Nature and Behavior of Mono- and Multi-Hydrogen Bonds, OH···π, CH···π, π···π, and Pn··X^+··Pn Interactions (X = H, F, Cl, Br, I; Pn = N, P, As, Sb) in Characteristic Systems, Elucidated with QTAIM Dual Functional Analysis

March 2024

Graduate School of Systems Engineering
Wakayama University

Taro Nishide

QTAIM2元関数解析法による特徴的な構造における単独および多重水素結合, OH···π, CH···π, π···πおよびPn··X^{+}··Pn (X = H, F, Cl, Br, I; Pn = N, P, As, Sb) 相互作用の特性と挙動解明

令和6年3月

和歌山大学大学院システム工学研究科

西出　太郎

Abstract

Inter- and intramolecular interactions are fundamental concepts in materials science. These interactions are closely associated with structural properties and stability, such as controlling molecular and crystal structures, creating novel materials, and stabilizing the duplex DNA structure using hydrogen bonds (HBs). Therefore, a methodology that can more effectively reveal the nature of such interactions must be established to develop materials science.

In this thesis, the author employs quantum theory of atoms-in-molecules dual functional analysis (QTAIM-DFA), a method with excellent potential for evaluating, classifying, characterizing, and understanding weak-to-strong interactions in a unified form. The QTAIM-DFA uncovers the dynamic and static behaviors of the interactions in question. The static behavior classifies the interactions, while the dynamic behavior characterizes them in detail. A method that can generate the perturbed structures is significant because the dynamic behavior must depend on them. Nakanishi and Hayashi proposed an innovative method to generate perturbed structures using coordinates derived from compliance force constants for internal vibrations (CIV), which are invariant to the choice of the coordinate system and minimize the effects of internal vibrations other than the interacting atoms under consideration. Accordingly, the QTAIM-DFA that applies the CIV elucidates the "intrinsic dynamic nature" of the interactions in question and characterizes them with high reliability.

Herein, the author aimed to establish and apply the QTAIM-DFA with CIV to various inter- and intramolecular interactions. The results are presented as follows:

1. The QTAIM-DFA with CIV effectively characterizes the nature of neutral intermolecular HBs, which are expected to have a wide range of interactions, such as van der Waals and charge transfer interactions (Chapter 3).
2. The nature of the intramolecular OH$\cdots\pi$ interactions in various π systems is elucidated to reveal the factors contributing to structural stabilization after comparing the stabilities of different conformations (Chapter 4).
3. A methodology to analyze each HB in multi-HB systems is established using acetic acid dimers and related species (Chapter 5). Subsequently, this methodology is applied to elucidate each HB in nucleobase pairs (Chapter 6).
4. The nature of Pn$\cdot\cdot$X$\cdot\cdot$Pn 3c–4e interactions (Pn = N, P, As, and Sb; X = H, F, Cl, Br, and I), which are formed in bicyclo[3.3.3] and [4.4.4] systems, is elucidated after clarifying the possibility of large X^+ atoms inside the cage (Chapter 7).
5. The dynamic and static behaviors of $\pi\cdots\pi$ interactions of each C atom in [*n*]helicenes (*n* = 4–12) are elucidated, revealing different trends of dynamic behaviors. Moreover, the nature of intermolecular interactions in [*n*]helicene dimers is clarified (Chapter 8).

The methodology elucidating the "intrinsic dynamic behavior" has been established and applied to different types of inter- and intramolecular interactions. Findings will help clarify the nature of similar inter- and intramolecular interactions for the development of various fields, such as molecular design with functionality and elucidation of biological phenomena.

概　要

分子間および分子内相互作用は物質科学において非常に重要な概念である．それらの性質は，物質の特性や構造と密接に関係している．その例は，結晶構造の配列制御および新奇な物性を有する分子設計，水素結合によって安定化されるDNA2重らせん構造など多く挙げられる．よって分子間および分子内相互作用特性の解明は物質科学の発展において非常に重要であり，それらを解明できる解析法の確立および適用範囲の拡大は不可欠である．

本論文では，量子化学計算および全相互作用を統一的に分類・評価できるquantum theory of atoms-in-molecules dual functional analysis (QTAIM2元関数解析法)を用いた．中西，林により提案されたQTAIM2元関数解析法は，着目原子間に生じる相互作用の静的および動的挙動を明らかにできる手法である．静的挙動は相互作用を分類するのに対し，動的挙動はより詳細に性質を評価できる．近年確立された摂動構造の作成法であるcoordinates derived from compliance force constants for internal vibrations (CIV法)は，他の内部座標由来の基準振動の影響を可能な限り削減した摂動構造を与える．よってCIV法を適用したQTAIM2元関数解析法により，着目原子間における「本質的な動的挙動」を明らかにできると期待される．

本論文ではCIV法を適用したQTAIM2元関数解析法によって，様々な分子間および分子内相互作用特性を明らかにできる解析法の適用範囲の拡大を目指した．以下に成果を示す．

1. 様々な中性種における分子間水素結合を対象とし，CIV法を適用したQTAIM2元関数解析法により広範な強さを持つ水素結合特性を解明し，その本質に迫ることができた (3章).
2. 分子内OH···π相互作用を形成すると期待される化合物において，様々な配座の安定性を比較した．化合物に生じる分子内OH···π相互作用を検出し，その特性を明らかにすることにより，構造の安定性との関係について解明した (4章).
3. 多重水素結合を形成する酢酸二量体およびその関連する化学種において，各水素結合を独立に評価・分類できる解析法を確立した (5章)．さらに複雑な多重水素結合を形成すると予測される核酸塩基対へ応用し，個々の水素結合の特性を解明した (6章).
4. 橋頭位をプニクトゲン(Pn)に置換したbicyclo[3.3.3]および[4.4.4]系において，分子内にプロトンおよびハロニウムイオン(X^+)が安定的に存在できる限界と構造特性を明らかにし，その安定化に寄与するPn··X··Pn相互作用の性質を解明した (7章).
5. [*n*]ヘリセン (*n* = 4–12)における微細構造の支配因子に寄与するπ···π相互作用の静的および動的挙動を炭素原子間単位で解明し，異なる動的挙動の傾向を見出した．さらに[*n*]ヘリセン二量体の安定化要因である分子間相互作用特性の解明も達成した (8章).

特徴的な構造下における様々な非結合相互作用において，静的挙動に加え「本質的な動的挙動」の解明および適用範囲の拡大を達成できた．この成果は，類似した分子間および分子内相互作用特性の解明に役立てられ，機能材料の分子設計や生体現象の解明など，多岐にわたる分野の発展に寄与できると期待される．

Contents

Chapter 1

General Introduction

The concept of chemical bonds is vital in materials science.[1] Materials consist of atoms connected through chemical bonds. Consequently, the nature of these chemical bonds must be closely related to material properties, encompassing structural features and stability.[2] Considerable efforts have been dedicated to elucidating the nature of chemical bonds and interactions.[3] Understanding chemical bonds and interactions requires effective methods to characterize their nature.[4] One such potent method is the quantum theory of the atoms-in-molecules (QTAIM) approach[5,6] introduced by Bader. This tool enables the analysis, characterization, and understanding of the nature of the considered inter- and intramolecular interactions. Recently, experimental chemists, not only theoretical chemists, have increasingly employed the QTAIM approach to clarify the nature of interactions.[7–11]

Furthermore, dynamic investigations of inter- and intramolecular interactions are performed to reveal the intrinsic strength between the interacting atoms involved based on the internal vibration, which minimizes the effects of other internal vibrations.[12] Considerable attention has been paid to the intrinsic strength of noncovalent interactions and classical covalent bonds.[12–14] However, characterizing the nature of interactions is challenging, although the concept of intrinsic strength is crucially useful.

Nakanishi et al. proposed and established QTAIM dual functional analysis (QTAIM-DFA),[15–19] which has excellent potential, for evaluating, classifying, characterizing, and understanding weak-to-strong interactions in a unified form, formulated based on the QTAIM approach. The QTAIM-DFA can elucidate the dynamic and static behaviors of the interactions in question. It has revealed the dynamic and static nature of various interactions, such as hydrogen bonds (HBs),[20] π···π interactions,[21] YX···π interactions (X = F, Cl, Br, and I; Y = F, Cl, Br, and I),[22] and hypervalent and extended-hypervalent bonds,[23,24] involving halogen and chalcogen atoms. Within the framework of QTAIM-DFA, perturbed structures are employed alongside optimized structures. The static behavior categorizes interactions into closed- and shared-shell natures, whereas the dynamic behavior presents a detailed characterization. The reliability of the dynamic behavior must depend on the quality of the perturbed structures. Therefore, the methods employed to generate perturbed structures are considerably significant within the context of QTAIM-DFA.

How are the perturbed structures generated? Three methods, namely, the partial optimization method (POM),[15–17] normal coordinates of internal vibrations (NIV),[18,19] and coordinates derived from compliance force constants for internal vibrations (CIV),[25] have been developed. First, the POM has been proposed to generate perturbed structures by optimizing structures in which the length between the interacting atoms in question is fixed. However, applying the POM to larger molecules

is challenging because the cost performance in the calculation is relatively poor. Second, the NIV method has been proposed to generate perturbed structures by employing the normal coordinates of internal vibrations that are most suitable for the interaction. The NIV overcomes the limitations of the POM because partial optimization processes are not required. However, the dynamic behavior elucidated by the QTAIM-DFA with NIV is always influenced by internal vibrations effects other than the interacting atoms in question, although this effect is usually small except in some cases.[18,19]

The third method, CIV, has been proposed to resolve NIV difficulty.[25] In CIV, the perturbed structures are generated using the internal vibration corresponding to compliance force constants (C_{ii}), calculated using the Compliance 3.0.2 program released by Grunenberg and Brandhorst.[26–28] The internal vibration corresponding to C_{ii} minimizes the effects of other internal vibrations. Therefore, C_{ii} (unit: Å mdyn^{-1}) indicates intrinsic flexibility between the interacting atoms in question. The dynamic behaviors elucidated by the QTAIM-DFA with CIV are the same as those with POM in terms of calculation errors.[25] Therefore, the CIV is anticipated to offer excellent applicability for generating the perturbed structures because of its invariance to the choice of the coordinate system and the lack of a need for partial optimization processes. However, the QTAIM-DFA with CIV was applied only to typical interactions in standard species.[25] The QTAIM-DFA with CIV must be established and applied to different inter- and intramolecular interactions. Therefore, the author aimed to elucidate the nature of various type of the inter- and intramolecular interactions by the QTAIM-DFA with CIV, which is expected to be high applicable to complex interactions in characteristic systems, such as multi-HBs, sterically compressed compounds, and helical molecules.

Chapter 2 presents the methodological details of the QTAIM-DFA, the methods generating the perturbed structures and their features, the basic concept of the QTAIM approach, and the results of typical interactions containing the fifth-period elements.

This thesis presents the intrinsic dynamic and static nature of different inter- and intramolecular interactions, elucidated by the QTAIM-DFA with CIV, in addition to the establishment and applications in Chapters 3–8. The chapters are introduced next.

As a first step, Chapter 3 elucidates the intrinsic dynamic and static nature of neutral HBs (Scheme 1-1) using the QTAIM-DFA with CIV and demonstrates the high applicability of CIV. HBs are crucial in various fields because of their ability to form molecular associations, which are caused by stabilization through 3c–4e interactions.[29–34] Neutral HBs are expected to have various interactions owing to a wide range of interaction energies (≤ 40 kJ mol^{-1}).[1,20,30–33] Accordingly, it was challenging

B---HY (**1-*n*** (*n* = 1–29)) 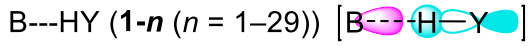

B = H_2Se, H_2S, H_2O, H_2CO, H_3N, and HX (X = I, Br, Cl, and F)
Y = SeH, SH, OH, NH_2, I, Br, Cl, and F

Scheme 1-1. Species of neutral HBs forming an asymmetric B···H–Y of σ(3c–4e) bond.

to characterize the nature of HBs spanning from van der Waals (vdW) to classical covalent interactions. In a previous study, the characteristics of neutral and charged HBs were elucidated using the QTAIM-DFA with POM and NIV.[20] The QTAIM-DFA with POM and NIV is well-suited to elucidate the nature of several HBs, which are characterized by vdW to trigonal bipyramidal adducts through charge transfer (CT) natures for neutral HBs and classical covalent interactions for charged HBs. However, the QTAIM-DFA with CIV has just been established. Therefore, it has few applications.[25] Can the QTAIM-DFA with CIV elucidate the nature of HBs, similar to the case with POM and NIV? It is inevitable to examine the applicability of the QTAIM-DFA with CIV by employing various neutral HBs (**1-1**–**1-29**), as shown in Scheme 1-1.

Intramolecular HBs are as fundamental as their intermolecular counterparts.[31,34,35] Notably, intramolecular HBs are sterically compressed compared to intermolecular HBs. The QTAIM-DFA with NIV elucidates the dynamic and static nature of the intermolecular HBs formed between EH_2 (E = O, S, Se, and Te) and π systems for benzene,[36] naphthalene,[37] and anthracene.[38] However, the dynamic and static characteristics of intramolecular HBs have not been elucidated using the QTAIM-DFA. How can the perturbed structures be generated to elucidate the dynamic behavior? It seems complicated for intramolecular interactions to generate perturbed structures because of the steric hindrance. The CIV appears well-suitable for intramolecular interactions because the perturbed structures are generated by minimizing the effects of the internal vibrations other than the interacting atoms in question. Consequently, it is challenging to elucidate the intrinsic dynamic and static behavior of various OH···π interactions for **1-30**–**1-44** (Scheme 1-2) using the QTAIM-DFA with CIV presented in Chapter 4.

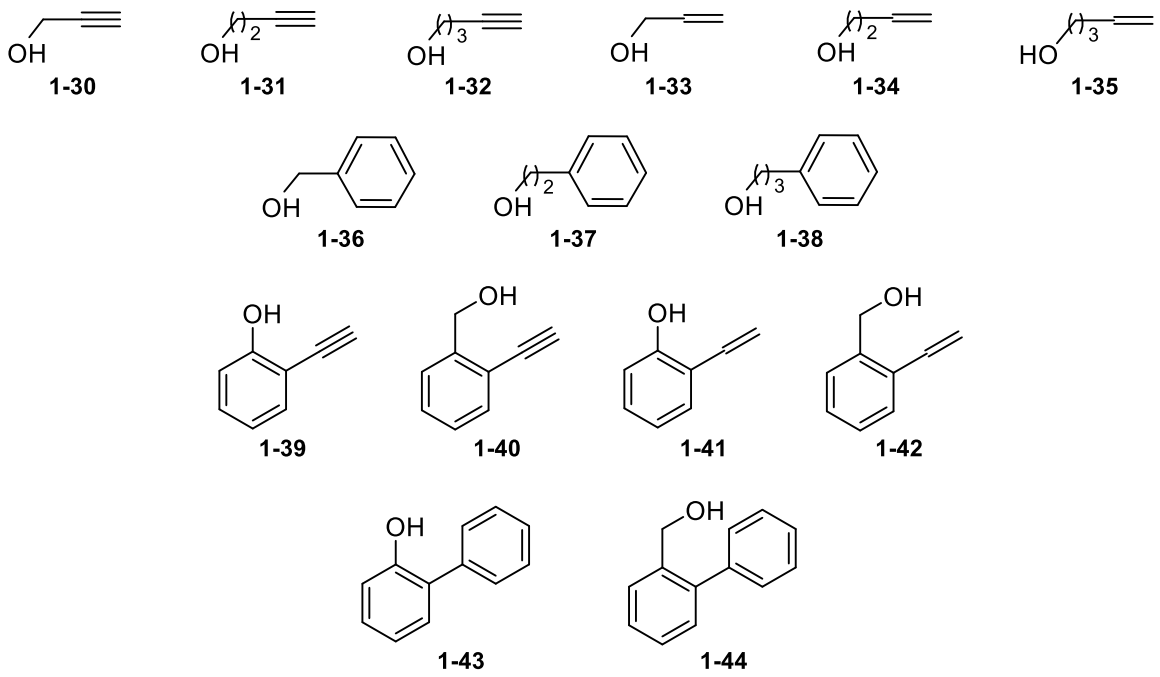

Scheme 1-2. Species to examine the various OH···π intramolecular interactions, which are expected to form with π systems for ethynyl, vinyl, and phenyl groups.

Subsequently, the author focused on multi-HB systems in which multi-HBs are formed in close proximity in space. Multi-HBs in the duplex DNA structure are a typical case.[39–41] It is inevitable to establish a methodology to elucidate the dynamic and static nature of each HB in a multi-HB system. Consequently, the QTAIM-DFA with CIV is suitable for generating perturbed structures. The multi-HBs will interact mutually and strongly. Acetic acid dimer (**1-45**), acetamide dimer (**1-46a**), and acetic acid-acetamide mixed dimer (**1-47**) would provide such a multi-HB system, together with the thio- and seleno-derivatives of **1-46a** (**1-46b** and **1-46c**, respectively). Scheme 1-3a illustrates the dimers, **1-45**–**1-47**. Furthermore, Chapter 5 elucidates the intrinsic dynamic and static nature of each HB formed in **1-45**–**1-47**, as well as the establishment of the methodology.

The natures of HBs in **1-45**$_{iso}$–**1-47**$_{isoC}$ (Scheme 1-3b) are also clarified for convenience of comparison with those of **1-45**–**1-47**. Notably, **1-45**$_{iso}$, **1-46a**$_{iso}$, **1-46b**$_{iso}$, and **1-46c**$_{iso}$ are isomers of **1-45**, **1-46a**, **1-46b**, and **1-46c**, respectively, whereas **1-47**$_{isoA}$–**1-47**$_{isoC}$ correspond to those of **1-47**. The factor contributing to the stabilization of **1-45**$_{iso}$–**1-47**$_{isoC}$ would mainly be single-HBs. The effects of stabilization through multi-HBs are expected to be well-revealed by comparing them with single-HBs.

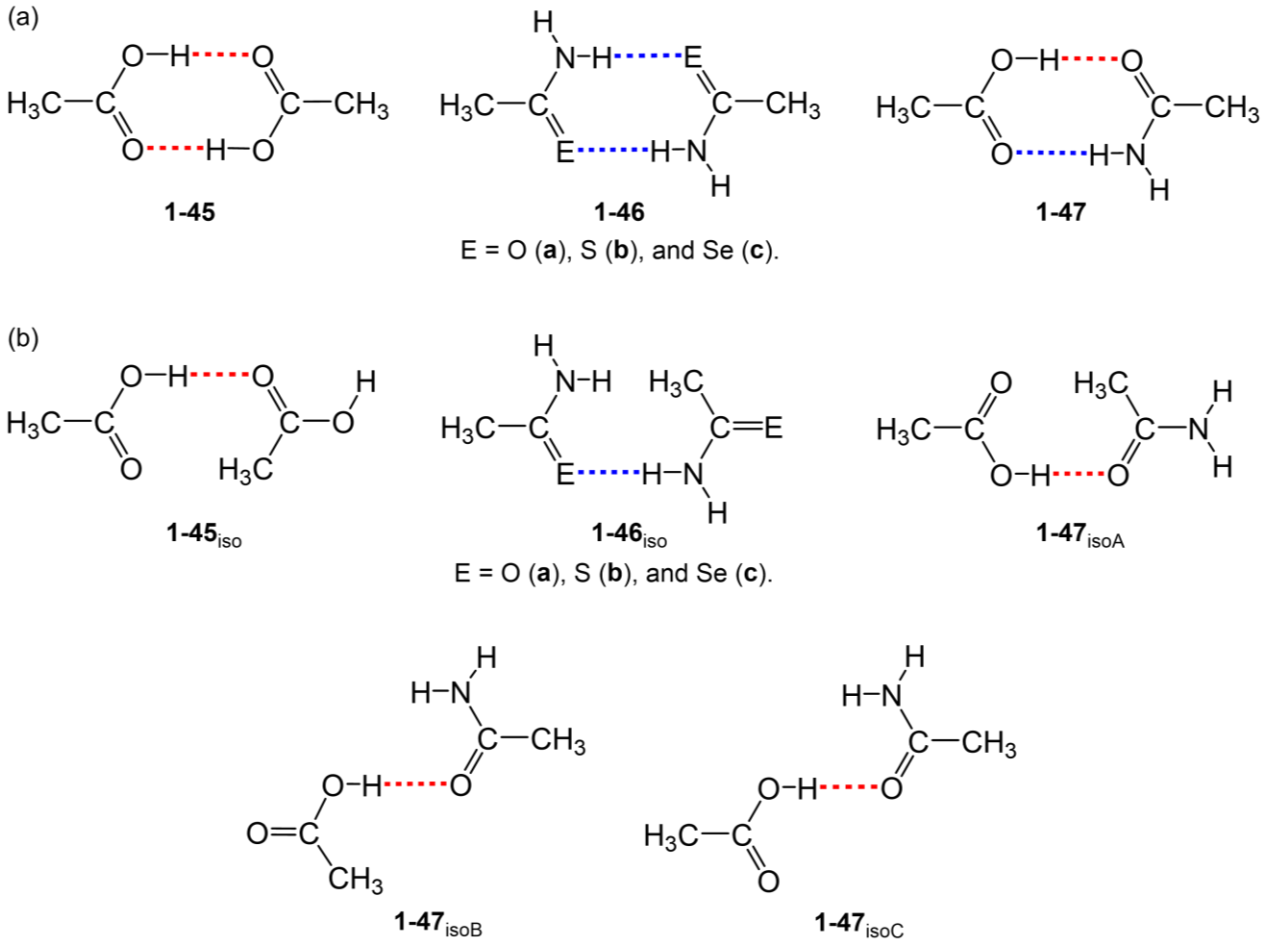

Scheme 1-3. Dimers of acetic acid (**1-45**) and related species (**1-46** and **1-47**) (a) and those isomers (**1-45**$_{iso}$, **1-46**$_{iso}$, **1-47**$_{isoA}$, **1-47**$_{isoB}$, and **1-47**$_{isoC}$) (b).

Chapter 6 presents an application of the QTAIM-DFA with CIV to intermolecular HBs in nucleobase pairs (Scheme 1-4), which are expected to be more complex than acetic acid dimer and related species. The duplex DNA structure is stabilized using multi HBs in adenine-thymine (A-T) and guanine-cytosine (G-C) pairs, together with π···π interactions.[39–41] In addition, these multi HBs are associated with replication of the duplex DNA structure at approximately room temperature, which first opens and then closes.[42] Therefore, understanding the dynamic and static nature of HBs in nucleobase pairs is significant. The dynamic behavior can be closely related to the initial stage of the opening and closing of the duplex DNA, although it is limited to the nucleobase-pairs moiety. The QTAIM-DFA with CIV would be suited to elucidate the intrinsic and static nature of multi HBs in nucleobase pairs because the high applicability of CIV to multi HBs is demonstrated by employing the acetic acid dimers and related species in Chapter 5. The relationships between each C_{ii} in multi HBs and the stabilization energies are also revealed.

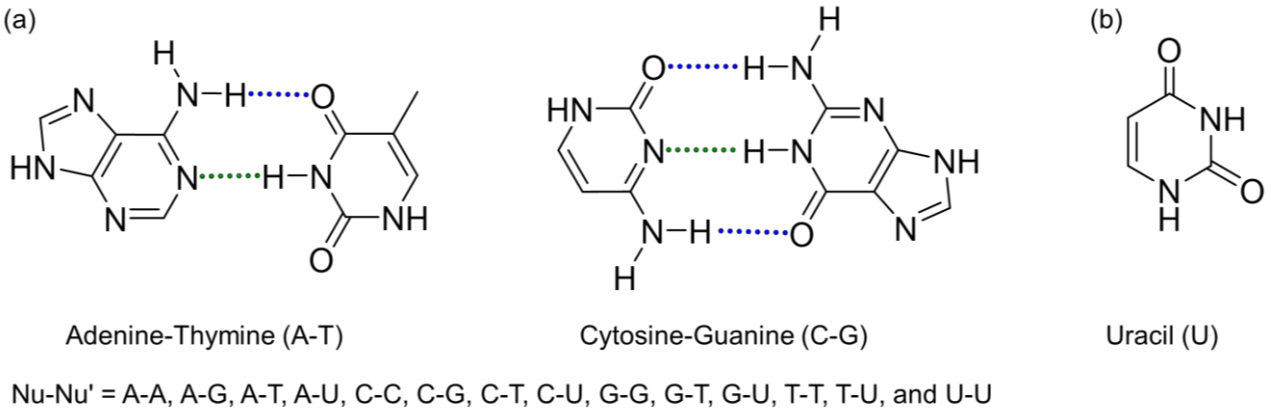

Scheme 1-4. Nucleobase pairs (Nu-Nu') for A-T, C-G, and other pairs (a), together with uracil (b).

In Chapter 7, the dynamic and static natures of $[^{A}Pn\cdot\cdot X\cdot\cdot{}^{B}Pn]^{+}$ in bicyclo[3.3.3] and [4.4.4] systems are elucidated using the QTAIM-DFA with CIV after clarifying the possibility of large X^{+} atoms inside the cage and the structural features. In addition, the stability between symmetric and nonsymmetric shapes is examined. The nature of charged HBs, such as $[H_3N\cdot\cdot H\cdot\cdot NH_3]^{+}$ and $[H_2O\cdot\cdot H\cdot\cdot OH_2]^{+}$, has been previously elucidated using the QTAIM-DFA with POM and NIV,[20] although the QTAIM-DFA with CIV has not been applied to charged HBs. Therefore, applying the QTAIM-DFA with CIV to charged HBs as well as neutral HBs is essential. Concerning the species that should be targeted to clarify the nature of charged HBs, the author focused on the nature of $[^{A}Pn\cdot\cdot X\cdot\cdot{}^{B}Pn]^{+}$ (^{A}Pn = ^{B}Pn = N, P, As, Sb; X = H, F, Cl, Br, and I) interactions in **1-48a**$^{+}$–**1-55e**$^{+}$ (Scheme 1-5), which are sterically compressed in medium cage structures. Alder et al. synthesized **1-48** and **1-53**.[43,44] Notably, **1-53** can contain a proton in the cage and form a compressed $[N\cdot\cdot H\cdot\cdot N]^{+}$

interaction.[45] Alder et al. mentioned that **1-48** protonated inside the cage might be kinetically persistent if formed, although **1-48** protonated to the N atom outside the cage.[46] Recently, a molecular design to form $[N\cdots F–N]^+$ halogen bonds has been theoretically proposed by employing the skeletons of **1-48** and **1-53**,[47] which are expected to be good candidates for forming strong $[N\cdot\cdot X\cdot\cdot N]^+$ bonds. Therefore, clarifying the possibility of small-to-large atoms in **1-48**–**1-55** and the nature of $[^{A}Pn\cdot\cdot X\cdot\cdot{}^{B}Pn]^+$ interactions will provide fundamental insights into designing molecules with high functionality and containing X^+.

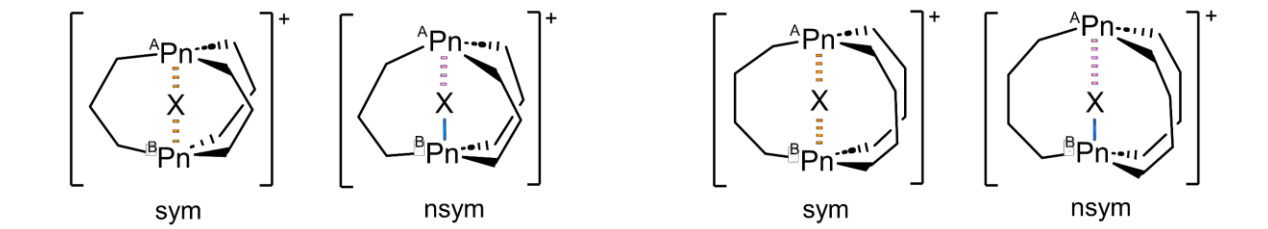

$^{A/B}Pn$ =
N (**1-48*x***$^+$), P (**1-49*x***$^+$), As (**1-50*x***$^+$), and Sb (**1-51*x***$^+$).

$^{A/B}Pn$ =
N (**1-52*x***$^+$), P (**1-53*x***$^+$), As (**1-54*x***$^+$), and Sb (**1-55*x***$^+$).

X = H (***x*** = **a**), F (**b**), Cl (**c**), Br (**d**), and I (**e**).

Scheme 1-5. Species **1-48a**$^+$–**1-55e**$^+$ and the definition of the symmetric (sym) and nonsymmetric (nsym) shapes.

Finally, Chapter 8 highlights the applications of QTAIM-DFA with CIV to the π···π interactions in [*n*]helicenes (*n* = 1–12) and the intermolecular interactions in helicene dimers, as shown in Schemes 1-6a and b, respectively. The fine structures of helicenes are primarily anticipated to be determined by the balance between the repulsion forces of adjacent aromatic rings and stabilization contributed by π···π interactions. Therefore, understanding the nature of π···π interactions between C atoms, detected by separating bay and cape areas, offers valuable insights into the structural features of helicenes and related species. The π···π interactions are expected to form for $n \geq 7$ because the aromatic rings (filled in green in Scheme 1-6c) are adjacent along the helical axis. For [12]helicene, all aromatic rings are adjacent, as shown in Scheme 1-6c. Consequently, more complex π···π interactions will form as *n* increases from 7 to 12.

The detection and characterization of the intermolecular interactions of helicene dimers yield valuable insights into the self-assembly phenomena. It is challenging to elucidate the intrinsic dynamic and static nature of each π···π interaction and intermolecular interaction, which are expected to be more complex with larger helicenes.

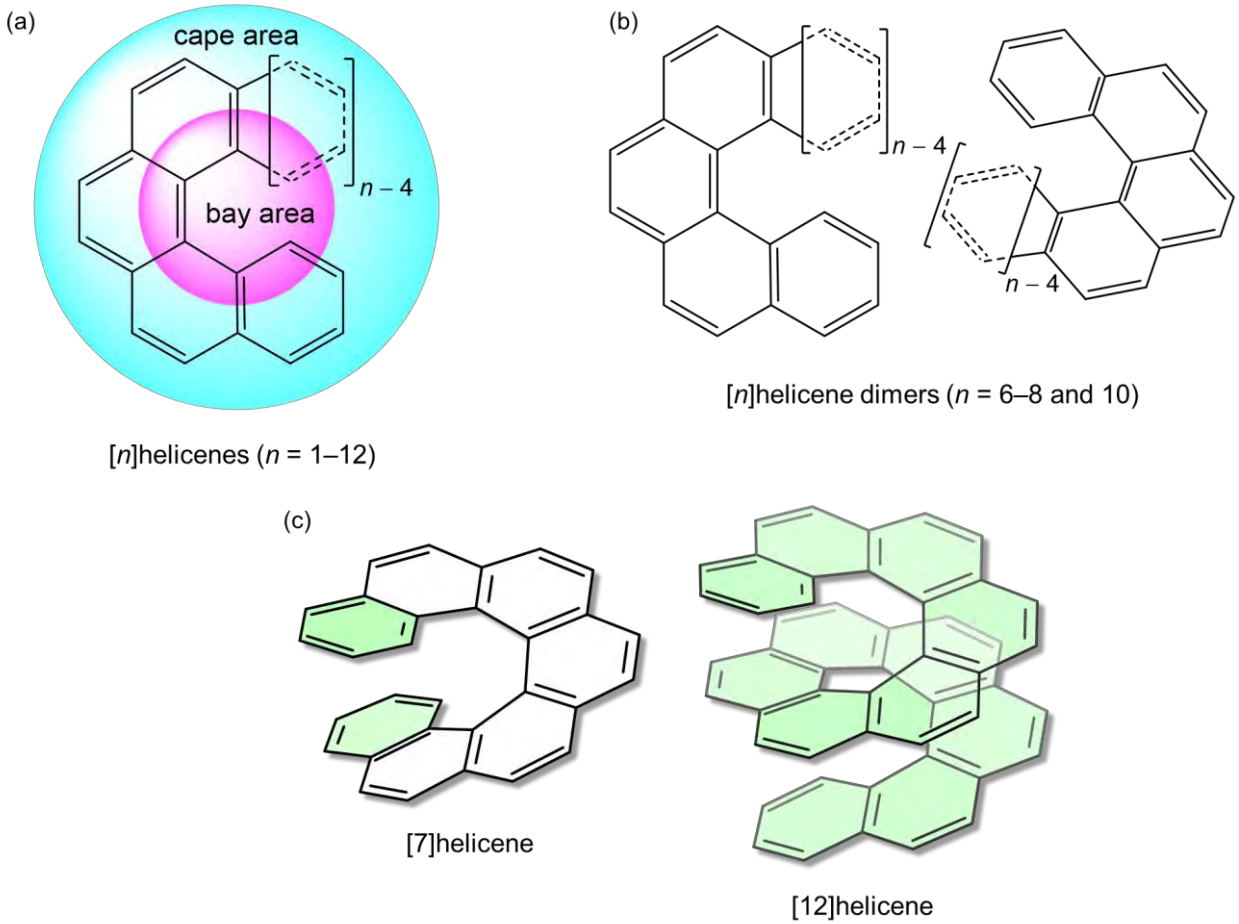

Scheme 1-6. [*n*]Helicenes and definition of bay and cape areas (a) and [*n*]helicene dimers (b), together with adjacent aromatic rings filled in green, exemplified by [7]helicene and [12]helicene (c). Benzene, naphthalene, and phenanthrene are defined corresponding to $n = 1$, 2, and 3, respectively.

Appendix

Abbreviated Words

QTAIM-DFA	Quantum theory of atoms-in-molecules dual functional analysis
POM	Partial optimization method
NIV	Normal coordinates of internal vibrations
CIV	Coordinates derived from compliance force constants for internal vibrations
C_{ii}	Compliance force constants (unit: Å $mdyn^{-1}$)
BCP	Bond critical point (denoted by asterisk: ∗)
RCP	Ring critical point
CCP	Cage critical point
BP	Bond path (denoted by A-∗-B for an interaction between A and B, together with the BCP (∗))
$\rho_b(\boldsymbol{r}_c)$	Charge densities at BCPs
$\nabla^2\rho_b(\boldsymbol{r}_c)$	Laplacian $\rho_b(\boldsymbol{r}_c)$, which is the second derivative of $\rho_b(\boldsymbol{r}_c)$
$H_b(\boldsymbol{r}_c)$	Total electron densities at BCPs
$G_b(\boldsymbol{r}_c)$	Kinetic energy densities at BCPs
$V_b(\boldsymbol{r}_c)$	Potential energy densities at BCPs
SS interaction	Shared-shell interaction ($\nabla^2\rho_b(\boldsymbol{r}_c) < 0$)
CS interaction	Closed-shell interaction ($\nabla^2\rho_b(\boldsymbol{r}_c) > 0$)
Pure CS (*p*-CS)	CS interaction for $H_b(\boldsymbol{r}_c) > 0$
Regular CS (*r*-CS)	CS interaction for $\nabla^2\rho_b(\boldsymbol{r}_c) > 0$ and $H_b(\boldsymbol{r}_c) < 0$
vdW	van der Waals interactions
HB	Hydrogen bond
t-HB_{nc}	Typical hydrogen bond with no covalency
t-HB_{wc}	Typical hydrogen bond with covalency
CT-MC	Molecular complexes through charge transfer (CT)
X_3^-	Trihalide ions
CT-TBP	Trigonal bipyramidal adducts through CT
Cov-w	Classical covalent interactions for weak cases
Cov-s	Classical covalent interactions for strong cases
3c–4e bonds	Three center–four electron bonds

References and Notes

1. L. Pauling, *The Nature of the Chemical Bond*, Cornell University Press, Ithaca, NY, **1960**.
2. A. S. Mahadevi, G. N. Sastry, *Chem. Rev.* **2016**, *116*, 2775–2825.
3. E. Pastorczak, C. Corminboeuf, *J. Chem. Phys.* **2017**, *146*, 120901.
4. N. Kumar, S. Saha, G. N. Sastry, *Phys. Chem. Chem. Phys.* **2021**, *23*, 8478–8488.
5. R. F. W. Bader, *Atoms in Molecules. A Quantum Theory*; Oxford University Press, Oxford, UK, **1990**.
6. C. F. Matta, R. J. Boyd, *An Introduction to the Quantum Theory of Atoms in Molecules* in *The Quantum Theory of Atoms in Molecules: From Solid State to DNA and Drug Design* (Eds.: C. F. Matta, R. J. Boyd), WILEY-VCH: Weinheim, Germany, **2007**, Ch. 1.
7. R. Mir, T. Dudding, *J. Org. Chem.* **2018**, *83*, 4384–4388.
8. M. Ciechańska, A. Jóźwiak, R. B. Nazarski, E. A. Skorupska, *J. Org. Chem.* **2019**, *84*, 11425–11440.
9. R. J. Somerville, A. M. Borys, M. Perez-Jimenez, A. Nova, D. Balcells, L. A. Malaspina, S. Grabowsky, E. Carmona, E. Hevia, J. Campos, *Chem. Sci.* **2022**, *13*, 5268–5276.
10. R. D. Alharthy, I. Urooj, M. Tasleem, M. Khalid, M. A. Asghar, S. I. Khan, M. Ajmal, N. Ahmed, Z. Shafiq, *RSC Adv.* **2023**, *13*, 15208–15221.
11. S. Rekha Boruah, M. Bhattacharjee, R. N. Dutta Purkayastha, S. Modak, T. Aktar, D. Maiti, L. Sieroń, W. Maniukiewicz, R. M. Gomila, A. Frontera, *ChemistrySelect* **2023**, *8*, e202204937.
12. E. Kraka, W. Zou, Y. Tao, *Wiley Interdiscip. Rev. Comput. Mol. Sci.* **2020**, *10*, e1480.
13. J. Grunenberg, *J. Am. Chem. Soc.* **2004**, *126*, 16310–16311.
14. J. Grunenberg, *Chem. A Eur. J.* **2016**, *22*, 18678–18681.
15. W. Nakanishi, S. Hayashi, K. Narahara, *J. Phys. Chem. A* **2008**, *112*, 13593–13599.
16. W. Nakanishi, S. Hayashi, K. Narahara, *J. Phys. Chem. A* **2009**, *113*, 10050–10057.
17. W. Nakanishi, S. Hayashi, *Curr. Org. Chem*. **2010**, *14*, 181–197.
18. W. Nakanishi, S. Hayashi, *J. Phys. Chem. A* **2010**, *114*, 7423–7430.
19. W. Nakanishi, S. Hayashi, K. Matsuiwa, M. Kitamoto, *Bull. Chem. Soc. Jpn*. **2012**, *85*, 1293–1305.
20. S. Hayashi, K. Matsuiwa, M. Kitamoto, W. Nakanishi, *J. Phys. Chem. A* **2013**, *117*, 1804–1816.
21. K. Matsuiwa, S. Hayashi, W. Nakanishi, *ChemistrySelect* **2017**, *2*, 1774–1782.
22. S. Hayashi, T. Kato, Y. Sugibayashi, W. Nakanishi, *Molecules* **2023**, *28*, 4219.
23. S. Hayashi, T. Nishide, W. Nakanishi, *Bioinorg. Chem. Appl.* **2020**, 2901439.
24. Y. Tsubomoto, S. Hayashi, W. Nakanishi, L. K. Mapp, S. J. Coles, *RSC Adv.* **2018**, *8*, 9651–9660.
25. W. Nakanishi, S. Hayashi, *Int. J. Quantum Chem.* **2018**, *118*, e25590.
26. K. Brandhorst, J. Grunenberg, *Chem. Soc. Rev.* **2008**, *37*, 1558–1567.
27. K. Brandhorst, J. Grunenberg, *J. Chem. Phys*. **2010**, *132*, 184101.
28. Compliance 3.0.2 program is available online: http://www.oc.tu-s.de/Grunenberg/compliance.html (accessed on 27 September 2023).
29. G. C. Pimentel, A. L. McClellan, *The Hydrogen Bond*, W. H. Freeman, San Francisco, CA, **1960**.

30. P. Schuster, G. Zundel, C. Sandorfy, *The Hydrogen Bond, Recent Developments in Theory and Experiments* (Eds.: P. Schuster, G. Zundel, C. Sandorfy), North-Holland Publishing Company, Amsterdam, **1976**.
31. G. A. Jeffrey, *An Introduction to Hydrogen Bonding*, Oxford University Press, New York, **1997**.
32. S. Scheiner, *Hydrogen Bonding, A Theoretical Perspective*, Oxford University Press, Oxford, **1997**.
33. G. R. Desiraju, T. Steiner, *The Weak Hydrogen Bond in Structural Chemistry and Biology*, International Union of Crystallography Monographs on Crystallography, Oxford University Press, New York, **1999**.
34. S. J. Grabowski, *Hydrogen Bonding – New Insights* (Ed.: S. J. Grabowski), Springer, The Netherlands, **2006**.
35. K.-L. Han, G.-J. Zhao, *Hydrogen Bonding and Transfer in the Excited State*, Wiley, Chichester, UK, **2010**.
36. Y. Sugibayashi, S. Hayashi, W. Nakanishi, *Phys. Chem. Chem. Phys.* **2016**, *18*, 9948–9960.
37. S. Hayashi, Y. Sugibayashi, W. Nakanishi, *RSC Adv.* **2016**, *6*, 49651–49660.
38. S. Hayashi, Y. Sugibayashi, W. Nakanishi, *RSC Adv.*,**2017**, *7*, 31858–31865.
39. F. H. C. Crick, *J. Mol. Biol.* **1968**, *38*, 367–379.
40. J. D. Watson, F. H. C. Crick, *Nature* **1953**, *171*, 737–738.
41. W. Saenger, *Principles of Nucleic Acid Structures*, *Springer*, Berlin, **1984**.
42. X. Wang, A. R. Chandrasekaran, Z. Shen, Y. P. Ohayon, T. Wang, M. E. Kizer, R. Sha, C. Mao, H. Yan, X. Zhang, S. Liao, B. Ding, B. Chakraborty, N. Jonoska, D. Niu, H. Gu, J. Chao, X. Gao, Y. Li, T. Ciengshin, N. C. Seeman, *Chem. Rev.* **2019**, *119*, 6273–6289; J.-L. Mergny, D. Sen, *Chem. Rev.* **2019**, *119*, 6290–6325; F. C. Simmel, B. Yurke, H. R. Singh, *Chem. Rev.* **2019**, *119*, 6326–6369; S. S. Wang, A. D. Ellington, *Chem. Rev.* **2019**, *119*, 6370–6383; M. Madsen, K. V. Gothelf, *Chem. Rev.* **2019**, *119*, 6384–6458.
43. R. W. Alder, R. B. Sessions, J. M. Mellor, M. F. Rawlins, *J. Chem. Soc. Chem. Commun.* **1977**, 747–748.
44. R. W. Alder, R. B. Sessions, *J. Am. Chem. Soc.* **1979**, *101*, 3651–3652.
45. R. W. Alder, A. G. Orpen, R. B. Sessions, *J. Chem. Soc. Chem. Commun.* **1983**, 999–1000.
46. R. W. Alder, R. E. Moss, R. B. Sessions, *J. Chem. Soc. Chem. Commun.* **1983**, 997–998.
47. S. A. Harry, S. Vemulapalli, T. Dudding, T. Lectka, *J. Org. Chem.* **2022**, *87*, 8413–8419.

Chapter 2

Methodological Details of Quantum Theory of Atoms-in-Molecules Dual Functional Analysis (QTAIM-DFA)

QTAIM Approach

The QTAIM approach, proposed by Bader, enables to analyze the nature of chemical bonds and interactions.[1,2] In QTAIM approach, the bond critical point (BCP: ∗[3]) is an important concept. The BCP is a point along the interatomic bond path at the interatomic surface where the charge density $\rho(\boldsymbol{r})$ reaches a minimum, while its maximum is on the interatomic surface separating the atomic basins. Figure 2-1 shows molecular graph with contour map, exemplified by Cl-∗-Cl, and three-dimensional saddle point of $\rho(\boldsymbol{r})$ illustrated as a model of a BCP. The first derivative of $\rho(\boldsymbol{r})$ at BCP is zero for each direction of x, y, and z ($\partial\rho_b(\boldsymbol{r}_c)/\partial r_i = 0$ for $r_i = x$, y, and z), where the $\rho(\boldsymbol{r})$ at BCP is denoted by $\rho_b(\boldsymbol{r}_c)$ (Figure 2-1a). The behavior of $\rho(\boldsymbol{r})$ around BCP can be understood by the image of the three-dimensional saddle point (Figure 2-1b). The sign of the second derivative of $\rho_b(\boldsymbol{r}_c)$ is positive in the bond direction ($\partial^2\rho_b(\boldsymbol{r}_c)/\partial z^2 > 0$, where the z is defined as the bond direction) and negative for the x- and y-directions perpendicular to z direction ($\partial^2\rho_b(\boldsymbol{r}_c)/\partial x^2 < 0$ and $\partial^2\rho_b(\boldsymbol{r}_c)/\partial y^2 < 0$). Therefore, at around BCP, the $\rho(\boldsymbol{r})$ is minimum in the z-direction and maximum in the x- and y-directions perpendicular to z one. The $\rho_b(\boldsymbol{r}_c)$ is strongly related to the binding energies[4–12] and bond orders.[1]

The sign of the Laplacian $\rho_b(\boldsymbol{r}_c)$ ($\nabla^2\rho_b(\boldsymbol{r}_c) = \partial^2\rho_b(\boldsymbol{r}_c)/\partial x^2 + \partial^2\rho_b(\boldsymbol{r}_c)/\partial y^2 + \partial^2\rho_b(\boldsymbol{r}_c)/\partial z^2$) indicates that $\rho_b(\boldsymbol{r}_c)$ is depleted or concentrated with respect to its surrounding, since $\nabla^2\rho_b(\boldsymbol{r}_c)$ is the second derivative of $\rho_b(\boldsymbol{r}_c)$. $\rho_b(\boldsymbol{r}_c)$ is locally depleted relative to the average distribution around $\boldsymbol{r}_c$ if $\nabla^2\rho_b(\boldsymbol{r}_c) > 0$, but it is concentrated when $\nabla^2\rho_b(\boldsymbol{r}_c) < 0$. Total electron energy densities at BCPs ($H_b(\boldsymbol{r}_c)$) must be a more appropriate measure for weak interactions on the energy basis.[1,2,11,13–29] $H_b(\boldsymbol{r}_c)$ are the sum

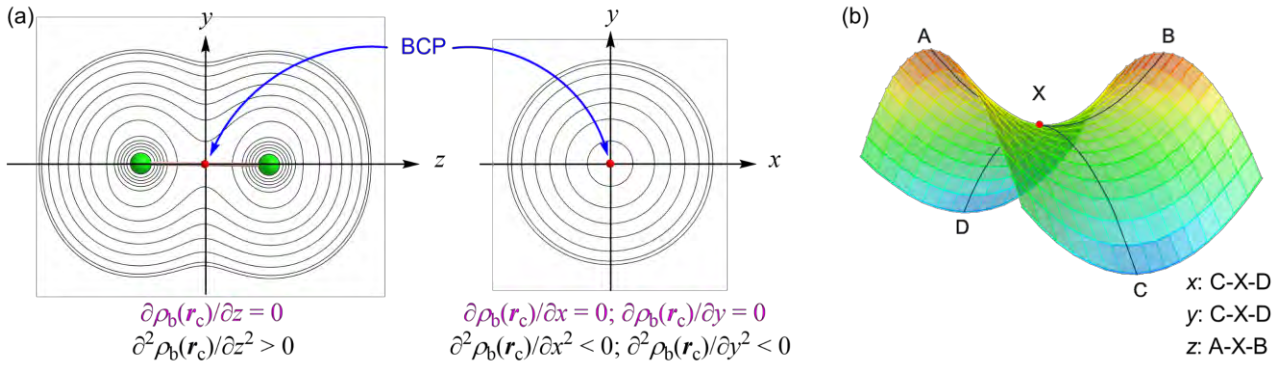

Figure 2-1. Molecular graph with contour plot of $\rho(\boldsymbol{r})$ of Cl-∗-Cl (a), three-dimensional saddle point of $\rho(\boldsymbol{r})$ illustrated as a model of BCP (b), BCPs and BPs are denoted by red dots and pink line, respectively, together with chlorine atoms are in light green.

of kinetic energy densities ($G_b(\boldsymbol{r}_c)$) and potential energy densities ($V_b(\boldsymbol{r}_c)$) at BCPs, as shown in Equation (2-1). Electrons at BCPs are stabilized when $H_b(\boldsymbol{r}_c) < 0$; therefore, interactions exhibit the covalent nature in this region, whereas they exhibit no covalency if $H_b(\boldsymbol{r}_c) > 0$, due to the destabilization of electrons at BCPs under the conditions.[1,2] Equation (2-2) represents the relation between $\nabla^2\rho_b(\boldsymbol{r}_c)$ and $H_b(\boldsymbol{r}_c)$, together with $G_b(\boldsymbol{r}_c)$ and $V_b(\boldsymbol{r}_c)$ (Equation (2-3)), which is closely related to the virial theorem.

$$H_b(\boldsymbol{r}_c) = G_b(\boldsymbol{r}_c) + V_b(\boldsymbol{r}_c) \quad (2\text{-}1)$$

$$(\hbar^2/8m)\nabla^2\rho_b(\boldsymbol{r}_c) = H_b(\boldsymbol{r}_c) - V_b(\boldsymbol{r}_c)/2 \quad (2\text{-}2)$$

$$= G_b(\boldsymbol{r}_c) + V_b(\boldsymbol{r}_c)/2 \quad (2\text{-}3)$$

Chemical bonds and interactions are classified by the signs of $\nabla^2\rho_b(\boldsymbol{r}_c)$ and $H_b(\boldsymbol{r}_c)$. They are called shared shell (SS) interactions when $\nabla^2\rho_b(\boldsymbol{r}_c) < 0$ and closed-shell (CS) interactions when $\nabla^2\rho_b(\boldsymbol{r}_c) > 0$. The CS interactions are especially called *pure* CS (*p*-CS) interactions for $H_b(\boldsymbol{r}_c) > 0$ and $\nabla^2\rho_b(\boldsymbol{r}_c) > 0$, since electrons at BCPs are depleted and destabilized under the conditions.[1] Electrons in the intermediate region between SS and *p*-CS, which belong to CS, are locally depleted but stabilized at BCPs, since $\nabla^2\rho_b(\boldsymbol{r}_c) > 0$ but $H_b(\boldsymbol{r}_c) < 0$.[1] Nakanishi et al. proposed to call the interactions of $H_b(\boldsymbol{r}_c) < 0$ and $\nabla^2\rho_b(\boldsymbol{r}_c) > 0$ *regular* CS (*r*-CS) interactions, which clearly distinguish these interactions from the *p*-CS interactions.[22–24] The sign of $\nabla^2\rho_b(\boldsymbol{r}_c)$ can be replaced by those of $H_b(\boldsymbol{r}_c) - V_b(\boldsymbol{r}_c)/2$ because $(\hbar^2/8m)\nabla^2\rho_b(\boldsymbol{r}_c) = H_b(\boldsymbol{r}_c) - V_b(\boldsymbol{r}_c)/2$ (see Equation (2-2)). While $H_b(\boldsymbol{r}_c) - V_b(\boldsymbol{r}_c)/2 = 0$ corresponds to the borderline between the classic covalent bonds (Cov) of SS and the noncovalent interactions of CS, $H_b(\boldsymbol{r}_c) = 0$ appears to be buried in the CS interactions. Scheme 2-1 summarizes the classification based on the signs of $\nabla^2\rho_b(\boldsymbol{r}_c)$ and $H_b(\boldsymbol{r}_c)$, together with $G_b(\boldsymbol{r}_c)$ and $V_b(\boldsymbol{r}_c)$. Consequently, it is difficult to characterize the CS interactions of van der Waals (vdW) type, typical hydrogen bonds (*t*-HBs) with no covalency (*t*-HB$_{nc}$), *t*-HBs with covalency (*t*-HB$_{wc}$), molecular complexes formed through charge transfer (CT-MCs), trihalide ions (X_3^-), and trigonal bipyramidal adducts formed through CT (CT-TBPs), if analyzed based on the signs of $H_b(\boldsymbol{r}_c) - V_b(\boldsymbol{r}_c)/2$ and/or $H_b(\boldsymbol{r}_c)$.

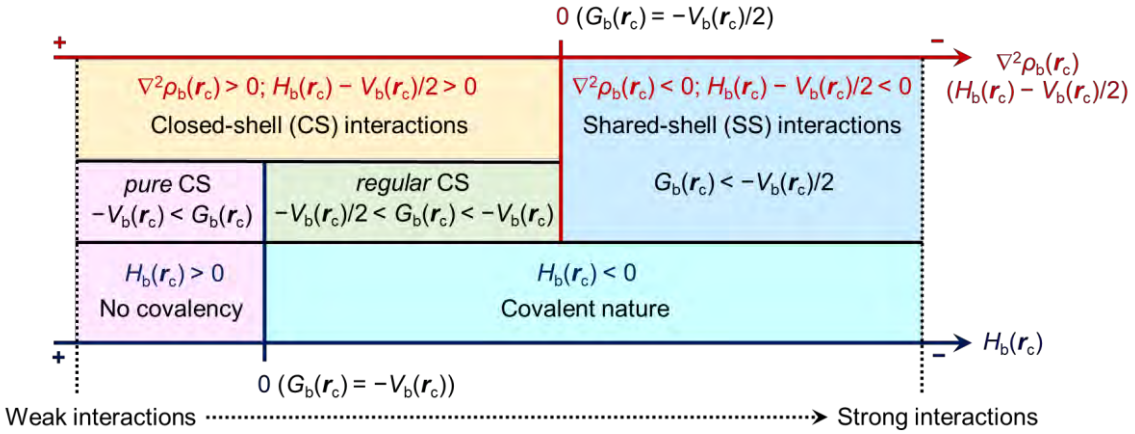

Scheme 2-1. Classification of interactions by the signs of $\nabla^2\rho_b(\boldsymbol{r}_c)$ and $H_b(\boldsymbol{r}_c)$, together with $G_b(\boldsymbol{r}_c)$ and $V_b(\boldsymbol{r}_c)$ according to Equations (2-1)–(2-3).

QTAIM Dual Functional Analysis (QTAIM-DFA)

QTAIM-DFA Plot of $H_b(r_c)$ versus $H_b(r_c) - H_b(r_c)/2$

QTAIM-DFA plot of $H_b(r_c)$ versus $H_b(r_c) - V_b(r_c)/2$ (= $(\hbar^2/8m)\nabla^2\rho_b(r_c)$)[22] has been proposed after the proposal of $H_b(r_c)$ versus $\nabla^2\rho_b(r_c)$.[23] This choice enables to analyze the plots much effectively, since the four arithmetic operations can be applied to analyze the plots by unifying the unit of both axes in the plot to energy. The QTAIM-DFA incorporates the classification of interactions by the signs of $\nabla^2\rho_b(r_c)$ and $H_b(r_c)$. Scheme 2-2 summarizes the QTAIM-DFA treatment. Interactions of *p*-CS appear in the first quadrant, those of *r*-CS in the fourth quadrant, and SS interactions do in the third quadrant. No interactions appear in the second one.

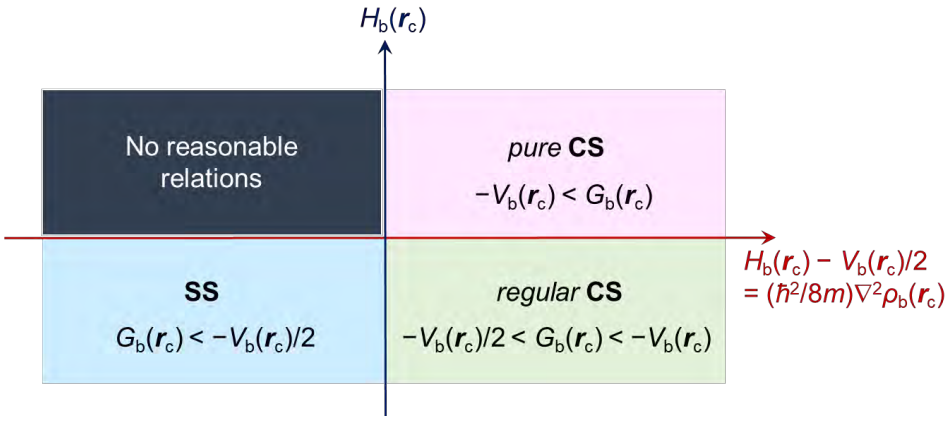

Scheme 2-2. QTAIM-DFA plot of $H_b(r_c)$ versus $H_b(r_c) - V_b(r_c)/2$, where the $H_b(r_c) - V_b(r_c)/2 = (\hbar^2/8m)\nabla^2\rho_b(r_c)$.

Application of the QTAIM-DFA to Typical Interactions

The QTAIM-DFA is applied to typical interactions, **2-1**–**2-56**, shown in Table 2-1. Figure 2-2 illustrates the QTAIM-DFA plots of the data for the typical interactions, evaluated with MP2/Sapporo-TZP + 1s1p, which is denoted as Sapporo-TZPsp. Data for the perturbed structures around the fully optimized structures are plotted in addition to data for the fully optimized structures, which are located on center of a plot of five digits.[22–24] The plots in Figure 2-2 have a spiral stream as a whole, and the interactions seem well separated. In *p*-CS, the plots of vdW and HB go upward and downward, respectively. The plots of CT-MC and CT-TBP in *r*-CS go downward to the right and left, respectively, through the those of X_3^- between them. The plots of Cov-w and Cov-s appear in SS region. The CS interactions are expected to be well classified and characterized with QTAIM-DFA. However, it must be careful when the dynamic nature of **2-34**, **2-35**, **2-39**, **2-40**, **2-43**, **2-44**, and **2-51** are discussed, since the plots show irregular stream, compared with others.[30] The Te and I atoms of the 5th period are contained in **2-34**, **2-35**, **2-39**, **2-43**, **2-44**, and **2-51**, while **2-40** contains Se-∗-Cl.

Table 2-1. Standard species for **2-1**–**2-56**, forming typical interactions.

vdW[a]	HB[b]	CT-MC[c]		X_3^-[d]
He-∗-HF: **2-1**	NN-∗-HF: **2-6**	Me_2O-∗-Cl_2: **2-11**	Me_2Se-∗-Cl_2: **2-17**	$[Cl\text{-}*\text{-}Cl_2]^-$: **2-23**
Ne-∗-HF: **2-2**	HF-∗-HF: **2-7**	Me_2O-∗-Br_2: **2-12**	Me_2Se-∗-Br_2: **2-18**	$[Br\text{-}*\text{-}Br_2]^-$: **2-24**
Ar-∗-HF: **2-3**	HCN-∗-HF: **2-8**	Me_2O-∗-I_2: **2-13**	Me_2Se-∗-I_2: **2-19**	$[I\text{-}*\text{-}I_2]^-$: **2-25**
Kr-∗-HF: **2-4**	H_2O-∗-HOH: **2-9**	Me_2S-∗-Cl_2: **2-14**	Me_2Te-∗-Cl_2: **2-20**	$[Cl\text{-}*\text{-}BrCl]^-$: **2-26**
Xe-∗-HF: **2-5**	Me_2O-∗-HOH: **2-10**	Me_2S-∗-Br_2: **2-15**	Me_2Te-∗-Br_2: **2-21**	$[Br\text{-}*\text{-}ClBr]^-$: **2-27**
		Me_2S-∗-I_2: **2-16**	Me_2Te-∗-I_2: **2-22**	$[Cl\text{-}*\text{-}ICl]^-$: **2-28**
				$[Br\text{-}*\text{-}IBr]^-$: **2-29**

CT-TBP[e]		Cov-w[f]	Cov-s[g]	
Me_2ClS-∗-Cl: **2-30**	Me_2S^+-∗-Cl: **2-37**	Me_2Te^+-∗-Cl: **2-43**	H_3C-∗-Cl: **2-49**	H_3C-∗-H: **2-55**
Me_2BrS-∗-Br: **2-31**	Me_2S^+-∗-Br: **2-38**	Me_2Te^+-∗-Br: **2- 44**	H_3C-∗-Br: **2-50**	H-∗-H: **2-56**
Me_2ClSe-∗-Cl: **2-32**	Me_2S^+-∗-I: **2-39**	Me_2Te^+-∗-I: **2-45**	H_3C-∗-I: **2-51**	
Me_2BrSe-∗-Br: **2-33**	Me_2Se^+-∗-Cl: **2-40**	Cl-∗-Cl: **2-46**	H_3C-∗-CH_3: **2-52**	
Me_2ClTe-∗-Cl: **2-34**	Me_2Se^+-∗-Br: **2-41**	Br-∗-Br: **2-47**	H_2C-∗-CH_2: **2-53**	
Me_2BrTe-∗-Br: **2-35**	Me_2Se^+-∗-I: **2-42**	I-∗-I: **2-48**	HC-∗-CH: **2-54**	
Me_2ITe-∗-I: **2-36**				

[a] van der Waals complexes. [b] Hydrogen bonds. [c] Molecular complexes through charge transfer. [d] Trihalide ions. [e] Trigonal bipyramidal adducts through charge transfer. [f] Weak covalent bonds. [g] Strong covalent bonds.

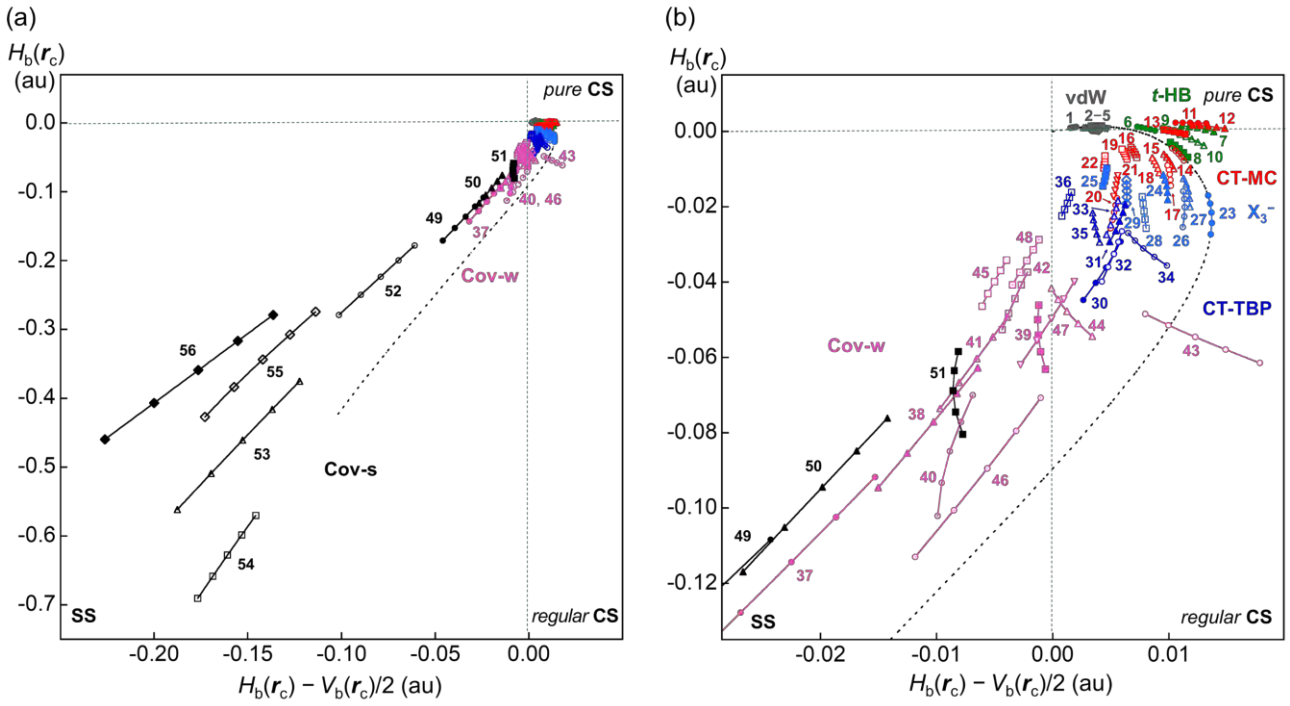

Figure 2-2. QTAIM-DFA plots of $H_b(r_c)$ versus $H_b(r_c) - V_b(r_c)/2$ for a fully optimized and four perturbed structures of each typical interaction (shown Table 2-1) in **2-1**–**2-56**, evaluated with MP2/Sapporo-TZPsp. The species numbers of ***n*** in **2-*n*** are also illustrated ("**2-**" was omitted for clarification). Whole picture (a) and magnified picture for *pure* and *regular* CS regions (b). The numbers and colors for the interactions are the same as those in Table 2-1. The perturbed structures are generated by employing partial optimization method (POM).

Calculation of QTAIM-DFA Parameters by Analyzing the QTAIM-DFA Plots

Plots of $H_b(\boldsymbol{r}_c)$ versus $H_b(\boldsymbol{r}_c) - V_b(\boldsymbol{r}_c)/2$ are analyzed by employing the polar coordinate (R, θ) representation, together with (θ_p, κ_p) parameters.[22,24–26] Figure 2-3 explains the treatment of those parameters. The R in (R, θ) is defined by Equation (2-4) and given in the energy unit; thus, the R corresponds to the energy for an interaction at BCP. The plots show a spiral stream, as a whole. The θ in (R, θ) defined by Equation (2-5), measured from the y-axis, controls the spiral stream of the plot, and classifies the interactions. The range is sub-divided into p-CS if $45.0^o < \theta < 90.0^o$ ($0 < H_b(\boldsymbol{r}_c)$, $0 < H_b(\boldsymbol{r}_c) - V_b(\boldsymbol{r}_c)/2$), r-CS if $90.0^o < \theta < 180.0^o$ ($H_b(\boldsymbol{r}_c) < 0$, $0 < H_b(\boldsymbol{r}_c) - V_b(\boldsymbol{r}_c)/2$), SS if $180.0^o < \theta < 206.6^o$ ($H_b(\boldsymbol{r}_c) < 0$, $H_b(\boldsymbol{r}_c) - V_b(\boldsymbol{r}_c)/2 < 0$). Each plot for an interaction shows a specific curve, which provides important information of the interaction (see Figure 2-2). The curve is expressed by θ_p and κ_p. While θ_p, defined by Equation (2-6) and measured from the y-direction, corresponds to the tangent line of a plot, where θ_p is calculated employing data of four perturbed structures with a fully optimized structure and κ_p is the curvature of the plot (Equation (2-7)). While (R, θ) correspond to the static nature, (θ_p, κ_p) represent the dynamic nature of interactions. The (R, θ) and (θ_p, κ_p) are called QTAIM-DFA parameters, whereas $\rho_b(\boldsymbol{r}_c)$, $\nabla^2\rho_b(\boldsymbol{r}_c)$, $G_b(\boldsymbol{r}_c)$, $V_b(\boldsymbol{r}_c)$, $H_b(\boldsymbol{r}_c)$, and $H_b(\boldsymbol{r}_c) - V_b(\boldsymbol{r}_c)/2$ belong to QTAIM functions. Table 2-2 collects the QTAIM functions and QTAIM-DFA parameters after analyzing each QTAIM-DFA plot of **2-1**–**2-56** according to Equations (2-4)–(2-7).

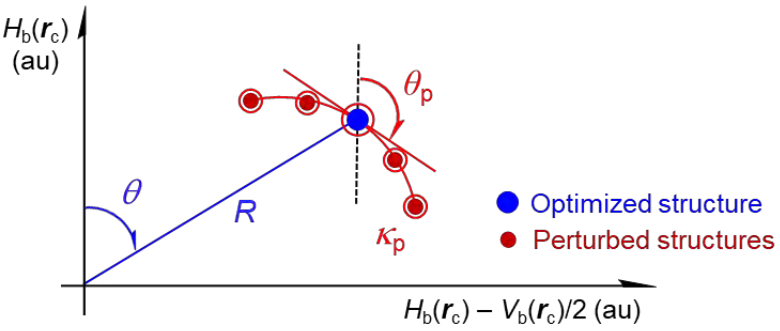

Figure 2-3. Polar (R, θ) coordinate representation of the QTAIM-DFA, together with (θ_p, κ_p) parameters.

$$R = (x^2 + y^2)^{1/2} \quad (2\text{-}4)$$

$$\theta = 90^o - \tan^{-1}(y/x) \quad (2\text{-}5)$$

$$\theta_p = 90^o - \tan^{-1}(dy/dx) \quad (2\text{-}6)$$

$$\kappa_p = |d^2y/dx^2|/[1 + (dy/dx)^2]^{3/2} \quad (2\text{-}7)$$

where the $(x, y) = (H_b(\boldsymbol{r}_c) - V_b(\boldsymbol{r}_c)/2, H_b(\boldsymbol{r}_c))$

Table 2-2. QTAIM functions and QTAIM-DFA parameters for **2-1**–**2-56**, evaluated with MP2/Sapporo-TZPsp, by employing the perturbed structures generated with POM.[a]

X-∗-Y: species	$\rho_b(\boldsymbol{r}_c)$ (au)	$c\nabla^2\rho_b(\boldsymbol{r}_c)^b$ (au)	$H_b(\boldsymbol{r}_c)$ (au)	R^c (au)	θ^d (º)	θ_p^e (º)	κ_p^f (au^{-1})	Predicted nature
He-∗-HF: **2-1**	0.0024	0.0018	0.0011	0.0020	58.9	62.3	69.8	*p*-CS/vdW
Ne-∗-HF: **2-2**	0.0048	0.0030	0.0011	0.0032	70.3	77.8	16.0	*p*-CS/vdW
Ar-∗-HF: **2-3**	0.0074	0.0037	0.0014	0.0040	69.1	83.4	157.2	*p*-CS/vdW
Kr-∗-HF: **2-4**	0.0104	0.0043	0.0008	0.0044	78.9	106.2	211.9	*p*-CS/*t*-HB_{nc}
Xe-∗-HF: **2-5**	0.0105	0.0036	0.0006	0.0037	81.3	109.9	278.8	*p*-CS/*t*-HB_{nc}
NN-∗-HF: **2-6**	0.0183	0.0080	0.0008	0.0081	84.2	123.3	157.9	*p*-CS/*t*-HB_{nc}
HF-∗-HF: **2-7**	0.0246	0.0124	0.0009	0.0125	85.8	117.9	124.5	*p*-CS/*t*-HB_{nc}
HCN-∗-HF: **2-8**	0.0336	0.0109	–0.0046	0.0118	113.0	159.1	51.2	*r*-CS/CT-MC
H_2O-∗-HOH: **2-9**	0.0242	0.0105	0.0004	0.0105	88.0	123.4	129.1	*p*-CS/*t*-HB_{nc}
Me_2O-∗-HOH: **2-10**	0.0315	0.0120	–0.0021	0.0122	99.8	145.3	78.9	*r*-CS/*t*-HB_{wc}
Me_2O-∗-Cl_2: **2-11**	0.0240	0.0118	0.0023	0.0121	79.1	93.2	53.2	*p*-CS/*t*-HB_{nc}
Me_2O-∗-Br_2: **2-12**	0.0302	0.0134	0.0013	0.0135	84.3	107.2	86.5	*p*-CS/*t*-HB_{nc}
Me_2O-∗-I_2: **2-13**	0.0280	0.0105	–0.0001	0.0105	90.3	122.4	123.2	*r*-CS/*t*-HB_{wc}
Me_2S-∗-Cl_2: **2-14**	0.0463	0.0108	–0.0060	0.0124	118.8	162.8	61.5	*r*-CS/CT-MC
Me_2S-∗-Br_2: **2-15**	0.0495	0.0100	–0.0078	0.0127	127.8	167.4	42.9	*r*-CS/CT-MC
Me_2S-∗-I_2: **2-16**	0.0372	0.0070	–0.0055	0.0089	128.0	169.1	43.9	*r*-CS/CT-MC
Me_2Se-∗-Cl_2: **2-17**	0.0597	0.0101	–0.0114	0.0152	138.6	176.9	18.8	*r*-CS/CT-MC
Me_2Se-∗-Br_2: **2-18**	0.0516	0.0089	–0.0088	0.0125	134.5	170.9	33.7	*r*-CS/CT-MC
Me_2Se-∗-I_2: **2-19**	0.0384	0.0062	–0.0059	0.0086	133.7	171.3	49.9	*r*-CS/CT-MC
Me_2Te-∗-Cl_2: **2-20**	0.0695	0.0053	–0.0215	0.0221	166.2	184.3	0.0	*r*-CS/CT-TBP
Me_2Te-∗-Br_2: **2-21**	0.0578	0.0055	–0.0143	0.0153	159.0	183.7	8.8	*r*-CS/CT-TBP
Me_2Te-∗-I_2: **2-22**	0.0416	0.0045	–0.0080	0.0092	150.8	182.2	24.9	*r*-CS/CT-TBP
$[Cl\text{-}∗\text{-}Cl_2]^-$: **2-23**	0.0837	0.0137	–0.0216	0.0255	147.6	178.4	15.0	*r*-CS/CT-MC
$[Br\text{-}∗\text{-}Br_2]^-$: **2-24**	0.0660	0.0098	–0.0145	0.0175	145.9	176.5	22.9	*r*-CS/CT-MC
$[I\text{-}∗\text{-}I_2]^-$: **2-25**	0.0508	0.0045	–0.0119	0.0128	159.1	183.8	14.7	*r*-CS/CT-TBP
$[Cl\text{-}∗\text{-}BrCl]^-$: **2-26**	0.0753	0.0114	–0.0201	0.0231	150.5	179.9	12.7	*r*-CS/CT-MC
$[Br\text{-}∗\text{-}ClBr]^-$: **2-27**	0.0717	0.0117	–0.0158	0.0197	143.6	175.5	23.1	*r*-CS/CT-MC
$[Cl\text{-}∗\text{-}ICl]^-$: **2-28**	0.0663	0.0079	–0.0212	0.0226	159.7	177.9	1.0	*r*-CS/CT-MC
$[Br\text{-}∗\text{-}IBr]^-$: **2-29**	0.0590	0.0064	–0.0158	0.0171	158.0	180.0	8.3	*r*-CS/CT-MC
Me_2ClS-∗-Cl: **2-30**	0.0964	0.0046	–0.0362	0.0364	172.8	191.5	6.2	*r*-CS/CT-TBP
Me_2BrS-∗-Br: **2-31**	0.0804	0.0058	–0.0238	0.0245	166.4	187.3	9.7	*r*-CS/CT-TBP
Me_2ClSe-∗-Cl: **2-32**	0.0860	0.0053	–0.0325	0.0330	170.8	187.4	3.6	*r*-CS/CT-TBP
Me_2BrSe-∗-Br: **2-33**	0.0742	0.0053	–0.0225	0.0231	166.8	186.0	12.7	*r*-CS/CT-TBP
Me_2ClTe-∗-Cl: **2-34**	0.0779	0.0078	–0.0311	0.0321	165.9	159.1	28.6	*r*-CS/CT-MC
Me_2BrTe-∗-Br: **2-35**	0.0695	0.0036	–0.0253	0.0256	171.8	175.7	10.5	*r*-CS/CT-MC
Me_2ITe-∗-I: **2-36**	0.0594	0.0013	–0.0191	0.0191	176.2	187.5	5.9	*r*-CS/CT-TBP
Me_2S^+-∗-Cl: **2-37**	0.1692	–0.0225	–0.1143	0.1165	191.1	197.9	0.3	SS/Cov-w
Me_2S^+-∗-Br: **2-38**	0.1389	–0.0103	–0.0771	0.0778	187.6	195.1	0.5	SS/Cov-w
Me_2S^+-∗-I: **2-39**	0.1071	–0.0012	–0.0541	0.0542	181.3	178.4	8.3	SS/Cov-w
Me_2Se^+-∗-Cl: **2-40**	0.1387	–0.0089	–0.0850	0.0854	185.9	186.0	4.2	SS/Cov-w
Me_2Se^+-∗-Br: **2-41**	0.1190	–0.0065	–0.0603	0.0607	186.2	193.5	0.1	SS/Cov-w
Me_2Se^+-∗-I: **2-42**	0.0967	–0.0032	–0.0444	0.0445	184.2	188.3	2.2	SS/Cov-w
Me_2Te^+-∗-Cl: **2-43**	0.1106	0.0123	–0.0546	0.0560	167.3	142.7	8.8	*r*-CS/*t*-HB_{wc}
Me_2Te^+-∗-Br: **2-44**	0.0996	0.0012	–0.0478	0.0478	178.5	164.9	14.9	*r*-CS/CT-MC
Me_2Te^+-∗-I: **2-45**	0.0870	–0.0050	–0.0399	0.0402	187.2	190.2	2.0	SS/Cov-w
Cl-∗-Cl: **2-46**	0.1606	–0.0056	–0.0895	0.0897	183.6	194.3	0.9	SS/Cov-w
Br-∗-Br: **2-47**	0.1130	–0.0001	–0.0497	0.0497	180.1	191.8	1.8	SS/Cov-w
I-∗-I: **2-48**	0.0825	–0.0022	–0.0343	0.0344	183.7	190.9	0.5	SS/Cov-w
H_3C-∗-Cl: **2-49**	0.1855	–0.0338	–0.1362	0.1404	193.9	199.1	0.2	SS/Cov-w
H_3C-∗-Br: **2-50**	0.1554	–0.0198	–0.0945	0.0965	191.9	197.0	0.1	SS/Cov-w
H_3C-∗-I: **2-51**	0.1243	–0.0086	–0.0689	0.0694	187.1	179.5	10.4	SS/Cov-w
H_3C-∗-CH_3: **2-52**	0.2462	–0.0791	–0.2233	0.2369	199.5	201.8	0.0	SS/Cov-s
H_2C-∗-CH_2: **2-53**	0.3545	–0.1527	–0.4608	0.4854	198.3	199.3	0.1	SS/Cov-s
HC-∗-CH: **2-54**[g]	0.4109	–0.1608	–0.6278	0.6481	194.4	194.4	0.1	SS/Cov-s
H_3C-∗-H: **2-55**	0.2851	–0.1420	–0.3436	0.3718	202.5	201.5	0.4	SS/Cov-s
H-∗-H: **2-56**	0.2730	–0.1763	–0.3593	0.4002	206.1	206.4	0.0	SS/Cov-s

[a] Data are given for the interaction in question at the BCP. [b] $c\nabla^2\rho_b(\boldsymbol{r}_c) = H_b(\boldsymbol{r}_c) - V_b(\boldsymbol{r}_c)/2$, where $c = \hbar^2/8m$. [c] $R = (x^2 + y^2)^{1/2}$, where $(x, y) = (H_b(\boldsymbol{r}_c) - V_b(\boldsymbol{r}_c)/2, H_b(\boldsymbol{r}_c))$. [d] $\theta = 90º - \tan^{-1}(y/x)$. [e] $\theta_p = 90º - \tan^{-1}(dy/dx)$. [f] $\kappa_p = |d^2y/dx^2|/[1 + (dy/dx)^2]^{3/2}$. [g] Data from $w = 0$, ±0.025, and ±0.5 were employed, since the (3, −3) attractor appeared at the center of the perturbed structure for $w = -0.1$ in Equation (2-8).

Standard Criteria to Classify and Characterize Interactions, Established by Applying the QTAIM-DFA to Typical Interactions

Figure 2-4 summarizes the areas for the standard interactions of vdW type, *t*-HB_{nc}, *t*-HB_{wc}, CT-MCs, X_3^-, and CT-TBPs, together with Cov-w and Cov-s, to be appeared in the QTAIM-DFA plot.[22–26] The areas seem defined uniquely for most interactions by the QTAIM-DFA parameters, while the areas are determined tentatively for some interactions, so as to be accepted by experimental scientists. Scheme 2-3 illustrates the standard criteria, derived from the areas illustrated in Figure 2-4, which are the most basic results in QTAIM-DFA. The (θ, θ_p) values of (75º, **90º**), (**90º**, 125º), (115º, 150º), (150º, **180º**), and (**180º**, 190º) correspond to the borderlines between the vdW/*t*-HB_{nc}, *t*-HB_{nc}/*t*-HB_{wc}, *t*-HB_{wc}/CT-MC, CT-MC/CT-TBP, and CT-TBP/Cov interactions, respectively. The classical covalent bonds of the SS ($180º < \theta$) will be Cov-s if $R > 0.15$ au, whereas they will be Cov-w for $R <$ 0.15 au. The basic values of (θ, θ_p), described in bold, are superior to the tentatively given values (in plane) in the classification and characterization of interactions. Table 2-2 also contains the predicted natures of typical interactions for **2-1**–**2-56**, evaluated with MP2/Sapporo-TZPsp, by characterizing based on the standard criteria. The CS interactions would be well characterized based on the θ and θ_p, together with the R for SS interactions. Thus, the criteria will be employed to discuss the nature of interactions in question, as a reference. It should be noted that the standard criteria have been

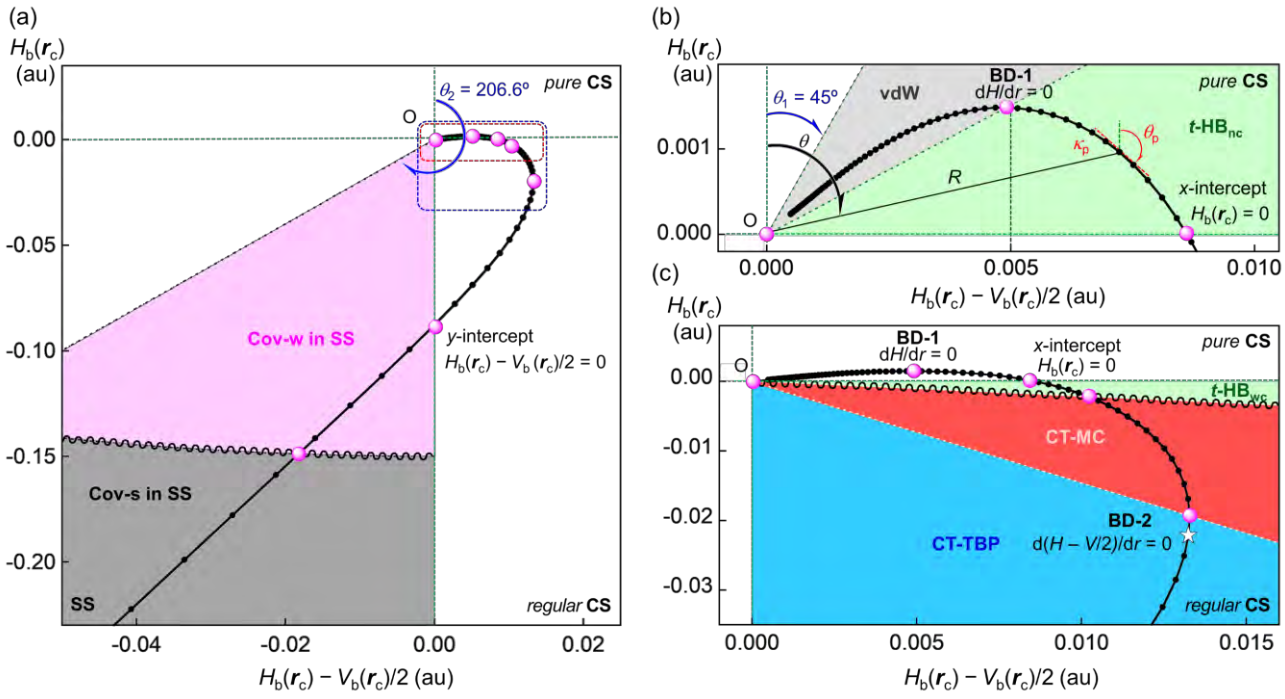

Figure 2-4. Areas for the weak to strong interactions to be appeared in the QTAIM-DFA plot of $H_b(r_c)$ versus $H_b(r_c) - V_b(r_c)/2$, calculated with MP2/6-311++G(3df,3pd). Data for **2-23**: $[Cl-*-Cl-Cl]^-$ of the wide range of w in Equation (2-8) being employed for the plot. Whole picture (a), magnified one for the *p*-CS region (b), and magnified one for the *r*-CS region (c). The white star symbol in (c) corresponds to the optimized structure. The θ_1 (= 45º) and θ_2 (= 206.6º) values correspond to the limited values. The definitions of (R, θ) and (θ_p, κ_p) are illustrated (b). First and second bending points of the plot (BD-1 and BD-2, respectively) are also shown in the figure.

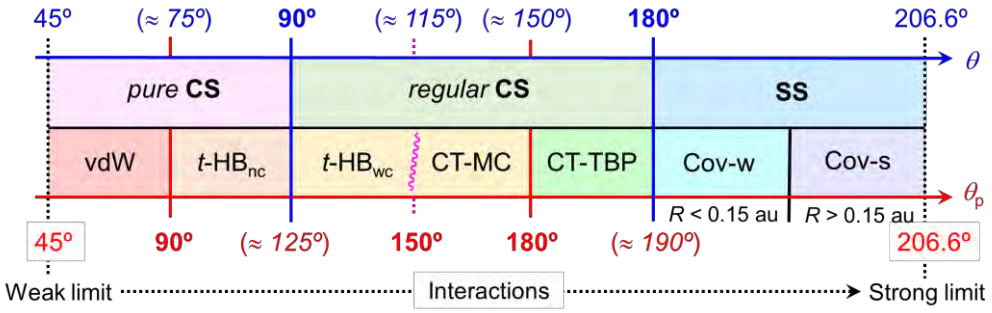

Scheme 2-3. Standard criteria to classify and characterize interactions by θ and θ_p, together with R for SS. The basic parameters, described in bold, are superior to the tentatively given parameters, described in italic, in the prediction of interactions.

proposed by applying the QTAIM-DFA to the typical interactions, evaluated with MP2/6-311++G(3df,3pd),[22–26] although the QTAIM-DFA is mainly explained using data for MP2/Sapporo-TZPsp here. The standard criteria would not be change because the similar results are given among MP2/(6-311++G(3df,3pd) + Sapporo-TZPsp), MP2/(aug-cc-pVTZ + Sapporo-TZPsp), and MP2/Sapporo-TZPsp for **2-1**–**2-56**, as shown in Tables 2-A1 and A2 of the Appendix and Table 2-2. However, some differences, especially for **2-1**–**2-19**, are obtained among the three methods (see also Figures 2-A1 and A2 of the Appendix). The further examination of basis set dependence is beyond the scope of this thesis, although it is very important issue in the QTAIM-DFA, as reported previously.[31]

The reliability of the dynamic behavior must depend on the quality of the perturbed structures. Therefore, the methods employed to generate perturbed structures are extremely significant in the QTAIM-DFA. How are the perturbed structures generated for evaluating the dynamic behavior of interactions in question? The methods to generate the perturbed structures will be explained next.

Methods to Generate the Perturbed Structures

Partial Optimization Method (POM)

POM is the primitive method to generate perturbed structure.[22–24] The perturbed structures are generated by the process of partial optimization with the length of interacting atoms in question (r) being fixed to satisfy Equation (2-8), where the r_o shows the distance in optimized structure with a_o of Bohr radius (0.52918 Å). Thus, the perturbed structures generated with POM must exist on the potential surface and should be related to the thermal process. Accordingly, r in the perturbed structures must be fixed longer or shorter than r_o by wa_o with other structural parameters being optimized. In QTAIM-DFA, each plot of $H_b(\boldsymbol{r}_c)$ versus $H_b(\boldsymbol{r}_c) - V_b(\boldsymbol{r}_c)/2$ for data of five digits (w = 0, ±0.05, and ±0.1 in Equation (2-8)), unless otherwise noted, is analyzed using a regression curve by assuming the cubic function as shown in Equation (2-9), where the $(x, y) = (H_b(\boldsymbol{r}_c) - V_b(\boldsymbol{r}_c)/2, H_b(\boldsymbol{r}_c))$ (R_c^2 = 0.99999 in usual).[26]

$$r = r_o + wa_o \ (w = (0), \pm 0.05, \text{ and } \pm 0.1;\ a_o = 0.52918 \text{ Å}) \tag{2-8}$$

$$y = c_o + c_1x + c_2x^2 + c_3x^3 \ (R_c^2\text{: square of correlation coefficient}) \tag{2-9}$$

POM is a simple method to generate the perturbed structures. However, it will be challenging to apply the POM to larger molecules because the cost performance in the calculation is relatively poor.

Normal Coordinates of Internal Vibrations (NIV)

Second, NIV method has been proposed to generate the perturbed structures by employing normal coordinates of internal vibrations obtained by frequency analysis.[25,26] NIV method is explained by Equation (2-10). A k-th perturbed structure in question ($\mathbf{S}_{kw}$) is generated by adding the normal coordinates of the k-th internal vibration ($\mathbf{N}_k$) to the standard orientation of a fully optimized structure ($\mathbf{S}_o$) in the matrix representation (In the $m \times n$ matrix representation, m corresponds to the number of atoms and n (= 3) to x, y, and z components of the space). The coefficient f_{kw} in Equation (2-10) controls the structural difference between $\mathbf{S}_{kw}$ and $\mathbf{S}_o$ to satisfy r in Equation (2-8), where the r is the distance of interacting atoms in question of the perturbed structure. The selected motion must be most effectively localized on the interaction in question among zero-point internal vibrations.

$$\mathbf{S}_{kw} = \mathbf{S}_o + f_{kw} \cdot \mathbf{N}_k \tag{2-10}$$

NIV overcomes the limitations of POM because the partial optimization processes are not required. Furthermore, NIV is most effective for analyzing the interactions in the transition structures (TSs) on intrinsic reaction coordinate (IRC) because the perturbed structures of TSs must be located on the IRC on the energy surface.[32] However, the dynamic behavior in equilibrium structures elucidated by the QTAIM-DFA with NIV is always affected by internals vibration other than the interacting atoms in question, although this effect is usually small except in some cases.[25,26]

Coordinates Derived from Compliance Force Constants for Internal Vibrations (CIV)

Third method, CIV, has been proposed to resolve the difficulty of NIV. In CIV, the perturbed structures are generated by employing the coordinates derived from compliance force constants for internal vibrations, which minimize the effects of other internal vibrations.[33] CIV method is explained by Equation (2-11). An *i*-th perturbed structure in question ($\mathbf{S}_{iw}$) is generated by adding the coordinates ($\mathbf{C}_i$), corresponding to compliance force constants (C_{ii}), to the standard orientation of a fully optimized structure ($\mathbf{S}_o$) as well as NIV (Equation 2-10). The $\mathbf{C}_i$ and C_{ii} are calculated with Compliance 3.0.2 program released by Grunenberg and Brandhorst,[34–36] by using the results of frequency analysis.

The C_{ij} is defined as the partial second derivatives of the potential energy due to an external force, as shown in Equation (2-12), for which *i* and *j* refer to internal coordinates, and the force constants f_i and f_j correspond to *i* and *j*, respectively. The value in Equation (2-12) corresponds to a lower numerical value (*i*) of a compliance force constant representing a stronger bond (*j*); that is, the compliance constants measure the flexibility (or compliance) of a particular bond.

$$\mathbf{S}_{iw} = \mathbf{S}_o + f_{iw} \cdot \mathbf{C}_i \quad (2\text{-}11)$$

$$C_{ij} = \partial^2 / \partial f_i \partial f_j \quad (2\text{-}12)$$

The QTAIM-DFA with CIV provides the same dynamic behaviors as those with POM in terms of calculation errors.[33] Figure 2-5 shows plots of $\theta_{p:POM}$ versus $\theta_{p:CIV}$ and $\kappa_{p:POM}$ versus $\kappa_{p:CIV}$ for

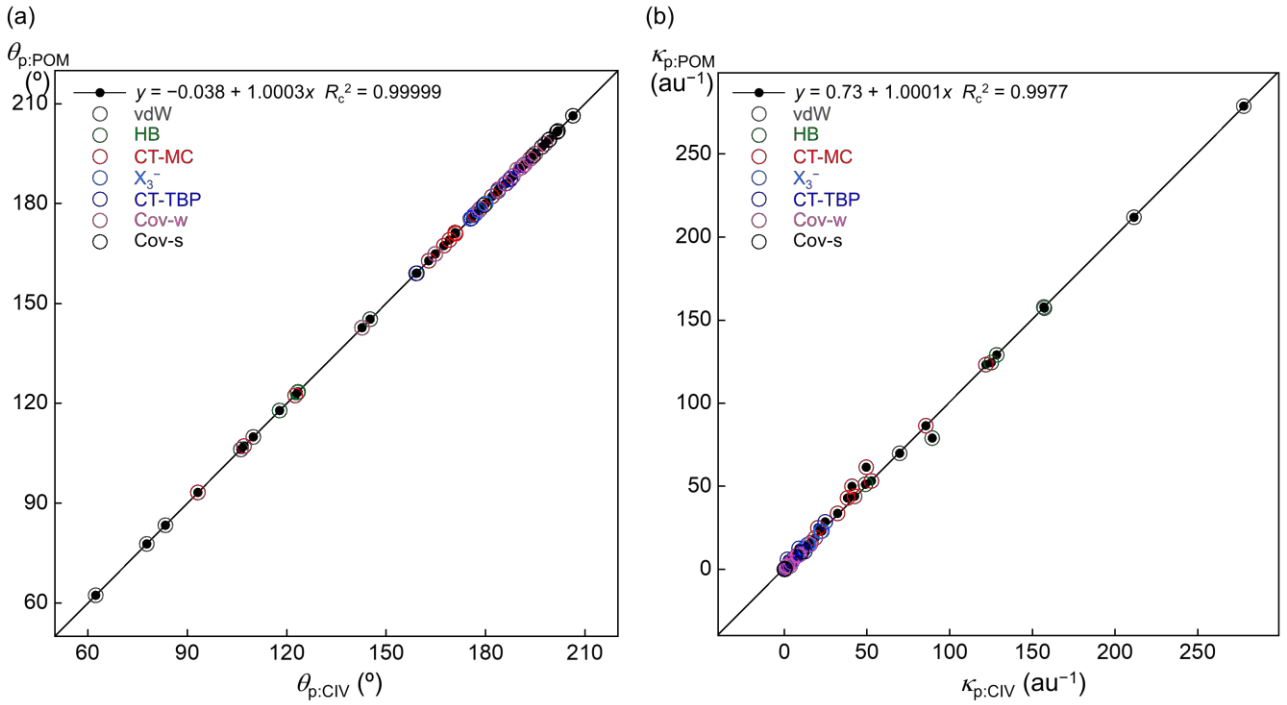

Figure 2-5. Plots of $\theta_{p:POM}$ versus $\theta_{p:CIV}$ (a) and $\kappa_{p:POM}$ versus $\kappa_{p:CIV}$ (b) for **2-1**–**2-56**, evaluated with MP2/Sapporo-TZPsp. The colors for the typical interactions are the same as those in Table 2-1.

2-1–**2-56**, evaluated with MP2/Sapporo-TZPsp, where the $\theta_{p:POM}$ and $\kappa_{p:POM}$, and $\theta_{p:CIV}$ and $\kappa_{p:CIV}$ are θ_p and κ_p calculated by employing the perturbed structures generated with POM and CIV, respectively. A highly excellent correlation is obtained for the $\theta_{p:POM}$ versus $\theta_{p:CIV}$ ($y = -0.038 + 1.0003x$: $R_c^2 = 0.99999$), whereas the plot of $\kappa_{p:POM}$ versus $\kappa_{p:CIV}$ gives a very good correlation ($y = 0.73 + 1.0001x$: $R_c^2 = 0.9977$). Consequently, CIV provides the perturbed structures, which are substantially the same as POM.

Table 2-3 summarizes the features of POM, NIV, and CIV. The CIV has some advantages in terms of computational cost, applicability, and reliability. The computational cost for CIV is good relative to POM due to no partial optimization process. For applicability for generating the perturbed structures, CIV is superior to NIV, because of invariant to the choice of the coordinate system. Additionally, CIV is expected to be high reliability to analyze the dynamic behavior, because the effects from other internal vibrations can be minimized. Therefore, CIV will be excellent method for generating the perturbed structures. The QTAIM-DFA with CIV will elucidate the "intrinsic dynamic nature" of the interactions in question with high reliability. In this thesis, CIV was mainly employed for generating the perturbed structures.

POM and NIV also have advantages; however, the further explanation of them is beyond the scope of this thesis.

Table 2-3. Features of methods to generate the perturbed structures, POM, NIV, and CIV.

Features	POM	NIV	CIV
Partial optimizations	yes	n.a.[a]	n.a.[a]
Computational cost	relatively poor[b]	relatively good[b]	relatively good[b]
Effect from other internal vibrations	n.a.[c,d]	always affected	minimized
Choice of the coordinate system	n.a.[c]	yes	invariant
Analyzing TS on IRC	n.a.	yes[e]	n.a.

[a] NIV and CIV generate the perturbed structures by employing the result of frequency analysis after the full optimization process. [b] POM requires four partial optimization processes in addition to full optimization, whereas NIV and CIV employ the result of a frequency analysis after the full optimization process. [c] In POM, the frequency result is not employed for generating the perturbed structures. [d] In POM, the effects from other internal coordinates are reduced by partial optimization process, which optimizes the internal coordinates on energy surface except for the length of interacting atoms in question. [e] NIV can elucidate dynamic behavior of the interaction in question on IRC by employing the internal vibration corresponding to the imaginary frequency, calculated by frequency analysis.

Appendix

Table 2-A1. QTAIM functions and QTAIM-DFA parameters for **2-1**–**2-56**, evaluated with MP2/(6-311++G(3df,3pd) + Sapporo-TZPsp), by employing the perturbed structures generated with POM.[a,b]

X-∗-Y: species	$\rho_b(\boldsymbol{r}_c)$ (au)	$c\nabla^2\rho_b(\boldsymbol{r}_c)$[c] (au)	$H_b(\boldsymbol{r}_c)$ (au)	R[d] (au)	θ[e] (°)	θ_p[f] (°)	κ_p[g] (au^{-1})	Predicted nature
He-∗-HF: **2-1**	0.0034	0.0022	0.0013	0.0025	59.9	57.2	8.2	*p*-CS/vdW
Ne-∗-HF: **2-2**	0.0076	0.0050	0.0019	0.0054	69.2	84.4	85.4	*p*-CS/vdW
Ar-∗-HF: **2-3**	0.0083	0.0043	0.0020	0.0048	65.0	76.4	163.1	*p*-CS/vdW
Kr-∗-HF: **2-4**	0.0086	0.0040	0.0017	0.0043	66.5	80.4	221.2	*p*-CS/vdW
Xe-∗-HF: **2-5**	0.0108	0.0040	0.0013	0.0042	72.6	94.7	336.9	*p*-CS/*t*-HB$_{nc}$
NN-∗-HF: **2-6**	0.0190	0.0087	0.0015	0.0088	80.0	126.8	240.0	*p*-CS/*t*-HB$_{nc}$
HF-∗-HF: **2-7**	0.0250	0.0125	–0.0002	0.0125	90.8	128.2	108.0	*r*-CS/*t*-HB$_{wc}$
HCN-∗-HF: **2-8**	0.0337	0.0107	–0.0053	0.0120	116.1	168.5	24.1	*r*-CS/CT-MC
H_2O-∗-HOH: **2-9**	0.0244	0.0106	0.0005	0.0107	87.3	123.7	159.3	*p*-CS/*t*-HB$_{nc}$
Me_2O-∗-HOH: **2-10**	0.0314	0.0121	–0.0021	0.0123	99.8	148.9	93.0	*r*-CS/*t*-HB$_{wc}$
Me_2O-∗-Cl_2: **2-11**	0.0283	0.0126	0.0007	0.0126	86.7	96.6	31.8	*p*-CS/*t*-HB$_{nc}$
Me_2O-∗-Br_2: **2-12**	0.0302	0.0120	–0.0004	0.0120	91.7	106.4	56.6	*r*-CS/*t*-HB$_{wc}$
Me_2O-∗-I_2: **2-13**	0.0302	0.0102	–0.0018	0.0103	99.9	121.0	77.6	*r*-CS/*t*-HB$_{wc}$
Me_2S-∗-Cl_2: **2-14**	0.0454	0.0108	–0.0055	0.0121	117.1	162.7	60.2	*r*-CS/CT-MC
Me_2S-∗-Br_2: **2-15**	0.0471	0.0092	–0.0076	0.0119	129.7	170.8	36.0	*r*-CS/CT-MC
Me_2S-∗-I_2: **2-16**	0.0365	0.0069	–0.0052	0.0087	127.2	168.5	44.7	*r*-CS/CT-MC
Me_2Se-∗-Cl_2: **2-17**	0.0602	0.0091	–0.0129	0.0157	144.9	182.8	9.1	*r*-CS/CT-TBP
Me_2Se-∗-Br_2: **2-18**	0.0501	0.0075	–0.0098	0.0124	142.6	180.7	15.8	*r*-CS/CT-TBP
Me_2Se-∗-I_2: **2-19**	0.0371	0.0061	–0.0056	0.0083	132.6	174.7	38.4	*r*-CS/CT-MC
Me_2Te-∗-Cl_2: **2-20**	0.0687	0.0054	–0.0206	0.0213	165.2	184.4	0.1	*r*-CS/CT-TBP
Me_2Te-∗-Br_2: **2-21**	0.0574	0.0048	–0.0149	0.0157	162.1	186.3	5.5	*r*-CS/CT-TBP
Me_2Te-∗-I_2: **2-22**	0.0415	0.0045	–0.0079	0.0091	150.5	181.9	21.2	*r*-CS/CT-TBP
$[Cl$-∗-$Cl_2]^-$: **2-23**	0.0836	0.0133	–0.0220	0.0257	149.0	181.6	11.1	*r*-CS/CT-TBP
$[Br$-∗-$Br_2]^-$: **2-24**	0.0667	0.0075	–0.0179	0.0194	157.3	184.3	7.8	*r*-CS/CT-TBP
$[I$-∗-$I_2]^-$: **2-25**	0.0508	0.0045	–0.0119	0.0128	159.1	183.8	14.7	*r*-CS/CT-TBP
$[Cl$-∗-$BrCl]^-$: **2-26**	0.0758	0.0097	–0.0224	0.0244	156.5	183.2	6.3	*r*-CS/CT-TBP
$[Br$-∗-$ClBr]^-$: **2-27**	0.0721	0.0103	–0.0178	0.0205	150.0	181.5	12.4	*r*-CS/CT-TBP
$[Cl$-∗-$ICl]^-$: **2-28**	0.0652	0.0080	–0.0199	0.0214	158.0	178.9	0.3	*r*-CS/CT-MC
$[Br$-∗-$IBr]^-$: **2-29**	0.0590	0.0060	–0.0165	0.0176	159.9	182.8	5.4	*r*-CS/CT-TBP
Me_2ClS-∗-Cl: **2-30**	0.0971	0.0044	–0.0369	0.0372	173.1	191.8	5.1	*r*-CS/CT-TBP
Me_2BrS-∗-Br: **2-31**	0.0802	0.0047	–0.0253	0.0257	169.5	188.7	7.4	*r*-CS/CT-TBP
Me_2ClSe-∗-Cl: **2-32**	0.0868	0.0047	–0.0341	0.0344	172.2	184.3	1.5	*r*-CS/CT-TBP
Me_2BrSe-∗-Br: **2-33**	0.0749	0.0030	–0.0259	0.0260	173.3	187.3	3.9	*r*-CS/CT-TBP
Me_2ClTe-∗-Cl: **2-34**	0.0774	0.0078	–0.0303	0.0313	165.5	160.5	28.8	*r*-CS/CT-MC
Me_2BrTe-∗-Br: **2-35**	0.0697	0.0033	–0.0264	0.0266	172.8	177.2	10.0	*r*-CS/CT-MC
Me_2ITe-∗I: **2-36**	0.0596	0.0012	–0.0193	0.0193	176.5	187.8	6.2	*r*-CS/CT-TBP
Me_2S^+-∗-Cl: **2-37**	0.1719	–0.0244	–0.1206	0.1230	191.5	198.2	0.4	SS/Cov-w
Me_2S^+-∗-Br: **2-38**	0.1390	–0.0110	–0.0788	0.0796	187.9	193.8	0.3	SS/Cov-w
Me_2S^+-∗-I: **2-39**	0.1069	–0.0014	–0.0537	0.0537	181.5	179.5	7.4	SS/Cov-w
Me_2Se^+-∗-Cl: **2-40**	0.1387	–0.0077	–0.0855	0.0858	185.2	185.4	1.5	SS/Cov-w
Me_2Se^+-∗-Br: **2-41**	0.1192	–0.0082	–0.0627	0.0632	187.5	190.7	0.5	SS/Cov-w
Me_2Se^+-∗-I: **2-42**	0.0983	–0.0048	–0.0474	0.0477	185.7	188.0	3.2	SS/Cov-w
Me_2Te^+-∗-Cl: **2-43**	0.1108	0.0120	–0.0548	0.0561	167.7	145.1	8.3	*r*-CS/*t*-HB$_{wc}$
Me_2Te^+-∗-Br: **2-44**	0.1007	0.0004	–0.0507	0.0507	179.6	165.7	14.1	*r*-CS/CT-MC
Me_2Te^+-∗-I: **2-45**	0.0866	–0.0049	–0.0395	0.0398	187.1	189.5	3.6	SS/Cov-w
Cl-∗-Cl: **2-46**	0.1641	–0.0087	–0.0985	0.0988	185.0	194.2	0.6	SS/Cov-w
Br-∗-Br: **2-47**	0.1154	–0.0044	–0.0574	0.0576	184.3	190.9	0.3	SS/Cov-w
I-∗-I: **2-48**	0.0825	–0.0022	–0.0343	0.0344	183.7	190.9	0.5	SS/Cov-w
H_3C-∗-Cl: **2-49**	0.1907	–0.0376	–0.1468	0.1515	194.4	198.4	0.2	SS/Cov-w
H_3C-∗-Br: **2-50**	0.1564	–0.0226	–0.0997	0.1022	192.8	195.9	0.3	SS/Cov-w
H_3C-∗-I: **2-51**	0.1267	–0.0109	–0.0758	0.0766	188.2	180.7	9.0	SS/Cov-w
H_3C-∗-CH_3: **2-52**	0.2445	–0.0718	–0.2097	0.2217	198.9	201.1	0.1	SS/Cov-s
H_2C-∗-CH_2: **2-53**	0.3496	–0.1345	–0.4226	0.4435	197.7	199.6	0.0	SS/Cov-s
HC-∗-CH: **2-54**	0.4077	–0.1529	–0.6048	0.6238	194.2	196.0	0.0	SS/Cov-s
H_3C-∗-H: **2-55**	0.2821	–0.1265	–0.3075	0.3325	202.4	202.3	0.1	SS/Cov-s
H-∗-H: **2-56**	0.2733	–0.1544	–0.3154	0.3512	206.1	206.4	0.0	SS/Cov-s

[a] Data are given for the interaction in question at the BCP. [b] The 6-311++G(3df,3pd) is applied to 1–4th period elements, together with the Sapporo-TZPsp for fifth period ones. [c] $c\nabla^2\rho_b(\boldsymbol{r}_c) = H_b(\boldsymbol{r}_c) - V_b(\boldsymbol{r}_c)/2$, where $c = \hbar^2/8m$. [d] $R = (x^2 + y^2)^{1/2}$, where $(x, y) = (H_b(\boldsymbol{r}_c) - V_b(\boldsymbol{r}_c)/2, H_b(\boldsymbol{r}_c))$. [e] $\theta = 90^o - \tan^{-1}(y/x)$. [f] $\theta_p = 90^o - \tan^{-1}(dy/dx)$. [g] $\kappa_p = |d^2y/dx^2|/[1 + (dy/dx)^2]^{3/2}$.

Table 2-A2. QTAIM functions and QTAIM-DFA parameters for **2-1**–**2-56**, evaluated with MP2/(aug-cc-pVTZ + Sapporo-TZPsp), by employing the perturbed structures generated with POM.[a,b]

X-∗-Y: species	$\rho_b(\boldsymbol{r}_c)$ (au)	$c\nabla^2\rho_b(\boldsymbol{r}_c)$[c] (au)	$H_b(\boldsymbol{r}_c)$ (au)	R[d] (au)	θ[e] (º)	θ_p[f] (º)	κ_p[g] (au^{-1})	Predicted nature
He-∗-HF: **2-1**	0.0033	0.0023	0.0013	0.0026	59.9	64.0	72.0	*p*-CS/vdW
Ne-∗-HF: **2-2**	0.0061	0.0038	0.0013	0.0041	71.0	78.9	15.7	*p*-CS/vdW
Ar-∗-HF: **2-3**	0.0088	0.0043	0.0015	0.0046	70.9	88.0	193.3	*p*-CS/vdW
Kr-∗-HF: **2-4**	0.0117	0.0047	0.0008	0.0048	80.0	111.9	265.3	*p*-CS/*t*-HB_{nc}
Xe-∗-HF: **2-5**	0.0156	0.0048	–0.0002	0.0048	92.4	136.6	281.3	*r*-CS/*t*-HB_{wc}
NN-∗-HF: **2-6**	0.0183	0.0079	0.0006	0.0079	85.6	132.8	176.0	*p*-CS/*t*-HB_{nc}
HF-∗-HF: **2-7**	0.0251	0.0122	0.0000	0.0122	90.0	131.4	94.9	*p*-CS/*t*-HB_{nc}
HCN-∗-HF: **2-8**	0.0332	0.0101	–0.0054	0.0115	118.2	163.2	25.7	*r*-CS/CT-MC
H_2O-∗-HOH: **2-9**	0.0247	0.0102	–0.0004	0.0102	92.3	136.9	128.0	*r*-CS/*t*-HB_{wc}
Me_2O-∗-HOH: **2-10**	0.0322	0.0114	–0.0035	0.0119	107.0	155.7	45.1	*r*-CS/CT-MC
Me_2O-∗-Cl_2: **2-11**	0.0268	0.0130	0.0018	0.0131	82.0	103.3	69.4	*p*-CS/*t*-HB_{nc}
Me_2O-∗-Br_2: **2-12**	0.0334	0.0141	0.0000	0.0141	90.2	119.4	85.3	*r*-CS/*t*-HB_{wc}
Me_2O-∗-I_2: **2-13**	0.0341	0.0121	–0.0019	0.0123	99.0	136.9	84.7	*r*-CS/*t*-HB_{wc}
Me_2S-∗-Cl_2: **2-14**	0.0521	0.0107	–0.0095	0.0143	131.6	172.1	29.5	*r*-CS/CT-MC
Me_2S-∗-Br_2: **2-15**	0.0521	0.0093	–0.0104	0.0139	138.2	173.1	24.3	*r*-CS/CT-MC
Me_2S-∗-I_2: **2-16**	0.0407	0.0071	–0.0072	0.0101	135.4	173.6	31.9	*r*-CS/CT-MC
Me_2Se-∗-Cl_2: **2-17**	0.0633	0.0091	–0.0149	0.0175	148.6	179.3	9.1	*r*-CS/CT-MC
Me_2Se-∗-Br_2: **2-18**	0.0545	0.0078	–0.0116	0.0140	146.0	176.2	17.6	*r*-CS/CT-MC
Me_2Se-∗-I_2: **2-19**	0.0413	0.0060	–0.0076	0.0097	141.8	175.8	25.8	*r*-CS/CT-MC
Me_2Te-∗-Cl_2: **2-20**	0.0718	0.0047	–0.0243	0.0247	169.1	183.8	1.5	*r*-CS/CT-TBP
Me_2Te-∗-Br_2**: 2- 1**	0.0603	0.0046	–0.0168	0.0175	164.7	185.3	6.2	*r*-CS/CT-TBP
Me_2Te-∗-I_2: **2-22**	0.0422	0.0044	–0.0084	0.0095	152.4	182.6	19.0	*r*-CS/CT-TBP
$[Cl$-∗-$Cl_2]^-$: **2-23**	0.0843	0.0125	–0.0246	0.0276	153.0	179.3	11.5	*r*-CS/CT-MC
$[Br$-∗-$Br_2]^-$: **2-24**	0.0669	0.0084	–0.0173	0.0192	154.1	178.8	15.4	*r*-CS/CT-MC
$[I$-∗-$I_2]^-$: **2-25**	0.0508	0.0045	–0.0119	0.0128	159.1	183.8	14.7	*r*-CS/CT-TBP
$[Cl$-∗-$BrCl]^-$**: 2-26**	0.0762	0.0102	–0.0227	0.0249	155.8	180.5	9.3	*r*-CS/CT-TBP
$[Br$-∗-$ClBr]^-$**: 2-27**	0.0726	0.0104	–0.0187	0.0214	150.8	177.1	16.8	*r*-CS/CT-MC
$[Cl$-∗-$ICl]^-$: **2-28**	0.0674	0.0077	–0.0228	0.0240	161.2	178.5	2.4	*r*-CS/CT-MC
$[Br$-∗-$IBr]^-$: **2-29**	0.0597	0.0059	–0.0172	0.0182	161.0	181.7	5.8	*r*-CS/CT-TBP
Me_2ClS-∗-Cl: **2-30**	0.0958	0.0041	–0.0370	0.0372	173.6	191.1	7.0	*r*-CS/CT-TBP
Me_2BrS-∗-Br: **2-31**	0.0808	0.0047	–0.0260	0.0264	169.7	187.6	7.6	*r*-CS/CT-TBP
Me_2ClSe-∗-Cl: **2-32**	0.0867	0.0047	–0.0342	0.0345	172.2	186.1	2.7	*r*-CS/CT-TBP
Me_2BrSe-∗-Br: **2-33**	0.0755	0.0040	–0.0251	0.0254	170.9	186.4	8.5	*r*-CS/CT-TBP
Me_2ClTe-∗-Cl: **2-34**	0.0789	0.0080	–0.0325	0.0335	166.3	159.5	25.1	*r*-CS/CT-MC
Me_2BrTe-∗-Br: **2-35**	0.0702	0.0032	–0.0268	0.0270	173.1	176.5	10.8	*r*-CS/CT-MC
Me_2ITe-∗I: **2-36**	0.0600	0.0011	–0.0196	0.0197	176.7	187.6	12.9	*r*-CS/CT-TBP
Me_2S^+-∗-Cl: **2-37**	0.1658	–0.0201	–0.1085	0.1103	190.5	197.7	0.6	SS/Cov-w
Me_2S^+-∗-Br: **2-38**	0.1377	–0.0097	–0.0757	0.0763	187.3	194.0	0.6	SS/Cov-w
Me_2S^+-∗-I: **2-39**	0.1081	–0.0017	–0.0562	0.0562	181.7	177.7	8.5	SS/Cov-w
Me_2Se^+-∗-Cl: **2-40**	0.1372	–0.0079	–0.0829	0.0833	185.5	186.1	2.9	SS/Cov-w
Me_2Se^+-∗-Br: **2-41**	0.1189	–0.0067	–0.0606	0.0609	186.3	192.1	0.1	SS/Cov-w
Me_2Se^+-∗-I: **2-42**	0.0981	–0.0041	–0.0467	0.0469	185.0	187.9	2.8	SS/Cov-w
Me_2Te^+-∗-Cl: **2-43**	0.1114	0.0120	–0.0567	0.0580	168.0	144.1	8.5	*r*-CS/*t*-HB_{wc}
Me_2Te^+-∗-Br: **2-44**	0.1004	0.0005	–0.0500	0.0500	179.5	165.5	14.9	*r*-CS/CT-MC
Me_2Te^+-∗-I: **2-45**	0.0873	–0.0051	–0.0403	0.0407	187.3	189.6	3.3	SS/Cov-w
Cl-∗-Cl: **2-46**	0.1582	–0.0049	–0.0872	0.0873	183.2	193.0	1.2	SS/Cov-w
Br-∗-Br: **2-47**	0.1132	–0.0013	–0.0517	0.0517	181.4	190.6	1.6	SS/Cov-w
I-∗-I: **2-48**	0.0825	–0.0022	–0.0343	0.0344	183.7	190.9	0.5	SS/Cov-w
H_3C-∗-Cl: **2-49**	0.1848	–0.0333	–0.1352	0.1392	193.8	199.0	0.3	SS/Cov-w
H_3C-∗-Br: **2-50**	0.1556	–0.0199	–0.0949	0.0969	191.8	196.3	0.1	SS/Cov-w
H_3C-∗-I: **2-51**	0.1265	–0.0092	–0.0725	0.0730	187.2	177.7	11.3	SS/Cov-w
H_3C-∗-CH_3: **2-52**	0.2461	–0.0787	–0.2227	0.2362	199.5	202.0	0.0	SS/Cov-s
H_2C-∗-CH_2: **2-53**	0.3549	–0.1578	–0.4696	0.4954	198.6	200.0	0.1	SS/Cov-s
HC-∗-CH: **2-54**[h]								
H_3C-∗-H: **2-55**	0.2845	–0.1388	–0.3298	0.3578	202.8	202.6	0.2	SS/Cov-s
H-∗-H: **2-56**	0.2724	–0.1548	–0.3161	0.3520	206.1	206.3	0.0	SS/Cov-s

[a] Data are given for the interaction in question at the BCP. [b] The 6-311++G(3df,3pd) is applied to 1–4th period elements, together with the Sapporo-TZPsp for fifth period ones. [c] $c\nabla^2\rho_b(\boldsymbol{r}_c) = H_b(\boldsymbol{r}_c) - V_b(\boldsymbol{r}_c)/2$, where $c = \hbar^2/8m$. [d] $R = (x^2 + y^2)^{1/2}$, where $(x, y) = (H_b(\boldsymbol{r}_c) - V_b(\boldsymbol{r}_c)/2, H_b(\boldsymbol{r}_c))$. [e] $\theta = 90^o - \tan^{-1}(y/x)$. [f] $\theta_p = 90^o - \tan^{-1}(dy/dx)$. [g] $\kappa_p = |d^2y/dx^2|/[1 + (dy/dx)^2]^{3/2}$. [h] The (3, −3) attractor appeared at the center of the species.

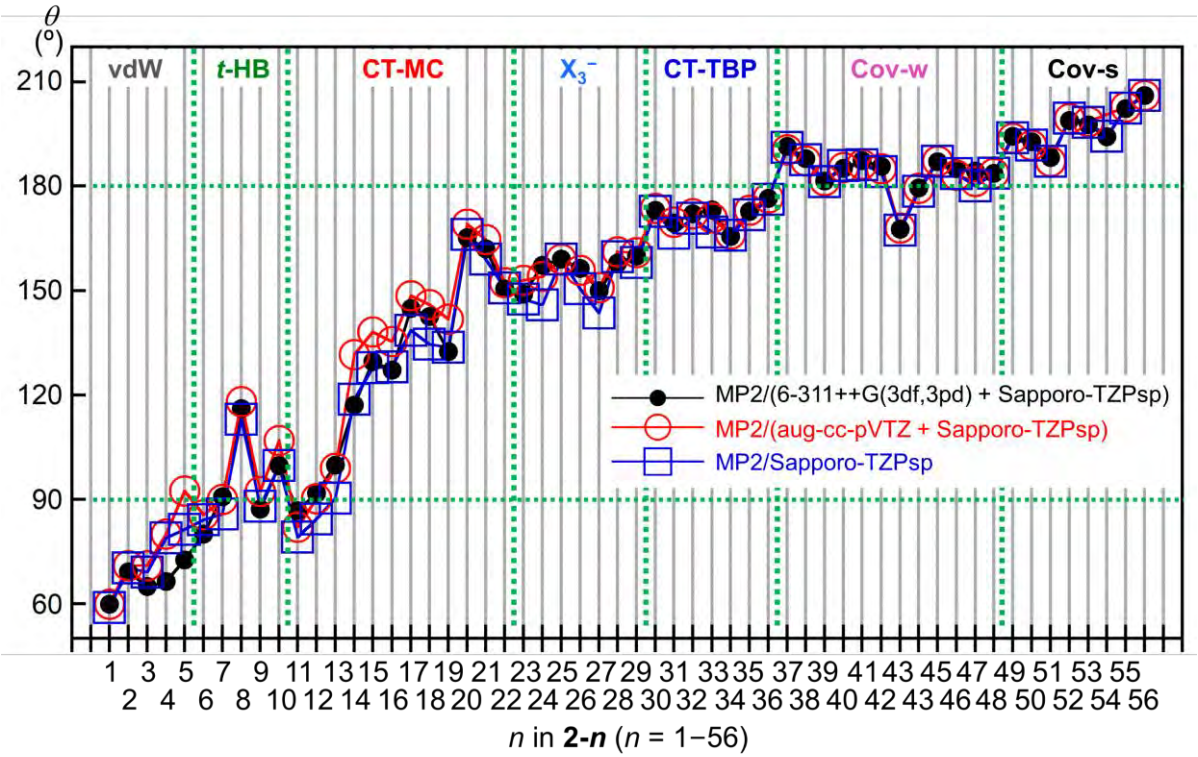

Figure 2-A1. Plots of θ versus n in **2-*n*** (n = 1–56), evaluated with MP2/(6-311++G(3df,3pd) + Sapporo-TZPsp), MP2/(aug-cc-pVTZ + Sapporo-TZPsp), and MP2/Sapporo-TZPsp.

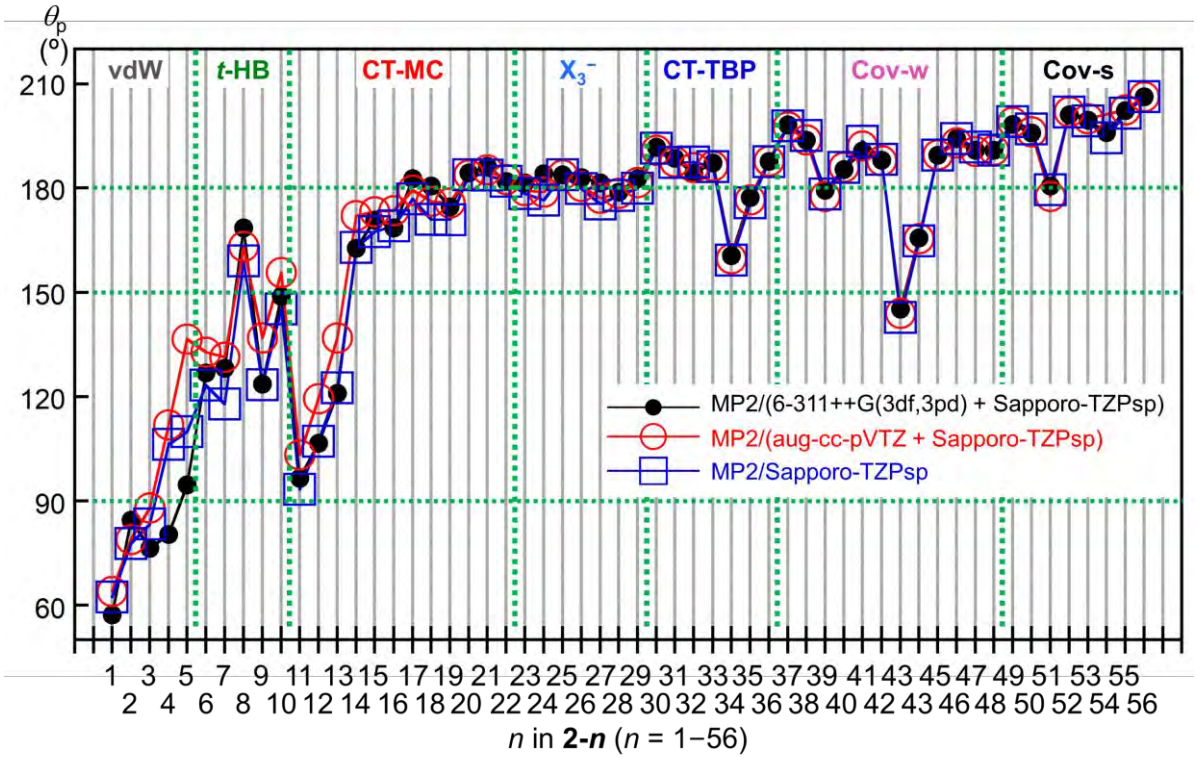

Figure 2-A2. Plots of θ_p versus n in **2-*n*** (n = 1–56), evaluated with MP2/(6-311++G(3df,3pd) + Sapporo-TZPsp), MP2/(aug-cc-pVTZ + Sapporo-TZPsp), and MP2/Sapporo-TZPsp.

References and Notes

1. R. F. W. Bader, *Atoms in Molecules. A Quantum Theory*; Oxford University Press, Oxford, UK, **1990**.
2. C. F. Matta, R. J. Boyd, *An Introduction to the Quantum Theory of Atoms in Molecules* in *The Quantum Theory of Atoms in Molecules: From Solid State to DNA and Drug Design* (Eds.: C. F. Matta, R. J. Boyd), WILEY-VCH: Weinheim, Germany, **2007**, Ch. 1.
3. Dots are usually employed to show BCPs in molecular graphs. Therefore, A-•-B would be more suitable to describe the BP with a BCP. Nevertheless, notation for A-∗-B is employed to emphasize the existence of a BCP on the BP in question in this thesis.
4. M. Nishio, *Cryst. Eng. Commun.* **2004**, *6*, 130–158.
5. R. J. Boyd, S. C. Choi, *Chem. Phys. Lett.* **1986**, *129*, 62–65.
6. M. T. Carroll, R. F. W. Bader, *Mol. Phys.* **1988**, *65*, 695–722.
7. S. J. Grabowski, *J. Phys. Chem. A* **2001**, *105*, 10739–10746.
8. M. Domagała, S. J. Grabowski, K. Urbaniak, G. Mlostoń, *J. Phys. Chem. A* **2003**, *107*, 2730–2736.
9. S. J. Grabowski, W. A. Sokalski, J. Leszczynski, *J. Phys. Chem. A* **2005**, *109*, 4331–4341.
10. M. Domagała, S. J. Grabowski, *J. Phys. Chem. A* **2005**, *109*, 5683–5688.
11. E. Espinosa, I. Alkorta, J. Elguero, E. Molins, *J. Chem. Phys.* **2002**, *117*, 5529–5542.
12. I. Rozas, I. Alkorta. J. Elguero, *J. Am. Chem. Soc.* **2000**, *122*, 11154–11161.
13. R. F. W. Bader, T. S. Slee. D. Cremer, E. Kraka, *J. Am. Chem. Soc.* **1983**, *105*, 5061–5068.
14. R. F. W. Bader, *Chem. Rev.* **1991**, *91*, 893–926.
15. R. F. W. Bader, *J. Phys. Chem. A* **1998**, *102*, 7314–7323.
16. F. Biegler-König, R. F. W. Bader, T. H. Tang, *J. Comput. Chem.* **1982**, *3*, 317–328.
17. R. F. W. Bader, *Acc. Chem. Res.* **1985**, *18*, 9–15.
18. T. H. Tang, R. F. W. Bader, P. MacDougall, *Inorg. Chem.* **1985**, *24*, 2047–2053.
19. F. Biegler-König, J. Schönbohm, D. Bayles, *J. Comput. Chem*. **2001**, *22*, 545–559.
20. F. Biegler-König, J. Schönbohm, *J. Comput. Chem.* **2002**, *23*, 1489–1494.
21. W. Nakanishi, T. Nakamoto, S. Hayashi, T. Sasamori, N. Tokitoh, *Chem. Eur. J.* **2007**, *13*, 255–268.
22. W. Nakanishi, S. Hayashi, K. Narahara, *J. Phys. Chem. A* **2009**, *113*, 10050–10057.
23. W. Nakanishi, S. Hayashi, K. Narahara, *J. Phys. Chem. A* **2008**, *112*, 13593–13599.
24. W. Nakanishi, S. Hayashi, *Curr. Org. Chem.* **2010**, *14*, 181–197.
25. W. Nakanishi, S. Hayashi, *J. Phys. Chem. A* **2010**, *114*, 7423–7430.
26. W. Nakanishi, S. Hayashi, K. Matsuiwa, M. Kitamoto, *Bull. Chem. Soc. Jpn.* **2012**, *85*, 1293–1305.
27. W. Grimme, J. Wortmann, D. Frowein, J. Lex, G. Chen, R. Gleiter, *J. Chem. Soc., Perkin Trans. 2* **1998,** 1893–1900.
28. C.-T. Lin, N.-J. Wang, Y.-L. Yeh, T.-C. Chou, Tetrahedron, **1995**, *51*, 2907–2928.
29. R. Bianchi, G. Gervasio, D. Marabello, *C. R. Chim.* **2005**, *8*, 1392–1399.

30. W. Nakanishi, S. Hayashi, R, Imanaka, T. Nishide, E. Tanaka, H. Matsuoka, *Int. J. Mol. Sci.* **2023**, *24*, 2798.
31. S. Hayashi, T. Nishide, K. Ueda, K. Hayama, W. Nakanishi, *ChemistrySelect* **2019**, *4*, 6198–6208.
32. W. Nakanishi, S. Hayashi, T. Nishide, S. Otsuki, *Int. J. Quantum Chem.* **2019**, *120*, e26073.
33. W. Nakanishi, S. Hayashi, *Int. J. Quantum Chem.* **2018**, *118*, e25590.
34. K. Brandhorst, J. Grunenberg, *Chem. Soc. Rev.* **2008**, *37*, 1558–1567.
35. K. Brandhorst, J. Grunenberg, *J. Chem. Phys*. **2010**, *132*, 184101.
36. Compliance 3.0.2 program is available online: http://www.oc.tu-s.de/Grunenberg/compliance.html (accessed on 27 September 2023).

Chapter 3

Intrinsic Dynamic Nature of Neutral Hydrogen Bonds Elucidated with QTAIM Dual Functional Analysis: Role of the Compliance Force Constants and QTAIM-DFA Parameters in Stability

Abstract

The dynamic and static nature of various neutral hydrogen bonds (nHBs) is elucidated with quantum theory of atoms-in-molecules dual functional analysis (QTAIM-DFA). The perturbed structures generated by using the coordinates derived from the compliance force constants (C_{ii}) of internal vibrations are employed for QTAIM-DFA. The method is called CIV. The dynamic nature of CIV is described as the "intrinsic dynamic nature," as the coordinates are invariant to the choice of the coordinate system. The nHBs are, for example, predicted to be van der Waals (H_2Se-∗-HSeH), *t*-HB_{nc} (typical-HBs with no covalency: HI-∗-HI), *t*-HB_{wc} (*t*-HBs with covalency: H_2C=O-∗-HI), CT-MC (molecular complexes formation through charge transfer (CT): H_2C=O-∗-HF), and CT-TBP (trigonal bipyramidal adducts formation through CT: H_3N-∗-HI) in nature. The results with CIV were the same as those with partial optimization method (POM) in the calculation errors. The highly excellent applicability of CIV for QTAIM-DFA was demonstrated for the various nHBs, as well as for the standard interactions previously reported. The stability of the HBs, evaluated by stabilization energies (ΔE), is well correlated with C_{ii} ($\Delta E \times C_{ii}$ = constant value of –165.64), and the QTAIM parameters, although a few deviations were detected.

Introduction

Hydrogen bonds (HBs) are fundamentally important because of their ability to form molecular associations, which stabilizes a system in terms of energy; the direction of the interacting three atoms in B···H–Y (see Chart 3-1) is controlled through the formation of a HB that is almost a linear asymmetric σ bond (3c–4e: three-center four-electron bond).[1–6] Weak HBs can be considered to be van der Waals (vdW) interactions, whereas strong HBs tend to be more covalent (Cov) in nature. The formation of HBs plays a crucial role in all fields of chemical and biological sciences. HBs control various chemical processes depending on their strength. It is imperative to clarify the nature of HBs for better understanding of chemical processes controlled by HBs.[7–11] Nakanishi et al. previously reported the dynamic and static nature of HBs in the neutral and charged forms by the quantum theory of atoms-in-molecules dual functional analysis (QTAIM-DFA).[10,12–17] The QTAIM-DFA has employed the perturbed structures generated by using the normal coordinates of the internal vibrations and/or by partial optimization method,[18–25] which are called NIV[15–17] and POM[12–14], respectively. Neutral HBs (nHBs) are predicted to be vdW to CT-TBP (trigonal bipyramidal adducts formation through charge transfer (CT)) in nature, whereas charged HBs are typically Cov in nature.[10]

Recently, a new method to generate the perturbed structures, called CIV, was proposed within the framework of QTAIM-DFA.[26] The method employs the coordinates corresponding to the compliance force constants (C_{ii}) for the internal vibrations.[27–32]

The very high applicability of CIV is demonstrated to generate the perturbed structures for QTAIM-DFA.[26] The dynamic nature of the interactions based on the perturbed structures with CIV is described as the "intrinsic dynamic nature of interactions," as the coordinates corresponding to C_{ii} are invariant to the choice of the coordinate system. The results with CIV are the same as those with POM in terms of the calculation errors. However, CIV has been applied only to the typical interactions of a limited number of HBs, and the default in NIV seems large for HBs.[26] The establishment of QTAIM-DFA on the firm basis of employing the perturbed structures with CIV for the wide range of nHBs is another purpose of this work. The neutral HBs in the species examined in this work are denoted by B-∗-HY (**3-1**–**3-29**), containing HI adducts, as shown in Chart 3-1.

B-∗-HY (**3-*n*** (*n* = 1–29)) [B---H—Y]

B = H_2Se, H_2S, H_2O, H_2CO, H_3N, and HX (X = I, Br, Cl, and F)
Y = SeH, SH, OH, NH_2, I, Br, Cl, and F

Chart 3-1. Species for neutral hydrogen bonds.

Herein, the author presents the results of investigations on the "intrinsic dynamic nature of nHBs," together with the static nature in B-∗-HY (**3-1**–**3-29**). To elucidate the nature, QTAIM-DFA is applied to B-∗-HY (**3-1**–**3-29**) by employing the perturbed structures generated with CIV. The applicability of CIV to QTAIM-DFA is also established in the nHBs of **3-1**–**3-29**, for which the QTAIM-DFA parameters elucidated by using CIV are compared with those elucidated by using NIV and POM. As a result, a firm basis for QTAIM-DFA by employing the perturbed structures generated with CIV is established over the wide range of the nHBs in **3-1**–**3-29**. The stability of **3-1**–**3-29** is discussed by examining the relations between the stability and the C_{ii}, (R, θ), and (θ_p, κ_p) values.

QTAIM-DFA is explained in Chapter 2, together with the methods to generate the perturbed structures, POM, NIV, and CIV. The basic concept of the QTAIM approach is also illustrated in Chapter 2.

Methodological Details in Calculations

The 6-311++G(3df,3pd) basis sets of the Gaussian 09 programs[33] were employed for the calculations of **3-1**–**3-29**, together with the basis set of the (7433111/743111/7411/2 + 1s1p1d1f) type for I, as implemented in the Sapporo Basis Set Factory.[34] The basis set system is called BSS-A. All calculations were performed under nonrelativistic conditions. The Møller-Plesset second-order energy correlation (MP2) level[35–37] was applied to the calculations (MP2/BSS-A). The optimized structures were confirmed by frequency analysis.

QTAIM functions are calculated by using the same basis sets at the MP2 level as in the optimizations (MP2/BSS-A) and are analyzed with the AIM2000 program.[38,39]

Results and Discussion

Optimized Structures of Neutral Hydrogen-Bonded Species and Stability

Neutral HB species for **3-1**–**3-29** were optimized with MP2/BSS-A, although some were optimized in a previous study.[10] The optimized B–H distances [r_o(B, H)] are collected in Table 3-A1 of the Appendix, together with the sum of the vdW radii[40] [$\Delta r = r_o(B, H) - \sum r_{vdW}(B, H)$]. Negative Δr values ($r_o(B, H) < \sum r_{vdW}(B, H)$) are obtained for **3-1**–**3-29**; thus, it is implied that the attractive interactions between B and H atoms in question formed. The energies for **3-1**–**3-29** on the energy surface (E) and the relative energies from the components (ΔE) [= E(HB) – E(components)] are collected in Table 3-1 of the Appendix. The ΔE values are plotted versus Δr for **3-1**–**3-29**. The plot is shown in Figure 3-1. The correlation is $\Delta E = 1.21 + 32.41 \times \Delta r$ ($R_c^2 = 0.876$) if the data for H_3N-∗-HF are omitted. The results show that the HB adducts become more stable as the distances are shortened, although H_3N-∗-HF is much more stable than that expected from the correlation.

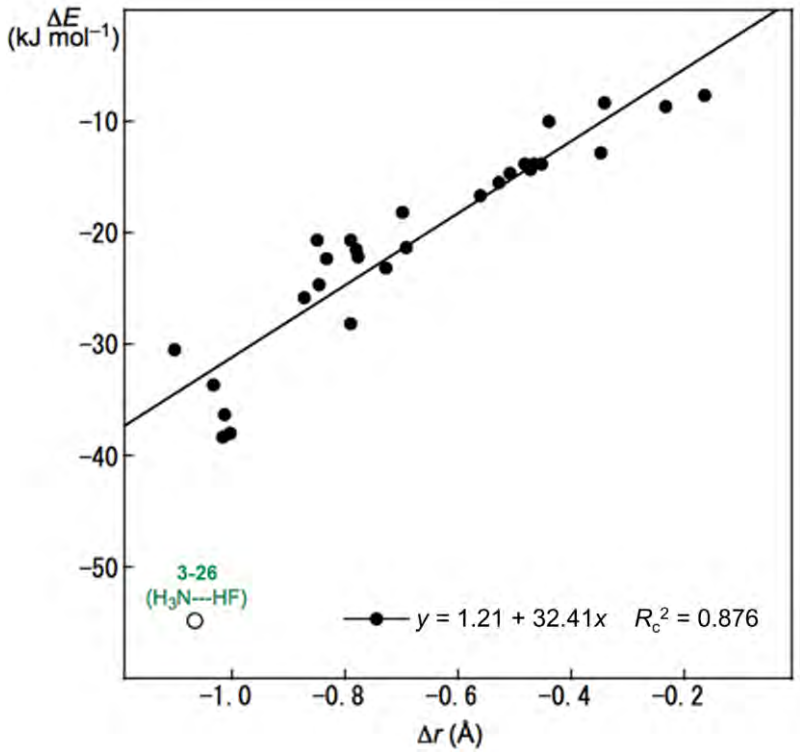

Figure 3-1. Plot of ΔE versus Δr for **3-1**–**3-29**.

Table 3-1. QTAIM functions and QTAIM-DFA parameters evaluated for the neutral hydrogen bonds (nHBs) in **3-1**–**3-29** by applying the QTAIM-DFA by employing the perturbed structures generated with CIV, NIV, and POM.[a,b]

Species (X-∗-Y)	$\rho_b(\boldsymbol{r}_c)$ (au)	$c\nabla^2\rho_b(\boldsymbol{r}_c)$[c] (au)	$H_b(\boldsymbol{r}_c)$ (au)	$k_b(\boldsymbol{r}_c)$[d] (au)	R (au)	θ (au)	C_{ii}[e] (Å mdyn^{-1})	$\theta_{p:CIV}$ (º)	$\kappa_{p:CIV}$ (au^{-1})
H_2Se-∗-HSeH (**3-1**)	0.0090	0.0026	0.0006	–0.858	0.0027	*76.0*[f]	23.4	88.1	194
H_2S-∗-HSH (**3-2**)	0.0102	0.0032	0.0008	–0.861	0.0033	76.3	19.2	91.8	229
H_3N-∗-HNH_2 (**3-3**)	0.0146	0.0059	0.0016	–0.844	0.0062	74.9	12.1	87.5	188
H_2O-∗-HOH (**3-4**)	0.0244	0.0106	0.0005	–0.976	0.0107	87.3	6.4	123.7	159
H_3N-∗-HOH (**3-5**)	0.0291	0.0094	–0.0020	–1.096	0.0096	*102.1*[f]	5.5	157.3	87.3
HI-∗-HI (**3-6**)	0.0130	0.0034	0.0004	–0.945	0.0034	84.1	13.8	102.6	304
HBr-∗-HBr (**3-7**)	0.0113	0.0038	0.0010	–0.853	0.0039	75.6	17.9	91.4	269
HCl-∗-HCl (**3-8**)	0.0127	0.0049	0.0015	–0.828	0.0052	73.6	16.1	95.0	294
HF-∗-HF (**3-9**)	0.0250	0.0125	–0.0002	–1.007	0.0125	90.8	5.9	128.2	107
H_2Se-∗-HI (**3-10**)	0.0162	0.0040	0.0001	–0.986	0.0040	88.5	12.7	*126.5*[f]	464
H_2Se-∗-HBr (**3-11**)	0.0159	0.0040	0.0002	–0.978	0.0040	87.6	13.0	*130.1*[f]	488
H_2Se-∗-HCl (**3-12**)	0.0168	0.0044	0.0001	–0.989	0.0044	88.7	11.2	*137.3*[f]	431
H_2Se-∗-HF (**3-13**)	0.0212	0.0051	–0.0013	–1.113	0.0053	*104.3*[f]	7.3	164.5	146
H_2S-∗-HI (**3-14**)	0.0164	0.0043	0.0001	–0.991	0.0043	89.0	13.4	124.5	334
H_2S-∗-HBr (**3-15**)	0.0175	0.0047	–0.0001	–1.010	0.0047	91.1	12.0	133.9	309
H_2S-∗-HCl (**3-16**)	0.0186	0.0051	–0.0002	–1.024	0.0051	92.8	10.3	140.5	269
H_2S-∗-HF (**3-17**)	0.0238	0.0061	–0.0020	–1.143	0.0064	*108.5*[f]	6.6	165.1	120
H_2O-∗-HI (**3-18**)	0.0228	0.0091	0.0009	–0.949	0.0091	84.5	10.1	113.6	217
H_2O-∗-HBr (**3-19**)	0.0274	0.0103	–0.0006	–1.028	0.0103	93.2	8.2	138.6	182
H_2O-∗-HCl (**3-20**)	0.0303	0.0112	–0.0018	–1.072	0.0114	98.9	6.4	149.9	116
H_2O-∗-HF (**3-21**)	0.0417	0.0131	–0.0089	–1.252	0.0158	124.0	3.4	166.1	6.9
H_2C=O-∗-HI (**3-22**)	0.0295	0.0102	–0.0009	–1.044	0.0103	95.3	9.7	139.7	216
H_2C=O-∗-HBr (**3-23**)	0.0321	0.0108	–0.0022	–1.093	0.0111	*101.6*[f]	8.2	154.4	138
H_2C=O-∗-HCl (**3-24**)	0.0340	0.0115	–0.0032	–1.122	0.0119	*105.9*[f]	6.6	160.4	92.0
H_2C=O-∗-HF (**3-25**)	0.0431	0.0127	–0.0099	–1.279	0.0161	127.8	3.5	170.1	6.7
H_3N-∗-HI (**3-26**)	0.0674	0.0050	–0.0268	–1.728	0.0272	169.4	19.8	194.1	4.2
H_3N-∗-HBr (**3-27**)	0.0563	0.0069	–0.0189	–1.579	0.0201	160.0	7.9	190.3	6.4
H_3N-∗-HCl (**3-28**)	0.0513	0.0080	–0.0155	–1.492	0.0174	152.7	5.5	186.9	9.3
H_3N-∗-HF (**3-29**)	0.0547	0.0085	–0.0195	–1.533	0.0213	156.4	2.8	182.0	2.8

[a] The functions and parameters were evaluated at the BCPs of the nHBs in the fully optimized structures. [b] With MP2/6-311++G(3df,3pd), except for I, for which calculations were performed with (7433111/743111/7411/2 + 1s1p1d1f) from the Sapporo Basis Set Factory, which is called MP2/BSS-A. [c] $c\nabla^2\rho_b(\boldsymbol{r}_c) = H_b(\boldsymbol{r}_c) - V_b(\boldsymbol{r}_c)/2$, for which $c = \hbar^2/8m$. [d] $k_b(\boldsymbol{r}_c) = V_b(\boldsymbol{r}_c)/G_b(\boldsymbol{r}_c)$. [e] Compliance force constants. [f] Minor values that do not satisfy the characterization from the major ones are shown in italics. [g] Internal vibrational frequency corresponding to the interaction. [h] Force constant corresponding to the frequency. [i] From the components. [j] The nature of *r*-CS/CT-MC was predicted with NIV. [k] On the borderline area between *r*-CS/*t*-HB_{wc} and *r*-CS/CT-MC if evaluated with CIV and POM.

(Table 3-1 continued.)

Species (X-∗-Y)	$\theta_{p:POM}$ (º)	$\kappa_{p:POM}$ (au^{-1})	ν [g] (cm^{-1})	k_f [h] (mdyn $Å^{-1}$)	$\theta_{p:NIV}$ (º)	$\kappa_{p:NIV}$ (au^{-1})	ΔE [i] (kJ mol^{-1})	Predicted Nature
H_2Se-∗-HSeH (**3-1**)	88.0	202	41.8	0.016	88.3	196	–7.6	*p*-CS/vdW
H_2S-∗-HSH (**3-2**)	91.8	232	69.1	0.009	93.3	263	–8.7	*p*-CS/*t*-HB_{nc}
H_3N-∗-HNH_2 (**3-3**)	87.5	151	141.2	0.036	86.6	159	–13.8	*p*-CS/vdW
H_2O-∗-HOH (**3-4**)	123.8	159	188.1	0.043	116.7	158	–22.2	*p*-CS/*t*-HB_{nc}
H_3N-∗-HOH (**3-5**)	157.5	88.1	200.2	0.050	158.6	83.0	–28.2	*r*-CS/CT-MC
HI-∗-HI (**3-6**)	102.7	309	43.5	0.024	102.5	296	–12.9	*p*-CS/*t*-HB_{nc}
HBr-∗-HBr (**3-7**)	91.4	269	48.8	0.028	91.2	259	–8.3	*p*-CS/*t*-HB_{nc}
HCl-∗-HCl (**3-8**)	95.0	295	76.4	0.021	94.8	267	–10.0	*p*-CS/*t*-HB_{nc}
HF-∗-HF (**3-9**)	128.3	109	166.9	0.081	128.5	103	–20.7	*r*-CS/*t*-HB_{wc}
H_2Se-∗-HI (**3-10**)	*126.5* [f]	464	52.5	0.031	*126.4* [f]	454	–14.5	*p*-CS/*t*-HB_{nc}
H_2Se-∗-HBr (**3-11**)	130.0	498	57.9	0.044	*129.9* [f]	480	–13.9	*p*-CS/*t*-HB_{nc}
H_2Se-∗-HCl (**3-12**)	137.4	438	79.3	0.057	137.1	423	–15.5	*p*-CS/*t*-HB_{nc}
H_2Se-∗-HF (**3-13**)	164.5	151	123.0	0.101	163.9	144	–21.3	*r*-CS/CT-MC
H_2S-∗-HI (**3-14**)	124.3	340	68.2	0.017	*125.3* [f]	325	–13.9	*p*-CS/*t*-HB_{nc}
H_2S-∗-HBr (**3-15**)	133.9	317	77.5	0.028	134.3	301	–14.6	*r*-CS/*t*-HB_{wc}
H_2S-∗-HCl (**3-16**)	140.6	274	98.2	0.042	140.7	260	–16.6	*r*-CS/*t*-HB_{wc}
H_2S-∗-HF (**3-17**)	165.1	121	145.7	0.096	164.6	117	–23.2	*r*-CS/CT-MC
H_2O-∗-HI (**3-18**)	112.9	212	97.6	0.013	122.9	227	–18.1	*p*-CS/*t*-HB_{nc}
H_2O-∗-HBr (**3-19**)	138.1	186	119.6	0.034	140.7	168	–20.7	*r*-CS/*t*-HB_{wc}
H_2O-∗-HCl (**3-20**)	149.9	120	150.1	0.048	*152.0* [j]	104	–24.7	*r*-CS/*t*-HB_{wc} [k]
H_2O-∗-HF (**3-21**)	166.1	8.5	229.9	0.079	167.6	7.1	–38.4	*r*-CS/CT-MC
H_2C=O-∗-HI (**3-22**)	139.8	202	141.9	0.049	138.3	219	–21.5	*r*-CS/*t*-HB_{wc}
H_2C=O-∗-HBr (**3-23**)	154.5	135	152.0	0.070	152.8	140	–22.4	*r*-CS/CT-MC
H_2C=O-∗-HCl (**3-24**)	160.4	91.7	176.0	0.115	158.6	91.8	–25.9	*r*-CS/CT-MC
H_2C=O-∗-HF (**3-25**)	170.0	8.0	246.7	0.267	168.3	5.7	–36.3	*r*-CS/CT-MC
H_3N-∗-HI (**3-26**)	194.2	5.3	100.7	0.025	193.9	4.2	–30.5	*r*-CS/CT-TBP
H_3N-∗-HBr (**3-27**)	190.3	8.1	148.1	0.059	189.8	6.3	–33.7	*r*-CS/CT-TBP
H_3N-∗-HCl (**3-28**)	186.9	11.7	186.8	0.105	186.2	9.3	–38.0	*r*-CS/CT-TBP
H_3N-∗-HF (**3-29**)	181.9	5.4	227.0	0.241	180.6	1.8	–54.8	*r*-CS/CT-TBP

[a] The functions and parameters were evaluated at the BCPs of the nHBs in the fully optimized structures. [b] With MP2/6-311++G(3df,3pd), except for I, for which calculations were performed with (7433111/743111/7411/2 + 1s1p1d1f) from the Sapporo Basis Set Factory, which is called MP2/BSS-A. [c] $c\nabla^2\rho_b(\boldsymbol{r}_c) = H_b(\boldsymbol{r}_c) - V_b(\boldsymbol{r}_c)/2$, for which $c = \hbar^2/8m$. [d] $k_b(\boldsymbol{r}_c) = V_b(\boldsymbol{r}_c)/G_b(\boldsymbol{r}_c)$. [e] Compliance force constants. [f] Minor values that do not satisfy the characterization from the major ones are shown in italics. [g] Internal vibrational frequency corresponding to the interaction. [h] Force constant corresponding to the frequency. [i] From the components. [j] The nature of *r*-CS/CT-MC was predicted with NIV. [k] On the borderline area between *r*-CS/*t*-HB_{wc} and *r*-CS/CT-MC if evaluated with CIV and POM.

Trends of Δ*E* for B-∗-HX (B = H_2Se, H_2S, H_2C=O, and H_3N; X = F, Cl, Br, and I) versus H_2O-∗-HX

The Δ*E* values of B-∗-HX (B = H_2Se, H_2S, H_2C=O, and H_3N; HX = HF, HCl, HBr, and HI) are plotted versus those of H_2O-∗-HX. The plot is shown in Figure 3-2, which also contains the plot of Δ*E* (H_2O-∗-HX versus Δ*E*(H_2O-∗-HX) as a reference. The correlations are very good (Table 3-2, entries 1–4). The results show that the Δ*E* values of B-∗-HX (B = H_2Se, H_2S, H_2C=O, and H_3N) are well correlated with each other if the Δ*E* values of common HX are compared, although the Δ*E* value of H_2Se-∗-HI seems somewhat smaller (more stable) than that predicted from the correlation for H_2Se-∗-HX. The magnitudes of Δ*E* become larger in the order $H_2Se \leq H_2S << H_2O \leq H_2C$=O << H_3N, although Δ*E*(H_2O-∗-HF) < Δ*E*(H_2C=O-∗-HF). The relations of Δ*E* in B-∗-HX is also confirmed in this work for HX = HI in addition to HX = HF, HCl, and HBr, although the *E* values are all evaluated under nonrelativistic conditions.

Next, molecular graphs with contour plots of $\rho(\boldsymbol{r})$ are examined before detailed discussion of the nature of the nHBs in **3-1**–**3-29**.

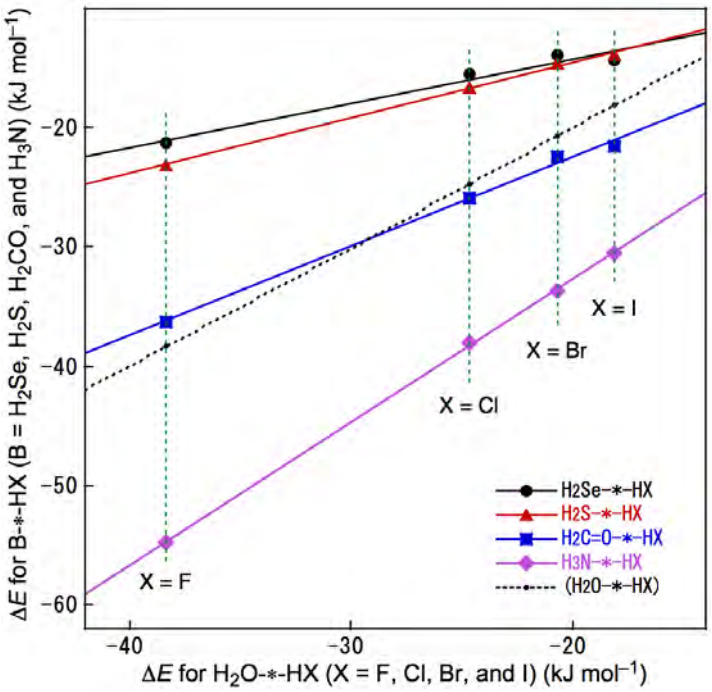

Figure 3-2. Plots of Δ*E* for B-∗-HX (B = H_2Se, H_2S, H_2C=O, and H_3N) versus those for H_2O-∗-HX (X = F, Cl, Br, and I), together with H_2O-∗-HX versus H_2O-∗-HX as a reference.

Table 3-2. Correlations in **3-1**–**3-29**, evaluated with NIV, POM, and CIV, under the MP2/BSS-A condition.[a]

Entry	Correlation	a	b	R_c^2	Correlation with n
1	$\Delta E_{H_2Se\text{-}HX}$ vs. $\Delta E_{H_2O\text{-}HX}$	0.371	–6.83	0.960	Fig. 3-2 (4)
2	$\Delta E_{H_2S\text{-}HX}$ vs. $\Delta E_{H_2O\text{-}HX}$	0.468	–5.13	0.997	Fig. 3-2 (4)
3	$\Delta E_{H_2CO\text{-}HX}$ vs. $\Delta E_{H_2O\text{-}HX}$	0.751	–7.39	0.996	Fig. 3-2 (4)
4	$\Delta E_{H_3N\text{-}HX}$ vs. $\Delta E_{H_2O\text{-}HX}$	1.200	–8.72	0.999_7	Fig. 3-2 (4)
5	$\theta_{p:NIV}$ vs. $\theta_{p:CIV}$	0.988	1.71	0.994	Fig. 3-5a (29)
6	$\theta_{p:NIV}$ vs. $\theta_{p:CIV}$	0.992	1.02	0.999	Fig. 3-5a (27[b])
7	$\theta_{p:POM}$ vs. $\theta_{p:CIV}$	1.001	–0.15	0.9999_7	Fig. 3-5b (29)
8	$\kappa_{p:NIV}$ vs. $\kappa_{p:CIV}$	0.980	–0.31	0.994	Fig. 3-6a (29)
9	$\kappa_{p:POM}$ vs. $\kappa_{p:CIV}$	1.009	–0.42	0.998	Fig. 3-6b (29)
10	ΔE vs. R	–2012.0	–3.83	0.866	Fig. 3-A1 (27[c])
11	ΔE vs. θ	–0.479	25.70	0.891	Fig. 3-8 (27[c])
12	$\theta_{p:CIV}$ vs. θ	2.390	–86.95	0.957	Fig. 3-A2 (23[d])
13	ΔE vs. $\theta_{p:CIV}$ (G(**A**))	–0.314	19.69	0.971	Fig. 3-9 (8[e])
14	ΔE vs. $\theta_{p:CIV}$ (G(**B**))	–0.219	14.01	0.957	Fig. 3-9 (8[f])
15	ΔE vs. $\theta_{p:CIV}$ (G(**C**))	–0.155	–0.05	0.838	Fig. 3-9 (6[g])
16	ΔE vs. $\theta_{p:CIV}$ (G(**D**))	1.994	–414.66	0.898	Fig. 3-9 (4[h])

[a] Analyzed by assuming the linear correlation $y = ax + b$ (R_c^2: square of correlation coefficient). [b] For **3-1**–**3-29**, except for **3-4** and **3-18**. [c] For **3-1**–**3-29**, except for **3-26** and **3-27**. [d] For **3-1**–**3-29**, except for **3-21**, **3-24**, and **3-25**–**3-29**. [e] For **3-1**–**3-9**, except for **3-3**. [f] For **3-10**–**3-17**. [g] For **3-18**–**3-25**, except for **3-21** and **3-25**. [h] For **3-24**–**3-29**.

Molecular Graphs with Contour Plots for B-∗-HX

Figure 3-3 illustrates molecular graphs for B-∗-HI (B = H_2Se, H_2S, H_2O, $H_2C{=}O$, H_3N, and HI) containing the contour plots of $\rho(\boldsymbol{r})$. All of the BCPs expected for B-∗-HI are clearly detected. They seem to be well located at three-dimensional saddle points of $\rho(\boldsymbol{r})$. The molecular graphs of **3-1**–**3-29**, other than B-∗-HI, were similarly drawn, and although they are not shown, they are very close to those of B-∗-HI.

The HB interactions seem straight for B-∗-HX based on the BPs, as shown in Figure 3-3. To examine the linearity of the BPs, further, the lengths of the BPs (r_{BP}) in question are collected in Table 3-A2 of the Appendix for **3-1**–**3-29**, together with the corresponding straight-line distances (R_{SL}). The differences between them ($\Delta r_{BP} = r_{BP} - R_{SL}$) are less than 0.04 Å. Consequently, the BPs for all B-∗-HY of **3-1**–**3-29** can be described by straight lines.

QTAIM functions were calculated for B-∗-HY (**3-1**–**3-29**) at the BCPs. Table 3-1 collects the $\rho_b(\boldsymbol{r}_c)$, $H_b(\boldsymbol{r}_c) - V_b(\boldsymbol{r}_c)/2$ $(= (\hbar^2/8m)\nabla^2\rho_b(\boldsymbol{r}_c))$, and $H_b(\boldsymbol{r}_c)$ values, whereas some were reported previously.[10] The $H_b(\boldsymbol{r}_c)$ values are plotted versus $H_b(\boldsymbol{r}_c) - V_b(\boldsymbol{r}_c)/2$ for the data shown in Table 3-1, together with those from the perturbed structures generated with CIV. Figure 3-4 shows the plots. The plots appear in the region of $H_b(\boldsymbol{r}_c) - V_b(\boldsymbol{r}_c)/2 > 0$; therefore, the HBs are all classified by closed-shell (CS) interactions. The behavior of the nHBs in **3-1**–**3-29** will be discussed in detail after evaluations of the QTAIM-DFA parameters.

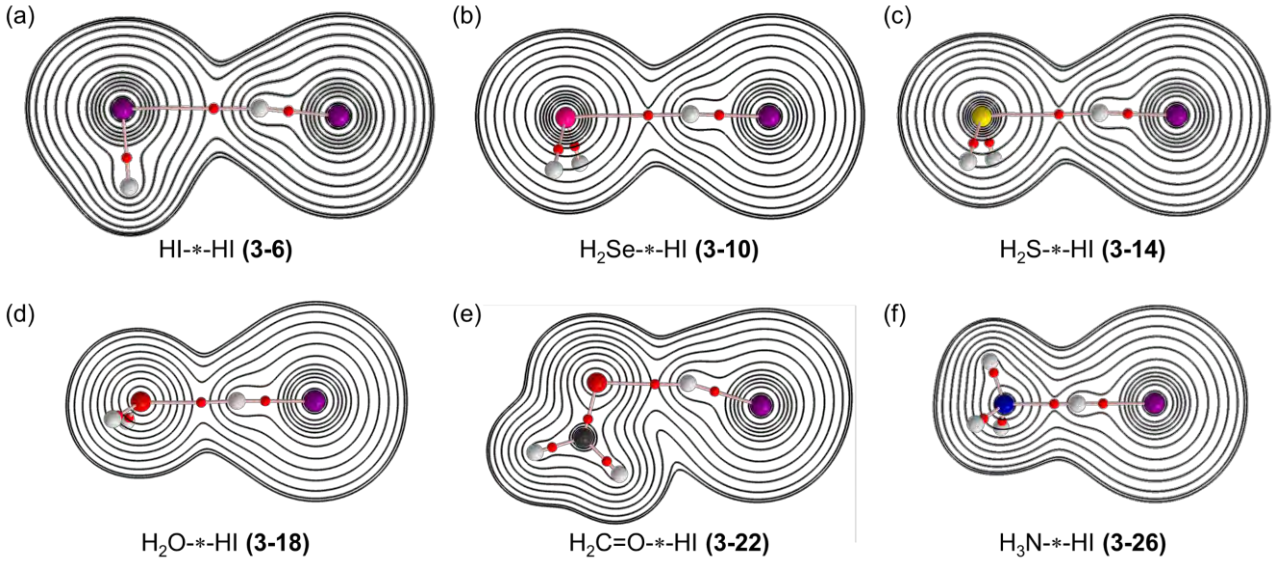

Figure 3-3. Molecular graphs with contour plots of $\rho(\boldsymbol{r})$ for HI-∗-HI (**3-6**) (a), H_2Se-∗-HI (**3-10**) (b), H_2S-∗-HI (**3-14**) (c), H_2O-∗-HI (**3-18**) (d), H_2C=O-∗-HI (**3-22**) (e), and H_3N-∗-HI (**3-26**) (f).

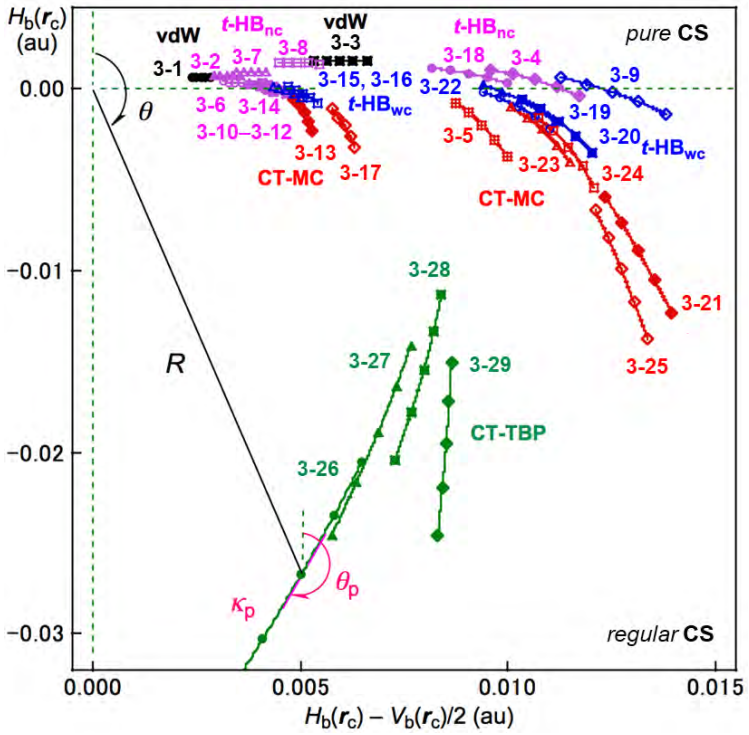

Figure 3-4. Plots of $H_b(\boldsymbol{r}_c)$ versus $H_b(\boldsymbol{r}_c) - V_b(\boldsymbol{r}_c)/2$ for **3-1**–**3-29**, for which data from the perturbed structures generated with CIV were employed, in addition to the data from the optimized structures. Definitions of (R, θ) and (θ_p, κ_p) are illustrated, as exemplified by H_3N-∗-HI (**3-26**).

QTAIM-DFA Parameters of (R, θ) and (θ_p, κ_p) for Neutral HBs in 3-1–3-29, Evaluated with POM, NIV, and CIV

The QTAIM-DFA parameters of (R, θ) and (θ_p, κ_p) were obtained by analyzing the plots of $H_b(\boldsymbol{r}_c)$ versus $H_b(\boldsymbol{r}_c) - V_b(\boldsymbol{r}_c)/2$. The ($\theta_p$, κ_p) values evaluated by employing the perturbed structures generated with CIV, POM, and NIV are denoted by ($\theta_{p:CIV}$, $\kappa_{p:CIV}$), ($\theta_{p:POM}$, $\kappa_{p:POM}$), and ($\theta_{p:NIV}$, $\kappa_{p:NIV}$), respectively. The ($\theta_{p:CIV}$, $\kappa_{p:CIV}$) values can be obtained if the plots shown in Figure 3-4 are analyzed. Table 3-1 collects the QTAIM-DFA parameters for **3-1**–**3-29**. Table 3-1 also contains the C_{ii} values for the nHBs in **3-1**–**3-29** together with the frequencies correlated to the NIVs employed to generate the perturbed structures and the force constants (k_f).

Behavior of $\theta_{p:CIV}$, $\theta_{p:POM}$, and $\theta_{p:NIV}$ Together with That of $\kappa_{p:CIV}$, $\kappa_{p:POM}$, and $\kappa_{p:NIV}$

Figure 3-5a shows the plot of $\theta_{p:NIV}$ versus $\theta_{p:CIV}$, which gives very good correlation. The correlation is shown in entry 5 of Table 3-2 (see also Figure 3-5a). The magnitudes of the differences between $\theta_{p:NIV}$ and $\theta_{p:CIV}$ ($\Delta\theta_{p:NIV–CIV} = \theta_{p:NIV} - \theta_{p:CIV}$) are less than 2.0º for most of the interactions. The magnitudes of $\Delta\theta_{p:NIV–CIV}$ are larger than 2.0º for H_2O-∗-HOH ($\Delta\theta_{p:NIV–CIV} = –7.0$º), H_2O-∗-HI (9.3º), H_2O-∗-HBr (2.1º), and H_2O-∗-HCl (2.1º). Large deviations are detected for H_2O-∗-HX (HX = HOH and HI). The selected internal vibration for H_2O-∗-HX could not be located effectively on O-∗-H by mixing with some other vibrational modes in the same symmetry,[26] although the selected mode is the best fit for the O-∗-H interaction. The correlation for the plot is much improved (Table 3-2, entry 6; see also Figure 3-5a) if the data for H_2O-∗-HX (X = HOH and HI) are omitted from the correlation. On the other hand, excellent correlation is obtained if $\theta_{p:POM}$ is plotted versus $\theta_{p:CIV}$, as shown in Figure 3-5b (for the correlation, also see Table 3-2, entry 7). The magnitudes of $\Delta\theta_{p:POM–CIV}$ are equal to or less than 0.1º for all HB adducts examined, except for H_3N-∗-HOH ($\Delta\theta_{p:POM–CIV} = 0.2$º), H_2S-∗-HI (–0.2º), H_2O-∗-HI (–0.7º), and H_2O-∗-HBr (–0.5º). The results must be a reflection of the fact that the perturbed structures generated with POM and CIV are very similar.[26] The results demonstrate the excellent applicability of CIV to generate the perturbed structures also for the nHB species in QTAIM-DFA.

Figures 3-6a and b show the plots of $\kappa_{p:NIV}$ versus $\kappa_{p:CIV}$ and $\kappa_{p:POM}$ versus $\kappa_{p:CIV}$, respectively. The correlations are given in entries 8 and 9 of Table 3-2 (see also Figures 3-6a and b, respectively). The correlations seem very good, although substantial deviations are observed in the plots. The magnitudes of $\Delta\kappa_{p:NIV–CIV}$ are larger than 10 au^{-1} for H_2S-∗-HSH ($\Delta\kappa_{p:NIV–CIV} = 34$ au^{-1}), H_3N-∗-HNH_2 (–29 au^{-1}), HBr-∗-HBr (–10 au^{-1}), HCl-∗-HCl (–27 au^{-1}), H_2O-∗-HI (10 au^{-1}), H_2O-∗-HBr (–14 au^{-1}), and H_2O-∗-HCl (–12 au^{-1}), together with magnitudes of 5 to 10 au^{-1} for HI-∗-HI (–8.7 au^{-1}), H_2Se-∗-HI (–9.3 au^{-1}), H_2Se-∗-HBr (–8.5 au^{-1}), H_2Se-∗-HCl (–7.6 au^{-1}), H_2S-∗-HI (–9.2 au^{-1}), H_2S-∗-HBr (–8.7 au^{-1}), and H_2S-∗-HCl (–9.1 au^{-1}). In the case of $\Delta\kappa_{p:POM–CIV}$, the magnitudes are less than 5 au^{-1} for most cases. The values are larger than 10 au^{-1} for H_3N-∗-HNH_2 ($\Delta\kappa_{p:POM–CIV} = –37$ au^{-1}), H_2Se-

∗-HBr (10 au^{-1}), and H_2C=O-∗-HI (–14 au^{-1}), together with magnitudes of 5 to 10 au^{-1} for H_2Se-∗-HSeH (8.0 au^{-1}), H_2Se-∗-HCl (7.1 au^{-1}), H_2S-∗-HI (6.2 au^{-1}), and H_2S-∗-HBr (8.0 au^{-1}). The magnitudes for $\Delta\kappa_{p:NIV–CIV}$ seem very large at first glance. However, the very large values of κ_p would

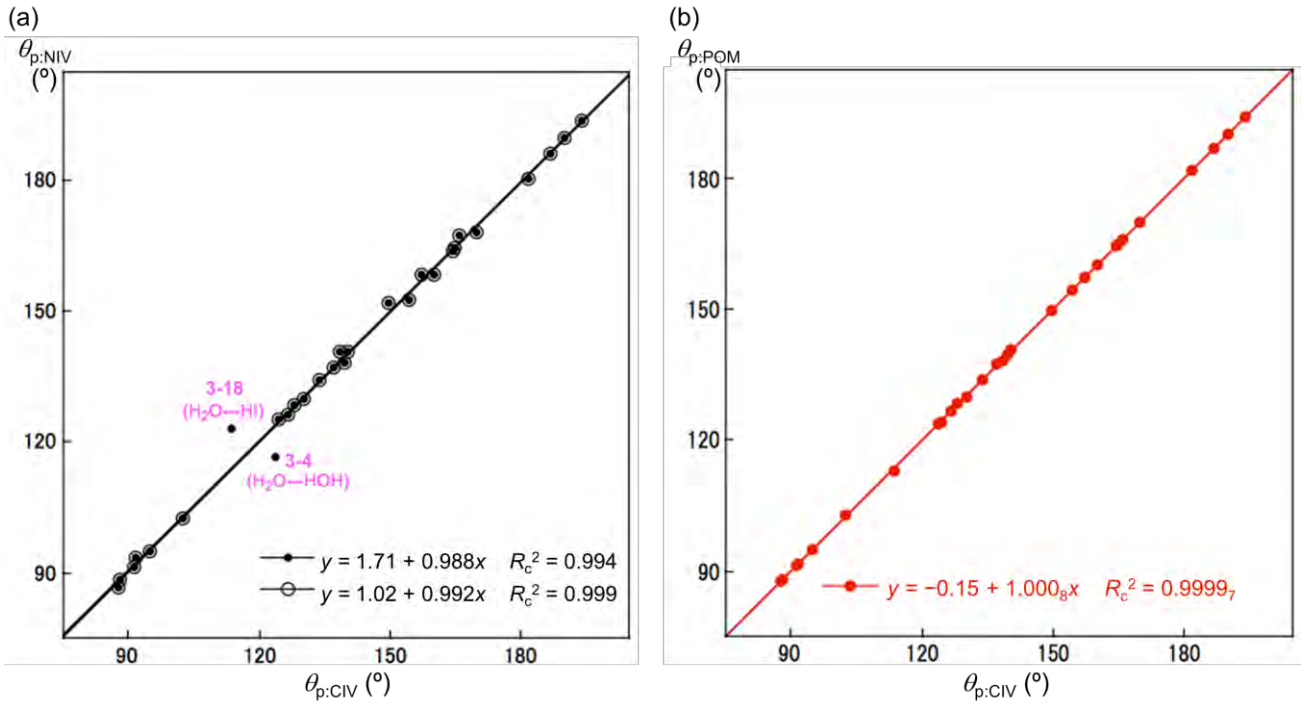

Figure 3-5. Plots of $\theta_{p:NIV}$ versus $\theta_{p:CIV}$ (a) and $\theta_{p:POM}$ versus $\theta_{p:CIV}$ (b) for **3-1**–**3-29**.

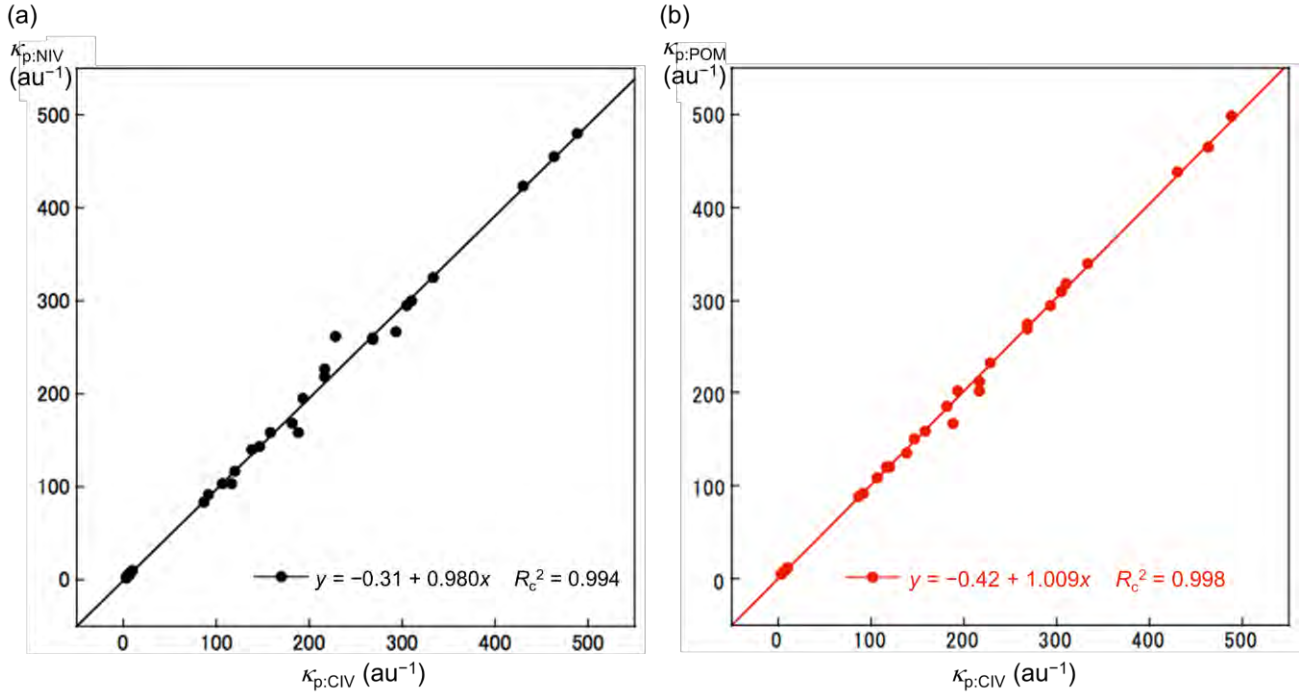

Figure 3-6. Plots of $\kappa_{p:NIV}$ versus $\kappa_{p:CIV}$ (a) and $\kappa_{p:POM}$ versus $\kappa_{p:CIV}$ (b) for **3-1**–**3-29**.

be responsible for the large magnitudes of $\Delta\kappa_p$ as a whole. The magnitudes of $\Delta\kappa_{p:POM–CIV}$ seem to be much improved relative to the case of $\Delta\kappa_{p:NIV–CIV}$; however, there are some severe deviations, such as H_3N-∗-HNH_2 (–37 au^{-1}).

The correlation of $\theta_{p:POM}$ versus $\theta_{p:CIV}$ is much better than that of $\kappa_{p:POM}$ versus $\kappa_{p:CIV}$ (see Table 3-2, entries 7 and 9). This observation seems curious at first glance, as the same perturbed structures are employed to evaluate θ_p and κ_p in QTAIM-DFA. The differences may be mainly attributable to the much more complex route to evaluate κ_p (= $|d^2y/dx^2|/[1+(dy/dx)^2]^{3/2}$) relative to the case of θ_p (= $90^o - \tan^{-1}(dy/dx)$). The θ_p and κ_p values are evaluated by using the common regression curve, as pointed out in a previous paper.[26] The small differences in the QTAIM functions based on the perturbed structures generated with CIV and POM will be magnified in the second derivatives of the regression curves used to evaluate κ_p.

As discussed above, the $\theta_{p:POM}$ values can be recognized to be the same as the $\theta_{p:CIV}$ values in terms of the calculation errors as a whole, although the $\Delta\theta_{p:POM-CIV}$ values of –0.7º for H_2O-∗-HI and –0.5º for H_2O-∗-HBr seem slightly larger than the calculation errors. There must be a reason for these results, but this point was not examined further. Larger magnitudes of $\Delta\kappa_{p:POM–CIV}$ are usually detected if κ_p is very large. However, the results will not damage the excellent reliability in the characterization of the nHBs, as the κ_p values are not used to characterize the interactions. Namely, the excellent applicability of CIV to generate the perturbed structures for QTAIM-DFA is also well established for the various nHBs, as discussed above.

Nature of Neutral HBs Evaluated with the (θ, θ_p) Values

The (θ, $\theta_{p:CIV}$) values of H_2Se-∗-HSeH (**3-1**) are (76.0º, 88.1º), and thus, it is classified by the *p*-CS interaction and is characterized by its vdW nature (*p*-CS/vdW). The $\theta_{p:CIV}$ value of 88.1º should be superior to θ = 76.0º (> 75º) to predict the nature. The HB interaction in H_3N-∗-HNH_2 (**3-3**) is also predicted to be *p*-CS/vdW in nature with (θ, $\theta_{p:CIV}$) = (74.9º, 87.5º) for the interaction. However, the HB interactions in **3-1** and **3-3** would be close to the borderline area between *p*-CS/vdW and *p*-CS/*t*-HB_{nc} judging from the (θ, $\theta_{p:CIV}$) values. HB interactions other than these two were similarly classified and characterized. The nHB interactions are predicted to have the *p*-CS/*t*-HB_{nc} nature for H_2S-∗-HSH (**3-2**), H_2O-∗-HOH (**3-4**), HX-∗-HX (**3-6** (HX = HI), **3-7** (HBr), and **3-8** (HCl)), H_2Se-∗-HX (**3-10** (HX = HI), **3-11** (HBr), and **3-12** (HCl)), H_2S-∗-HI (**3-14**), and H_2O-∗-HI (**3-18**). The *r*-CS/*t*-HB_{wc} nature is predicted for HF-∗-HF (**3-9**), H_2S-∗-HX (**3-15** (HX = HBr) and **3-16** (HCl)), H_2O-∗-HX (**3-19** (HX = HBr) and **3-20** (HCl)), and H_2C=O-∗-HI (**3-22**). On the other hand, the *r*-CS/CT-MC nature is predicted for H_3N-∗-HOH (**3-5**), H_2Se-∗-HF (**3-13**), H_2S-∗-HF (**3-17**), H_2O-∗-HF (**3-21**), and H_2C=O-∗-HX (**3-23** (HX = HBr), **3-24** (HCl), and **3-25** (HF)), whereas the *r*-CS/CT-TBP nature is predicted for H_3N-∗-HX (**3-26** (HX = HI), **3-27** (HBr), **3-28** (HCl), and **3-29** (HF)). The results are summarized in Table 3-1.

The characterization based on POM is the same as that based on CIV, and the characterization based on NIV is equal to that based on CIV and POM, except for **3-20** (H_2O-∗-HCl). The nature of *r*-CS/CT-MC is predicted for **3-20** with NIV, whereas it is just borderline between *r*-CS/*t*-HB_{wc} and *r*-CS/CT-MC if evaluated with CIV and POM. The results show that the HB interactions can also be characterized satisfactorily by employing $\theta_{p:NIV}$ for most cases, irrespective of the substantial differences between $\theta_{p:NIV}$ and $\theta_{p:CIV}$ in some cases. The predicted nature for B-∗-HX is summarized in Table 3-3, exemplified by the formation of B-∗-HX from B (= H_2Se, H_2S, H_2O, $H_2C{=}O$, and H_3N) and HX (= HI, HBr, HCl, and HF). It enables to visualize the roles of B and HX in the formation of B-∗-HX. The HB interactions are predicted to be stronger in the order shown in Equations (3-1) and (3-2). The results shown in Table 3-3 and Equations (3-1) and (3-2) can be essentially explained on the basis of the results shown in Figure 3-2, although there are some differences, namely, the order shown in Equation (3-2) holds for B = H_2Se, H_2S, H_2O, and $H_2C{=}O$ in B-∗-HX, but it is reversed for B = H_3N. The indirect B···(H)–X soft–soft interactions may affect the (θ, $\theta_{p:CIV}$) values in H_2Se-∗-HI and H_2S-∗-HI.

$$B = H_2Se < H_2S \leq H_2O < H_2C{=}O << H_3N \quad (3\text{-}1)$$
$$HX = HI < HBr \leq HCl << HF \quad (3\text{-}2)$$

The wide range of nHB interactions in **3-1**–**3-29** were satisfactorily classified and characterized by employing the perturbed structures generated with CIV in QTAIM-DFA, resulting in the prediction of the reliable intrinsic dynamic nature of these interactions.

Table 3-3. The predicted natures of the nHBs in B-∗-HX with the (θ, θ_p) values, for which B = H_2Se, H_2S, H_2O, $H_2C{=}O$, and H_3N with HX = HI, HBr, HCl, and HF.[a–c]

HX	B = H_2Se	H_2S	H_2O	$H_2C{=}O$	H_3N
	(θ, θ_p)/º	(θ, θ_p)/º	(θ, θ_p)/º	(θ, θ_p)/º	(θ, θ_p)/º
	nature	nature	nature	nature	nature
HI	(**88.5**, *126.5*)	(**89.0**, 124.5)	(**84.5**, 113.5)	(95.3, **139.7**)	(164.9, **194.1**)
	t-HB_{nc}	*t*-HB_{nc}	*t*-HB_{nc}	*t*-HB_{wc}	CT-TBP
HBr	(**87.6**, *130.1*)	(**91.1**, 133.9)	(**93.2**, 138.6)	(*101.6*, **154.6**)	(160.0, **190.3**)
	t-HB_{nc}	*t*-HB_{wc}	*t*-HB_{wc}	CT-MC	CT-TBP
HCl	(**88.7**, *137.3*)	(**92.8**, 140.5)	(98.9, **149.9**[d])	(*105.9*, **160.4**)	(152.7, **186.9**)
	t-HB_{nc}	*t*-HB_{wc}	*t*-HB_{wc}	CT-MC	CT-TBP
HF	(*104.3*, **164.5**)	(*108.5*, **165.1**)	(124.0, **166.1**)	(127.8, **170.1**)	(156.4, **182.0**)
	CT-MC	CT-MC	CT-MC	CT-MC	CT-TBP

[a] Evaluated with MP2/BSS-A by employing the perturbed structures generated by using CIV. [b] Basic (superior) parameters are shown in bold. In the case of *t*-HB_{wc}, θ is basic if it is close to 90º, whereas θ_p becomes basic if it is close to 150º. [c] Nonsuperior parameters are shown in italic if they do not satisfy the predicted nature based on the superior parameters. [d] The value shows that the nature is borderline between *t*-HB_{wc} and CT-MC.

Behavior of Neutral HBs, Examined by the Parameters

What is the behavior of the nHBs in **3-1**–**3-29**? The behavior was examined on the basis of the relation of ΔE with the compliance force constants (C_{ii}) and the QTAIM-DFA parameters (R, θ) and (θ_p, κ_p) for **3-1**–**3-29**. Figure 3-7 draws the plot of ΔE versus C_{ii}. It seems that the plot can be well described by an inverse relationship, although data for $H_3N\cdots HX$ (**3-26** (X = I) and **3-27** (Br)) deviate from the correlation. Equation (3-3) shows the inverse relationship for **3-1**–**3-29**, except for **3-26** and **3-27**. No effort was made to get a best-fit relationship; instead, the averaged value of $\Delta E \times C_{ii}$ (= –165.64) for **3-1**–**3-25**, **3-28**, and **3-29** was employed in Equation (3-3). The regression curve, given in Equation (3-3), is drawn in Figure 3-7 by a dotted line. The ΔE values for the nHBs seem to be well correlated to C_{ii} if the data for **3-26** and **3-27** are omitted. As a result, the stability of B-∗-HY, denoted by ΔE, can be well described by the inverse nature of the compliance for the B-∗-HY interactions, evaluated by C_{ii}, in **3-1**–**3-25**, **3-28**, and **3-29**.

$$\Delta E \times C_{ii} = -165.64 \tag{3-3}$$

The ΔE values for **3-1**–**3-29** were next plotted versus R in (R, θ), which is drawn in Figure 3-A1 of the Appendix. The correlation is given in Table 3-2 (entry 10), although the data for **3-26** and **3-27** are again omitted from the correlation. The ΔE values in the nHBs of **3-1**–**3-25**, **3-28**, and **3-29** seem well correlated to R, for which both have the energy unit, although the ΔE values are on the energy surface, whereas the R values are at the BCPs corresponding to the HBs.

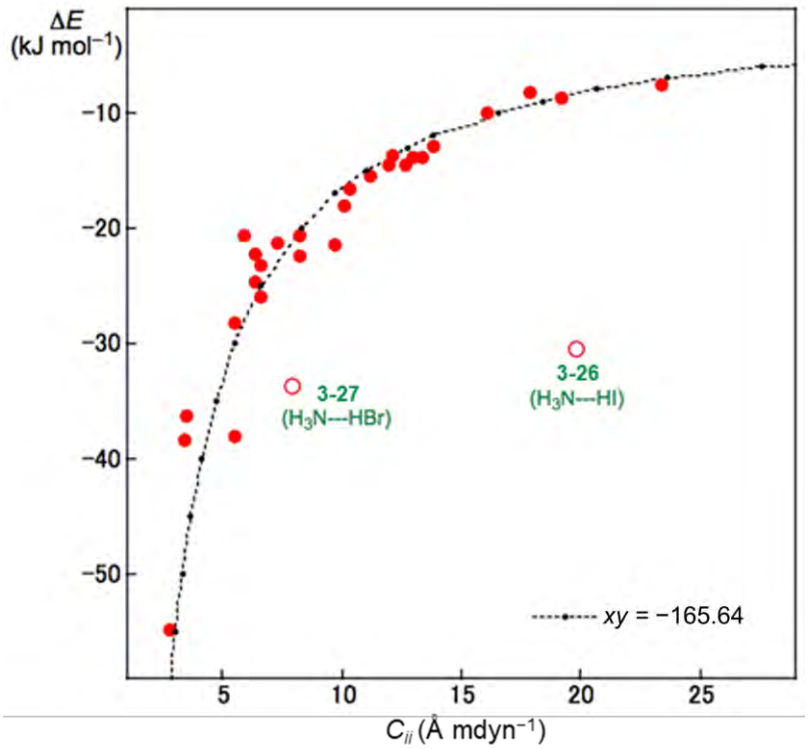

Figure 3-7. Plot of ΔE versus C_{ii} for **3-1**–**3-29**.

Figure 3-8 shows the plot of ΔE versus θ for **3-1**–**3-29**. The correlation seems good if the data of **3-26** and **3-27** are omitted from the correlation. The correlation is given in Table 3-2 (entry 11) (see also Figure 3-8). Why does ΔE correlate rather well with θ for **3-1**–**3-25**, **3-28**, and **3-29**? One may not expect such a correlation. However, it is of interest that the plot of θ versus R for **3-1**–**3-29** gives a good correlation, although this data is not shown ($\theta = 3956.3R + 64.73$: $R_c^2 = 0.813$). The correlation of ΔE versus R through θ versus R leads to the correlation of ΔE versus θ.

The relations between ΔE and (θ_p, κ_p) are next discussed. Before a detailed discussion is given, the relation between θ_p and θ is examined. The θ_p values are plotted versus θ in Figure 3-A2 of the Appendix. A good correlation is obtained for **3-1**–**3-20** and **3-22**–**3-24**, which is given in Table 3-2 (entry 12); the data for **3-21** ($H_2O\cdots HF$), **3-25** ($H_2CO\cdots HF$), and **3-26**–**3-29** (H_3N–HX: X = I, Br, Cl, and F) are omitted from the correlation. Figure 3-9 illustrates the plot of ΔE versus θ_p for **3-1**–**3-29**. The plot was analyzed separately for four groups. Data for **3-1**–**3-9** (HA-∗-HA) belong to group A [G(**A**)]. A very good correlation is obtained for G(**A**), although data for **3-3** (H_3N-∗-HNH_2) deviate from the correlation. The correlation is shown in Table 3-2 (entry 13). The data for **3-10**–**3-17** (H_2Se-∗-HX and H_2S-∗-HX: X = I, Br, Cl and F) make up group B [G(**B**)]. Very good correlation is also obtained for G(**B**), which is shown in Table 3-2 (entry 14). The data for **3-18**–**3-25** (H_2O-∗-HX and H_2C=O-∗-HX: X = I, Br, Cl, and F) form group C [G(**C**)]. The correlation seems poorer than those for G(**A**) and G(**B**), and the data for **3-21** (H_2O-∗-HF) and **3-25** (H_2C=O-∗-HF) deviate from the correlation. The correlation is given in Table 3-2 (entry 15). Group D [G(**D**)] consists of **3-26**–**3-29**

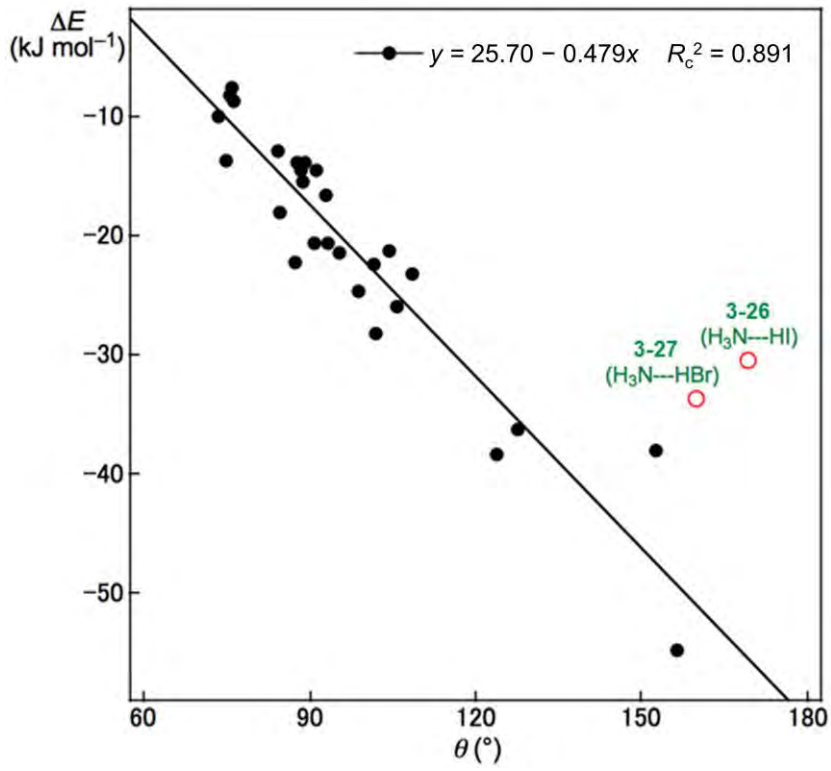

Figure 3-8. Plot of ΔE versus θ for **3-1**–**3-29**.

(H_3N-∗-HX: X = I, Br, Cl, and F). A positive correlation constant is predicted for G(**D**) (a = 1.99 > 0; see Table 3-2, entry 16), contrary to the cases of G(**B**) and G(**C**) with negative correlations (a < 0; see Table 3-2, entries **3-13**–**3-15**). As shown in Figure 3-9, ΔE correlates rather well with θ_p as a whole, with a few deviations. The correlation of ΔE versus θ_p should be a reflection of the correlation of ΔE versus θ through the correlation of θ_p versus θ.

The stability of the HBs in **3-1**–**3-29**, evaluated by ΔE, is well explained on the basis of C_{ii}, R, θ, and θ_p. For the plots of ΔE versus C_{ii}, the magnitudes of ΔE for **3-26** and **3-27** seem to be overestimated relative to those expected on the basis of the correlations for **3-1**–**3-25**, **3-28**, and **3-29**. On the other hand, the magnitudes of ΔE for **3-26** and **3-27** would be underestimated relative to those expected from the correlations of ΔE versus R and θ for **3-1**–**3-25**, **3-28**, and **3-29**. As shown in Figure 3-9, the plot for ΔE versus θ_p could be recognized as a correlation as a whole, with deviation for G(**D**) (H_3N-∗-HX) from the whole correlation for G(**A**)–G(**C**), if the correlation constants for the a values for the groups are compared.

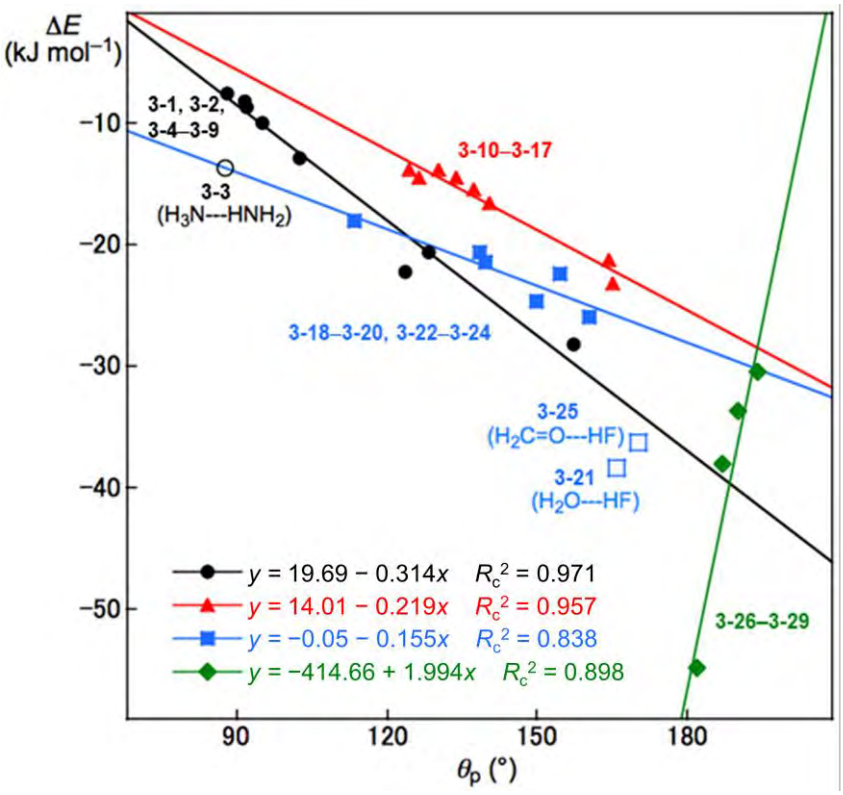

Figure 3-9. Plots of ΔE versus θ_p for **3-1**–**3-29**. Black dots for **3-1**–**3-9** belong to G(**A**), red triangles for **3-10**–**3-17** to G(**B**), blue squares for **3-18**–**3-25** to G(**C**), and green diamonds for **3-26**–**3-29** to G(**D**), although a few deviations are also included.

Summary

Hydrogen bonds (HBs) are fundamentally important in all fields of chemical and biological sciences. Thus, HBs have been variously investigated. However, it has been difficult to characterize the nature of HBs spread over the range of van der Waals (vdW) type for pure closed-shell (CS) interactions to the covalent type of shared-shell (SS) interactions. In this work, the HBs of the neutral form were characterized by applying quantum theory of atoms-in-molecules dual functional analysis (QTAIM-DFA) by employing the perturbed structures generated with CIV. The neutral hydrogen bond (nHB) interactions were characterized on the basis of the static and dynamic behavior predicted with QTAIM-DFA. The dynamic nature of the interactions could be described as the "intrinsic dynamic nature of interactions" if the perturbed structures were generated with CIV, as the coordinates corresponding to the compliance force constants (C_{ii}), used in CIV, are invariant to the choice of the coordinate system. The method was applied to nHBs and the interactions were characterized. Some of them are as follows: nHBs in H_2Se-∗-HSeH and H_3N-∗-HNH_2 were characterized by the *p*-CS (*pure* CS)/vdW nature. The *p*-CS/*t*-HB_{nc} (typical hydrogen bond with no covalency) nature was predicted for H_2S-∗-HSH, H_2O-∗-HOH, and HX-∗-HX (HX = HI, HBr, and HCl), whereas the *r*-CS (*regular* CS)/*t*-HB_{wc} (typical-HB interactions with covalency) nature was predicted for HF-∗-HF, H_2S-∗-HX (HX = HBr and HCl), and H_2O-∗-HX (HX = HBr and HCl). On the other hand, HBs in H_2C=O-∗-HX (HX = HBr, HCl, and HF) were predicted to have the *r*-CS/CT-MC (interactions in the molecular complex formation through CT) nature, whereas the *r*-CS/CT-TBP (trigonal bipyramidal adduct formation through CT) nature was predicted for H_3N-∗-HX (HX = HI, HBr, HCl, and HF). Characterization based on POM was the same as that based on CIV, and characterization based on NIV was equal to that based on CIV and POM, except for **3-20** (H_2O-∗-HCl). The *r*-CS/CT-MC nature was predicted for **3-20** with NIV, whereas it was borderline between *r*-CS/*t*-HB_{wc} and *r*-CS/CT-MC if evaluated with CIV and POM. The highly excellent applicability of CIV is well demonstrated in QTAIM-DFA by applying the method to nHBs, in addition to the standard interactions in a previous study.

Relations between ΔE and C_{ii} or the QTAIM-DFA parameters were examined, together with the reasons. A relation of $\Delta E \times C_{ii} = -165.64$ was found for **3-1**–**3-25**, **3-28**, and **3-29**. Namely, ΔE could be well described by the inverse nature of C_{ii}. Similarly, the R, θ, and θ_p values correlated linearly well with ΔE. The results showed that the values became larger as the stability of the HBs, described by ΔE, increased in the region examined, although there were a few deviations.

Appendix

Table 3-A1. The optimized B···H distances (r_o(B, H)) in **3-1**–**3-29** and those from the sum of the vdW radii. The energies on the energy surface (E) and those from the components (ΔE) [= E(HB) – E(components)], together with the symmetries, for the optimized structures of **3-1**–**3-29**.[a]

Species (B-∗-H)	r_o(B, H) (Å)	Σr_{vdW}(B, H) (Å)	Δr[b] (Å)	E (au)	ΔE[c] (kJ mol^{-1})	Sym-metry
H_2Se-∗-HSeH (**3-1**)	2.9375	3.10	–0.1625	–4802.2815	–7.6	C_s
H_2S-∗-HSH (**3-2**)	2.7668	3.00	–0.2332	–797.8022	–8.7	C_s
H_3N-∗-HNH_2 (**3-3**)	2.2845	2.75	–0.4655	–112.9189	–13.8	C_s
H_2O-∗-HOH (**3-4**)	1.9427	2.72	–0.7773	–152.6570	–22.2	C_s
H_3N-∗-HOH (**3-5**)	1.9585	2.75	–0.7915	–132.7919	–28.2	C_1
HI-∗-HI (**3-6**)	2.8321	3.18	–0.3479	–13837.3469	–12.9	C_s
HBr-∗-HBr (**3-7**)	2.7078	3.05	–0.3422	–5146.2776	–8.3	C_s
HCl-∗-HCl (**3-8**)	2.5109	2.95	–0.4391	–920.6082	–10.0	C_s
HF-∗-HF (**3-9**)	1.8196	2.67	–0.8504	–200.6735	–20.7	C_1[e]
H_2Se-∗-HI (**3-10**)	2.6280	3.10	–0.4720	–9319.9821	–14.5	C_s
H_2Se-∗-HBr (**3-11**)	2.6194	3.10	–0.4806	–4974.2818	–13.9	C_s
H_2Se-∗-HCl (**3-12**)	2.5726	3.10	–0.5274	–2861.4474	–15.5	C_s
H_2Se-∗-HF (**3-13**)	2.4078	3.10	–0.6922	–2501.4802	–21.3	C_s
H_2S-∗-HI (**3-14**)	2.5466	3.00	–0.4534	–7317.5757	–13.9	C_s
H_2S-∗-HBr (**3-15**)	2.4919	3.00	–0.5081	–2972.0422	–14.6	C_s
H_2S-∗-HCl (**3-16**)	2.4410	3.00	–0.5590	–859.2079	–16.6	C_s
H_2S-∗-HF (**3-17**)	2.2719	3.00	–0.7281	–499.2411	–23.2	C_s
H_2O-∗-HI (**3-18**)	2.0207	2.72	–0.6993	–6995.0022	–18.1	C_s
H_2O-∗-HBr (**3-19**)	1.9304	2.72	–0.7896	–2649.4694	–20.7	C_s
H_2O-∗-HCl (**3-20**)	1.8727	2.72	–0.8473	–536.6359	–24.7	C_s
H_2O-∗-HF (**3-21**)	1.7054	2.72	–1.0146	–176.6717	–38.4	C_s
H_2C=O-∗-HI (**3-22**)	1.9399	2.72	–0.7801	–7032.9891	–21.5	C_s
H_2C=O-∗-HBr (**3-23**)	1.8868	2.72	–0.8332	–2687.4556	–22.4	C_s
H_2C=O-∗-HCl (**3-24**)	1.8477	2.72	–0.8723	–574.6219	–25.9	C_s
H_2C=O-∗-HF (**3-25**)	1.7069	2.72	–1.0131	–214.6565	–36.3	C_s
H_3N-∗-HI (**3-26**)	1.6488	2.75	–1.1012	–6975.1394	–30.5	C_{3v}
H_3N-∗-HBr (**3-27**)	1.7176	2.75	–1.0324	–2629.6069	–33.7	C_{3v}
H_3N-∗-HCl (**3-28**)	1.7459	2.75	–1.0041	–516.7735	–38.0	C_{3v}
H_3N-∗-HF (**3-29**)	1.6837	2.75	–1.0663	–156.8105	–54.8	C_{3v}

[a] Calculated with the MP2/6-311++G(3df,3pd) method, except for I of which calculations being performed with (7433111/743111/7411/2 + 1s1p1d1f) type from the Sapporo Basis Set Factory. [b] Δr = r_o(X, Y) – Σr_{vdW} (vdW radii of Bondi being employed; see, ref 40). [c] ΔE = E(HB adduct) – E(components)].

Table 3-A2. Lengths of bond paths (r_{BP}) with components (r_{BP-1} and r_{BP-2}) and the corresponding straight-line distances (R_{SL}) in **3-1**–**3-29**.[a]

Species (B-∗-H)	r_{BP-1} (Å)	r_{BP-2} (Å)	r_{BP}[b] (Å)	R_{SL}[c] (Å)	Δr_{BP}[d] (Å)
H_2Se-∗-HSeH (**3-1**)	1.9169	1.0352	2.9520	2.9375	0.0145
H_2S-∗-HSH (**3-2**)	1.8044	0.9804	2.7848	2.7668	0.0180
H_3N-∗-HNH_2 (**3-3**)	1.4502	0.8606	2.3108	2.2845	0.0263
H_2O-∗-HOH (**3-4**)	1.2645	0.7081	1.9727	1.9427	0.0300
H_3N-∗-HOH (**3-5**)	1.3011	0.6873	1.9884	1.9585	0.0299
HI-∗-HI (**3-6**)	1.8974	0.9481	2.8455	2.8321	0.0134
HBr-∗-HBr (**3-7**)	1.7863	0.9380	2.7244	2.7078	0.0166
HCl-∗-HCl (**3-8**)	1.6481	0.8835	2.5316	2.5109	0.0207
HF-∗-HF (**3-9**)	1.1899	0.6668	1.8568	1.8196	0.0372
H_2Se-∗-HI (**3-10**)	1.7490	0.8926	2.6416	2.6280	0.0136
H_2Se-∗-HBr (**3-11**)	1.7577	0.8786	2.6363	2.6194	0.0169
H_2Se-∗-HCl (**3-12**)	1.7418	0.8512	2.5930	2.5726	0.0204
H_2Se-∗-HF (**3-13**)	1.6826	0.7604	2.4429	2.4078	0.0351
H_2S-∗-HI (**3-14**)	1.6816	0.8800	2.5616	2.5466	0.0150
H_2S-∗-HBr (**3-15**)	1.6617	0.8481	2.5099	2.4919	0.0180
H_2S-∗-HCl (**3-16**)	1.6425	0.8199	2.4624	2.4410	0.0214
H_2S-∗-HF (**3-17**)	1.5792	0.7287	2.3079	2.2719	0.0360
H_2O-∗-HI (**3-18**)	1.2762	0.7591	2.0354	2.0207	0.0147
H_2O-∗-HBr (**3-19**)	1.2414	0.7068	1.9482	1.9304	0.0178
H_2O-∗-HCl (**3-20**)	1.2194	0.6745	1.8939	1.8727	0.0212
H_2O-∗-HF (**3-21**)	1.1619	0.5792	1.7411	1.7054	0.0357
H_2C=O-∗-HI (**3-22**)	1.2378	0.7159	1.9537	1.9399	0.0138
H_2C=O-∗-HBr (**3-23**)	1.2198	0.6839	1.9037	1.8868	0.0169
H_2C=O-∗-HCl (**3-24**)	1.2068	0.6612	1.8680	1.8477	0.0203
H_2C=O-∗-HF (**3-25**)	1.1624	0.5795	1.7419	1.7069	0.0350
H_3N-∗-HI (**3-26**)	1.1302	0.5291	1.6593	1.6488	0.0105
H_3N-∗-HBr (**3-27**)	1.1680	0.5642	1.7322	1.7176	0.0146
H_3N-∗-HCl (**3-28**)	1.1863	0.5781	1.7644	1.7459	0.0185
H_3N-∗-HF (**3-29**)	1.1756	0.5410	1.7166	1.6837	0.0329

[a] Calculated with the MP2/6-311++G(3df,3pd) method, except for I of which calculations being performed with (7433111/743111/7411/2 + 1s1p1d1f) type from the Sapporo Basis Set Factory. [b] The lengths of BPs, where $r_{BP} = r_{BP-1} + r_{BP-2}$. [c] Straight-line distances. [d] $\Delta r_{BP} = r_{BP} - R_{SL}$.

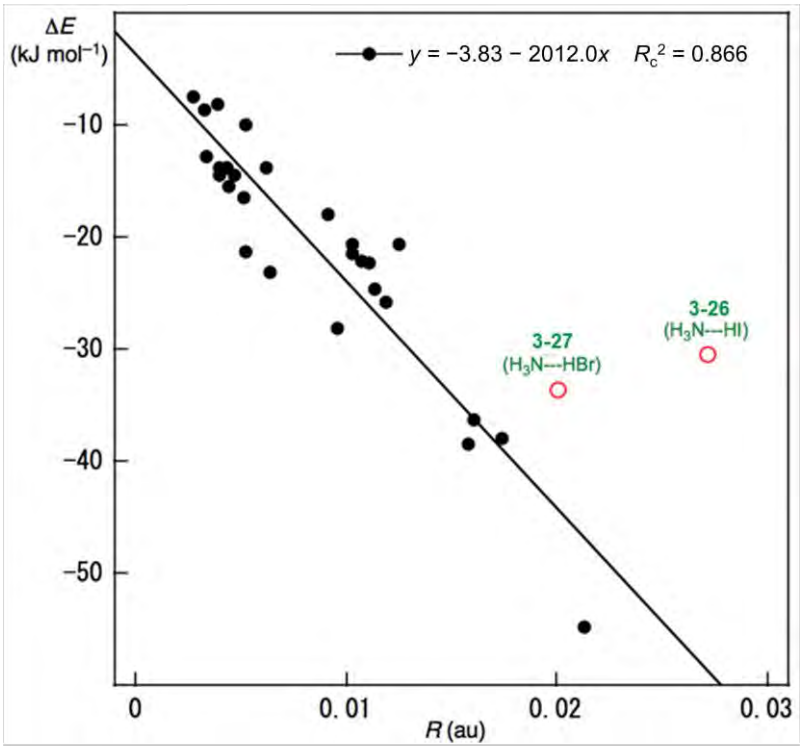

Figure 3-A1. Plot of ΔE versus R for **3-1**–**3-29**.

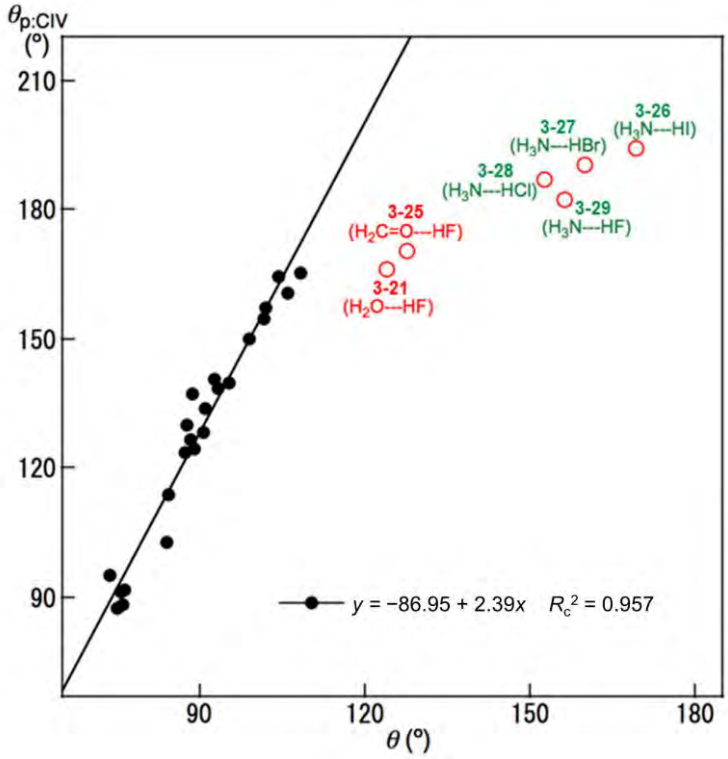

Figure 3-A2. Plot of θ_p values versus θ for **3-1**–**3-29**.

References and Notes

1. L. Pauling, *The Nature of the Chemical Bond*, Cornell University Press, Ithaca, NY, **1960**.
2. G. C. Pimentel, A. L. McClellan, *The Hydrogen Bond*, W. H. Freeman, San Francisco, CA, **1960**.
3. P. Schuster, G. Zundel, C. Sandorfy, *The Hydrogen Bond, Recent Developments in Theory and Experiments* (Eds.: P. Schuster, G. Zundel, C. Sandorfy), North-Holland Publishing Company, Amsterdam, **1976**.
4. G. A. Jeffrey, *An Introduction to Hydrogen Bonding*, Oxford University Press, New York, **1997**.
5. S. Scheiner, *Hydrogen Bonding, A Theoretical Perspective*, Oxford University Press, Oxford, **1997**.
6. G. R. Desiraju, T. Steiner, *The Weak Hydrogen Bond in Structural Chemistry and Biology*, International Union of Crystallography Monographs on Crystallography, Oxford University Press, New York, **1999**.
7. S. J. Grabowski, *Hydrogen Bonding – New Insights* (Ed.: S. J. Grabowski), Springer, The Netherlands, **2006**.
8. G. Buemi, *Intramolecular Hydrogen Bonds. Methodologies and Strategies for Their Strength Evaluation* in *Hydrogen Bonding – New Insights* (Eds.: S. J. Grabowski), Springer, New York, **2006**. Ch. 2.
9. K.-L. Han, G.-J. Zhao, *Hydrogen Bonding and Transfer in the Excited State*, Wiley, Chichester, UK, **2010**.
10. S. Hayashi, K. Matsuiwa, M. Kitamoto, W. Nakanishi, *J. Phys. Chem. A* **2013**, *117*, 1804–1816.
11. See the refs cited in ref. 10.
12. W. Nakanishi, S. Hayashi, K. Narahara, *J. Phys. Chem. A* **2008**, *112*, 13593–13599.
13. W. Nakanishi, S. Hayashi, K. Narahara, *J. Phys. Chem. A* **2009**, *113*, 10050–10057.
14. W. Nakanishi, S. Hayashi, *Curr. Org. Chem.* **2010**, *14*, 181–197.
15. W. Nakanishi, S. Hayashi, *J. Phys. Chem. A* **2010**, *114*, 7423–7430.
16. W. Nakanishi, S. Hayashi, *Bull. Chem. Soc. Jpn.* **2012**, *85*, 1293–1305.
17. W. Nakanishi, S. Hayashi, *J. Phys. Chem. A* **2013**, *117*, 1795–1803.
18. W. Nakanishi, S. Hayashi, M. B. Pitak, M. B. Hursthouse, S. J. Coles, *J. Phys. Chem. A* **2011**, *115*, 11775–11787.
19. Y. Sugibayashi, S. Hayashi, W. Nakanishi, *Phys. Chem. Chem. Phys.* **2015**, *17*, 28879–28891.
20. S. Hayashi, Y. Sugibayashi, W. Nakanishi, *Phys. Chem. Chem. Phys.* **2016**, *18*, 9948–9960.
21. Y. Sugibayashi, S. Hayashi, W. Nakanishi, *ChemPhysChem* **2016**, *17*, 1804–1816.
22. S. Hayashi, Y. Sugibayashi, W. Nakanishi, *RSC Adv.* **2016**, *6*, 49651–49660.
23. S. Hayashi, Y. Sugibayashi, W. Nakanishi, *RSC Adv.* **2017**, *7*, 31858–31865.
24. S. Hayashi, K. Nagata, S. Otsuki, W. Nakanishi, *J. Phys. Chem. A* **2017**, *121*, 2482–2496.
25. Y. Tsubomoto, S. Hayashi, W. Nakanishi, L. K. Mapp, S. J. Coles, *RSC Adv.* **2018**, *8*, 9651–9660.
26. W. Nakanishi, S. Hayashi, *Int. J. Quantum Chem.* **2018**, *118*, e25590.
27. K. Brandhorst, J. Grunenberg, *J. Chem. Phys.* **2010**, *132*, 184101–184107.
28. K. Brandhorst, J. Grunenberg, *Chem. Soc. Rev.* **2008**, *37*, 1558–1567.

29. J. Grunenberg, *J. Am. Chem. Soc.* **2004**, *126*, 16310–16311.
30. J. Grunenberg, *Angew. Chem. Int. Ed.* **2001**, *40*, 4027-4029; *Angew. Chem.* **2001**, *113*, 4150–4153.
31. J. Böhnke, H. Braunschweig, P. Constantinidis, T. Dellermann, W. C. Ewing, I. Fischer, K. Hammond, F. Hupp, J. Mies, H.-C. Schmitt, A. Vargas, *J. Am. Chem. Soc.* **2015**, *137*, 1766–1769.
32. The C_{ii} values and the coordinates corresponding to C_{ii} were calculated by using the Compliance 3.0.2 program released by Grunenberg and Brandhorst.
33. *Gaussian 09, Revision D.01*, M. J. Frisch, G. W. Trucks, H. B. Schlegel, G. E. Scuseria, M. A. Robb, J. R. Cheeseman, G. Scalmani, V. Barone, B. Mennucci, G. A. Petersson, H. Nakatsuji, M. Caricato, X. Li, H. P. Hratchian, A. F. Izmaylov, J. Bloino, G. Zheng, J. L. Sonnenberg, M. Hada, M. Ehara, K. Toyota, R. Fukuda, J. Hasegawa, M. Ishida, T. Nakajima, Y. Honda, O. Kitao, H. Nakai, T. Vreven, J. A. Montgomery, Jr., J. E. Peralta, F. Ogliaro, M. Bearpark, J. J. Heyd, E. Brothers, K. N. Kudin, V. N. Staroverov, R. Kobayashi, J. Normand, K. Raghavachari, A. Rendell, J. C. Burant, S. S. Iyengar, J. Tomasi, M. Cossi, N. Rega, J. M. Millam, M. Klene, J. E. Knox, J. B. Cross, V. Bakken, C. Adamo, J. Jaramillo, R. Gomperts, R. E. Stratmann, O. Yazyev, A. J. Austin, R. Cammi, C. Pomelli, J. W. Ochterski, R. L. Martin, K. Morokuma, V. G. Zakrzewski, G. A. Voth, P. Salvador, J. J. Dannenberg, S. Dapprich, A. D. Daniels, Ö. Farkas, J. B. Foresman, J. V. Ortiz, J. Cioslowski, D. J. Fox, Gaussian, Inc., Wallingford CT, **2009**.
34. T. Noro, M. Sekiya, T. Koga, Theor. *Chem. Acc.* **2012**, *131*, 1124–1128.
35. C. Møller, M. S. Plesset, *Phys. Rev.* **1934**, *46*, 618–622.
36. J. Gauss, *J. Chem. Phys.* **1993**, *99*, 3629–3643.
37. J. Gauss, Ber. Bunsenges, *Phys. Chem.* **1995**, *99*, 1001–1008.
38. R. F. W. Bader, *Atoms in Molecules: A Quantum Theory* (Ed.: R. F. W. Bader), Oxford University Press, Oxford, **1990**.
39. F. Biegler-König, *J. Comput. Chem.* **2000**, *21*, 1040–1048.
40. A. Bondi, *J. Phys. Chem.* **1964**, *68*, 441–451.

Chapter 4

Nature of Intramolecular O–H···π Interactions as Elucidated by QTAIM Dual Functional Analysis with QC Calculations

Abstract

The intrinsic dynamic and static nature of intramolecular OH-∗-π interactions is elucidated with QTAIM dual functional analysis (QTAIM-DFA) by employing perturbed structures generated with coordinates derived from compliance force constants for internal vibrations (CIV), after clarifying the structural features. Seven intramolecular OH-∗-C(π) interactions were detected in six-membered rings, with six bond paths (BPs) and bond critical points (BCPs) for each, among the 72 conformers of the species examined in this work. The interactions are predicted to have a vdW or *t*-HB_{nc} (typical hydrogen bonds with no covalency) nature, which appeared in the pure closed shell region in QTAIM-DFA plot. They appear to be stronger than the corresponding intermolecular interactions. Nine BPs with BCPs were also detected for the intramolecular O-∗-X interactions (X = C(π) and H(π), joined to C(π)) in the five to seven-membered rings. The second perturbation energies, as obtained by natural bond orbital analysis, are discussed in relation to the stabilities of the conformers and the BPs with BCPs.

Introduction

Hydrogen bonds (HBs) are of ongoing interest in all fields of chemical and biological sciences.[1–4] The conventional HBs in the shared proton interaction type (cv-HBs: B···H–X) are basic HBs. The B···H–X directions are controlled through the formation of HBs from X–H and B due to the contribution of the unsymmetric σ(3c–4e) (three center–four electron interactions of the σ-type).[5–7] The energies involved in the formation of cv-HBs are typically 10–40 kJ mol^{-1} for the neutral form.[5] Another type of HBs will form if π-orbitals are provided from ethyne, ethene, benzene, and the derivatives to X–H. These X–H···π interactions, which are called π-HBs here, seem weaker than cv-HBs. The weaker proton-accepting ability of π-orbitals relative to the lone pair orbitals must primarily be responsible for the differences. Recently, the behavior of cv-HBs among the neutral and charged forms were elucidated by applying QTAIM dual functional analysis (QTAIM-DFA).[4,8] The cv-HBs of the neutral form are predicted to have vdW to CT-TBP (trigonal bipyramidal adduct formation through charge transfer) nature, while the cv-HBs of the charged form show a covalent bond nature (Cov), due to the wide range of interaction energies of HBs.[4] The natures of the XH···π interactions were also reported recently for the π-systems of benzene,[9,10] naphthalene,[11] anthracene,[12] and/or coronene,[13] where X = F, Cl, Br, I, HO, HS, HSe, MeO, H_2N, MeHN, and/or Me_2N.

The author also closely observed the intramolecular π-HBs since they play a very important role in the chemical and biological sciences.[14,15] What is the behavior of the intramolecular π-HBs? What are the differences and similarities between the intramolecular and intermolecular π-HBs? How does steric hindrance affect the strength of the intermolecular π-HBs? It is challenging to clarify the nature of intramolecular π-HBs to understand the fundamental behavior of π-HBs.[14,15] Chart 4-1 illustrates

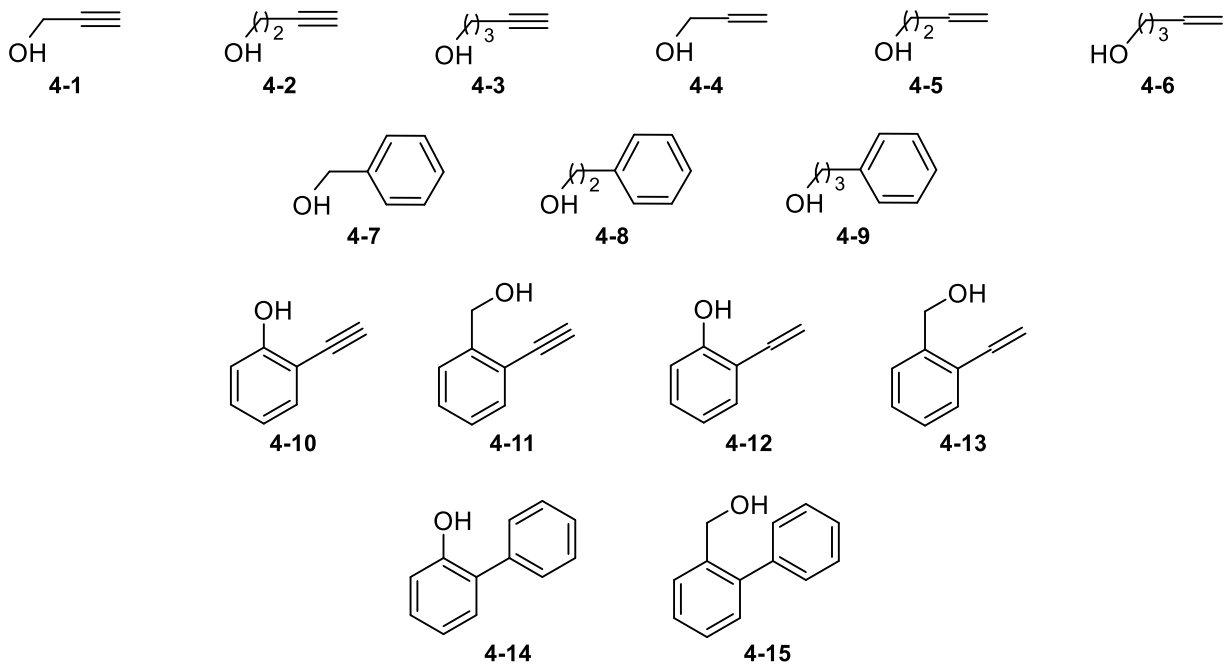

Chart 4-1. Candidates **4-1**–**4-15**, to examine the intramolecular HB interactions.

species **4-1**–**4-15**, which were examined in this work.

When employing the perturbed structures generated with the coordinates derived from compliance force constants for internal vibrations (CIV),[16] the author considers QTAIM dual functional analysis (QTAIM-DFA)[17–20] to be well-suited for elucidating the nature of the intramolecular π-HB interactions in **4-1**–**4-15**. Herein, the results of investigations on the intrinsic dynamic and static nature of the intramolecular π-HBs are presented. Bond paths (BPs) with bond critical points (BCPs) corresponding to the intramolecular OH-∗-π(C) interactions are detected in seven conformers, together with four intramolecular O-∗-C(π) and five O-∗-H(π) interactions among 72 conformers examined in **4-1**–**4-15**, where H(π) indicates an H joined directly to a C(π). The nature of the intramolecular interactions is clarified for those detected by the BPs with BCPs. The natural orbital (NBO) analysis[21] is applied to some selected conformers of **4-1**–**4-15**. The nature of the intramolecular interactions will be discussed in relation to the results of the NBO analysis and the structural features.

Methodological Details in Calculations

The Gaussian 09 programs[22] were employed for the calculations. The calculations containing the NBO analysis[21] were performed with the 6-311++G(3df,3pd) basis set (BSS-A) at a second order Møller-Plesset energy correlation (MP2) level (MP2/BSS-A).[23] The optimized structures were confirmed by the frequency analysis. The results of the frequency analysis were used to obtain the compliance force constants (C_{ii}) values and the coordinates corresponding to C_{ii}.[24–27] The B3LYP[28]/BSS-A and M06-2X[29]/BSS-A methods were also applied to the limited cases for the examination of the effect from the DFT level.

QTAIM functions were calculated using the same basis set system and the level as in the optimizations, unless otherwise noted, and were analyzed with the AIM2000[30] and AIMAll[31] programs. In QTAIM-DFA, $H_b(\boldsymbol{r}_c)$ are plotted versus $H_b(\boldsymbol{r}_c) - V_b(\boldsymbol{r}_c)/2$ for the five data points of w = 0, ±0.05, and ±0.1 (see Chapter 2), unless otherwise noted.

QTAIM-DFA is explained in Chapter 2, together with the basic concept of the QTAIM approach.[32,33]

Results and Discussion

Optimizations of Species, 4-1–4-15

Species **4-1**–**4-15** were optimized with MP2/BSS-A. The most extended conformer was optimized for each of **4-1**–**4-15**, first. The conformers were searched by the optimizations with the changing all torsional angles for each species. 72 conformers were optimized for **4-1**–**4-15**. The conformers are explained first, exemplified by **4-3**. Figure 4-1 illustrates the conformers of **4-3** with $\phi(C_\beta C_\gamma OH) \approx 180^o$ (***t***), which are the ***ttt***, ***tgt***, ***gtt***, ***ggt***, and ***gg't*** conformers around C_β, C_γ, and O. Three conformers around C_α in **4-3** are identical, as shown in Figure 4-1. Therefore, the conformers will be distinguished by the conformations around C_β, C_γ, and O. The *gauche* (***g***) and *gauche'* (***g'***) notations are used for $\phi(C_\beta C_\gamma OH) \approx 60^o$ and -60^o, respectively, for example, in addition to the *trans* (***t***) notation for $\phi(C_\beta C_\gamma OH) \approx 180^o$. The ***g*** and ***g'*** conformers around C_β (from the ***ttt*** conformer) are the same in this work. The optimizations were further performed with the torsional angles changing compared with those of the optimized structures, as mentioned above. 14 conformers were optimized for **4-3**, although the systematic conformation analysis is not applied. The optimized conformer of the shortest OH···C(π) distance [r(H···C(π))] in **4-3** is called **4-3a**. The optimized conformers will be called **4-3b**, **4-3c**, …, **4-3m**, and **4-3n**, in the increasing order of the optimized OH···C(π) distances.

In the case of **4-5**, the most extended structure of the C_s symmetry (**4-5** (C_s)) has one imaginary frequency. The optimization converged a conformer of the C_1 symmetry (**4-5A** (C_1)) with the torsional angle of $\phi(C_{sp2}C_{sp2}C_{H2}H) \approx 8.5^o$ if started from the C_1 structure, close to **4-5** (C_s). However, the similar conformer with $\phi(C_{sp2}C_{sp2}C_{H2}H) \approx 173.5^o$ (**4-5A'** (C_1)) was not optimized. Another type of conformer with C_s symmetry (**4-5B** (C_s)) was optimized, of which $\phi(C_{sp2}C_{sp2}C_{H2}C_{H2}) = 0$. Figure 4-1 contains the process from **4-5** (C_s) to **4-5A** (C_1) and **4-5B** (C_s) with **4-5A'** (C_1). The optimizations for **4-5** were performed by changing the torsional angles around the $-CH_2OH$ group in **4-5A** (C_1) and **4-5B** (C_s). As a result, fifteen different conformers were optimized for **4-5**. Conformers **4-5** (C_s), **4-5A** (C_1), and **4-5B** (C_s) correspond to **4-5n**, **4-5m**, and **4-5o**, respectively, among the 15 conformers.

The optimizations of **4-1**–**4-15** other than **4-3** and **4-5** were performed in a similar way. There were greater efforts to search for the conformers with the shorter OH···C(π) distances than the ones with the longer distances, which would prevent the trivial optimizations of the conformers with no intramolecular OH···C(π) interactions. Finally, 72 conformers were optimized for **4-1**–**4-15**. The optimized conformers in this study are denoted as ***x*a**, ***x*b**, … (***x*** = **4-1**–**4-15**), similar to **4-3**. The selected structural parameters around the intramolecular OH···C(π) interactions in **4-1**–**4-15**, r(O–H), r(H···C(π)), ∠OHC(π), and ∠HC(π)C(π), are collected in Table 4-A1 of the Appendix. The optimized structures of **4-1**–**4-15** are not shown in the figures, but they can be found in the molecular graphs drawn on the optimized structures (see Figure 4-3 and Figures 4-A1–4-A3 of the Appendix). The relative energies (ΔE) in **4-1**–**4-15** are calculated on the energy surface (ΔE_{ES}) and those with the

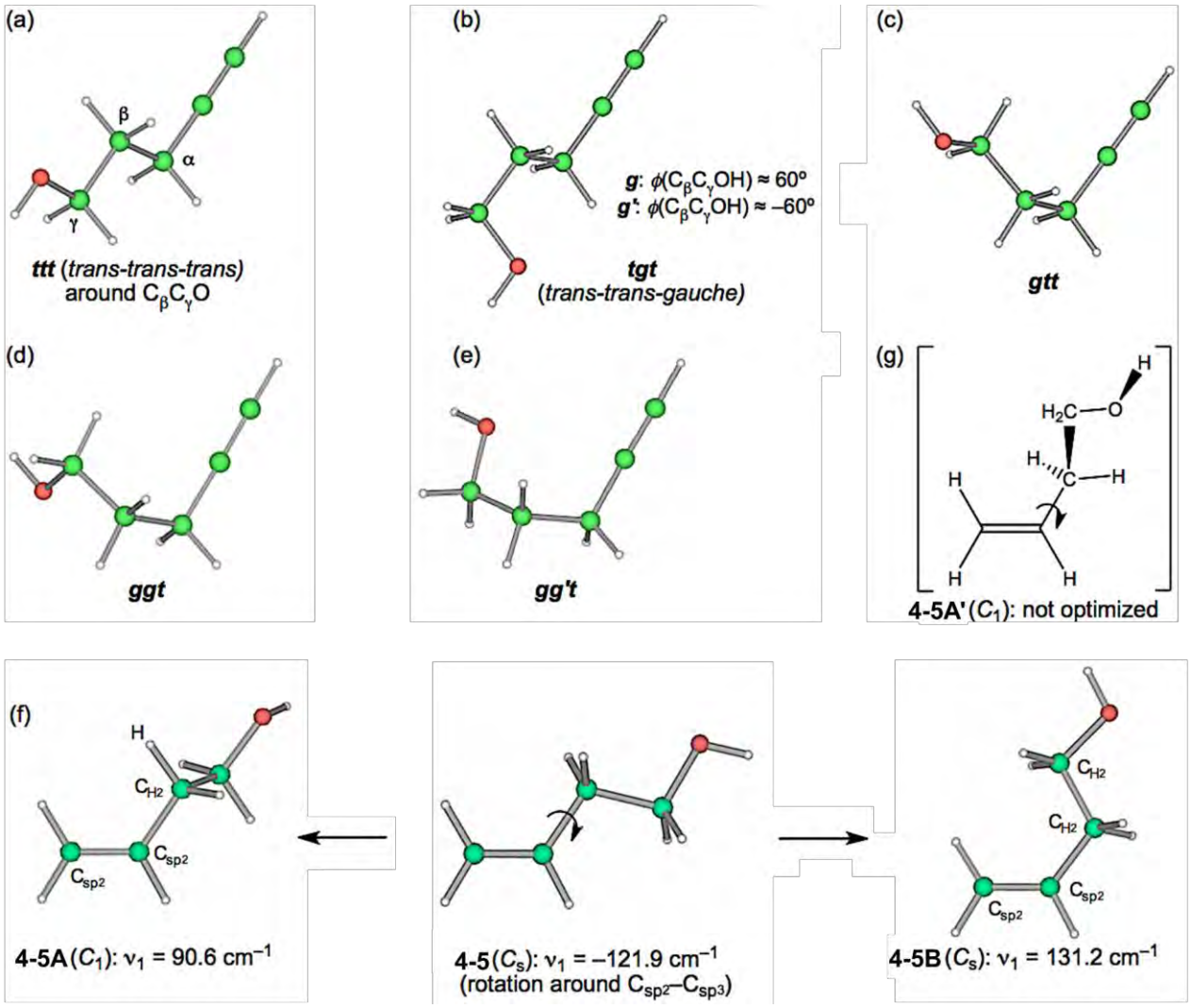

Figure 4-1. Survey of the structural optimizations for **4-3** ((a)–(e)) and **4-5** ((g) and (f)), calculated with MP2/BSS-A.

corrections for the zero-point energies (ΔE_{ZP}). The energies of the conformers in **4-1**–**4-15**, with the smallest r(H···C(π)) values among the optimized ones (called **4-1a**–**4-15a**, respectively), were chosen as the standards. The ΔE values (ΔE_{ES} and ΔE_{ZP}) for **4-1**–**4-15** are also presented in Table 4-A1 of the Appendix.

Figure 4-2 shows the plot of ΔE_{ZP} versus ΔE_{ES} for the optimized 14 conformers in **4-3**. The plot showed an excellent correlation ($y = 0.906x - 0.56$: $R_c^2 = 0.995$). The dependence of ΔE on the conformers in **4-3** seems well understood based on Figure 4-2. The ΔE values for the conformers increase in the order shown in Equation (4-1) (less stable in the order), if ϕ(CβCγOH) are limited to 180º (***t***). The ***ttt*** conformer is predicted to be the second-most unstable one in the stability sequence shown in Equation (4-1).

ggt **(4-3e)** < ***tgt*** **(4-3m)** < ***gtt*** **(4-3k)** < ***ttt*** **(4-3n)** < ***gg't*** **(4-3d)** (4-1)

The prediction seems unusual at first glance since the conformers in **4-3** are expected to be less stable as the steric crowding increases if no mechanisms other than the steric one are operating to stabilize the conformer. The repulsive energy from the steric hindrance is expected to be the lowest in ***ttt*** (**4-3n**). However, ***ggt*** (**4-3e**), ***tgt*** (**4-3m**), and ***gtt*** (**4-3k**) are predicted to be more stable than ***ttt*** (**4-3n**), although ***gg′t*** (**4-3d**) is predicted to be most unstable relative to the others. The ΔE_{ES} values are calculated to be 14.0 and 8.0 kJ mol^{-1} for ***gg′t*** (**4-3d**) and ***gg′g′*** (**4-3b**), respectively, which are the most and second-most unstable conformers in **4-3**. They seem to be the second and third-most sterically crowded ones in **4-3**, respectively. The conformer **4-3a** is expected to be the most sterically crowded one among those in **4-3**, where the ΔE_{ES} value for ***gg′g*** (**4-3a**) is used as the standard (0.0 kJ mol^{-1}) for the conformers of **4-3**. However, ***gg′g*** (**4-3a**) is close to the most stabilized conformer among those in **4-3**. The intramolecular OH-∗-C(π) interaction contributes to stabilizing ***gg′g*** (**4-3a**) by approximately 15 kJ mol^{-1} in **4-3**. Similar phenomena were observed among the optimized conformers in **4-1**–**4-15**.

The ΔE_{ZP} values are similarly plotted versus the ΔE_{ES} for the 72 conformers. The plot is shown in Figure 4-A4 of the Appendix. The plot also gave a very good correlation ($y = 0.897x - 0.20$: $R_c^2 = 0.990$). As a result, ΔE_{ES} can be employed for the discussion of ΔE.

Before presenting a detailed discussion of the nature of the intramolecular OH-∗-C(π) interactions, it is instructive to examine the molecular graphs with the contour plots.

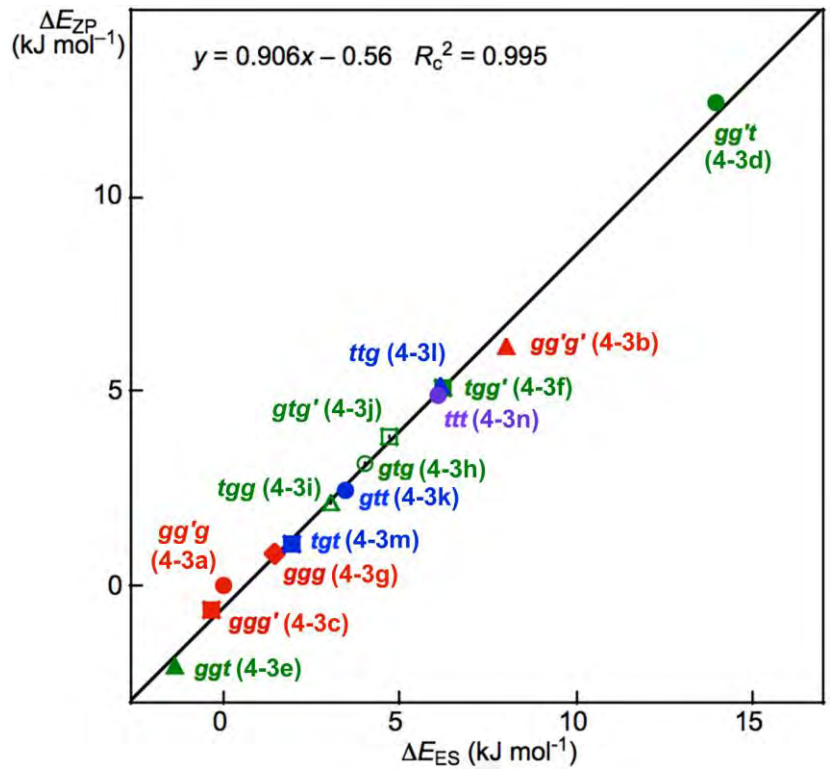

Figure 4-2. Plot of ΔE_{ZP} versus ΔE_{ES} for the conformers in **4-3**, as optimized with MP2/BSS-A.

Molecular Graphs with Contour Plots for 4-1–4-15

A BCP on a BP corresponding to the intramolecular OH-∗-C(π) interaction was detected for **4-3a**, **4-6a**, **4-9a**, **4-11a**, **4-12a**, **4-13a**, and **4-15a**, whereas one corresponding to the intramolecular O-∗-C(π) interaction was recorded for **4-3b**, **4-6c**, **4-9b**, and **4-14b,** and that corresponding to the intramolecular O-∗-H(π) interaction was for **4-5e**, **4-5i**, **4-12b**, **4-15b**, and **4-15c**, where the H(π) joined directly to the C(π). Figure 4-3 illustrates the molecular graphs with the contour plots for the intramolecular OH-∗-C(π), O-∗-C(π), and O-∗-H(π) interactions for the conformers discussed above. All the expected BCPs are clearly detected, and they contain the components for the intramolecular interactions.

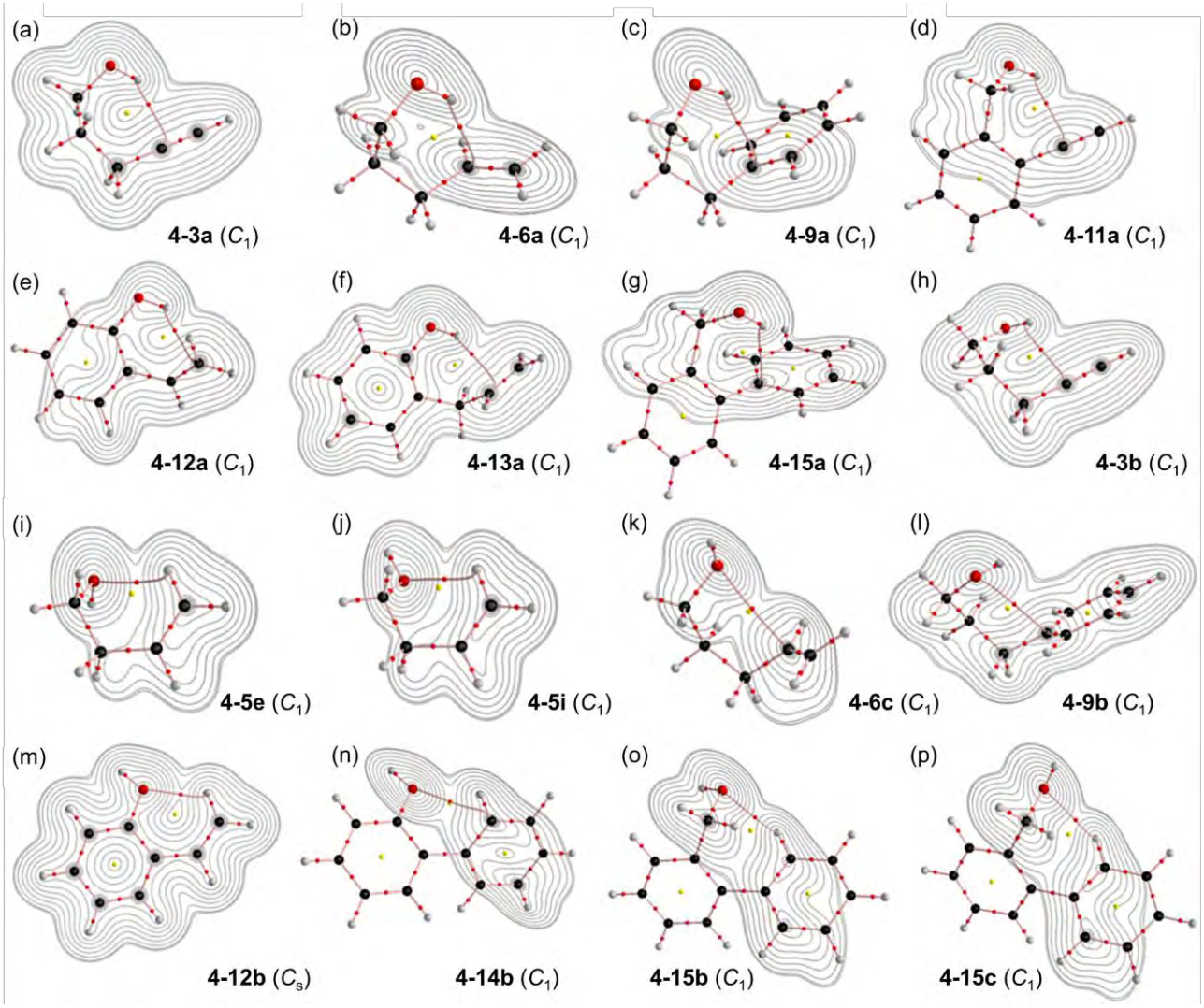

Figure 4-3. Molecular graphs for the 16 conformers of **4-3a**, **4-6a**, **4-9a**, **4-11a**, **4-12a**, **4-13a**, **4-15a**, **4-3b**, **4-5e**, **4-5i**, **4-6c**, **4-9b**, **4-12b**, **4-14b**, **4-15b**, and **4-15c** ((a)–(p), respectively), calculated with MP2/BSS-A, where BPs with BCP corresponding to the intramolecular non-covalent interactions around the OH group are detected. The BCPs are denoted by red dots, RCPs (ring critical points) are indicated by yellow dots and BPs are indicated by pink lines. The carbon, hydrogen, and oxygen atoms are shown in black, grey, and red, respectively. Contour plots are drawn on the planes containing the intramolecular interaction for each.

As shown in Figure 4-3, each BP with BCP corresponding to the intramolecular OH-∗-C(π) interaction appears in the six-membered ring of the –COH-∗-CCC type. However, each BP with BCP corresponding to the intramolecular O-∗-C(π) or O-∗-H(π) interaction appears in the five, six, or seven-membered ring. A BCP on a BP corresponding to the intramolecular OH-∗-C(π), O-∗-C(π) or O-∗-H(π) interaction is not detected for HOCC≡CH (**4-1**), HOCCC≡CH (**4-2**), HOCC=CH (**4-4**), HOCCC=CH (**4-5**), $HOCH_2Ph$ (**4-7**), $HOCH_2CH_2Ph$ (**4-8**), and HOC_6H_4C=CH-*o* (**4-10**). The cyclic interaction seems not to satisfy the conditions for the appearance of BP with BCP in each of the above species. BPs with BCPs corresponding to both intramolecular OH-∗-C(π) and O-∗-C(π) interactions are detected in **4-6**, while BPs with BCPs corresponding to the intramolecular OH-∗- C(π) and O-∗-H(π) interactions are detected in **4-12** and **4-15**. However, only BP with BCP corresponding to the intramolecular OH-∗-C(π) interaction appears in **4-13**, whereas only BP with BCP corresponding to the intramolecular O-∗-C(π) interaction appears in **4-14**. The intramolecular OH-∗-C(π) interactions, appearing in the six-membered rings, show clear contrast to the similar CH-∗-C(π) interaction, expected to occur in the five-membered ring in the species similar to **4-5**.[34]

Molecular graphs are given in Figures 4-A1–4-A3 of the Appendix for the conformers in **4-1**–**4-15** without a BCP on a BP corresponding to the OH-∗-C(π) or O-∗-X interaction being recorded for each.

Survey of HB Interactions in 4-1–4-15

The BPs corresponding to the intramolecular OH-∗-C(π), O-∗-C(π), and O-∗-H(π) interactions shown in Figure 4-3 appear somewhat curved, especially around the area close to the atoms at the ends of the BPs. To examine the linearity of the interactions further, the lengths of the BPs (r_{BP}) in question and the corresponding straight-line distances (R_{SL}) are calculated for those shown in Figure 4-3. The values calculated with MP2/BSS-A are collected in Table 4-A2 of the Appendix, together with the differences between them ($\Delta r_{BP} = r_{BP} - R_{SL}$). The magnitudes of Δr_{BP} are 0.01–0.30 Å for the BPs. Consequently, the intramolecular OH-∗-C(π) interactions should be recognized as the curved ones, more or less. The curved nature of the intramolecular interactions would have originated from the twisted interaction due to the steric constraints in the optimized conformers. The r_{BP} values are plotted versus the R_{SL}, which is displayed in Figure 4-A5 of the Appendix. The Δr_{BP} values seem to increase in the order O-∗-H(π) < O-∗-C(π) < OH-∗-C(π) in the average.

The QTAIM functions of $\rho_b(\boldsymbol{r}_c)$, $H_b(\boldsymbol{r}_c) - V_b(\boldsymbol{r}_c)/2$, $H_b(\boldsymbol{r}_c)$, and $k_b(\boldsymbol{r}_c)$ are calculated at the BCP on the BP corresponding to the intramolecular OH-∗-C(π) interaction for **4-3a**, **4-6a**, **4-9a**, **4-11a**, **4-12a**, **4-13a**, and **4-15a** and at the factor corresponding to the intramolecular O-∗-C(π) interaction for **4-3b**, **4-6b**, **4-9b**, and **4-14b**, together with that corresponding to the intramolecular O-∗-H(π) interaction for **4-5e**, **4-5i**, **4-12b**, **4-15b**, and **4-15c**. Table 4-1 shows the values, as evaluated with MP2/BSS-A. Figure 4-4 shows the plots of $H_b(\boldsymbol{r}_c)$ versus $H_b(\boldsymbol{r}_c) - V_b(\boldsymbol{r}_c)/2$ for OH-∗-C(π), O-∗-C(π), and O-∗-H(π) interactions in them.

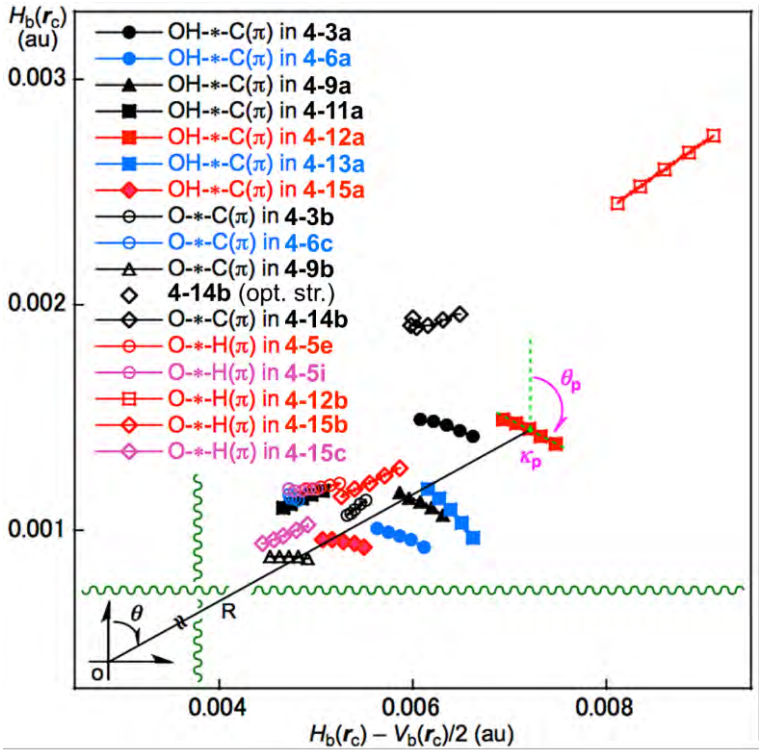

Figure 4-4. Plots of $H_b(\boldsymbol{r}_c)$ versus $H_b(\boldsymbol{r}_c) - V_b(\boldsymbol{r}_c)/2$ for the intramolecular interactions around the OH group in **4-3a**, **4-3b**, **4-5e**, **4-5i**, **4-6a**, **4-6c**, **4-9a**, **4-9b**, **4-11a**, **4-12a**, **4-12b**, **4-13a**, **4-14b**, **4-15a**, **4-15b**, and **4-15c**, as evaluated with MP2/BSS-A. The perturbed structures are generated with CIV.

the perturbed structures generated with CIV. The (R, θ) and ($\theta_{p:CIV}$, $\kappa_{p:CIV}$) values were calculated by analyzing the plots in Figure 4-4. The values are collected in Table 4-1, together with the C_{ii} values.

Nature of Intramolecular OH-∗-C(π), O-∗-C(π), and O-∗-H(π) Interactions in the Conformers of 4-1–4-15

The intramolecular OH-∗-C(π), O-∗-C(π), and O-∗-H(π) interactions in the conformers of **4-1**–**4-15** given in Table 4-1 are classified and characterized based on the (θ, $\theta_{p:CIV}$) values and evaluated with MP2/BSS-A. While θ classifies interactions, θ_p characterizes them.

In the case of the intramolecular OH-∗-C(π) interactions in Table 4-1, the (θ, $\theta_{p:CIV}$) values are (77.0–80.5°, 94.0–115.9°) for all the intramolecular OH-∗-C(π) interactions, except for **4-11a**, of which (θ, $\theta_{p:CIV}$) = (76.8°, 79.3°). Therefore, the intramolecular OH-∗-C(π) interactions in **4-3a**, **4-6a**, **4-9a**, **4-12a**, **4-13a**, and **4-15a** are predicted to have a t-HB$_{nc}$ nature, as appeared in the p-CS region (p-CS/t-HB$_{nc}$), whereas the nature of the interaction in **4-11a** has a p-CS/vdW nature. The intramolecular O-∗-C(π) interactions show a similar trend relative to the intramolecular OH-∗-C(π) interactions. The (θ, $\theta_{p:CIV}$) values are (76.4–79.4°, 90.8–107.2°) for **4-6c** and **4-9b**, whereas the values are (72.0–78.5°, 49.7–86.1°) for **4-3b** and **4-14b**. Consequently, the nature of the intramolecular O-∗-C(π) interactions in **4-6c** and **4-9b** is predicted to have a p-CS/t-HB$_{nc}$ nature, while the predicted nature is p-CS/vdW for **4-3b** and **4-14b**. However, the (θ, $\theta_{p:CIV}$) values are (73.2–78.2° and 73.4–

88.5º) for the intramolecular O-∗-H(π) interactions in **4-5e**, **4-5i**, **4-12b**, **4-15b**, and **4-15c**, and thus they have a *p*-CS/vdW nature. The strength of the three types of interactions is roughly predicted to be smaller in the order OH-∗-C(π) > O-∗-C(π) > O-∗-H(π).

Table 4-1. QTAIM functions and QTAIM-DFA parameters for the intramolecular interactions around the O–H group, as elucidated with MP2/BSS-A, together with the predicted nature for the interactions.[a,b]

A-∗-B(π) (Compounds)	$\rho_b(\boldsymbol{r}_c)$ (ea_o^{-3})	$c\nabla^2\rho_b(\boldsymbol{r}_c)$[c] (au)	$H_b(\boldsymbol{r}_c)$ (au)	$k_b(\boldsymbol{r}_c)$[d]	R[e] (au)	θ[f] (º)	C_{ii}[g] (Å mdyn^{-1})	$\theta_{p:CIV}$[h] (º)	$\kappa_{p:CIV}$[i] (au^{-1})	Predicted Nature
OH-∗-C(π)										
OH-∗-^{o}C(π) (**4-3a**)	0.0161	0.0063	0.0015	–0.870	0.0065	77.0	7.81	97.7	335	*p*-CS/*t*-HB$_{nc}$
OH-∗-^{o}C(π) (**4-6a**)	0.0162	0.0059	0.0010	–0.909	0.0059	80.5	8.02	99.2	387	*p*-CS/*t*-HB$_{nc}$
OH-∗-^{i}C(π) (**4-9a**)	0.0155	0.0061	0.0011	–0.898	0.0062	79.5	7.46	101.8	288	*p*-CS/*t*-HB$_{nc}$
OH-∗-^{o}C(π) (**4-11a**)	0.0117	0.0048	0.0011	–0.867	0.0050	76.8	14.93	79.3	56.2	*p*-CS/vdW
OH-∗-$^{\beta}$C(π) (**4-12a**)	0.0170	0.0072	0.0014	–0.888	0.0073	78.6	5.85	101.8	236	*p*-CS/*t*-HB$_{nc}$
OH-∗-^{o}C(π) (**4-13a**)	0.0178	0.0064	0.0011	–0.907	0.0065	80.3	7.58	115.9	420	*p*-CS/*t*-HB$_{nc}$
OH-∗-^{i}C(π) (**4-15a**)	0.0135	0.0053	0.0009	–0.901	0.0054	79.8	12.45	94.0	193	*p*-CS/*t*-HB$_{nc}$
O-∗-C(π)										
O-∗-^{o}C(π) (**4-3b**)[j]	0.0125	0.0054	0.0011	–0.887	0.0055	78.5	7.31	49.7	5035	*p*-CS/vdW
O-∗-^{o}C(π) (**4-6c**)	0.0098	0.0047	0.0011	–0.863	0.0049	76.4	7.48	107.2	7373	*p*-CS/*t*-HB$_{nc}$
O-∗-^{i}C(π) (**4-9b**)	0.0108	0.0047	0.0009	–0.897	0.0048	79.4	9.14	90.8	85.0	*p*-CS/*t*-HB$_{nc}$
O-∗-^{o}C(π) (**4-14b**)[k]	0.0108	0.0060	0.0019	–0.807	0.0063	72.0	4.79	86.1	1631	*p*-CS/vdW
O-∗-H(π)[l]										
O-∗-$^{\beta}$H(π) (**4-5e**)	0.0107	0.0051	0.0012	–0.867	0.0052	76.8	12.74	86.3	266	*p*-CS/vdW
O-∗-$^{\beta}$H(π) (**4-5i**)	0.0102	0.0049	0.0012	–0.862	0.0050	76.3	15.97	88.5	577	*p*-CS/vdW
O-∗-$^{\beta}$H(π) (**4-12b**)	0.0164	0.0086	0.0026	–0.822	0.0090	73.2	4.43	73.4	19.8	*p*-CS/vdW
O-∗-^{o}H(π) (**4-15b**)	0.0129	0.0056	0.0012	–0.877	0.0057	77.7	13.09	77.9	0.4	*p*-CS/vdW
O-∗-^{o}H(π) (**4-15c**)	0.0112	0.0047	0.0010	–0.883	0.0048	78.2	16.49	79.9	24.3	*p*-CS/vdW
OH-∗-C(π)										
OH-∗-^{o}C(π) (**4-3a**)[m]	0.0147	0.0061	0.0018	–0.832	0.0063	73.9	7.95	82.7	185	*p*-CS/vdW
OH-∗-^{o}C(π) (**4-3a**)[n]	0.0132	0.0050	0.0016	–0.813	0.0053	72.5	9.68	81.0	199	*p*-CS/vdW

[a] Data are given at BCPs. [b] MP2/6-311+G(3df,3pd) for MP2/BSS-A. [c] $c\nabla^2\rho_b(\boldsymbol{r}_c) = H_b(\boldsymbol{r}_c) - V_b(\boldsymbol{r}_c)/2$, where $c = \hbar^2/8m$. [d] $k_b(\boldsymbol{r}_c) = V_b(\boldsymbol{r}_c)/G_b(\boldsymbol{r}_c)$. [e] $R = (x^2 + y^2)^{1/2}$, where $(x, y) = (H_b(\boldsymbol{r}_c) - V_b(\boldsymbol{r}_c)/2, H_b(\boldsymbol{r}_c))$. [f] $\theta = 90^o - \tan^{-1}(y/x)$. [g] Defined in Equation (2-12) in Chapter 2. [h] $\theta_p = 90^o - \tan^{-1}(dy/dx)$. [i] $\kappa_p = |d^2y/dx^2|/[1 + (dy/dx)^2]^{3/2}$. [j] Data from $w = 0$, ±0.0125, and ±0.025 were employed for the evaluation. [k] Data from $w = -0.0625$, –0.050, –0.0375, –0.025, and –0.0125 are employed for the evaluation. [l] H(π) bonded directly to C(π). [m] Calculated with M06-2X/BSS-A (r(H···C(π)) = 2.3277 Å versus 2.2797 Å (MP2)). [n] Calculated with B3LYP/BSS-A (r(H···C(π)) = 2.3782 Å versus 2.2797 Å (MP2)).

The calculated $\theta_{p:CIV}$ values are usually larger than or close to the θ values for the usual interactions. However, the $\theta_{p:CIV}$ in **4-3b** (49.7º) is predicted to be much smaller than θ (78.5º) for the O-∗-C(π) interaction. The reason is unclear when using the data in Table 4-1. It would have originated from the substantially distorted nature of the O-∗-C(π) interaction in **4-3b** (Δr_{BP} = 0.295 Å). The BP for the intramolecular O-∗-C(π) interaction in **4-3b** seems to be very close to the O–H bond in **4-3b**, which would also be a reason for this phenomena.

The effects from basis sets and levels on the optimized structures and the calculated natures of the interactions in question must be an important issue of QTAIM approach. The effects on the standard interactions, containing hydrogen bonds, were carefully examined.[35] The effects from the DFT level of M06-2X (M06-2X/BSS-A//M06-2X/BSS-A: M06-2X/BSS-A) and B3LYP (B3LYP/BSS-A//B3LYP/BSS-A: B3LYP/BSS-A) on the nature of OH-∗-$^{\alpha}$C(π) in **4-3a** were examined. Table 4-1 shows the results. The r(H···C(π)) values were optimized as 2.3277 and 2.3782 Å at the M06-2X and B3LYP levels, respectively, which are 0.048 and 0.099 Å longer, relative to that optimized at the MP2 level (2.2797 Å). On the other hand, the (θ, $\theta_{p:CIV}$) values of (73.9º, 82.7º) and (72.5º, 81.0º) were calculated for OH-∗-$^{\alpha}$C(π) in **4-3a** at the M06-2X and B3LYP levels, respectively, irrespective of the calculated r(H···C(π)) values, while the (77.0º, 97.7º) values were calculated at the MP2 level. As a result, the *p*-CS/vdW nature was predicted for OH-∗-$^{\alpha}$C(π) in **4-3a** at the M06-2X and B3LYP levels, whereas the *p*-CS/*t*-HB_{nc} nature was at the MP2 level. The effects from M06-2X/BSS-A and B3LYP/BSS-A seem not small, relative to the case of MP2/BSS-A.

The strength of the intramolecular interactions is discussed in relation to those of the NBO analysis in the next section.

NBO Analysis for Intramolecular Interactions

The stabilization energy $E(2)$ is calculated by NBO analysis for each donor NBO (i) and acceptor NBO (j) based on the second-order perturbation theory according to Equation (4-2). The q_i values in Equation (4-2) are the donor orbital occupancy, E_i and E_j are diagonal elements (orbital energies) and $F(i,j)$ is the off-diagonal NBO Fock matrix element. The treatments will evaluate the CT terms of the intramolecular interactions.

$$E(2) = q_i F(i,j)^2/(E_j - E_i) \quad (4\text{-}2)$$

The NBO analysis was applied to the conformers, where BPs with BCPs corresponding to the intramolecular OH-∗-C(π), O-∗-C(π), and/or O-∗-H(π) interactions were detected. The NBO analysis was also applied to the conformers for which the OH···C(π) distances are less than 2.9 Å. The $E(2)$ values were successfully obtained under the threshold of 0.5 kcal mol^{-1} (2.1 kJ mol^{-1}). Table 4-2 collects the results of the NBO analysis, as calculated with MP2/BSS-A. The CT terms of the

π(C≡C/C=C)→σ*(H–O) type contribute to $E(2)$ in **4-3a**, **4-5a**, **4-5b**, **4-6a**, **4-8a**, **4-9a**, **4-10a**, **4-11a**, **4-12a**, **4-13a**, **4-14a**, and **4-15a**, together with the inverse σ(H–O)→π*(C≡C/C=C) type for **4-10a** and **4-15b**. The CT terms of the n_p(O)→π*(C≡C) type contribute to $E(2)$ in **4-1a**, **4-3b**, **4-4a**, **4-4c**, **4-6a**, **4-6b**, **4-6c**, and **4-7a**. However, the CT term of the n_p(O)→σ*(C–H) type was detected in

Table 4-2. Results of the NBO analysis for the intramolecular interactions around the OH group, as evaluated with MP2/BSS-A.

Species	$E(2)^a$ (kJ mol^{-1})	$E(j)–E(i)^b$ (au)	$F(i,j)^c$ (au)	r(H···C(π)) (Å)
CT term of the π(C≡C/C=C)→σ*(H–O) type				
4-3a	10.0	1.14	0.047	2.2797
4-5a	4.8	1.09	0.032	2.4802
4-5b	3.7	1.10	0.028	2.6111
4-6a	13.8	1.11	0.054	2.3020
4-8a	2.7	1.02	0.025	2.5218
4-9a	7.2	1.05	0.042	2.3316
4-10a	4.5	1.52	0.036	2.2584
4-11a	2.1	1.13	0.021	2.4507
4-12a	11.6	1.08	0.049	2.4139
4-13a	20.1	1.09	0.065	2.2783
4-14a	8.9	1.00	0.045	2.3601
4-15a	4.4	1.05	0.032	2.3869
CT term of the σ(H–O)→π*(C≡C/C=C) type				
4-10a	3.6	1.27	0.029	2.2584
4-15b	2.1	1.47	0.027	4.1125
CT term of the n_p(O)→π*(C≡C/C=C) type				
4-1a	5.7	0.82	0.030	2.5155[d]
4-3b	2.3	0.79	0.018	2.4272[e]
4-4a	6.9	0.72	0.031	2.5383[f]
4-4c	5.4	0.73	0.027	2.6315[g]
4-6a	2.3	0.70	0.017	2.3020[h]
4-6b	3.7	0.73	0.023	3.4771[i]
4-6c	3.8	0.73	0.023	3.5116[j]
4-7a	3.7	0.67	0.024	2.5311[k]
CT term of the n_p(O)→σ*(C–H) type				
4-15c	2.3	1.34	0.024	4.2452[l]
CT term of the n_s(O)→π*(C–H) type				
4-10b	3.5	1.18	0.028	3.6982[m]
CT term of the n_s(O)→σ*(C–H) type				
4-12b	3.3	1.59	0.032	3.8536[n]
4-15b	19.3	7.82	0.170	4.1125[o]

[a] Second order perturbation energy given by Equation (4-2). [b] The diagonal elements (orbital energies). [c] The off-diagonal NBO Fock matrix element. [d] 2.4027 Å for r(O···C(π)). [e] 2.9757 Å for r(O···C(π)). [f] 2.4170 Å for r(O···C(π)). [g] 2.4305 Å for r(O···C(π)). [h] 3.0039 Å for r(O···C(π)). [i] 3.0044 Å for r(O···C(π)). [j] 2.9581 Å for r(O···C(π)). [k] 3.0080 Å for r(O···C(π)). [l] 2.4484 Å for r(HO···H). [m] 2.74345 Å for r(O···C(π)). [n] 2.2155 Å for r(HO···H). [o] 2.3578 Å for r(HO···H).

4-15c and that of the n_s(O)→π*(C–H) type was in **4-10b**, while the term of the n_s(O)→σ*(C–H) type was in **4-12b** and **4-15b**.

The *E*(2) values larger than 7.0 kJ mol^{-1} were predicted for the CT terms of the π(C≡C/C=C)→σ*(H–O) interactions in **4-3a**, **4-6a**, **4-9a**, **4-13a**, and **4-14a**, for which the OH···C(π) distances are less than 2.36 Å. A BP with a BCP corresponding to the intramolecular OH-∗-C(π) interaction was detected for each case, except for **4-14a**. The *E*(2) values of less than 4.8 kJ mol^{-1} were similarly predicted for **4-5a**, **4-5b**, **4-8a**, **4-11a**, and **4-15a**, among which the OH···C(π) distances were longer than 2.38 Å. In this case, the BP with the BCP was detected for **4-11a**, **4-12a**, and **4-15a**, whereas it was not detected for **4-5a**, **4-5b**, **4-8a**, and **4-10a**. The *E*(2) value of 20.1 kJ mol^{-1} was evaluated for the intramolecular OH-∗-C(π) interaction in **4-13a**, which is larger than those in **4-3a**, **4-6a**, **4-9a**, **4-11a**, **4-12a**, and **4-15a** (2.1–13.8 kJ mol^{-1}). This must be the reason for the stronger intramolecular OH-∗-C(π) interaction in **4-13a**, relative to the cases in **4-3a**, **4-6a**, **4-9a**, **4-11a**, **4-12a**, and **4-15a** evaluated with QTAIM-DFA. The large *E*(2) value of 20.1 kJ mol^{-1} in **4-13a** may come from the short OH···C(π) distance (2.28 Å), although the other advantageous structural parameters around the OH-∗-C(π)-predicted CT interaction in **4-11a** are not of the π(C≡C)→σ*(H–O) type but rather the inverse type of σ(H–O)→π*(C≡C). The *E*(2) value was evaluated to be 2.1 kJ mol^{-1} for the intramolecular interaction of **4-11a**.

Substantially, large *E*(2) values are evaluated for the intramolecular OH···C(π) interaction by NBO, if a BP with a BCP corresponding to the intramolecular OH-∗-C(π) interaction was detected for the conformer. In the case of **4-12b**, a rather small *E*(2) value (3.3 kJ mol^{-1}) was evaluated for the n_p(O)→σ*(H–C) interaction.

However, a much larger *E*(2) value of 19.3 kJ mol^{-1} was predicted for the n_s(O)→σ*(C–H) interaction in **4-15b**, which must be the reason for the predicted strong intramolecular O-∗-H(π) interaction for **4-15b** evaluated with QTAIM-DFA. The CT terms were not printed out for the intramolecular interactions in **4-5e** and **4-5i**, although the BPs with the BCPs of the O-∗-$^{\beta}$H(π) type were detected. The results seem to be queries at first glance. They would be the results from the intramolecular vdW type interactions in **4-5e** and **4-5i**. The contributions of the CT terms must be (very) small for the vdW type interactions; therefore, the *E*(2) values should be evaluated to be (very) small, which would be buried in the threshold value of 2.1 kJ mol^{-1} (0.5 kcal mol^{-1}).

The results of the NBO analysis are discussed in relation to the ΔE_{ES} values in the next section.

Intramolecular π(C≡C/C=C)→σ*(H–O) Interactions as the Factor to Stabilize the Conformers

Are the conformers effectively stabilized through the intramolecular CT interactions? The stability of the conformers are discussed in relation to the $E(2)$ values calculated with the NBO analysis, as exemplified by the energy differences between conformer **a** and **b**, $\Delta E_{ES}(\boldsymbol{x}\mathbf{b}/\boldsymbol{x}\mathbf{a})$ [= $\Delta E_{ES}(\boldsymbol{x}\mathbf{b}) - \Delta E_{ES}(\boldsymbol{x}\mathbf{a})$]. The ***x*** were limited to **4-3**, **4-6**, **4-9**, **4-11**–**4-13**, and **4-15**, where the BP with BCP of the OH-∗-C(π) type were detected in ***x*a**. The OH···C(π) distance must be the shortest in ***x*a** by definition; therefore, the steric hindrance is expected to reach its maximum in ***x*a**, although the ***x*a** will contain the attractive factor based on the intramolecular OH···C(π) interaction. The intramolecular OH···C(π) distance in ***x*b** is the second shortest, by definition, and therefore the steric hindrance in ***x*b** would be somewhat released in most cases due to the change of $\phi(C_\beta C_\gamma OH)$ from ***x*a**. As a result, the $\Delta E_{ES}(\boldsymbol{x}\mathbf{b}/\boldsymbol{x}\mathbf{a})$ is expected to be a rough measure for the contribution from the intramolecular interaction in ***x*a** if the contribution from the intramolecular interaction is (almost) varnished in ***x*b**.

The nature of the interactions in question can be clarified based on the BPs with the BCPs, but the intramolecular interactions are carefully discussed based on BPs with BCPs. The theoretical treatment for the appearance and/or disappearance of BPs is very complex and very difficult.[36] Namely, the theoretical treatment for the intramolecular interactions in detail is beyond the scope of this work. Therefore, the $\Delta E_{ES}(\boldsymbol{x}\mathbf{b}/\boldsymbol{x}\mathbf{a})$ values are discussed here, where the BPs with BCPs are detected for some of the conformers from **4-1**–**4-15**, whereas some are not. The $\Delta E_{ES}(\boldsymbol{x}\mathbf{b}/\boldsymbol{x}\mathbf{a})$ values are discussed in relation to the $E(2)$ values for the intramolecular interactions evaluated with the NBO and the steric effect in the conformers.

Figure 4-5 shows the plots of $E(2)$ and $\Delta E_{ES}(\boldsymbol{x}\mathbf{b}/\boldsymbol{x}\mathbf{a})$ for ***x*** = **4-3**, **4-6**, **4-9**, **4-11**–**4-13**, and **4-15**

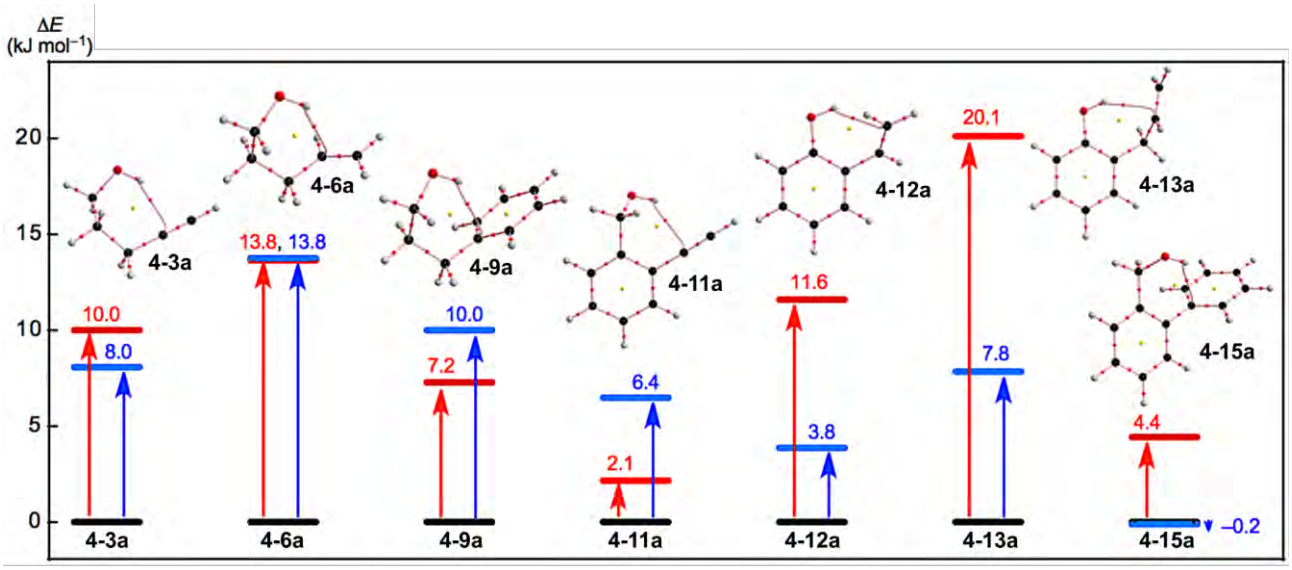

Figure 4-5. Plots of $E(2)$ and $\Delta E_{ES}(\boldsymbol{x}\mathbf{b}/\boldsymbol{x}\mathbf{a})$ for ***x*** = **4-3**, **4-6**, **4-9**, **4-11**–**4-13**, and **4-15** in red and blue, respectively. Molecular graphs for ***x*a** are shown, where BCP with BPs corresponding to the intramolecular OH-∗-C(π), O-∗-C(π), or O-∗-H(π) interactions are given for each. Molecular graphs other than ***x*a** are drawn in Figures 4-A3–4-A5 of the Appendix.

in red and blue, respectively. The ΔE_{ES}(***x*b**/***x*a**) values are evaluated over a range of $3.8 \leq \Delta E_{ES} \leq 13.8$ kJ mol^{-1} for **4-3b**/**4-3a**, **4-6b**/**4-6a**, **4-9b**/**4-9a**, and **4-11b**/**4-11a**–**4-13b**/**4-13a** with ΔE_{ES} = –0.2 kJ mol^{-1} for **4-15b**/**4-15a**. However, the $E(2)$ values are calculated at a range of $2.1 \leq \Delta E_{ES} \leq 13.8$ kJ mol^{-1} for ***x*a** (***x*** = **4-3**, **4-6**, **4-9**, **4-11**, **4-12**, and **4-15**) with 20.1 kJ mol^{-1} for **4-13a**, as shown in Figure 4-5 and Table 4-2. The ΔE_{ES} values of **4-3b**/**4-3a** (8.0 kJ mol^{-1}), **4-6b**/**4-6a** (13.8 kJ mol^{-1}), and **4-9b**/**4-9a** (10.0 kJ mol^{-1}) are close to the $E(2)$ values of **4-3a** (10.0 kJ mol^{-1}), **4-6a** (13.8 kJ mol^{-1}), and **4-9a** (7.2 kJ mol^{-1}). The results can be reasonably explained by assuming that the intramolecular π(C≡C/C=C)→σ*(H–O) interactions can effectively stabilize the conformers of the ethenyl and ethynyl derivatives of the aliphatic alcohols. In the case of the phenol and benzyl alcohol derivatives, the ΔE_{ES} values of **4-12b**/**4-12a** (3.8 kJ mol^{-1}), **4-13b**/**4-13a** (7.8 kJ mol^{-1}), and **4-15b**/**4-15a** (–0.2 kJ mol^{-1}) are substantially smaller than the $E(2)$ values of **4-12a** (11.6 kJ mol^{-1}), **4-13a** (20.1 kJ mol^{-1}), and **4-15a** (4.4 kJ mol^{-1}), respectively. Other factors seem to waste the contributions from the attractive intramolecular π(C≡C/C=C)→σ*(H–O) interactions. A repulsive steric effect would greatly waste the attractive interactions in **4-12a** and **4-13a**. The intramolecular interactions operate more effectively to stabilize **4-12a** and **4-13a** relative to **4-12b** and **4-13b**, respectively, which would come from the steric hindrance in **4-12b** and **4-13b** larger than **4-12a** and **4-13a**, respectively. The ΔE_{ES}(**4-15b**/**4-15a**) value is predicted to be –0.2 kJ mol^{-1}. The intramolecular n_p(O)→σ*(C–H) interaction stabilizes **4-15b**, very effectively, as shown by the NBO analysis (see, Table 4-2). In fact, the π(C≡C/C=C)→σ*(H–O) interaction acts to stabilize **4-15a** (4.4 kJ mol^{-1}), but the σ(H–O)→π*(C≡C/C=C), n_p(O)→σ*(C–H), and n_s(O)→σ*(C–H) interactions also operate to stabilize **4-15b** (2.1 kJ mol^{-1}), **4-15c** (2.3 kJ mol^{-1}), and **4-15b** (19.3 kJ mol^{-1}), respectively. The contributions from the intramolecular interactions to stabilize **4-15a** and **4-15b** must be the primary factor in the negative value of ΔE_{ES}(**4-15b**/**4-15a**), although the mechanism, similar to the case of **4-11b**/**4-11a** and **4-11b**/**4-11a**, must also be working.

The ΔE_{ES}(**4-1b**/**4-1a**) (6.6 kJ mol^{-1}) and ΔE_{ES}(**4-5b**/**4-5a**) (6.8 kJ mol^{-1}) values seem close to the ΔE_{ES}(**4-3b**/**4-3a**) (8.0 kJ mol^{-1}) and smaller than the ΔE_{ES}(**4-6b**/**4-6a**) (13.8 kJ mol^{-1}), for example. The intramolecular n_p(O)→π*(C≡C/C=C) and π(C≡C/C=C)→σ*(H–O) interactions operate to stabilize **4-1a** (5.7 kJ mol^{-1}) and **4-5a** (4.8 kJ mol^{-1}), respectively, while **4-3a** (10.0 kJ mol^{-1}) and **4-6a** (13.8 kJ mol^{-1}) are stabilized by the π(C≡C/C=C)→σ*(H–O) interaction. In this case, a BP with a BCP is detected for **4-3a** and **4-6a**, whereas a BP with a BCP is not detected in **4-1a** and **4-5a**. The conditions for the appearance of the BP with BCP would not be satisfied for the corresponding interaction in **4-1a** and **4-5a**.

Summary

Intramolecular cv-HBs are extremely important in the all fields of the chemical and biological sciences as are intramolecular π-HBs as well as the intermolecular HBs. The intrinsic dynamic and static nature of intramolecular π-HBs is elucidated with QTAIM-DFA by employing the perturbed structures generated with CIV. Over 70 conformers were optimized for **4-1**–**4-15**. BPs with BCPs corresponding to the intramolecular OH-∗-C(π) interactions were detected in seven conformers that appeared in the six-membered rings of the –COH-∗-CCC type. Those corresponding to the intramolecular O-∗-C(π) interactions are also detected in four conformers together with those for the intramolecular O-∗-H(π) interactions in five conformers. The intramolecular O-∗-C(π) and O-∗-H(π) interactions appeared in the 5–7-membered rings. The BPs are somewhat curved. The intramolecular OH-∗-C(π) interactions are predicted to have a *p*-CS/vdW or *p*-CS/*t*-HB_{nc} nature. The strength of the intramolecular interactions appears to be generally weaker in the order OH-∗-C(π) > O-∗-C(π) > O-∗-H(π). The contributions from the intramolecular OH-∗-C(π), O-∗-C(π) and O-∗-H(π) interactions towards stabilizing the conformers are also confirmed by the NBO analysis. The contributions of the intramolecular interactions used to stabilize the conformers are considered, even for the conformers with no appearance of BPs, which corresponds to the intramolecular interactions. The intramolecular interactions between the OH and C≡C/C=C groups, such as the OH-∗-C(π), O-∗-C(π), or O-∗-H(π) types, may help to stabilize the conformers even if this interaction is not detected as a BP with BCP. The intramolecular OH-∗-π interactions appear to be evaluated as somewhat stronger than the intermolecular interactions.

Appendix

Table 4-A1. Selected structural parameters of r(O–H), r(H···C(π)), ∠OHC(π), and ∠HC(π)C(π) around the intramolecular OH-∗-C(π) interactions in **4-1**–**4-15**, together with the ΔE_{ES} and ΔE_{ZP} values, evaluated with MP2/BSS-A.[a] Each conformer is called **a**, **b**, …, in the order of the increase of the r(H···C(π)) values.

Species (symm)	r(O–H) (Å)	r(OH···C(π)) (Å)	∠OHC(π) (º)	∠HC(π)C(π) (º)	ΔE_{ES}[b] (kJ mol^{-1})	ΔE_{ZP}[c] (kJ mol^{-1})
4-1: $HOCH_2C{\equiv}CH$						
4-1a (C_1)	0.9604	2.5155	72.2	127.9	0.0	0.0
4-1b (C_s)	0.9604	3.1663	26.0	156.5	6.6	5.9
4-2: $HO(CH_2)_2C{\equiv}CH$						
4-2a (C_1)	0.9625	2.5009	104.6	100.1	0.0	0.0
4-2b (C_1)	0.9601	3.2663	63.3	127.8	10.3	9.3
4-2c (C_1)	0.9593	3.7298	27.6	121.7	9.4	8.2
4-2d (C_1)	0.9597	4.0049	65.8	157.4	6.0	5.3
4-2e (C_s)	0.9594	4.3819	37.1	147.9	5.1	4.2
4-3: $HO(CH_2)_3C{\equiv}CH$						
4-3a (C_1)	0.9624	2.2797	133.5	83.6	0.0	0.0
4-3b (C_1)	0.9609	2.4272	115.9	91.2	8.0	6.2
4-6: $HO(CH_2)_3CH{=}CH_2$						
4-6a (C_1)	0.9621	2.3020	129.2	83.5	0.0	0.0
4-6b (C_1)	0.9599	3.4771	53.3	119.3	13.8	12.0
4-9: $HO(CH_2)_3Ph$						
4-9a (C_1)	0.9623	2.3316	129.6	77.1	0.0	0.0
4-9b (C_1)	0.9610	2.6756	101.7	85.6	10.0	8.7
4-11: $HOCH_2C_6H_4C{\equiv}CH$						
4-11a (C_1)	0.9625	2.4507	123.3	88.1	0.0	0.0
4-11b (C_1)	0.9611	3.7307	53.9	117.0	6.4	5.6
4-12: $HOC_6H_4CH{=}CH_2$						
4-12a (C_1)	0.9655	2.4139	113.1	68.3	0.0	0.0
4-12b (C_s)	0.9620	3.8536	7.8	77.1	3.8	3.5
4-13: $HOC_6H_4CH_2CH{=}CH_2$						
4-13a (C_1)	0.9661	2.2783	137.7	76.4	0.0	0.0
4-13b (C_1)	0.9616	4.1427	20.7	81.9	7.8	6.7
4-15: $HOCH_2C_6H_4Ph$						
4-15a (C_1)	0.9633	2.3869	126.9	82.1	0.0	0.0
4-15b (C_1)	0.9615	4.1125	52.1	67.7	–0.2	0.1

[a] With the MP2/6-311++G(3df,3pd) (MP2/BSS-A) method of the Gaussian 09 program. [b] The energies on the energy surface from the components (ΔE_{ES}) [= E_{ES}(***xm***) – E_{ES}(***x*****a**): ***x*** = **4-1**–**4-15**]. [c] The energies with the zero-point energy collections from the components (ΔE_{ZP}) [= E_{ZP}(***xm***) – E_{ZP}(***x*****a**): ***x*** = **4-1**–**4-15**].

Table 4-A2. Lengths of bond paths (BPs: r_{BP}) and the corresponding straight-line distances (R_{SL}), corresponding to the intramolecular non-covalent interactions around the OH group, evaluated with MP2/BSS-A, together with the differences between them ($\Delta r_{BP} = r_{BP} - R_{SL}$).[a]

Species (symm)	r_{BP}[b] (Å)	R_{SL}[c] (Å)	Δr_{BP}[d] (Å)
OH-∗-C(π)			
4-3a (C_1)	2.4248	2.2797	0.1452
4-6a (C_1)	2.4390	2.3020	0.1370
4-9a (C_1)	2.4786	2.3316	0.1470
4-11a (C_1)	2.5670	2.4507	0.1164
4-12a (C_1)	2.3970	2.2867	0.1103
4-13a (C_1)	2.5238	2.2782	0.2456
4-15a (C_1)	2.4569	2.3869	0.0699
O-∗-C(π)			
4-3b (C_1)	3.2709	2.9757	0.2951
4-6c (C_1)	2.9645	2.9580	0.0065
4-9b (C_1)	3.0586	3.0214	0.0372
4-14b (C_1)	3.0502	2.9122	0.1380
O-∗-H			
4-5e (C_1)	2.6129	2.4974	0.1155
4-5i (C_1)	2.6296	2.5373	0.0924
4-12b (C_1)	2.2717	2.2155	0.0562
4-15b (C_1)	2.3901	2.3578	0.0323
4-15c (C_1)	2.4920	2.4484	0.0436

[a] With the MP2/6-311++G(3df,3pd) for MP2/BSS-A method of the Gaussian 09 program. [b] The length of BPs. [c] Straight-line distances. [d] $\Delta r_{BP} = r_{BP} - R_{SL}$.

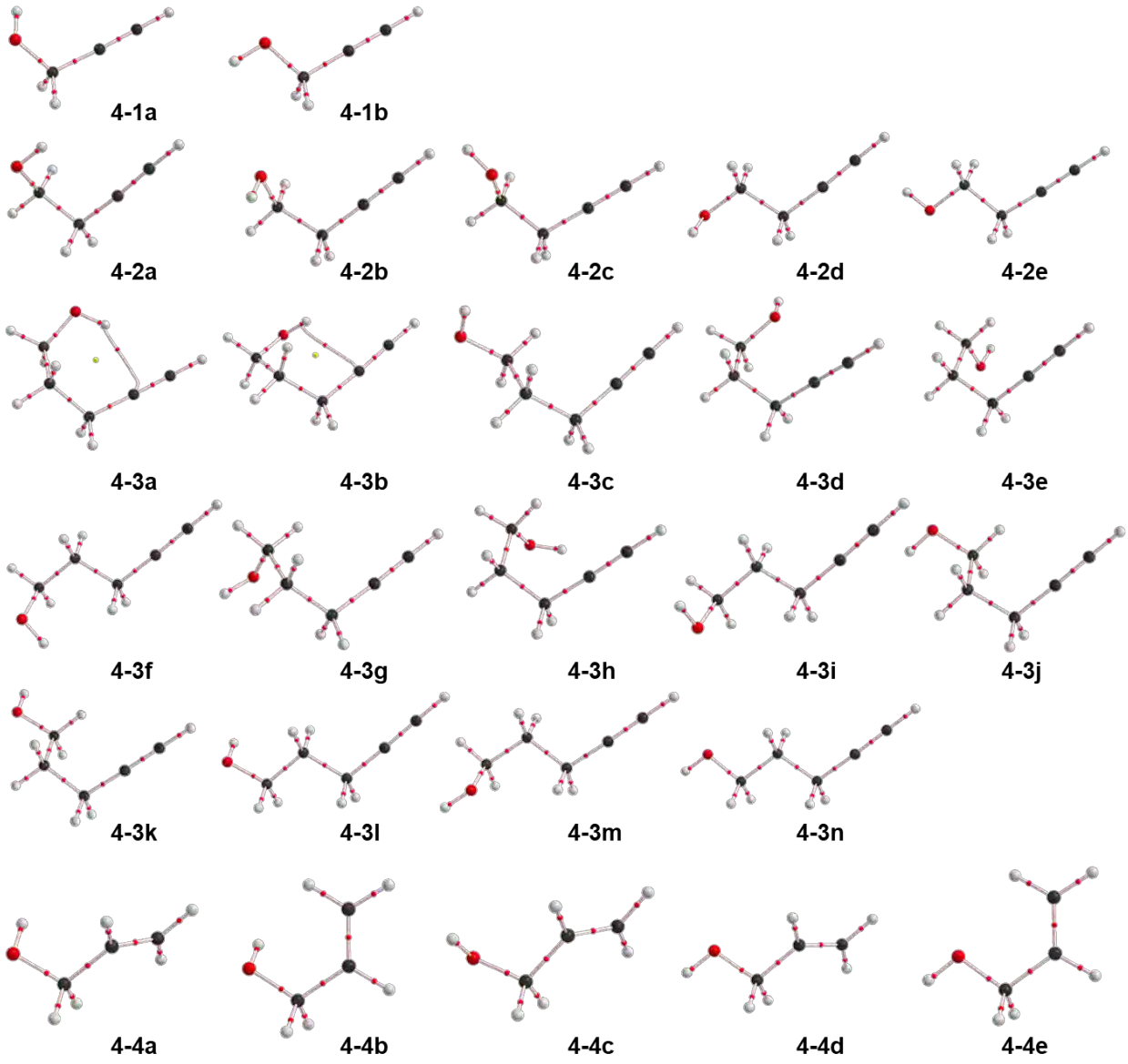

Figure 4-A1. Molecular graphs, drawn on the optimized structures, for the conformers in **4-1**–**4-4**, calculated with MP2/BSS-A.

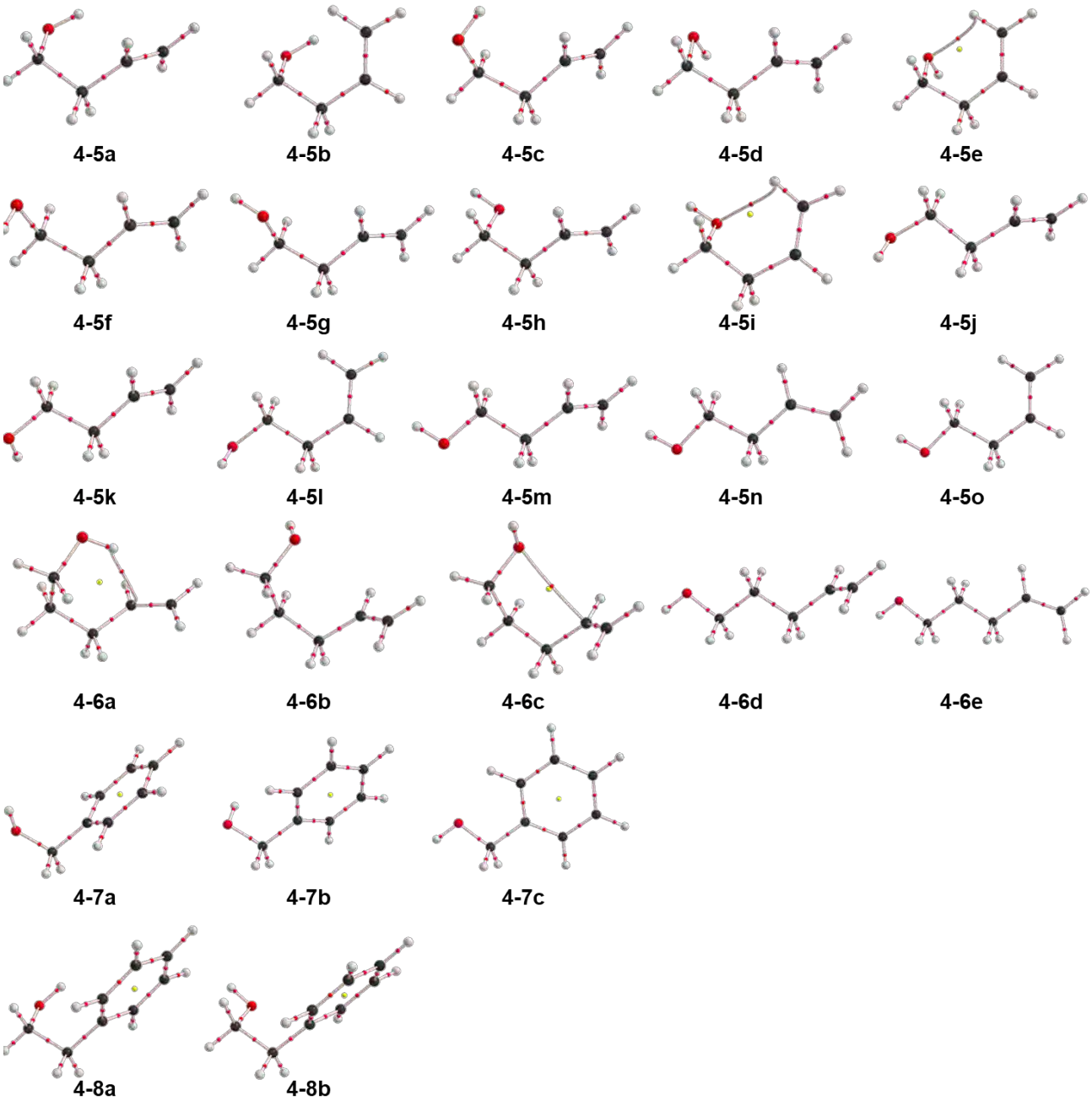

Figure 4-A2. Molecular graphs, drawn on the optimized structures, for the conformers in **4-5**–**4-8**, calculated with MP2/BSS-A.

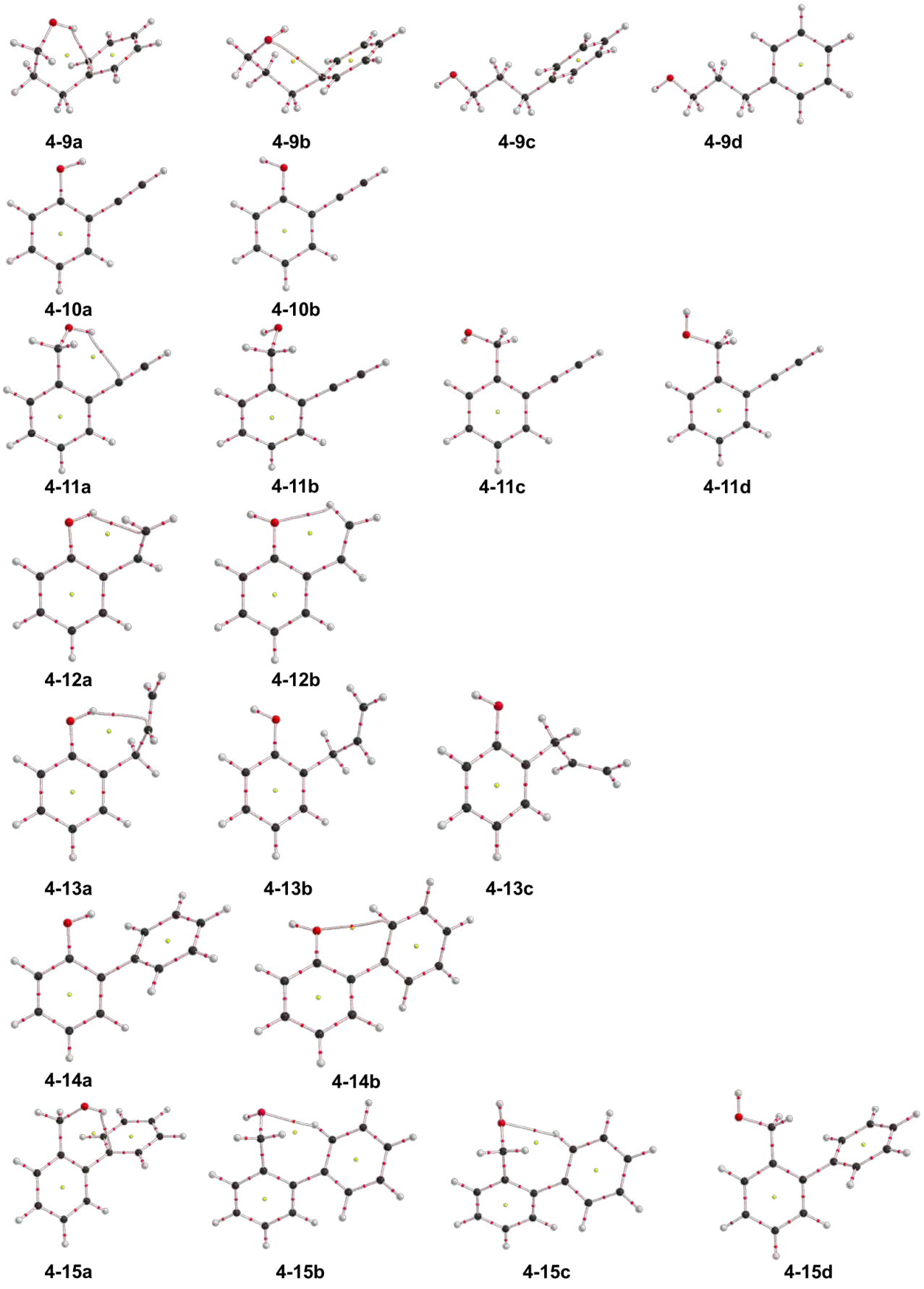

Figure 4-A3. Molecular graphs, drawn on the optimized structures, for the conformers in **4-9**–**4-15**, calculated with MP2/BSS-A.

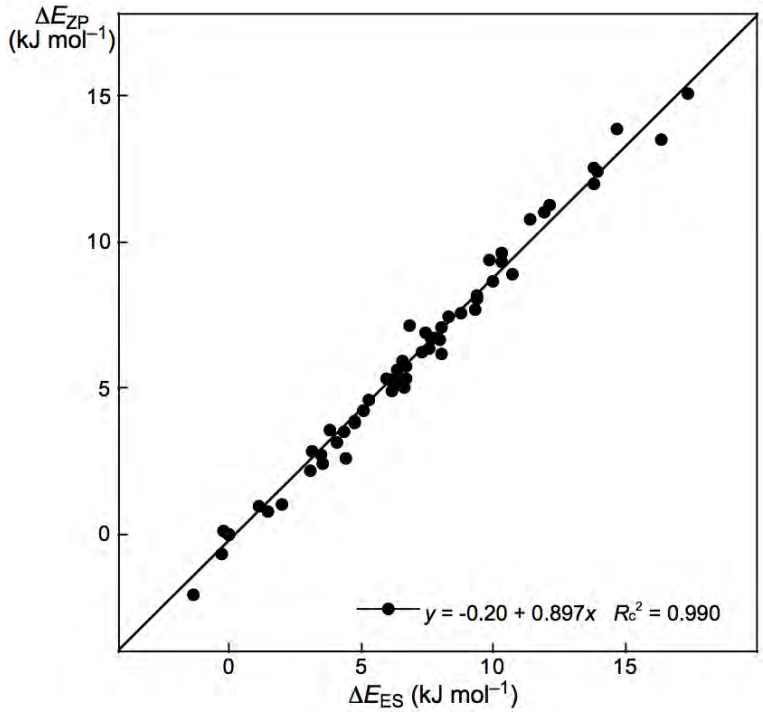

Figure 4-A4. Plot of ΔE_{ZP} versus ΔE_{ES} for the conformers in **4-1**–**4-15**, evaluated with MP2/BSS-A.

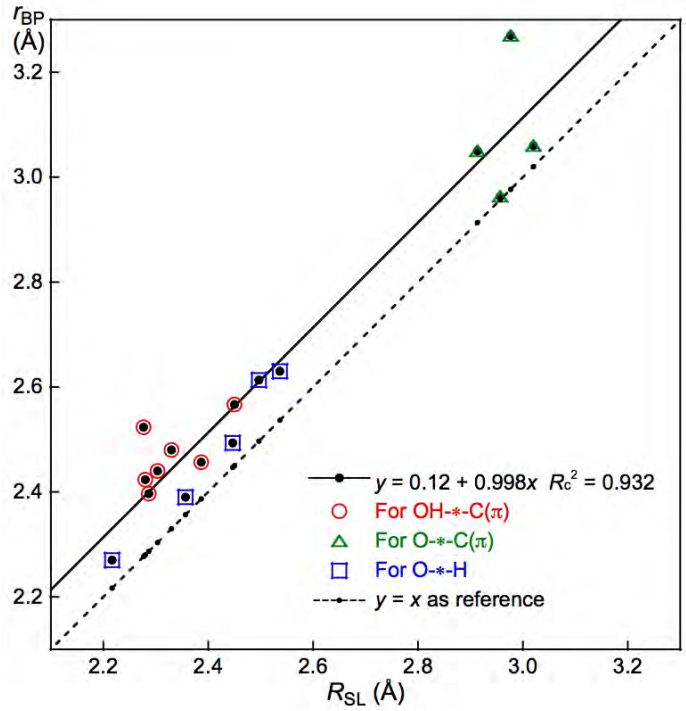

Figure 4-A5. Plot of r_{BP} versus R_{SL} for the intramolecular OH-∗-C(π) and O-∗-X (X = C(π) and H (bonded to C(π))) in some conformers of **4-3a**, **4-6a**, **4-9a**, **4-11a**, **4-12a**, **4-13a**, **4-15a**, **4-3b**, **4-5e**, **4-5i**, **4-6c**, **4-9b**, **4-12b**, **4-14b**, **4-15b**, and **4-15** evaluated with MP2/BSS-A.

References and Notes

1. S. Scheiner, *Hydrogen Bonding, A Theoretical Perspective*, Oxford University Press, Oxford, U.K., **1997**.
2. G. R. Desiraju, T. Steiner, *The Weak Hydrogen Bond in Structural Chemistry and Biology* (*IUCr Monographs on Crystallography*), Oxford University Press, Oxford, **1999**.
3. G. Gilli, P. Gilli, *The Nature of the Hydrogen Bond: Outline of a Comprehensive Hydrogen Bond Theory* (*IUCr Monographs on Crystallography*), Oxford University Press, Oxford, **2009**.
4. S. Hayashi, K. Matsuiwa, M. Kitamoto, W. Nakanishi, *J. Phys. Chem. A* **2013**, *117*, 1804–1816.
5. G. Buemi, *Intramolecular Hydrogen Bonds. Methodologies and Strategies for Their Strength Evaluation* in *Hydrogen Bonding – New Insights* (Eds.: S. J. Grabowski), Springer, New York, **2006**. Ch. 2.
6. *Chemistry of Hypervalent Compounds* (Ed.: K.-y. Akiba), Wiley-VCH, New York, **1999**.
7. W. Nakanishi*, Hypervalent Chalcogen Compounds* in *Handbook of Chalcogen Chemistry: New Perspectives in Sulfur, Selenium and Tellurium* (Ed.: F. A. Devillanova), Royal Society of Chemistry, Cambridge, **2006**, Ch. 10.3, pp. 644–668.
8. T. Nishide, S. Hayashi, W. Nakanishi, *ChemistryOpen* **2018**, *7*, 565–575.
9. Y. Sugibayashi, S. Hayashi, W. Nakanishi, *Phys. Chem. Chem. Phys.* **2015**, *17*, 28879–28891.
10. Y. Sugibayashi, S. Hayashi, W. Nakanishi, *Phys. Chem. Chem. Phys.* **2016**, *18*, 9948–9960.
11. S. Hayashi, Y. Sugibayashi, W. Nakanishi, *RSC Adv.* **2016**, *6*, 49651–49660.
12. S. Hayashi, Y. Sugibayashi, W. Nakanishi, *RSC Adv.* **2017**, *7*, 31858–31865.
13. S. Hayashi, Y. Sugibayashi, W. Nakanishi, *RSC Adv.* **2018**, *8*, 16349–16361.
14. *Hydrogen Bonding: New – Insights* (Ed.: S. J. Grabowski), Springer, The Netherlands, **2006**.
15. K.-L. Han, G.-J. Zhao, *Hydrogen Bonding and Transfer in the Excited State*, Wiley, Chichester, UK, **2010**.
16. W. Nakanishi, S. Hayashi, *Int. J. Quantum Chem.* **2018**, *118*, e25590.
17. a) W. Nakanishi, S. Hayashi, K. Narahara, *J. Phys. Chem. A* **2009**, *113*, 10050–10057; b) W. Nakanishi, S. Hayashi, K. Narahara, *J. Phys. Chem. A* **2008**, *112*, 13593–13599.
18. W. Nakanishi, S. Hayashi, *Curr. Org. Chem*. **2010**, *14*, 181–197.
19. W. Nakanishi, S. Hayashi, *J. Phys. Chem. A* **2010**, *114*, 7423–7430.
20. W. Nakanishi, S. Hayashi, K. Matsuiwa, M. Kitamoto, *Bull. Chem. Soc. Jpn*. **2012**, *85*, 1293–1305.
21. E. D. Glendening, A. E. Reed, J. E. Carpenter, F. Weinhold, NBO 3.0 Program Manual, Theoretical Chemistry Institute, University of Wisconsin, Madison, WI, USA, **1990**.
22. *Gaussian 09, Revision D.01*, M. J. Frisch, G. W. Trucks, H. B. Schlegel, G. E. Scuseria, M. A. Robb, J. R. Cheeseman, G. Scalmani, V. Barone, B. Mennucci, G. A. Petersson, H. Nakatsuji, M. Caricato, X. Li, H. P. Hratchian, A. F. Izmaylov, J. Bloino, G. Zheng, J. L. Sonnenberg, M. Hada, M. Ehara, K. Toyota, R. Fukuda, J. Hasegawa, M. Ishida, T. Nakajima, Y. Honda, O. Kitao, H. Nakai, T. Vreven, J. A. Montgomery, Jr., J. E. Peralta, F. Ogliaro, M. Bearpark, J. J. Heyd, E. Brothers, K. N. Kudin, V. N. Staroverov, R. Kobayashi, J. Normand, K. Raghavachari, A.

Rendell, J. C. Burant, S. S. Iyengar, J. Tomasi, M. Cossi, N. Rega, J. M. Millam, M. Klene, J. E. Knox, J. B. Cross, V. Bakken, C. Adamo, J. Jaramillo, R. Gomperts, R. E. Stratmann, O. Yazyev, A. J. Austin, R. Cammi, C. Pomelli, J. W. Ochterski, R. L. Martin, K. Morokuma, V. G. Zakrzewski, G. A. Voth, P. Salvador, J. J. Dannenberg, S. Dapprich, A. D. Daniels, Ö. Farkas, J. B. Foresman, J. V. Ortiz, J. Cioslowski, D. J. Fox, Gaussian, Inc., Wallingford CT, **2009**.

23. a) C. Møller, M. S. Plesset, *Phys. Rev.* **1934**, *46*, 618–622; b) J. Gauss, *J. Chem. Phys.* **1993**, *99*, 3629–3643; c) J. Gauss, *Ber. Bunsen-Ges. Phys. Chem.* **1995**, *99*, 1001–1008.
24. The C_{ii} values and the coordinates corresponding to C_{ii} were calculated by using the Compliance 3.0.2 program released by Grunenberg and Brandhorst.
25. K. Brandhorst, J. Grunenberg, *J. Chem. Phys.* **2010**, *132*, 184101.
26. K. Brandhorst, J. Grunenberg, *Chem. Soc. Rev.* **2008**, *37*, 1558–1567.
27. J. Grunenberg, *Chem. Sci.* **2015**, *6*, 4086–4088.
28. a) A. D. Becke, *Phys. Rev. A: At., Mol., Opt. Phys.* **1988**, *38*, 3098−3100; b) A. D. Becke, *J. Chem. Phys.* **1993**, *98*, 5648−5652; c) C. Lee, W. Yang, R. G. Parr, *Phys. Rev. B: Condens. Matter Mater. Phys.* **1988**, *37*, 785−789.
29. Y. Zhao, D. G. Truhlar, *Theor. Chem. Acc.* **2008**, *120*, 215–241.
30. F. Biegler-König, *J. Comput. Chem.* **2000**, *21*, 1040–1048.
31. T. A. Keith, AIMAll (Version 17.11.14), TK Gristmill Software, Overland Park, KS, USA, **2017**, http://www.aim.tkgristmill.com.
32. R. F. W. Bader, *Atoms in Molecules*. *A Quantum Theory* (Ed.: R. F. W. Bader), Oxford University Press, Oxford, UK, **1990**.
33. C. F. Matta, R. J. Boyd, *An Introduction to the Quantum Theory of Atoms in Molecules* in *The Quantum Theory of Atoms in Molecules: From Solid State to DNA and Drug Design* (Eds.: C. F. Matta, R. J. Boyd), WILEY-VCH: Weinheim, Germany, **2007**, Ch. 1.
34. M. Nishio, *Phys. Chem. Chem. Phys.* **2011**, *13*, 13873–13900.
35. S. Hayashi, T. Nishide, K. Ueda, K. Hayama, W. Nakanishi, *ChemistrySelect* **2019**, *4*, 6198–6208.
36. It is demonstrated that the detection of the BPs between two atoms in a molecule emerging from natural alignment of the gradient vector held of the one-electron density of a molecule is neither necessary nor a sufficient condition for the presence of a chemical bond between those atoms.[37] In this connection, it is pointed out that the terms line paths (LPs) and line critical points (LCPs) should be used in place of BPs and BCPs, respectively.[37b] However, BPs and BCPs are used in this work.
37. a) R. F. W. Bader, *J. Phys. Chem. A* **2009**, *113*, 10391–10396; b) C. Foroutan-Nejad, S. Shahbazian, R. Marek, *Chem. Eur. J.* **2012**, *18*, 4982–4993; c) M. Garcıa-Revilla, E. Francisco, P. L. A. Popelier, A. M. Pend´as, *ChemPhysChem* **2013**, *14*, 1211–1218; d) Z. A. Keyvani, S. Shahbazian, M. Zahedi, *Chem. Eur. J.* **2016**, *22*, 5003–5009.

Chapter 5

Behavior of Multi-HBs in Acetic Acid Dimer and Related Species: QTAIM Dual Functional Analysis Employing Perturbed Structures Generated Using Coordinates from Compliance Force Constants

Abstract

The dynamic and static nature of each hydrogen bond (HB) in acetic acid dimer (**5-1**), acetamide dimer (**5-2a**), thio- and seleno-derivatives of **5-2a** (**5-2b** and **5-2c**, respectively), and acetic acid-acetamide complex (**5-3**) was elucidated with QTAIM dual functional analysis (QTAIM-DFA). Such multi-HBs will form in **5-1**–**5-3**, in close proximity in space, and interact mutually and strongly with each other. Perturbed structures generated using coordinates derived from the compliance force constants (C_{ii}: the method being called CIV) are employed in QTAIM-DFA, for the establishment of the methodology to elucidate the nature of each HB in the multi-HBs. Each HB in the multi-HBs of **5-1**–**5-3** are predicted to have the nature of CT-MC (molecular complex through charge transfer) appear at the regular closed shell region, which are stronger than each HB of the isomers of **5-1**–**5-3**. The methodology to elucidate the nature of multi-HBs is well established, which employs the perturbed structures generated with CIV within the framework of QTAIM-DFA.

Introduction

Water, alcohols, and carboxylic acids construct dimers, oligomers, and/or polymers in crystals, liquid phase, and even gas phase. They combine through hydrogen bonds (HBs), where HBs are fundamentally important because of their molecular association due to the stabilization of the system in energy.[1–6] The comprehension of HBs has been growing much through analysis; however, it is still inevitable to clarify the nature of HBs further for better understanding of chemical processes controlled by HBs.[7–12] In previous study, the nature of a wide range of HBs has been reported, employing the QTAIM dual functional analysis (QTAIM-DFA), where only one HB is contained in each HB species.[10,12]

The author has paid much attention to multi-HB systems, where plural HBs are formed in close proximity in space. The multi-HBs will interact mutually and strongly with each other. Acetic acid dimer (**5-1**), acetamide dimer (**5-2a**), and the acetic acid-acetamide complex (**5-3**) would provide such a multi-HB system, together with the thio- and seleno-derivatives of **5-2a** (**5-2b** and **5-2c**, respectively). Chart 5-1 shows the dimers of **5-1**–**5-3**. How can the nature of each HB in the multi-HBs be clarified? It is necessary to establish the methodology to elucidate the nature of each HB in such multi-HB system. The QTAIM-DFA will be suited to elucidate each HB in multi-HB system if the perturbed structures are generated with coordinates derived from compliance force constants for internal vibrations (CIV).[13–19] The QTAIM-DFA is explained in Chapter 2

Herein, he presents the results of the investigations on the intrinsic dynamic and static nature of each HB in the multi-HBs, exemplified by the acetic acid dimers and related species **5-1**–**5-3**, elucidated with QTAIM-DFA, by employing the perturbed structures generated with CIV. The nature of each HB in the isomers of **5-1**–**5-3**, is also clarified for convenience of comparison. The methodology, necessary for the analysis of such multi-HBs, is established through this investigation.

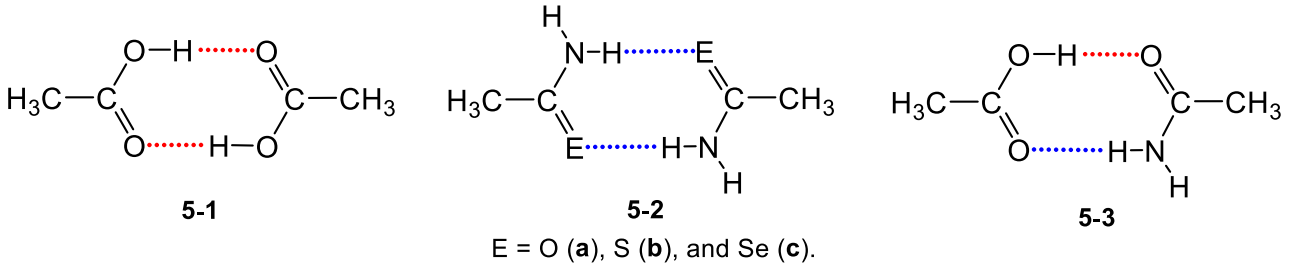

5-1 **5-2** **5-3**

E = O (**a**), S (**b**), and Se (**c**).

Chart 5-1. Dimers of acetic acid (**5-1**) and related species (**5-2a**, **5-2b**, **5-2c**, and **5-3**).

Methodological Details in Calculations

Calculations were performed by employing the Gaussian 09 program.[20] To obtain suitable basis set systems (BSSs) for the calculations, various BSSs were examined. Table 5-1 lists the BSSs. BSS-B′a and BSS-B′b were examined to know the effect of lower BSSs for the atoms other than A, H, and B in an AH–B interaction. The Møller-Plesset second order energy correlation (MP2) level[21] and the DFT level of M06-2X[22,23] were applied for the examinations. The optimized structures were confirmed by the frequency analysis. The results of the frequency analysis are used to obtain the compliance force constants (C_{ii}) and the coordinates corresponding to C_{ii}.[24–27] The basis set superposition errors (BSSE) were not corrected.

QTAIM functions were calculated using the same basis set system and the level as in the optimizations, unless otherwise noted, and were analyzed with the AIM2000[28] and AIMAll[29] programs. In QTAIM-DFA, $H_b(\boldsymbol{r}_c)$ are plotted versus $H_b(\boldsymbol{r}_c) - V_b(\boldsymbol{r}_c)/2$ for the five data points of w = 0, ±0.025, and ±0.05 in Equations (2-4)–(2-7) of Chapter 2.

Table 5-1. Basis set systems (BSSs), employed for the calculations.

BSS	H, C, N, O, S, and Se	BSS	H, C, N, O, S, and Se
BSS-A	6-311++G(3df,3pd)	BSS-A′	6-311+G(3df,3pd)
BSS-B′a	6-311+G(3df,3pd)[a]	BSS-B′b	6-311+G(3df,3pd)[b]
BSS-C	6-311++G(3df,3p)	BSS-C′	6-311+G(3df,3p)
BSS-D	6-311++G(3d,3p)	BSS-E	6-311++G(d,p)

[a] The 6-311+G(3d) basis set being employed for C. [b] The 6-311+G(d) basis set for C.

Results and Discussion

Search of Suitable BSSs for Evaluation, Employing the Observed Structure of 5-1

The structure of **5-1** has been determined by the neutron diffraction measurement.[30] The static nature of HBs is examined employing the observed structure of **5-1**, before detailed discussion on the intrinsic dynamic nature of each HB in the multi-HB system of **5-1**–**5-3**. The QTAIM functions of $\rho_b(\boldsymbol{r}_c)$, $H_b(\boldsymbol{r}_c) - V_b(\boldsymbol{r}_c)/2$ (= $\hbar^2/8m\nabla^2\rho_b(\boldsymbol{r}_c)$), $H_b(\boldsymbol{r}_c)$, and $k_b(\boldsymbol{r}_c)$ (= $V_b(\boldsymbol{r}_c)/G_b(\boldsymbol{r}_c)$) are calculated for the observed structure of **5-1**, with various BSSs shown in Table 5-1 at the MP2 and M06-2X levels. The values are collected in Table 5-2.

$H_b(\boldsymbol{r}_c)$ are plotted versus $H_b(\boldsymbol{r}_c) - V_b(\boldsymbol{r}_c)/2$ for the data given in Table 5-2. The plot is shown in Figure 5-1. The basis set and level dependence are well visualized by the plot. The data appear as three groups in the figure, group A (G(**A**)), group B (G(**B**)), and group C (G(**C**)). The data for the observed structure of **5-1** form G(**A**), if evaluated with BSS-A, BSS-A′, BSS-B′a, and BSS-B′b, at the MP2 and M06-2X levels. The data belong to G(**B**), when calculated with BSS-C, BSS-C′, and BSS-D, at the MP2 and M06-2X levels, and G(**C**) consists of the data evaluated with BSS-E, at the MP2 and M06-2X levels. The notation of G(**A**), G(**B**), and G(**C**) will also be used to show the basis set groups in addition to those of the data. It is of interest that the substantially different three data (points) align linearly in the plot. (The linearity is described as $y = 1.623x - 0.0368$: $R_c^2 = 0.987$). The results show that BSSs (and levels) must be carefully examined when the nature of interactions is discussed on the basis of the calculated values.

Table 5-2. QTAIM functions and QTAIM-DFA parameters for HBs in the observed structure of acetic acid dimer (**5-1**), calculated with various BSSs at MP2 and M06-2X levels.[a,b]

Level BSS	X-∗-Y	$\rho_b(\boldsymbol{r}_c)$ (au)	$c\nabla^2\rho_b(\boldsymbol{r}_c)$[c] (au)	$H_b(\boldsymbol{r}_c)$ (au)	$k_b(\boldsymbol{r}_c)$[d]	R (au)	θ (°)	Classifi- cation
MP2								
BSS-A	OH-∗-O	0.0540	0.0131	–0.0158	–1.376	0.0205	140.4	*r*-CS
BSS-A′	OH-∗-O	0.0540	0.0131	–0.0158	–1.376	0.0205	140.3	*r*-CS
BSS-B′a	OH-∗-O	0.0540	0.0130	–0.0159	–1.379	0.0205	140.6	*r*-CS
BSS-B′b	OH-∗-O	0.0540	0.0130	–0.0159	–1.378	0.0205	140.6	*r*-CS
BSS-C	OH-∗-O	0.0526	0.0154	–0.0115	–1.271	0.0192	126.7	*r*-CS
BSS-C′	OH-∗-O	0.0526	0.0154	–0.0115	–1.271	0.0192	126.7	*r*-CS
BSS-D	OH-∗-O	0.0526	0.0155	–0.0112	–1.265	0.0192	125.8	*r*-CS
BSS-E	OH-∗-O	0.0521	0.0178	–0.0085	–1.193	0.0197	115.6	*r*-CS
M06-2X								
BSS-A	OH-∗-O	0.0545	0.0128	–0.0161	–1.387	0.0205	141.6	*r*-CS
BSS-A′	OH-∗-O	0.0545	0.0128	–0.0161	–1.387	0.0205	141.6	*r*-CS
BSS-B′a	OH-∗-O	0.0545	0.0127	–0.0162	–1.390	0.0206	141.9	*r*-CS
BSS-B′b	OH-∗-O	0.0545	0.0127	–0.0162	–1.388	0.0206	141.8	*r*-CS
BSS-C	OH-∗-O	0.0531	0.0152	–0.0117	–1.277	0.0192	127.5	*r*-CS
BSS-C′	OH-∗-O	0.0531	0.0152	–0.0117	–1.277	0.0192	127.4	*r*-CS
BSS-D	OH-∗-O	0.0529	0.0154	–0.0112	–1.266	0.0191	126.0	*r*-CS
BSS-E	OH-∗-O	0.0520	0.0179	–0.0082	–1.187	0.0197	114.7	*r*-CS

[a] Data are given at BCPs. [b] See Table 5-1 for BSSs. [c] $c\nabla^2\rho_b(\boldsymbol{r}_c) = H_b(\boldsymbol{r}_c) - V_b(\boldsymbol{r}_c)/2$, where $c = \hbar^2/8m$. [d] $k_b(\boldsymbol{r}_c) = V_b(\boldsymbol{r}_c)/G_b(\boldsymbol{r}_c)$.

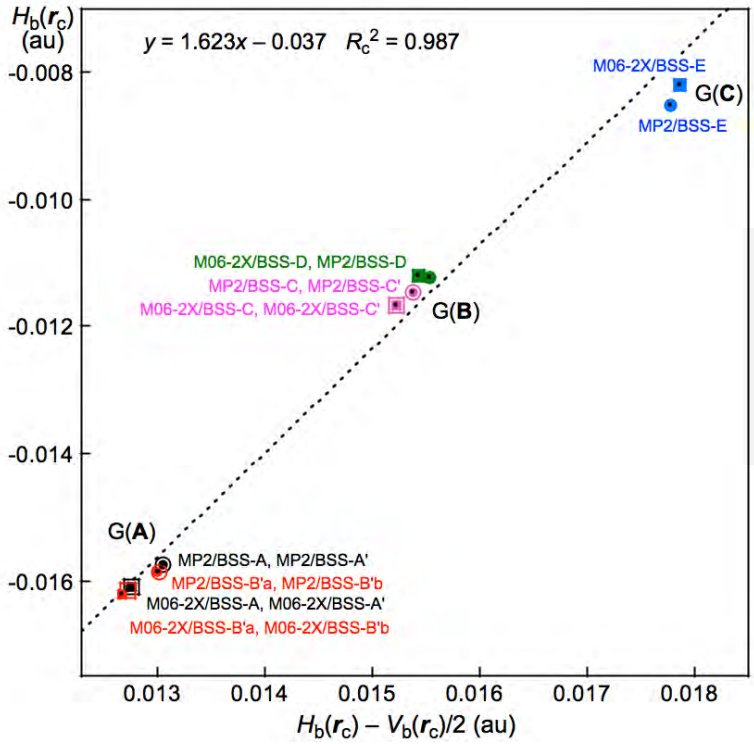

Figure 5-1. Plot of $H_b(\boldsymbol{r}_c)$ versus $H_b(\boldsymbol{r}_c) - V_b(\boldsymbol{r}_c)/2$ for the observed structure of **5-1**, evaluated with various basis set at MP2 and M06-2X levels.

The QTAIM-DFA parameters of (R, θ) are calculated for the HB in the observed structure of **5-1**. The values are collected in Table 5-2. As shown in the table, three ranges of θ are typically predicted depending on the calculation levels, G(**A**), G(**B**), and G(**C**). The θ values of 140–142º are predicted with G(**A**), at the MP2 and M06-2X levels. On the other hand, 126º $\leq \theta \leq$ 128º are predicted with G(**B**), at the MP2 and M06-2X levels. The smaller range of θ around 115–116º is predicted similarly with G(**C**) at the MP2 and M06-2X levels. Such trend is also observed for R: $R \approx 0.0205$ au with G(**A**) and $R \approx 0.0192$ au with G(**B**), while $R \approx 0.0197$ au with G(**C**). QTAIM functions show similar trend, as seen in Table 5-2. The results in (R, θ) must come from the evaluated values of QTAIM functions, which are differently predicted with G(**A**), G(**B**), and G(**C**) at the MP2 and M06-2X levels. One may feel curious for the substantially large differences in (R, θ), predicted with various BSSs, employing the common observed structure of **5-1**, at first glance. The differences arise from the basis set (and level) dependence on the values of QTAIM functions, even if the common observed structure of **5-1** is employed for the calculations.

Suitable Methods to Elucidate the Nature of Each HB of a Multi-HB System, Examined Exemplified by 5-1

To examine a suitable method to evaluate the nature of each HB in multi-HB system, the structure of **5-1** was optimized with various BSSs at the MP2 and M06-2X levels. The optimized structure of **5-1** is not shown in figures but it can be found in molecular graph of **5-1** drawn on the optimized structure with MP2/BSS-A. The optimized structural parameters selected for **5-1**, r(O–H), r(O···H), and ∠OHO, are collected in Table 5-3. The table contains the selected structural parameters of **5-1**, determined by the neutron diffraction measurement. The differences between the calculated and observed values are also given in the table, $\Delta P = P_{calcd} - P_{obsd}$, where P stands for r(O–H), r(O···H), or ∠OHO: Δr(O···H) = 0.007 Å if calculated with MP2/BSS-A, 0.007 Å with MP2/BSS-A′, 0.0003 Å with MP2/BSS-B′a, and –0.006 Å with MP2/BSSB′b (MP2/G(**A**)). They reproduce very well the observed structure of **5-1**, especially for the r(O–H) and r(O···H) distances, although Δ(∠OHO) = 13.5º. MP2/G(**A**) seems very suitable for the optimization of **5-1**. The magnitudes of Δr(O···H) become larger when MP2/BSS-C (0.026 Å), MP2/BSS-C′ (0.026 Å), and MP2/BSS-D (0.028 Å) (MP2/G(**B**)) are applied. The methods would also be suitable for the optimization of **5-1**, together

Table 5-3. Structural parameters and stabilization energies for $CH_3COOH•HOOCCH_3$ (**5-1**), calculated with the various BSSs at MP2 and M06-2X levels, together with $\Delta P = P_{calcd} - P_{obsd}$ (P = r(O–H), r(O···H), and ∠O–H···O).[a]

Level BSS	r(O–H) (Å)	Δr(O–H)[b] (Å)	r(O···H) (Å)	Δr(O···H)[b] (Å)	∠O–H···O (º)	Δ∠O–H···O[b] (º)	ΔE_{ES}[c] (kJ mol^{-1})	ΔE_{ZP}[d] (kJ mol^{-1})
MP2								
BSS-A	0.9966	–0.0038	1.6491	0.0071	178.54	13.54	–72.4	–66.2
BSS-A′	0.9966	–0.0038	1.6491	0.0071	178.53	13.53	–72.4	–66.2
BSS-B′a	0.9971	–0.0033	1.6423	0.0003	178.59	13.59	–73.9	–67.5
BSS-B′b	0.9975	–0.0030	1.6365	–0.0055	178.53	13.54	–75.4	–68.6
BSS-C	0.9956	–0.0049	1.6681	0.0261	178.66	13.66	–71.3	–65.0
BSS-C′	0.9956	–0.0048	1.6681	0.0261	178.65	13.65	–70.7	–64.5
BSS-D	0.9955	–0.0050	1.6706	0.0286	178.23	13.23	–71.6	–65.3
BSS-E	0.9907	–0.0098	1.7043	0.0623	179.87	14.87	–64.5	–59.5
M06-2X								
BSS-A	0.9997	–0.0008	1.6257	–0.0163	179.79	14.79	–73.3	–69.6
BSS-A′	0.9997	–0.0007	1.6256	–0.0164	179.79	14.79	–73.4	–69.7
BSS-B′a	1.0001	–0.0003	1.6232	–0.0188	179.77	14.77	–73.2	–69.5
BSS-B′b	0.9996	–0.0009	1.6257	–0.0163	179.82	14.82	–73.6	–69.9
BSS-C	0.9980	–0.0025	1.6395	–0.0025	179.65	14.65	–72.4	–69.0
BSS-C′	0.9980	–0.0024	1.6392	–0.0028	179.66	14.66	–72.5	–69.1
BSS-D	0.9984	–0.0020	1.6379	–0.0041	179.80	14.80	–72.4	–68.8
BSS-E	0.9920	–0.0084	1.6850	0.0430	176.83	11.83	–72.3	–69.0
Obsd value[e]	1.0005	0.0000	1.6420	0.0000	165.00	0.00		

[a] See Table 5-1 for BSSs. [b] $\Delta P = P_{calcd} - P_{obsd}$ (P = r(O–H), r(O···H), and ∠O–H···O), where $P_{calcd} - P_{obsd}$ are observed and calculated values, respectively. [c] The energies on the energy surface from the components (ΔE_{ES}) [= E_{ES}(HB) – E_{ES}(components)]. [d] The energies with the zero-point energy correction from the components (ΔE) [= E(HB) – E(components)]. [e] Ref. 30.

with M06-2X/BSS-A (–0.016 Å), M06-2X/BSS-A′ (–0.016 Å), M06-2X/BSS-B′a (–0.019 Å), M06-2X/BSS-B′b (–0.016 Å), M06-2X/BSS-C (–0.003 Å), M06-2X/BSS-C′ (–0.003 Å), and M06-2X/BSS-D (–0.004 Å) (M06-2X/G(**A**) and M06-2X/G(**B**)). The magnitudes of Δr(O···H) become much larger if evaluated with MP2/BSS-E (0.062 Å) and M06-2X/BSS-E (0.043 Å) (MP2/G(**C**) and M06-2X/G(**C**)).

The QTAIM functions of $\rho_b(\boldsymbol{r}_c)$, $H_b(\boldsymbol{r}_c) - V_b(\boldsymbol{r}_c)/2$, $H_b(\boldsymbol{r}_c)$, and $k_b(\boldsymbol{r}_c)$ are calculated for the optimized structures of **5-1** with the same methods of optimization. Table 5-4 collects the selected values of the QTAIM functions. $H_b(\boldsymbol{r}_c)$ are plotted versus $H_b(\boldsymbol{r}_c) - V_b(\boldsymbol{r}_c)/2$ for the data of **5-1**, given in Table 5-4, together with those for the perturbed structures generated with CIV, although the data in Table 5-4 are somewhat selected. The plot is shown in Figure 5-2, which also contains some data given in Table 5-2, for convenience of comparison. The results show that the data (points) for the optimized structures appear near to those for the observed structure of **5-1**, if those evaluated with BSSs of the same group are employed.

QTAIM-DFA parameters of (R, θ) and (θ_p, κ_p) are calculated for **5-1** by analyzing the plots in Figure 5-2. The (θ_p, κ_p) values are denoted by ($\theta_{p:CIV}$, $\kappa_{p:CIV}$) and ($\theta_{p:NIV}$, $\kappa_{p:NIV}$), if the perturbed structures are generated with CIV and NIV, respectively. Table 5-4 summarizes the (R, θ) and ($\theta_{p:CIV}$, $\kappa_{p:CIV}$) values, together with the C_{ii} values, for the optimized structures of **5-1**, calculated with various BSSs at the MP2 and M06-2X levels. The $\theta_{p:CIV}$ values are evaluated to be 172.5–173.0º if evaluated

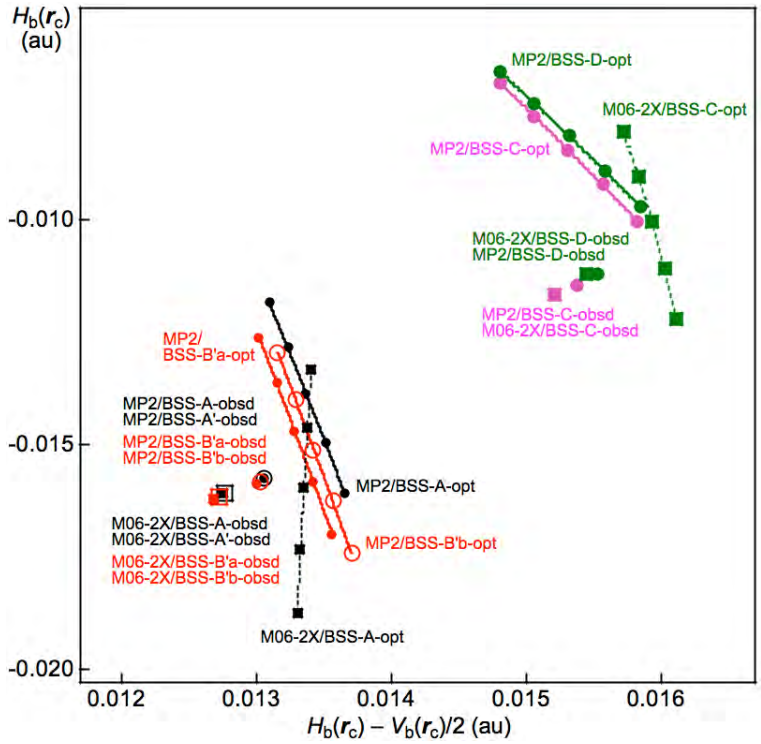

Figure 5-2. Plots of $H_b(\boldsymbol{r}_c)$ versus $H_b(\boldsymbol{r}_c) - V_b(\boldsymbol{r}_c)/2$ for the observed and optimized structures of **5-1**, evaluated with various methods.

with MP2/BSS-A, MP2/BSS-B′a, and MP2/BSS-B′b (MP2/G(**A**)), while the values are 160.9–161.7º with MP2/BSS-C and MP2/BSS-D (MP2/G(**B**)). The former is larger than the latter by 11–12º. The $\theta_{p:CIV}$ value is evaluated to be 181.2º with M06-2X/BSS-A, which seems overestimated by 8.2–8.7º, relative to the cases with MP2/G(**A**). On the other hand, the $\theta_{p:CIV}$ value is evaluated to be 174.7º with M06-2X/BSS-C, which is (very) close to those evaluated with MP2/G(**A**) ($\Delta\theta_{p:CIV}$ = 1.7–2.2º). Consequently, MP2/G(**A**) are highly recommended in the application to QTAIM-DFA. MP2/BSS-B′b would be the best method among MP2/G(**A**) in the calculations of larger systems, since it requires the least number of (primitive) Gaussian functions in the calculations.

QTAIM-DFA, employing the perturbed structures generated with CIV, is shown to be suitable to evaluate each HB in multi-HBs. However, the calculation methods should be carefully examined when the nature of interactions is discussed on the basis of the predicted values, since the values somewhat change depending on the methods for the prediction. MP2/BSS-A will be mainly employed in this work, together with MP2/BSS-B′a and MP2/BSS-B′b. M06-2X/BSS-A and M06-2X/BSS-C are also employed, if necessary. M06-2X/BSS-C would be more suitable than M06-2X/BSS-A, in the applications to QTAIM-DFA, since the latter seems overestimate the θ_p values.

Before detailed discussion of the nature of each HB in multi-HB system of **5-1**–**5-3**, it is instructive to examine the molecular graphs and the contour plots for **5-1**–**5-3**.

Molecular Graphs with Contour Plots for 5-1–5-3

Species **5-1**–**5-3** were optimized mainly with MP2/G(**A**). The structural parameters of r(A–H), r(H···X), and ∠AHX of AH-∗-X, evaluated with MP2/BSS-A are collected in Table 5-A1 of the Appendix. Figure 5-3 illustrates the molecular graphs for **5-1**–**5-3**, containing the contour plots of $\rho(\boldsymbol{r})$, drawn on the planes containing at least one side of HB. All BCPs expected, containing those of each HB, are clearly detected. The optimized structures are not shown in figures. They can be found in the molecular graphs for **5-1**–**5-3** illustrated in Figure 5-3, which are drawn on the structures optimized with MP2/BSS-A.

The HB interactions in **5-1**–**5-3** seem straight, judging from the BPs corresponding to the HBs in Figure 5-3. To examine the linearity of the HB interactions further, the lengths of BPs (r_{BP}) in question and the corresponding straight-line distances (R_{SL}) are calculated for **5-1**–**5-3**. The values evaluated with MP2/BSS-A are collected in Table 5-A2 of the Appendix, together with the differences between them ($\Delta r_{BP} = r_{BP} - R_{SL}$). The magnitudes of Δr_{BP} are less than 0.031 Å for the BPs; therefore, all HB interactions in **5-1**–**5-3** can be approximated by the straight lines.

The energies of **5-1**–**5-3** from the components, $\Delta E(\boldsymbol{n})$ (= $E(\boldsymbol{n}) - E$(components) (ΔE_{ES} and ΔE_{ZP})), evaluated with MP2/BSS-A, are also collected in Table 5-A1 of the Appendix, where ΔE_{ES} and ΔE_{ZP} represent ΔE on the energy surface and ΔE with the zero-point energy collections, respectively. The

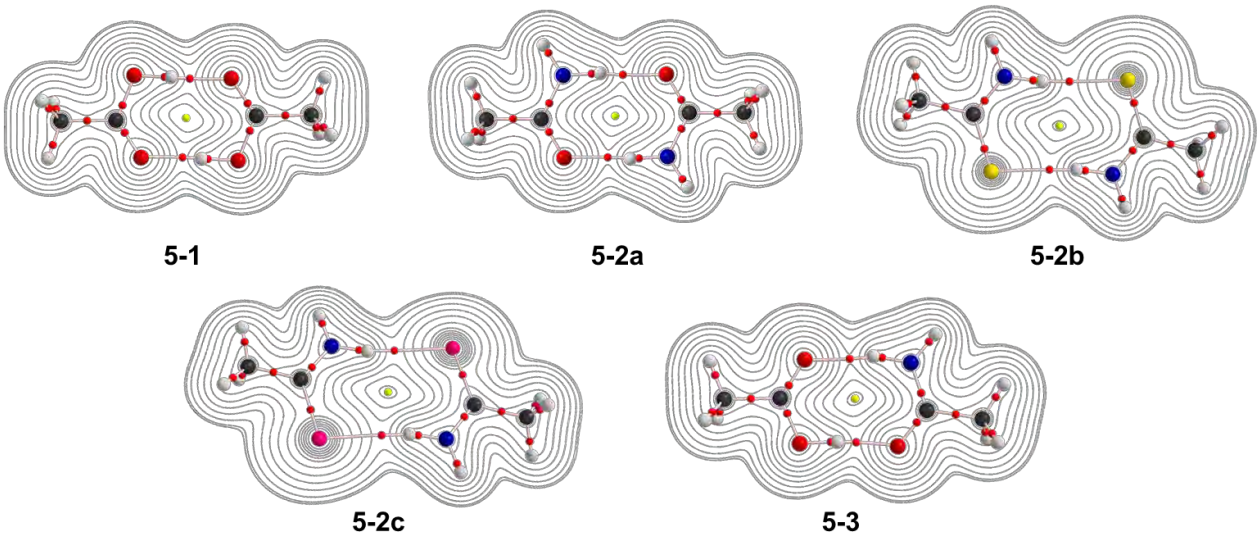

Figure 5-3. Molecular graphs for **5-1** (C_{2h}), **5-2a** (C_i), **5-2b** (C_i), **5-2c** (C_i), and **5-3** (C_1), evaluated with MP2/BSS-A. BCPs are denoted by red dots, RCPs (ring critical points) by yellow dots, and BPs are by pink lines. Carbon atoms are in black and hydrogen atoms are in grey, with oxygen, nitrogen, sulfur, and selenium atoms in red, blue, dark yellow, and deep pink, respectively. Contour plots are drawn on the planes containing at least one side of HB.

plot of ΔE_{ZP} versus ΔE_{ES} gave a (very) good correlation ($\Delta E_{ZP} = 0.900\Delta E_{ES} + 0.59$: $R_c^2 = 0.975$ (n (number of data points) = 5)).

QTAIM functions of $\rho_b(\boldsymbol{r}_c)$, $H_b(\boldsymbol{r}_c) - V_b(\boldsymbol{r}_c)/2$, $H_b(\boldsymbol{r}_c)$, and $k_b(\boldsymbol{r}_c)$ are calculated at BCP on the BP corresponding to each HB in **5-1**–**5-3**. Table 5-4 collects the values, evaluated with MP2/BSS-A, MP2/BSS-B′a, and MP2/BSS-B′b (MP2/G(**A**)) for **5-1**–**5-3**, together those with MP2/BSS-C, MP2/BSS-D, M06-2X/BSS-A and M06-2X/BSS-C for **5-1**. $H_b(\boldsymbol{r}_c)$ are plotted versus $H_b(\boldsymbol{r}_c) - V_b(\boldsymbol{r}_c)/2$ for the data shown in Table 5-4 and those from the perturbed structures, generated with CIV. Figure 5-4 shows the plots, evaluated with MP2/BSS-A and MP2/BSS-B′b. Two plots for **5-1**–**5-3** almost coincide. The (R, θ) and ($\theta_{p:CIV}$, $\kappa_{p:CIV}$) values were calculated for **5-1**–**5-3** by analyzing the plots in Figure 5-4. The parameters evaluated with MP2/BSS-A, MP2/BSS-B′a, and MP2/BSS-B′b (MP2/G(**A**)) are very close with each other.

Table 5-4. QTAIM functions and QTAIM-DFA parameters for each HB of multi-HBs in acetic acid dimer (**5-1**) and the derivatives (**5-2a**, **5-2b**, **5-2c**, and **5-3**), evaluated with various calculation conditions.[a]

Species Level/BSS	X-∗-Y	$\rho_b(\boldsymbol{r}_c)$ (au)	$c\nabla^2\rho_b(\boldsymbol{r}_c)$[b] (au)	$H_b(\boldsymbol{r}_c)$ (au)	$k_b(\boldsymbol{r}_c)$[c]	R[d] (au)	θ[e] (°)	C_{ii} (unit[h])	$\theta_{p:CIV}$[f] (°)	$\kappa_{p:CIV}$[g] (au^{-1})	Predicted Nature
Acetic acid dimer: **5-1** (C_{2h})											
MP2/BSS-A	OH-∗-O	0.0511	0.0134	–0.0139	–1.342	0.0193	136.1	3.19	172.5	3.0	*r*-CS/CT-MC
MP2/BSS-B′a	OH-∗-O	0.0521	0.0133	–0.0147	–1.356	0.0198	137.9	3.10	173.0	1.8	*r*-CS/CT-MC
MP2/BSS-B′b	OH-∗-O	0.0528	0.0134	–0.0151	–1.360	0.0202	138.4	3.05	173.0	1.9	*r*-CS/CT-MC
MP2/BSS-C	OH-∗-O	0.0474	0.0153	–0.0084	–1.216	0.0175	118.9	3.34	161.7	10.1	*r*-CS/CT-MC
MP2/BSS-D	OH-∗-O	0.0471	0.0153	–0.0081	–1.210	0.0174	118.0	3.40	160.9	11.8	*r*-CS/CT-MC
M06-2X/BSS-A	OH-∗-O	0.0545	0.0134	–0.0160	–1.374	0.0208	140.1	3.49	181.2	1.4	*r*-CS/CT-TBP
M06-2X/BSS-C	OH-∗-O	0.0511	0.0159	–0.0100	–1.240	0.0188	122.2	4.04	174.7	9.5	*r*-CS/CT-MC
Acetamide dimer: **5-2a** (C_i)											
MP2/BSS-A	NH-∗-O	0.0394	0.0123	–0.0038	–1.134	0.0128	107.3	4.41	158.4	54.4	*r*-CS/CT-MC
MP2/BSS-B′a	NH-∗-O	0.0354	0.0123	–0.0040	–1.141	0.0130	108.1	4.35	159.6	50.4	*r*-CS/CT-MC
MP2/BSS-B′b	NH-∗-O	0.0360	0.0124	–0.0043	–1.148	0.0132	109.1	4.30	160.1	46.5	*r*-CS/CT-MC
Thio-derivative of **5-2a**: **5-2b** (C_i)											
MP2/BSS-A	NH-∗-S	0.0227	0.0059	–0.0012	–1.090	0.0060	101.2	5.82	151.6	238	*r*-CS/CT-MC
MP2/BSS-B′a	NH-∗-S	0.0229	0.0059	–0.0012	–1.094	0.0060	101.7	5.74	152.3	198	*r*-CS/CT-MC
MP2/BSS-B′b	NH-∗-S	0.0229	0.0059	–0.0012	–1.093	0.0060	101.5	5.77	152.0	201	*r*-CS/CT-MC
Seleno-derivative of **5-2a**: **5-2c** (C_i)											
MP2/BSS-A	NH-∗-Se	0.0213	0.0051	–0.0009	–1.085	0.0052	100.6	5.93	153.7	186	*r*-CS/CT-MC
MP2/BSS-B′a	NH-∗-Se	0.0226	0.0053	–0.0013	–1.109	0.0054	103.8	5.55	157.8	159	*r*-CS/CT-MC
MP2/BSS-B′b	NH-∗-Se	0.0227	0.0053	–0.0013	–1.111	0.0054	104.0	5.56	158.2	157	*r*-CS/CT-MC
Acetic acid-acetamide mixed dimer: **5-3** (C_1)											
MP2/BSS-A	OH-∗-O	0.0538	0.0132	–0.0158	–1.374	0.0206	140.1	3.01	173.2	2.8	*r*-CS/CT-MC
	NH-∗-O	0.0328	0.0124	–0.0024	–1.089	0.0126	101.1	4.72	153.7	76.2	*r*-CS/CT-MC
MP2/BSS-B′a	OH-∗-O	0.0548	0.0131	–0.0166	–1.387	0.0212	141.6	2.93	173.7	2.0	*r*-CS/CT-MC
	NH-∗-O	0.0333	0.0125	–0.0027	–1.097	0.0128	102.1	4.65	155.6	69.2	*r*-CS/CT-MC
MP2/BSS-B′b	OH-∗-O	0.0554	0.0132	–0.0170	–1.391	0.0215	142.1	2.89	173.8	2.2	*r*-CS/CT-MC
	NH-∗-O	0.0339	0.0126	–0.0029	–1.104	0.0130	103.1	4.60	156.3	63.7	*r*-CS/CT-MC

[a] Data are given at BCPs. [b] $c\nabla^2\rho_b(\boldsymbol{r}_c) = H_b(\boldsymbol{r}_c) - V_b(\boldsymbol{r}_c)/2$, where $c = \hbar^2/8m$. [c] $k_b(\boldsymbol{r}_c) = V_b(\boldsymbol{r}_c)/G_b(\boldsymbol{r}_c)$. [d] $R = (x^2 + y^2)^{1/2}$, where $(x, y) = (H_b(\boldsymbol{r}_c) - V_b(\boldsymbol{r}_c)/2, H_b(\boldsymbol{r}_c))$. [e] $\theta = 90° - \tan^{-1}(y/x)$. [f] $\theta_p = 90° - \tan^{-1}(dy/dx)$. [g] $\kappa_p = |d^2y/dx^2|/[1 + (dy/dx)^2]^{3/2}$. [h] Å mdyn^{-1}.

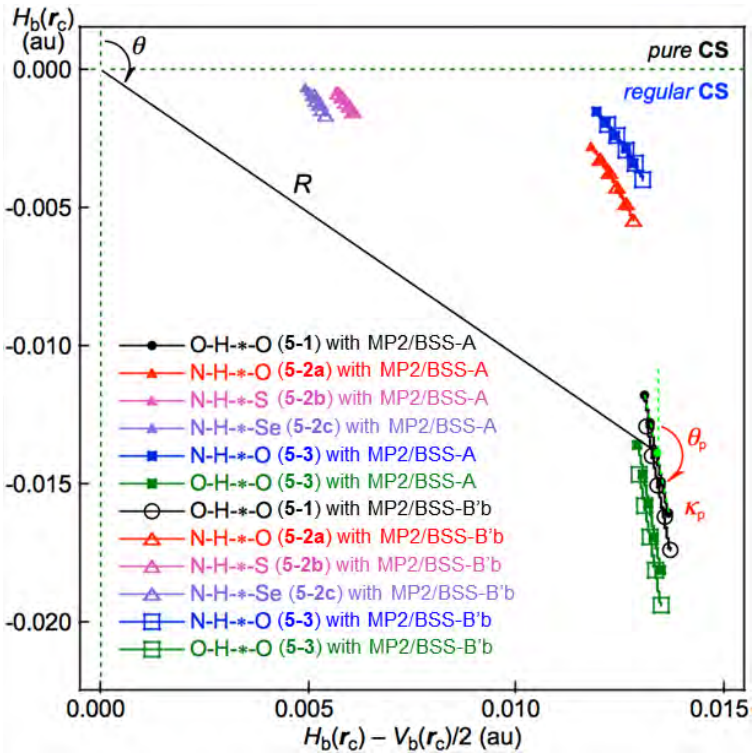

Figure 5-4. Plots of $H_b(\boldsymbol{r}_c)$ versus $H_b(\boldsymbol{r}_c) - V_b(\boldsymbol{r}_c)/2$ for **5-1**, **5-2a**–**5-2c**, and **5-3**, evaluated with MP2/BSS-A and MP2/BSS-B′b.

Nature of Each HB in Multi-HBs of 5-1–5-3

Each HB in multi-HBs of **5-1**–**5-3** are classified and characterized on the basis of the (θ, $\theta_{p:CIV}$) values, evaluated with MP2/BSS-A, given in Table 5-4. The (θ, $\theta_{p:CIV}$) values are (136.1º, 172.5º) for OH-∗-O in **5-1**, which is typically classified by the *r*-CS interaction and characterized as the CT-MC nature (*r*-CS/CT-MC). Each NH-∗-O interaction in **5-2a** is also predicted to have the nature of *r*-CS/CT-MC, since (θ, $\theta_{p:CIV}$) = (107.3º, 158.4º) for the interactions. Indeed, θ = 107.3º is less than the tentatively given θ value for CT-MC (115º), but the θ_p = 158.4º (> 150º) should be superior to θ, in this case. Each NH-∗-S interaction in **5-2b** and each NH-∗-Se interaction in **5-2c** are similarly predicted to have the nature of *r*-CS/CT-MC, since (θ, $\theta_{p:CIV}$) = (101.2º, 151.6º) and (100.6º, 153.7º) for **5-2b** and **5-2c**, respectively, although the θ values are predicted to be less than 115º. The $\theta_{p:CIV}$ values should be superior to θ in the characterization of **5-2b** and **5-2c**. The NH-∗-E interactions in **5-2** are predicted to be stronger in the order of E = S < Se < O because the order of $H_b(\boldsymbol{r}_c)$/au values for NH-∗-O (**5-2a**), NH-∗-S (**5-2b**), and NH-∗-Se (**5-2c**) are –0.0038 < –0.0012 < –0.0009, respectively. The same result for $H_b(\boldsymbol{r}_c)$ is also observed for $\rho_b(\boldsymbol{r}_c)$, *R*, and C_{ii}. Both OH-∗-O and NH-∗-O interactions in **5-3** are predicted to have the nature of *r*-CS/CT-MC, since (θ, $\theta_{p:CIV}$) = (140.1º, 173.2º) for OH-∗-O and (101.1º, 153.7º) for NH-∗-O, although θ = 101.1º < 115º for NH-∗-O. The $\theta_{p:CIV}$ value is superior to the θ value in the characterization of **5-3**, again.

The OH-∗-O interaction in **5-3** is predicted to be slightly stronger than that in **5-1**, whereas NH-

∗-O in **5-3** is predicted to be weaker than that in **5-2a**. As a result, each HB interaction in **5-1**–**5-3** is shown to be weaker in the order shown in Equation (5-1), based on the $\theta_{p:CIV}$ values.

OH-∗-O (**5-3**) > OH-∗-O (**5-1**) > NH-∗-O (**5-2a**) > NH-∗-O (**5-3**) > NH-∗-Se (**5-2c**) > NH-∗-S (**5-2b**) (5-1)

The QTAIM-DFA parameters for OH-∗-O and NH-∗-E (E = O, S, and Se) in **5-1**–**5-3** predicted with MP2/BSS-B′a and MP2/BSS-B′b are very close to those predicted with MP2/BSS-A. The predicted nature is substantially the same, if predicted with MP2/G(**A**). However, the nature of OH-∗-O in **5-1** is predicted be *r*-CS/CT-TBP with M06-2X/BSS-A, which seems somewhat overestimated, relative to the case with MP2/BSS-A, as aforementioned.

Perturbed structures generated with CIV are demonstrated to operate (very) effectively in QTAIM-DFA to elucidate the nature of each HB of the multi-HB system in **5-1**–**5-3**. To examine the applicability of the method to the multi-HB system further, the ($\theta_{p:NIV}$, $\kappa_{p:NIV}$) values are similarly evaluated for **5-1**–**5-3** with QTAIM-DFA. The perturbed structures are employed, generated using the normal coordinates for the anti-symmetric and symmetric vibrations around the multi-HBs of **5-1**–**5-3** under MP2/BSS-A. Table 5-5 collects the $\theta_{p:NIV:a}$ and $\theta_{p:NIV:s}$ values, together with the differences between them ($\Delta\theta_{p:NC} = \theta_{p:NIV} - \theta_{p:CIV}$) for **5-1**–**5-3**. The subscripts of a and s in $\theta_{p:NIV}$ show that the normal coordinates corresponding to the anti-symmetric and symmetric vibrations, respectively, around the multi-HBs, which are used to generate the perturbed structures for QTAIM-DFA. In the case of **5-3**, a suitable internal vibration, located on OH-∗-O or NH-∗-O, is searched in place of the anti-symmetric or symmetric vibration, since **5-3** retains the C_1 symmetry after optimizations. However, no suitable internal vibration was found, located on OH-∗-O, in present calculation conditions.

The magnitudes of $\Delta\theta_{p:NC:a}$ are two to six times larger than those of $\Delta\theta_{p:NC:s}$. The results show that the perturbed structures generated with NIV based on the symmetric vibration, is closer to those with CIV than the case with NIV based on the antisymmetric vibration. One may imagine that NIV based on the symmetric vibration can be used effectively to generate the perturbed structures for **5-1**–**5-3**, in place of CIV. However, the perturbed structures of **5-3**, suitable for OH-∗-O, could not be effectively generated with NIV, since such vibration could not be found that located effectively on the OH-∗-O interaction of **5-3**, as mentioned above. As a result, QTAIM-DFA employing the perturbed structures generated with CIV is demonstrated to be a highly reliable method to elucidate nature of each HB in the multi-HB system. The magnitudes of $\Delta\theta_{p:NC:a}$ amount to about –5º, which seems smaller than those for the accurate analysis of the behavior for each HB of the multi-HB system.

Much attention has also been paid to the nature of HBs in the isomers of **5-1**–**5-3**, if formed. The nature of HBs in the isomers is discussed, next.

Table 5-5. The $\theta_{p:CIV}$ and $\theta_{p:NIV}$ values for each HB in **5-1**–**5-3**, evaluated with QTAIM-DFA under MP2/BSS-A, employing the perturbed structures generated with CIV and NIV, together with $\Delta\theta_{p:NC} = \theta_{p:NIV} - \theta_{p:CIV}$.[a]

θ_p[b]	**5-1** (C_{2h})	**5-2a** (C_i)	**5-2b** (C_i)	**5-2c** (C_i)	**5-3** (C_1)[c]
$\theta_{p:CIV}$	172.5	158.4	151.6	153.7	173.2/153.7
$\theta_{p:NIV:a}$[d]	167.8	155.6	147.7	149.6	171.4/150.0
$\Delta\theta_{p:NC:a}$	–4.7	–2.8	–3.9	–4.1	–1.8/3.7
$\theta_{p:NIV:s}$[e]	171.4	158.6	152.2	155.2	*f*/155.2
$\Delta\theta_{p:NC:s}$	–1.1	0.2	0.6	1.5	*f*/1.5

[a] Coordinates from anti-symmetric (a) and symmetric (s) vibrations around the multi-HBs of **5-1**–**5-3** are employed. [b] $\theta_p = 90^o - \tan^{-1}(dy/dx)$, where $(x, y) = (H_b(\boldsymbol{r}_c) - V_b(\boldsymbol{r}_c)/2, H_b(\boldsymbol{r}_c))$. [c] Values are given for OH-∗-O/NH-∗-O. Suitable vibrations located on OH-∗-O and NH-∗-O were searched for, in place of the a and s vibrations, since **5-3** has C_1 symmetry. [d] Based on the anti-symmetric vibration around the multi-HBs. [e] Based on the symmetric vibration around the multi-HBs. [f] Not obtained since no suitable vibration was found located on OH-∗-O.

Nature of Each HB in Multi-HBs for the Isomers of 5-1–5-3

To examine the nature of each HB in **5-1**–**5-3** further, isomers of **5-1**–**5-3** were looked for, starting from the structures of **5-1**–**5-3** by the torsional angles around the HBs being changed suitably, although a systematic conformer search was not applied. The optimizations converged to some isomers of **5-1**–**5-3** or to the original structures of **5-1**–**5-3** in a few cases, if optimized with MP2/BSS-A. A conformer **5-1**$_{iso}$ was obtained as an isomer of **5-1**, while **5-2a**$_{iso}$ was from **5-2a**, together with the topological isomer, **5-2a**′. In the case of **5-2b** and **5-2c**, the optimizations were performed to **5-2b**$_{iso}$ and **5-2c**$_{iso}$, respectively, which were ascribed as the isomers of **5-2b** and **5-2c**, respectively. A similar isomer search of **5-3** gave **5-3**$_{isoA}$, **5-3**$_{isoB}$, and **5-3**$_{isoC}$. Figure 5-5 illustrates the molecular graphs of **5-1**$_{iso}$–**5-3**$_{isoC}$, drawn on the optimized structures. Double HBs of the OH-∗-O and CH-∗-O types are formed in **5-1**$_{iso}$ and **5-3**$_{isoA}$ and double HBs of the OH-∗-O and NH-∗-O types are formed in the six membered rings in **5-3**$_{isoB}$ and **5-3**$_{isoC}$. On the other hand, triple HBs of the NH-∗-N, NH-∗-E, and CH-∗-E types are formed in the bicycle 1,3,3-systems of **5-2a**$_{iso}$, **5-2b**$_{iso}$, and **5-2c**$_{iso}$, where E = O, S, and Se, respectively.

QTAIM functions of $\rho_b(\boldsymbol{r}_c)$, $H_b(\boldsymbol{r}_c) - V_b(\boldsymbol{r}_c)/2$, $H_b(\boldsymbol{r}_c)$, and $k_b(\boldsymbol{r}_c)$ are calculated at BCP of BP corresponding to each HB in **5-1**$_{iso}$–**5-3**$_{isoC}$. Table 5-6 collects the values, evaluated with MP2/BSS-A. $H_b(\boldsymbol{r}_c)$ are plotted versus $H_b(\boldsymbol{r}_c) - V_b(\boldsymbol{r}_c)/2$ for the data shown in Table 5-6 and those from the perturbed structures, generated with CIV. Figure 5-6 shows the plots. The QTAIM-DFA parameters of (R, θ) and ($\theta_{p:CIV}$, $\kappa_{p:CIV}$) were calculated for **5-1**$_{iso}$–**5-3**$_{isoC}$ by analyzing the plots in Figure 5-6. Table 5-6 also collects the (R, θ) and ($\theta_{p:CIV}$, $\kappa_{p:CIV}$) values, together with the C_{ii} values.

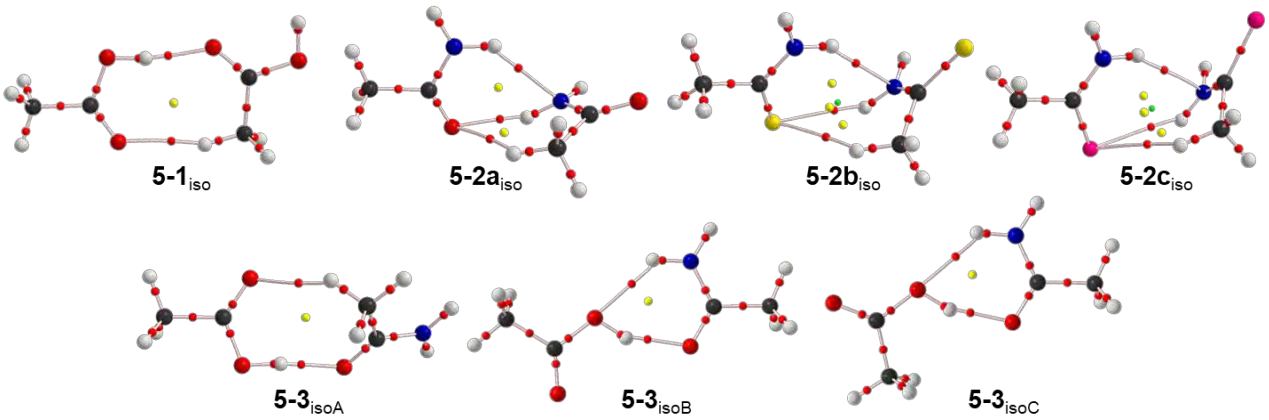

Figure 5-5. Molecular graphs for **5-1**$_{iso}$ (C_s), **5-2a**$_{iso}$ (C_1), **5-2b**$_{iso}$ (C_1), **5-2c**$_{iso}$ (C_1), **5-3**$_{isoA}$ (C_1), **5-3**$_{isoB}$ (C_1), and **5-3**$_{isoC}$ (C_1), evaluated with MP2/BSS-A. BCPs are denoted by red dots, RCPs by yellow dots, and BPs are by pink lines. Carbon atoms are in black and hydrogen atoms are in grey, with oxygen, nitrogen, sulfur, and selenium atoms in red, blue, dark yellow, and deep pink, respectively.

Table 5-6. QTAIM functions and QTAIM-DFA parameters for each HB of multi-HBs in **5-1**$_{iso}$–**5-3**$_{isoC}$, evaluated with MP2/BSS-A.

Species (symm)	X-∗-Y[a]	$\rho_b(\boldsymbol{r}_c)$ (au)	$c\nabla^2\rho_b(\boldsymbol{r}_c)$[b] (au)	$H_b(\boldsymbol{r}_c)$ (au)	$k_b(\boldsymbol{r}_c)$[c]	R[d] (au)	θ[e] (°)	C_{ii} (unit[h])	$\theta_{p:CIV}$[f] (°)	$\kappa_{p:CIV}$[g] (au^{-1})	Predicted Nature
5-1$_{iso}$ (C_s)	OH-∗-O	0.0356	0.0129	–0.0044	–1.144	0.0136	108.6	4.16	159.2	36.3	*r*-CS/CT-MC
	CH-∗-O	0.0132	0.0058	0.0015	–0.852	0.0060	75.6	11.48	78.9	32.4	*p*-CS/vdW
5-2a$_{iso}$ (C_1)	NH-∗-O	0.0247	0.0104	0.0005	–0.975	0.0104	87.2	8.38	121.1	221	*p*-CS/*t*-HB$_{nc}$
	NH-∗-N	0.0143	0.0058	0.0014	–0.864	0.0060	76.5	15.31	85.1	121	*p*-CS/vdW
	CH-∗-O	0.0079	0.0032	0.0007	–0.886	0.0033	78.5	25.76	85.0	109	*p*-CS/vdW
5-2b$_{iso}$ (C_1)	NH-∗-S	0.0167	0.0050	0.0004	–0.962	0.0050	85.8	16.55	119.3	415	*p*-CS/*t*-HB$_{nc}$
	NH-∗-N	0.0150	0.0061	0.0013	–0.876	0.0062	77.6	17.25	93.9	159	*p*-CS/*t*-HB$_{nc}$
	CH-∗-S	0.0088	0.0030	0.0006	–0.877	0.0030	77.6	20.32	87.6	96.5	*p*-CS/vdW
5-2c$_{iso}$ (C_1)	NH-∗-Se	0.0155	0.0043	0.0004	–0.951	0.0044	84.7	16.56	114.0	562	*p*-CS/*t*-HB$_{nc}$
	NH-∗-N	0.0141	0.0059	0.0015	–0.857	0.0061	75.9	18.55	92.6	141	*p*-CS/*t*-HB$_{nc}$
	CH-∗-Se	0.0082	0.0026	0.0006	–0.874	0.0026	77.4	21.93	86.1	89.1	*p*-CS/vdW
5-3$_{isoA}$ (C_1)	OH-∗-O	0.0461	0.0135	–0.0106	–1.283	0.0172	128.2	3.35	169.8	8.0	*r*-CS/CT-MC
	CH-∗-O	0.0134	0.0058	0.0014	–0.858	0.0060	76.1	13.66	77.8	43.6	*p*-CS/vdW
5-3$_{isoB}$ (C_1)	OH-∗-O	0.0436	0.0133	–0.0086	–1.246	0.0158	123.1	4.62	171.5	15.9	*r*-CS/CT-MC
	NH-∗-O	0.0138	0.0074	0.0023	–0.820	0.0078	73.1	12.92	77.1	44.5	*p*-CS/vdW
5-3$_{isoC}$ (C_1)	OH-∗-O	0.0496	0.0137	–0.0124	–1.312	0.0185	132.2	3.21	173.0	6.8	*r*-CS/CT-MC
	NH-∗-O	0.0151	0.0082	0.0024	–0.826	0.0086	73.5	11.20	79.1	55.3	*p*-CS/vdW

[a] Data are given at BCP. [b] $c\nabla^2\rho_b(\boldsymbol{r}_c) = H_b(\boldsymbol{r}_c) - V_b(\boldsymbol{r}_c)/2$, where $c = \hbar^2/8m$. [c] $k_b(\boldsymbol{r}_c) = V_b(\boldsymbol{r}_c)/G_b(\boldsymbol{r}_c)$. [d] $R = (x^2 + y^2)^{1/2}$, where $(x, y) = (H_b(\boldsymbol{r}_c) - V_b(\boldsymbol{r}_c)/2, H_b(\boldsymbol{r}_c))$. [e] $\theta = 90° - \tan^{-1}(y/x)$. [f] $\theta_p = 90° - \tan^{-1}(dy/dx)$. [g] $\kappa_p = |d^2y/dx^2|/[1 + (dy/dx)^2]^{3/2}$. [h] Å mdyn^{-1}.

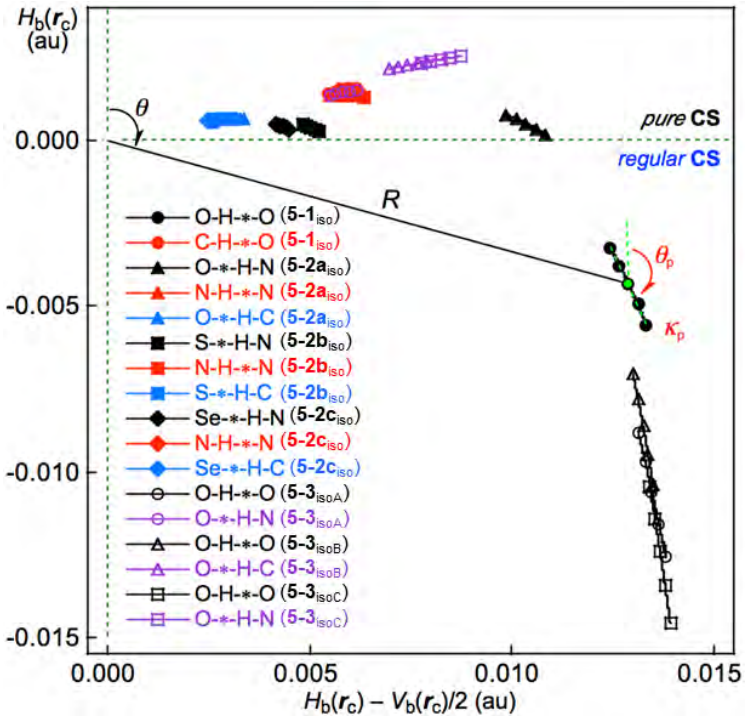

Figure 5-6. Plots of $H_b(\boldsymbol{r}_c)$ versus $H_b(\boldsymbol{r}_c) - V_b(\boldsymbol{r}_c)/2$ for **5-1**$_{iso}$–**5-3**$_{isoC}$, calculated with MP2/BSS-A, where the perturbed structures are generated with CIV.

Each HB in multi-HBs of **5-1**$_{iso}$–**5-3**$_{isoC}$ are similarly classified and characterized on the basis of the (θ, $\theta_{p:CIV}$) values evaluated with MP2/BSS-A, employing the criteria as a reference. The (θ, $\theta_{p:CIV}$) values are (108.6–132.2º, 159.2–173.0º) for OH-∗-O in **5-1**$_{iso}$ and **5-3**$_{isoA}$–**5-3**$_{isoC}$, which are classified by the *r*-CS interactions and characterized as the CT-MC nature (*r*-CS/CT-MC). The (θ, $\theta_{p:CIV}$) values for NH-∗-E in **5-2a**$_{iso}$, **5-2b**$_{iso}$, and **5-2c**$_{iso}$ (E = O, S, and Se, respectively) are (84.7–87.2º, 114.0–121.1º); therefore, the interactions are classified and characterized as *p*-CS/*t*-HB$_{nc}$ (the typical HB nature with no covalency). The NH-∗-E interactions in **5-2a**$_{iso}$, **5-2b**$_{iso}$, and **5-2c**$_{iso}$ are predicted to be stronger in the order of E = Se < S < O. The NH-∗-N interactions in **5-2b**$_{iso}$ and **5-2c**$_{iso}$ are also predicted to have the nature of *p*-CS/*t*-HB$_{nc}$, due to the (θ, $\theta_{p:CIV}$) values of (75.9–77.6º, 92.6–93.9º), whereas NH-∗-N in **5-2a**$_{iso}$ is classified and characterized as the *p*-CS/vdW nature, because both θ (= 76.5º) and $\theta_{p;CIV}$ (= 85.1º) are less than 90º. The CH-∗-O, CH-∗-S, and CH-∗-Se interactions in **5-1**$_{iso}$–**5-3**$_{isoC}$ are all classified and characterized as the *p*-CS/vdW nature with θ < 90º and $\theta_{p;CIV}$ < 90º, so are the NH-∗-O interactions in **5-3**$_{isoA}$–**5-3**$_{isoC}$. The results demonstrate that each HB interaction in **5-1**–**5-3** is predicted to be stronger than the corresponding HB in **5-1**$_{iso}$–**5-3**$_{isoC}$, respectively. The formation of multi-HBs seems to enhance the strength of original single HB.

Each HB in multi-HB system in **5-1**–**5-3** and **5-1**$_{iso}$–**5-3**$_{isoC}$ are reasonably analyzed with QTAIM-DFA. The results demonstrate the high applicability of QTAIM-DFA to the system, by employing the perturbed structures generated with CIV.

Summary

It is inevitable to clarify the nature of each HB in multi-HBs for better understanding of chemical processes controlled by multi-HBs, as well as single-HBs. The dynamic and static nature of each HB in multi-HBs was elucidated, exemplified by those in acetic acid dimer (**5-1**), acetamide dimer (**5-2a**), the acetic acid acetamide complex (**5-3**), together with the thio- and seleno-derivatives of **5-2a** (**5-2b** and **5-2c**, respectively). However, it is necessary to establish the methodology to elucidate the nature of such multi-HBs, since the multi-HBs are formed in close proximity in space, and they will interact mutually and strongly with each other. It must be careful when the nature of interactions is discussed on the basis of the calculated values, since substantially large basis set and level dependence will appear. Suitable method to calculate HBs in multi-HB system was carefully explored by employing **5-1** in this work.

QTAIM-DFA well elucidated the intrinsic dynamic and static nature of each HB in multi-HB system by employing CIV method for generating perturbed structures. The nature of each HB of **5-1**–**5-3** are all predicted to have the nature of CT-MC appearing in the *r*-CS region. The nature of each HB in **5-1**$_{iso}$–**5-3**$_{isoC}$ of the isomers of **5-1**–**5-3** is also investigated for convenience of comparison. Each HB in **5-1**–**5-3** is predicted to be stronger than the corresponding interactions in **5-1**$_{iso}$–**5-3**$_{isoC}$. Each HB is confirmed to be enhanced by the formation of multi-HBs such as those in **5-1**–**5-3** with QTAIM-DFA. The high applicability of QTAIM-DFA, employing the perturbed structures generated with CIV, is demonstrated. Each HB in the multi-HBs will be able to be elucidated in dimers, oligomers, and/or polymers of water, alcohols, and carboxylic acids. Multi-HBs formed not only in vitro but also in vivo are expected to be clarified by applying the method, although some devise seems necessary.

Appendix

Table 5-A1. The structural parameters of the r(H···X) and ∠AHX values of AH-∗-X, evaluated with MP2/BSS-A for HBs in **5-1**–**5-3** and the isomers, **5-1**$_{iso}$–**5-3**$_{isoC}$, together with the ΔE_{ES} and ΔE_{ZP} values.[a]

Species (symm)	AH-∗-X	r(H···X) (Å)	∠AHX (º)	ΔE_{ES}[b] (kJ mol^{-1})	ΔE_{ZP}[c] (kJ mol^{-1})
5-1 (C_{2h})	OH-∗-O	1.6491	178.54	–72.4	–66.2
5-2a (C_i)	NH-∗-O	1.8199	175.72	–65.0	–55.3
5-2b (C_i)	NH-∗-S	2.3513	171.05	–55.2	–49.0
5-2c (C_i)	NH-∗-Se	2.4672	168.69	–55.6	–50.7
5-3 (C_1)	OH-∗-O	1.6304	173.30	–70.6	–62.8
	NH-∗-O	1.8399	167.25		
5-1$_{iso}$ (C_s)	OH-∗-O	1.7746	169.66	–41.0	–36.1
	CH-∗-O	2.2782	161.70		
5-2a$_{iso}$ (C_1)	NH-∗-O	1.9853	154.79	–40.8	–32.9
	NH-∗-N	2.3152	139.64		
	CH-∗-O	2.5972	142.31		
5-2b$_{iso}$ (C_1)	NH-∗-S	2.5315	143.24	–43.1	–37.6
	NH-∗-N	2.2933	149.37		
	CH-∗-S	2.8800	145.83		
5-2c$_{iso}$ (C_1)	NH-∗-Se	2.6590	139.95	–45.1	–40.7
	NH-∗-N	2.3322	150.21		
	CH-∗-Se	3.0065	144.63		
5-3$_{isoA}$ (C_1)	OH-∗-O	1.6832	173.82	–50.7	–44.4
	CH-∗-O	2.2848	146.42		
5-3$_{isoB}$ (C_1)	OH-∗-O	1.7282	154.70	–41.5	–35.9
	NH-∗-O	2.1827	133.07		
5-3$_{isoC}$ (C_1)	OH-∗-O	1.6809	159.83	–37.0	–30.5
	NH-∗-O	2.1455	132.27		

[a] Calculated with MP2/6-311++G(3df,3pd). [b] The energies on the energy surface from the components (ΔE_{ES}) [= E_{ES}(HB) – E_{ES}(components)]. [c] The energies with the zero-point energy collections from the components (ΔE) [= E(HB) – E(components)].

Table 5-A2. The r_{BP} and R_{SL} values evaluated with MP2/BSS-A for HBs in **5-1**–**5-3** and the isomers, **5-1**$_{iso}$–**5-3**$_{isoC}$, together with the Δr_{BP} values.[a]

Compound (symm)	AH-∗-X	r_{BP} (H···X)[b] (Å)	R_{SL} (H···X)[c] (Å)	Δr_{BP}[d] (Å)
5-1 (C_{2h})	OH-∗-O	1.6806	1.6491	0.0314
5-2a (C_i)	NH-∗-O	1.8484	1.8199	0.0285
5-2b (C_i)	NH-∗-S	2.3776	2.3513	0.0263
5-2c (C_i)	NH-∗-Se	2.4933	2.4672	0.0261
5-3 (C_1)	OH-∗-O	1.6613	1.6304	0.0309
	NH-∗-O	1.8690	1.8399	0.0291
5-1$_{iso}$ (C_s)	OH-∗-O	1.8064	1.7746	0.0318
	CH-∗-O	2.3035	2.2782	0.0252
5-2a$_{iso}$ (C_1)	NH-∗-O	2.0147	1.9853	0.0294
	NH-∗-N	2.3444	2.3152	0.0292
	CH-∗-O	2.6337	2.5972	0.0365
5-2b$_{iso}$ (C_1)	NH-∗-S	2.5669	2.5315	0.0353
	NH-∗-N	2.3274	2.2933	0.0341
	CH-∗-S	2.9098	2.8800	0.0298
5-2c$_{iso}$ (C_1)	NH-∗-Se	2.6969	2.6590	0.0379
	NH-∗-N	2.3921	2.3322	0.0599
	CH-∗-Se	3.0349	3.0065	0.0284
5-3$_{isoA}$ (C_1)	OH-∗-O	1.7147	1.6832	0.0315
	CH-∗-O	2.3144	2.2848	0.0296
5-3$_{isoB}$ (C_1)	OH-∗-O	1.7583	1.7282	0.0301
	NH-∗-O	2.2192	2.1827	0.0366
5-3$_{isoC}$ (C_1)	OH-∗-O	1.7102	1.6809	0.0292
	NH-∗-O	2.1843	2.1455	0.0387

[a] Calculated with MP2/6-311++G(3df,3pd). [b] The lengths of BPs. [c] Straight-line distances. [d] $\Delta r_{BP} = r_{BP} - R_{SL}$.

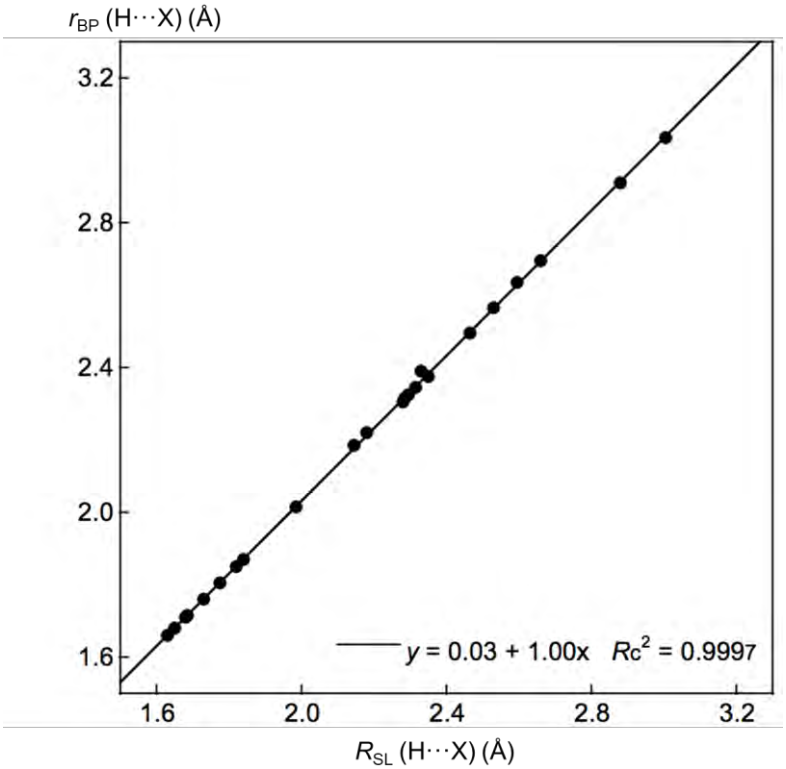

Figure 5-A1. Plot of r_{BP} (H···X) versus R_{SL} (H···X) for the optimized structures of **5-1**–**5-3** and **5-1**$_{iso}$–**5-3**$_{isoC}$ with the MP2/6-311++G(3df,3pd) method.

References and Notes

1. L. Pauling, *The Nature of the Chemical Bond*, Cornell University Press, Ithaca, NY, **1960**.
2. G. C. Pimentel, A. L. McClellan, *The Hydrogen Bond*, W. H. Freeman, San Francisco, CA, **1960**.
3. P. Schuster, G. Zundel, C. Sandorfy, *The Hydrogen Bond, Recent Developments in Theory and Experiments*, North-Holland Publishing Company, Amsterdam, **1976**.
4. G. A. Jeffrey, *An Introduction to Hydrogen Bonding*, Oxford University Press, New York, **1997**.
5. S. Scheiner, *Hydrogen Bonding, A Theoretical Perspective*, Oxford University Press, Oxford, **1997**.
6. G. R. Desiraju, T. Steiner, *The Weak Hydrogen Bond in Structural Chemistry and Biology; International Union of Crystallography Monographs on Crystallography*, Oxford University Press, New York, **1999**.
7. *Hydrogen Bonding – New Insights*, (Ed.: S. J. Grabowski), Springer, The Netherlands, Dordrecht, **2006**.
8. G. Buemi, *Intramolecular Hydrogen Bonds. Methodologies and Strategies for Their Strength Evaluation* in *Hydrogen Bonding – New Insights* (Eds.: S. J. Grabowski), Springer, New York, **2006**. Ch. 2.
9. K.-L. Han, G.-J. Zhao, *Hydrogen Bonding and Transfer in the Excited State*, Wiley, Chichester, UK, **2010**.
10. S. Hayashi, K. Matsuiwa, M. Kitamoto, W. Nakanishi, *J. Phys. Chem. A* **2013**, *117*, 1804–1816.
11. See the references cited in ref. 10.
12. T. Nishide, S. Hayashi, W. Nakanishi, *ChemistryOpen* **2018**, *7*, 565–575.
13. W. Nakanishi, S. Hayashi, K. Narahara, *J. Phys. Chem. A* **2008**, *112*, 13593–13599.
14. W. Nakanishi, S. Hayashi, K. Narahara, *J. Phys. Chem. A* **2009**, *113*, 10050–10057.
15. W. Nakanishi, S. Hayashi, *Curr. Org. Chem.* **2010**, *14*, 181–197.
16. W. Nakanishi, S. Hayashi, *J. Phys. Chem. A* **2010**, *114*, 7423–7430.
17. W. Nakanishi, S. Hayashi, K. Matsuiwa, M. Kitamoto, *Bull. Chem. Soc. Jpn.* **2012**, *85*, 1293–1305.
18. W. Nakanishi, S. Hayashi, *J. Phys. Chem. A* **2013**, *117*, 1795–1803.
19. W. Nakanishi, S. Hayashi, *Int. J. Quantum Chem.* **2018**, *118*, e25590.
20. *Gaussian 09, Revision D.01*, M. J. Frisch, G. W. Trucks, H. B. Schlegel, G. E. Scuseria, M. A. Robb, J. R. Cheeseman, G. Scalmani, V. Barone, B. Mennucci, G. A. Petersson, H. Nakatsuji, M. Caricato, X. Li, H. P. Hratchian, A. F. Izmaylov, J. Bloino, G. Zheng, J. L. Sonnenberg, M. Hada, M. Ehara, K. Toyota, R. Fukuda, J. Hasegawa, M. Ishida, T. Nakajima, Y. Honda, O. Kitao, H. Nakai, T. Vreven, J. A. Montgomery, Jr., J. E. Peralta, F. Ogliaro, M. Bearpark, J. J. Heyd, E. Brothers, K. N. Kudin, V. N. Staroverov, R. Kobayashi, J. Normand, K. Raghavachari, A. Rendell, J. C. Burant, S. S. Iyengar, J. Tomasi, M. Cossi, N. Rega, J. M. Millam, M. Klene, J. E. Knox, J. B. Cross, V. Bakken, C. Adamo, J. Jaramillo, R. Gomperts, R. E. Stratmann, O. Yazyev, A. J. Austin, R. Cammi, C. Pomelli, J. W. Ochterski, R. L. Martin, K. Morokuma, V. G. Zakrzewski,

G. A. Voth, P. Salvador, J. J. Dannenberg, S. Dapprich, A. D. Daniels, Ö. Farkas, J. B. Foresman, J. V. Ortiz, J. Cioslowski, D. J. Fox, Gaussian, Inc., Wallingford CT, **2009**.

21. a) C. Møller, M. S. Plesset, *Phys. Rev.* **1934**, *46*, 618–622; b) J. Gauss, *J. Chem. Phys.* **1993**, *99*, 3629–3643; c) J. Gauss, *Ber. Bunsen-Ges. Phys. Chem.* **1995**, *99*, 1001–1008.
22. Y. Zhao, D. G. Truhlar, *Theor. Chem. Acc.* **2008**, *120*, 215–241.
23. The M06-2X level seems one of nice candidates for the evaluations, since the optimizations at the level reproduce well the observed structures, containing the HB species, relative to other DFT levels, although the structures of molecular complexes would not. QTAIM functions and QTAIM-DFA parameters evaluated at the M06-2X level seem close to those obtained at the MP2 level in the average. QTAIM functions evaluated at the MP2 level are shown to be very close to those determined by the high-resolution X-ray determination of electron densities of some interactions.[31,32]
24. The unit of C_{ij} is Å mdyn^{-1}. Å^3 mdyn^{-1} in refs 12 and 19 should read Å mdyn^{-1}.
25. K. Brandhorst, J. Grunenberg, *J. Chem. Phys.* **2010**, *132*, 184101.
26. K. Brandhorst, J. Grunenberg, *Chem. Soc. Rev.* **2008**, *37*, 1558–1567.
27. J. Grunenberg, *Chem. Sci.* **2015**, *6*, 4086–4088.
28. F. Biegler-König, *J. Comput. Chem.* **2000**, *21*, 1040–1048.
29. T. A. Keith, AIMAll (Version 17.11.14), TK Gristmill Software, Overland Park, KS, USA, **2017**, http://www.aim.tkgristmill.com.
30. *Kagakubinran Kisohen II 5th ed.* (Ed.; Y. Iwasawa), The Chemical Society of Japan Edition, Ch. 11, Maruzen, Tokyo, Japan, **2004**.
31. W. Nakanishi, S. Hayashi, M. B. Pitak, M. B. Hursthouse, S. J. Coles, *J. Phys. Chem. A* **2011**, *115*, 11775–11787.
32. Y. Tsubomoto, S. Hayashi, W. Nakanishi, L. K. Mapp, S. J. Coles, *RSC Adv.* **2018**, *8*, 9651–9660.

Chapter 6

Intrinsic Dynamic and Static Nature of Each HB in the Multi-HBs between Nucleobase Pairs and its Behavior, Elucidated with QTAIM Dual Functional Analysis and QC Calculations

Abstract

The intrinsic dynamic and static nature of each HB in the multi-HBs between nucleobase pairs (Nu-Nu') is elucidated with QTAIM dual functional analysis (QTAIM-DFA), by employing the perturbed structures generated with coordinates derived from the compliance force constants (C_{ii}) for internal vibrations (CIV). Two, three, or four HBs are detected for Nu-Nu'. Each HB in Nu-Nu' is predicted to have the nature of CT-TBP (trigonal bipyramidal adduct through charge transfer (CT)), CT-MC (molecular complex through CT), or *t*-HB_{wc} (typical HB with covalency), while the vdW nature is predicted for the C–H···X interactions, for example. Energies for the formation of the pairs (ΔE) are linearly correlated with the total values of C_{ii}^{-1} in Nu-Nu'. The total C_{ii}^{-1} values are obtained by summing each C_{ii}^{-1} value, similarly to the case of Ohm's law for the parallel connection in the electric resistance. The total ΔE value for a nucleobase pair could be fractionalized to each HB, based on each C_{ii}^{-1} value. The perturbed structures generated with CIV are very close to those generated with the partial optimization method, when the changes in the distances of interacting atoms are very small. The results provide useful insights for better understanding DNA processes, although they are highly enzymatic.

Introduction

Hydrogen bonds (HBs) are fundamentally important in all fields of chemical and biological sciences.[1–9] One of the most important roles of HBs in biological sciences is the operation of the genetic code.[10] The two helical chains of nucleotides in DNA associate through the multi-HBs between adenine-thymine (A-T) and guanine-cytosine (G-C) pairs, as proposed by Watson and Crick.[3,10–13] The duplex DNA structure first opens and then closes in active proliferation at approximately room temperature, which is a typical event in DNA induced by the action of HBs. The processes must be highly enzymatically catalyzed.[14] The multi-HBs between A-T and G-C pairs are formed in close proximity in space and will mutually and strongly interact with each other. Therefore, clarifying the nature of each HB in the multi-HBs between nucleobase pairs (Nu-Nu'), containing A-T and G-C, is very important. The results will provide useful insights for better understanding DNA processes, although they are highly enzymatic. The ability to image the initial stage of the opening and closing of duplex DNA through a simple mechanism based on the nature of each HB in the multi-HBs between Nu-Nu' would be helpful. The basic behavior and stability of the duplex DNA structure should be closely related to the nature of each HB in Nu-Nu'. The ability to fractionalize the energy for the formation of Nu-Nu' from the components (Nu and Nu') to each HB in the multi-HBs between Nu-Nu' is also very interested. Such considerations led to elucidate the dynamic and static nature of each HB in the multi-HBs between Nu-Nu'. Figure 6-1 shows the structures of the nucleobases adenine (A), guanine (G), cytosine (C), thymine (T), and uracil (U) as molecular graphs, which are calculated with MP2/BSS-B'a (seeTable 6-1 for BSS-B'a). Indeed, there are some possibilities in the structures of Nu-Nu', and these possibilities, which control the functionalities of the pairs in the DNA chains, seem promising;[15] however, the typical cases are discussed in this work.

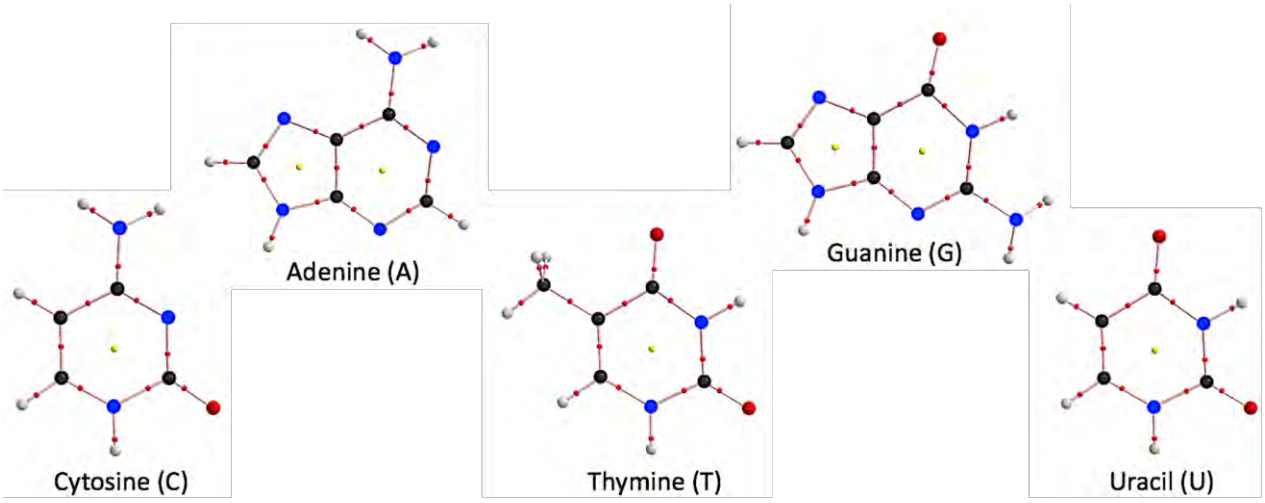

Figure 6-1. Molecular graphs for the nucleobases adenine (A), guanine (G), cytosine (C), thymine (T), and uracil (U), optimized with MP2/BSS-B'a (see Table 6-1 for BSS-B'a).

The understanding of HBs has been considerably growing recently,[1–9,16,17] but evaluating, characterizing, and understanding the nature of each HB in multi-HBs, especially in nucleobase pairs, is inevitably needed to obtain a better understanding of DNA processes. How can the dynamic and static nature of each HB in the multi-HBs between Nu-Nu', where the multi-HBs are formed in close proximity in space and interact mutually and strongly with each other, be clarified? Grunenberg and Brandhorst calculated the strength of each HB of the multi-HBs in the A-T and C-G pairs by applying the compliance force constants (C_{ii}).[18–20] The elucidation of the intrinsic dynamic and static nature of each HB in multi-HBs, exemplified by the acetic acid dimer and derivatives, was attempted by employing the perturbed structures generated with CIV[21] to examine the effective applicability of the QTAIM dual functional analysis (QTAIM-DFA)[22–25] to the system.[26]

The QTAIM-DFA would be well suited to elucidate the nature of each HB in the multi-HBs between Nu-Nu' by employing the perturbed structures generated with CIV, with above discussion in mind. Weak interactions in Nu-Nu' may sometimes be called HBs here, even if they should be assigned to other categories of interactions. Herein, the author presents the results of investigations on the intrinsic dynamic and static nature of each HB in the multi-HBs between nucleobase pairs. Each HB interaction in Nu-Nu' can be classified and characterized effectively with QTAIM-DFA, employing the perturbed structures generated with CIV. The behavior of the pairs is also discussed based on the nature. The mechanism for the formation the Nu-Nu' pairs will also be clarified in more detail based on the C_{ii} parameters.

The QTAIM-DFA is explained in Chapter 2, together with the basic concept of the QTAIM approach.[27,28]

Methodological Details in Calculations

Calculations were performed employing the Gaussian 09 program package.[29] Table 6-1 summarizes the basis set systems (BSSs) used in this work. The Møller-Plesset second-order energy correlation (MP2) level[30] was applied for the calculations, together with the DFT level of M06-2X.[31,32] It was reported that MP2/BSS-A, MP2/BSS-A', MP2/BSS-B'a, and MP2/BSS-B'b gave excellent results of very similar quality in the evaluation of the nature of each HB in the acetic acid dimer and related species.[26] Optimized structures were confirmed by all real frequencies in the possible cases. The reliability of the structures optimized with MP2/BSS-B'a was also examined by comparison with structures optimized with MP2/BSS-A'. The results of the frequency analysis were used to obtain the C_{ii} values.[30–35] The M06-2X level was also employed, if necessary. The results obtained with MP2/BSS-B'a are mainly discussed. BSS-D or lower basis sets were employed for pre-optimizations.

QTAIM functions were calculated using the same basis set system and the level as in the optimizations and were analyzed with the AIM2000[36] and AIMAll[37] programs. In QTAIM-DFA, $H_b(\boldsymbol{r}_c)$ are plotted versus $H_b(\boldsymbol{r}_c) - V_b(\boldsymbol{r}_c)/2$ for the five data points of $w = 0$, ±0.025, and ±0.05 (see Chapter 2). The perturbed structures were also generated by the partial optimization method (POM)[22,24] of the Z-matrix and/or ModRedundant types.[38]

Table 6-1. Basis set systems (BSSs) employed for the calculations.

BSS	H, C, N, and O	BSS	H, C, N, and O
BSS-A	6-311++G(3df,3pd)	BSS-A'	6-311+G(3df,3pd)
BSS-B'a	6-311+G(3df,3pd)[a]	BSS-B'b	6-311+G(3df,3pd)[b]
BSS-C	6-311++G(3df,3p)	BSS-C'	6-311+G(3df,3p)
BSS-D	6-311++G(3d,3p)	BSS-D'	6-311+G(3d,3p)

[a] The 6-311+G(3d) basis set being employed for C. [b] The 6-311+G(d) basis set being employed for C.

Results and Discussion

Optimization of Nucleobase Pairs, Nu-Nu'

The nucleobase pairs are optimized with various BSSs at the MP2 and M06-2X levels, where many results have been reported.[39] The HB distances (r(H, B); r) in Nu-Nu' optimized with MP2/BSS-A', MP2/BSS-B'a, MP2/BSS-B'b, M06-2X/BSS-A, M06-2X/BSS-C, and M06-2X/BSS-D are collected in Table 6-A1 of the Appendix. Energies for the formation of Nu-Nu' from the components (Nu and Nu') ΔE [= E(Nu-Nu') – (E(Nu) + E(Nu'))] are evaluated with various methods. The ΔE_{ES} and ΔE_{ZP} values correspond to those on the energy surface and those containing the zero-point corrections, respectively. The values evaluated with MP2/BSS-B'a, MP2/BSS-B'b, M06-2X/BSS-A, M06-2X/BSS-C, and M06-2X/BSS-D are collected in Table 6-A2 of the Appendix, which also contains the ΔE_{ES} values evaluated with MP2/BSS-A'. The results for the C_1 structures of Nu-Nu' (Nu-Nu' (C_1)) are mainly employed for the discussion, and the results for A-T (C_s), T-T (C_i), and U-U (C_s) are essentially the same as those for the corresponding C_1 pairs. In the case of G-G, it is optimized as the C_i structure. The optimized structures are not shown in the figures, but they can be found in the molecular graphs drawn on the structures optimized with MP2/BSS-B'a (see Figure 6-2).

The r(H, B) values in Nu-Nu' evaluated with the various methods are plotted versus those evaluated with MP2/BSS-A'. The plot is shown in Figure 6-A1 of the Appendix. This plot gave very good correlations, as shown in the figure. The high similarities in r(H, B) correspond to the high similarities of the structures of Nu-Nu' optimized with the methods employed in the calculations.[20,35,40] The similarities are excellent, especially for the structures optimized with MP2/BSS-B'a, MP2/BSS-B'b, and MP2/BSS-A', although frequency analysis could not be performed on those with MP2/BSS-A'.

Molecular Graphs with Contour Plots of $\rho(r)$ and Negative Laplacians around HBs in Nu-Nu'

Figure 6-2 illustrates the molecular graphs with the contour plots of $\rho(\boldsymbol{r})$ for Nu-Nu' drawn on the structures optimized with MP2/BSS- B'a. As expected, a BP with a BCP is clearly detected for each HB. Figure 6-3 shows the negative Laplacians of $\rho(\boldsymbol{r})$, exemplified by A-T and C-G. All BCPs for HBs exist in the blue area (the outsides of the red area) in the figure, which means that the HBs in A-T and C-G are all classified as CS interactions. For example, the ΔE_{ES} values evaluated with MP2/BSS-B'a are –70.3, –70.6, and –123.5 kJ mol^{-1} for A-T, A-U, and C-G, respectively. The values for A-T and A-U are very close to each other due to their structural similarity.[13] The ΔE_{ZP} values are plotted versus the ΔE_{ES} values calculated with MP2/BSS-B'a. The plot, which is shown in Figure 6-A2 of the Appendix, gives a very good correlation ($\Delta E_{ZP} = 0.968\Delta E_{ES} + 1.80$: $R_c^2 = 0.9993$). Therefore, either ΔE_{ES} or ΔE_{ZP} can be employed for the discussion of the energy terms.

Next, the nature of each HB in multi-HBs of Nu-Nu' will be clarified by QTAIM-DFA with CIV.

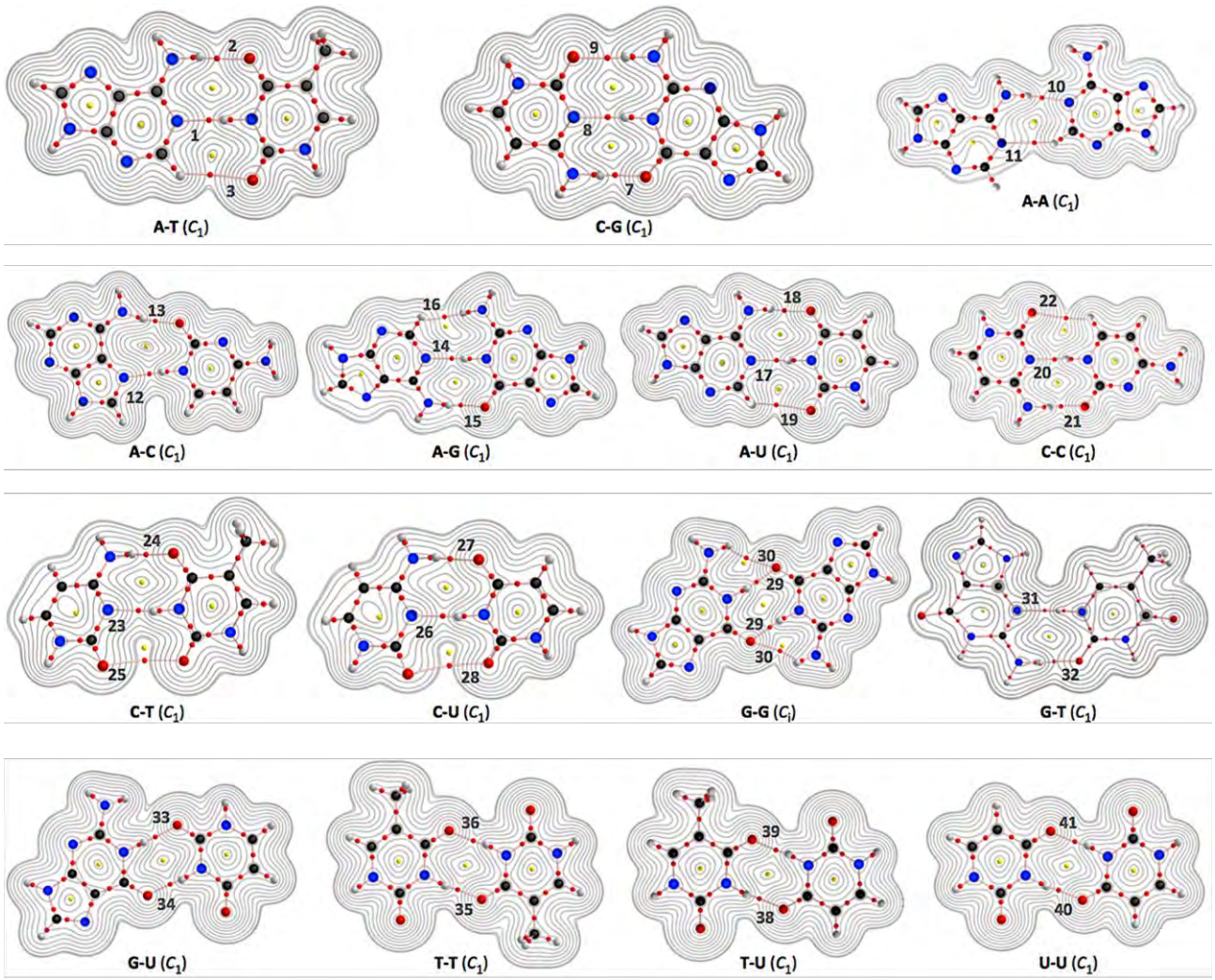

Figure 6-2. Molecular graphs for nucleobase pairs (Nu-Nu'), with the contour plots of $\rho(\boldsymbol{r})$, evaluated with MP2/BSS-B'a. The numbers for the bonds are the same as those in Figure 6-4 and Table 6-2. Bond critical points (BCPs) are denoted by red dots, ring critical points (RCPs) are denoted by yellow dots and bond paths (BPs) are denoted by pink lines. Oxygen, nitrogen, carbon, and hydrogen atoms are in red, blue, black, and gray, respectively. Contour plots are drawn on the planes containing at least one side of the HB interaction.

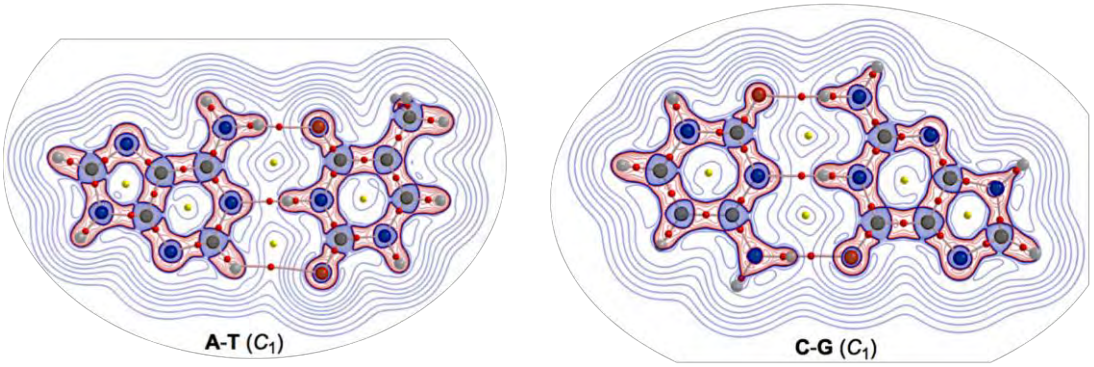

Figure 6-3. Negative Laplacians of $\rho(\boldsymbol{r})$ for the A-T and C-G pairs, calculated with MP2/BSS-B'a. Positive and negative areas are in blue and red lines, respectively.

Survey of the HB Interactions in Nu-Nu'

The HB interactions in Nu-Nu' seem straight, considering the BPs corresponding to the HBs shown in Figure 6-2. To examine the linearity of the HB interactions further, the lengths of the BPs (r_{BP}) in question and the corresponding straight-line distances (R_{SL}) are calculated for Nu-Nu'. The values evaluated with MP2/BSS-B'a are collected in Table 6-A3 of the Appendix, together with the differences between them ($\Delta r_{BP} = r_{BP} - R_{SL}$). The magnitudes of Δr_{BP} are less than 0.072 Å for the BPs; therefore, all HBs in Nu-Nu' can be approximated by straight lines, except for CH-∗-HN in A-G (Δr_{BP}: 0.1972 Å).

QTAIM functions are calculated at each BCP on the BP corresponding to each HB in Nu-Nu'. Table 6-2 collects the $\rho_b(\boldsymbol{r}_c)$, $H_b(\boldsymbol{r}_c) - V_b(\boldsymbol{r}_c)/2$ (= $(\hbar^2/8m)\nabla^2\rho_b(\boldsymbol{r}_c)$) and $H_b(\boldsymbol{r}_c)$ values evaluated with MP2/BSS-B'a, where each HB in a nucleobase pair is numbered in the order of decreasing $\rho_b(\boldsymbol{r}_c)$ values. $H_b(\boldsymbol{r}_c)$ is plotted versus $H_b(\boldsymbol{r}_c) - V_b(\boldsymbol{r}_c)/2$ for the data shown in Table 6-2, together with those data from the perturbed structures generated with CIV. Figure 6-4 illustrates the plots. Figure 6-4a shows the whole picture of the plots, and Figure 6-4b presents the magnified plots that appeared in the *p*-CS region of $H_b(\boldsymbol{r}_c) - V_b(\boldsymbol{r}_c)/2 > 0$ and $H_b(\boldsymbol{r}_c) > 0$. The data (points) in Figure 6-4 are divided into three groups: (a) NH-∗-N appeared in the *r*-CS region, (b) NH-∗-O appeared in the *r*-CS region, and (c) very weak O-∗-O and CH-∗-X (X = O, N and HN) interactions appeared in the *p*-CS region, where the weaker NH-∗-O interaction in G-G (**30**) is also contained. The three groups are called G(**A**), G(**B**), and G(**C**), respectively, here. Relative to those from G(**B**), data from G(**A**) appear more on the left and lower sides overall. The results would show that interactions in G(**A**) are stronger than those corresponding to G(**B**) as a whole. As shown later, interactions in G(**C**) are predicted to have the vdW nature. The QTAIM-DFA parameters of (R, θ) and (θ_p, κ_p) are calculated for each HB in Nu-Nu' by analyzing each plot shown in Figure 6-4. Table 6-2 collects the (R, θ) and (θ_p, κ_p) values evaluated with MP2/BSS-B'a, together with the C_{ii} values.

Nature of each HB in Nu-Nu' elucidated by the QTAIM-DFA with CIV are discussed in the following.

Table 6-2. QTAIM functions and QTAIM-DFA parameters for each hydrogen bond in nucleobase pairs evaluated with MP2/BSS-B'a.[a]

AH-*-B in Nu-Nu'[b] (symmetry: No[c])	$\rho_b(\boldsymbol{r}_c)$ (ea_o^{-3})	$c\nabla^2\rho_b(\boldsymbol{r}_c)$[d] (au)	$H_b(\boldsymbol{r}_c)$ (au)	R[e] (au)	θ[f] (°)	C_{il}[g] (Å mdyn^{-1})	θ_p[h] (°)	κ_p[i] (au^{-1})	Predicted Nature
N-*-HN in A-T (C_1: 1)	0.0498	0.0094	–0.0143	0.0171	146.7	3.12	182.4	8.5	*r*-CS/CT-TBP
NH-*-O in A-T (C_1: 2)	0.0291	0.0114	–0.0012	0.0115	95.9	5.78	145.4	115.3	*r*-CS/*t*-HB$_{wc}$
CH-*-O in A-T (C_1: 3)	0.0059	0.0025	0.0007	0.0026	74.5	16.31	80.6	64.9	*p*-CS/vdW
N-*-HN in A-T (C_s: 4)	0.0498	0.0094	–0.0143	0.0171	146.7	3.12	182.4	8.5	*r*-CS/CT-TBP
NH-*-O in A-T (C_s: 5)	0.0291	0.0114	–0.0012	0.0115	95.9	5.78	145.4	115.2	*r*-CS/*t*-HB$_{wc}$
CH-*-O in A-T (C_s: 6)	0.0059	0.0025	0.0007	0.0026	74.5	16.30	80.6	64.9	*p*-CS/vdW
NH-*-O in C-G (C_1: 7)	0.0449	0.0134	–0.0096	0.0165	125.5	3.20	169.9	11.4	*r*-CS/CT-MC
N-*-HN in C-G (C_1: 8)	0.0377	0.0099	–0.0062	0.0117	122.2	2.15	175.0	30.8	*r*-CS/CT-MC
O-*-HN in C-G (C_1: 9)	0.0305	0.0118	–0.0017	0.0119	98.2	4.08	148.3	101.3	*r*-CS/*t*-HB$_{wc}$
NH-*-N in A-A (C_1: 10)	0.0289	0.0093	–0.0018	0.0095	100.9	5.74	158.6	99.6	*r*-CS/CT-MC
N-*-HC in A-A (C_1: 11)	0.0119	0.0045	0.0013	0.0047	74.1	17.10	75.6	55.8	*p*-CS/vdW
N-*-HN in A-C (C_1: 12)	0.0391	0.0101	–0.0071	0.0123	125.1	3.70	174.1	23.3	*r*-CS/CT-MC
NH-*-O in A-C (C_1: 13)	0.0364	0.0135	–0.0042	0.0141	107.5	3.72	158.2	40.2	*r*-CS/CT-MC
N-*-HN in A-G (C_1: 14)	0.0424	0.0098	–0.0091	0.0133	132.8	3.52	178.6	22.5	*r*-CS/CT-MC
NH-*-O in A-G (C_1: 15)	0.0361	0.0125	–0.0044	0.0133	109.5	4.45	161.0	45.0	*r*-CS/CT-MC
CH-*-HN in A-G (C_1: 16)	0.0056	0.0026	0.0009	0.0027	71.1	29.31	78.8	111.5	*p*-CS/vdW
N-*-HN in A-U (C_1: 17)	0.0500	0.0093	–0.0145	0.0172	147.2	3.10	182.6	8.2	*r*-CS/CT-TBP
NH-*-O in A-U (C_1: 18)	0.0289	0.0114	–0.0011	0.0115	95.5	5.79	141.5	117.4	*r*-CS/*t*-HB$_{wc}$
CH-*-O in A-U (C_1: 19)	0.0060	0.0025	0.0007	0.0026	74.5	16.06	80.3	77.2	*p*-CS/vdW
N-*-HN in C-C (C_1: 20)	0.0488	0.0099	–0.0134	0.0167	143.5	2.63	180.6	2.3	*r*-CS/CT-TBP
NH-*-O in C-C (C_1: 21)	0.0421	0.0131	–0.0079	0.0153	121.0	3.86	168.1	17.8	*r*-CS/CT-MC
O-*-HC in C-C (C_1: 22)	0.0050	0.0021	0.0006	0.0022	73.0	14.60	82.4	61.9	*p*-CS/vdW
N-*-HN in C-T (C_1: 23)	0.0406	0.0096	–0.0083	0.0127	130.7	4.77	178.1	24.7	*r*-CS/CT-MC
NH-*-O in C-T (C_1: 24)	0.0348	0.0125	–0.0037	0.0130	106.5	4.81	158.6	55.6	*r*-CS/CT-MC
O-*-O in C-T (C_1: 25)	0.0026	0.0013	0.0006	0.0014	67.2	32.13	86.3	344.8	*p*-CS/vdW
N-*-HN in C-U (C_1: 26)	0.0410	0.0096	–0.0085	0.0129	131.6	4.73	178.5	23.5	*r*-CS/CT-MC
NH-*-O in C-U (C_1: 27)	0.0347	0.0125	–0.0036	0.0130	106.2	4.79	158.4	55.9	*r*-CS/CT-MC
O-*-O in C-U (C_1: 28)	0.0028	0.0014	0.0006	0.0015	67.9	30.90	87.4	325.6	*p*-CS/vdW
NH-*-O G-G (C_i: 29)	0.0500	0.0136	–0.0124	0.0184	132.4	2.86	172.4	7.6	*r*-CS/CT-MC
O-*-HN G-G (C_i: 30)	0.0083	0.0044	0.0015	0.0046	71.6	12.98	73.0	10.5	*p*-CS/vdW
N-*-HN in G-T (C_1: 31)	0.0416	0.0100	–0.0087	0.0133	130.8	3.90	177.1	19.7	*r*-CS/CT-MC
NH-*-O in G-T (C_1: 32)	0.0335	0.0123	–0.0030	0.0127	103.7	4.92	155.6	68.9	*r*-CS/CT-MC
NH-*-O in G-U (C_1: 33)	0.0419	0.0138	–0.0072	0.0155	117.5	3.09	165.7	21.7	*r*-CS/CT-MC
O-*-HN in G-U (C_1: 34)	0.0404	0.0127	–0.0070	0.0145	118.8	4.32	167.5	22.2	*r*-CS/CT-MC
NH-*-O in T-T (C_1: 35)	0.0375	0.0129	–0.0051	0.0139	111.4	4.29	163.5	34.1	*r*-CS/CT-MC
O-*-HN in T-T (C_1: 36)	0.0375	0.0129	–0.0051	0.0139	111.4	4.29	163.5	34.1	*r*-CS/CT-MC
NH-*-O in T-T (C_i: 37)	0.0375	0.0129	–0.0051	0.0139	111.4	4.29	163.5	34.1	*r*-CS/CT-MC
NH-*-O in T-U (C_1: 38)	0.0381	0.0130	–0.0054	0.0141	112.6	4.17	164.2	30.9	*r*-CS/CT-MC
O-*-HN in T-U (C_1: 39)	0.0366	0.0128	–0.0046	0.0136	109.8	4.42	162.5	38.2	*r*-CS/CT-MC
NH-*-O in U-U (C_1: 40)	0.0373	0.0129	–0.0050	0.0138	111.1	4.29	163.3	34.5	*r*-CS/CT-MC
O-*-HN in U-U (C_1: 41)	0.0373	0.0129	–0.0050	0.0138	111.1	4.29	163.3	34.5	*r*-CS/CT-MC
NH-*-O in U-U (C_s: 42)	0.0373	0.0129	–0.0050	0.0138	111.1	4.29	163.3	34.5	*r*-CS/CT-MC
O-*-HN in U-U (C_s: 43)	0.0373	0.0129	–0.0050	0.0138	111.1	4.29	163.3	33.6	*r*-CS/CT-MC

[a] See Table 6-1 for BSS-B'a. [b] Data are given at the BCPs. [c] Numbers given for the interactions are the same as those in Figures 6-2 and 6-4. [d] $c\nabla^2\rho_b(\boldsymbol{r}_c) = H_b(\boldsymbol{r}_c) - V_b(\boldsymbol{r}_c)/2$, where $c = \hbar^2/8m$. [e] $R = (x^2 + y^2)^{1/2}$, where $(x, y) = (H_b(\boldsymbol{r}_c) - V_b(\boldsymbol{r}_c)/2, H_b(\boldsymbol{r}_c))$. [f] $\theta = 90° - \tan^{-1}(y/x)$. [g] Compliance force constants. [h] $\theta_p = 90° - \tan^{-1}(dy/dx)$. [i] $\kappa_p = |d^2y/dx^2|/[1 + (dy/dx)^2]^{3/2}$.

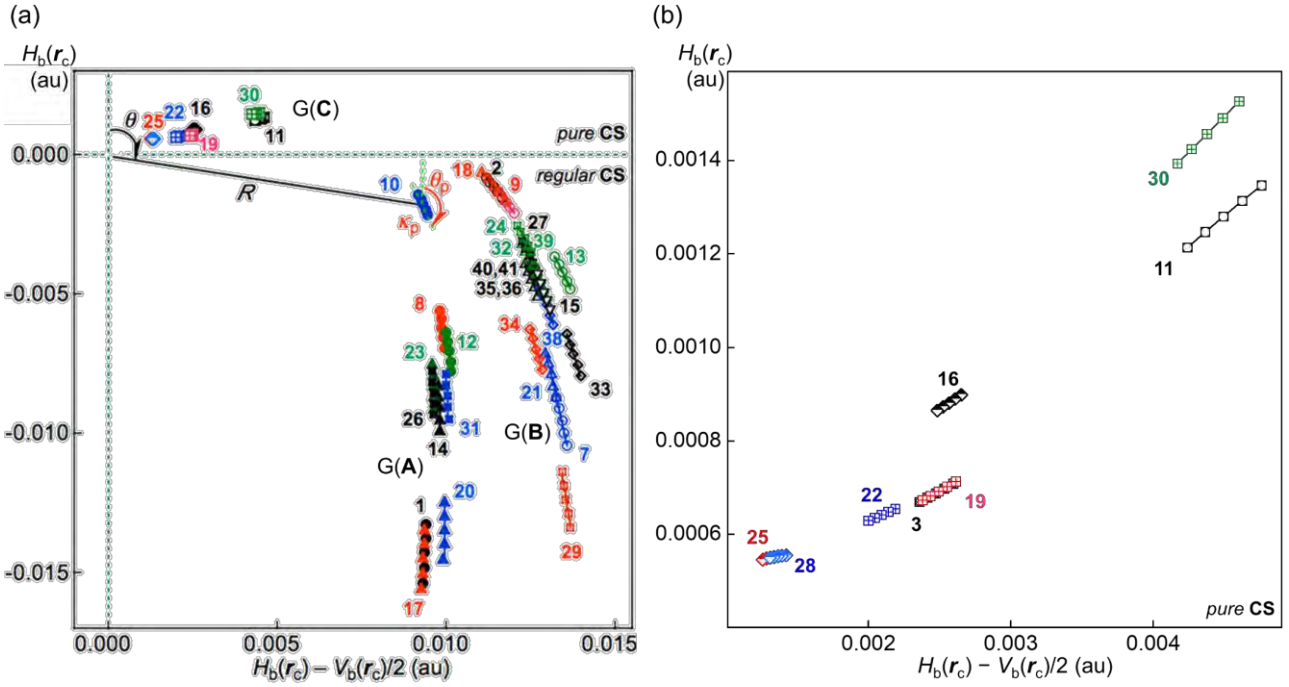

Figure 6-4. Plots of $H_b(\boldsymbol{r}_c)$ versus $H_b(\boldsymbol{r}_c) - V_b(\boldsymbol{r}_c)/2$ for each HB in Nu-Nu', evaluated with MP2/BSS-B'a. For the whole picture (a) and the magnified image for the *pure* CS region (b). The numbers for the interactions are the same as those in Figure 6-2 and Table 6-2, respectively. Two streams appear in the plots of (a) by NH-∗-N G(**A**) and NH-∗-O G(**B**), which are shown by the solid and hollow marks, respectively, together with weak interactions G(**C**) in *p*-CS region. The definitions of (R, θ) and (θ_p, κ_p) are also illustrated.

Nature of Each HB in Multi-HBs of Nu-Nu'

The (θ, θ_p) values are (67.2–74.5º, 73.0–87.4º) for O-∗-O in C-U (28) and C-T (25); CH-∗-O in C-C (22), A-T (3, 6), and A-U (19); CH-∗-HN in A-G (16); CH-∗-N in A-A (11); and the weaker O-∗-HN in G-G (30). Therefore, the interactions are classified as *p*-CS interactions ($45^\circ < \theta < 90^\circ$) and characterized as having the vdW nature ($45^\circ < \theta_p < 90^\circ$), which is denoted by *p*-CS/vdW. The ∠NHO angle for the weaker NH-∗-O interaction in G-G (30) is 135.0º (<< 180º); therefore, it is much weaker than expected. The NH-∗-O interactions in A-T (2, 5) and A-U (18) along with the weaker O-∗-HN in C-G (9) are predicted to be *r*-CS/*t*-HB_{wc} since the (θ, θ_p) values are (95.5–98.2º, 141.5–148.3º) ($90^\circ < \theta, \theta_p < 150^\circ$), although the weaker NH-∗-O in C-G (9) seems fairly close to the borderline area with *r*-CS/CT-MC, of which (θ, θ_p) = (98.2º, 148.3º). The NH-∗-O interactions in A-C (13), A-G (15), C-C (21), C-T (24), C-U (27), G-G (29), G-T (32), G-U (33, 34), T-T (35, 36, 37), T-U (38, 39), and U-U (40, 41, 42, 43), together with the stronger NH-∗-O in C-G (7), are predicted to have the *r*-CS/CT-MC nature since the (θ, θ_p) values are (103.7–132.4º, 155.6–172.4º) ($150^\circ < \theta_p < 180^\circ$). On the other hand, the (θ, θ_p) values for N-∗-HN in A-T (1, 4), A-U (17) and C-C (20) are (143.5–147.2º, 180.6–182.6º); therefore, the interactions are predicted to have the *r*-CS/CT-TBP nature ($\theta_p > 180^\circ$), while the NH-∗-N interactions in A-A (10), A-C (12), A-G (14), C-T (23), C-U (26), and G-T (31)

along with the weaker NH-∗-N in C-G (8) are predicted to be the *r*-CS/CT-MC nature since (θ, θ_p) = (100.9–132.8º, 158.6–178.6º) (150º < θ_p < 180º). The NH-∗-N interactions in A-G (14), C-T (23), and C-U (26) seem fairly close to the borderline area with *r*-CS/CT-TBP (θ_p = 180º) since the θ_p values are 178.6º, 178.1º, and 178.5º, respectively, which are fairly close to 180º. The results are summarized in Table 6-2. The nature of each HB in the multi-HBs between Nu-Nu', calculated with MP2/BSS-B'a, together with the number, is illustrated in Figure 6-A3 of the Appendix.

The total orders for NH-∗-N and NH-∗-O, based on θ and θ_p, are shown in Equations (6-1) and (6-2), respectively. The NH···N interactions are again demonstrated to be stronger than the NH···O interactions, overall. The orders shown in Equations (6-1) and (6-2) are similar with each other, although the similarity is not necessarily. These results would arise from the specific nature of each HB in multi-HBs of Nu-Nu'. The applicability of QTAIM-DFA, which employs the perturbed structures generated with CIV, is also demonstrated to elucidate the nature of each HB of the multi-HB system in Nu-Nu'. However, there are some differences as shown in the orders by italic. The differences seem large for NH-∗-O (G-G: 29), NH-∗-N (C-G: 8), NH-∗-O (A-C: 13), and NH-∗-N (A-A: 10), among them, as shown by italic.

For both NH-∗-N and NH-∗-O, based on θ:

NH-∗-N (A-U: 17) ≥ NH-∗-N (A-T: 1) > NH-∗-N (C-C: 20) > NH-∗-N (A-G: 14) ≥ *NH-∗-O (G-G: 29)* ≥ *NH-∗-N (C-U: 26)* ≥ NH-∗-N (G-T: 31) ≥ *NH-∗-N (C-T: 23)* > *NH-∗-O (C-G: 7)* ≥ *NH-∗-N (A-C: 12)* > *NH-∗-N (C-G: 8)* > NH-∗-O (C-C: 21) > NH-∗-O (G-U: 34) > NH-∗-O (G-U: 33) > NH-∗-O (T-U: 38) > NH-∗-O (T-T: 35, 36) ≥ NH-∗-O (U-U: 40, 41) > NH-∗-O (T-U: 39) ≥ NH-∗-O (A-G: 15) > *NH-∗-O (A-C: 13)* > NH-∗-O (C-T: 24) ≥ NH-∗-O (C-U: 27) > *NH-∗-O (G-T: 32)* > *NH-∗-N (A-A: 10)* > NH-∗-O (C-G: 9) > NH-∗-O (A-T: 2) ≥ NH-∗-O (A-U: 18) >> NH-∗-O (G-G: 30) (6-1)

For both NH-∗-N and NH-∗-O, based on θ_p:

NH-∗-N (A-U: 17) ≥ NH-∗-N (A-T: 1) > NH-∗-N (C-C: 20) > NH-∗-N (A-G: 14) ≥ *NH-∗-N (C-U: 26)* ≥ *NH-∗-N (C-T: 23)* > NH-∗-N (G-T: 31) > *NH-∗-N (C-G: 8)* > *NH-∗-N (A-C: 12)* > *NH-∗-O (G-G: 29)* > *NH-∗-O (C-G: 7)* > NH-∗-O (C-C: 21) > NH-∗-O (G-U: 34) > NH-∗-O (G-U: 33) > NH-∗-O (T-U: 38) > NH-∗-O (T-T: 35, 36) > NH-∗-O (U-U: 40, 41) > NH-∗-O (T-U: 39) > NH-∗-O (A-G: 15) > *NH-∗-N (A-A: 10)* > NH-∗-O (C-T: 24) ≥ NH-∗-O (C-U: 27) ≥ *NH-∗-O (A-C: 13)* > NH-∗-O (G-T: 32) > NH-∗-O (C-G: 9) > NH-∗-O (A-T: 2) > NH-∗-O (A-U: 18) >> NH-∗-O (G-G: 30) (6-2)

After elucidation of the nature of each HB in Nu-Nu', the next extension is to consider the behavior of the HBs.

Relations between R, θ, θ_p, and $\rho_b(r_c)$ for Each HB in Nu-Nu'

Relations between the QTAIM-DFA parameters of (R, θ, θ_p) and QTAIM functions, such as $\rho_b(\boldsymbol{r}_c)$, are examined, first. Good correlations are detected for the relations. The R values are plotted versus $\rho_b(\boldsymbol{r}_c)$ for each HB in Nu-Nu', as shown in Figure 6-A4 in the Appendix. The plot can be analyzed as three correlations of G(**A**), G(**B**), and G(**C**), which are closely related to the plot shown in Figure 6-4. The data point for the weaker NH-∗-O in G-G (**30**) is just on the correlation line for G(**B**); therefore, it is added to G(**B**) in the analysis. The correlations are shown in Table 6-3 (entries 1–3). The results seem to promise similar relations between the parameters.

Figure 6-5 shows the plot of θ versus $\rho_b(\boldsymbol{r}_c)$. The plot is analyzed as three correlations for G(**A**) of NH-∗-N, G(**B**) of NH-∗-O, and G(**C**) of vdW interactions. The correlations are shown in Table 6-3 (entries 4 and 5), except for the very poor correlation for G(**C**), which is given in the figure. The plot of θ versus R is illustrated in Figure 6-A5 of the Appendix. The plot is also analyzed as two correlations, similar to the case of the plot in Figure 6-5. The correlations are given in the figure.

Good linear correlations are not found in the plots of θ_p versus $\rho_b(\boldsymbol{r}_c)$ and θ_p versus R. The plot of θ_p versus θ also does not give a good linear correlation. Instead, the relation between θ_p and θ is analyzed using a cubic function as a regression curve. The correlation was much improved when analyzed as two correlations, which are shown in Figure 6-A6 of the Appendix. The correlations are given in the figure.

Table 6-3. Correlations between $\rho_b(\boldsymbol{r}_c)$, R, θ, ΔE, $(1/C_{ij})_{\text{Nu-Nu'}}$, $R_{\text{Nu-Nu'}}$, and $\theta_{\text{Nu-Nu'}}$, where $(1/C_{ij})_{\text{Nu-Nu'}}$, $R_{\text{Nu-Nu'}}$ and $\theta_{\text{Nu-Nu'}}$ are defined in Equations (6-4) and (6-6).[a]

Entry	Correlation	a	b	c	Correlation with n
1	R vs. $\rho_b(\boldsymbol{r}_c)$	0.388	–0.003	0.963	Fig. 6-A4 (G(**A**): 10)
2	R vs. $\rho_b(\boldsymbol{r}_c)$	0.320	0.002	0.993	Fig. 6-A4(G(**B**): 20[b])
3	R vs. $\rho_b(\boldsymbol{r}_c)$	0.355	0.001	0.992	Fig. 6-A4 (G(**C**): 7[c])
4	θ vs. $\rho_b(\boldsymbol{r}_c)$	2110.5	42.5	0.985	Fig. 6-5 (G(**A**): 10)
5	θ vs. $\rho_b(\boldsymbol{r}_c)$	1811.6	43.4	0.989	Fig. 6-5 (G(**B**): 19)
6	ΔE vs. $(1/C_{ii})_{\text{Nu-Nu'}}$	–121.1	–7.52	0.954	Fig. 6-6 (15)
7	ΔE vs. $(1/C_{ii})_{\text{Nu-Nu'}}$	–136.6	–0.02	0.956	Fig. 6-6 (14[d])
8	$(w'/w)_{\text{POM}}$ vs. $(w'/w)_{\text{CIV}}$	1.021	–0.001	0.9997	Fig. 6-7 (15)
9	$(w'/w)_{\text{POM}}$ vs. $(w'/w)_{\text{CIV}}$	1.046	–0.004	0.997	Fig. 6-A10 (15)

[a] Evaluated with MP2/BSS-B'a. [b] Data from weaker NH-∗-O of G-G (30) being added to G(**B**). [c] Omitting the data from weaker NH-∗-O of G-G (30). [d] Omitting the data from C-G.

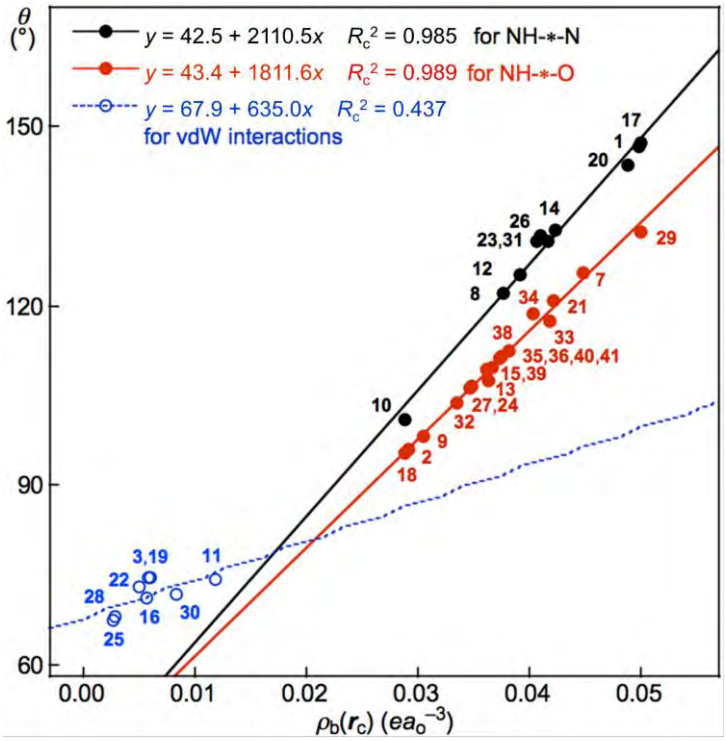

Figure 6-5. Plots of θ versus $\rho_b(\boldsymbol{r}_c)$ for each HB in Nu-Nu', calculated with MP2/BSS-B'a. While data for G(**A**) of NH-∗-N are shown by black solid circles, those for G(**B**) of NH-∗-O are by red solid circles, together with those for G(**C**) of CH-∗-X (X = O, N, and HN) and O-∗-O by blue hole circles. The numbers for the interactions are the same as those in Table 6-2 and Figure 6-4.

Relations between ΔE and C_{ii} for Nu-Nu'

A good inverse correlation between ΔE and C_{ii} ($\Delta E \bullet C_{ii}$ = constant) for the neutral mono-HB species was reported, previously.[17] Therefore, Equation (6-3) is expected to hold between ΔE and $1/C_{ii}$ in the multi-HB system of Nu-Nu', where $1/C_{ii}$ should be the total values for Nu-Nu', together with ΔE. How can the total values of $1/C_{ii}$ for the multi-HBs of Nu-Nu' be calculated from the value of each HB in Nu-Nu'? Equation (6-4) is applied for the purpose, where $(1/C_{ii})_{\text{Nu-Nu'}}$ is the total value of $1/C_{ii}$ for a nucleobase pair and $(1/C_{ii})_{\text{Nu-Nu':}k}$ is the $1/C_{ii}$ value for the k-th HB in the nucleobase pair. The $(1/C_{ii})_{\text{Nu-Nu':}k}$ values of the vdW interactions are also contained in the summation.

$$\Delta E = a(1/C_{ii}) + b \tag{6-3}$$

$$(1/C_{ii})_{\text{Nu-Nu'}} = \Sigma_k (1/C_{ii})_{\text{Nu-Nu':}k} \tag{6-4}$$

The ΔE values are plotted versus $(1/C_{ii})_{\text{Nu-Nu'}}$ for Nu-Nu' in Figure 6-6. A (very) good correlation was obtained for the plot, which is shown in Table 6-3 (entry 6). In this case, a y-intercept value (b in Equation (6-3)) very close to zero is obtained (b = 0.02 kJ mol^{-1}) if data from C-G are omitted from the correlation, although the correlation seems not very improved. The correlation is shown in Table 6-3 (entry 7). The inverse proportion also holds for the multi-HB system of Nu-Nu' in this case. The constant value (in $\Delta E \bullet C_{ii}$ = constant), as the averaged value of $\Delta E \bullet C_{ij}$ for Nu-Nu', is evaluated to be

–137.04 without C-G. The constant value for Nu-Nu' (–137.04) is close to but somewhat smaller than that reported for the neutral mono-HB species (–165.64) in magnitude.[17] The constant value for all Nu-Nu' is evaluated to be –135.96, which is very close to that without the data from C-G. The results show that the compliance constants (C_{ii}) are closely related to ΔE for the formation of not only the neutral mono-HB species but also the multi-HB system of Nu-Nu'. A similar mechanism would be operative in both processes of ΔE and C_{ii} in the multi-HB systems of Nu-Nu'. Equation (6-4) reminds that the total value of resistance of a parallel connection should be calculated for each one according to Ohm's law for the electric resistance of resistors connected in parallel.[41]

The total contributions of ΔE and C_{ii} should be calculated as the summations of the contributions from each HB. As a result, it is expected that the ΔE value for a nucleobase pair can be fractionalized to each HB in the multi-HB system of the Nu-Nu'. Based on the good relation with Equations (6-3) and (6-4) shown in Figure 6-6 (see entry 6 or 7 in Table 6-3), the ΔE value for a nucleobase pair is expected to be fractionalized to each HB (ΔE_e) by the ratio of $1/C_{ii}$ of each HB, according to Equation (6-5), where $\Delta E_{e:1}$ and $(1/C_{ii})_{Nu\text{-}Nu':1}$ stand for the fractionalized energy to the first HB and for the $1/C_{ii}$ values of the first HB in the Nu-Nu', respectively. The results are collected in Table 6-4.

$$\Delta E_{e:1}:\Delta E_{e:2}:\ \ldots = (1/C_{ii})_{Nu\text{-}Nu':1}:(1/C_{ii})_{Nu\text{-}Nu':2}:\ \ldots \qquad (6\text{-}5)$$

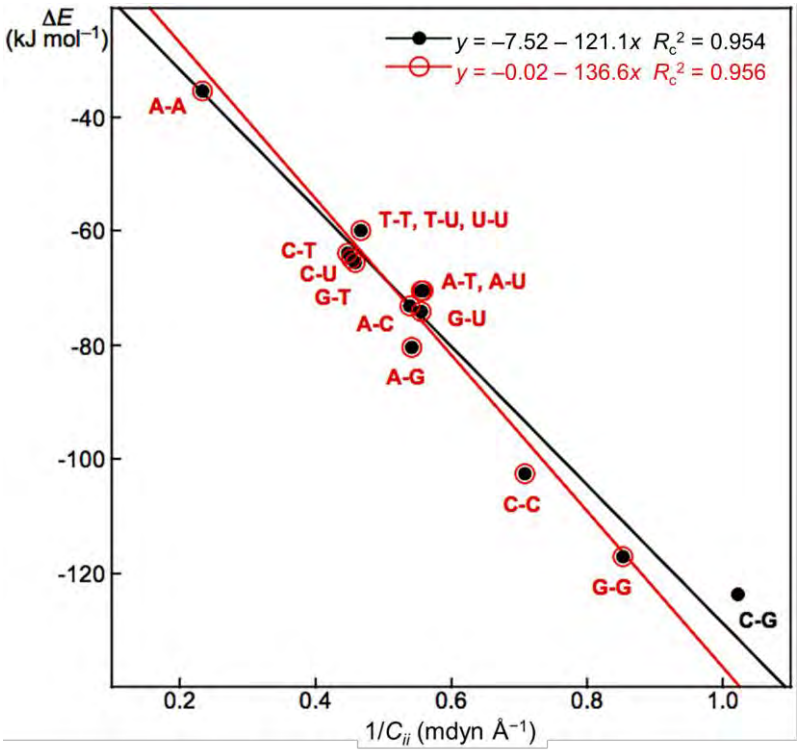

Figure 6-6. Plots of ΔE versus $(1/C_{ii})_{Nu\text{-}Nu'}$ in Nu-Nu', calculated with MP2/BSS-B'a.

Table 6-4. Fractionalization of the total values of ΔE for Nu-Nu' to each HB (ΔE_e), calculated with MP2/BSS-B'a.[a]

Nu-Nu' (symm)	ΔE	ΔE_e (No[b])	ΔE_e (No[b])	ΔE_e (No[b])
A-T (C_1)	–70.3	–40.6 (1)	–21.9 (2)	–7.8 (3)
C-G (C_1)	–123.5	–37.7 (7)	–56.2 (8)	–29.6 (9)
A-A (C_1)	–35.4	–26.5 (10)	–8.9 (11)	
A-C (C_1)	–73.1	–36.6 (12)	–36.5 (13)	
A-G (C_1)	–80.5	–42.1 (14)	–33.3 (15)	–5.1 (16)
A-U (C_1)	–70.6	–40.8 (17)	–21.9 (18)	–7.9 (19)
C-C (C_1)	–102.6	–55.1 (20)	–37.6 (21)	–9.9 (22)
C-T (C_1)	–64.0	–29.9 (23)	–29.7 (24)	–4.4 (25)
C-U (C_1)	–64.9	–30.3 (26)	–29.9 (27)	–4.6 (28)
G-G (C_1)	–117.1	–48.0 (29)	–10.6 (30)	
G-T (C_1)	–65.4	–36.5 (31)	–28.9 (32)	
G-U (C_1)	–74.2	–43.3 (33)	–30.9 (34)	
T-T (C_1)	–60.0	–30.0 (35)	–30.0 (36)	
T-U (C_1)	–59.9	–30.8 (38)	–29.1 (39)	
U-U (C_1)	–59.8	–29.9 (40)	–29.9 (41)	

[a] The values are given in kJ mol^{-1}. [b] The number for each HB, containing the vdW interaction, is the same as that given in Table 6-2.

Relations among the Total Values of R, θ, θ_p, and ΔE for Nu-Nu'

What are the relations among the total values of R, θ, θ_p, and ΔE for Nu-Nu'? The total values of $P_{Nu\text{-}Nu'}$ (= $R_{Nu\text{-}Nu'}$, $\theta_{Nu\text{-}Nu'}$, and $\theta_{p:Nu\text{-}Nu'}$) of Nu-Nu' are necessary for the analysis. The total values are calculated according to Equation (6-6), where $P_{Nu\text{-}Nu':k}$ is the $P_{Nu\text{-}Nu'}$ value for each HB in Nu-Nu'. The $P_{Nu\text{-}Nu':k}$ values from the vdW interactions are also contained in Equation (6-6).

$$P_{Nu\text{-}Nu'} = \Sigma_k P_{Nu\text{-}Nu':k} \tag{6-6}$$

The ΔE values are plotted versus $R_{Nu\text{-}Nu'}$, $\theta_{Nu\text{-}Nu'}$, and $\theta_{p:Nu\text{-}Nu'}$, and the plots are shown in Figures 6-A7–6-A9 of the Appendix. The correlation is greatly improved by analyzing the plot as two or three correlations instead of one correlation. The correlations are shown in the figure. The correlation for ΔE versus $\theta_{p:Nu\text{-}Nu'}$ seems poorer than that for ΔE versus $\theta_{Nu\text{-}Nu'}$.

It is also instructive to clarify the structural feature in the perturbed structures of Nu-Nu' to discuss the behavior of each HB of Nu-Nu' in more detail, which is examined in the following.

Structural Feature in the Perturbed Structures of Nu-Nu'

How can the perturbed structures of Nu-Nu′ generated with CIV and POM be simply and effectively visualized? Equations (6-7)–(6-9) are applied to a tri-HB system for the purpose. Subscribes 1, 2, and 3 in Equations (6-7)–(6-9) correspond to the first, second, and third HBs in tri-HBs of Nu-Nu′, while k (= 1, 2, and 3) designates the role of each HB in the calculations. In Equation (6-7), r_{k1} will be r_{11} when k = 1, which means that the first HB in Nu-Nu′ is selected as the major HB and therefore is fixed in POM. In this case, relative to r_{11}, r_{12} for the second HB in Equation (6-8), and r_{13} for the third HB in Equation (6-9) (k = 1) are the minor HBs, which are (partially) optimized in POM. Similarly, Equation (6-8) defines r_{22} with k = 2, and Equation (6-9) does r_{33} with k = 3, where the second and third HBs are selected as the major interactions, respectively, for Nu-Nu'. Compared to r_{22}, the r_{21} and r_{23} values are the minor HBs, while compared to r_{33}, r_{31}, and r_{32} are the minor HBs. The w_{k1}, w_{k2}, and w_{k3} values are calculated according to Equations (6-7)–(6-9), where w_{11}, w_{22}, and w_{33} are the fixed values. Equations (6-7) and (6-8) with k = 1 and 2 are applied to the di-HB system of Nu-Nu′.

$$r_{k1} = r_{k1\mathrm{o}} + w_{k1}a_{\mathrm{o}} \quad (6\text{-}7)$$
$$r_{k2} = r_{k2\mathrm{o}} + w_{k2}a_{\mathrm{o}} \quad (6\text{-}8)$$
$$r_{k3} = r_{k3\mathrm{o}} + w_{k3}a_{\mathrm{o}} \quad (6\text{-}9)$$

(k = 1, 2, and 3)

The structural feature in the perturbed structures of Nu-Nu' is examined by dividing them into four groups, G(**AT**), G(**CG**), G(**AA**), and G(**TT**).[42] Nu-Nu' of A-T, C-G, A-A, and T-T are the typical members of the groups, respectively. The feature is discussed by employing A-T, C-G, A-A, and T-T, together with U-U. The feature in U-U will supply a small structural difference from that in T-T, although U-U belongs to G(**TT**).

The values of $(w'_{ij}/w_{ii})_{\mathrm{CIV}}$ and $(w'_{ij}/w_{ii})_{\mathrm{POM}}$ (i, j = 1, 2, and/or 3) are calculated for each HB in A-T, C-G, A-A, T-T, and U-U with MP2/BSS-B'a at w_{ii} = 0.05 by applying in Equations (6-7)–(6-9).[23–25,38] The values are collected in Table 6-A6 of the Appendix. Small differences in (w'_{ij}/w_{ii}) between T-T and U-U are detected. A positive value of w'_{ij}/w_{ii} implies that the minor (HB) interaction in Nu-Nu′ moves in the same direction as the major interaction. On the other hand, relative to the major interaction, the minor HB interaction moves in the inverse direction for negative w'_{ij}/w_{ii} values. Compared to that of the major interaction, the magnitudes in the movement of the minor HB interactions would be negligible when the w'_{ij}/w_{ii} values are close to zero. Figure 6-7 shows the plot of $(w'_{ij}/w_{ii})_{\mathrm{POM}}$ versus $(w'_{ij}/w_{ii})_{\mathrm{CIV}}$ for the HB interactions. The plot gave an excellent correlation, which is shown in Table 6-3 (entry 8). The results show that the perturbed structures generated with CIV and POM are very close to each other, approximately at w_{ii} = 0.05, in the multi-HB system of Nu-Nu′, as well as in the case of the mono-HB system.[17]

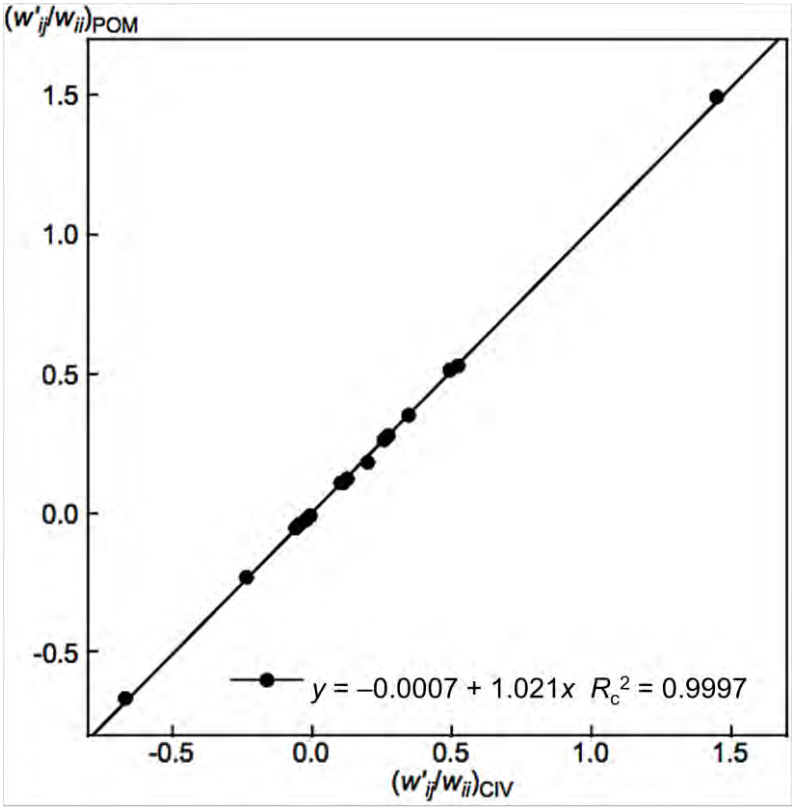

Figure 6-7. Plot of $(w'_{ij}/w_{ii})_{POM}$ versus $(w'_{ij}/w_{ii})_{CIV}$ for each HB of multi-HB system in A-T, C-G, A-A, U-U, and T-T, calculated at $w_{ii} = 0.05$ with MP2/BSS-B'a.

What happens if the H···B distance (r(H, B)) in each HB of Nu-Nu′ is elongated further, where Δr(H, B) (= r(H, B) – r_o(H, B)) is defined as the difference in H···B distance between the perturbed structure and the fully optimized structure. Relative to that of M06-2X/BSS-A, the reliability of M06-2X/BSS-C′ is confirmed for the optimization. That is, the r_o(H, B) values calculated with M06-2X/BSS-C′ differ from the corresponding values calculated with M06-2X/BSS-A by less than 0.01 Å in magnitude. Therefore, these perturbed structures are calculated with POM by fixing the r(H, B) distances in question in the wider range of –0.05 Å ≤ Δr(H, B) ≤ 0.50 Å for all HBs in A-T, C-G, A-A, T-T, and U-U with M06-2X/BSS-C′ for improved calculation cost. The ΔE_{ESps} (= E_{ESps} – E_{ESo}) values are also calculated for each HB in A-T, C-G, A-A, T-T, and U-U based on the partially optimized structures. The E_{ESps} values are the energies of the perturbed structures at r(H, B) on the energy surface, and the E_{ESo} values are those for the fully optimized structures. The magnitudes of the differences between ΔE_{ESps} calculated with M06-2X/BSS-C' and those calculated with M06-2X/BSS-A are less than 0.3 kJ mol^{-1} for A-T, C-G, A-A, T-T, and U-U if the corresponding values are compared at Δr(H, B) = 0.025 Å. The results again support the reliability of M06-2X/BSS-C' relative to M06-2X/BSS-A in the optimizations.

The perturbed structures of A-T, C-G, A-A, T-T, and U-U are also generated by employing CIV with M06-2X/BSS-C' in a wider range of –0.1 ≤ w_{ii} ≤ 1.0 (*cf*: –0.05 Å ≤ Δr ≤ 0.50 Å for POM). The

w_{ij} values of the minor HBs are calculated, corresponding to w_{ij} at w_{ii} = 0.05 for the Nu-Nu'. The results are also summarized in Table 6-A7 of the Appendix in the $(w'_{ij}/w_{ii})_{CIV}$ form. The $(w'_{ij}/w_{ii})_{POM}$ values are plotted versus $(w'_{ij}/w_{ii})_{CIV}$ calculated at w_{ii} = 0.05 with M06-2X/BSS-C′, as shown in Figure 6-A10 of the Appendix. The plot also gives a very good correlation, which is shown in Table 6-3 (entry 9). The quality of the correlation based on M06-2X/BSS-C′ is noticeably the same as that of the correlation based on MP2/BSS-B′a.

The ΔE_{ESps} values are plotted versus a wide range of –0.05 Å ≤ Δr(H, B) ≤ 0.50 Å and –0.1 ≤ w_{ii} ≤ 1.0 for each HB in A-T, C-G, A-A, T-T, and U-U evaluated with POM and CIV, respectively. The plot is illustrated in Figure 6-8, where r(H, B) in the x axis with POM is replaced by w_{ii}. As shown in the figure, the differences in ΔE_{ESps} between the structures evaluated with CIV and those evaluated with POM are negligible at approximately w_{ii} < 0.2. Indeed, the ΔE_{ESps} curves evaluated with CIV show a similar trend as those evaluated with POM for w_{ii} < 0.3, but overall, the curves begin to grow rather exponentially for w_{ii} > 0.4 as w_{ii} increases. The results show that the perturbed structures generated with POM and CIV are very similar for w_{ii} < 0.2 and similar for 0.2 < w_{ii} < 0.3 but become different for 0.4 < w_{ii}.

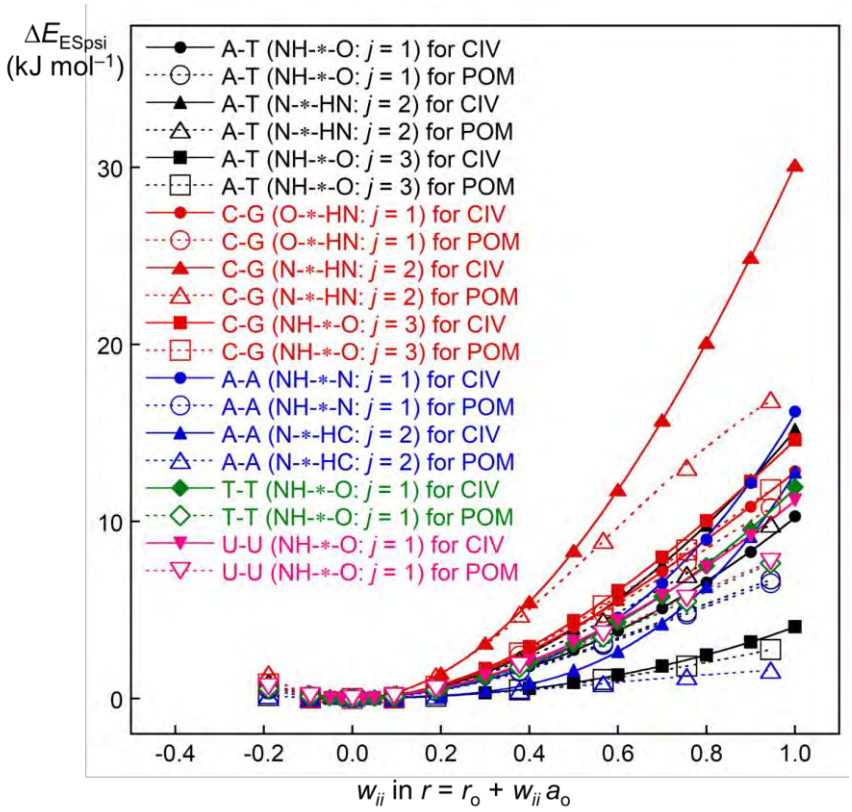

Figure 6-8. Plots of ΔE_{ESpsi} versus w_{ii} in $r = r_o + w_{ii}a_o$ for each HB in A-T, C-G, A-A, T-T, and U-U calculated with CIV and POM of ModRedundant under M06-2X/BSS-C'.

The gradient for ΔE_{ESps} is largest for N–H···N in C-G, which must be the reflection of the largest magnitude of ΔE_{ES} for C-G (–117.2 kJ mol^{-1}) among A-T, C-G, A-A, T-T, and U-U. The gradient for ΔE_{ESps} decreases in the order shown in Equation (6-10). The order seems to not necessarily reflect the strength of each HB in the A-T and C-G pairs.

N–H···N (C-G) >> N–H···O (C-G) ≥ O···H–N (C-G) > N–H···N (A-T) > N–H···O (U-U) > N–H···O (T-T) > N–H···N (A-A) ≈ N–H···O (A-T: j = 1) > C–H···N (A-A) > N–H···O (A-T: j = 3) (6-10)

The gradient increased when POM or CIV is applied to the central N–H···N interaction for both the A-T and C-G pairs. The behavior of ΔE_{ESps} evaluated with POM may correspond to that in the initial stage for the scission of Nu-Nu′ to Nu and Nu′ under the simple mechanism for each HB. Such large ΔE_{ESps} values must be effectively decreased by the enzyme-catalyzed reactions in vivo at approximately room temperature. However, it is helpful to understand the behavior of HBs in Nu-Nu′ through a simple mechanism.

Indeed, the behavior of HBs, containing those of multi-HBs in Nu-Nu', will be revealed in more detail, if the magnitudes in the movement of HBs is directly investigated. The NVT ensemble method seems typical one of such methods.[43] The predicted nature will change depending on the quality of the calculation levels, especially for weak HBs. However, the results in the framework of QTAIM-DFA with CIV should be reasonable, if calculated with MP2/BSS-B′a.

Summary

The intrinsic dynamic and static nature of each HB in the multi-HBs of Nu-Nu' is elucidated with QTAIM-DFA by employing CIV. The initial stage of the opening or closing of the duplex DNA structure and the stability can be understand based on the nature of the interactions through the simple mechanism. The QTAIM-DFA plot consists of three groups of data: G(**A**) of NH-∗-N, G(**B**) of NH-∗-O, and G(**C**) of the very weak interactions of the vdW type. Each NH-∗-N in G(**A**) is predicted to have the nature of *r*-CS/CT-MC to *r*-CS/CT-TBP, and each NH-∗-O in G(**B**) is of the nature of *r*-CS/*t*-HB_{wc} to *r*-CS/CT-MC. The results show that NH-∗-N in G(**A**) is stronger than NH-∗-O in G(**B**) overall. It is demonstrated that the total values of ΔE_{ES} are (directly) proportional to $(1/C_{ii})_{Nu\text{-}Nu'}$, the total values of $1/C_{ii}$ for Nu-Nu', where $(1/C_{ii})_{Nu\text{-}Nu'}$ is calculated by $\Sigma_k(1/C_{ij})_{Nu\text{-}Nu':k}$, similar to Ohm's law for a parallel connection. The results demonstrate that ΔE_{ES} values are closely related to C_{ii} values. As a result, the total value of ΔE_{ES} for Nu-Nu' can be fractionalized to each HB in multi-HB systems, even if the HBs in multi-HB systems, containing the weak vdW interactions, are formed in close proximity in space and interact mutually and strongly with each other. The differences in the perturbed structures generated with POM and CIV are negligible for $w_{ii} < 0.2$ and very small for $0.2 < w_{ii} < 0.3$, but they become larger for $0.4 < w_{ii}$.

Many multi-HB systems play a crucial role in the chemical and biological sciences, not only in vitro but also in vivo. Each HB in such multi-HB systems will interact mutually and strongly with each other due to their close proximity in space. It is of very interest if the proposed method can open the door to elucidate each HB in such multi-HB systems, although some devices seem necessary for the effective analysis.

Appendix

Table 6-A1. The interaction for multi-HB in Nu-Nu′ distances r_o(X, Y), evaluated with various methods.

AH-∗-B in Nu-Nu′ (Symmetry: No)	r_o(X, Y)/Å MP2/BSS-A′ [a]	r_o(X, Y)/Å MP2/BSS-B′a[b]	r_o(X, Y)/Å MP2/BSS-B′b[c]
N-∗-HN in A-T (C_1: 1)	1.7602	1.7527	1.7493
NH-∗-O in A-T (C_1: 2)	1.8932	1.8861	1.8770
CH-∗-O in A-T (C_1: 3)	2.7316	2.7138	2.7129
NH-∗-N in A-T (C_s: 4)	1.7602	1.7527	1.7493
NH-∗-O in A-T (C_s: 5)	1.8932	1.8861	1.8770
CH-∗-O in A-T (C_s: 6)	2.7316	2.7138	2.7130
NH-∗-O in C-G (C_1: 7)	1.7189	1.7104	1.7041
N-∗-HN in C-G (C_1: 8)	1.8706	1.8677	1.8643
O-∗-HN in C-G (C_1: 9)	1.8780	1.8687	1.8614
NH-∗-N in A-A (C_1: 10)	1.9814	1.9722	1.9664
CH-∗-N in A-A (C_1: 11)	2.4555	2.4455	2.4412
N-∗-HN in A-C (C_1: 12)	1.8485	1.8451	1.8406
NH-∗-O in A-C (C_1: 13)	1.7907	1.7823	1.7731
N-∗-HN in A-G (C_1: 14)	1.8302	1.8241	1.8192
NH-∗-O in A-G (C_1: 15)	1.8092	1.8019	1.7959
CH-∗-HN in A-G (C_1: 16)	2.3914	2.3822	2.3798
N-∗-HN in A-U (C_1: 17)	1.7579	1.7508	1.7472
NH-∗-O in A-U (C_1: 18)	1.8952	1.8880	1.8796
CH-∗-O in A-U (C_1: 19)	2.7262	2.7094	2.7076
NH-∗-N in C-C (C_1: 20)	1.7613	1.7559	1.7522
O-∗-HN in C-C (C_1: 21)	1.7432	1.7371	1.7270
CH-∗-O in C-C (C_1: 22)	2.8352	2.8195	2.8203
N-∗-HN in C-T (C_1: 23)	1.8406	1.8292	1.8292
NH-∗-O in C-T (C_1: 24)	1.8204	1.8152	1.8059
O-∗-O in C-T (C_1: 25)	3.5797	3.5675	3.5725
N-∗-HN in C-U (C_1: 26)	1.8364	1.8258	1.8255
NH-∗-O in C-U (C_1: 27)	1.8213	1.8159	1.8072
O-∗-O in C-U (C_1: 28)	3.5543	3.5419	3.5456
NH-∗-O G-G (C_i: 29)	1.6928	1.6888	1.6825
O-∗-HN G-G (C_i: 30)	2.4331	2.4270	2.4259
N-∗-HN in G-T (C_1: 31)	1.8277	1.8194	1.8164
NH-∗-O in G-T (C_1: 32)	1.8359	1.8310	1.8218
NH-∗-O in G-U (C_1: 33)	1.7486	1.7440	1.7353
O-∗-HN in G-U (C_1: 34)	1.7607	1.7544	1.7468
NH-∗-O in T-T (C_1: 35)	1.7857	1.7788	1.7723
O-∗-HN in T-T (C_1: 36)	1.7857	1.7788	1.7724
NH-∗-O in T-T ([g]: 37)	1.7858	1.7788	1.7722
NH-∗-O in T-U (C_1: 38)	1.7783	1.7718	1.7649
O-∗-HN in T-U (C_1: 39)	1.7940	1.7871	1.7809
NH-∗-O in U-U (C_1: 40)	1.7863	1.7798	1.7733
O-∗-HN in U-U (C_1: 41)	1.7863	1.7798	1.7733
NH-∗-O in U-U (C_s: 42)	1.7863	1.7798	1.7733
O-∗-HN in U-U (C_s: 43)	1.7863	1.7798	1.7733

[a] BSS-A′: 6-311+G(3df,3pd). [b] BSS-B′a: 6-311+G(3df,3pd) for O, N, H, and 6-311+G(3d) for C. [c] BSS-B′b: 6-311+G(3df,3pd) for O, N, H, and 6-311+G(d) for C. [d] BSS-A: 6-311++G(3df,3pd). [e] BSS-C: 6-311++G(3df,3p). [f]6-311++G(3d,3p). [g] The higher symmetry for T-T calculated with MP2/BSS-A′, MP2/BSS-B′a, MP2/BSS-B′b, M06-2X/BSS-A, M06-2X/BSS-C, and M06-2X/BSS-D are C_s, C_i, C_s, C_{2h}, C_{2h}, C_{2h}, and C_{2h}, respectively.

(Table 6-A1 continued.)

AH-∗-B in Nu-Nu′ (Symmetry: No)	r_o(X, Y)/Å M06-2X/BSS-A[d]	r_o(X, Y)/Å M06-2X/BSS-C[e]	r_o(X, Y)/Å M06-2X/BSS-D[f]
N-∗-HN in A-T (C_1: 1)	1.7775	1.7792	1.7765
NH-∗-O in A-T (C_1: 2)	1.9343	1.9384	1.9372
CH-∗-O in A-T (C_1: 3)	2.7452	2.7443	2.7441
NH-∗-N in A-T (C_s: 4)	1.7741	1.7759	1.7736
NH-∗-O in A-T (C_s: 5)	1.9367	1.9402	1.9382
CH-∗-O in A-T (C_s: 6)	2.7357	2.7359	2.7376
NH-∗-O in C-G (C_1: 7)	1.7490	1.7616	1.7625
N-∗-HN in C-G (C_1: 8)	1.9020	1.9103	1.9073
O-∗-HN in C-G (C_1: 9)	1.9017	1.9066	1.9102
NH-∗-N in A-A (C_1: 10)	2.0308	2.0368	2.0347
CH-∗-N in A-A (C_1: 11)	2.4942	2.4943	2.4956
N-∗-HN in A-C (C_1: 12)	1.9124	1.9199	1.9172
NH-∗-O in A-C (C_1: 13)	1.8261	1.8335	1.8372
N-∗-HN in A-G (C_1: 14)	1.8793	1.8873	1.8769
NH-∗-O in A-G (C_1: 15)	1.8520	1.8604	1.8624
CH-∗-HN in A-G (C_1: 16)	2.3888	2.3893	2.4124
N-∗-HN in A-U (C_1: 17)	1.7699	1.7713	1.7692
NH-∗-O in A-U (C_1: 18)	1.9353	1.9390	1.9370
CH-∗-O in A-U (C_1: 19)	2.7321	2.7315	2.7335
NH-∗-N in C-C (C_1: 20)	1.7953	1.8008	1.7967
O-∗-HN in C-C (C_1: 21)	1.7748	1.7868	1.7894
CH-∗-O in C-C (C_1: 22)	2.8769	2.8763	2.8704
N-∗-HN in C-T (C_1: 23)	1.9205	1.9309	1.9270
NH-∗-O in C-T (C_1: 24)	1.8559	1.8629	1.8631
O-∗-O in C-T (C_1: 25)	3.6389	3.6451	3.6532
N-∗-HN in C-U (C_1: 26)	1.9091	1.9212	1.9172
NH-∗-O in C-U (C_1: 27)	1.8521	1.8593	1.8591
O-∗-O in C-U (C_1: 28)	3.6239	3.6285	3.6382
NH-∗-O G-G (C_i: 29)	1.7240	1.7378	1.7344
O-∗-HN G-G (C_i: 30)	2.4119	2.4150	2.4211
N-∗-HN in G-T (C_1: 31)	1.8884	1.8964	1.9006
NH-∗-O in G-T (C_1: 32)	1.8547	1.8622	1.8665
NH-∗-O in G-U (C_1: 33)	1.7785	1.7882	1.7858
O-∗-HN in G-U (C_1: 34)	1.8098	1.8222	1.8203
NH-∗-O in T-T (C_1: 35)	1.8377	1.8450	1.8423
O-∗-HN in T-T (C_1: 36)	1.8377	1.8450	1.8423
NH-∗-O in T-T ([g]: 37)	1.8409	1.8483	1.8454
NH-∗-O in T-U (C_1: 38)	1.8315	1.8392	1.8368
O-∗-HN in T-U (C_1: 39)	1.8419	1.8488	1.8464
NH-∗-O in U-U (C_1: 40)	1.8524	1.8584	1.8566
O-∗-HN in U-U (C_1: 41)	1.8501	1.8561	1.8541
NH-∗-O in U-U (C_s: 42)	1.8511	1.8567	1.8549
O-∗-HN in U-U (C_s: 43)	1.8460	1.8526	1.8514

[a] BSS-A′: 6-311+G(3df,3pd). [b] BSS-B′a: 6-311+G(3df,3pd) for O, N, H, and 6-311+G(3d) for C. [c] BSS-B′b: 6-311+G(3df,3pd) for O, N, H, and 6-311+G(d) for C. [d] BSS-A: 6-311++G(3df,3pd). [e] BSS-C: 6-311++G(3df,3p). [f]6-311++G(3d,3p). [g] The higher symmetry for T-T calculated with MP2/BSS-A′, MP2/BSS-B′a, MP2/BSS-B′b, M06-2X/BSS-A, M06-2X/BSS-C, and M06-2X/BSS-D are C_s, C_i, C_s, C_{2h}, C_{2h}, C_{2h}, and C_{2h}, respectively.

Table 6-A2. The ΔE_{ES} (kJ mol^{-1}) and ΔE_{ZP} (kJ mol^{-1}) values for Nu-Nu′, evaluated with various methods.

Compds	ΔE_{ES}[a]	ΔE_{ES}[a]	ΔE_{ZP}[a]	ΔE_{ES}[a]	ΔE_{ZP}[a]
(Symm)	MP2/BSS-A′[b]	MP2/BSS-B′a[c]		MP2/BSS-B′b[d]	
A-T (C_1)	–68.4	–70.3	–66.5	–71.3	–67.6
A-T (C_s)	–68.4	–70.3	–66.5	–71.3	–67.6
C-G (C_1)	–121.4	–123.5	–117.2	–125.0	–118.6
A-U (C_1)	–68.7	–70.6	–66.6	–71.4	–67.6
A-A (C_1)	–34.1	–35.4	–32.1	–35.8	–32.8
A-C (C_1)	–71.2	–73.1	–68.4	–74.2	–69.6
A-G (C_1)	–78.8	–80.5	–75.5	–81.2	–76.4
C-C (C_1)	–100.7	–102.6	–96.6	–104.2	–98.4
C-T (C_1)	–62.2	–64.0	–60.2	–64.8	–61.2
C-U (C_1)	–63.1	–64.9	–60.9	–65.5	–61.8
G-G (C_i)	–115.3	–117.1	–112.7	–118.3	–113.7
G-T (C_1)	–63.6	–65.4	–62.6	–66.3	–63.5
G-U (C_1)	–72.8	–74.2	–70.4	–75.4	–71.5
T-T (C_1)	–58.5	–60.0	–56.3	–61.6	–57.7
T-T (*h*)	–58.7	–60.0	–56.3	–61.6	–57.7
T-U (C_1)	–58.5	–59.9	–56.2	–61.2	–57.3
U-U (C_1)	–58.4	–59.8	–55.9	–60.8	–56.9
U-U (C_s)	–58.4	–59.8	–55.9	–60.8	–56.9

[a] The units of ΔE_{ES} and ΔE_{ZP} are given in kJ mol^{-1}. [b] BSS-A': 6-311+G(3df,3pd). [c] BSS-B'a: 6-311+G(3df,3pd) for O, N, H, and 6-311+G(3d) for C. [d] BSS-B′b: 6-311+G(3df,3pd) for O, N, H, and 6-311+G(d) for C. [e] BSS-A: 6-311++G(3df,3pd). [f] BSS-C: 6-311++G(3df,3p). [g]6-311++G(3d,3p). [h] The higher symmetry for T-T calculated with MP2/BSS-A', MP2/BSS-B′a, MP2/BSS-B'b, M06-2X/BSS-A, M06-2X/BSS-C, and M06-2X/BSS-D are C_s, C_i, C_s, C_{2h}, C_{2h}, C_{2h}, and C_{2h}, respectively.

(Table 6-A2 continued.)

Compds	ΔE_{ES}[a]	ΔE_{ZP}[a]	ΔE_{ES}[a]	ΔE_{ZP}[a]	ΔE_{ES}[a]	ΔE_{ZP}[a]
(Symm)	M06-2X/BSS-A[e]		M06-2X/BSS-C[f]		M06-2X/BSS-D[g]	
A-T (C_1)	–58.9	–54.9	–58.7	–53.7	–58.8	–54.5
A-T (C_s)	–59.1	–54.9	–58.9	–53.7	–59.0	–54.5
C-G (C_1)	–113.6	–108.7	–113.3	–108.2	–112.3	–107.7
A-U (C_1)	–59.6	–56.4	–59.4	–56.0	–59.5	–56.5
A-A (C_1)	–26.6	–22.8	–26.5	–22.8	–26.7	–23.4
A-C (C_1)	–60.1	–55.7	–59.9	–55.5	–59.8	–55.5
A-G (C_1)	–68.7	–63.2	–68.5	–63.0	–68.7	–64.1
C-C (C_1)	—91.3	–86.2	–90.9	–85.8	–91.1	–86.1
C-T (C_1)	–52.7	–48.3	–52.5	–47.1	–52.6	–47.7
C-U (C_1)	–54.0	–50.4	–53.8	–50.0	–53.9	–50.5
G-G (C_i)	–109.4	–106.7	–108.8	–106.2	–107.8	–104.9
G-T (C_1)	–54.9	–52.3	–54.7	–51.2	–54.0	–50.7
G-U (C_1)	–65.1	–61.7	–64.9	–61.3	–64.9	–61.4
T-T (C_1)	–50.1	–47.3	–50.0	–45.3	–50.3	–45.8
T-T (*h*)	–50.0	–48.1	–50.0	–46.1	–50.2	–46.6
T-U (C_1)	–50.8	–47.9	–50.7	–46.7	–51.0	–47.0
U-U (C_1)	–49.3	–46.6	–49.3	–46.2	–49.5	–46.4
U-U (C_s)	–49.5	–46.5	–49.4	–46.1	–49.6	–46.3

[a] The units of ΔE_{ES} and ΔE_{ZP} are given in kJ mol^{-1}. [b] BSS-A': 6-311+G(3df,3pd). [c] BSS-B'a: 6-311+G(3df,3pd) for O, N, H, and 6-311+G(3d) for C. [d] BSS-B'b: 6-311+G(3df,3pd) for O, N, H, and 6-311+G(d) for C. [e] BSS-A: 6-311++G(3df,3pd). [f] BSS-C: 6-311++G(3df,3p). [g]6-311++G(3d,3p). [h] The higher symmetry for T-T calculated with MP2/BSS-A', MP2/BSS-B'a, MP2/BSS-B'b, M06-2X/BSS-A, M06-2X/BSS-C, and M06-2X/BSS-D are C_s, C_i, C_s, C_{2h}, C_{2h}, C_{2h}, and C_{2h}, respectively.

Table 6-A3. The lengths of bond paths (r_{BP}) and the corresponding straight-line distances (R_{SL}) in each HB for Nu-Nu′, Evaluated with MP2/BSS-B'a.

AH-∗-B in Nu-Nu′ (symmetry: No.)	r_{BP}[a] (Å)	R_{SL}[b] (Å)	Δr[c] (Å)
N-∗-HN in A-T (C_1: 1)	1.7785	1.7527	0.0258
NH-∗-O in A-T (C_1: 2)	1.9156	1.8861	0.0295
CH-∗-O in A-T (C_1: 3)	2.7494	2.7138	0.0356
NH-∗-N in A-T (C_s: 4)	1.7785	1.7527	0.0258
NH-∗-O in A-T (C_s: 5)	1.9156	1.8861	0.0295
CH-∗-O in A-T (C_s: 6)	2.7495	2.7138	0.0357
NH-∗-O in C-G (C_1: 7)	1.7393	1.7104	0.0289
N-∗-HN in C-G (C_1: 8)	1.8938	1.8677	0.0261
O-∗-HN in C-G (C_1: 9)	1.8971	1.8687	0.0284
NH-∗-N in A-A (C_1: 10)	2.0004	1.9722	0.0282
CH-∗-N in A-A (C_1: 11)	2.4675	2.4455	0.0220
N-∗-HN in A-C (C_1: 12)	1.8716	1.8451	0.0265
NH-∗-O in A-C (C_1: 13)	1.8116	1.7823	0.0293
N-∗-HN in A-G (C_1: 14)	1.8501	1.8241	0.0260
NH-∗-O in A-G (C_1: 15)	1.8308	1.8019	0.0289
CH-∗-HN in A-G (C_1: 16)	2.5794	2.3822	0.1972
N-∗-HN in A-U (C_1: 17)	1.7766	1.7508	0.0258
NH-∗-O in A-U (C_1: 18)	1.9176	1.8880	0.0296
CH-∗-O in A-U (C_1: 19)	2.7450	2.7094	0.0356
NH-∗-N in C-C (C_1: 20)	1.7822	1.7559	0.0263
O-∗-HN in C-C (C_1: 21)	1.7664	1.7371	0.0293
CH-∗-O in C-C (C_1: 22)	2.8704	2.8195	0.0509
N-∗-HN in C-T (C_1: 23)	1.8566	1.8292	0.0274
NH-∗-O in C-T (C_1: 24)	1.8441	1.8152	0.0289
O-∗-O in C-T (C_1: 25)	3.5785	3.5675	0.0110
N-∗-HN in C-U (C_1: 26)	1.8531	1.8258	0.0273
NH-∗-O in C-U (C_1: 27)	1.8448	1.8159	0.0289
O-∗-O in C-U (C_1: 28)	3.5526	3.5419	0.0107
NH-∗-O G-G (C_i: 29)	1.7152	1.6888	0.0264
O-∗-HN G-G (C_i: 30)	2.4985	2.4270	0.0715
N-∗-HN in G-T (C_1: 31)	1.8462	1.8194	0.0268
NH-∗-O in G-T (C_1: 32)	1.8593	1.8310	0.0283
NH-∗-O in G-U (C_1: 33)	1.7714	1.7440	0.0274
O-∗-HN in G-U (C_1: 34)	1.7837	1.7544	0.0293
NH-∗-O in T-T (C_1: 35)	1.8082	1.7788	0.0294
O-∗-HN in T-T (C_1: 36)	1.8082	1.7788	0.0294
NH-∗-O in T-T (C_i: 37)	1.8082	1.7788	0.0294
NH-∗-O in T-U (C_1: 38)	1.8012	1.7718	0.0294
O-∗-HN in T-U (C_1: 39)	1.8167	1.7871	0.0296
NH-∗-O in U-U (C_1: 40)	1.8093	1.7798	0.0295
O-∗-HN in U-U (C_1: 41)	1.8093	1.7798	0.0295
NH-∗-O in U-U (C_s: 42)	1.8093	1.7798	0.0295
O-∗-HN in U-U (C_s: 43)	1.8093	1.7798	0.0295

[a] The lengths of BPs. [b] Straight-line distances. [c] $\Delta r_{BP} = r_{BP} - R_{SL}$.

Table 6-A4. QTAIM functions and QTAIM-DFA parameters for each HB of multi-HBs in nucleobase pairs, together with the nature of each HB, elucidated with MP2/BSS-B'b.[a,b]

AH-∗-B in Nu-Nu′ (Symmetry: No.)	$\rho_b(\boldsymbol{r}_c)$ (au)	$c\nabla^2\rho_b(\boldsymbol{r}_c)$[c] (au)	$H_b(\boldsymbol{r}_c)$ (au)	$k_b(\boldsymbol{r}_c)$[d]	R[e] (au)	θ[f] (°)	C_{ii}[g] (unit[j])	θ_p[h] (°)	κ_p[i] (au^{-1})	Predicted Nature
N-∗-HN in A-T (C_1: 1)	0.0502	0.0093	–0.0147	–1.441	0.0173	147.6	3.13	182.6	6.5	*r*-CS/CT-TBP
NH-∗-O in A-T (C_1: 2)	0.0298	0.0116	–0.0014	–1.057	0.0117	96.9	5.63	146.7	106.3	*r*-CS/*t*-HB_{wc}
CH-∗-O in A-T (C_1: 3)	0.0060	0.0025	0.0006	–0.849	0.0025	75.3	16.27	81.9	69.8	*p*-CS/vdW
NH-∗-N in A-T (C_s: 4)	0.0502	0.0093	–0.0147	–1.441	0.0173	147.6	3.13	182.6	6.4	*r*-CS/CT-TBP
NH-∗-O in A-T (C_s: 5)	0.0298	0.0116	–0.0014	–1.057	0.0117	96.9	5.63	146.7	106.3	*r*-CS/*t*-HB_{wc}
CH-∗-O in A-T (C_s: 6)	0.0060	0.0025	0.0006	–0.849	0.0025	75.3	16.27	81.9	69.8	*p*-CS/vdW
O-∗-HN in C-G (C_1: 7)	0.0455	0.0136	–0.0099	–1.266	0.0168	126.0	3.16	169.6	10.9	*r*-CS/CT-MC
N-∗-HN in C-G (C_1: 8)	0.0380	0.0099	–0.0064	–1.245	0.0118	123.0	2.15	175.2	26.6	*r*-CS/CT-MC
NH-∗-O in C-G (C_1: 9)	0.0311	0.0119	–0.0020	–1.076	0.0120	99.4	4.03	149.6	91.6	*r*-CS/*t*-HB_{wc}
NH-∗-N in A-A (C_1: 10)	0.0292	0.0093	–0.0020	–1.095	0.0095	101.8	5.67	160.1	91.1	*r*-CS/CT-MC
CH-∗-N in A-A (C_1: 11)	0.0120	0.0045	0.0012	–0.841	0.0047	74.7	16.53	76.0	51.0	*p*-CS/vdW
N-∗-HN in A-C (C_1: 12)	0.0395	0.0101	–0.0074	–1.267	0.0125	126.1	3.67	174.5	21.0	*r*-CS/CT-MC
NH-∗-O in A-C (C_1: 13)	0.0372	0.0136	–0.0046	–1.145	0.0144	108.7	3.61	158.4	36.5	*r*-CS/CT-MC
N-∗-HN in A-G (C_1: 14)	0.0429	0.0097	–0.0094	–1.326	0.0135	134.1	3.50	179.0	9.5	*r*-CS/CT-MC
NH-∗-O in A-G (C_1: 15)	0.0366	0.0126	–0.0046	–1.154	0.0135	110.1	4.40	161.1	42.4	*r*-CS/CT-MC
CH-∗-HN in A-G (C_1: 16)	0.0056	0.0026	0.0009	–0.796	0.0027	71.3	30.25	78.4	108.3	*p*-CS/vdW
N-∗-HN in A-U (C_1: 17)	0.0505	0.0092	–0.0149	–1.446	0.0175	148.1	3.12	182.8	6.2	*r*-CS/CT-TBP
NH-∗-O in A-U (C_1: 18)	0.0295	0.0116	–0.0013	–1.053	0.0116	96.3	5.66	145.8	109.3	*r*-CS/*t*-HB_{wc}
CH-∗-O in A-U (C_1: 19)	0.0061	0.0025	0.0006	–0.850	0.0026	75.4	16.27	81.7	69.8	*p*-CS/vdW
NH-∗-N in C-C (C_1: 20)	0.0492	0.0099	–0.0137	–1.409	0.0170	144.2	2.61	180.7	4.5	*r*-CS/CT-TBP
O-∗-HN in C-C (C_1: 21)	0.0431	0.0133	–0.0084	–1.241	0.0157	122.4	3.77	168.3	15.7	*r*-CS/CT-MC
CH-∗-O in C-C (C_1: 22)	0.0050	0.0021	0.0006	–0.824	0.0022	73.3	14.38	83.4	57.2	*p*-CS/vdW
N-∗-HN in C-T (C_1: 23)	0.0406	0.0096	–0.0083	–1.303	0.0127	131.0	4.81	178.1	19.4	*r*-CS/CT-MC
NH-∗-O in C-T (C_1: 24)	0.0356	0.0126	–0.0040	–1.138	0.0132	107.7	4.66	159.4	49.7	*r*-CS/CT-MC
O-∗-O in C-T (C_1: 25)	0.0027	0.0013	0.0005	–0.762	0.0014	69.0	31.80	88.7	369.5	*p*-CS/vdW
N-∗-HN in C-U (C_1: 26)	0.0410	0.0096	–0.0086	–1.310	0.0128	131.9	4.76	178.5	12.3	*r*-CS/CT-MC
NH-∗-O in C-U (C_1: 27)	0.0354	0.0126	–0.0039	–1.135	0.0132	107.3	4.67	159.0	50.5	*r*-CS/CT-MC
O-∗-O in C-U (C_1: 28)	0.0029	0.0013	0.0005	–0.774	0.0014	69.7	30.68	89.8	344.2	*p*-CS/vdW
NH-∗-O G-G (C_i: 29)	0.0507	0.0137	–0.0127	–1.316	0.0187	132.8	2.83	172.2	8.1	*r*-CS/CT-MC
O-∗-HN G-G (C_i: 30)	0.0083	0.0044	0.0014	–0.804	0.0046	71.9	13.06	73.2	20.2	*p*-CS/vdW
N-∗-HN in G-T (C_1: 31)	0.0419	0.0100	–0.0089	–1.308	0.0134	131.6	3.88	177.2	16.0	*r*-CS/CT-MC
NH-∗-O in G-T (C_1: 32)	0.0343	0.0124	–0.0034	–1.120	0.0129	105.2	4.82	156.9	60.3	*r*-CS/CT-MC
NH-∗-O in G-U (C_1: 33)	0.0428	0.0139	–0.0077	–1.216	0.0159	118.9	3.02	165.9	19.4	*r*-CS/CT-MC
O-∗-HN in G-U (C_1: 34)	0.0411	0.0128	–0.0073	–1.221	0.0148	119.6	4.24	167.5	20.9	*r*-CS/CT-MC
NH-∗-O in T-T (C_1: 35)	0.0380	0.0130	–0.0053	–1.169	0.0141	112.1	4.23	163.7	32.2	*r*-CS/CT-MC
O-∗-HN in T-T (C_1: 36)	0.0380	0.0131	–0.0053	–1.169	0.0141	112.1	4.22	163.7	32.2	*r*-CS/CT-MC
NH-∗-O in T-T (C_i: 37)	0.0380	0.0131	–0.0053	–1.169	0.0141	112.1	4.22	163.7	28.4	*r*-CS/CT-MC
NH-∗-O in T-U (C_1: 38)	0.0387	0.0131	–0.0057	–1.178	0.0143	113.4	4.10	164.5	29.0	*r*-CS/CT-MC
O-∗-HN in T-U (C_1: 39)	0.0372	0.0130	–0.0048	–1.157	0.0138	110.4	4.35	162.4	36.2	*r*-CS/CT-MC
NH-∗-O in U-U (C_1: 40)	0.0379	0.0130	–0.0052	–1.166	0.0140	111.8	4.23	163.3	32.6	*r*-CS/CT-MC
O-∗-HN in U-U (C_1: 41)	0.0379	0.0130	–0.0052	–1.166	0.0140	111.8	4.23	163.3	32.6	*r*-CS/CT-MC
NH-∗-O in U-U (C_s: 42)	0.0379	0.0130	–0.0052	–1.166	0.0140	111.8	4.23	163.3	28.8	*r*-CS/CT-MC
O-∗-HN in U-U (C_s: 43)	0.0379	0.0130	–0.0052	–1.166	0.0140	111.8	4.23	163.3	28.8	*r*-CS/CT-MC

[a] BSS-B'b: 6-311+G(3df,3pd) for O, N, H, and 6-311+G(d) for C. [b] Data are given at BCPs. [c] $c\nabla^2\rho_b(\boldsymbol{r}_c) = H_b(\boldsymbol{r}_c) - V_b(\boldsymbol{r}_c)/2$, where $c = \hbar^2/8m$. [d] $k_b(\boldsymbol{r}_c) = V_b(\boldsymbol{r}_c)/G_b(\boldsymbol{r}_c)$. [e] $R = (x + y)^{1/2}$, where (x, $y = H_b(\boldsymbol{r}_c) - V_b(\boldsymbol{r}_c)/2$, $H_b(\boldsymbol{r}_c)$). [f] $\theta = 90° - \tan^{-1}(y/x)$. [g] Compliance force constants. [h] $\theta_p = 90° - \tan^{-1}(dy/dx)$. [i] $\kappa_p = |d^2y/dx^2|/[1 + (dy/dx)^2]^{3/2}$. [j] Å $mdyn^{-1}$.

Table 6-A5. QTAIM functions and QTAIM-DFA parameters for each HB of multi-HBs in some nucleobase pairs, together with the nature of each HB, evaluated with various basis sets for M06-2X level.[a]

AH-∗-B in Nu-Nu′ (Symmetry: No.)	$\rho_b(\boldsymbol{r}_c)$ (au)	$c\nabla^2\rho_b(\boldsymbol{r}_c)$[b] (au)	$H_b(\boldsymbol{r}_c)$ (au)	$k_b(\boldsymbol{r}_c)$[c]	R[d] (au)	θ[e] (º)	C_{il}[f] (unit[j])	θ_p[g] (º)	κ_p[h] (au^{-1})	Predicted Nature
M06-2X/BSS-A[i]										
N-∗-HN in A-T (C_1: 1)	0.0470	0.0092	–0.0125	–1.404	0.0155	143.6	3.81	186.0	3.6	*r*-CS/CT-TBP
NH-∗-O in A-T (C_1: 2)	0.0252	0.0115	0.0011	–0.949	0.0116	84.5	6.07	124.4	218.8	*p*-CS/*t*-HB_{nc}
CH-∗-O in A-T (C_1: 3)	0.0055	0.0023	0.0007	–0.823	0.0024	73.3	20.49	78.9	103.9	*p*-CS/vdW
O-∗-HN in C-G (C_1: 7)	0.0402	0.0137	–0.0061	–1.181	0.0150	113.9	3.88	174.8	36.4	*r*-CS/CT-MC
N-∗-HN in C-G (C_1: 8)	0.0342	0.0103	–0.0037	–1.153	0.0110	109.8	2.22	178.1	45.3	*r*-CS/CT-MC
NH-∗-O in C-G (C_1: 9)	0.0273	0.0121	0.0005	–0.981	0.0121	87.8	3.95	135.4	199.8	*p*-CS/*t*-HB_{nc}
NH-∗-O in T-T (C_1: 35)	0.0311	0.0133	–0.0008	–1.030	0.0133	93.6	5.50	153.4	126.8	*r*-CS/CT-MC
NH-∗-O in T-U (C_1: 38)	0.0317	0.0133	–0.0011	–1.040	0.0134	94.7	4.84	155.8	118.0	*r*-CS/CT-MC
O-∗-HN in T-U (C_1: 39)	0.0308	0.0132	–0.0007	–1.026	0.0132	93.0	4.76	152.4	133.2	*r*-CS/CT-MC
NH-∗-O in U-U (C_1: 40)	0.0298	0.0132	–0.0001	–1.005	0.0132	90.6	4.97	147.3	152.1	*r*-CS/*t*-HB_{wc}
M06-2X/BSS-C[k]										
N-∗-HN in A-T (C_1: 1)	0.0460	0.0107	–0.0097	–1.313	0.0144	132.3	4.04	184.0	11.6	*r*-CS/CT-TBP
NH-∗-O in A-T (C_1: 2)	0.0248	0.0117	0.0015	–0.933	0.0118	82.8	5.91	112.1	164.8	*p*-CS/*t*-HB_{nc}
CH-∗-O in A-T (C_1: 3)	0.0055	0.0023	0.0007	–0.815	0.0024	72.6	20.18	77.7	86.4	*p*-CS/vdW
O-∗-HN in C-G (C_1: 7)	0.0381	0.0149	–0.0032	–1.097	0.0152	102.1	3.89	161.4	68.9	*r*-CS/CT-MC
N-∗-HN in C-G (C_1: 8)	0.0329	0.0111	–0.0020	–1.083	0.0113	100.3	2.22	168.4	100.7	*r*-CS/CT-MC
NH-∗-O in C-G (C_1: 9)	0.0268	0.0124	0.0010	–0.958	0.0124	85.4	3.89	120.4	170.2	*p*-CS/*t*-HB_{nc}
NH-∗-O in T-T (C_1: 35)	0.0302	0.0137	0.0003	–0.990	0.0137	88.9	5.26	136.8	150.2	*p*-CS/*t*-HB_{nc}
NH-∗-O in T-U (C_1: 38)	0.0307	0.0138	0.0001	–0.997	0.0138	89.7	4.58	139.1	146.5	*p*-CS/*t*-HB_{nc}
O-∗-HN in T-U (C_1: 39)	0.0299	0.0136	0.0003	–0.988	0.0136	88.6	4.53	136.0	153.7	*p*-CS/*t*-HB_{nc}
NH-∗-O in U-U (C_1: 40)	0.0291	0.0136	0.0007	–0.972	0.0136	86.9	4.80	131.4	158.7	*p*-CS/*t*-HB_{nc}
M06-2X/BSS-C[l]										
N-∗-HN in A-T (C_1: 1)	0.0460	0.0107	–0.0097	–1.313	0.0144	132.3	4.03	184.0	11.6	*r*-CS/CT-TBP
NH-∗-O in A-T (C_1: 2)	0.0248	0.0117	0.0015	–0.933	0.0118	82.8	5.91	112.2	164.1	*p*-CS/*t*-HB_{nc}
CH-∗-O in A-T (C_1: 3)	0.0055	0.0023	0.0007	–0.814	0.0024	72.6	20.75	77.8	74.1	*p*-CS/vdW
O-∗-HN in C-G (C_1: 7)	0.0381	0.0149	–0.0032	–1.097	0.0152	102.1	3.89	161.4	68.6	*r*-CS/CT-MC
N-∗-HN in C-G (C_1: 8)	0.0330	0.0111	–0.0020	–1.083	0.0113	100.3	2.22	168.4	100.5	*r*-CS/CT-MC
NH-∗-O in C-G (C_1: 9)	0.0268	0.0124	0.0010	–0.958	0.0124	85.4	3.90	120.4	170.3	*p*-CS/*t*-HB_{nc}
NH-∗-N in A-A (C_1: 10)	0.0239	0.0097	0.0011	–0.938	0.0098	83.3	6.34	127.1	261.8	*p*-CS/*t*-HB_{nc}
CH-∗-N in A-A (C_1: 11)	0.0106	0.0041	0.0014	–0.795	0.0044	71.2	18.21	70.6	35.0	*p*-CS/vdW
NH-∗-O in T-T (C_1: 35)	0.0302	0.0137	0.0003	–0.990	0.0137	88.9	5.24	136.8	150.2	*p*-CS/*t*-HB_{nc}
NH-∗-O in U-U (C_1: 40)	0.0290	0.0135	0.0007	–0.973	0.0135	87.0	4.82	131.5	160.2	*p*-CS/*t*-HB_{nc}
M06-2X/BSS-D[m]										
N-∗-HN in A-T (C_1: 1)	0.0459	0.0109	–0.0092	–1.299	0.0143	130.4	4.03	183.5	14.3	*r*-CS/CT-TBP
NH-∗-O in A-T (C_1: 2)	0.0247	0.0117	0.0017	–0.922	0.0118	81.7	5.84	109.8	161.2	*p*-CS/*t*-HB_{nc}
CH-∗-O in A-T (C_1: 3)	0.0055	0.0023	0.0007	–0.823	0.0024	73.3	20.41	78.6	90.7	*p*-CS/vdW
O-∗-HN in C-G (C_1: 7)	0.0377	0.0150	–0.0027	–1.082	0.0152	100.1	3.87	158.9	73.6	*r*-CS/CT-MC
N-∗-HN in C-G (C_1: 8)	0.0329	0.0112	–0.0017	–1.071	0.0114	98.7	2.29	167.4	104.5	*r*-CS/CT-MC
NH-∗-O in C-G (C_1: 9)	0.0264	0.0123	0.0013	–0.944	0.0124	83.9	4.00	116.6	170.5	*p*-CS/*t*-HB_{nc}
NH-∗-O in T-T (C_1: 35)	0.0303	0.0137	0.0004	–0.983	0.0138	88.1	5.21	135.3	152.1	*p*-CS/*t*-HB_{nc}
NH-∗-O in T-U (C_1: 38)	0.0307	0.0138	0.0003	–0.990	0.0138	88.8	4.55	137.5	149.1	*p*-CS/*t*-HB_{nc}
O-∗-HN in T-U (C_1: 39)	0.0299	0.0136	0.0005	–0.980	0.0137	87.8	4.50	134.5	155.9	*p*-CS/*t*-HB_{nc}
NH-∗-O in U-U (C_1: 40)	0.0290	0.0136	0.0009	–0.965	0.0136	86.1	4.77	129.7	160.1	*p*-CS/*t*-HB_{nc}

[a] Data are given at BCPs. [b] $c\nabla^2\rho_b(\boldsymbol{r}_c) = H_b(\boldsymbol{r}_c) - V_b(\boldsymbol{r}_c)/2$, where $c = \hbar^2/8m$. [c] $k_b(\boldsymbol{r}_c) = V_b(\boldsymbol{r}_c)/G_b(\boldsymbol{r}_c)$. [d] $R = (x + y)^{1/2}$, where $(x, y = H_b(\boldsymbol{r}_c) - V_b(\boldsymbol{r}_c)/2, H_b(\boldsymbol{r}_c))$. [e] $\theta = 90º - \tan^{-1}(y/x)$. [f] Compliance force constants. [g] $\theta_p = 90º - \tan^{-1}(dy/dx)$. [h] $\kappa_p = |d^2y/dx^2|/[1 + (dy/dx)^2]^{3/2}$. [i] Å $mdyn^{-1}$. [j] BSS-A: 6-311++G(3df,3pd). [k] BSS-C: 6-311++G(3df,3p). [l] BSS-C: 6-311++G(3df,3p). [m] 6-311++G(3d,3p).

Table 6-A6. The w'_{ij}/w_{ii} ratios for the interactions of each HB in Nu-Nu' evaluated with CIV and POM of the under MP2/BSS-B′a.[a–c]

Interaction	$(w'_{1j}/w_1)_{CIV}$[d]	$(w'_{2j}/w_2)_{CIV}$[d]	$(w'_{3j}/w_3)_{CIV}$[d]	$(w'_{1j}/w_1)_{POM}$[d]	$(w'_{2j}/w_2)_{POM}$[d]	$(w'_{3j}/w_3)_{POM}$[d]
AH-∗-B (j)	(i = 1)	(i = 2)	(i = 3)	(i = 1)	(i = 2)	(i = 3)
A-T (C_1)						
NH-∗-O (j = 1)	1.0000	0.1969	–0.2370	1.0000	0.1807	–0.2320
N-∗-HN (j = 2)	0.1058	1.0000	0.2774	0.1051	1.0000	0.2800
NH-∗-O (j = 3)	–0.6674	1.4505	1.0000	–0.6674	1.4909	1.0000
C-G (C_1)						
O-∗-HN (j = 1)	1.0000	0.4951	–0.0537	1.0000	0.5155	–0.0563
N-∗-HN (j = 2)	0.2589	1.0000	0.3481	0.2619	1.0000	0.3481
NH-∗-O (j = 3)	–0.0420	0.5204	1.0000	–0.0420	0.5291	1.0000
A-A (C_1)						
NH-∗-N (j = 1)	1.0000	–0.0076		1.0000	–0.0098	
N-∗-HC (j = 2)	–0.0204	1.0000		–0.0231	1.0000	
T-T (C_1)						
NH-∗-O (j = 1)	1.0000			1.0000		
(j = 2)	0.1126			0.1088		
U-U (C_1)						
NH-∗-O (j = 1)	1.0000			1.0000		
(j = 2)	0.1232			0.1194		

[a] BSS-B'a: The 6-311+G(3df,3pd) for O, N, H, and 6-311+G(3d) for C. [b] The w'_{ij}/w_i values are calculated at w = 0.05. [c] i and j for w'_{ij}/w_i represent the interaction in question and the other ones, respectively. [d] The w'_{ij}/w_i values are calculated with w = 0.05.

Table 6-A7. The w'_{ij}/w_i ratios for the interactions of each HB in Nu-Nu' evaluated with CIV and POM with M06-2X/BSS-C'.[a–c]

Interaction	$(w'_{1j}/w_1)_{CIV}$[d]	$(w'_{2j}/w_2)_{CIV}$[d]	$(w'_{3j}/w_3)_{CIV}$[d]	$(w'_{1j}/w_1)_{POM}$[d]	$(w'_{2j}/w_2)_{POM}$[d]	$(w'_{3j}/w_3)_{POM}$[d]
AH-∗-B (j)	(i = 1)	(i = 2)	(i = 3)	(i = 1)	(i = 2)	(i = 3)
A-T (C_1)						
NH-∗-O (j = 1)	1.0000	0.1281	–0.2101	1.0000	0.0695	–0.2094
N-∗-HN (j = 2)	0.0877	1.0000	0.3095	0.0945	1.0000	0.3100
NH-∗-O (j = 3)	–0.7381	1.5903	1.0000	–0.7203	1.7082	1.0000
C-G (C_1)						
O-∗-HN (j = 1)	1.0000	0.5321	–0.0737	1.0000	0.5431	–0.0782
N-∗-HN (j = 2)	0.3031	1.0000	0.3685	0.3046	1.0000	0.3677
NH-∗-O (j = 3)	–0.0737	0.6455	1.0000	–0.0741	0.6553	1.0000
A-A (C_1)						
NH-∗-N (j = 1)	1.0000	–0.0008		1.0000	–0.0181	
N-∗-HC (j = 2)	0.0034	1.0000		–0.0185	1.0000	
T-T (C_1)						
NH-∗-O (j = 1)	1.0000			1.0000		
	–0.0008			0.0106		
U-U (C_1)						
NH-∗-O (j = 1)	1.0000			1.0000		
	0.0612			0.0559		

[a] BSS-B'a: The 6-311+G(3df,3pd) for O, N, H, and 6-311+G(3d) for C. [b] The w'_{ij}/w_i values are calculated with w = 0.05 and 0.1. [c] i and j for w'_{ij}/w_i represent the interaction in question and the other ones, respectively. [d] The w'_{ij}/w_i values are calculated with w = 0.05.

Table 6-A8. QTAIM-DFA parameters for each HB of multi-HBs in Some nucleobase pairs, elucidated by employing the perturbed structures generated with CIV and POM methods, together with the nature of each HB and the differences between $\theta_{p:CIV}$ and $\theta_{p:POM}$, $\kappa_{p:CIV}$ and $\kappa_{p:POM}$, evaluated with M06-2X/BSS-C'.[a]

AH-∗-B in Nu-Nu′ (Symmetry: No.)	$\theta_{p:CIV}$ (º)	$\theta_{p:POM}$ (º)	$\Delta\theta_p$[b] (º)	$\kappa_{p:CIV}$ (au^{-1})	$\kappa_{p:POM}$ (au^{-1})	$\Delta\kappa_p$[c] (au^{-1})	Predicted Nature
N-∗-HN in A-T (C_1: 1)	184.0	184.0	0.0	16.5	11.6	4.9	*r*-CS/CT-TBP
NH-∗-O in A-T (C_1: 2)	112.1	112.2	–0.1	163.9	164.1	–0.2	*p*-CS/*t*-HB_{nc}
CH-∗-O in A-T (C_1: 3)	77.8	77.8	0.0	75.9	74.1	1.8	*p*-CS/vdW
O-∗-HN in C-G (C_1: 7)	161.4	161.4	0.0	74.6	68.6	6.0	*r*-CS/CT-MC
N-∗-HN in C-G (C_1: 8)	168.4	168.4	0.0	109.8	100.5	9.3	*r*-CS/CT-MC
NH-∗-O in C-G (C_1: 9)	120.4	120.4	0.0	171.9	170.3	1.6	*p*-CS/*t*-HB_{nc}
NH-∗-N in A-A (C_1: 10)	127.1	127.1	0.0	268.0	261.8	6.2	*p*-CS/*t*-HB_{nc}
CH-∗-N in A-A (C_1: 11)	70.5	70.6	–0.1	38.5	35.0	3.5	*p*-CS/vdW
NH-∗-O in T-T (C_1: 35)	136.8	136.8	0.0	155.8	150.2	5.6	*p*-CS/*t*-HB_{nc}
NH-∗-O in U-U (C_1: 40)	131.4	131.5	–0.1	164.5	160.2	4.3	*p*-CS/*t*-HB_{nc}

[a] BSS-C': The 6-311+G(3df,3p) basis sets. [b] $\Delta\theta_p = \theta_{p:CIV} - \theta_{p:POM}$. [c] $\Delta\kappa_p = \kappa_{p:CIV} - \kappa_{p:POM}$.

Table 6-A9. ΔE_{psi} (= $E_{psi} - E_o$) for A-T, C-G, A-A, T-T, and U-U, calculated with M06-2X/BSS-C'.[a]

w	Δr (Å)	$\Delta E_{ES:CIV:(j=1)}$ (kJ mol^{-1})	$\Delta E_{ES:POM:(j=1)}$ (kJ mol^{-1})	$\Delta E_{ES:CIV:(j=2)}$ (kJ mol^{-1})	$\Delta E_{ES:POM:(j=2)}$ (kJ mol^{-1})	$\Delta E_{ES:CIV:(j=3)}$ (kJ mol^{-1})	$\Delta E_{ES:POM:(j=3)}$ (kJ mol^{-1})
A-T (C_1)							
–0.18897	–0.10000		0.58286		0.90317		0.16278
–0.10000	–0.05292	0.15228		0.23735		0.04437	
–0.09449	–0.05000		0.13653		0.20479		0.03676
–0.05000	–0.02646	0.03649		0.05592		0.01050	
–0.02500	–0.01323	0.00893		0.01365		0.00263	
0.00000	0.00000	0.00000	0.00000	0.00000	0.00000	0.00000	0.00000
0.02500	0.01323	0.00866		0.01260		0.00236	
0.05000	0.02646	0.03413		0.04883		0.00945	
0.09449	0.05000		0.11552		0.16541		0.03413
0.10000	0.05292	0.13285		0.18457		0.03649	
0.18897	0.10000		0.44371		0.60912		0.12602
0.20000	0.10584	0.50593		0.68841		0.13968	
0.30000	0.15875	1.08302		1.50651		0.31480	
0.37794	0.20000		1.57793		2.19229		0.48834
0.40000	0.21167	1.83732		2.60187		0.57498	
0.50000	0.26459	2.75625		3.97606		0.91682	
0.56691	0.30000		3.12697		4.38984		1.07645
0.60000	0.31751	3.84006		5.62067		1.33402	
0.70000	0.37043	5.09793		7.55330		1.84415	
0.75589	0.40000		4.87293		7.00221		1.83522
0.80000	0.42334	6.56428		9.78078		2.46246	
0.90000	0.47626	8.28345		12.32042		3.19418	
0.94486	0.50000		6.71865		9.85613		2.76203
1.00000	0.52918	10.29327		15.18379		4.05824	
C-G (C_1)							
–0.18897	–0.10000		0.86642		1.39677		0.82703
–0.10000	–0.05292	0.23157		0.38674		0.22684	
–0.09449	–0.05000		0.05776		0.09714		0.05776
–0.05000	–0.02646	0.05592		0.09583		0.05540	
–0.02500	–0.01323	0.01365		0.02363		0.01365	
0.00000	0.00000	0.00000	0.00000	0.00000	0.00000	0.00000	0.00000
0.02500	0.01323	0.01313		0.02337		0.01313	
0.05000	0.02646	0.05198		0.09347		0.05225	
0.09449	0.05000		0.05251		0.09452		0.05251
0.10000	0.05292	0.20138		0.36810		0.20269	
0.18897	0.10000		0.68263		1.27074		0.69313
0.20000	0.10584	0.75903		1.42565		0.77951	
0.30000	0.15875	1.61600		3.12933		1.70579	
0.37794	0.20000		2.43384		4.77316		2.57299
0.40000	0.21167	2.72133		5.45605		2.92953	
0.50000	0.26459	4.03618		8.36143		4.40506	
0.56691	0.30000		4.83355		8.93458		5.24575
0.60000	0.31751	5.52930		11.79716		6.10140	
0.70000	0.37043	7.17208		15.72569		7.98940	
0.75589	0.40000		7.69009		13.06974		8.39110
0.80000	0.42334	8.94193		20.11422		10.04884	
0.90000	0.47626	10.82940		24.92728		12.26502	
0.94486	0.50000		10.77505		16.88459		11.80162
1.00000	0.52918	12.83318		30.13654		14.62036	

[a] BSS-C': The 6-311+G(3df,3p) basis sets.

(Table 6-A9 continued.)

w	Δr (Å)	$\Delta E_{ES:CIV:(j=1)}$ (kJ mol^{-1})	$\Delta E_{ES:POM:(j=1)}$ (kJ mol^{-1})	$\Delta E_{ES:CIV:(j=2)}$ (kJ mol^{-1})	$\Delta E_{ES:POM:(j=2)}$ (kJ mol^{-1})	$\Delta E_{ES:CIV:(j=3)}$ (kJ mol^{-1})	$\Delta E_{ES:POM:(j=3)}$ (kJ mol^{-1})
A-A (C_1)							
–0.18897	–0.10000		0.51985		0.17328		
–0.10000	–0.05292	0.13495		0.05514			
–0.09449	–0.05000		0.12602		0.03676		
–0.05000	–0.02646	0.03177		0.01392			
–0.02500	–0.01323	0.00735		0.00394			
0.00000	0.00000	0.00000	0.00000	0.00000	0.00000		
0.02500	0.01323	0.00893		0.00158			
0.05000	0.02646	0.03439		0.00866			
0.09449	0.05000		0.10765		0.03938		
0.10000	0.05292	0.13154		0.03991			
0.18897	0.10000		0.42008		0.14703		
0.20000	0.10584	0.50147		0.18090			
0.30000	0.15875	1.10061		0.44686			
0.37794	0.20000		1.52016		0.47259		
0.40000	0.21167	1.94838		0.88847			
0.50000	0.26459	3.08759		1.59105			
0.56691	0.30000		3.03508		0.84541		
0.60000	0.31751	4.57677		2.66068			
0.70000	0.37043	6.50730		4.20789			
0.75589	0.40000		4.74953		1.23399		
0.80000	0.42334	8.99680		6.33244			
0.90000	0.47626	12.18232		9.15249			
0.94486	0.50000		6.51649		1.59630		
1.00000	0.52918	16.20616		12.80509			
T-T (C_1)							
–0.18897	–0.10000		0.56973				
–0.10000	–0.05292	0.16908					
–0.09449	–0.05000		0.14965				
–0.05000	–0.02646	0.04122					
–0.02500	–0.01323	0.01024					
0.00000	0.00000	0.00000	0.00000				
0.02500	0.01323	0.00998					
0.05000	0.02646	0.03965					
0.09449	0.05000		0.13915				
0.10000	0.05292	0.15412					
0.18897	0.10000		0.51197				
0.20000	0.10584	0.57498					
0.30000	0.15875	1.21561					
0.37794	0.20000		1.76959				
0.40000	0.21167	2.05603					
0.50000	0.26459	3.08523					
0.56691	0.30000		3.48141				
0.60000	0.31751	4.32000					
0.70000	0.37043	5.75956					
0.75589	0.40000		5.49255				
0.80000	0.42334	7.50158					
0.90000	0.47626	9.55026					
0.94486	0.50000		7.63758				
1.00000	0.52918	11.95364					

[a] BSS-C': The 6-311+G(3df,3p) basis sets.

(Table 6-A9 continued.)

w	Δr (Å)	$\Delta E_{ES:CIV:(j=1)}$ (kJ mol^{-1})	$\Delta E_{ES:POM:(j=1)}$ (kJ mol^{-1})	$\Delta E_{ES:CIV:(j=2)}$ (kJ mol^{-1})	$\Delta E_{ES:POM:(j=2)}$ (kJ mol^{-1})	$\Delta E_{ES:CIV:(j=3)}$ (kJ mol^{-1})	$\Delta E_{ES:POM:(j=3)}$ (kJ mol^{-1})
U-U (C_1)							
–0.18897	–0.10000		0.66688				
–0.10000	–0.05292	0.18221					
–0.09449	–0.05000		0.16016				
–0.05000	–0.02646	0.04463					
–0.02500	–0.01323	0.01103					
0.00000	0.00000	0.00000	0.00000				
0.02500	0.01323	0.01103					
0.05000	0.02646	0.04253					
0.09449	0.05000		0.14440				
0.10000	0.05292	0.16331					
0.18897	0.10000		0.53823				
0.20000	0.10584	0.60859					
0.30000	0.15875	1.28571					
0.37794	0.20000		1.86936				
0.40000	0.21167	2.15790					
0.50000	0.26459	3.20337					
0.56691	0.30000		3.64682				
0.60000	0.31751	4.42029					
0.70000	0.37043	5.81995					
0.75589	0.40000		5.65795				
0.80000	0.42334	7.40811					
0.90000	0.47626	9.19660					
0.94486	0.50000		7.74260				
1.00000	0.52918	11.21587					

[a] BSS-C': The 6-311+G(3df,3p) basis sets.

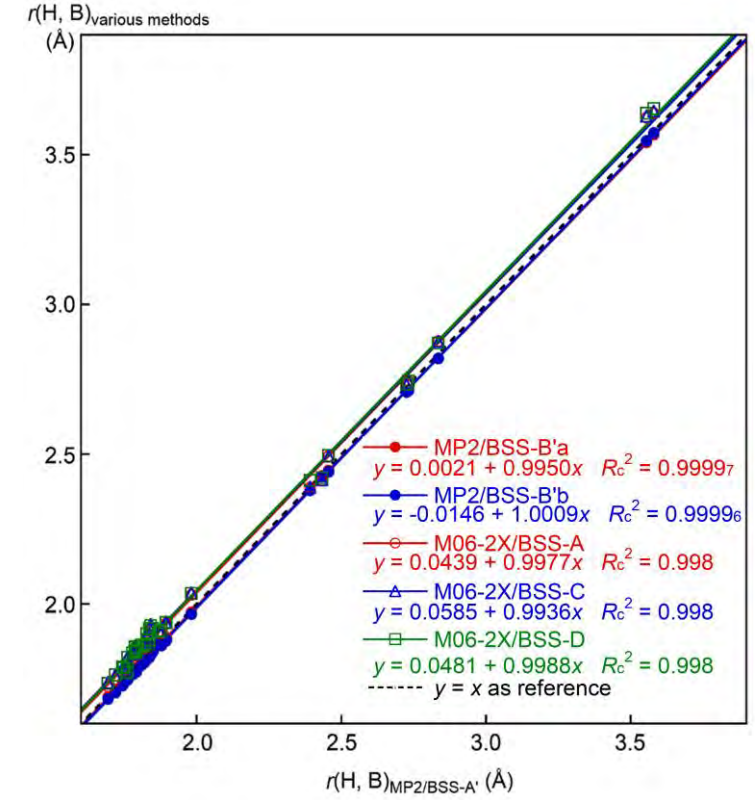

Figure 6-A1. Plots of r(H, B) for each HB in Nu-Nu′ calculated with various methods (r(H, B)$_{\text{various methods}}$) versus those with MP2/BSS-A′ (r(H, B)$_{\text{MP2/BSS-A′}}$).

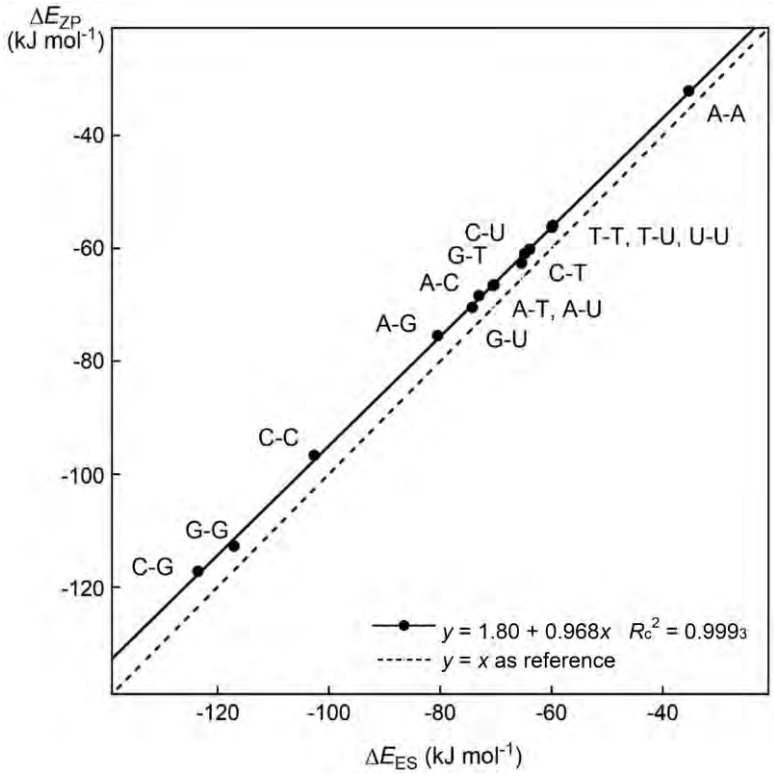

Figure 6-A2. Plot of ΔE_{ZP} versus ΔE_{ES}, together with ΔE_{ES} versus ΔE_{ES}, calculated with MP2/BSS-B′a.

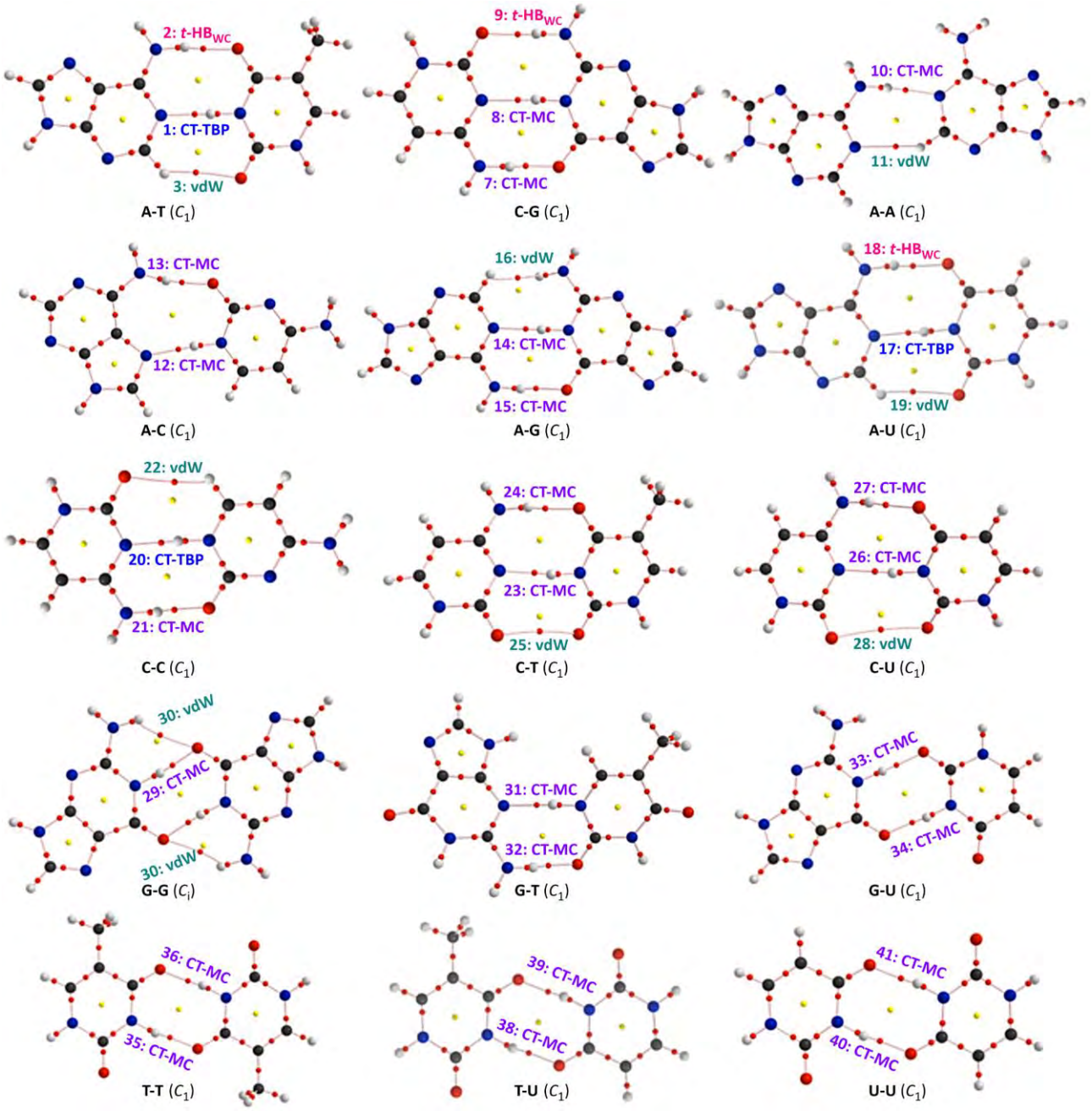

Figure 6-A3. Molecular graphs for nucleobase pairs, with numbers and predicted natures, evaluated with MP2/BSS-B′a. BCPs (bond critical points) are denoted by red dots, RCPs (ring critical points) by yellow dots, and BPs (bond paths) are by pink lines. Oxygen, nitrogen, carbon, and hydrogen atoms are in red, blue, black, and grey, respectively.

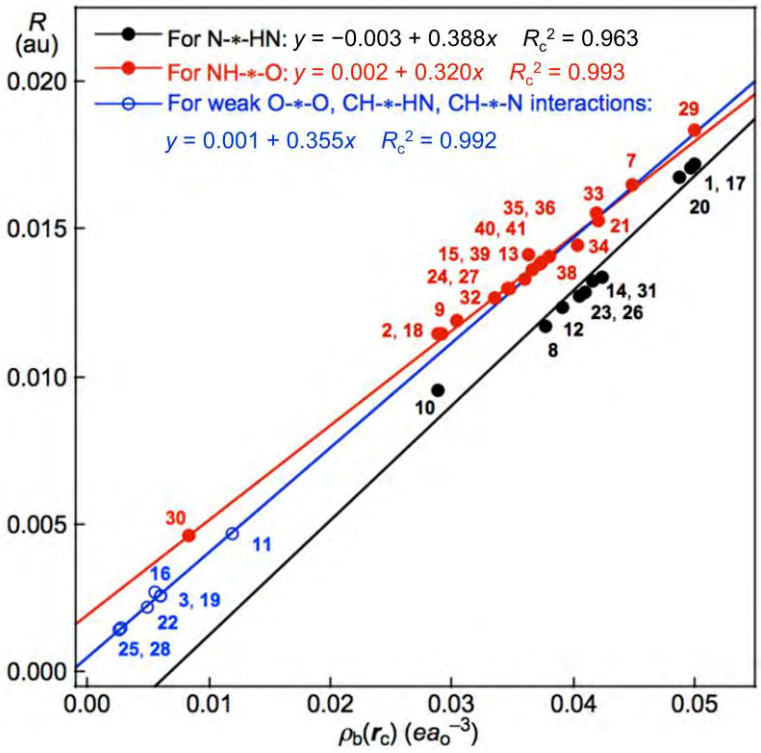

Figure 6-A4. Plots of R versus $\rho_b(\boldsymbol{r}_c)$ for each HB in Nu-Nu′, calculated with MP2/BSS-B′a. While data for G(**A**) of NH-∗-N are shown by black solid circles, those for G(**B**) of NH-∗-O are by red solid circles, together with those for G(**C**) of CH-∗-X (X = O, N, and HN) and O-∗-O by blue hole circles. Numbers for the interactions are the same as those in Table 6-2 and Figure 6-4 of the text, respectively.

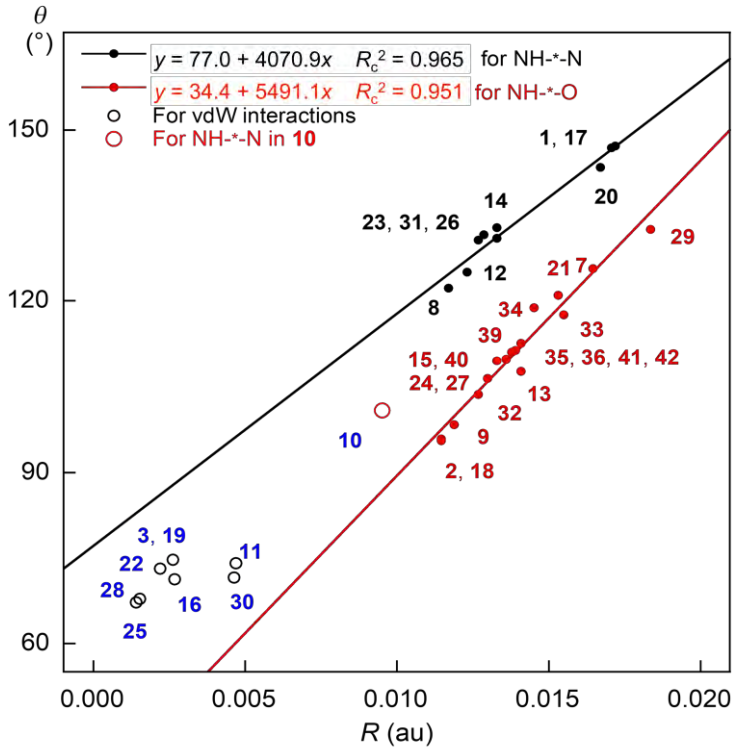

Figure 6-A5. Plots of θ versus R for Nu-Nu′, calculated with MP2/BSS-B′a, black line for θ versus R of N-∗-HN (NH-∗-N), CH-∗-O, O-∗-O, and CH-∗-HN, except for 10: NH-∗-N, red line for θ versus R of NH-∗-O (O-∗-HN) and CH-∗-N, blue square digit for 10: NH-∗-N.

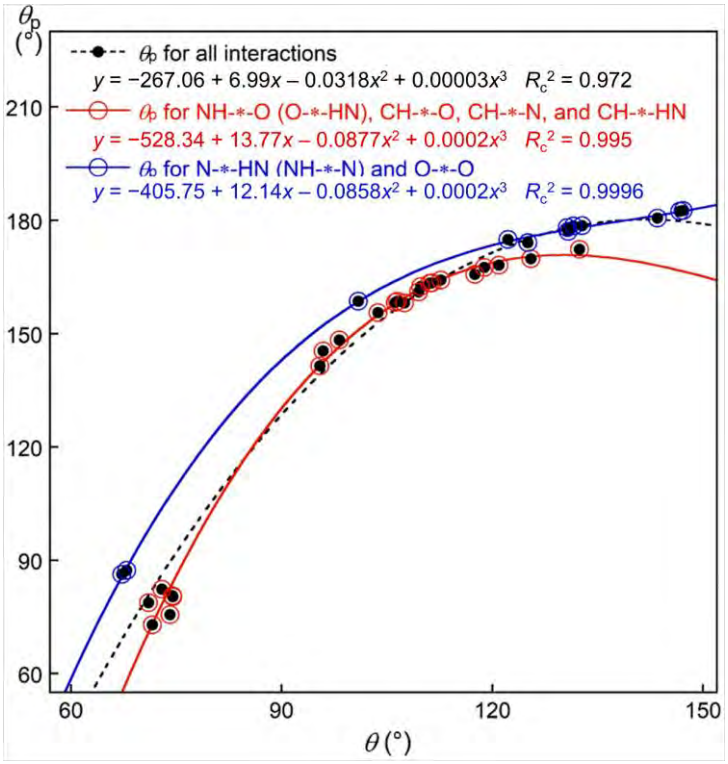

Figure 6-A6. Plots of θ_p versus θ for Nu-Nu′, calculated with MP2/BSS-B′a, black dot-line for θ_p versus θ of all interaction, red line for θ_p versus θ of NH-*-O (O-*-HN), CH-*-O, CH-*-N, and CH-*-HN, blue line for θ_p versus θ of N-*-HN (NH-*-N) and O-*-O.

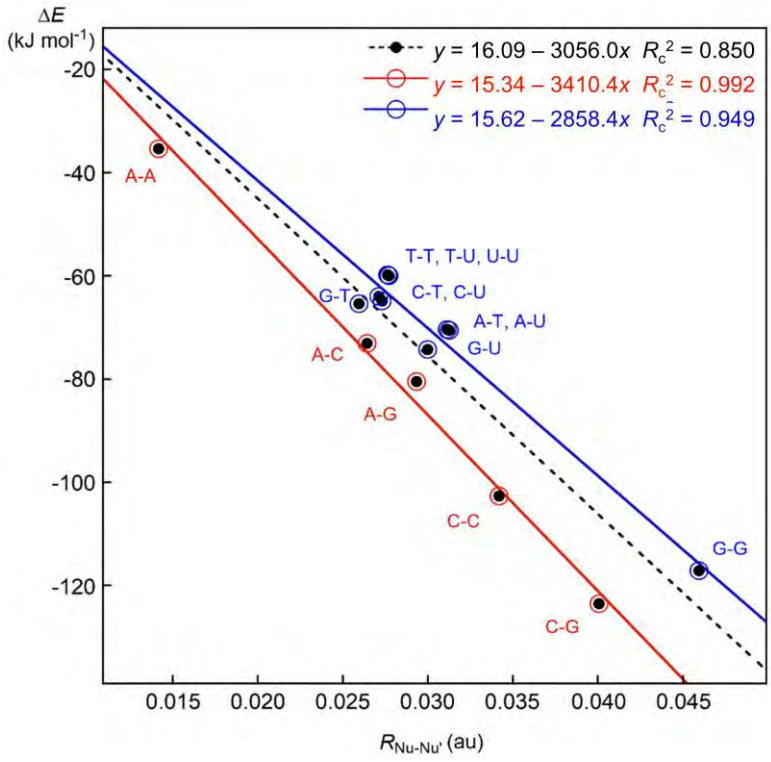

Figure 6-A7. Plots of ΔE versus $R_{Nu\text{-}Nu'}$ in Nu-Nu′, calculated with MP2/BSS-B′a.

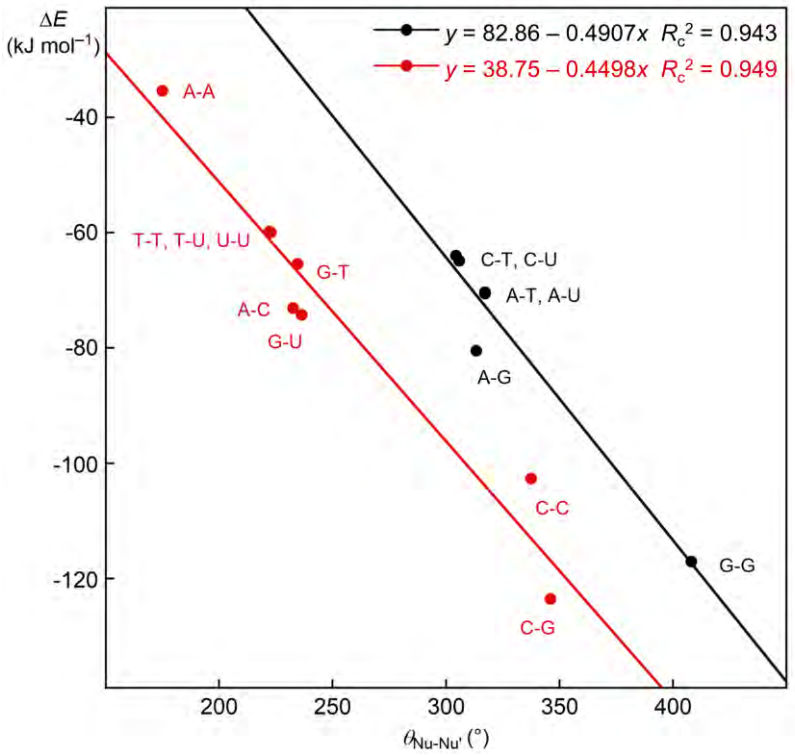

Figure 6-A8. Plots of ΔE versus $\theta_{\text{Nu-Nu}'}$ in Nu-Nu′, calculated with MP2/BSS-B′a.

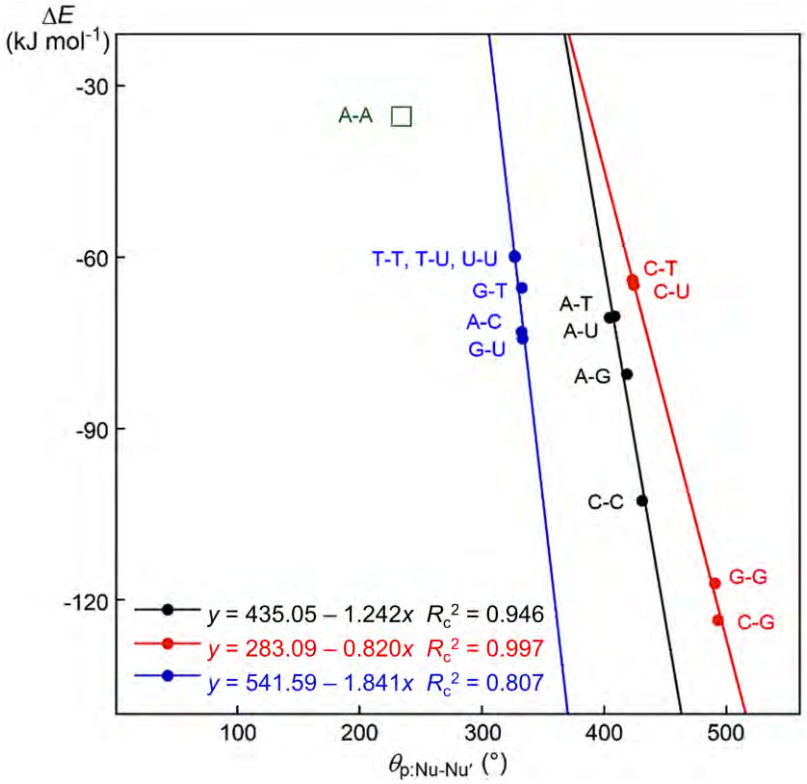

Figure 6-A9. Plots of ΔE versus $\theta_{\text{p:Nu-Nu}'}$ for Nu-Nu′, calculated with MP2/BSS-B′a.

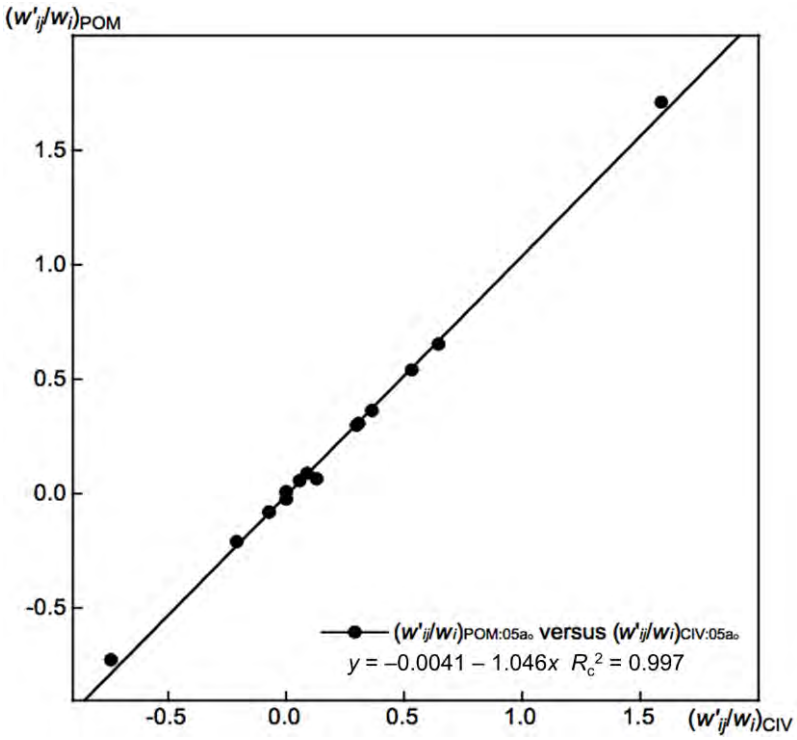

Figure 6-A10. Plot of $(w'_{ij}/w_i)_{POM}$ versus $(w'_{ij}/w_i)_{CIV}$ for each HB of multi-HB system in A-T, C-G, A-A, T-T, and U-U, calculated with M06-2X/BSS-C′.

References and Notes

1. L. Pauling, *The Nature of the Chemical Bond*, Cornell University Press, Ithaca, NY, **1960**.
2. *The Hydrogen Bond, Recent Developments in Theory and Experiments*, eds. P. Schuster, G. Zundel, C. Sandorfy, North-Holland Publishing Company, Amsterdam, **1976**.
3. G. A. Jeffrey, W. Saenger, *Hydrogen Bonding in Biological Structures*, Springer, Berlin, **1991**.
4. G. A. Jeffrey, *An Introduction to Hydrogen Bonding*, Oxford University Press, New York, **1997**.
5. A. D. Buckingham, A. C. Legon, S. M. Roberts, *Principles of Molecular Recognition*, Blackie Academic & Professional, London, **1993**.
6. S. Scheiner, *Hydrogen Bonding, A Theoretical Perspective*, Oxford University Press, Oxford, **1997**.
7. G. R. Desiraju, T. Steiner, *The Weak Hydrogen Bond in Structural Chemistry and Biology, International Union of Crystallography Monographs on Crystallography*, Oxford University Press, New York, **1999**.
8. S. J. Grabowski, *Hydrogen Bonding – New Insights*, *Vol. 3, Challenges and Advances in Computational Chemistry and Physics* (Ed.: J. Leszczynski), Springer, The Netherlands, Dordrecht, **2006**.
9. G. Buemi, *Intramolecular Hydrogen Bonds. Methodologies and Strategies for Their Strength Evaluation* in *Hydrogen Bonding – New Insights* (Ed.: S. J. Grabowski), Springer, New York, **2006**, Ch. 2.
10. F. H. C. Crick, *J. Mol. Biol.* **1968**, *38*, 367–379.
11. J. D. Watson, F. H. C. Crick, *Nature* **1953**, *171*, 737–738.
12. W. Saenger, *Principles of Nucleic Acid Structures*, *Springer*, Berlin, **1984**.
13. The adenine-uracil (A-U) pair also plays an important role in the process, containing RNA.[44] However, A-U will be discussed as a simple derivative of A-T in this work, since the difference seems small.
14. X. Wang, A. R. Chandrasekaran, Z. Shen, Y. P. Ohayon, T. Wang, M. E. Kizer, R. Sha, C. Mao, H. Yan, X. Zhang, S. Liao, B. Ding, B. Chakraborty, N. Jonoska, D. Niu, H. Gu, J. Chao, X. Gao, Y. Li, T. Ciengshin, N. C. Seeman, *Chem. Rev.* **2019**, *119*, 6273−6289; J.-L. Mergny, D. Sen, *Chem. Rev.* **2019**, *119*, 6290−6325; F. C. Simmel, B. Yurke, H. R. Singh, *Chem. Rev.* **2019**, *119*, 6326−6369; S. S. Wang, A. D. Ellington, *Chem. Rev.* **2019**, *119*, 6370−6383; M. Madsen, K. V. Gothelf, *Chem. Rev.* **2019**, *119*, 6384−6458.
15. a) B. Yang, A. R. Moehlig, C. E. Frieler, M. T. Rodgers, *J. Phys. Chem. B* **2015**, *119*, 1857−1868; b) Q. Hu, H. Li, L. Wang, H. Gu, C. Fan, *Chem. Rev.* **2019**, *119*, 6459−6506.
16. S. Hayashi, K. Matsuiwa, M. Kitamoto, W. Nakanishi, *J. Phys. Chem. A* **2013**, *117*, 1804–1816.
17. T. Nishide, S. Hayashi, W. Nakanishi, *ChemistryOpen* **2018**, *7*, 565–575.
18. The basic concept for the compliance constants was introduced by Taylor and Pitzer,[45] followed by Konkoli and Cremer.[46] Equation (2-12) in Chapter 2 was formulated based on the concept.[20a,47,48]
19. K. Brandhorst, J. Grunenberg, *Chem. Soc. Rev.* **2008**, *37*, 1558–1567.

20. a) J. Grunenberg, *J. Am. Chem. Soc.* **2004**, *126*, 16310–16311; b) J. Grunenberg, G. Barone, *RSC Adv.* **2013**, *3*, 4757–4762.
21. W. Nakanishi, S. Hayashi, *Int. J. Quantum Chem.* **2018**, *118*, e25590.
22. W. Nakanishi, S. Hayashi, K. Narahara, *J. Phys. Chem. A* **2008**, *112*, 13593–13599.
23. W. Nakanishi, S. Hayashi, K. Narahara, *J. Phys. Chem. A* **2009**, *113*, 10050–10057.
24. W. Nakanishi, S. Hayashi, *Curr. Org. Chem*. **2010**, *14*, 181–197.
25. W. Nakanishi, S. Hayashi, K. Matsuiwa, M. Kitamoto, *Bull. Chem. Soc. Jpn*. **2012**, *85*, 1293–1305.
26. S. Hayashi, T. Nishide, W. Nakanishi, *Bull. Chem. Soc. Jpn.* **2019**, *92*, 87–96.
27. R. F. W. Bader, *Atoms in Molecules. A Quantum Theory*; Oxford University Press, Oxford, UK, **1990**.
28. C. F. Matta, R. J. Boyd, *An Introduction to the Quantum Theory of Atoms in Molecules* in *The Quantum Theory of Atoms in Molecules: From Solid State to DNA and Drug Design* (Eds.: C. F. Matta, R. J. Boyd), WILEY-VCH: Weinheim, Germany, **2007**, Ch. 1.
29. *Gaussian 09, Revision D.01*, M. J. Frisch, G. W. Trucks, H. B. Schlegel, G. E. Scuseria, M. A. Robb, J. R. Cheeseman, G. Scalmani, V. Barone, B. Mennucci, G. A. Petersson, H. Nakatsuji, M. Caricato, X. Li, H. P. Hratchian, A. F. Izmaylov, J. Bloino, G. Zheng, J. L. Sonnenberg, M. Hada, M. Ehara, K. Toyota, R. Fukuda, J. Hasegawa, M. Ishida, T. Nakajima, Y. Honda, O. Kitao, H. Nakai, T. Vreven, J. A. Montgomery, Jr., J. E. Peralta, F. Ogliaro, M. Bearpark, J. J. Heyd, E. Brothers, K. N. Kudin, V. N. Staroverov, R. Kobayashi, J. Normand, K. Raghavachari, A. Rendell, J. C. Burant, S. S. Iyengar, J. Tomasi, M. Cossi, N. Rega, J. M. Millam, M. Klene, J. E. Knox, J. B. Cross, V. Bakken, C. Adamo, J. Jaramillo, R. Gomperts, R. E. Stratmann, O. Yazyev, A. J. Austin, R. Cammi, C. Pomelli, J. W. Ochterski, R. L. Martin, K. Morokuma, V. G. Zakrzewski, G. A. Voth, P. Salvador, J. J. Dannenberg, S. Dapprich, A. D. Daniels, Ö. Farkas, J. B. Foresman, J. V. Ortiz, J. Cioslowski, D. J. Fox, Gaussian, Inc., Wallingford CT, **2009**.
30. a) C. Møller, M. S. Plesset, *Phys. Rev.* **1934**, *46*, 618–622; b) J. Gauss, *J. Chem. Phys.* **1993**, *99*, 3629–3643; c) J. Gauss, *Ber. Bunsen-Ges. Phys. Chem.* **1995**, *99*, 1001–1008.
31. Y. Zhao, D. G. Truhlar, *Theor. Chem. Acc.* **2008**, *120*, 215–241.
32. The M06-2X level seems a nice candidate for the evaluations, since the optimizations at the level reproduce well the observed structures, containing the HB species, relative to other DFT levels, although the structures of molecular complexes would not. QTAIM functions and QTAIM-DFA parameters evaluated at the M06-2X level seem close to those obtained at the MP2 level on average. QTAIM functions evaluated at the MP2 level are shown to be very close to those determined by the high-resolution X-ray determination of electron densities of some interactions.[49,50]
33. The C_{ij} values and the coordinates corresponding to C_{ii} were calculated by using the Compliance 3.0.2 program released by J. Grunenberg and K. Brandhorst.
34. K. Brandhorst, J. Grunenberg, *J. Chem. Phys.* **2010**, *132*, 184101.
35. J. Grunenberg, *Chem. Sci.* **2015**, *6*, 4086–4088.

36. F. Biegler-König, *J. Comput. Chem.* **2000**, *21*, 1040.
37. T. A. Keith, AIMAll (Version 17.11.14), TK Gristmill Software, Overland Park, KS, USA, **2017**, http://www.aim.tkgristmill.com.
38. Indeed, the "standard orientation" and "ModRedundant method" are specific to the Gaussian program, but the terms are used in this work. The results based on the perturbed structures generated with the Z-matrix method are very similar to those using the ModRedundant method. However, the convergence is much better with the ModRedundant method, relative to the case with the Z-matrix method, if the species to be optimized becomes complex and/or larger. Therefore, the results with ModRedundant method are employed for the discussion in this work.
39. P. Jure ka, P, Hobza, *J. Am. Chem. Soc.* **2003**, *125*, 15608–15613; J. poner, P. Jure ka, P. Hobza, *J. Am. Chem. Soc.* **2004**, *126*, 10142−10151; B. Yang, A. R. Moehlig, C. E. Frieler, M. T. Rodgers, *J. Phys. Chem. B* **2015**, *119*, 1857−1868; H. Sun, S. Zhanga, Z. Sun, *Phys. Chem. Chem. Phys.* **2015**, *17*, 4337–4345; M. Roomana, R. Wintjens, *J. Biomol. Struct. Dyn.* **2014**, *32*, 532–545; see also A. Müller, F. Talbot, S. Leutwyler, *J. Am. Chem. Soc.* **2002**, *124*, 14486–14494.
40. S. Hayashi, T. Nishide, K. Ueda, K. Hayama, W. Nakanishi, *ChemistrySelect* **2019**, *4*, 6198 – 6208.
41. The similarity of Equation (6-4) for C_{ii} to the Ohm's low for the resistors in parallel is of very interest. The mechanism to hold Equation (6-4) would be close to that for the Ohm's low of the parallel resistors, however, the similarity could be superficial rather than intrinsic. The strong mutual interactions between each HB in the multi-HB system will occur in the HB interaction network between Nu-Nu′, whereas no such interactions are supposed in the parallel resistor network, although the two network systems seem close with each other. It is beyond the scope of this work to clarify the mechanism for Equation (6-4); however, it would be instructive to consider the common behavior between the two networks. A parallel resistive circuit is defined as one where the resistors are connected to the same two points (or nodes) and is identified by the fact that it has more than one current path connected to a common voltage source. As a result, the total reciprocal value of the resistance (R_T^{-1}) is given by the sum of the reciprocal individual resistance (R_i^{-1}) ($R_T^{-1} = S_i R_i^{-1}$) under a common voltage across the resistors in parallel, while the total current (I_T) is given by the sum of the individual current (I_i) in each current path ($I_T = S_i I_i$). Here, $(1/C_{ii})$Nu-Nu′ and $(1/C_{ii})$Nu-Nu′$_{:k}$ in Equation (6-4) correspond to R_T^{-1} and R_i^{-1}, respectively, for the parallel resistor network, while ΔE and $\Delta E_{e:i}$ in Equation (6-5) do to I_T and I_i, respectively. Namely, the total and each C_{ii} in the multi-HB system between Nu-Nu′ work as if they are R_T and R_i in the parallel resistor network, according to the Ohm's low, while the total and each energies for Nu–Nu′ (ΔE and $\Delta E_{e:i}$, respectively) act as if they are I_T and I_i, respectively. The energy for the strong mutual interactions between each HB in the multi-HBs between Nu-Nu′ would be reasonably fractionalized to each HB based on $1/C_{ii}$, which would be the reason for Equations (6-3)–(6-5) to be hold.
42. To simplify the discussion of the behavior of multi-HBs in Nu-Nu', Nu-Nu' are divided into four groups based on the multi-HBs types. The first group is G(**AT**), which consists of two strong

NH-∗-N and NH-∗-O with a weak vdW interaction. G(**AT**) contains A-U, C-C, C-T, C-U, A-G, and G-T. A-C contains strong NH-∗-N and NH-∗-O with a negligibly weak undetected CH···HC interaction as a BP, therefore, A-C is tentatively regarded to be G(**AT**). The second group is G(**CG**), which contains three strong NH-∗-N, NH-∗-O and NH-∗-O. C-G is the only one member in G(**CG**). The third group is G(**AA**), which contains one strong NH-∗-N and a weak CH-∗-N. A-A is the only one member in G(**AA**). The fourth group is called G(**TT**), where double strong NH-*-O are contained in T-T. TU and UU belong to G(**TT**). G-G is tentatively contained in G(**TT**), although it contains two strong NH-∗-O interactions and two weak NH-∗-O interactions.

43. M. Z. Brela, O. Klimas, E. Surmiak, M. Boczar, T. Nakajima, M. J. Wójcik, *J. Phys. Chem. A* **2019**, *123*, 10757−10763.
44. A. Rich, S. Zhang, *Nat. Rev. Genet.* **2003**, *3*, 566–572; U. Nagaswamy, M. Larios-Sanz, J. Hury, S. Collins, Z. Zhang, Q. Zhao, G. E. Fox, *Nucleic Acids Res.* **2002**, *30*, 395−397; N. B. Leontis, A. Lescoute, E. Westhof, *Curr. Opin. Struct. Biol.* **2006**, *16*, 279−287; W. A. Cantara, P. F. Crain, J. Rozenski, J. A. McCloskey, K. A. Harris, X. Zhang, F. A. Vendeix, D. Fabris, P. F. Agris, *Nucleic Acids Res.* **2011**, *39*, D195−201; Genesilico. *Modomics: A Database of RNA Modification Pathways*, http://modomics.genesilico.pl/; Accessed Sept 15, 2013.
45. W. T. Taylor, K. S. Pitzer, *J. Res. Natl. Bur. Stand.* **1947**, *38*, 1–17.
46. Z. Konkoli, D. Cremer, *Int. J. Quantum Chem*. **1998**, *67*, 1–9.
47. a) J. Grunenberg, N. Goldberg, *J. Am. Chem. Soc.* **2000**, *122*, 6045–6047; b) J. Grunenberg, R. Streubel, G. v. Frantzius, W. Marten, *J. Chem. Phys.* **2003**, *119*, 165–169.
48. Y. Xie, H. F. I. Schaefer, *Z. Phys. Chem.* **2003**, *217*, 189–203.
49. W. Nakanishi, S. Hayashi, M. B. Pitak, M. B. Hursthouse, S. J. Coles, *J. Phys. Chem. A* **2011**, *115*, 11775–11787.
50. Y. Tsubomoto, S. Hayashi, W. Nakanishi, L. K. Mapp, S. J. Coles, *RSC Adv.* **2018**, *8*, 9651–9660.

Chapter 7

Intrinsic Dynamic and Static Natures of $^{A}Pn\cdot\cdot X^{+}\cdot\cdot{}^{B}Pn$ σ(3c–4e) Type Interactions ($^{A}Pn = {}^{B}Pn$ = N, P, As, and Sb; X = H, F, Cl, Br, and I) in Bicyclo[3.3.3] and Bicyclo[4.4.4] Systems and the Behavior, Elucidated with QTAIM Dual Functional Analysis

Abstract

The intrinsic dynamic and static natures of $^{A}Pn\cdot\cdot X^{+}\cdot\cdot{}^{B}Pn$ ($^{A}Pn = {}^{B}Pn$: N, P, As, and Sb; X = H, F, Cl, Br, and I) in **7-1a**$^{+}$–**7-8c**$^{+}$ were elucidated with the quantum theory of atoms-in-molecules dual functional analysis (QTAIM-DFA). Species **7-1a**$^{+}$–**7-8c**$^{+}$ were formed by incorporating X^{+} between ^{A}Pn and ^{B}Pn of $^{A}Pn(CH_2CH_2CH_2)_3{}^{B}Pn$ (**7-1**–**7-4**) and $^{A}Pn(CH_2CH_2CH_2CH_2)_3{}^{B}Pn$ (**7-5**–**7-8**). The relative stabilities between the symmetric and nonsymmetric structures along with their transition states were investigated. Various natures from typical hydrogen bonds (*t*-HB) to classical covalent bonds were predicted for the $^{A}Pn–X/{}^{B}Pn–X$ interactions in $^{A}Pn\cdot\cdot X^{+}\cdot\cdot{}^{B}Pn$ with QTAIM-DFA. The secondary interactions of H–H and X–C were also detected. The vdW to molecular complexes through charge transfer natures were predicted for them. Natural bond orbital analysis clarified that the CT terms were caused by not only $n(^{A}Pn)\rightarrow\sigma^{*}(X–{}^{B}Pn)$ but also $\sigma(^{A}Pn–C)\rightarrow\sigma^{*}(X–{}^{B}Pn)$, $\sigma(^{A}Pn–C/{}^{B}Pn–C)\rightarrow n_p(X^{+})$ and $n(X)\rightarrow n_s(Pn^{+})$. The direction and magnitude of the p-character of $n(^{A}Pn)$ were the factors that determined the types of donor-acceptor interactions. Estimating the order of the interaction strengths was attempted. The σ(3c–4e) characters of $^{A}Pn\cdot\cdot X^{+}\cdot\cdot{}^{B}Pn$ were also examined by analyzing the charge distributions on $^{A}Pn\cdot\cdot X^{+}\cdot\cdot{}^{B}Pn$. These results would provide fundamentally important insight into designing molecules with high functionality containing X^{+} in symmetric and nonsymmetric structures.

Introduction

Many cage compounds have been prepared, so far, and they play an important role in chemistry.[1,2] Bicyclo[3.3.3]undecane (**7-I**) and bicyclo[4.4.4]tetradecane (**7-II**) provide typical types of the frameworks. The bridgehead carbon distances in **7-I** and **7-II** are considered to be the medium size. The original interactions between the methine groups in **7-I** and **7-II** would be negligibly small. However, if the methine groups are replaced by A and A' of the main group atoms or the derivatives in the neutral and charged forms, the A···A' interactions become much stronger. The A···A' interactions make it possible to investigate the natures of the interactions in more detail. The interactions would consist of the repulsive and/or attractive terms. The A···A' interactions change greatly the energy profiles around the interactions relative to the original cases. The changes have profound effects not only on the fine details of the structures but also on the natures of the interactions, which are to be elucidated.

Among a lot of such species,[3–7] the research group of Kawashima demonstrated that 1-hydro-5-carbaphosphatrane and 1-hydro-6-carbaphosphatrane could form an "anti- apicophilic" arrangement.[8–11] Thus, the skeletons of **7-I** and **7-II** could supply the diverse electronic structures and have unique functionalities, such as superbase,[12–14] catalysis,[15–17] and biological activity.[18–21] Alder and coworkers synthesized various derivatives of **7-I** and **7-II** and related species.[3,5,22–25] 1,5-Diazabicyclo[3.3.3]undecane (**7-1**)[22] and 1,6-diazabicyclo[4.4.4]tetradecane (**7-5**)[23] are the typical examples. They reported protonation in cages of various sizes.[26–30] Much attention has been paid to prepare the species with the interactions of the so-called proton sponges and to clarify the properties. While **7-5** could contain a proton in the cage to form a $[N{\cdot\cdot}H{\cdot\cdot}N]^+$ bond, N is protonated from outside the cage in **7-1**. However, Alder mentioned that **7-1** containing a proton in the cage could potentially be kinetically persistent if once formed.[28]

Recently, molecular designs to form $[N\cdots F{-}N]^+$ were theoretically proposed by using the skeletons of **7-1** and **7-5**,[31] in addition to $[C{\cdot\cdot}H{\cdot\cdot}C]^-$ using the bicyclo[3.3.3]undecane backborn.[32,33] Much effort has been made experimentally and theoretically to clarify properties of the symmetric

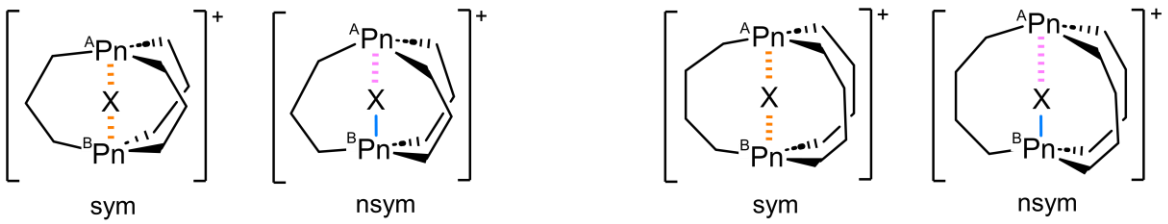

$^{A/B}$Pn = N (**7-1*x*$^+$**), P (**7-2*x*$^+$**), As (**7-3*x*$^+$**), and Sb (**7-4*x*$^+$**). $^{A/B}$Pn = N (**7-5*x*$^+$**), P (**7-6*x*$^+$**), As (**7-7*x*$^+$**), and Sb (**7-8*x*$^+$**).

X = H (***x*** = **a**), F (**b**), Cl (**c**), Br (**d**), and I (**e**).

Chart 7-1. Species **7-1a**$^+$–**7-8e**$^+$ and the definition of the symmetric (sym) and nonsymmetric (nsym) shapes.

(sym) and nonsymmetric (nsym) interactions of the $[N\cdot\cdot X\cdot\cdot N]^+$ (X = F, Cl, Br, and I) form.[34–38] However, few reports seem to contain the systematic research on the compressed $[N\cdot\cdot X\cdot\cdot N]^+$ interactions (X = F, Cl, Br, and I) in cage structures of the medium size.

Investigations in this work were focused to elucidate the natures and the properties of the interactions in $[N\cdot\cdot X\cdot\cdot N]^+$ (X = H, F, Cl, Br, and I) and the pnictogen derivatives. Chart 7-1 shows the structures of **7-1a**$^+$–**7-8e**$^+$ and the definition of the symmetric (sym) and nonsymmetric (nsym) shapes. The $[^{A}Pn\cdot\cdot X\cdot\cdot{}^{B}Pn]^+$ interaction will form through the incorporation of X^+ into $^{A}Pn\cdots{}^{B}Pn$ of **7-1**–**7-8**. Herein, the author reports the results of the investigations on $[^{A}Pn\cdot\cdot X\cdot\cdot{}^{B}Pn]^+$ in **7-1a**$^+$–**7-8e**$^+$, using the original frameworks of **7-I** and **7-II**, where $^{A}Pn = {}^{B}Pn$ = N (**7-1*x***$^+$/**7-5*x***$^+$), P (**7-2*x***$^+$/**7-6*x***$^+$), As (**7-3*x***$^+$/**7-7*x***$^+$), and Sb (**7-4*x***$^+$/**7-8*x***$^+$); X = H (***x*** = **a**), F (**b**), Cl (**c**), Br (**d**), and I (**e**) (see Chart 7-1). The nature of $[^{A}Pn\cdot\cdot X\cdot\cdot{}^{B}Pn]^+$ in **7-1a**$^+$–**7-8e**$^+$ was elucidated after clarifying the structural features and energetic behavior of the species. The subscribe $^+$ as in $[^{A}Pn\cdot\cdot X\cdot\cdot{}^{B}Pn]^+$ will be often omitted from the interaction as in $^{A}Pn\cdot\cdot X\cdot\cdot{}^{B}Pn$, in this work. It is the second issue of this study to clarify the stabilities and the properties of **7-1**–**7-8** and **7-1a**$^+$–**7-8e**$^+$ with the larger pnictogen atoms, in place of the CH groups, at the bridgehead positions of **7-I** and **7-II**. The results of this study will provide useful insight into the $^{A}Pn\cdot\cdot X\cdot\cdot{}^{B}Pn$ σ(3c–4e) interactions such as those in **7-1a**$^+$–**7-8e**$^+$.

The dynamic nature of the $^{A}Pn\cdots X\cdots{}^{B}Pn$ interactions in **7-1a**$^+$–**7-8e**$^+$ under sterically severe conditions need to be clarified. The natures of these interactions are elucidated with QTAIM dual functional analysis (QTAIM-DFA),[39–42] based on the QTAIM approach introduced by Bader.[43,44] In QTAIM-DFA, CIV is employed to generate the perturbed structures (see Chapter 2).[45] The QTAIM-DFA with CIV would be suited to elucidate dynamic and static nature of $^{A}Pn\cdots X\cdots{}^{B}Pn$ under sterically severe conditions in **7-1a**$^+$–**7-8e**$^+$.

Methodological Details in Calculations

Gaussian 09 program was used for the calculations.[46] Various basis set systems (BSSs) were examined to determine suitable BSSs. Table 7-1 shows typical BSSs, examined. The BSS-A employs the basis sets of the Sapporo-TZP with diffuse functions of the 1s1p type (Sapporo-TZP + 1s1p) for all atoms, as implemented from the Sapporo Basis Set Factory.[47] BSS-B employs Sapporo-TZP + 1s1p for ^{A}Pn, ^{B}Pn, and X (= H, F, Cl, Br, and I), together with Sapporo-DZP + 1s1p for C and H. For BSS-C, Sapporo-TZP + 1s1p is applied to ^{A}Pn, ^{B}Pn, and X, whereas Sapporo-DZP is applied to C and H. The Møller–Plesset second order energy correlation (MP2) level[48] was employed for the calculations (MP2/BSS-A, MP2/BSS-B, and MP2/BSS-C). The optimized structures were confirmed by frequency analysis. The results of frequency analysis were used to calculate the coordinates derived from compliance force constants (C_{ii}) for internal vibrations.[49,50] Natural bond orbital (NBO) analysis was performed by the NBO6 program[51] under M06-2X/BSS-B//MP2/BSS-B. The relativistic effects were not considered, which would be the next them of the study, especially on the element of 5th period of Sb and I.

QTAIM functions were calculated using the same basis set system and the level as in the optimizations, unless otherwise noted, and were analyzed with the AIM2000[52] and AIMAll[53] programs. In QTAIM-DFA, $H_b(\boldsymbol{r}_c)$ are plotted versus $H_b(\boldsymbol{r}_c) - V_b(\boldsymbol{r}_c)/2$ for the five data points of w = 0, ±0.05, and ±0.1 in Equations (2-2)–(2-8) of Chapter 2.

Table 7-1. Basis set systems (BSSs) employed for the calculations.

BSSs	C and H	^{A}Pn, ^{B}Pn, and X (= H, F, Cl, Br, and I)
BSS-A	Sapporo-TZP + 1s1p	Sapporo-TZP + 1s1p
BSS-B	Sapporo-DZP + 1s1p	Sapporo-TZP + 1s1p
BSS-C	Sapporo-DZP	Sapporo-TZP + 1s1p

Results and Discussion

Exploring a suitable method for calculations

The structures of **7-2**, **7-5**, and **7-5a**$^+$, optimized with MP2/BSS-A, MP2/BSS-B, and MP2/BSS-C, were carefully compared with the structures, determined by X-ray crystallography.[24,29] Scheme 7-1 illustrates the structural parameters of θ (θ_A and θ_B), d (d_A and d_B), and the least-square planes σ (σ_A and σ_B) for the three C atoms bonding to Pn (^{A}Pn or ^{B}Pn) of **7-1**–**7-4** and **7-5**–**7-8**. The d values are defined to be positive and negative, respectively, if Pn are located outside and inside the σ plane with respect to the molecular center. The "*out*" and "*in*" notations[54] correspond to the positive and negative d values, respectively.

Table 7-2 lists the selected observed and calculated structural parameters for the interaction lengths between ^{A}Pn and ^{B}Pn (r(^{A}Pn–^{B}Pn)), θ_A, θ_B, d_A, and d_B. The differences between the calculated and observed r(^{A}Pn–^{B}Pn) values (Δr(^{A}Pn–^{B}Pn) = r_{calc}(^{A}Pn–^{B}Pn) – r_{obsd}(^{A}Pn–^{B}Pn)) are also provided in Table 7-2. The Δr(^{A}Pn–^{B}Pn) values were 0.027 Å, 0.041 Å, and 0.022 Å for **7-2**, respectively, when calculated with MP2/BSS-A, MP2/BSS-B, and MP2/BSS-C. The values were −0.035 Å, −0.024 Å, and −0.054 Å for **7-5**, respectively, if the three methods were applied. The Δr(^{A}Pn–^{B}Pn) values were 0.003–0.006 Å for **7-5a**$^+$ by the three methods. The coincidence between the calculated and observed values are excellent for **7-5a**$^+$.

The MP2/BSS-A method provided excellent quality results; however, the cost performance in the calculations were poorer if the numbers of primitive gaussian functions necessary for the calculations became larger in **7-1**–**7-8** and **7-1a**$^+$–**7-8e**$^+$. Both MP2/BSS-B and MP2/BSS-C were (very) good with some advantages, whereas disadvantages were observed for purpose of this work. MP2/BSS-B was employed for calculations since the results with MP2/BSS-B were closer to those with MP2/BSS-A relative to those with MP2/BSS-C. One imaginary frequency was predicted for ^{A}N··H··^{B}N in **7-1a**$^+_{sym}$ with MP2/BSS-A and MP2/BSS-B, but all real frequencies were predicted

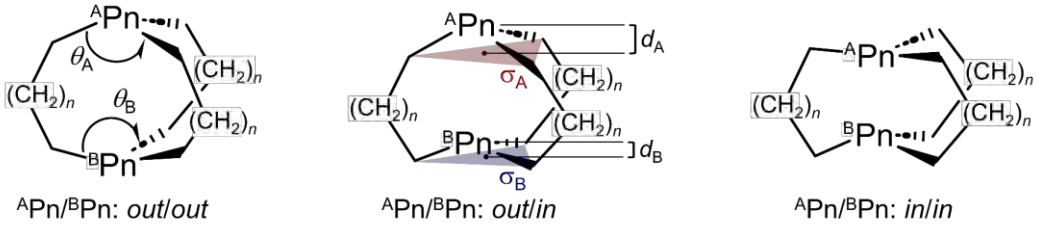

Scheme 7-1. Selected structural parameters of θ (θ_A and θ_B) and d (d_A and d_B) for **7-1**–**7-4** (n = 1) and **7-5**–**7-8** (n = 2) with the least-square planes σ (σ_A and σ_B) for the three C atoms bonded to Pn (^{A}Pn and ^{B}Pn). The d values are defined to be positive and negative, respectively, if Pn are located outside and inside the σ plane with respect to the molecular center. The "*out*" and "*in*" notations correspond to the positive and negative d values, respectively.

with MP2/BSS-C. All real frequencies were predicted for **7-1a**$^{+}_{\mathrm{nsym}}$ with MP2/BSS-B. The results led to select MP2/BSS-B for the calculations. The diffuse functions appeared to play an important role in predicting an imaginary frequency around the bridgehead symmetric interactions in **7-1a**$^{+}$.

Table 7-2. Selected structural parameters of $r(^{A}\mathrm{Pn}–^{B}\mathrm{Pn})$, θ_A, θ_B, d_A, and d_B for **7-2**, **7-5**, and **7-5a**$^{+}$, optimized with MP2/BSS-A, MP2/BSS-B, and MP2/BSS-C, together with the differences for θ_A, θ_B, d_A, and d_B between calculated and observed structures.[a]

BSSs	$r(^{A}\mathrm{Pn}–^{B}\mathrm{Pn})$ (Å)	$\Delta r(^{A}\mathrm{Pn}–^{B}\mathrm{Pn})$[b] (Å)	θ_A[c] (º)	$\Delta\theta_A$[d] (º)	θ_B[c] (º)	$\Delta\theta_B$[e] (º)	d_A[c] (Å)	Δd_A[f] (Å)	d_B[c] (Å)	Δd_B[g] (Å)	Type[h] ^{A}Pn/^{B}Pn
7-2 (^{A}Pn and ^{B}Pn: P; X: null)											
BSS-A	4.1001	0.0268	105.1	–0.7	105.1	–0.4	0.742	0.021	0.742	0.016	*out*/*out*
BSS-B	4.1145	0.0412	105.2	–0.6	105.2	–0.3	0.740	0.019	0.740	0.014	*out*/*out*
BSS-C	4.0957	0.0224	105.6	–0.2	105.6	0.0	0.731	0.010	0.731	0.005	*out*/*out*
Obsd	4.0733	0.0000	105.8	0.0	105.6	0.0	0.721	0.000	0.726	0.000	*out*/*out*
7-5 (^{A}Pn and ^{B}Pn: P; X: null)											
BSS-A	2.7720	–0.0345	115.1	0.2	115.1	0.2	0.323	0.013	–0.323	–0.013	*in*/*in*
BSS-B	2.7826	–0.0239	115.0	0.0	115.0	0.0	0.330	0.020	–0.330	–0.020	*in*/*in*
BSS-C	2.7522	–0.0543	114.9	0.0	114.9	0.0	0.331	0.021	–0.331	–0.021	*in*/*in*
Obsd	2.8065	0.0000	115.0	0.0	115.0	0.0	0.310	0.000	–0.310	–0.000	*in*/*in*
7-5a^{+} (^{A}Pn and ^{B}Pn: P; X: H)											
BSS-A	2.5328	0.0059	112.9	–0.7	112.9	–0.7	0.402	0.020	–0.402	–0.020	*in*/*in*
BSS-B	2.5332	0.0063	112.8	–0.9	112.8	–0.9	0.407	0.025	–0.407	–0.025	*in*/*in*
BSS-C	2.5294	0.0025	112.9	–0.7	112.9	–0.7	0.404	0.022	–0.404	–0.022	*in*/*in*
Obsd	2.5269	0.0000	113.6	0.0	113.6	0.0	0.382	0.000	–0.382	–0.000	*in*/*in*

[a] See Table 7-1 in the text for BSS-A, BSS-B, and BSS-C. [b] $\Delta r(^{A}\mathrm{Pn}–^{B}\mathrm{Pn}) = r_{\mathrm{calc}}(^{A}\mathrm{Pn}–^{B}\mathrm{Pn}) - r_{\mathrm{obsd}}(^{A}\mathrm{Pn}–^{B}\mathrm{Pn})$, where the $r_{\mathrm{calc}}(^{A}\mathrm{Pn}–^{B}\mathrm{Pn})$ and $r_{\mathrm{obsd}}(^{A}\mathrm{Pn}–^{B}\mathrm{Pn})$ are calculated and observed $r(^{A}\mathrm{Pn}–^{B}\mathrm{Pn})$ values, respectively. [c] See Scheme 7-1 in the text for the definition for the selected structural parameters. [d] $\Delta\theta_A = \theta_{A:calc} - \theta_{A:obsd}$, where the $\theta_{A:calc}$ and $\theta_{A:obsd}$ are calculated and observed θ_A values, respectively. [e] $\Delta\theta_B = \theta_{B:calc} - \theta_{B:obsd}$, where the $\theta_{B:calc}$ and $\theta_{B:obsd}$ are calculated and observed θ_B values, respectively. [f] $\Delta d_A = d_{A:calc} - d_{A:obsd}$, where the $d_{A:calc}$ and $d_{A:obsd}$ are calculated and observed d_A values, respectively. [g] $\Delta d_B = d_{B:calc} - d_{B:obsd}$, where the $d_{B:calc}$ and $d_{B:obsd}$ are calculated and observed d_B values, respectively. [h] See Scheme 7-1 in the text for the definition for "*in*" and "*out*" notation. [i] The optimized structures of sym shape are employed for the examination, since the observed structure is very close to D_3 symmetry if Cl^{-} of a counter anion is omitted.

Optimizations and structural features of 7-1–7-8 and 7-1a$^+$–7-8c$^+$

Optimizations were started assuming the C_{3h} symmetry for **7-1a**$^+$–**7-4e**$^+$ and the D_3 symmetry for **7-5a**$^+$–**7-8e**$^+$,[55] although the symmetries were often broken during the optimizations. The minimal structures were optimized with MP2/BSS-B for **7-1a**$^+$–**7-1c**$^+$ (X = H, F, and Cl), **7-2a**$^+$–**7-4b**$^+$ (X = H and F), **7-5a**$^+$–**7-6e**$^+$ (X = H, F, Cl, Br, and I), **7-7a**$^+$–**7-7d**$^+$ (X = H, F, Cl, and Br), and **7-8a**$^+$–**7-8c**$^+$ (X = H, F, and Cl). The optimized minimal structures are collectively written as **7-1a**$^+$–**7-8c**$^+$. The optimized minimal structures were only the symmetric shape for **7-1c**$^+$, **7-4b**$^+$, **7-5c**$^+$–**7-5e**$^+$, and **7-6e**$^+$ and only the nonsymmetric shape for **7-1a**$^+$, **7-5a**$^+$, and **7-7a**$^+$, while they were both for **7-1b**$^+$, **7-2a**$^+$, **7-2b**$^+$, **7-3a**$^+$, **7-3b**$^+$, **7-4a**$^+$, **7-5a**$^+$, **7-5b**$^+$, **7-6a**$^+$–**7-6d**$^+$, **7-7b**$^+$–**7-7d**$^+$, and **7-8a**$^+$–**7-8c**$^+$. The difference between ^{A}Sb··H (1.8823 Å) and ^{B}Sb··H (1.8815 Å) in the optimized structure of **7-4a**$^+$ in the C_3 symmetry was negligibly small in magnitude (0.0008 Å); therefore, it could be recognized to have the symmetric shape. The optimizations were not successfully performed for **7-1e**$^+$–**7-4e**$^+$ (X = I). The reason would be the too large size of I$^+$ to incorporate into ^{A}Pn···^{B}Pn to give the stable species of **7-1e**$^+$–**7-4e**$^+$. Moreover, the optimizations were successful for those other than above species, but multiple imaginary frequencies were predicted after the frequency analysis. Efforts were made to search the minimal structures for the species. However, the trials were unsuccessful under the calculation conditions. The structures of the symmetric and nonsymmetric shapes are conveniently denoted by **7-*mx***$^+_{sym}$ and **7-*mx***$^+_{nsym}$ (***mx*** = **1a**–**8e**), respectively.

Two types of the transition states (TSs) were optimized. One type appears in the site exchange process between the topological isomers of the nsym shape, where the longer and shorter distances in $^{A/B}$Pn··X··$^{B/A}$Pn are changed. Another type appears between the sym and nsym shapes. While the TSs will be **7-*mx***$^+_{tp:TS}$ if the optimized minimal structures are only **7-*mx***$^+_{nsym}$, they will be **7-*mx***$^+_{s\text{-}ns:TS}$ if both **7-*mx***$^+_{sym}$ and **7-*mx***$^+_{nsym}$ are optimized for a species. No TSs will be optimized for a species if the optimized structure is only **7-*mx***$^+_{sym}$. As a result, **7-*mx***$^+_{tp:TS}$ will be optimized for **7-1a**$^+$, **7-5a**$^+$, and **7-7a**$^+$, while **7-*mx***$^+_{s\text{-}ns:TS}$ will appear for **7-1b**$^+$, **7-2a**$^+$, **7-2b**$^+$, **7-3a**$^+$, **7-3b**$^+$, **7-4a**$^+$, **7-5b**$^+$, **7-6a**$^+$–**7-6d**$^+$, **7-7b**$^+$–**7-7d**$^+$, and **7-8a**$^+$–**7-8c**$^+$, under the calculation conditions. Only one imaginary frequency was predicted for each TS. The vibrational motions of TSs corresponding to the imaginary frequencies are shown in Figure 7-A1 of the Appendix, which confirms the intervention of the TSs between the corresponding two structures. Figure 7-1 explains the processes via **7-*mx***$^+_{tp:TS}$ (a) and **7-*mx***$^+_{s\text{-}ns:TS}$ (b), exemplified by **7-5a**$^+_{tp:TS}$ and **7-6b**$^+_{s\text{-}ns:TS}$, respectively. Figure 7-1a illustrates the exchange the longer and shorter distances of $^{A/B}$Pn··X··$^{B/A}$Pn in **7-5a**$^+_{nsym}$ via **7-5a**$^+_{tp:TS}$, where **7-5a**$^+_{nsym}$ is (very) close to **7-5a**$^+_{tp:TS}$, since **7-5a**$^+_{nsym}$ is almost symmetric. Figure 7-1b shows the clear exchange of the geometries around ^{A}P and ^{B}P between **7-6b**$^+_{sym}$ and **7-6b**$^+_{nsym}$ via **7-6b**$^+_{s\text{-}ns:TS}$.

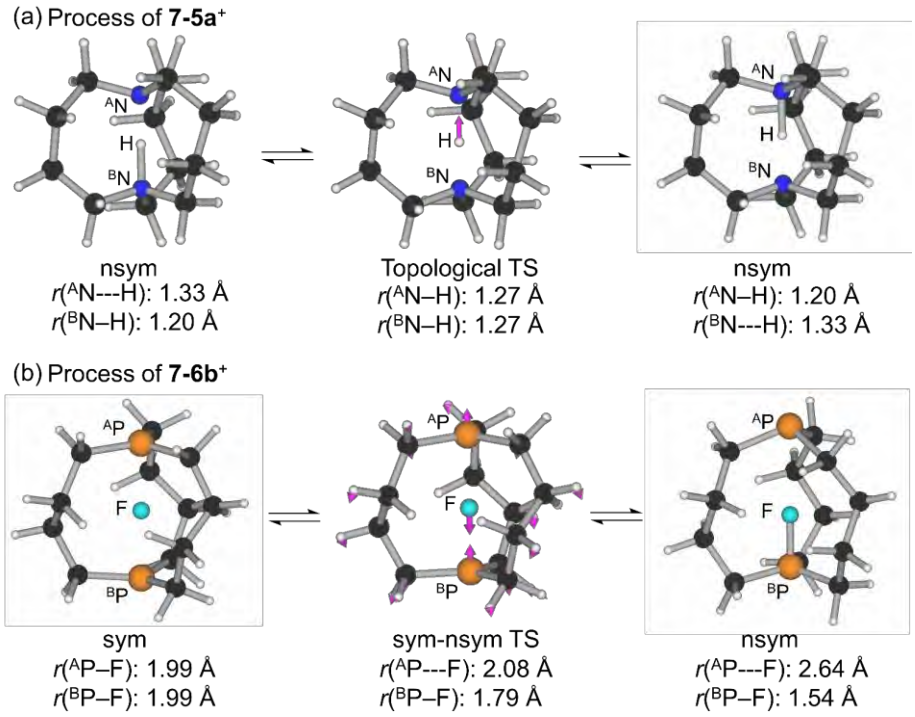

Figure 7-1. Processes via the TSs, exemplified by **7-5*x***$^{+}_{\text{tp:TS}}$ (a) and of **7-6b**$^{+}_{\text{s-ns:TS}}$ (b).

The selected structural parameters optimized with MP2/BSS-B are listed in Table 7-A1 of the Appendix; this table contains the lengths between ^{A}Pn and X (r(^{A}Pn–X)) and between ^{B}Pn and X (r(^{B}Pn–X)), θ_A, θ_B, d_A, d_B, and the types of ^{A}Pn and ^{B}Pn, defined in Scheme 7-1. The *in*/*in* type was predicted for **7-1a**$^{+}_{\text{tp:TS}}$, **7-1a**$^{+}_{\text{nsym}}$, **7-5a**$^{+}_{\text{tp:TS}}$, **7-5a**$^{+}_{\text{nsym}}$, **7-5b**$^{+}_{\text{sym}}$, **7-5c**$^{+}_{\text{sym}}$, **7-5d**$^{+}_{\text{sym}}$, **7-6a**$^{+}_{\text{sym}}$, and **7-7a**$^{+}_{\text{tp:TS}}$, whereas the *out*/*in* type was for the nonsymmetric shape of **7-2a**$^{+}$, **7-5b**$^{+}$, **7-6a**$^{+}$–**7-6d**$^{+}$, **7-7a**$^{+}$–**7-7c**$^{+}$, **7-8a**$^{+}$, and **7-8b**$^{+}$. The *out*/*out* type was optimized for those other than the one listed above. The optimized structures are not shown in the figures, but they can be found in molecular graphs of **7-1**–**7-8** and **7-1a**$^{+}$–**7-8c**$^{+}$, drawn on the optimized structures with MP2/BSS-B.

The Δr_{Cov}($^{A/B}$Pn–X) values for r($^{A/B}$Pn–X) of **7-1a**$^{+}$–**7-8c**$^{+}$ in the optimized structures were calculated from the sum of the covalent radii[56] (r_{Cov}($^{A/B}$Pn–X)). The Δr_{vdW}($^{A/B}$Pn–X) values were similarly calculated from the sum of the van der Waals radii[57,58] (r_{vdW}($^{A/B}$Pn–X)). The values are listed in Table 7-A1 of the Appendix. Each r($^{A/B}$Pn–X) was smaller than the corresponding r_{vdW}($^{A/B}$Pn–X), respectively. The Δr_{Cov}($^{A/B}$Pn–X) values were plotted versus the species numbers, which was shown in Figure 7-2. Each r($^{A/B}$Pn–X) of the symmetric shape was larger than the corresponding r_{Cov}($^{A/B}$Pn–X) (Δr_{Cov}($^{A/B}$Pn–X) > 0), respectively, except for r($^{A/B}$Sb–F) of **7-4b**$^{+}_{\text{sym}}$. While r(^{A}Pn···X) and r(^{B}Pn–H) in each of **7-*mx***$^{+}_{\text{nsym}}$ was longer and shorter than the corresponding r_{Cov}(Pn–X), respectively, except for r(^{B}N–H) in **7-1a**$^{+}_{\text{nsym}}$ and **7-5a**$^{+}_{\text{nsym}}$ and r(^{B}N–F) in **7-1b**$^{+}_{\text{nsym}}$ and **7-5b**$^{+}_{\text{nsym}}$. The overall order of the lengths was r(^{A}Pn···X)$_{\text{nsym}}$ > r(^{A}Pn–X)$_{\text{sym}}$ > r(^{B}Pn–X)$_{\text{nsym}}$. While r(^{A}Pn···X)$_{\text{nsym}}$ and r(^{A}Pn–X)$_{\text{sym}}$ seem noncovalent with the exception of r(^{A}Sb–F) in **7-4b**$^{+}_{\text{sym}}$, r(^{B}Pn–X)$_{\text{nsym}}$ became covalent, except for r(^{B}N–H) of **7-1a**$^{+}_{\text{nsym}}$ and **7-5a**$^{+}_{\text{nsym}}$ and r(^{B}N–F) of **7-1b**$^{+}_{\text{nsym}}$ and **7-5b**$^{+}_{\text{nsym}}$.

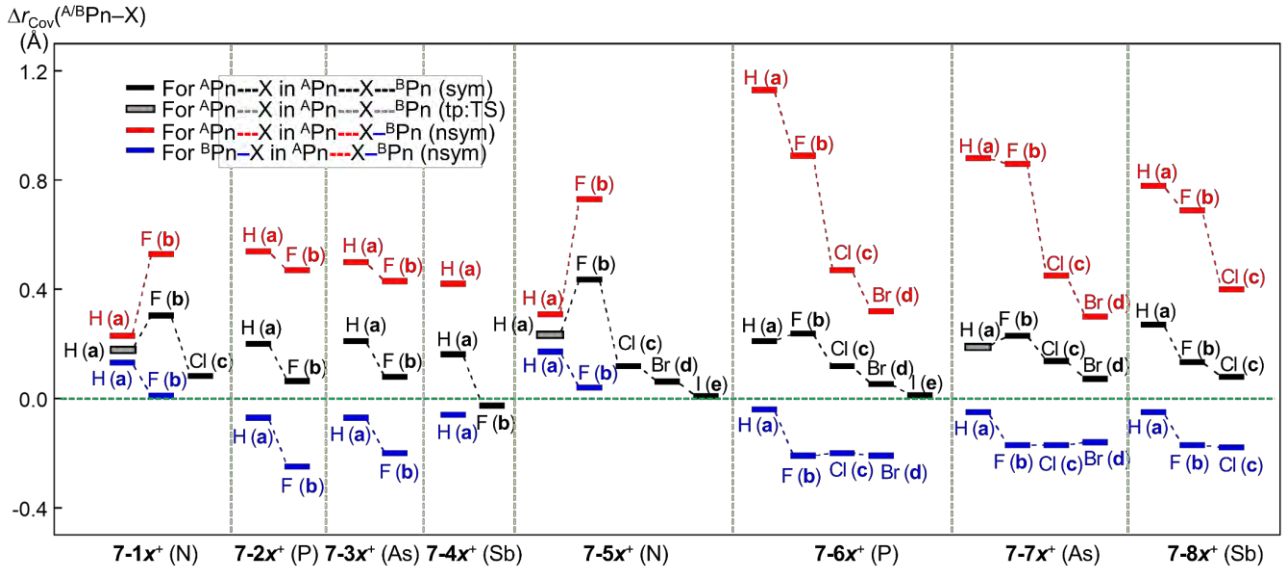

Figure 7-2. Plots of $\Delta r_{Cov}(^{A/B}Pn–X)$ for **7-1a**$^+$–**7-8c**$^+$ of **7-*mx*$^+_{sym}$** and/or **7-*mx*$^+_{nsym}$**, together with **7-1a**$^+$, **7-5a**$^+$, and **7-7a**$^+$ of **7-*mx*$^+_{tp:TS}$**, optimized with MP2/BSS-B, where $\Delta r_{Cov}(^{A/B}Pn–X) = r_{calcd}(^{A/B}Pn–X) - r_{Cov}(^{A/B}Pn–X)$.

Stability of symmetric and nonsymmetric shapes and TSs

The energy values (E: E_{ES} and E_{ZP}) for **7-*mx*$^+_{sym}$**, **7-*mx*$^+_{nsym}$**, **7-*mx*$^+_{s\text{-}ns:TS}$**, and/or **7-*mx*$^+_{tp:TS}$** (***mx*** = **1a**–**8e**) are collected in Table 7-A2 of the Appendix, where E_{ES} and E_{ZP} are E on the energy surface and those corrected with the zero-point energy, respectively. The relative energies (ΔE: ΔE_{ES} and ΔE_{ZP}) are also shown in the table for the species from the global minimum in each group. Each group contains one **7-*mx*$^+_{sym}$**, one **7-*mx*$^+_{nsym}$**, one **7-*mx*$^+_{s\text{-}ns:TS}$**, and/or one **7-*mx*$^+_{tp:TS}$**. A very good correlation was obtained in the plot of ΔE_{ZP} versus ΔE_{ES} ($y = -0.73 + 0.93x$, $R_c^2 = 0.991$), as shown in Figure 7-A2 of the Appendix. As a result, the energy profiles can be discussed using the ΔE_{ES} values.

What are the energies of **7-*mx*$^+_{sym}$**, **7-*mx*$^+_{nsym}$**, **7-*mx*$^+_{s\text{-}ns:TS}$**, and/or **7-*mx*$^+_{tp:TS}$** (***mx*** = **1a**–**8c**), originally? It is instructive to consider the energies of (**7-*mx*$^+_{sym}$** and **7-*mx*$^+_{nsym}$**) from (**7-1**–**7-8** and X^+). The energy differences correspond to those for the formation of (**7-*mx*$^+_{sym}$** and **7-*mx*$^+_{nsym}$**) from (**7-1**–**7-8** and X^+); therefore, they are denoted by ΔE_f ($\Delta E_{f:ES}$ and $\Delta E_{f:ZP}$) (= E(**7-*mx*$^+$**) – E(**7-*mx*** + X^+)), here. $\Delta E_{f:ES}$ must strongly reflect the binding energies around the Pn··X··Pn moieties. The ΔE_f values are calculated for **7-*mx*$^+_{sym}$**, **7-*mx*$^+_{nsym}$**, **7-*mx*$^+_{s\text{-}ns:TS}$**, and/or **7-*mx*$^+_{tp:TS}$**, which are collected in Table 7-A2 of the Appendix.

Figure 7-3 illustrates the $\Delta E_{f:ES}$ values for the global minimum in each group, **7-*mx*$^+_{sym}$** or **7-*mx*$^+_{nsym}$**. The energy levels and arrows are shown in black if **7-*mx*$^+_{sym}$** are the global minima whereas they are in red if **7-*mx*$^+_{nsym}$** is the global minima. Figure 7-3 clearly tells that **7-1**–**7-4** react with H and F to give the stable **7-*m*a**$^+$ and **7-*m*b**$^+$ (m = 1–4), respectively. The structures are all **7-*mx*$^+_{sym}$** for X = F, while they are all **7-*mx*$^+_{nsym}$** for X = H, except for **7-4a**$^+_{sym}$. The cavity size of the bicyclo[3.3.3]

system would not be enough large to give the stable moieties of $[Pn\cdot\cdot X\cdot\cdot Pn]^+$ with X^+ (X = Cl and Br). Indeed, Cl^+ reacts with **7-1** to give **7-1c**$^+_{sym}$, but it is less stable than the components by 307 kJ mol^{-1}. The high energy barrier inside the cavity in **7-1c**$^+_{sym}$ prevents Cl^+ to escape from the cavity, irrespective of the less stable property of **7-1c**$^+_{sym}$ in energy. It is of interest that H^+ tends to give **7-*mx*$^+_{nsym}$**, whereas F^+ to **7-*mx*$^+_{sym}$**.

Species of **7-5**–**7-8** essentially react with all X^+ (X = H, F, Cl, Br, and I) to give stable species. While **7-6** (Pn = P) reacts with all X^+ to give stable species, the adduct of **7-5** (Pn = N) with I^+ was optimized but it is less stable than the components. The adduct of **7-7** (Pn = As) with I^+ was not optimized; moreover, those of **7-8** (Pn = Sb) with Br^+ and I^+ were not, either. The larger cavities in **7-5**–**7-8** of the bicyclo[4.4.4] system seem superior to the narrower ones in **7-1**–**7-4** of the bicyclo[3.3.3] system to give the stable species in the reaction with X^+, especially for X = Br and I. It is also confirmed that the Pn atom affects on the stability of the adducts.

The ΔE_{ES} values for (**7-1a**$^+_{tp:TS}$ from **7-1a**$^+_{nsym}$) and (**7-5a**$^+_{tp:TS}$ from **7-5a**$^+_{nsym}$) were predicted to be very small values of 0.02 and 0.04 kJ mol^{-1}, respectively, in magnitudes. Therefore, it would be difficult to distinguish the two structures clearly. The optimized structures of **7-*mx*$^+_{tp:TS}$** (***mx*** = **1a** and **5a**) must be very close to the corresponding **7-*mx*$^+_{nsym}$** (and **7-*mx*$^+_{sym}$**) (see Table 7-A2 for **7-1a** and **7-5a**). However, ΔE_{ES} for **7-7a**$^+_{tp:TS}$ from **7-7a**$^+_{nsym}$ were predicted to be very large value of 76.2 kJ mol^{-1}. **7-7a**$^+_{tp:TS}$ must be substantially different from **7-7a**$^+_{nsym}$. The optimized structure of **7-7a**$^+_{tp:TS}$ seems symmetric. The differences between Pn = As in **7-7a**$^+$ and Pn = N in **7-1a**$^+$ and **7-5a**$^+$ would be responsible for the results.

Figure 7-4 shows the relative values of ΔE_{ES} (**7-*mx*$^+_{sym}$**), ΔE_{ES} (**7-*mx*$^+_{s\text{-}ns:TS}$**), and ΔE_{ES} (**7-*mx*$^+_{nsym}$**) from the global minimum of each group. As a result, all ΔE_{ES} (**7-*mx*$^+$**) are plotted upside of the corresponding global minimum. The energy levels and the model lines for the reaction coordinates are illustrated in black if ΔE_{ES} (**7-*mx*$^+_{sym}$**) < ΔE_{ES} (**7-*mx*$^+_{nsym}$**), whereas they are in red when ΔE_{ES} (**7-*mx*$^+_{sym}$**) > ΔE_{ES} (**7-*mx*$^+_{nsym}$**). The colors in Figures 7-3 and 7-4 are related to each other. Only one plot in black appeared for each of **7-1b**$^+$, **7-4a**$^+$, and **7-5b**$^+$; therefore, the plots are shown as Figure 7-4a. The plots for (**7-2a**$^+$ and **7-2b**$^+$), (**7-3a**$^+$ and **7-3b**$^+$), (**7-6a**$^+$–**7-6d**$^+$), (**7-7b**$^+$–**7-7d**$^+$), and (**7-8a**$^+$–**7-8c**$^+$) are drawn in Figures 7-4b–f, respectively.

The ΔE_{ES} values for (**7-1b**$^+_{nsym}$ and **7-1b**$^+_{s\text{-}ns:TS}$ from **7-1b**$^+_{sym}$), (**7-4a**$^+_{nsym}$ and **7-4a**$^+_{s\text{-}ns:TS}$ from **7-4a**$^+_{sym}$), and (**7-5b**$^+_{nsym}$ and **7-5b**$^+_{s\text{-}ns:TS}$ from **7-5b**$^+_{sym}$) were predicted to be (70.7 and 72.7 kJ mol^{-1}), (10.0 and 14.8 kJ mol^{-1}), and (91.9 and 95.3 kJ mol^{-1}), respectively, in magnitudes. The results are illustrated in Figure 7-4a with the ΔE_{ES} values. Similarly, the calculated ΔE_{ES} values for **7-*mx*$^+_{nsym}$** and **7-*mx*$^+_{s\text{-}ns:TS}$** from **7-*mx*$^+_{sym}$** (***mx*$^+$** = **2a**$^+$–**8c**$^+$) are drawn in Figures 7-4b–f, respectively.

Figures 7-3 and 7-4 are illustrated in such a way that all processes can be visualized for the formation of **7-*mx*$^+_{sym}$**, **7-*mx*$^+_{nsym}$**, **7-*mx*$^+_{s\text{-}ns:TS}$**, and **7-*mx*$^+_{tp:TS}$** (***mx*** = **1a**–**8c**) from the components, **7-**

1–**7-8** and X^+ (X = H, F, Cl, Br, and I), by overlapping the energy levels of the common species in the two figures. While the red lines should connect to the red ones, the black lines to the black ones, in this process. The $\Delta E_{f:ES}$ values for all species are obtained by adding the values along the processes via the global minimum in a group. (The memory widths on the vertical axes are different.) The ΔE_{ES} values are given in the figures, which are also found in Table 7-A2 of the Appendix.

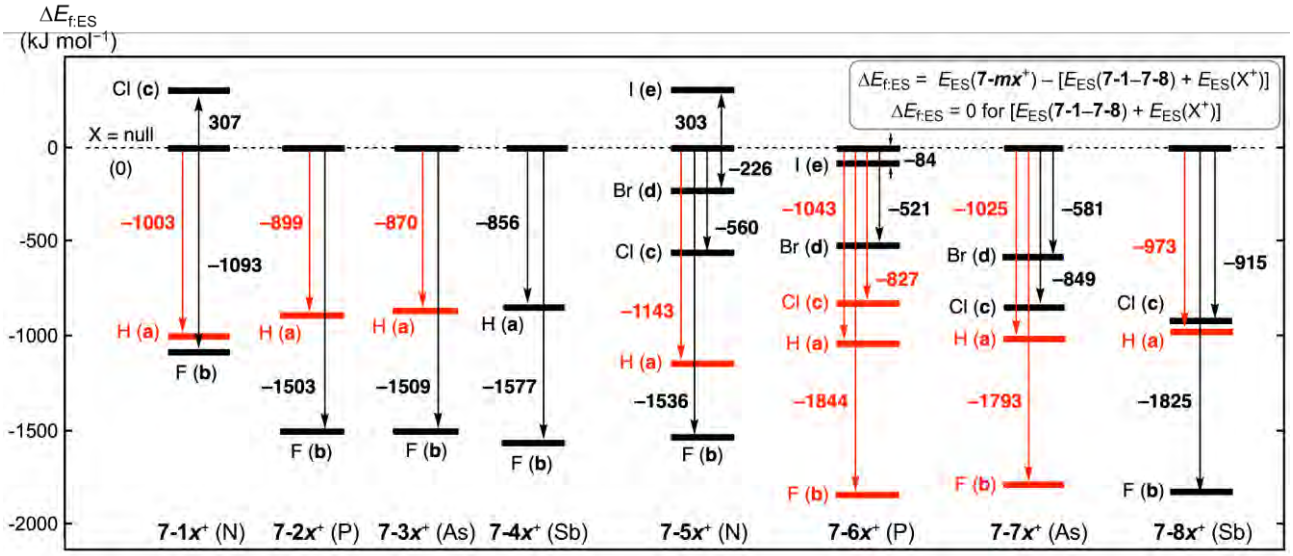

Figure 7-3. Energy profiles for the formation of **7-*mx*$^+$$_{sym}$** and/or **7-*mx*$^+$$_{nsym}$** of the minimal structures from **7-1**–**7-8** and X^+ (X = H, F, Cl, Br, and I), optimized with MP2/BSS-B. The energy of each combination of **7-1**–**7-8** and X^+ was taken as the standard for each energy producing **7-*mx*$^+$$_{sym}$** and/or **7-*mx*$^+$$_{nsym}$**, which are given in kJ mol^{-1}. The energy levels and the values are described in black for **7-*mx*$^+$$_{sym}$**, whereas they are given in red for **7-*mx*$^+$$_{nsym}$** in the diagram.

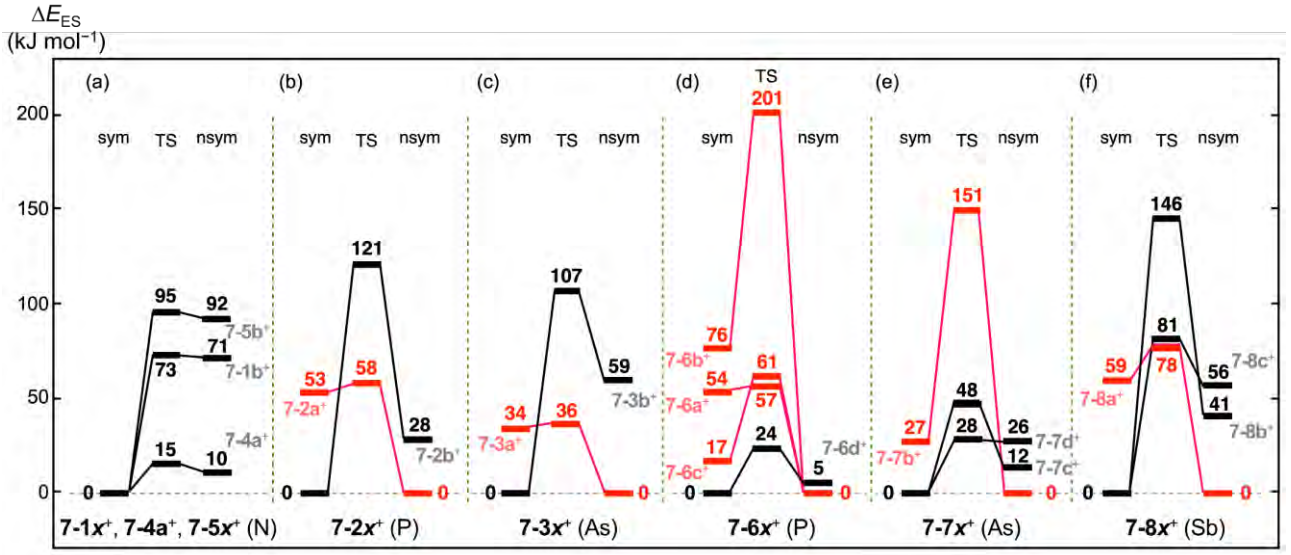

Figure 7-4. Plots of ΔE_{ES} (**7-*mx*$^+$$_{sym}$**), ΔE_{ES} (**7-*mx*$^+$$_{s\text{-}ns:TS}$**), and ΔE_{ES} (**7-*mx*$^+$$_{nsym}$**), optimized with MP2/BSS-B. Plots are for **7-1b**$^+$, **7-4a**$^+$, and **7-5b**$^+$ (a), **7-2a**$^+$ and **7-2b**$^+$ (b), **7-3a**$^+$, and **7-3b**$^+$ (c), **7-6a**$^+$–**7-6d**$^+$ (d), **7-7b**$^+$–**7-7d**$^+$ (e), and **7-8a**$^+$–**7-8c**$^+$ (f). The energy levels and the model lines for the reaction coordinates are illustrated in black when ΔE_{ES} (**7-*mx*$^+$$_{sym}$**) < ΔE_{ES} (**7-*mx*$^+$$_{nsym}$**) and in red if ΔE_{ES} (**7-*mx*$^+$$_{sym}$**) > ΔE_{ES} (**7-*mx*$^+$$_{nsym}$**).

The ΔE_{ES} values for both **7-*mx*$^{+}_{nsym}$** and **7-*mx*$^{+}_{s\text{-}ns:TS}$** increase in the order of Pn = P (in **7-6c**$^{+}$) < As (in **7-7c**$^{+}$) < Sb (in **7-8c**$^{+}$). However, the orders for others are unclear, since some data are lacking due to unsuccessful optimizations and some disorders seem to occur. In the case of **7-6b**$^{+}$–**7-6d**$^{+}$ and **7-7b**$^{+}$–**7-7d**$^{+}$, the ΔE_{ES} values for **7-*mx*$^{+}_{nsym}$** increase in the order of X = F < Cl < Br whereas the values for **7-*mx*$^{+}_{s\text{-}ns:TS}$** decreased in the order of X = F > Cl > Br. The opposite trends between **7-*mx*$^{+}_{nsym}$** and **7-*mx*$^{+}_{s\text{-}ns:TS}$** are of interest. The similar trend was detected in **7-8b**$^{+}_{nsym}$ and **7-8c**$^{+}_{nsym}$, of which ΔE_{ES} values increased in the order of X = F < Cl.

The ^{A}Pn··X··^{B}Pn and/or ^{A}Pn···X–^{B}Pn interactions plays an important role in stabilizing the symmetric and nonsymmetric shapes of **7-1a**$^{+}$–**7-8c**$^{+}$, respectively, together with the TSs, although the contributions seem complex. The secondary interactions also contribute to control the fine details of the structures.

Molecular graphs with contour plots for 7-1–7-8 and 7-1a^{+}–7-8c^{+}

Figure 7-5 shows the molecular graphs with contour plots drawn on the selected minimal structures of **7-1a**$^{+}$–**7-8c**$^{+}$, optimized with MP2/BSS-B. Those of others, containing those for **7-1**–**7-8**, are shown in Figures 7-A3–A5 of the Appendix. The BCPs corresponding to the ^{A}Pn···^{B}Pn interactions were detected for ^{A}N-∗-^{B}N in **7-1** and **7-5** and ^{A}P-∗-^{B}P in **7-6**, although such BCPs were not detected for **7-2**–**7-4**, **7-7**, and **7-8**, due to the clear *out*/*out* structures with the large ^{A}Pn···^{B}Pn distances for **7-7** and **7-8**. The BCPs were detected for ^{A}Pn··X··^{B}Pn in **7-1a**$^{+}$–**7-8c**$^{+}$, along with those for the secondary H-∗-H and X-∗-C interactions in **7-2**–**7-8** and **7-1b**$^{+}$–**7-8c**$^{+}$, together with that for H-∗-^{B}Sb in **7-8a**$^{+}_{sym}$.

The BPs in ^{A}Pn--∗--^{B}Pn and ^{A}Pn-∗-X appeared straight, as shown in Figure 7-5 and Figures 7-A3–A5 of the Appendix. What is the linearity of the BPs for ^{A}Pn--∗--^{B}Pn and Pn-∗-X? The lengths of BPs (r_{BP}) and the straight-line distances (R_{SL}) corresponding to r_{BP} of ^{A}Pn--∗--^{B}Pn in **7-1**, **7-5**, and **7-6** and Pn-∗-X in **7-1a**$^{+}$–**7-8c**$^{+}$ are listed in Table 7-A3 of the Appendix, along with the differences between r_{BP} and R_{SL}, Δr_{BP} (= r_{BP} −R_{SL}). The ^{A}Pn--∗--^{B}Pn and Pn-∗-X interactions in **7-1**, **7-5**, **7-6**, and **7-1a**$^{+}$–**7-8c**$^{+}$ were recognized to be straight, since the Δr_{BP} values were less than 0.01 Å. However, the BPs for H--∗--H and H--∗--^{B}Sb in **7-8a**$^{+}_{nsym}$ and some X--∗--C were bent compared with those of ^{A}Pn--∗--^{B}Pn and Pn-∗-X, of which Δr_{BP} values are provided in Table 7-A4 of the Appendix. The Δr_{BP} values were 0.02–0.23 Å for H--∗--H, H--∗--^{B}Sb in **7-8a**$^{+}_{nsym}$, Cl--∗--C in **7-6c**$^{+}_{nsym}$, Br--∗--C in **7-6d**$^{+}_{sym}$ and **7-6d**$^{+}_{nsym}$, I--∗--C in **7-6e**$^{+}_{sym}$, and F--∗--C in **7-7b**$^{+}_{nsym}$, **7-8b**$^{+}_{sym}$, and **7-8b**$^{+}_{nsym}$. For other X--∗--C, the Δr_{BP} values were less than 0.20 Å; thus, they were approximately straight.

The values of QTAIM functions for $\rho_b(\boldsymbol{r}_c)$, $V_b(\boldsymbol{r}_c)$, $G_b(\boldsymbol{r}_c)$, and $H_b(\boldsymbol{r}_c)$ were calculated at the BCPs that appeared in molecular graphs, as shown in Figure 7-5, for example. Table 7-3 lists the values of the QTAIM functions of $\rho_b(\boldsymbol{r}_c)$, $H_b(\boldsymbol{r}_c) - V_b(\boldsymbol{r}_c)/2$, and $H_b(\boldsymbol{r}_c)$, evaluated with MP2/BSS-B.

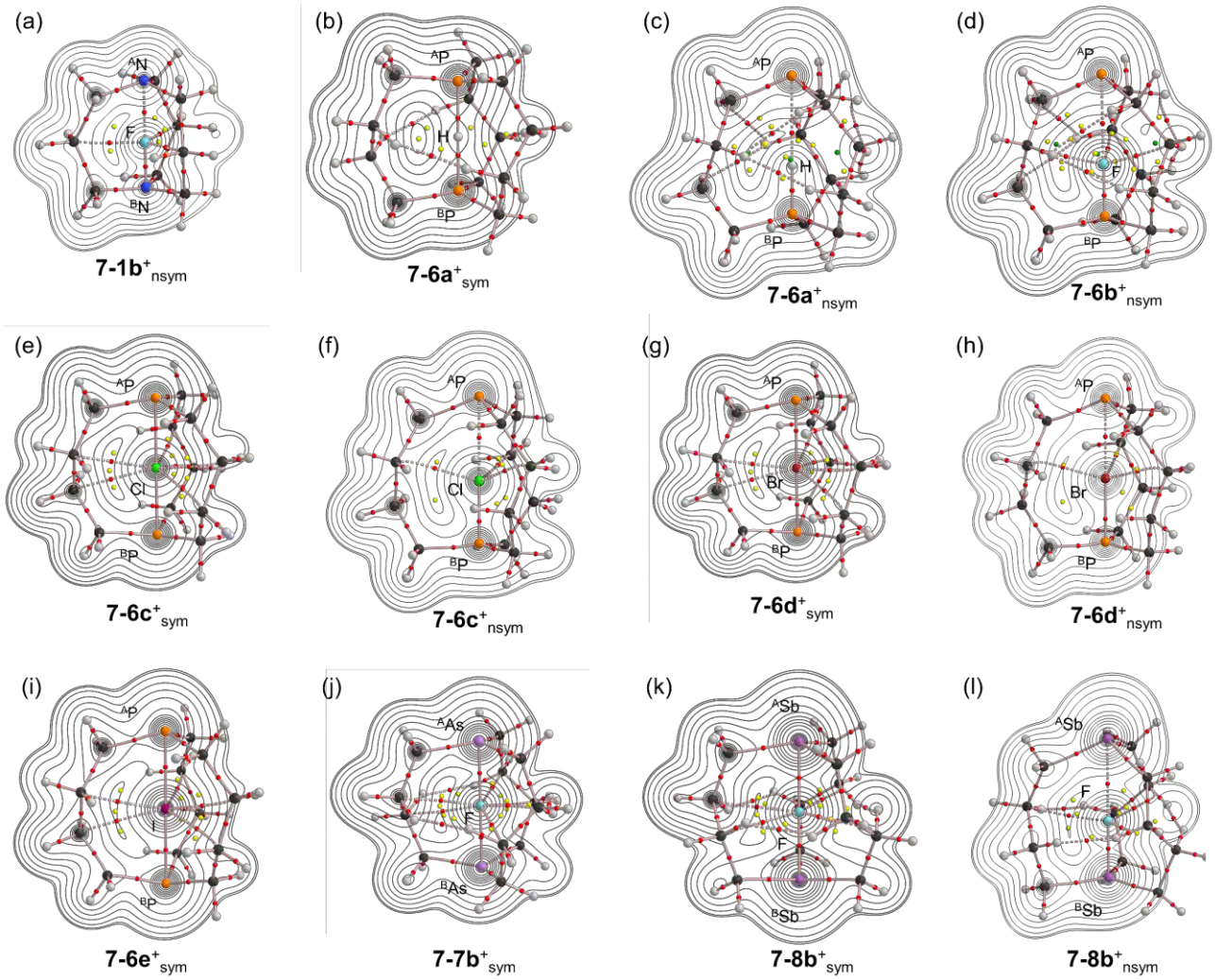

Figure 7-5. Molecular graphs with contour plots for **7-1b**$^{+}_{nsym}$, **7-6a**$^{+}_{sym}$, **7-6a**$^{+}_{nsym}$, **7-6b**$^{+}_{nsym}$, **7-6c**$^{+}_{sym}$, **7-6c**$^{+}_{nsym}$, **7-6d**$^{+}_{sym}$, **7-6d**$^{+}_{nsym}$, **7-6e**$^{+}_{sym}$, **7-7b**$^{+}_{sym}$, **7-8b**$^{+}_{sym}$, and **7-8b**$^{+}_{nsym}$ ((a)–(l), respectively), calculated with MP2/BSS-B. The BCPs are denoted by red dots, RCPs (ring critical points) by yellow dots, CCPs (cage critical points) by green dots, and BPs by pink lines. Carbon, hydrogen, nitrogen, phosphorus, arsenic, antimony, fluorine, chlorine, bromine, and iodine atoms are shown in black, grey, blue, orange, light purple, purple, light green, green, dark red, and dark purple, respectively. Contour plots are drawn on the planes containing at least ^{A}Pn, ^{B}Pn, and X.

Table 7-3. QTAIM functions and QTAIM-DFA parameters of $^{A/B}$Pn-∗-X, ^{A}Pn--∗--X, and/or ^{B}Pn-∗-X for **7-1a**$^+$–**7-8c**$^+$, together with the C_{ii} values and the predicted natures, evaluated with MP2/BSS-B[a,b]

Species (symmetry) **7-*mx*$^+$**$_{sym/nsym}$ ($^{A/B}$Pn-∗-X)	$\rho_b(\boldsymbol{r}_c)$ (ea_o^{-3})	$c\nabla^2\rho_b(\boldsymbol{r}_c)$[c] (au)	$H_b(\boldsymbol{r}_c)$ (au)	R[d] (au)	θ[e] (º)	C_{ii}[f] (Å mdyn^{-1})	θ_p[g] (º)	κ_p[h] (au^{-1})	Predicted nature
7-1a$^+_{nsym}$ (C_1) (^{A}N--∗--H)	0.1815	–0.0445	–0.1805	0.1859	193.9	19.190	205.2	0.1	SS/Cov-s
(^{B}N-∗-H)	0.2364	–0.1009	–0.2959	0.3126	198.8	12.800	206.6	0.0	SS/Cov-s
7-1b$^+_{sym}$ (C_{3h}) ($^{A/B}$N-∗-F)	0.1518	0.0626	–0.0590	0.0860	133.3	0.155	155.0	7.4	*r*-CS/CT-MC
7-1b$^+_{nsym}$ (C_3) (^{A}N--∗--F)	0.0860	0.0520	–0.0155	0.0543	106.6	0.506	146.5	20.1	*r*-CS/*t*-HB$_{wc}$
(^{B}N-∗-F)	0.3334	–0.0212	–0.3316	0.3323	183.7	0.302	199.0	0.1	SS/Cov-s
7-1c$^+_{sym}$ (C_{3h}) (^{A}N-∗-Cl)	0.1790	0.0087	–0.1148	0.1151	175.6	0.547	196.2	1.0	*r*-CS/CT-TBP
7-2a$^+_{sym}$ (C_{3h}) ($^{A/B}$P-∗-H)	0.1088	–0.0180	–0.0709	0.0732	194.2	0.613	198.5	2.2	SS/Cov-w
7-2a$^+_{nsym}$ (C_3) (^{A}P--∗--H)	0.0464	0.0098	–0.0108	0.0146	137.7	0.860	182.7	28.9	*r*-CS/CT-TBP
(^{B}P-∗-H)	0.1980	–0.0091	–0.2209	0.2211	182.4	0.238	128.3	1.7	SS/Cov-s
7-2b$^+_{sym}$ (C_{3h}) ($^{A/B}$P-∗-F)	0.0968	0.0237	–0.0645	0.0687	159.8	0.247	116.8	39.8	*r*-CS/*t*-HB$_{wc}$
7-2b$^+_{nsym}$ (C_3) (^{A}P--∗--F)	0.0455	0.0230	–0.0039	0.0234	99.7	0.480	157.6	79.2	*r*-CS/CT-MC
(^{B}P-∗-F)	0.1987	0.1707	–0.1335	0.2167	128.0	0.125	106.4	0.1	*r*-CS/*t*-HB$_{wc}$
7-3a$^+_{sym}$ (C_{3h}) ($^{A/B}$As-∗-H)	0.0924	–0.0047	–0.0487	0.0489	185.6	0.800	187.1	4.0	SS/Cov-w
7-3a$^+_{nsym}$ (C_3) (^{A}As--∗--H)	0.0438	0.0089	–0.0101	0.0134	138.7	0.981	180.8	21.5	*r*-CS/CT-TBP
(^{B}As-∗-H)	0.1800	–0.0177	–0.1457	0.1468	186.9	0.279	168.6	2.4	SS/Cov-w
7-3b$^+_{sym}$ (C_{3h}) ($^{A/B}$As-∗-F)	0.0918	0.0404	–0.0321	0.0516	128.5	0.267	123.2	0.7	*r*-CS/*t*-HB$_{wc}$
7-3b$^+_{nsym}$ (C_3) (^{A}As--∗--F)	0.0431	0.0213	–0.0036	0.0216	99.6	0.584	140.7	22.0	*r*-CS/*t*-HB$_{wc}$
(^{B}As-∗-F)	0.1848	0.1156	–0.1202	0.1668	136.1	0.154	128.8	1.4	*r*-CS/*t*-HB$_{wc}$
7-4a$^+_{sym}$ (C_3) ($^{A/B}$Sb-∗-H)[i]	0.0764	0.0084	–0.0305	0.0316	164.5	0.646	148.9	4.9	*r*-CS/*t*-HB$_{wc}$
7-4a$^+_{nsym}$ (C_3) (^{A}Sb--∗--H)	0.0409	0.0076	–0.0097	0.0123	142.0	1.174	169.6	15.4	*r*-CS/CT-MC
(^{B}Sb-∗-H)	0.1308	0.0123	–0.0744	0.0754	170.6	0.435	158.1	1.4	*r*-CS/CT-MC
7-4b$^+_{sym}$ (C_{3h}) ($^{A/B}$Sb-∗-F)[j]	0.0856	0.0654	–0.0111	0.0663	99.7	0.282	109.3	164.4	*r*-CS/*t*-HB$_{wc}$
7-5a$^+_{nsym}$ (C_3) (^{A}N--∗--H)	0.1491	–0.0306	–0.1291	0.1327	193.3	10.360	204.6	0.2	SS/Cov-w
(^{B}N-∗-H)	0.2108	–0.0895	–0.2519	0.2673	199.6	6.953	206.1	0.0	SS/Cov-s
7-5b$^+_{sym}$ (D_3) ($^{A/B}$N-∗-F)	0.1116	0.0487	–0.0264	0.0554	118.5	0.305	148.0	9.8	*r*-CS/*t*-HB$_{wc}$
7-5b$^+_{nsym}$ (C_3) (^{A}N--∗--F)	0.0542	0.0330	–0.0015	0.0331	92.5	1.156	128.4	30.8	*r*-CS/*t*-HB$_{wc}$
(^{B}N-∗-F)	0.3091	–0.0186	–0.2833	0.2839	183.8	0.284	197.7	0.0	SS/Cov-s
7-5c$^+_{sym}$ (C_3) ($^{A/B}$N-∗-Cl)	0.1722	0.0049	–0.1042	0.1043	177.3	0.424	194.3	1.6	*r*-CS/CT-TBP
7-5d$^+_{sym}$ (C_2) (^{A}N-∗-Br)	0.1508	0.0072	–0.0963	0.0966	175.7	0.405	186.5	2.2	*r*-CS/CT-TBP
7-5e$^+_{sym}$ (D_3) (^{A}N-∗-I)	0.1262	0.0225	–0.0729	0.0763	162.8	0.403	149.6	14.8	*r*-CS/*t*-HB$_{wc}$

[a] See Table 7-1 for BSS-B. [b] Data are given at the BCPs. [c] $c\nabla^2\rho_b(\boldsymbol{r}_c) = H_b(\boldsymbol{r}_c) - V_b(\boldsymbol{r}_c)/2$, where $c = \hbar^2/8m$. [d] $R = (x^2 + y^2)^{1/2}$, where $(x, y) = (H_b(\boldsymbol{r}_c) - V_b(\boldsymbol{r}_c)/2, H_b(\boldsymbol{r}_c))$. [e] $\theta = 90^o - \tan^{-1}(y/x)$. [f] $C_{ij} = \partial^2 E/\partial f_i \partial f_j$, where i and j refer to internal coordinates, and f_i and f_j, corresponding to i and j, respectively, are the external force components acting on the system. [g] $\theta_p = 90^o - \tan^{-1}(dy/dx)$. [h] $\kappa_p = |d^2y/dx^2|/[1 + (dy/dx)^2]^{3/2}$. [j] Two sets of very close data are predicted from ^{A}Sb-∗-H and ^{B}Sb-∗-H. One set of data are shown here. [j] Data from $w = \pm0.05$, ±0.025, and 0 are used for the plot because a poor correlation is obtained for the data from $w = \pm0.1$, ±0.05, and 0.0.

(Table 7-3 continued.)

Species (symmetry)	$\rho_b(\boldsymbol{r}_c)$	$c\nabla^2\rho_b(\boldsymbol{r}_c)$[c]	$H_b(\boldsymbol{r}_c)$	R[d]	θ[e]	C_{it}[f]	θ_p[g]	κ_p[h]	Predicted
7-*mx*$^+$ $_{sym/nsym}$ ($^{A/B}$Pn-∗-X)	(ea_o^{-3})	(au)	(au)	(au)	(º)	(Å mdyn^{-1})	(º)	(au^{-1})	nature
7-6a$^+_{sym}$ (C_2) ($^{A/B}$P-∗-H)	0.1242	–0.0228	–0.0736	0.0771	197.2	2.470	206.0	0.1	SS/Cov-w
7-6a$^+_{nsym}$ (C_2) (^{A}P--∗--H)	0.0161	0.0048	–0.0003	0.0048	93.9	3.611	134.2	260.5	*r*-CS/*t*-HB$_{wc}$
(^{B}P-∗-H)	0.1857	–0.0217	–0.2041	0.2053	186.1	0.269	129.7	2.6	SS/Cov-s
7-6b$^+_{sym}$ (D_3) ($^{A/B}$P-∗-F)	0.0738	0.0095	–0.0352	0.0365	164.8	0.594	184.0	10.6	*r*-CS/CT-TBP
7-6b$^+_{nsym}$ (C_3) (^{A}P--∗--F)	0.0212	0.0116	0.0023	0.0118	78.9	1.017	91.6	56.9	*p*-CS/*t*-HB$_{nc}$
(^{B}P-∗-F)	0.1843	0.1406	–0.1248	0.1880	131.6	0.149	105.3	0.3	*r*-CS/*t*-HB$_{wc}$
7-6c$^+_{sym}$ (C_1) ($^{A/B}$P-∗-Cl)	0.0895	–0.0016	–0.0488	0.0488	181.8	0.331	192.8	0.1	SS/Cov-w
7-6c$^+_{nsym}$ (C_1) (^{A}P--∗--Cl)	0.0433	0.0123	–0.0074	0.0144	120.8	0.623	170.1	56.4	*r*-CS/CT-MC
(^{B}P-∗-Cl)	0.1670	0.0120	–0.1657	0.1661	175.9	0.201	121.4	3.4	*r*-CS/*t*-HB$_{wc}$
7-6d$^+_{sym}$ (C_3) ($^{A/B}$P-∗-Br)	0.0899	–0.0014	–0.0445	0.0445	181.8	0.326	193.8	1.9	SS/Cov-w
7-6d$^+_{nsym}$ (C_3) (^{A}P--∗--Br)	0.0498	0.0112	–0.0109	0.0157	134.3	0.590	181.3	32.2	*r*-CS/CT-TBP
(^{B}P-∗-Br)	0.1572	–0.0297	–0.1594	0.1621	190.6	0.259	155.2	20.3	SS/Cov-s
7-6e$^+_{sym}$ (D_3) ($^{A/B}$P-∗-I)	0.0851	–0.0014	–0.0397	0.0397	182.1	0.586	196.9	1.0	SS/Cov-w
7-7a$^+_{nsym}$ (C_1) (^{A}As--∗--H)	0.0222	0.0054	–0.0014	0.0056	104.8	3.013	153.3	199.5	*r*-CS/CT-MC
(^{B}As-∗-H)	0.1717	–0.0211	–0.1337	0.1354	189.0	0.301	168.3	2.9	SS/Cov-w
7-7b$^+_{sym}$ (D_3) ($^{A/B}$As-∗-F)	0.0689	0.0226	–0.0186	0.0293	129.4	0.622	133.6	17.3	*r*-CS/*t*-HB$_{wc}$
7-7b$^+_{nsym}$ (C_3) (^{A}As--∗--F)	0.0200	0.0104	0.0020	0.0106	79.2	1.190	91.0	69.7	*p*-CS/*t*-HB$_{nc}$
(^{B}As-∗-F)	0.1734	0.0999	–0.1094	0.1481	137.6	0.174	130.0	1.3	*r*-CS/*t*-HB$_{wc}$
7-7c$^+_{sym}$ (C_2) ($^{A/B}$As-∗-Cl)	0.0757	0.0083	–0.0301	0.0312	164.6	0.362	168.4	11.2	*r*-CS/CT-MC
7-7c$^+_{nsym}$ (C_1) (^{A}As--∗--Cl)	0.0394	0.0113	–0.0061	0.0129	118.3	0.712	166.0	57.7	*r*-CS/CT-MC
(^{B}As-∗-Cl)	0.1471	0.0113	–0.0972	0.0979	173.4	0.245	157.5	2.7	*r*-CS/CT-MC
7-7d$^+_{sym}$ (C_2) ($^{A/B}$As-∗-Br)	0.0754	0.0057	–0.0296	0.0302	169.2	0.358	176.5	6.9	*r*-CS/CT-MC
7-7d$^+_{nsym}$ (C_3) (^{A}As--∗--Br)	0.0464	0.0101	–0.0098	0.0140	134.2	0.743	198.7	46.2	*r*-CS/CT-TBP
(^{B}As-∗-Br)	0.1256	–0.0038	–0.0759	0.0760	182.9	0.504	178.4	14.9	SS/Cov-w
7-8a$^+_{sym}$ (C_3) ($^{A/B}$Sb-∗-H)	0.0689	0.0017	–0.0267	0.0267	176.3	1.108	164.5	25.4	*r*-CS/CT-MC
7-8a$^+_{nsym}$ (C_1) (^{A}Sb--∗--H)	0.0220	0.0047	–0.0019	0.0051	111.8	2.545	162.3	136.5	*r*-CS/CT-MC
(^{B}Sb-∗-H)	0.1320	0.0098	–0.0754	0.0760	172.6	0.357	153.0	1.4	*r*-CS/CT-MC
7-8b$^+_{sym}$ (C_3) ($^{A/B}$Sb-∗-F)	0.0632	0.0345	–0.0072	0.0353	101.8	0.596	99.8	5.0	*r*-CS/*t*-HB$_{wc}$
7-8b$^+_{nsym}$ (C_3) (^{A}Sb--∗--F)	0.0208	0.0096	0.0010	0.0096	84.3	1.821	102.6	66.6	*p*-CS/*t*-HB$_{nc}$
(^{B}Sb-∗-F)	0.1353	0.1004	–0.0465	0.1106	114.8	0.200	121.6	1.5	*r*-CS/*t*-HB$_{wc}$
7-8c$^+_{sym}$ (D_3) ($^{A/B}$Sb-∗-Cl)	0.0640	0.0162	–0.0183	0.0244	138.5	0.418	124.0	7.8	*r*-CS/*t*-HB$_{wc}$
7-8c$^+_{nsym}$ (C_3) (^{A}Sb--∗--Cl)	0.0336	0.0094	–0.0051	0.0107	118.7	0.908	154.0	4.6	*r*-CS/CT-MC
(^{B}Sb-∗-Cl)	0.1130	0.0314	–0.0488	0.0580	147.3	0.272	134.6	2.0	*r*-CS/*t*-HB$_{wc}$

[a] See Table 7-1 for BSS-B. [b] Data are given at the BCPs. [c] $c\nabla^2\rho_b(\boldsymbol{r}_c) = H_b(\boldsymbol{r}_c) - V_b(\boldsymbol{r}_c)/2$, where $c = \hbar^2/8m$. [d] $R = (x^2 + y^2)^{1/2}$, where $(x, y) = (H_b(\boldsymbol{r}_c) - V_b(\boldsymbol{r}_c)/2, H_b(\boldsymbol{r}_c))$. [e] $\theta = 90^o - \tan^{-1}(y/x)$. [f] $C_{ij} = \partial^2 E/\partial f_i \partial f_j$, where i and j refer to internal coordinates, and f_i and f_j, corresponding to i and j, respectively, are the external force components acting on the system. [g] $\theta_p = 90^o - \tan^{-1}(dy/dx)$. [h] $\kappa_p = |d^2y/dx^2|/[1 + (dy/dx)^2]^{3/2}$. [j] Two sets of very close data are predicted from ^{A}Sb-∗-H and ^{B}Sb-∗-H. One set of data are shown here. [J] Data from $w = \pm 0.05$, ± 0.025, and 0 are used for the plot because a poor correlation is obtained for the data from $w = \pm 0.1$, ± 0.05, and 0.0.

Intrinsic dynamic and static natures of ^{A}Pn-∗-X and ^{B}Pn-∗-X in 7-1a^{+}–7-8c^{+}, elucidated with QTAIM-DFA

The natures of the interactions in question in the optimized minimal species are mainly discussed in this section. Figure 7-6 shows the QTAIM-DFA plots of $H_b(\boldsymbol{r}_c)$ versus $H_b(\boldsymbol{r}_c) - V_b(\boldsymbol{r}_c)/2$ for $^{A/B}$Pn-∗-X in **7-*mx*$^{+}_{sym}$** and ^{A}Pn--∗--X and ^{B}Pn-∗-X in **7-*mx*$^{+}_{nsym}$** (see Table 7-3 for the data). The 17 (data) points appeared in the SS region. While the plots for others than those above appeared in the *r*-CS region, except for three, which appeared in the *p*-CS region. The results imply that ^{A}Pn-∗-X, ^{A}Pn--∗--X, and ^{B}Pn-∗-X show various natures of the wide ranges over the *p*-CS to SS regions.

The nature of each Pn-∗-X interaction in **7-1a**$^{+}$–**7-8c**$^{+}$ was classified and characterized with the QTAIM-DFA parameters of (R, θ, θ_p). Table 7-3 lists the analyzed QTAIM-DFA parameters of (R, θ) and (θ_p, κ_p), along with the C_{ii} values, evaluated with MP2/BSS-B. Table 7-3 also provides the intrinsic dynamic and static natures predicted for the interactions.

The (R, θ, θ_p) values are (0.162–0.332 au, 182.4–199.6º, 128.3–206.6º), for ^{A}N--∗--H and ^{B}N-∗-H (**7-1a**$^{+}_{nsym}$), ^{B}N-∗-F (**7-1b**$^{+}_{nsym}$ and **7-5b**$^{+}_{nsym}$), ^{B}P-∗-H (**7-2a**$^{+}_{nsym}$ and **7-6a**$^{+}_{nsym}$), ^{B}N-∗-H (**7-5a**$^{+}_{nsym}$), and ^{B}P-∗-Br (**7-6d**$^{+}_{nsym}$); therefore, the interactions are predicted to have the SS/Cov-s nature. Similarly, the (R, θ, θ_p) values were (0.040–0.147 au, 181.8–197.2º, 168.3–206.0º) for $^{A/B}$P-∗-H (**7-2a**$^{+}_{sym}$ and **7-6a**$^{+}_{nsym}$), $^{A/B}$As-∗-H (**7-3a**$^{+}_{sym}$), ^{B}As-∗-H (**7-3a**$^{+}_{nsym}$ and **7-7a**$^{+}_{nsym}$), ^{A}N--∗--H (**7-5a**$^{+}_{nsym}$), $^{A/B}$P-∗-Cl (**7-6c**$^{+}_{sym}$), $^{A/B}$P-∗-Br (**7-6d**$^{+}_{sym}$), $^{A/B}$P-∗-I (**7-6e**$^{+}_{sym}$), and ^{B}As-∗-Br (**7-7d**$^{+}_{nsym}$); thus, these were predicted to be the SS/Cov-w nature. In the case of CS interactions, the *r*-CS/CT-TBP nature was predicted for $^{A/B}$N-∗-Cl (**7-1c**$^{+}_{sym}$ and **7-5c**$^{+}_{sym}$), ^{A}P--∗--H (**7-2a**$^{+}_{nsym}$), ^{A}As--∗--H (**7-3a**$^{+}_{nsym}$), $^{A/B}$N-∗-Br (**7-5d**$^{+}_{sym}$), $^{A/B}$P-∗-F (**7-6b**$^{+}_{sym}$), ^{A}P--∗--Br (**7-6d**$^{+}_{nsym}$), and ^{A}As--∗--Br (**7-7d**$^{+}_{nsym}$), of which the (θ, θ_p) values were (134.2–177.3º, 180.8–198.7º). The *r*-CS/CT-MC nature was predicted for $^{A/B}$N-∗-F (**7-1b**$^{+}_{sym}$), ^{A}P--∗--F (**7-2b**$^{+}_{nsym}$), ^{A}Sb--∗--H/^{B}Sb-∗-H (**7-4a**$^{+}_{nsym}$ and **7-8a**$^{+}_{nsym}$), ^{A}P--∗--Cl (**7-6c**$^{+}_{nsym}$), ^{A}As--∗--H (**7-7a**$^{+}_{nsym}$), $^{A/B}$As-∗-Cl (**7-7c**$^{+}_{sym}$), ^{A}As--∗--Cl/^{B}As-∗-Cl (**7-7c**$^{+}_{nsym}$), $^{A/B}$As-∗-Br (**7-7d**$^{+}_{sym}$), $^{A/B}$Sb-∗-H (**7-8a**$^{+}_{sym}$), and ^{A}Sb--∗--Cl (**7-8c**$^{+}_{nsym}$), due to the (θ, θ_p) values of (99.7–176.3º, 153.0–176.5º).

The *r*-CS/*t*-HB$_{wc}$ nature was predicted for ^{A}N--∗--F (**7-1b**$^{+}_{nsym}$ and **7-5b**$^{+}_{nsym}$), $^{A/B}$P-∗-F (**7-2b**$^{+}_{sym}$), ^{B}P-∗-F (**7-2b**$^{+}_{nsym}$ and **7-6b**$^{+}_{nsym}$), $^{A/B}$As-∗-F (**7-3b**$^{+}_{sym}$ and **7-7b**$^{+}_{sym}$), ^{A}As--∗--F (**7-3b**$^{+}_{nsym}$), ^{B}As-∗-F (**7-3b**$^{+}_{nsym}$ and **7-7b**$^{+}_{nsym}$), $^{A/B}$Sb-∗-H (**7-4a**$^{+}_{sym}$), $^{A/B}$Sb-∗-F (**7-4b**$^{+}_{sym}$ and **7-8b**$^{+}_{sym}$), $^{A/B}$N-∗-F (**7-5b**$^{+}_{sym}$), $^{A/B}$N-∗-I (**7-5b**$^{+}_{sym}$), ^{A}P--∗--H (**7-6a**$^{+}_{nsym}$), ^{B}P-∗-Cl (**7-6c**$^{+}_{nsym}$), ^{B}Sb-∗-F (**7-8b**$^{+}_{nsym}$), $^{A/B}$Sb-∗-Cl (**7-8c**$^{+}_{sym}$), and ^{B}Sb-∗-Cl (**7-8c**$^{+}_{nsym}$), of which (θ, θ_p) values were (92.5–175.9º, 99.8–149.6º). The (θ, θ_p) values for ^{A}P--∗--F (**7-6b**$^{+}_{nsym}$), ^{A}As--∗--F (**7-7b**$^{+}_{nsym}$), and ^{A}Sb--∗--F (**7-8b**$^{+}_{nsym}$) were (78.9–84.3º, 91.0–102.6º); thus, they were predicted to be the *p*-CS/*t*-HB$_{nc}$ nature.

The differences between θ and θ_p ($\Delta\theta_p = \theta_p - \theta$) are positive for usual interactions, which show normal behavior. However, the $\Delta\theta_p$ values are sometimes negative, which show inverse behavior. The inverse versus normal behavior of interactions in relation to the $\Delta\theta_p$ values, which was proposed

recently, would correspond to some basic properties of interactions.[59] The inverse behavior is often observed when the interaction occurs between the atoms, of which atomic numbers are (very) large. Such cases can be easily found in Table 7-3. The abnormal character of $G_b(\boldsymbol{r}_c)$ at the BCP for the interactions seems responsible for the inverse behavior.

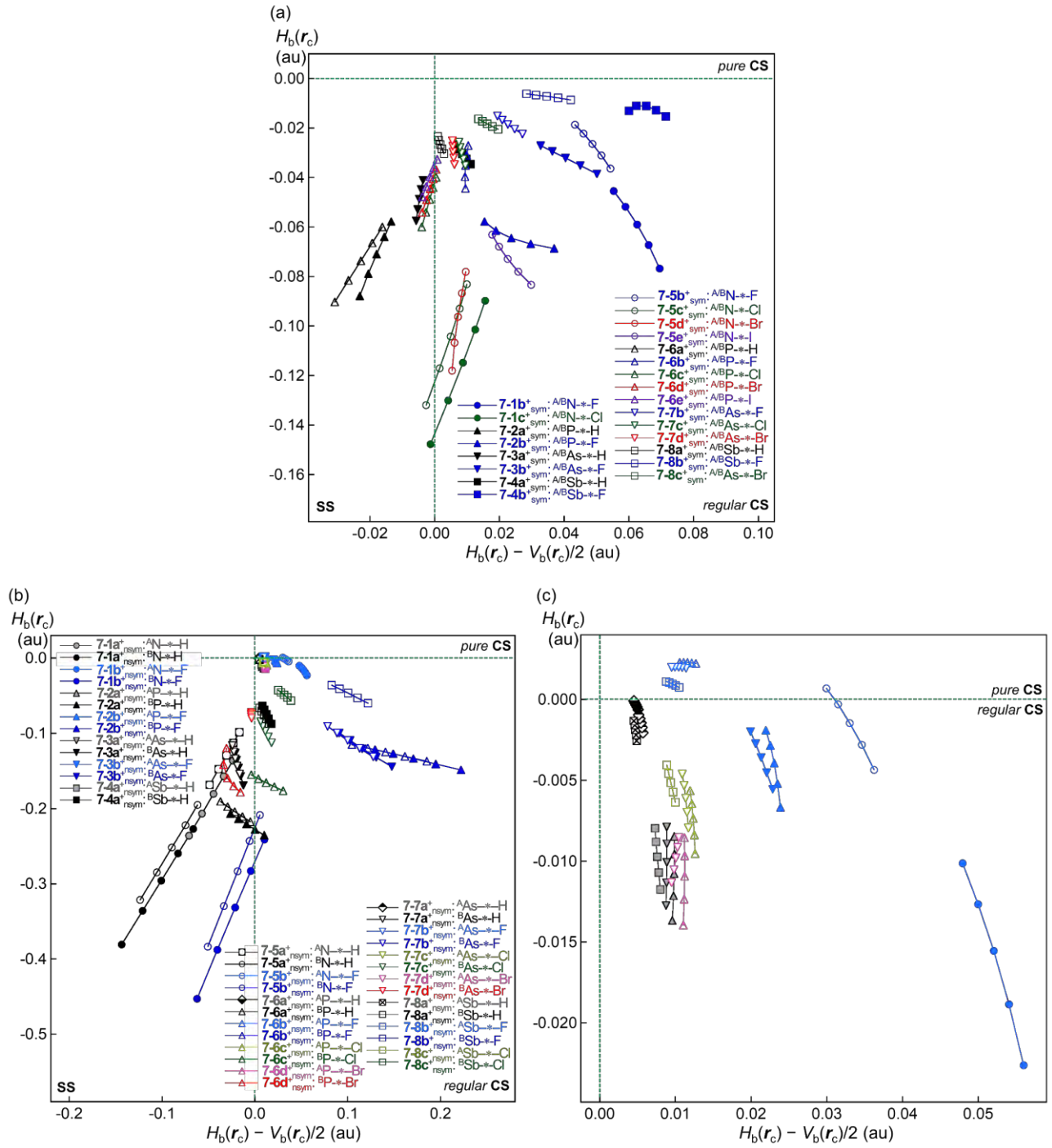

Figure 7-6. QTAIM-DFA plots of $^{A/B}$Pn-∗-X in **7-*mx*$^+_{sym}$** for **7-1b$^+$**, **7-1c$^+$**, **7-2a$^+$**, **7-2b$^+$**, **7-3a$^+$**, **7-3b$^+$**, **7-4a$^+$**, **7-4b$^+$**, **7-5b$^+$**–**7-5e$^+$**, **7-6a$^+$**–**7-6e$^+$**, **7-7b$^+$**–**7-7d$^+$**, and **7-8a$^+$**–**7-8c$^+$** (a), ^{A}Pn--∗--X and ^{B}Pn-∗-X in **7-*m*$^+_{nsym}$** for **7-1a$^+$**, **7-1b$^+$**, **7-2a$^+$**, **7-2b$^+$**, **7-3a$^+$**, **7-3b$^+$**, **7-4a$^+$**, **7-5a$^+$**, **7-5b$^+$**, **7-6a$^+$**–**7-6d$^+$**, **7-7a$^+$**–**7-7d$^+$**, and **7-8a$^+$**–**7-8c$^+$** (b), and a magnified picture of pure and regular CS region around the origin (c), evaluated with MP2/BSS-B.

While the negative $\nabla^2\rho_b(\boldsymbol{r}_c)$ values (= $8m/\hbar^2(H_b(\boldsymbol{r}_c) - V_b(\boldsymbol{r}_c)/2)$) were predicted for some interactions, irrespective of the negative $\Delta r_{Cov}(^{A/B}Pn–X)$ values, which were examined in more detail through the negative Laplacian maps. Figure 7-7 shows the maps for **7-5a**$^+_{tp:TS}$, **7-5a**$^+_{nsym}$, **7-6b**$^+_{nsym}$, **7-6c**$^+_{nsym}$, **7-7b**$^+_{nsym}$, and **7-8a**$^+_{nsym}$, where the maps for **7-5a**$^+_{tp:TS}$ and **7-5a**$^+_{nsym}$ were very close to those previously reported.[60] Similar maps for those other than those above are shown in Figures 7-A6 and A7 of the Appendix. The negative $\nabla^2\rho(\boldsymbol{r})$ area near the electronegative atoms around the ^{B}Pn–X interactions was more widely extended relative to that near the electropositive atoms for **7-2b**$^+_{nsym}$, **7-3b**$^+_{nsym}$, **7-4a**$^+_{nsym}$, **7-6b**$^+_{nsym}$, **7-6c**$^+_{nsym}$, **7-7b**$^+_{nsym}$, **7-7c**$^+_{nsym}$, **7-8a**$^+_{nsym}$, **7-8b**$^+_{nsym}$, and **7-8c**$^+_{nsym}$, along with $^{A/B}$Pn–X one in **7-4b**$^+_{sym}$.

Cremer and Kraka reported that the homonuclear covalent bonds resided in the negative $\nabla^2\rho_b(\boldsymbol{r}_c)$ area, except for F_2, whereas the positive $\nabla^2\rho_b(\boldsymbol{r}_c)$ values sometimes appeared around the heteronuclear bonds.[61] They also demonstrated that distances from the hydrogen atoms to the BCPs changed depending on the differences in the electronegativities of the interacting atoms. As a result, the BCPs moved towards the electropositive atoms rather than the electronegative ones since the electronegative atoms were more negatively charged than the electropositive ones. Similar conditions were observed for ^{B}P-∗-F (**7-2b**$^+_{nsym}$ and **7-6b**$^+_{nsym}$), ^{B}As-∗-F (**7-3b**$^+_{nsym}$ and **7-7b**$^+_{nsym}$), ^{B}Sb-∗-H (**7-4a**$^+_{nsym}$ and **7-8a**$^+_{nsym}$), $^{A/B}$Sb-∗-F (**7-4b**$^+_{sym}$), ^{B}P-∗-Cl (**7-6c**$^+_{nsym}$), ^{B}As-∗-Cl (**7-7c**$^+_{nsym}$), ^{B}Sb-∗-F (**7-8b**$^+_{nsym}$), and ^{B}Sb-∗-Cl (**7-8c**$^+_{nsym}$).

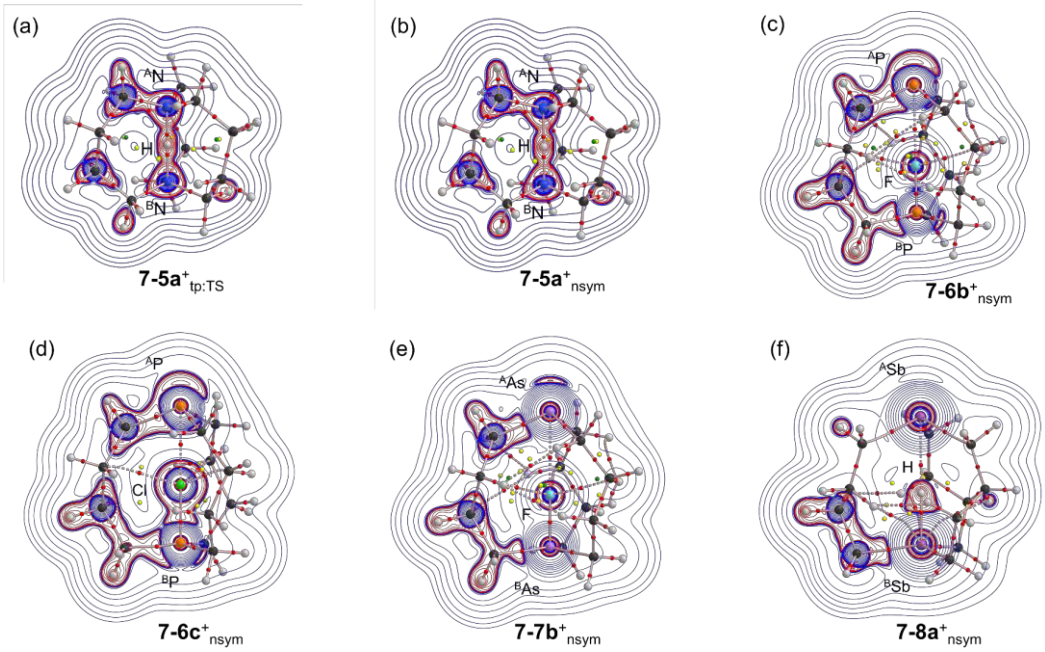

Figure 7-7. Negative Laplacian maps of **7-5a**$^+_{tp:TS}$, **7-5a**$^+_{nsym}$, **7-6b**$^+_{nsym}$, **7-6c**$^+_{nsym}$, **7-7b**$^+_{nsym}$, and **7-8a**$^+_{nsym}$ ((a)–(f), respectively), evaluated with MP2/BSS-B. The BCPs are denoted by red dots, RCPs (ring critical points) by yellow dots, CCPs (cage critical points) by green dots, and BPs by pink lines. Carbon, hydrogen, phosphorus, arsenic, antimony, fluorine, and chlorine atoms are shown in black, grey, orange, light purple, purple, light green, and green, respectively. Contour plots are drawn on the planes containing at least ^{A}Pn, ^{B}Pn, and X. The red and blue lines correspond to the negative and positive areas of $\nabla^2\rho(\boldsymbol{r})$, respectively.

$H_b(\boldsymbol{r}_c)$ is a better indicator than $\nabla^2\rho_b(\boldsymbol{r}_c)$ to elucidate the nature of the CS interactions.[61] The $H_b(\boldsymbol{r}_c)$ values for all Pn···X···Pn bonds in question collected in Table 7-3 are arranged increasing order, which is shown in Equation (7-A1) of Appendix. Equations (7-1)–(7-3) show the partial orders from Equation (7-A1) of Appendix for X = H, X = F, and X = Cl, Br, and I, respectively. Equation (7-1) shows that (i) $H_b(\boldsymbol{r}_c)$ for Pn-∗-H increases in the order of ^{B}Pn-∗-H (**7-*m*a**$^{+}_{nsym}$) < $^{A/B}$Pn-∗-H (**7-*m*a**$^{+}_{sym}$) < ^{A}Pn--∗--H (**7-*m*a**$^{+}_{nsym}$); (ii) Regarding **7-*m***, $H_b(\boldsymbol{r}_c)$ increases in the order of **7-*m*** = (**7-1** and **7-5**: Pn = N) < (**7-2** and **7-6**: Pn = P) < (**7-3** and **7-7**: Pn = As) < (**7-4** and **7-8**: Pn = Sb); (iii) The order in (ii) is clearly observed for the strong interactions in ^{B}Pn-∗-H and $^{A/B}$Pn-∗-H whereas the order becomes vague for the weak ^{A}Pn--∗--H. In the case of Equation (7-2), the trends for X = F are very close to that observed X = H in Equation (7-1), although some discrepancies are observed in the order, such as ^{A}N--∗--F (**7-1b**$^{+}_{nsym}$: –0.016 and **7-5b**$^{+}_{nsym}$: -0.001_5) and $^{A/B}$P-∗-F (**7-2b**$^{+}_{sym}$: –0.065 and **7-6b**$^{+}_{sym}$: –0.035). The order in Equation (7-3) implies that (i) $H_b(\boldsymbol{r}_c)$ of Pn-∗-X increases in the order of X = Cl < Br < I; (ii) The same order for $H_b(\boldsymbol{r}_c)$ of ^{B}Pn-∗-X (**7-*mx***$^{+}_{nsym}$) < $^{A/B}$Pn-∗-X (**7-*mx***$^{+}_{sym}$) < ^{A}Pn--∗--X (**7-*mx***$^{+}_{nsym}$) was also observed for X = Cl, Br, and I. However, the order becomes unclear between ^{B}Pn-∗-X (**7-*mx***$^{+}_{nsym}$) and $^{A/B}$Pn-∗-X (**7-*mx***$^{+}_{sym}$); (iii) The difference in the reactivity between the bicyclo[4.4.4] system versus the bicyclo[3.3.3] system becomes much larger for X = Cl, Br, and I, if compared with the case of X = H and F. The strengths of interactions become weakened inversely proportional to $H_b(\boldsymbol{r}_c)$ being increased. Therefore, the orders in Equations (7-1)–(7-3) show the rough orders of the strengths of the interactions being weakened. However, some deviations were observed.

Order of $H_b(\boldsymbol{r}_c)$ for Pn-∗-X (X = H):

^{B}N-∗-H (**7-1a**$^{+}_{nsym}$: $H_b(\boldsymbol{r}_c)$/au = –0.296) < ^{B}N-∗-H (**7-5a**$^{+}_{nsym}$: –0.252) < ^{B}P-∗-H (**7-2a**$^{+}_{nsym}$: –0.221) < ^{B}P-∗-H (**7-6a**$^{+}_{nsym}$: –0.204) < ^{A}N--∗--H (**7-1a**$^{+}_{nsym}$: –0.181) < ^{B}As-∗-H (**7-3a**$^{+}_{nsym}$: –0.146) < ^{B}As-∗-H (**7-7a**$^{+}_{nsym}$: –0.134) < ^{A}N--∗--H (**7-5a**$^{+}_{nsym}$: –0.129) < ^{B}Sb-∗-H (**7-8a**$^{+}_{nsym}$: –0.075) ≤ ^{B}Sb-∗-H (**7-4a**$^{+}_{nsym}$: -0.074_4) ≤ $^{A/B}$P-∗-H (**7-6a**$^{+}_{sym}$: -0.073_6) < $^{A/B}$P-∗-H (**7-2a**$^{+}_{sym}$: –0.071) < $^{A/B}$As--∗--H (**7-3a**$^{+}_{sym}$: –0.049) < $^{A/B}$Sb-∗-H (**7-4a**$^{+}_{sym}$: –0.030) < $^{A/B}$Sb-∗-H (**7-8a**$^{+}_{sym}$: –0.027) < ^{A}P--∗--H (**7-2a**$^{+}_{nsym}$: -0.010_8) ≤ ^{A}As--∗--H (**7-3a**$^{+}_{nsym}$: -0.010_1) < ^{A}Sb--∗--H (**7-4a**$^{+}_{nsym}$: -0.009_7) < ^{A}Sb--∗--H (**7-8a**$^{+}_{nsym}$: -0.001_9) ≤ ^{A}As--∗--H (**7-7a**$^{+}_{nsym}$: -0.001_4) ≤ ^{A}P--∗--H (**7-6a**$^{+}_{nsym}$: -0.000_3) (7-1)

Order of $H_b(\boldsymbol{r}_c)$ for Pn-∗-X (X = F):

^{B}N-∗-F (**7-1b**$^{+}_{nsym}$: $H_b(\boldsymbol{r}_c)$/au = –0.332) < ^{B}N-∗-F (**7-5b**$^{+}_{nsym}$: –0.283) < ^{B}P-∗-F (**7-2b**$^{+}_{nsym}$: –0.134) < ^{B}P-∗-F (**7-6b**$^{+}_{nsym}$: –0.125) < ^{B}As-∗-F (**7-3b**$^{+}_{nsym}$: –0.120) < ^{B}As-∗-F (**7-7b**$^{+}_{nsym}$: –0.109) < $^{A/B}$P-∗-F (**7-2b**$^{+}_{sym}$: –0.065) < $^{A/B}$N-∗-F (**7-1b**$^{+}_{sym}$: –0.059) < ^{B}Sb-∗-F (**7-8b**$^{+}_{nsym}$: –0.047) < $^{A/B}$P-∗-F (**7-6b**$^{+}_{sym}$: –0.035) < $^{A/B}$As-∗-F (**7-3b**$^{+}_{sym}$: –0.032) < $^{A/B}$N-∗-F (**7-5b**$^{+}_{sym}$: -0.026_4) < $^{A/B}$As-∗-F (**7-7b**$^{+}_{sym}$: –0.019) < ^{A}N--∗--F (**7-1b**$^{+}_{nsym}$: –0.016) < $^{A/B}$Sb-∗-F (**7-4b**$^{+}_{sym}$: -0.011_1) < $^{A/B}$Sb-∗-F (**7-8b**$^{+}_{sym}$: -0.007_2) < ^{A}P--∗--F (**7-2b**$^{+}_{nsym}$: -0.003_9) ≤ ^{A}As--∗--F (**7-3b**$^{+}_{nsym}$: -0.003_6)) < ^{A}N--∗--F (**7-5b**$^{+}_{nsym}$: -0.001_5) ≤ ^{A}Sb--∗--F (**7-8b**$^{+}_{nsym}$: 0.001_0) ≤ ^{A}As--∗--F (**7-7b**$^{+}_{nsym}$: 0.002_0) ≤ ^{A}P--∗--F (**7-6b**$^{+}_{nsym}$: 0.002_3) (7-2)

Order of $H_b(\boldsymbol{r}_c)$ for Pn-*-X (X = Cl, Br, and I):

^{B}P-*-Cl (**7-6c**$^{+}_{nsym}$: $H_b(\boldsymbol{r}_c)$/au = –0166) < ^{B}P-*-Br (**7-6d**$^{+}_{nsym}$: –0.159) > $^{A/B}$N-*-Cl (**7-1c**$^{+}_{sym}$: –0.115) < $^{A/B}$N-*-Cl (**7-5c**$^{+}_{sym}$: –0.104) < ^{B}As-*-Cl (**7-7c**$^{+}_{nsym}$: –0.097) ≤ $^{A/B}$N-*-Br (**7-5d**$^{+}_{sym}$: –0.096) < ^{B}As-*-Br (**7-7d**$^{+}_{nsym}$: –0.076) < $^{A/B}$N-*-I (**7-5e**$^{+}_{sym}$: –0.072$_9$) < $^{A/B}$P-*-Cl (**7-6c**$^{+}_{sym}$: –0.048$_{81}$) ≤ ^{B}Sb-*-Cl (**7-8c**$^{+}_{nsym}$: –0.048$_{80}$) < $^{A/B}$P-*-Br (**7-6d**$^{+}_{sym}$: –0.045) < $^{A/B}$P-*-I (**7-6e**$^{+}_{sym}$: –0.040) < $^{A/B}$As-*-Cl (**7-7c**$^{+}_{sym}$: –0.030$_1$) ≤ $^{A/B}$As-*-Br (**7-7d**$^{+}_{sym}$: –0.029$_6$) < $^{A/B}$Sb-*-Cl (**7-8c**$^{+}_{sym}$: –0.018) < ^{A}P--*--Br (**7-6d**$^{+}_{nsym}$: –0.010$_9$) ≤ ^{A}As--*--Br (**7-7d**$^{+}_{nsym}$: –0.009$_8$) < ^{A}P--*--Cl (**7-6c**$^{+}_{nsym}$: –0.007$_4$) ≤ ^{A}As--*--Cl (**7-7c**$^{+}_{nsym}$: –0.006$_1$) ≤ ^{A}Sb--*--Cl (**7-8c**$^{+}_{nsym}$: –0.005$_1$) (7-3)

What is the behavior of $H_b(\boldsymbol{r}_c)$ in **7-1a**$^{+}$–**7-8c**$^{+}$? Figure 7-8 shows the plot of $H_b(\boldsymbol{r}_c)$ versus $\rho_b(\boldsymbol{r}_c)$ for the sym and nsym shapes of **7-1a**$^{+}$–**7-8c**$^{+}$. The plot was analyzed, assuming the linear correlations, by the four groups of Group A (G(**A**)), G(**B**), G(**C**), and G(**D**). The correlations are very good for G(**A**) ($y = 0.090 - 1.57x$: $R_c^2 = 0.992$), G(**B**) ($y = 0.099 - 1.35x$: $R_c^2 = 0.987$), and G(**C**) ($y = 0.136 - 1.38x$: $R_c^2 = 0.994$) and fairly good for G(**D**) ($y = 0.007 - 0.35x$: $R_c^2 = 0.78$). The plot for G(**A**) appears most downside of the four and that for G(**C**) does most upside, while that for G(**B**) exists between the two. The data for G(**D**) correspond to those from the much weaker bonds of ^{A}Pn--*--X in the nsym shapes; therefore, the (data) points are located near the origin of the plots. The correlation constant for G(**D**) is about one-fourth to one-fifth of those for G(**A**), G(**B**), and G(**C**). Most of the data are contained in G(**A**), which consists of the data from 14 sym shapes and

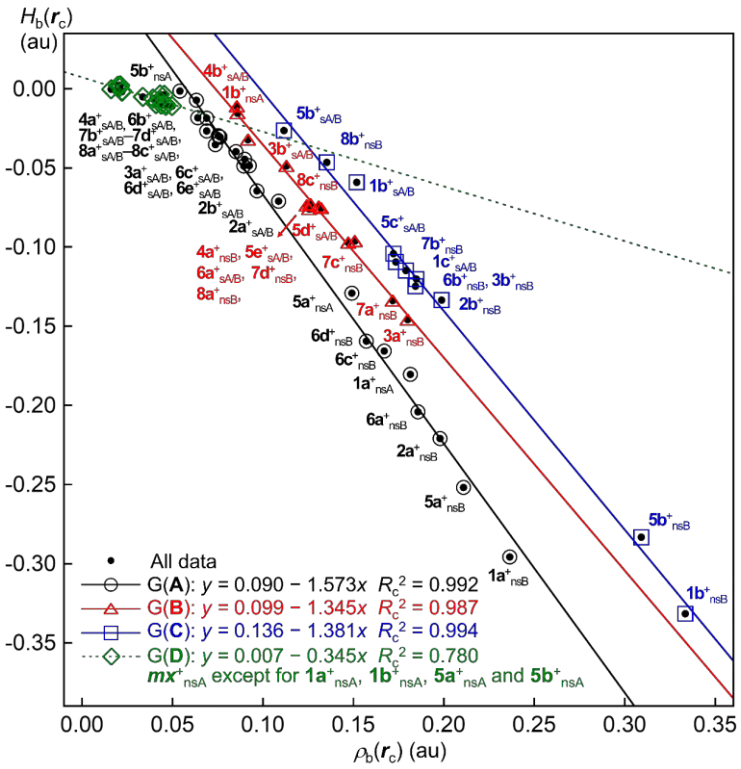

Figure 7-8. Plots of $H_b(\boldsymbol{r}_c)$ versus $\rho_b(\boldsymbol{r}_c)$ for Pn-*-X in **1a**$^{+}$–**8c**$^{+}$, evaluated with MP2/BSS-B. The $^{A/B}$Pn-*-X of **7-*mx***$^{+}_{sym}$ and ^{A}Pn--*--X and ^{B}Pn-*-X of **7-*mx***$^{+}_{nsym}$ are also illustrated in the figure as ***mx***$^{+}_{sA/B}$, ***mx***$^{+}_{nsA}$, and ***mx***$^{+}_{nsB}$, respectively ("**7-**" was omitted for clarification).

seven nsym shapes. G(**B**) contains those from five sym shapes and eight nsym shapes. While G(**C**) contains four sym shapes seven nsym shapes G(**D**) does those for 16 nsym shapes, except for four. (See Figure 7-8 for the interactions and the species.)

The trend in the correlations can be variously explained, but the explanation is as follows: Almost common mechanisms are operating to give $H_b(\boldsymbol{r}_c)$ and $\rho_b(\boldsymbol{r}_c)$ for both sym and nsym shapes of **7-1a**$^+$–**7-8c**$^+$. The mechanisms to give $H_b(\boldsymbol{r}_c)$ and/or $\rho_b(\boldsymbol{r}_c)$ would be very similar for most species but somewhat different for some species. The species with the negligibly small differences in the mechanisms forms a group of G(**A**), G(**B**), G(**C**), or G(**D**); however, there are some differences among the groups. The differences would be caused by the consisting interactions of the groups. G(**C**) and G(**D**) mainly consist of Pn-∗-X (X = F or Cl) and ^{A}Pn--∗--X, respectively, whereas G(**B**) mainly consists of $^{A/B}$Pn-∗-X of ***mx***$^+_{sym}$ and ^{B}Pn-∗-X of ***mx***$^+_{nsym}$, and G(**A**) contains others.

The natures of the secondary interactions of X--∗--C and H--∗--H for **7-1**–**7-8** and **7-1a**$^+$–**7-8c**$^+$ were also investigated with MP2/BSS-B, along with ^{A}Pn--∗--^{B}Pn of **7-1**, **7-5**, and **7-6**. The QTAIM functions and QTAIM-DFA parameters are provided in Table 7-A5 of the Appendix, along with the C_{ii} values and the predicted natures. Various natures of *p*-CS/vdW, *p*-CS/*t*-HB$_{nc}$, *r*-CS/*t*-HB$_{wc}$, and *r*-CS/CT-MC were predicted for X--∗--C and H--∗--H, together with ^{A}Pn--∗--^{B}Pn. These interactions contributed to stabilizing the system, in addition to $^{A/B}$Pn-∗-X, ^{A}Pn--∗--X, and ^{B}Pn-∗-X.

The natures were also elucidated for the interactions in question in the transition states. The analyzed results by QTAIM-DFA are collected in Table 7-A6 of the Appendix, along with molecular graphs and negative Laplacian maps shown in Figures 7-A8 and A9 of the Appendix, respectively.

Second-perturbation energies *E*(2), evaluated with NBO analysis

The contributions from the CT terms of NBO (*i*)→NBO (*j*) to **7-1a**$^+$–**7-8c**$^+$ were estimated through the second-perturbation energies (*E*(2)), calculated using the NBO analysis with M06-2X/BSS-B//MP2/BSS-B. Table 7-4 lists the *E*(2) values for **7-1a**$^+$–**7-8c**$^+$. Several types of the CT terms contribute to stabilize the species. The first is the n(^{A}Pn)→σ*(X–^{B}Pn) type, which operates in 17 species. The *E*(2) values are shown in parenthesis after the compound: The values larger than 30 kcal mol^{-1} are **7-1a**$^+_{nsym}$ (*E*(2) = 78 kcal mol^{-1}), **7-5a**$^+_{nsym}$ (80 kcal mol^{-1}), **7-1b**$^+_{sym}$ (344 kcal mol^{-1}), **7-1c**$^+_{sym}$ (230 kcal mol^{-1}), **7-2b**$^+_{sym}$ (565 kcal mol^{-1}), **7-5b**$^+_{sym}$ (243 kcal mol^{-1}), **7-5c**$^+_{sym}$ (191 kcal mol^{-1}), **7-5d**$^+_{sym}$ (171 kcal mol^{-1}), **7-5e**$^+_{sym}$ (132 kcal mol^{-1}), **7-6a**$^+_{sym}$ (288 kcal mol^{-1}), **7-6c**$^+_{sym}$ (357 kcal mol^{-1}), **7-7c**$^+_{sym}$ (506 kcal mol^{-1}), **7-8a**$^+_{sym}$ (349 kcal mol^{-1}), **7-8b**$^+_{sym}$ (429 kcal mol^{-1}), and **7-8c**$^+_{sym}$ (762 kcal mol^{-1}). The *E*(2) values for the nsym shapes are small to moderate, whereas the values are very large for the sym shapes. The shorter interaction distances in the sym shapes would be responsible for the results.

Table 7-4. Contributions from the CT terms of the NBO (*i*)→NBO (*j*) form to the interactions in **7-1a**$^+$–**7-8c**$^+$, estimated through the second-perturbation energies (*E*(2)), evaluated with NBO analysis under the M06-2X/BSS-B//MP2/BSS-B conditions.[a]

Species (^{A}Pn (^{B}Pn), X)	NBO (*i*)→NBO (*j*)	*E*(2)[b] (kcal mol^{-1})	*E* (*j*) – *E* (*i*)[c] (au)	*F* (*i*,*j*)[d] (au)
7-1a$^+_{nsym}$ (N, H)	n(^{A}N)→σ*(H–^{B}N)	77.6	0.73	0.212
7-1b$^+_{sym}$ (N, F)	n($^{A/B}$N)→σ*(F–$^{B/A}$N)	344.2[e]	0.14	0.198
7-1b$^+_{nsym}$ (N, F)	n(^{A}N)→σ*(F–^{B}N)	11.1	0.46	0.064
7-1c$^+_{sym}$ (N, Cl)	n($^{A/B}$N)→σ*(Cl–$^{B/A}$N)	229.6[e]	0.42	0.277
7-2a$^+_{sym}$ (P, H)	n(^{A}P/^{B}P)→σ(H$^+$)	31.9	0.14	0.060
	σ(^{A}P–C/^{B}P–C)→σ(H$^+$)	55.8[f] (334.8)[g]	0.40	0.134
7-2a$^+_{nsym}$ (P, H)	σ(^{A}P–C)→σ*(H–^{B}P)	10.1[h] (30.3)[g]	0.86	0.083
7-2b$^+_{sym}$ (P, F)	n(^{A}P)→σ*(F–^{B}P)	565.0	0.05	0.142
7-2b$^+_{nsym}$ (P, F)	σ(^{A}P–C)→σ*(F–^{B}P)	1.2[h] (3.6)[g]	0.80	0.027
7-3a$^+_{sym}$ (As, H)	σ(^{A}As–C/^{B}As–C)→σ(H$^+$)	74.6[f] (447.6)[g]	0.32	0.138
7-3a$^+_{nsym}$ (As, H)	σ(^{A}As–C)→σ*(H–^{B}As)	13.5[h] (40.5)[g]	0.76	0.091
7-3b$^+_{sym}$ (As, F)	σ(^{A}As–C)→σ*(F–^{B}As)	3.3[h] (9.8)[g]	0.52	0.037
7-3b$^+_{nsym}$ (As, F)	σ(^{A}As–C)→σ*(F–^{B}As)	1.2[h] (3.6)[g]	0.66	0.025
7-4a$^+_{sym}$ (Sb, H)	σ(^{A}Sb–C/^{B}Sb–C)→σ(H$^+$)	94.3[f] (565.7)[g]	0.20	0.123
7-4a$^+_{nsym}$ (Sb, H)	σ(^{A}Sb–C)→σ*(H–^{B}Sb)	14.3[h] (43.0)[g]	0.64	0.086
7-4b$^+_{sym}$ (Sb, F)	n(F)→n(Sb$^+$)	66.8	0.08	0.066
7-5a$^+_{nsym}$ (N, H)	n($^{A/B}$N)→σ*(H–$^{B/A}$N)	80.4[e]	0.75	0.220
7-5b$^+_{sym}$ (N, F)	n($^{A/B}$N)→σ*(F–$^{B/A}$N)	242.7[e]	0.14	0.162
7-5b$^+_{nsym}$ (N, F)	n(^{A}N)→σ*(F–^{B}N)	12.0	0.35	0.058
7-5c$^+_{sym}$ (N, Cl)	n($^{A/B}$N)→σ*(Cl–$^{B/A}$N)	191.4[e]	0.44	0.259
7-5d$^+_{sym}$ (N, Br)	n($^{A/B}$N)→σ*(Br–$^{B/A}$N)	170.5[e]	0.46	0.251
7-5e$^+_{sym}$ (N, I)	n($^{A/B}$N)→σ*(I–$^{B/A}$N)	131.8[e]	0.51	0.231
7-6a$^+_{sym}$ (P, H)	n($^{A/B}$P)→σ*(H–$^{B/A}$P)	288.1[e]	0.28	0.256
7-6a$^+_{nsym}$ (P, H)	σ(^{A}P–C)→σ*(H–^{B}P)	4.2[h] (12.6)[g]	0.82	0.052
7-6b$^+_{sym}$ (P, F)	n(F)→σ*(^{A}P–^{B}P)	101.8	0.36	0.171
7-6b$^+_{nsym}$ (P, F)	*i*	*i*	*i*	*i*
7-6c$^+_{sym}$ (P, Cl)	n($^{A/B}$P)→σ*(Cl–$^{B/A}$P)	356.9[e]	0.10	0.171
7-6c$^+_{nsym}$ (P, Cl)	σ(^{A}P–C)→σ*(Cl–^{B}P)	1.4[h] (4.1)[g]	0.86	0.031
7-6d$^+_{sym}$ (P, Br)	σ(^{A}P–C/^{B}P–C)→n(Br$^+$)	61.5[f] (369.2)[g]	0.27	0.116
7-6d$^+_{nsym}$ (P, Br)	σ(^{A}P–C)→σ*(Br–^{B}P)	8.3[h] (24.8)[g]	0.65	0.066
7-6e$^+_{sym}$ (P, I)	σ(^{A}P–C/^{B}P–C)→n(I$^+$)	58.9[f] (353.2)[g]	0.32	0.122
7-7a$^+_{nsym}$ (As, H)	σ(^{A}As–C)→σ*(H–^{B}As)	7.0[h] (21.0)[g]	0.76	0.065
7-7b$^+_{sym}$ (As, F)	n(F)→σ*(^{A}As–^{B}As)	80.0	0.34	0.147
7-7b$^+_{nsym}$ (As, F)	*i*	*i*	*i*	*i*
7-7c$^+_{sym}$ (As, Cl)	n($^{A/B}$As)→σ*(Cl–$^{B/A}$As)	505.8[e]	0.06	0.151
7-7c$^+_{nsym}$ (As, Cl)	σ(^{A}As–C)→σ*(Cl–^{B}As)	4.3[h] (12.8)[g]	0.62	0.046
7-7d$^+_{sym}$ (As, Br)	σ(^{A}As–C/^{B}As–C)→n(Br$^+$)	76.6[f] (459.5)[g]	0.20	0.111
7-7d$^+_{nsym}$ (As, Br)	σ(^{A}As–C)→σ*(Br–^{B}As)	9.9[h] (29.7)[g]	0.56	0.067
7-8a$^+_{sym}$ (Sb, H)	n($^{A/B}$Sb)→σ*(H–$^{B/A}$Sb)	348.6[e]	0.12	0.184
7-8a$^+_{nsym}$ (Sb, H)	σ(^{A}Sb–C)→σ*(H–^{B}Sb)	6.7[h] (20.0)[g]	0.66	0.059
7-8b$^+_{sym}$ (Sb, F)	n(^{A}Sb)→σ*(F–^{B}Sb)	429.2	0.02	0.086
7-8b$^+_{nsym}$ (Sb, F)	n(F)→σ*(^{A}Sb–C)	1.7[h] (5.1)[g]	1.34	0.042
7-8c$^+_{sym}$ (Sb, Cl)	n($^{A/B}$Sb)→σ*(Cl–$^{B/A}$Sb)	762.1[e]	0.03	0.130
7-8c$^+_{nsym}$ (Sb, Cl)	σ(^{A}Sb–C)→σ*(H–^{B}Sb)	2.9[h] (8.6)[g]	0.54	0.035

[a] See Table 7-1 for BSS-B. [b] Second-perturbation energy. [c] Differences between the energies of NBO (*i*) and NBO (*j*). [d] The off-diagonal NBO Fock matrix elements. [e] Detected as σ(3c–4e). [f] Six CT contributions are detected. [g] Total values are given in parenthesis. [h] Three CT contributions are detected. [i] No CT contributions in question are detected.

The second is the σ(^{A}Pn–C/^{B}Pn–C)→n_p(X^+) type, which operates in 6 species of **7-2a**$^+_{sym}$ (335 kcal mol^{-1}), **7-3a**$^+_{sym}$ (448 kcal mol^{-1}), **7-4a**$^+_{sym}$ (566 kcal mol^{-1}), **7-6d**$^+_{sym}$ (369 kcal mol^{-1}), **7-6e**$^+_{sym}$ (353 kcal mol^{-1}), and **7-7d**$^+_{sym}$ (460 kcal mol^{-1}). Total six equivalent σ(Pn–C) bonds from three σ(^{A}Pn–C) and three σ(^{B}Pn–C) bonds contribute to this type; therefore, the total contribution is six times larger than that of each contribution. The total values are also very large. The third case is the σ(^{A}Pn–C)→σ*(X–^{B}Pn) form, which operates in 14 species. The total contribution is three times larger than that of each contribution. The total contributions larger than 30 kcal mol^{-1} are **7-3a**$^+_{nsym}$ (41 kcal mol^{-1}), **7-4a**$^+_{nsym}$ (43 kcal mol^{-1}). The fourth is the n_p(F)→σ*(^{A}Pn–^{B}Pn), which operated in **7-6b**$^+_{sym}$ (102 kcal mol^{-1}) and **7-7b**$^+_{sym}$ (80 kcal mol^{-1}). Other cases of which contributions larger than 10 kcal mol^{-1} are n(^{A}P/^{B}P)→s(H^+) (32 kcal mol^{-1}) in **7-2a**$^+_{sym}$ and n(F)→n(Sb^+) (67 kcal mol^{-1}) in **7-4b**$^+_{sym}$.

The high contributions from the CT terms mainly arise from the n(^{A}Pn)→σ*(X–^{B}Pn) types. The σ(^{A}Pn–C/^{B}Pn–C)→n_p(X^+) type interactions also have the substantially high contributions. The reason for the contributions was intriguing at first glance but it would be difficult to explain. The reason could be interpreted by considering the through space and the through bond mechanisms. The contributions increased rapidly as the interaction distances became shorter. The contributions in question could be understood based on the same reason. A similar mechanism would also operate in the CT interactions in σ(^{A}Pn–C/^{B}Pn–C)→n_p(X^+).

The very high contributions from the of n(^{A}Pn)→σ*(X–^{B}Pn) type, accompanied by the very large *E*(2) values, must correlate deeply to the (very) high p-characters in n(^{A}Pn). The occupancy ratios between s- and p-characters in n(^{A}Pn) were calculated under the same conditions. The results are shown in Table 7-5. The planarity around ^{A}Pn will affect much to the ratio of the p-character, together with the energy difference between atomic s- and p-orbitals of ^{A}Pn. High ratios of p-characters over 70% were predicted for n(^{A}Pn) in **7-1a**$^+$–**7-1c**$^+$ (86.0–98.7%), **7-2b**$^+$ (97.6%), **7-3b**$^+$ (97.4%), **7-5a**$^+$–**7-5e**$^+$ (84.4–99.6%), **7-6a**$^+$ (87.9%), **7-6c**$^+$ (96.2%), **7-7c**$^+$ (96.5%), **7-8a**$^+$ (92.6%), **7-8b**$^+$(97.7%), and **7-8c**$^+$ (96.3%). However, the predicted rations were 32.1–62.4% for the others. Indeed, high ratios of the p-characters are expected to enlarge *E*(2) for n(^{A}Pn)→σ*(X–^{B}Pn), but the correlation between the ratio and *E*(2) seems unclear, as shown in Table 7-4. Other factors, such as the atomic types of ^{A}Pn, X, and ^{B}Pn, must also operate to control the *E*(2) values.

The NBO analysis demonstrated the large contributions from the ^{A}Pn··X··^{B}Pn and ^{A}Pn···X–^{B}Pn interactions and clarified the reasons for the high contributions from n(^{A}Pn)→σ*(X–^{B}Pn). While the σ(^{A}Pn–C/^{B}Pn–C)→n_p(X^+) interactions also contribute much to stabilize the system, the contributions from σ(^{A}Pn–C)→σ*(X–^{B}Pn) seem smaller. The contribution from n(F)→n_s(Sb^+) was also of interest. The n(F)→n_s(Sb^+) interaction, in place of n_p(Sb)→σ*(F–Sb), contributed to **7-4b**$^+_{sym}$. A heavy CT occurred from Sb to F^+ due to the very large electronegativity of F, relative to Sb, resulting in the formation of F and Sb^+, which led to the above interaction, as listed in Table 7-4.

Table 7-5. The s- and p-characters (abbreviated by s-char. and p-char., respectively) of n(^{A}Pn) for **7-1a**$^{+}$–**7-8c**$^{+}$ of **7-*mx***$^{+}_{sym}$ and/or **7-*mx***$^{+}_{nsym}$, calculated by NBO analysis under the M06-2X/BSS-B//MP2/BSS-B conditions.[a]

Species (^{A}Pn (^{B}Pn), X)	s-char. (n(^{A}Pn)) (%)	p-char. (n(^{A}Pn)) (%)		s-char. (n(^{A}Pn)) (%)	p-char. (n(^{A}Pn)) (%)
7-1a$^{+}_{nsym}$ (N, H)	1.1	98.7	**7-6a**$^{+}_{sym}$ (P, H)	12.0	87.9
7-1b$^{+}_{sym}$ (N, F)	2.7	97.3	**7-6a**$^{+}_{nsym}$ (P, H)	47.9	52.0
7-1b$^{+}_{nsym}$ (N, F)	15.4	84.4	**7-6b**$^{+}_{sym}$ (P, F)	*b*	*b*
7-1c$^{+}_{sym}$ (N, Cl)	13.6	86.0	**7-6b**$^{+}_{nsym}$ (P, F)	50.0	50.0
7-2a$^{+}_{sym}$ (P, H)	37.5	62.4	**7-6c**$^{+}_{sym}$ (P, Cl)	3.6	96.2
7-2a$^{+}_{nsym}$ (P, H)	54.1	45.8	**7-6c**$^{+}_{nsym}$ (P, Cl)	54.9	45.0
7-2b$^{+}_{sym}$ (P, F)	2.4	97.6	**7-6d**$^{+}_{sym}$ (P, Br)	52.9	47.0
7-2b$^{+}_{nsym}$ (P, F)	59.5	40.5	**7-6d**$^{+}_{nsym}$ (P, Br)	57.6	42.4
7-3a$^{+}_{sym}$ (As, H)	54.2	45.7	**7-6e**$^{+}_{sym}$ (P-*-I)	56.7	43.1
7-3a$^{+}_{nsym}$ (As, H)	63.3	36.7	**7-7a**$^{+}_{nsym}$ (As, H)	53.8	46.2
7-3b$^{+}_{sym}$ (As, F)	2.6	97.4	**7-7b**$^{+}_{sym}$ (As, F)	*b*	*b*
7-3b$^{+}_{nsym}$ (As, F)	67.5	32.5	**7-7b**$^{+}_{nsym}$ (As, F)	59.6	40.4
7-4a$^{+}_{sym}$ (Sb, H)	67.5	32.5	**7-7c**$^{+}_{sym}$ (As, Cl)	3.3	96.5
7-4a$^{+}_{nsym}$ (Sb, H)	67.5	32.5	**7-7c**$^{+}_{nsym}$ (As, Cl)	64.2	35.8
7-4b$^{+}_{sym}$ (Sb, F)	*b*	*b*	**7-7c**$^{+}_{sym}$ (As, Br)	67.9	32.1
7-5a$^{+}_{nsym}$ (N, H)	13.1	86.8	**7-7c**$^{+}_{nsym}$ (As, Br)	66.5	33.5
7-5b$^{+}_{sym}$ (N, F)	2.7	97.3	**7-8a**$^{+}_{sym}$ (Sb, H)	7.3	92.6
7-5b$^{+}_{nsym}$ (N, F)	0.4	99.6	**7-8a**$^{+}_{nsym}$ (Sb, H)	59.9	40.1
7-5c$^{+}_{sym}$ (N, Cl)	13.4	86.3	**7-8b**$^{+}_{sym}$ (Sb, F)	2.1	97.7
7-5d$^{+}_{sym}$ (N, Br)	13.8	86.0	**7-8b**$^{+}_{nsym}$ (Sb, F)	62.5	37.4
7-5e$^{+}_{sym}$ (N, I)	14.9	84.8	**7-8c**$^{+}_{sym}$ (Sb, Cl)	3.6	96.3
			7-8c$^{+}_{nsym}$ (Sb, Cl)	67.5	32.5

[a] See Table 7-1 in the text for BSS-B. [b] Not detected.

Characteristic nature of [Pn··X··Pn]$^{+}$ with the behavior of charge

What is the character of Pn··X^{+}··Pn in **7-1a**$^{+}$–**7-8c**$^{+}$? The ψ_3, ψ_2, and ψ_1 orbitals of σ(3c–4e) are looked for among MOs in **7-1a**$^{+}$–**7-8c**$^{+}$. Figure 7-9 shows HOMO-5, HOMO, and LUMO of **7-6c**$^{+}_{sym}$, for example, which correspond to the orbitals, respectively. The results clearly demonstrate the σ(3c–4e) nature for Pn··X^{+}··Pn. the changes of *Qn*, so are **7-5**$^{+}$, **7-7**$^{+}$, and **7-8**$^{+}$. Figure 7-10 shows the plot of *Qn* (^{A}P), *Qn* (X), *Qn* (^{B}P), and *Qn* (Total) (= *Qn* (T) = *Qn* (^{A}P) + *Qn* (X) + *Qn* (^{B}P)) for **7-6a**$^{+}_{sym}$–**7-6e**$^{+}_{sym}$, and **7-6a**$^{+}_{nsym}$–**7-6d**$^{+}_{nsym}$ versus X. The values of *Qn* (^{A}P), *Qn* (X), *Qn* (^{B}P), and *Qn* (T) for **7-1**–**7-8** and **7-1a**$^{+}$–**7-8c**$^{+}$ are collected in Table 7-A7 of the Appendix.

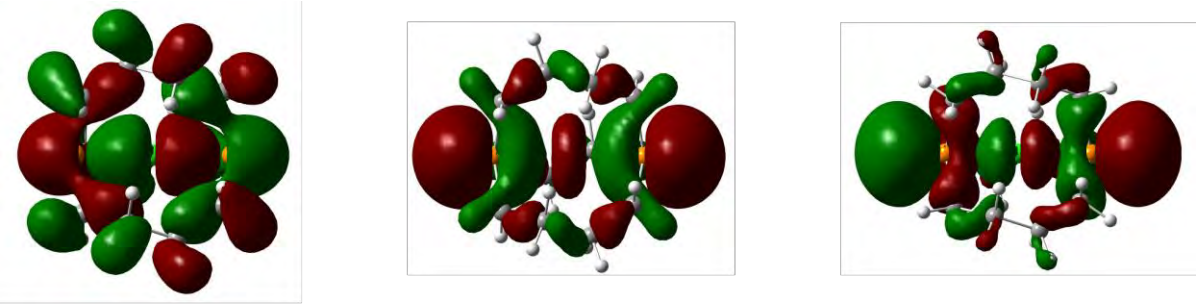

ψ_{66} (HOMO−5): −15.8 eV ψ_{71} (HOMO): −9.6 eV ψ_{72} (LUMO): −3.8 eV

Figure 7-9. HOMO-5, HOMO, and LUMO in **7-6c**$^{+}_{sym}$ (Pn = P, X = Cl), which correspond to ψ_1, ψ_2, and ψ_3 of σ(3c–4e), respectively.

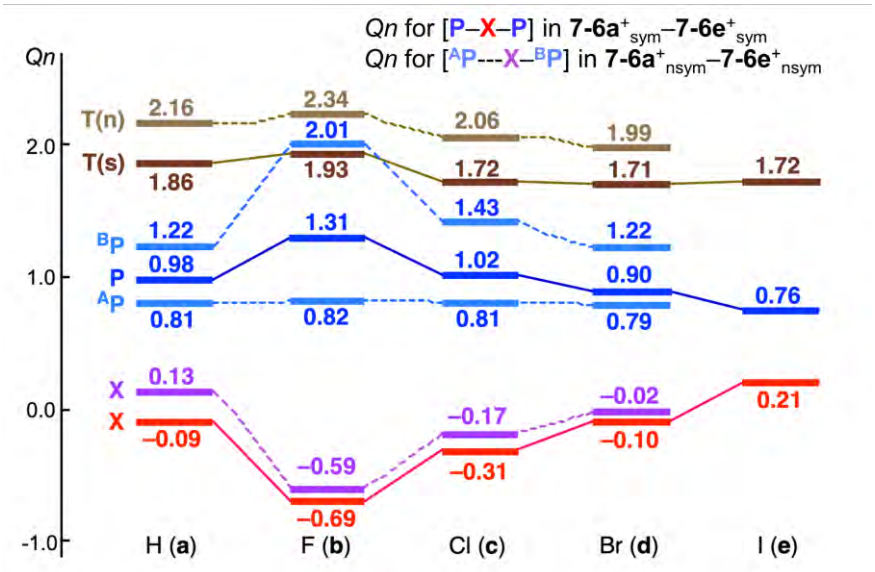

Figure 7-10. Plots of *Qn* (^{A}Pn), *Qn* (X), *Qn* (^{B}Pn), and *Qn* (T) versus X for **7-6a**$^{+}$–**7-6e**$^{+}$.

The *Qn* (X) values in sym and nsym shapes of **7-6a**$^{+}$–**7-6e**$^{+}$ become larger in the order of X = F < Cl < Br < I, as expected, where *Qn* (H) seems close to *Qn* (Cl) or *Qn* (Br). *Qn* (P) behaves the exact opposite of *Qn* (X). The exact opposite behavior between *Qn* (P) (or *Qn* (^{B}Pn)) and *Qn* (X) are confirmed by examining *Qn* (T), which are almost constant for both shapes. It is noteworthy that *Qn* (^{A}P) are almost constant in the nsym shapes, irrespective of the large changes in *Qn* (X) and *Qn* (^{B}Pn). The results may support the formation of the (very) strong ^{B}P–X bond with the (very) weak ^{A}Pn···X in the nsym shapes. The plots for **7-5**$^{+}$, **7-7**$^{+}$, and **7-8**$^{+}$, drawn in Figure 7-A10 of the Appendix, are very similar to that in Figure 7-10.

It seems curious that the *Qn* (T) values of **7-6a**$^{+}_{sym}$–**7-6e**$^{+}_{sym}$ are close to 2 (e^{+}), which is much larger than 1 (e^{+}), originated from X^{+}, at first glance. The results could be very different from those generally expected for the formation of σ(3c–4e). Scheme 7-2 explains the changes of *Qn* ($^{A/B}$P) and *Qn* (X) in the formation of **7-6c**$^{+}_{sym}$, starting from **7-6**$_{nsym}$ + Cl^{+}, via [**7-6c**$^{+}_{nsym}$]$_{CT=0}$. The explanation for the change in *Qn* is as follows. The mechanism for the change is explained by the three processes, starting from the neutral **7-6**$_{nsym}$ + Cl^{+}. (i) The *Qn* (^{A}Pn/^{B}Pn) values in **7-6**$_{nsym}$ are 0.78 e^{+} and 0.82 e^{+}, respectively. (ii) When Cl^{+} is incorporated into P···P of **7-6**$_{nsym}$, the double donation occurs from the lone pair electrons of P to the vacant p-orbital of Cl^{+}. The *Qn* (Pn) and *Qn* (Cl) values would be 1.8 e^{+} and –1.0 e^{+}, respectively, where the donated electrons are assumed to share equally between P and Cl. The primitive structure with no CT is denoted by [**7-6c**$^{+}_{nsym}$]$_{CT=0}$. (iii) The charges in P··Cl··P of [**7-6c**$^{+}_{nsym}$]$_{CT=0}$ redistribute to form **7-6c**$^{+}_{sym}$.

The CT occurs from [**7-6c**$^{+}_{nsym}$]$_{CT=0}$ to **7-6c**$^{+}_{sym}$, contrary to the electronegativities of P and Cl, in this process, resulting in *Qn* (Pn) = 1.02 e^{+} and *Qn* (Cl) = –0.31 e^{+}. The σ(3c–4e) character of ^{A}Pn··X^{+}··^{B}Pn is demonstrated again, through the examination of the changes of the charges on the

atoms. Indeed, some Pn··X^{+}··Pn interactions would not be typical σ(3c–4e), depending on the combination of Pn and X, but the bonds, analyzed in this work, are recognized to be the σ(3c–4e) type, for the unified understanding of the bonds.

The σ-hole on a halogen atom must correlate deeply in the behavior of ^{A}Pn··X^{+}··^{B}Pn and/or Pn···X^{+}–Pn. Molecular electrostatic potentials (MEPs) will present a fine picture for the visualization. The MEPs are shown in Figure 7-11, exemplified by **7-6d**$^{+}_{nsym}$, [H–C(CH$_2$CH$_2$CH$_2$CH$_2$)$_3$P–Br]$^{+}$ (**7-9d**$^{+}$), and [H–C(CH$_2$CH$_2$CH$_2$CH$_2$)$_3$P–I]$^{+}$ (**7-9e**$^{+}$). Indeed, the charge depletion, corresponding to the σ-hole, is confirmed on the surface of X in the direction of P–X in **7-6d**$^{+}_{nsym}$, **7-9d**$^{+}$, and especially, **7-9e**$^{+}$, as expected.

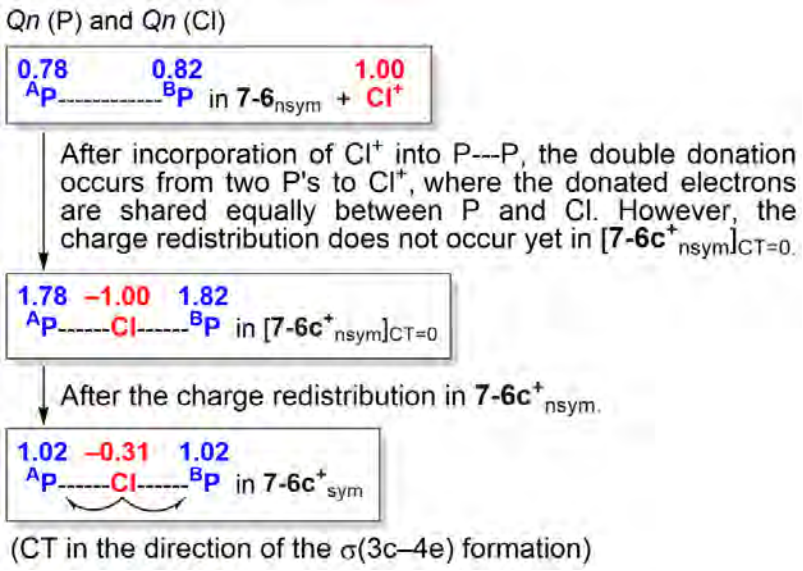

Scheme 7-2. Changes in *Qn* ($^{A/B}$Pn) and *Qn* (X) in the formation of **7-6c**$^{+}_{sym}$ via [**7-6c**$^{+}_{nsym}$]$_{CT=0}$.

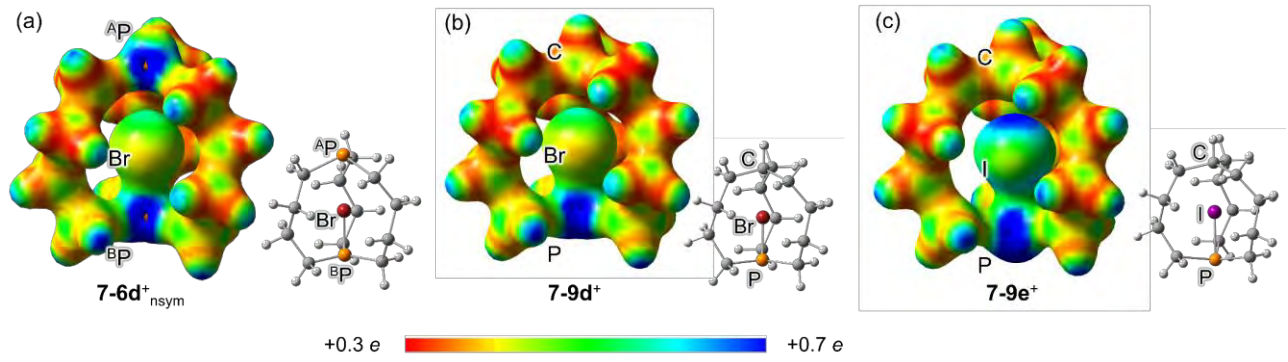

Figure 7-11. Molecular electrostatic potentials (MEPs) for the Pn–X, exemplified by **7-6d**$^{+}_{nsym}$ (a), [H–C(CH$_2$CH$_2$CH$_2$CH$_2$)$_3$P–Br]$^{+}$ (**7-9d**$^{+}$) (b) and [H–C(CH$_2$CH$_2$CH$_2$CH$_2$)$_3$P–I]$^{+}$ (**7-9e**$^{+}$) (c), calculated with MP2/BSS-B. The MEPs are calculated by the isovalue of 0.075 au. Positive range of electron density for 0.3–0.7 e^{+} was employed to show color gradiant on the MEPs for clarification due to the cationic forms of **7-6d**$^{+}_{nsym}$, **7-9d**$^{+}$, and **7-9e**$^{+}$.

Summary

The possibility of large atoms to incorporate in stable cage compounds of medium rings was examined with the atoms X of H (**a**), F (**b**), Cl (**c**), Br (**d**), and I (**e**). The skeletons of bicyclo[3.3.3]undecane and bicyclo[4.4.4]tetradecane were employed for the purpose, in which the bridgehead atoms were substituted by pnictogens (^{A}Pn = ^{B}Pn =N, P, As, and Sb: **7-1*x*$^{+}$**–**7-8*x*$^{+}$**). In this system, X acted as X^{+} to form the linear ^{A}Pn··X^{+}··^{B}Pn σ(3c–4e) type interactions, which were fixed by the bicyclo systems. Moreover, **7-1**$^{+}$ (^{A}Pn = ^{B}Pn = N) was successfully optimized for X of each H, F and Cl, and **7-2*x***$^{+}$ (^{A}Pn = ^{B}Pn = P), **7-3*x***$^{+}$ (^{A}Pn = ^{B}Pn = As), and **7-4*x***$^{+}$ (^{A}Pn = ^{B}Pn = Sb) were carefully optimized when X = H and F. In the case of **7-5*x***$^{+}$ (^{A}Pn = ^{B}Pn = N) and **7-6*x***$^{+}$ (^{A}Pn = ^{B}Pn = P) were successfully optimized for X of H, F, Cl, Br, and I, **7-7*x***$^{+}$ (^{A}Pn = ^{B}Pn = As) was optimized for X of H, F, Cl, and Br, and **7-8*x***$^{+}$ (^{A}Pn = ^{B}Pn = Sb) was optimized for X of H, F and Cl. The structures of the symmetric and nonsymmetric shapes were optimized for **7-1a**$^{+}$–**7-8c**$^{+}$, with their relative stabilities, and their transition states. The symmetric shapes appeared to be more stabilized as ^{A}Pn, ^{B}Pn, and X became larger, except for ^{A}Pn = ^{B}Pn = N.

The intrinsic dynamic and static natures of the Pn-∗-X interactions were elucidated for **7-1a**$^{+}$–**7-8c**$^{+}$ with QTAIM-DFA by employing CIV. Various natures from vdW to Cov-s were predicted. The ^{B}P-∗-F (**7-2b**$^{+}_{nsym}$ and **7-6b**$^{+}_{nsym}$), ^{B}As-∗-F (**7-3b**$^{+}_{nsym}$ and **7-7b**$^{+}_{nsym}$), ^{B}Sb-∗-H (**7-4a**$^{+}_{nsym}$ and **7-8a**$^{+}_{nsym}$), $^{A/B}$Sb-∗-F (**7-4b**$^{+}_{sym}$), ^{B}P-∗-Cl (**7-6c**$^{+}_{nsym}$), ^{B}As-∗-Cl (**7-7c**$^{+}_{nsym}$), ^{B}Sb-∗-F (**7-8b**$^{+}_{nsym}$), and ^{B}Sb-∗-Cl (**7-8c**$^{+}_{nsym}$) interactions were predicted to be *r*-CS/*t*-HB_{wc} or *r*-CS/CT-MC, respectively, although their *r*($^{A/B}$Pn–X) were shorter than the r_{Cov}($^{A/B}$Pn–X). In contrast, the SS/Cov-w or SS/Cov-s natures were predicted for ^{B}Pn-∗-X interactions than the above such as ^{B}N-∗-H in **7-1a**$^{+}_{nsym}$ and **7-5a**$^{+}_{nsym}$ (with **7-1a**$^{+}_{tp:TS}$ and **7-5a**$^{+}_{tp:TS}$). The secondary interactions of H-∗-H and X-∗-C were also detected, of which the predicted natures were *p*-CS/vdW, *p*-CS/*t*-HB_{nc}, *r*-CS/*t*-HB_{wc}, and *r*-CS/CT-MC. They also contributed to stabilizing the systems, along with the main interactions. The order of the interaction strengths was estimated using the $H_b(\boldsymbol{r}_c)$ values.

The NBO analysis was applied to the interactions and evaluated the contributions from the CT terms to the interactions in question. Several types of NBO (*i*) to NBO (*j*) interactions were detected in this case. Among the several types, the $n_p(^{A}Pn)\rightarrow\sigma^*(X–^{B}Pn)$ interactions highly contributed, together with $\sigma(^{A}Pn–C)\rightarrow\sigma^*(X–^{B}Pn)$ and $\sigma(^{A}Pn–C/^{B}Pn–C)\rightarrow n_p(X^{+})$. In the case of **7-4b**$^{+}$, the CT interaction was described by $n_p(F)\rightarrow n_s(Sb^{+})$, not by $n_p(Sb)\rightarrow\sigma^*(F–Sb)$. The very large electronegativity of F was likely responsible for the change. The charge distributions on the atoms of ^{A}Pn··X^{+}··^{B}Pn were confirmed to show the σ(3c–4e) type behavior.

The results provide important insights into the nature of the interactions, especially the hypervalent 3c–4e interactions of the symmetric and nonsymmetric shapes, where the interactions are fixed linearly by the bicyclo systems. These interactions can also be considered as the extension of the hydrogen and halogen bonds. These results are useful to design materials containing X^{+}, as in **7-1**–**7-8**.

Appendix

Table 7-A1. Selected structural parameters of r(A–B), θ_A, θ_B, d_A, and d_B, Δr(A–B)$_{vdW}$ and Δr_{Cov}(A–B) for **7-1**–**7-8**, **7-1a**$^+$–**7-8c**$^+$ of **7-*mx*$^+_{sym}$**, **7-*mx*$^+_{nsym}$** and **7-1a**$^+_{tp:TS}$, **7-5a**$^+_{tp:TS}$, and **7-7a**$^+_{tp:TS}$, optimized with MP2/BSS-B, together with the types of ^{A}Pn and ^{B}Pn.[a]

Species (A, B)[b]	r(A–B) (Å)	Δr(A–B)$_{vdW}$[c] (Å)	Δr_{Cov}(A–B)[d] (Å)	θ_A[e] (º)	θ_B[e] (º)	d_A[e] (Å)	d_B[e] (Å)	Type[f] ^{A}Pn/^{B}Pn
7-1 (^{A}N, ^{B}N)	3.0094	–0.09	1.59	118.2	118.2	0.195	0.195	*out*/*out*
7-2 (^{A}P, ^{B}P)	4.1145	0.51	1.89	105.2	105.2	0.740	0.740	*out*/*out*
7-3 (^{A}As, ^{B}As)	4.2590	0.56	1.84	103.8	103.8	0.825	0.825	*out*/*out*
7-4 (^{A}Sb, ^{B}Sb)	4.5021	0.38	1.70	102.1	102.1	0.956	0.956	*out*/*out*
7-5 (^{A}N, ^{B}N)	2.7826	–0.32	1.36	115.0	115.0	–0.330	–0.330	*in*/*in*
7-6 (^{A}P, ^{B}P)	3.2493	–0.35	1.03	105.5	106.1	0.723	0.729	*out*/*in*
7-7 (^{A}As, ^{B}As)	4.8399	1.14	2.42	109.9	109.9	0.650	0.650	*out*/*out*
7-8 (^{A}Sb, ^{B}Sb)	5.1101	0.99	2.31	107.5	107.5	0.800	0.800	*out*/*out*
7-1a$^+_{tp:TS}$ ($^{A/B}$N, H)	1.2086	–1.54	0.18	119.7	119.7	–0.088	–0.088	*in*/*in*
7-1a$^+_{nsym}$ (^{A}N, H)	1.2603	–1.49	0.23	119.8	119.4	–0.112	–0.060	*in*/*in*
(^{B}N, H)	1.1620	–1.59	0.13	119.8	119.4	–0.112	–0.060	*in*/*in*
7-1b$^+_{sym}$ ($^{A/B}$N, F)	1.6539	–1.37	0.30	117.8	117.8	0.231	0.231	*out*/*out*
7-1b$^+_{nsym}$ (^{A}N, F)	1.8750	–1.14	0.53	114.8	120.0	0.352	0.019	*out*/*out*
(^{B}N, F)	1.3611	–1.66	0.01	114.8	120.0	0.352	0.019	*out*/*out*
7-1c$^+_{sym}$ ($^{A/B}$N, Cl)	1.7827	–1.52	0.08	117.5	117.5	0.265	0.265	*out*/*out*
7-2a$^+_{sym}$ ($^{A/B}$P, H)	1.6322	–1.37	0.20	116.9	116.9	0.331	0.331	*out*/*out*
7-2a$^+_{nsym}$ (^{A}P, H)	1.9665	–1.03	0.54	105.2	119.8	0.761	–0.086	*out*/*in*
(^{B}P, H)	1.3593	–1.64	–0.07	105.2	119.8	0.761	–0.086	*out*/*in*
7-2b$^+_{sym}$ ($^{A/B}$P, F)	1.8149	–1.46	0.06	114.5	114.5	0.447	0.447	*out*/*out*
7-2b$^+_{nsym}$ (^{A}P, F)	2.2180	–1.05	0.47	103.5	119.7	0.823	0.094	*out*/*out*
(^{B}P, F)	1.5032	–1.77	–0.25	103.5	119.7	0.823	0.094	*out*/*out*
7-3a$^+_{sym}$ ($^{A/B}$As, H)	1.7398	–1.31	0.21	115.1	115.1	0.446	0.446	*out*/*out*
7-3a$^+_{nsym}$ (^{A}As, H)	2.0337	–1.02	0.50	103.4	120.0	0.859	0.008	*out*/*out*
(^{B}As, H)	1.4551	–1.59	–0.07	103.4	120.0	0.859	0.008	*out*/*out*
7-3b$^+_{sym}$ ($^{A/B}$As, F)	1.9288	–1.39	0.08	111.9	111.9	0.582	0.582	*out*/*out*
7-3b$^+_{nsym}$ (^{A}As, F)	2.2784	–1.04	0.43	102.0	118.2	0.913	0.266	*out*/*out*
(^{B}As, F)	1.6519	–1.67	–0.20	102.0	118.2	0.913	0.266	*out*/*out*
7-4a$^+_{sym}$ (^{A}Sb, H)	1.8823	–1.38	0.16	112.8	113.5	0.567	0.599	*out*/*out*
7-4a$^+_{sym}$ (^{B}Sb, H)	1.8815	–1.38	0.16	112.8	113.5	0.567	0.599	*out*/*out*
7-4a$^+_{nsym}$ (^{A}Sb, H)	2.1416	–1.12	0.42	101.3	119.1	1.001	0.211	*out*/*out*
(^{B}Sb, H)	1.6628	–1.60	–0.06	101.3	119.1	1.001	0.211	*out*/*out*
7-4b$^+_{sym}$ ($^{A/B}$Sb, F)	2.0150	–1.52	–0.03	111.7	111.7	0.652	0.652	*out*/*out*

[a] See Table 7-1 in the text for BSS-B. [b] The (A, B) shows (^{A}Pn, ^{B}Pn) for **7-1**–**7-8** and ($^{A/B}$Pn, X) for **7-1a**$^+$–**7-8c**$^+$. [c] The Δr_{vdW}(A–B) = r_{calcd}(A–B) − r_{vdW}(A–B), where the r_{calcd}(A–B) and r_{vdW}(A–B) are the calculated r(A–B) values and sum of van der Waals radii of A and B, respectively. [d] The Δr_{Cov}(A–B) = r_{calcd}(A–B) − r_{Cov}(A–B), where the r_{calcd}(A–B) and r_{Cov}(A–B) are the calculated r(A–B) values and sum of covalent radii of A and B, respectively. [e] See Scheme 7-1 in the text for the definition for the selected structural parameters. [f] See Scheme 7-1 in the text for the definition for "*in*" and "*out*" notation.

(Table 7-A1 continued.)

Species (A, B)[b]	r(A–B) (Å)	Δr(A–B)$_{vdW}$[c] (Å)	Δr_{Cov}(A–B)[d] (Å)	θ_A[e] (º)	θ_B[e] (º)	d_A[e] (Å)	d_B[e] (Å)	Type[f] ^{A}Pn/^{B}Pn
7-5a$^{+}_{tp:TS}$ ($^{A/B}$N, H)	1.2667	–1.48	0.24	112.8	112.8	–0.407	–0.407	*in*/*in*
7-5a$^{+}_{nsym}$ (^{A}N, H)	1.3379	–1.41	0.31	112.7	112.9	–0.407	–0.404	*in*/*in*
(^{B}N, H)	1.2022	–1.55	0.17	112.7	112.9	–0.407	–0.404	*in*/*in*
7-5b$^{+}_{sym}$ ($^{A/B}$N, F)	1.7864	–1.23	0.44	119.7	119.7	–0.075	–0.075	*in*/*in*
7-5b$^{+}_{nsym}$ (^{A}N, F)	2.0799	–0.94	0.73	119.9	116.4	0.035	0.291	*out*/*in*
(^{B}N, F)	1.3924	–1.63	0.04	119.9	116.4	0.035	0.291	*out*/*in*
7-5c$^{+}_{sym}$ ($^{A/B}$N, Cl)	1.8189	–1.48	0.12	119.5	119.5	–0.109	–0.109	*in*/*in*
7-5d$^{+}_{sym}$ ($^{A/B}$N, Br)	1.9131	–1.47	0.06	119.9	119.9	–0.055	–0.055	*in*/*in*
7-5e$^{+}_{sym}$ ($^{A/B}$N, I)	2.0499	–1.48	0.01	120.0	120.0	0.022	0.022	*out*/*out*
7-6a$^{+}_{sym}$ ($^{A/B}$P, H)	1.6387	–1.36	0.21	118.1	118.1	–0.253	–0.253	*in*/*in*
7-6a$^{+}_{nsym}$ (^{A}P, H)	2.5622	–0.44	1.13	107.3	114.4	0.693	0.433	*out*/*in*
(^{B}P, H)	1.3942	–1.61	–0.04	107.3	114.4	0.693	–0.433	*out*/*in*
7-6b$^{+}_{sym}$ ($^{A/B}$P, F)	1.9884	–1.28	0.24	119.6	119.6	0.119	0.119	*out*/*out*
7-6b$^{+}_{nsym}$ (^{A}P, F)	2.6414	–0.63	0.89	107.2	117.2	0.699	–0.303	*out*/*in*
(^{B}P, F)	1.5386	–1.73	–0.21	107.2	117.2	0.699	–0.303	*out*/*in*
7-6c$^{+}_{sym}$ ($^{A/B}$P, Cl)	2.2188	–1.33	0.12	117.9	117.9	0.274	0.274	*out*/*out*
7-6c$^{+}_{nsym}$ (^{A}P, Cl)	2.5650	–0.98	0.47	107.8	119.3	0.791	–0.159	*out*/*in*
(^{B}P, Cl)	1.9004	–1.65	–0.20	107.8	119.3	0.791	–0.159	*out*/*in*
7-6d$^{+}_{sym}$ ($^{A/B}$P, Br)	2.3038	–1.33	0.05	116.9	116.9	0.343	0.343	*out*/*out*
7-6d$^{+}_{nsym}$ (^{A}P, Br)	2.5694	–1.06	0.32	108.2	119.9	0.698	–0.058	*out*/*in*
(^{B}P, Br)	2.0431	–1.59	–0.21	108.2	119.9	0.698	–0.058	*out*/*in*
7-6e$^{+}_{sym}$ ($^{A/B}$P, I)	2.4524	–1.33	0.01	114.7	114.7	0.466	0.466	*out*/*out*
7-7a$^{+}_{tp:TS}$ ($^{A/B}$As, H)	1.7226	–1.33	0.19	119.2	119.2	–0.175	–0.175	*in*/*in*
7-7a$^{+}_{nsym}$ (^{A}As, H)	2.4109	–0.64	0.88	110.4	115.6	0.636	–0.413	*out*/*in*
(^{B}As, H)	1.4810	–1.57	–0.05	110.4	115.6	0.636	–0.413	*out*/*in*
7-7b$^{+}_{sym}$ ($^{A/B}$As, F)	2.0795	–1.24	0.23	118.9	118.9	0.210	0.210	*out*/*out*
7-7b$^{+}_{nsym}$ (^{A}As, F)	2.7087	–0.61	0.86	105.2	118.8	0.801	–0.210	*out*/*in*
(^{B}As, F)	1.6826	–1.64	–0.17	105.2	118.8	0.801	–0.210	*out*/*in*
7-7c$^{+}_{sym}$ ($^{A/B}$As, Cl)	2.3378	–1.26	0.14	116.0	116.0	0.408	0.408	*out*/*out*
7-7c$^{+}_{nsym}$ (^{A}As, Cl)	2.6470	–0.95	0.45	106.1	120.0	0.796	–0.030	*out*/*in*
(^{B}As, Cl)	2.0293	–1.57	–0.17	106.1	120.0	0.796	–0.030	*out*/*in*
7-7d$^{+}_{sym}$ ($^{A/B}$As, Br)	2.4227	–1.26	0.07	114.6	114.6	0.484	0.484	*out*/*out*
7-7d$^{+}_{nsym}$ (^{A}As, Br)	2.6467	–1.03	0.30	107.0	119.6	0.777	0.134	*out*/*out*
(^{B}As, Br)	2.1903	–1.49	–0.16	107.0	119.6	0.777	0.134	*out*/*out*
7-8a$^{+}_{sym}$ ($^{A/B}$Sb, H)	1.9903	–1.27	0.27	118.9	118.9	0.231	0.231	*out*/*out*
7-8a$^{+}_{nsym}$ (^{A}Sb, H)	2.5024	–0.76	0.78	108.3	118.0	0.778	–0.306	*out*/*in*
(^{B}Sb, H)	1.6703	–1.59	–0.05	108.3	118.0	0.778	–0.306	*out*/*in*
7-8b$^{+}_{sym}$ ($^{A/B}$Sb, F)	2.1742	–1.36	0.13	117.7	117.7	0.329	0.329	*out*/*out*
7-8b$^{+}_{nsym}$ (^{A}Sb, F)	2.7265	–0.80	0.69	107.2	119.8	0.814	–0.102	*out*/*in*
(^{B}Sb, F)	1.8672	–1.66	–0.17	107.2	119.8	0.814	–0.102	*out*/*in*
7-8c$^{+}_{sym}$ ($^{A/B}$Sb, Cl)	2.4712	–1.34	0.08	114.8	114.8	0.515	0.515	*out*/*out*
7-8c$^{+}_{nsym}$ (^{A}Sb, Cl)	2.7908	–1.02	0.40	103.8	119.6	0.944	0.140	*out*/*out*
(^{B}Sb, Cl)	2.2143	–1.60	–0.18	103.8	119.6	0.944	0.140	*out*/*out*

[a] See Table 7-1 in the text for BSS-B. [b] The (A, B) shows (^{A}Pn, ^{B}Pn) for **7-1**–**7-8** and (^{A}Pn, X) for **7-1a**$^{+}$–**7-8c**$^{+}$. [c] The Δr_{vdW}(A–B) = r_{calcd}(A–B) − r_{vdW}(A–B), where the r_{calcd}(A–B) and r_{vdW}(A–B) are the calculated r(A–B) values and sum of van der Waals radii of A and B, respectively. [d] The Δr_{Cov}(A–B) = r_{calcd}(A–B) − r_{Cov}(A–B), where the r_{calcd}(A–B) and r_{Cov}(A–B) are the calculated r(A–B) values and sum of covalent radii of A and B, respectively. [e] See Scheme 7-1 in the text for the definition for the selected structural parameters. [f] See Scheme 7-1 in the text for the definition for "*in*" and "*out*" notation.

Table 7-A2. Total energies (E_{ES}) and those corrected with zero-point energies (E_{ZP}) for **7-1a**$^+$–**7-8c**$^+$, together with the relative energies of ΔE_{ES} and ΔE_{ZP} and stabilization energies of $\Delta E_{f:ES}$ and $\Delta E_{f:ZP}$, evaluated with MP2/BSS-B.[a]

Species (^{A}Pn (^{B}Pn), X)	E_{ES}[b] (au)	E_{ZP}[c] (au)	ΔE_{ES}[d] (kJ mol^{-1})	ΔE_{ZP}[e] (kJ mol^{-1})	$\Delta E_{f:ES}$[f] (kJ mol^{-1})	$\Delta E_{f:ZP}$[g] (kJ mol^{-1})
7-1a$^+_{tp:TS}$ (N, H)	–462.308591	–462.026619	0.0_2	-1.1_8	–1002.8	–972.3
7-1a$^+_{nsym}$ (N, H)	–462.308600	–462.026170	0.0_0	0.0_0	–1002.8	–971.1
7-1b$^+_{sym}$ (N, F)	–561.167117	–560.894422	0.0	0.0	–1092.9	–1086.8
7-1b$^+_{s\text{-}ns:TS}$ (N, F)	–561.139424	–560.870602	72.7	62.5	–1020.2	–1024.3
7-1b$^+_{nsym}$ (N, F)	–561.140193	–560.870202	70.7	63.6	–1022.3	–1023.2
7-1c$^+_{sym}$ (N, Cl)	–920.858235	–920.601827	0.0	0.0	307.0	270.4
7-2a$^+_{sym}$ (P, H)	–1034.676634	–1034.409301	53.2	51.9	–846.3	–821.1
7-2a$^+_{s\text{-}ns:TS}$ (P, H)	–1034.674955	–1034.410137	57.6	49.7	–841.8	–823.3
7-2a$^+_{nsym}$ (P, H)	–1034.696909	–1034.429081	0.0	0.0	–899.5	–873.0
7-2b$^+_{sym}$ (P, F)	–1133.750908	–1133.487446	0.0	0.0	–1502.9	–1487.9
7-2b$^+_{s\text{-}ns:TS}$ (P, F)	–1133.704662	–1133.446655	121.4	107.1	–1381.4	–1380.8
7-2b$^+_{nsym}$ (P, F)	–1133.740056	–1133.481328	28.5	16.1	–1474.4	–1471.8
7-3a$^+_{sym}$ (As, H)	–4821.732494	–4821.469699	34.4	32.1	–836.0	–814.3
7-3a$^+_{s\text{-}ns:TS}$ (As, H)	–4821.731716	–4821.470357	36.4	30.4	–834.0	–816.0
7-3a$^+_{nsym}$ (As, H)	–4821.745592	–4821.481919	0.0	0.0	–870.4	–846.4
7-3b$^+_{sym}$ (As, F)	–4920.813120	–4920.553684	0.0	0.0	–1509.3	–1496.4
7-3b$^+_{s\text{-}ns:TS}$ (As, F)	–4920.772283	–4920.517446	107.2	95.1	–1402.1	–1401.2
7-3b$^+_{nsym}$ (As, F)	–4920.790607	–4920.535646	59.1	47.4	–1450.2	–1449.0
7-4a$^+_{sym}$ (Sb, H)	–12980.025582	–12979.766525	0.0	0.0	–855.9	–833.7
7-4a$^+_{s\text{-}ns:TS}$ (Sb, H)	–12980.019945	–12979.763031	14.8	9.2	–841.1	–824.6
7-4a$^+_{nsym}$ (Sb, H)	–12980.021769	–12979.763544	10.0	7.8	–845.9	–825.9
7-4b$^+_{sym}$ (Sb, F)	–13079.124590	–13078.810940	0.0	0.0	–1577.5	–1412.0
7-5a$^+_{tp:TS}$ (N, H)	–579.925482	–579.557381	0.0_4	-2.8_0	–1143.6	–1112.3
7-5a$^+_{nsym}$ (N, H)	–579.925498	–579.556316	0.0_0	0.0_0	–1143.6	–1109.5
7-5b$^+_{sym}$ (N, F)	–678.899250	–678.535227	0.0	0.0	–1536.3	–1515.7
7-5b$^+_{s\text{-}ns:TS}$ (N, F)	–678.862934	–678.502626	95.3	85.6	–1440.9	–1430.1
7-5b$^+_{nsym}$ (N, F)	–678.864259	–678.502612	91.9	85.6	–1444.4	–1430.1
7-5c$^+_{sym}$ (N, Cl)	–1038.751889	–1038.395342	0.0	0.0	–560.4	–559.5
7-5d$^+_{sym}$ (N, Br)	–3151.656733	–3151.303871	0.0	0.0	–226.9	–235.6
7-5e$^+_{sym}$ (N, I)	–7496.968552	–7496.621733	0.0	0.0	303.4	278.8
7-6a$^+_{sym}$ (P, H)	–1152.260169	–1151.909698	53.8	40.9	–989.2	–967.7
7-6a$^+_{s\text{-}ns:TS}$ (P, H)	–1152.259137	–1151.908475	56.5	44.1	–986.5	–964.5
7-6a$^+_{nsym}$ (P, H)	–1152.280674	–1151.925259	0.0	0.0	–1043.1	–1008.6
7-6b$^+_{sym}$ (P, F)	–1251.381136	–1251.029676	75.9	84.6	–1768.4	–1744.3
7-6b$^+_{s\text{-}ns:TS}$ (P, F)	–1251.333331	–1250.987154	201.4	196.3	–1642.9	–1632.7
7-6b$^+_{nsym}$ (P, F)	–1251.410043	–1251.061914	0.0	0.0	–1844.3	–1828.9
7-6c$^+_{sym}$ (P, Cl)	–1611.240732	–1610.896316	16.5	20.0	–810.8	–805.2
7-6c$^+_{s\text{-}ns:TS}$ (P, Cl)	–1611.223802	–1610.881788	61.0	58.1	–766.4	–767.1
7-6c$^+_{nsym}$ (P, Cl)	–1611.247029	–1610.903926	0.0	0.0	–827.4	–825.2
7-6d$^+_{sym}$ (P, Br)	–3724.162396	–3723.821094	0.0	0.0	–521.5	–524.1
7-6d$^+_{s\text{-}ns:TS}$ (P, Br)	–3724.153401	–3723.813670	23.6	19.5	–497.9	–504.6
7-6d$^+_{nsym}$ (P, Br)	–3724.160566	–3723.820192	4.8	2.4	–516.7	–521.7
7-6e$^+_{sym}$ (P, I)	–8069.509412	–8069.172757	0.0	0.0	–83.6	–98.3
7-7a$^+_{tp:TS}$ (As, H)	–4939.297557	–4938.949524	0.0	0.0	–948.7	–931.1
7-7a$^+_{nsym}$ (As, H)	–4939.326574	–4938.974924	–76.2	–66.7	–1024.8	–997.7
7-7b$^+_{sym}$ (As, F)	–5038.433061	–5038.085622	27.5	35.2	–1766.0	–1750.0
7-7b$^+_{s\text{-}ns:TS}$ (As, F)	–5038.386065	–5038.042607	150.9	148.2	–1642.6	–1637.0
7-7b$^+_{nsym}$ (As, F)	–5038.443529	–5038.099041	0.0	0.0	–1793.5	–1785.2
7-7c$^+_{sym}$ (As, Cl)	–5398.308350	–5397.967596	0.0	0.0	–849.6	–851.1
7-7c$^+_{s\text{-}ns:TS}$ (As, Cl)	–5398.290092	–5397.951142	47.9	43.2	–801.7	–807.9
7-7c$^+_{nsym}$ (As, Cl)	–5398.303599	–5397.963741	12.5	10.1	–837.2	–841.0
7-7d$^+_{sym}$ (As, Br)	–7511.238058	–7510.900223	0.0	0.0	–581.4	–590.6
7-7d$^+_{s\text{-}ns:TS}$ (As, Br)	–7511.227432	–7510.890571	27.9	25.3	–553.5	–565.3
7-7d$^+_{nsym}$ (As, Br)	–7511.228088	–7510.890879	26.2	24.5	–555.2	–566.1
7-8a$^+_{sym}$ (Sb, H)	–13097.585073	–13097.237730	58.8	59.1	–914.3	–889.9
7-8a$^+_{s\text{-}ns:TS}$ (Sb, H)	–13097.577873	–13097.234019	77.7	68.9	–895.4	–880.2
7-8a$^+_{nsym}$ (Sb, H)	–13097.607485	–13097.260257	0.0	0.0	–973.1	–949.1
7-8b$^+_{sym}$ (Sb, F)	–13196.756294	–13196.411894	0.0	0.0	–1825.4	–1808.8
7-8b$^+_{s\text{-}ns:TS}$ (Sb, F)	–13196.700559	–13196.360424	146.3	135.1	–1679.1	–1673.7
7-8b$^+_{nsym}$ (Sb, F)	–13196.740628	–13196.399765	41.1	31.8	–1784.3	–1777.0
7-8c$^+_{sym}$ (Sb, Cl)	–13556.634184	–13556.295721	0.0	0.0	–915.8	–914.8
7-8c$^+_{s\text{-}ns:TS}$ (Sb, Cl)	–13556.603163	–13556.267375	81.4	74.4	–834.4	–840.4
7-8c$^+_{nsym}$ (Sb, Cl)	–13556.612690	–13556.275925	56.4	52.0	–859.4	–862.8

[a] See Table 7-1 in the text for BSS-B. [b] Total energies. [c] Total energies corrected with the zero-point energies. [d] Relative E_{ES} taken as standard for those values for **7-*m***$^+_{sym}$ or **7-*m***$^+_{nsym}$ of global minimum. [e] Relative E_{ZP} taken as standard for those values for **7-*m***$^+_{sym}$ or **7-*m***$^+_{nsym}$ of global minimum. [f] Stabilization energies defined by $\Delta E_{f:ES} = E_{ES}(\mathbf{7\text{-}m}^+) - (E_{ES}(\mathbf{7\text{-}m}) + E_{ES}(X^+))$, where X = F, Cl, Br and I. [g] Stabilization energies defined by $\Delta E_{f:ZP} = E_{ZP}(\mathbf{7\text{-}m}^+) - (E_{ZP}(\mathbf{7\text{-}m}) + E_{ZP}(X^+))$, where X = F, Cl, Br, and I.

Table 7-A3. The lengths of BPs (r_{BP}) and straight-lines (R_{SL}) of ^{A}Pn-∗-^{B}Pn and Pn-∗-X in **7-1**, **7-5**, **7-6** and **7-1a**$^{+}$–**7-8c**$^{+}$ of **7-*mx*$^{+}_{sym}$** and/or **7-*mx*$^{+}_{nsym}$**, evaluated with MP2/BSS-B, together with the differences between r_{BP} and R_{SL} (Δr_{BP}).[a]

Species (A-∗-B)[b]	r_{BP}[c] (Å)	R_{SL}[d] (Å)	Δr_{BP}[e] (Å)	Species (A-∗-B)[b]	r_{BP}[c] (Å)	R_{SL}[d] (Å)	Δr_{BP}[e] (Å)
7-1 (^{A}N-∗-^{B}N)	3.0094	3.0094	0.0000	**7-6a**$^{+}_{sym}$ ($^{A/B}$P-∗-H)	1.6387	1.6387	0.0000
7-5 (^{A}N-∗-^{B}N)	2.7826	2.7826	0.0000	**7-6a**$^{+}_{nsym}$ (^{A}P--∗--H)	2.5709	2.5622	0.0087
7-6 (^{A}P-∗-^{B}P)	3.2493	3.2493	0.0000	(^{B}P-∗-H)	1.3856	1.3942	–0.0086
7-1a$^{+}_{nsym}$ (^{A}N--∗--H)	1.1587	1.1620	–0.0033	**7-6b**$^{+}_{sym}$ ($^{A/B}$P-∗-F)	1.9884	1.9884	0.0000
(^{B}N-∗-H)	1.2086	1.2086	0.0000	**7-6b**$^{+}_{nsym}$ (^{A}P--∗--F)	2.6414	2.6414	0.0000
7-1b$^{+}_{sym}$ ($^{A/B}$N-∗-F)	1.6539	1.6539	0.0000	(^{B}P-∗-F)	1.5386	1.5386	0.0000
7-1b$^{+}_{nsym}$ (^{A}N--∗--F)	1.8750	1.8750	0.0000	**7-6c**$^{+}_{sym}$ ($^{A/B}$P-∗-Cl)	2.2188	2.2188	0.0000
(^{B}N-∗-F)	1.3611	1.3611	0.0000	**7-6c**$^{+}_{nsym}$ (^{A}P--∗--Cl)	2.5650	2.5650	0.0000
7-1c$^{+}_{sym}$ ($^{A/B}$N-∗-Cl)	1.7827	1.7827	0.0000	(^{B}P-∗-Cl)	1.9004	1.9004	0.0000
7-2a$^{+}_{sym}$ ($^{A/B}$P-∗-H)	1.6322	1.6322	0.0000	**7-6d**$^{+}_{sym}$ ($^{A/B}$P-∗-Br)	2.3038	2.3038	0.0000
7-2a$^{+}_{nsym}$ (^{A}P--∗--H)	1.9746	1.9665	0.0080	**7-6d**$^{+}_{nsym}$ (^{A}P--∗--Br)	2.5694	2.5694	0.0000
(^{B}P-∗-H)	1.3513	1.3593	–0.0080	(^{B}P-∗-Br)	2.0431	2.0431	0.0000
7-2b$^{+}_{sym}$ ($^{A/B}$P-∗-F)	1.8149	1.8149	0.0000	**7-6e**$^{+}_{sym}$ ($^{A/B}$P-∗-I)	2.4524	2.4524	0.0000
7-2b$^{+}_{nsym}$ (^{A}P--∗--F)	2.2180	2.2180	0.0000	**7-7a**$^{+}_{nsym}$ (^{A}As--∗--H)	2.4188	2.4109	0.0079
(^{B}P-∗-F)	1.5032	1.5032	0.0000	(^{B}As-∗-H)	1.4731	1.4810	–0.0079
7-3a$^{+}_{sym}$ ($^{A/B}$As-∗-H)	1.7398	1.7398	0.0000	**7-7b**$^{+}_{sym}$ ($^{A/B}$As-∗-F)	2.0795	2.0795	0.0000
7-3a$^{+}_{nsym}$ (^{A}As--∗--H)	2.0407	2.0337	0.0070	**7-7b**$^{+}_{nsym}$ (^{A}As--∗--F)	2.7087	2.7087	0.0000
(^{B}As-∗-H)	1.4481	1.4551	–0.0070	(^{B}As-∗-F)	1.6826	1.6826	0.0000
7-3b$^{+}_{sym}$ ($^{A/B}$As-∗-F)	1.9288	1.9288	0.0000	**7-7c**$^{+}_{sym}$ ($^{A/B}$As-∗-Cl)	2.3378	2.3378	0.0000
7-3b$^{+}_{nsym}$ (^{A}As--∗--F)	2.2784	2.2784	0.0000	**7-7c**$^{+}_{nsym}$ (^{A}As--∗--Cl)	2.6470	2.6470	0.0000
(^{B}As-∗-F)	1.6519	1.6519	0.0000	(^{B}As-∗-Cl)	2.0293	2.0293	0.0000
7-4a$^{+}_{sym}$ (^{A}Sb-∗-H)	1.8823	1.8823	0.0000	**7-7d**$^{+}_{sym}$ ($^{A/B}$As-∗-Br)	2.4227	2.4227	0.0000
7-4a$^{+}_{sym}$ (^{B}Sb-∗-H)	1.8815	1.8815	0.0000	**7-7d**$^{+}_{nsym}$ (^{A}As--∗--Br)	2.6467	2.6467	0.0000
7-4a$^{+}_{nsym}$ (^{A}Sb--∗--H)	2.1469	2.1416	0.0053	(^{B}As-∗-Br)	2.1903	2.1903	0.0000
~~**7-4a**$^{+}_{nsym}$~~ (^{B}Sb-∗-H)	1.6575	1.6628	–0.0053	**7-8a**$^{+}_{sym}$ ($^{A/B}$Sb-∗-H)	1.9903	1.9903	0.0000
7-4b$^{+}_{sym}$ ($^{A/B}$Sb-∗-F)	2.0150	2.0150	0.0000	**7-8a**$^{+}_{nsym}$ (^{A}Sb--∗--H)	2.5088	2.5024	0.0064
7-5a$^{+}_{nsym}$ (^{A}N--∗--H)	1.1983	1.2022	–0.0039	(^{B}Sb-∗-H)	1.6639	1.6703	–0.0064
(^{B}N-∗-H)	1.2667	1.2667	0.0000	**7-8b**$^{+}_{sym}$ ($^{A/B}$Sb-∗-F)	2.1742	2.1742	0.0000
7-5b$^{+}_{sym}$ ($^{A/B}$N-∗-F)	1.7864	1.7864	0.0000	**7-8b**$^{+}_{nsym}$ (^{A}Sb--∗--F)	2.7265	2.7265	0.0000
7-5b$^{+}_{nsym}$ (^{A}N--∗--F)	2.0800	2.0799	0.0001	(^{B}Sb-∗-F)	1.8672	1.8672	0.0000
(^{B}N-∗-F)	1.3924	1.3924	0.0000	**7-8c**$^{+}_{sym}$ ($^{A/B}$Sb-∗-Cl)	2.4712	2.4712	0.0000
7-5c$^{+}_{sym}$ ($^{A/B}$N-∗-Cl)	1.8189	1.8189	0.0000	**7-8c**$^{+}_{nsym}$ (^{A}Sb--∗--Cl)	2.7908	2.7908	0.0000
7-5d$^{+}_{sym}$ ($^{A/B}$N-∗-Br)	1.9131	1.9131	0.0000	(^{B}Sb-∗-Cl)	2.2143	2.2143	0.0000
7-5e$^{+}_{sym}$ ($^{A/B}$N-∗-I)	2.0499	2.0499	0.0000				

[a] See Table 7-1 in the text for BSS-B. [b] Interactions in question can be found in Figure 7-5 in the text and Figures 7-A4 and A5 of the Appendix. [c] Bond path lengths between A and B. [c] Straight-line distances between A and B. [d] $\Delta r_{BP} = r_{BP} - R_{SL}$.

Table 7-A4. The lengths of BPs (r_{BP}), straight-lines (R_{SL}), and the differences between r_{BP} and R_{SL} (Δr_{BP}) of H-∗-H and/or X-∗-C (X = F, Cl, Br, and I) in **7-2**–**7-8** and **7-1b**$^+$–**7-8c**$^+$ of **7-*mx*$^+_{sym}$** and/or **7-*mx*$^+_{nsym}$**, together with H-∗-^{B}Sb in **7-8a**$^+_{nsym}$, evaluated with MP2/BSS-B.[a]

Species (^{u}A-∗-^{v}B)[b,c]	r_{BP}[d] (Å)	R_{SL}[e] (Å)	Δr_{BP}[f] (Å)
7-2 (^{2}H-∗-^{7}H)	2.3545	2.2051	0.1495
7-3 (^{2}H-∗-^{7}H)	2.3528	2.2201	0.1326
7-4 (^{2}H-∗-^{7}H)	2.4928	2.3426	0.1502
7-5 (^{3}H-∗-^{8}H)	2.6531	2.5706	0.0826
7-6 (^{2}H-∗-^{9}H)	1.9088	1.8453	0.0635
7-7 (^{3}H-∗-^{8}H)	1.8006	1.7431	0.0575
7-8 (^{3}H-∗-^{8}H)	1.8199	1.7636	0.0564
7-1b$^+_{sym}$ (F-∗-^{3}C)	2.1016	2.0942	0.0074
7-1b$^+_{nsym}$ (F-∗-^{2}C)	2.1179	2.1100	0.0079
7-1c$^+_{sym}$ (Cl-∗-^{3}C)	2.2531	2.2498	0.0034
7-3a$^+_{nsym}$ (^{2}H-∗-^{7}H)	2.3755	2.2427	0.1328
7-3b$^+_{sym}$ (F-∗-^{3}C)	2.3563	2.3465	0.0099
7-3b$^+_{sym}$ (^{2}H-∗-^{7}H)	2.5742	2.3603	0.2138
7-3b$^+_{nsym}$ (^{2}H-∗-^{7}H)	2.4387	2.3024	0.1363
7-4a$^+_{nsym}$ (^{2}H-∗-^{7}H)	2.3296	2.3465	0.1020
7-5b$^+_{sym}$ (^{3}H-∗-^{8}H)	2.4824	2.3890	0.0934
7-5b$^+_{nsym}$ (^{3}H-∗-^{8}H)	2.4328	2.3465	0.0863
7-5c$^+_{sym}$ (Cl-∗-^{3}C)	2.5481	2.5291	0.0190
7-5d$^+_{sym}$ (Br-∗-^{3}C)	2.5842	2.5672	0.0170
7-5e$^+_{sym}$ (I-∗-^{3}C)	2.6475	2.6383	0.0092
7-6a$^+_{nsym}$ (^{2}H-∗-^{9}H)	2.2671	2.1411	0.1260
7-6a$^+_{nsym}$ (^{4}H-∗-^{9}H)	2.3596	2.2793	0.0804
7-6b$^+_{nsym}$ (F-∗-^{2}C)	2.5307	2.5252	0.0055
7-6b$^+_{nsym}$ (^{2}H-∗-^{9}H)	2.4058	2.2698	0.1360
7-6b$^+_{nsym}$ (^{4}H-∗-^{9}H)	2.3754	2.3033	0.0721
7-6c$^+_{nsym}$ (Cl-∗-^{3}C)	2.6376	2.6176	0.0200
7-6d$^+_{sym}$ (Br-∗-^{3}C)	2.7615	2.7324	0.0291
7-6d$^+_{nsym}$ (Br-∗-^{3}C)	2.7155	2.6690	0.0465
7-6e$^+_{sym}$ (I-∗-^{3}C)	2.8226	2.8024	0.0202
7-7a$^+_{nsym}$ (^{3}H-∗-^{8}H)	2.0422	1.9777	0.0645
7-7b$^+_{nsym}$ (F-∗-^{3}C)	2.5907	2.5441	0.0465
7-7b$^+_{nsym}$ (^{2}H-∗-^{9}H)	2.3305	2.2277	0.1028
7-7b$^+_{nsym}$ (^{4}H-∗-^{9}H)	2.3507	2.2819	0.0687
7-7c$^+_{sym}$ (Cl-∗-^{3}C)	2.7573	2.7388	0.0185
7-7c$^+_{nsym}$ (Cl-∗-^{3}C)	2.6685	2.6601	0.0085
7-7d$^+_{sym}$ (Br-∗-^{3}C)	2.7983	2.7807	0.0175
7-7d$^+_{nsym}$ (Br-∗-^{3}C)	2.7402	2.7248	0.0153
7-8a$^+_{nsym}$ (^{3}H-∗-^{8}H)	2.0343	1.9731	0.0611
7-8a$^+_{nsym}$ (^{3}H-∗-^{B}Sb)	2.8452	2.6788	0.1664
7-8b$^+_{sym}$ (F-∗-^{3}C)	2.7362	2.6708	0.0655
7-8b$^+_{sym}$ (^{3}H-∗-^{8}H)	2.0487	1.9909	0.0578
7-8b$^+_{nsym}$ (F-∗-^{3}C)	2.8560	2.6217	0.2344
7-8b$^+_{nsym}$ (^{3}H-∗-^{8}H)	2.0244	1.9619	0.0625
7-8c$^+_{sym}$ (Cl-∗-^{3}C)	2.8137	2.8042	0.0095
7-8c$^+_{nsym}$ (Cl-∗-^{3}C)	2.7309	2.7245	0.0064

[a] See Table 7-1 in the text for BSS-B. [b] Interactions in question can be found in Figure 7-5 in the text and Figures 7-A4 and A5 of the Appendix. [c] The *u* and *v* are the position numbers of C or C bonding to H. [d] Bond path lengths between A and B. [e] Straight-line distances between A and B. [f] $\Delta r_{BP} = r_{BP} - R_{SL}$.

Table 7-A5. The QTAIM functions and QTAIM-DFA parameters of H-∗-H, X-∗-C, and Pn-∗-H for **7-2**–**7-8** and **7-1a**$^+$–**7-8c**$^+$ of **7-*mx*$^+_{sym}$** and/or **7-*mx*$^+_{nsym}$**, together with the C_{ii} values and the predicted natures, evaluated with MP2/BSS-B.[a,b]

Species (^{u}A-∗-^{v}B^c: symm)	$\rho_b(\boldsymbol{r}_c)$ (ea_o^{-3})	$c\nabla^2\rho_b(\boldsymbol{r}_c)^d$ (au)	$H_b(\boldsymbol{r}_c)$ (au)	R^e (au)	θ^f (º)	$C_{ii}{}^g$ (Å mdyn^{-1})	$\theta_p{}^h$ (º)	$\kappa_p{}^i$ (au^{-1})	Predicted nature
7-2 (^{2}H-∗-^{7}H: C_{3h})	0.0094	0.0044	0.0014	0.0046	72.0	14.926	109.5	262.9	*p*-CS/*t*-HB$_{nc}$
7-3 (^{2}H-∗-^{7}H: C_{3h})	0.0089	0.0041	0.0013	0.0043	72.3	18.005	106.9	317.4	*p*-CS/*t*-HB$_{nc}$
7-4 (^{2}H-∗-^{7}H: C_{3h})	0.0069	0.0032	0.0012	0.0034	69.4	36.961	95.3	401.6	*p*-CS/*t*-HB$_{nc}$
7-5 (^{2}H-∗-^{7}H: C_3)	0.0041	0.0018	0.0009	0.0020	65.0	26.853	74.0	390.5	*p*-CS/vdW
7-6 (^{2}H-∗-^{7}H: C_3)	0.0171	0.0059	–0.0004	0.0059	93.4	7.427	140.6	9.6	*r*-CS/*t*-HB$_{wc}$
7-7 (^{2}H-∗-^{7}H: D_3)	0.0220	0.0078	–0.0007	0.0078	95.1	4.620	130.4	29.1	*r*-CS/*t*-HB$_{wc}$
7-8 (^{2}H-∗-^{7}H: D_3)	0.0211	0.0076	–0.0006	0.0076	94.5	4.808	130.2	18.9	*r*-CS/*t*-HB$_{wc}$
7-1b$^+_{sym}$ (F-∗-^{3}C: C_{3h})	0.0520	0.0331	–0.0018	0.0331	93.0	0.536	131.6	28.1	*r*-CS/*t*-HB$_{wc}$
7-1b$^+_{nsym}$ (F-∗-^{2}C: C_3)	0.0501	0.0328	–0.0006	0.0328	91.0	0.574	130.8	4.3	*r*-CS/*t*-HB$_{wc}$
7-1c$^+_{sym}$ (Cl-∗-^{3}C: C_{3h})	0.0629	0.0250	–0.0126	0.0280	116.8	0.679	166.0	36.3	*r*-CS/CT-MC
7-3a$^+_{nsym}$ (^{2}H-∗-^{7}H: C_3)	0.0082	0.0037	0.0012	0.0039	71.6	17.234	101.9	408.1	*p*-CS/*t*-HB$_{nc}$
7-3b$^+_{sym}$ (F-∗-^{3}C: C_{3h})[j]	0.0297	0.0205	0.0041	0.0209	78.6	1.117	99.9	48.2	*p*-CS/*t*-HB$_{nc}$
(^{2}H-∗-^{7}H)[k]	0.0065	0.0032	0.0013	0.0035	68.1	16.721	98.2	427.8	*p*-CS/*t*-HB$_{nc}$
7-3b$^+_{nsym}$ (^{2}H-∗-^{7}H: C_3)	0.0071	0.0034	0.0013	0.0036	69.5	17.625	95.8	365.1	*p*-CS/*t*-HB$_{nc}$
7-4a$^+_{nsym}$ (^{2}H-∗-^{7}H: C_3)	0.0080	0.0034	0.0010	0.0036	73.5	19.964	104.7	438.6	*p*-CS/*t*-HB$_{nc}$
7-5b$^+_{sym}$ (^{3}H-∗-^{8}H: D_3)	0.0055	0.0025	0.0010	0.0028	67.9	16.505	87.0	474.3	*p*-CS/vdW
7-5b$^+_{nsym}$ (^{3}H-∗-^{8}H: C_3)	0.0061	0.0027	0.0010	0.0029	69.7	15.600	91.7	459.7	*p*-CS/*t*-HB$_{nc}$
7-5c$^+_{sym}$ (Cl-∗-^{3}C: C_3)[l]	0.0364	0.0177	–0.0008	0.0177	92.7	0.670	134.3	26.6	*r*-CS/*t*-HB$_{wc}$
7-5d$^+_{sym}$ (Br-∗-^{3}C: C_2)[l]	0.0390	0.0172	–0.0021	0.0173	97.0	0.639	141.3	31.6	*r*-CS/*t*-HB$_{wc}$
7-5e$^+_{sym}$ (I-∗-^{3}C: D_3)	0.0423	0.0154	–0.0051	0.0162	108.3	0.650	161.9	51.7	*r*-CS/CT-MC
7-6a$^+_{nsym}$ (^{2}H-∗-^{9}H: C_2)	0.0106	0.0047	0.0012	0.0048	75.5	26.283	119.5	291.0	*p*-CS/*t*-HB$_{nc}$
7-6a$^+_{nsym}$ (^{4}H-∗-^{9}H: C_2)	0.0071	0.0030	0.0009	0.0031	73.7	34.331	102.5	474.1	*p*-CS/*t*-HB$_{nc}$
7-6b$^+_{nsym}$ (F-∗-^{2}C: C_3)	0.0188	0.0131	0.0044	0.0139	71.4	1.796	77.9	29.7	*p*-CS/vdW
(^{2}H-∗-^{9}H)	0.0080	0.0038	0.0013	0.0040	70.6	29.049	105.7	212.6	*p*-CS/*t*-HB$_{nc}$
(^{4}H-∗-^{9}H)	0.0080	0.0038	0.0013	0.0040	70.6	23.418	125.4	140.9	*p*-CS/*t*-HB$_{nc}$
7-6c$^+_{nsym}$ (Cl-∗-^{3}C: C_1)[l]	0.0289	0.0150	0.0011	0.0151	85.7	1.191	120.1	21.5	*p*-CS/*t*-HB$_{nc}$
7-6d$^+_{sym}$ (Br-∗-^{3}C: C_3)	0.0279	0.0130	0.0007	0.0130	87.0	1.166	116.3	254.5	*p*-CS/*t*-HB$_{nc}$
7-6d$^+_{nsym}$ (Br-∗-^{3}C: C_3)[k]	0.03130	0.0148	0.0005	0.0148	88.1	1.187	130.1	79.9	*p*-CS/*t*-HB$_{nc}$
7-6e$^+_{sym}$ (I-∗-^{3}C: D_3)	0.0310	0.0124	–0.0009	0.0125	94.0	2.085	134.6	82.0	*r*-CS/*t*-HB$_{wc}$
7-7a$^+_{nsym}$ (^{3}H-∗-^{8}H: C_1)	0.0127	0.0046	0.0002	0.0046	87.8	9.059	129.0	127.1	*p*-CS/*t*-HB$_{nc}$
7-7b$^+_{nsym}$ (F-∗-^{3}C: C_3)	0.0186	0.0129	0.0044	0.0136	71.2	1.867	77.3	31.2	*p*-CS/vdW
(^{2}H-∗-^{9}H)	0.0084	0.0038	0.0012	0.0040	72.8	25.941	108.5	404.7	*p*-CS/*t*-HB$_{nc}$
(^{4}H-∗-^{9}H)	0.0066	0.0028	0.0009	0.0030	72.8	31.114	105.2	512.4	*p*-CS/*t*-HB$_{nc}$
7-7c$^+_{sym}$ (Cl-∗-^{3}C: C_2)[l]	0.0234	0.0123	0.0019	0.0124	81.4	1.433	108.3	43.9	*p*-CS/*t*-HB$_{nc}$
7-7c$^+_{nsym}$ (Cl-∗-^{3}C: C_1)	0.0265	0.0141	0.0016	0.0142	83.6	1.336	112.4	64.6	*p*-CS/*t*-HB$_{nc}$
7-7d$^+_{sym}$ (Br-∗-^{3}C: C_2)	0.0255	0.0121	0.0011	0.0121	84.8	1.458	112.1	61.5	*p*-CS/*t*-HB$_{nc}$
7-7d$^+_{nsym}$ (Br-∗-^{3}C: C_3)	0.0278	0.0134	0.0009	0.0135	86.1	1.523	114.0	74.5	*p*-CS/*t*-HB$_{nc}$
7-8a$^+_{nsym}$ (^{3}H-∗-^{8}H: C_1)	0.0129	0.0046	0.0001	0.0046	88.7	8.635	129.9	113.1	*p*-CS/*t*-HB$_{nc}$
(^{3}H-∗-^{8}Sb)	0.0170	0.0063	0.0005	0.0063	85.2	5.574	157.1	67.0	*p*-CS/*t*-HB$_{nc}$
7-8b$^+_{sym}$ (F-∗-^{3}C: C_3)	0.0156	0.0101	0.0034	0.0107	71.6	2.014	73.7	39.8	*p*-CS/vdW
(^{3}H-∗-^{8}H)	0.0119	0.0044	0.0002	0.0044	87.1	8.913	127.8	130.4	*p*-CS/*t*-HB$_{nc}$
7-8b$^+_{nsym}$ (F-∗-^{3}C: C_3)	0.0169	0.0111	0.0038	0.0117	70.9	2.080	76.1	26.5	*p*-CS/vdW
(^{3}H-∗-^{8}H)	0.0122	0.0041	–0.0001	0.0041	91.4	10.159	133.3	78.9	*r*-CS/*t*-HB$_{wc}$
7-8c$^+_{sym}$ (Cl-∗-^{3}C: D_3)	0.0205	0.0111	0.0023	0.0113	78.5	2.083	100.9	82.4	*p*-CS/*t*-HB$_{nc}$
7-8c$^+_{nsym}$ (Cl-∗-^{3}C: C_3)	0.0233	0.0128	0.0021	0.0130	80.5	1.762	105.6	73.2	*p*-CS/*t*-HB$_{nc}$

[a] See Table 7-1 in the text for BSS-B. [b] Data are given at the BCPs. [c] The *u* and *v* are the position numbers of C or C bonding to H. [d] $c\nabla^2\rho_b(\boldsymbol{r}_c) = H_b(\boldsymbol{r}_c) - V_b(\boldsymbol{r}_c)/2$, where $c = \hbar^2/8m$. [e] $R = (x^2 + y^2)^{1/2}$, where $(x, y) = (H_b(\boldsymbol{r}_c) - V_b(\boldsymbol{r}_c)/2, H_b(\boldsymbol{r}_c))$. [f] $\theta = 90^o - \tan^{-1}(y/x)$. [g] $C_{ij} = \partial^2 E/\partial f_i \partial f_j$, where *i* and *j* refer to internal coordinates, and f_i and f_j corresponding to *i* and *j*, respectively, are the external force components acting on the system. [h] $\theta_p = 90^o - \tan^{-1}(dy/dx)$. [i] $\kappa_p = |d^2y/dx^2|/[1 + (dy/dx)^2]^{3/2}$. [j] Data from $w = -0.075$, -0.05, -0.025, 0.0, and 0.025 were employed for the calculating θ_p and κ_p because the BCPs were not detected for $w = 0.05$ and 0.1. [k] Data from $w = -0.1$, -0.075, -0.05, -0.025, and 0.0 were employed for the calculating θ_p and κ_p because the BCPs were not detected for $w = 0.025$, 0.05, and 0.1. [l] Data from $w = \pm 0.05$, ± 0.025, and 0.0 were employed for the calculating θ_p and κ_p because the BCPs were not detected for $w = 0.1$.

Table 7-A6. The QTAIM functions and QTAIM-DFA parameters of $^{A/B}$Pn-∗-X in **7-1a**$^{+}_{tp:TS}$, **7-5a**$^{+}_{tp:TS}$, and **7-7a**$^{+}_{tp:TS}$, ^{A}Pn--∗--X/^{B}Pn-∗-X in **7-1b**$^{+}$–**7-8c**$^{+}$ of **7-*mx***$^{+}_{s\text{-}ns:TS}$ and X-∗-H and H-∗-H in them, together with the C_{ii} values and the predicted natures, evaluated with MP2/BSS-B[a,b]

Species (^{u}A-∗-^{v}B[c]: symm)	$\rho_b(\boldsymbol{r}_c)$ (ea_o^{-3})	$c\nabla^2\rho_b(\boldsymbol{r}_c)$[d] (au)	$H_b(\boldsymbol{r}_c)$ (au)	R[e] (au)	θ[f] (º)	C_{ii}[g] (Å mdyn^{-1})	θ_p[h] (º)	κ_p[i] (au^{-1})	Predicted nature
$^{A/B}$Pn-∗-X, ^{A}Pn--∗--X and ^{B}Pn-∗-X interactions									
7-1a$^{+}_{tp:TS}$ ($^{A/B}$N-∗-H: C_s)	0.2084	–0.0708	–0.2351	0.2456	196.8	-32.869	206.1	0.0	SS/Cov-s
7-5a$^{+}_{tp:TS}$ ($^{A/B}$N-∗-H: C_3)	0.1786	–0.0568	–0.1847	0.1933	197.1	-16.412	205.7	0.0	SS/Cov-s
7-7a$^{+}_{tp:TS}$ ($^{A/B}$As-∗-H: C_3)	0.1108	–0.0155	–0.0613	0.0632	194.2	1.552	200.1	2.0	SS/Cov-w
7-1b$^{+}_{s\text{-}ns:TS}$ (^{A}N--∗--F: C_3)	0.1070	0.0544	–0.0282	0.0613	117.4	–0.099	212.9	17.9	*r*-CS/CT-TBP
(^{B}N-∗-F)	0.2778	0.0228	–0.2151	0.2163	173.9	–0.171	205.3	1.1	*r*-CS/CT-TBP
7-2a$^{+}_{s\text{-}ns:TS}$ (^{A}P--∗--H: C_3)	0.0927	–0.0089	–0.0501	0.0509	190.1	0.514	194.5	0.1	SS/Cov-w
(^{B}P-∗-H)	0.1250	–0.0276	–0.0906	0.0947	196.9	0.353	194.3	5.4	SS/Cov-w
7-2b$^{+}_{s\text{-}ns:TS}$ (^{A}P--∗--F: C_3)	0.0793	0.0134	–0.0370	0.0393	160.2	0.246	181.6	5.9	*r*-CS/CT-TBP
(^{B}P-∗-F)	0.1262	0.0448	–0.0920	0.1023	154.0	0.139	92.6	6.9	*r*-CS/*t*-HB$_{wc}$
7-3a$^{+}_{s\text{-}ns:TS}$ (^{A}As--∗--H: C_3)	0.0783	–0.0013	–0.0360	0.0360	182.0	0.379	162.1	61.7	SS/Cov-w
(^{B}As-∗-H)	0.1072	–0.0092	–0.0625	0.0631	188.4	0.224	131.5	10.5	SS/Cov-w
7-3b$^{+}_{s\text{-}ns:TS}$ (^{A}As--∗--F: C_3)	0.0688	0.0238	–0.0186	0.0302	128.0	0.285	125.3	25.7	*r*-CS/*t*-HB$_{wc}$
(^{B}As-∗-F)	0.1243	0.0541	–0.0601	0.0808	138.0	0.128	122.4	5.3	*r*-CS/*t*-HB$_{wc}$
7-4a$^{+}_{s\text{-}ns:TS}$ (^{A}Sb--∗--H: C_3)	0.0528	0.0062	–0.0165	0.0176	159.3	0.537	129.2	49.2	*r*-CS/*t*-HB$_{wc}$
(^{B}Sb-∗-H)[j]	0.1019	0.0078	–0.0496	0.0502	171.1	0.113	240.4	8.1	*r*-CS/CT-TBP
7-5b$^{+}_{s\text{-}ns:TS}$ (^{A}N--∗--F: C_3)	0.0809	0.0392	–0.0132	0.0414	108.6	0.204	202.0	49.4	*r*-CS/CT-TBP
(^{B}N-∗-F)	0.2504	0.0234	–0.1697	0.1713	172.1	–0.119	209.6	3.0	*r*-CS/CT-TBP
7-6a$^{+}_{s\text{-}ns:TS}$ (^{A}P--∗--H: C_1)	0.0866	–0.0074	–0.0391	0.0398	190.7	-1.076	204.1	2.2	SS/Cov-w
(^{B}P-∗-H)	0.1434	–0.0357	–0.0967	0.1030	200.2	0.485	201.5	2.4	SS/Cov-w
7-6b$^{+}_{s\text{-}ns:TS}$ (^{A}P--∗--F: C_3)	0.0718	0.0116	–0.0236	0.0264	153.8	0.476	186.5	16.3	*r*-CS/CT-TBP
(^{B}P-∗-F)	0.1170	0.0081	–0.0928	0.0932	175.0	0.339	112.8	37.2	*r*-CS/*t*-HB$_{wc}$
7-6c$^{+}_{s\text{-}ns:TS}$ (^{A}P--∗--Cl: C_1)	0.0812	0.0028	–0.0339	0.0340	175.2	0.366	191.1	7.9	*r*-CS/CT-TBP
(^{B}P-∗-Cl)	0.1193	–0.0137	–0.0791	0.0803	189.8	0.201	194.3	2.6	SS/Cov-w
7-6d$^{+}_{s\text{-}ns:TS}$ (^{A}P--∗--Br: C_1)	0.0720	0.0053	–0.0259	0.0264	168.4	0.307	182.6	10.3	*r*-CS/CT-TBP
(^{B}P-∗-Br)[j]	0.1145	–0.0103	–0.0676	0.0684	188.7	0.092	179.3	23.2	SS/Cov-w
7-7b$^{+}_{s\text{-}ns:TS}$ (^{A}As--∗--F: C_1)	0.0612	0.0161	–0.0142	0.0215	131.4	0.582	150.7	8.7	*r*-CS/CT-MC
(^{B}As-∗-F)	0.1065	0.0320	–0.0463	0.0563	145.4	0.342	128.9	3.1	*r*-CS/*t*-HB$_{wc}$
7-7c$^{+}_{s\text{-}ns:TS}$ (^{A}As--∗--Cl: C_1)	0.0625	0.0078	–0.0196	0.0211	158.4	0.425	174.5	6.1	*r*-CS/CT-MC
(^{B}As-∗-Cl)	0.1004	0.0035	–0.0496	0.0497	176.0	0.163	154.8	55.6	*r*-CS/CT-MC
7-7d$^{+}_{s\text{-}ns:TS}$ (^{A}As--∗--Br: C_1)	0.0539	0.0086	–0.0141	0.0165	148.8	0.276	136.5	79.1	*r*-CS/*t*-HB$_{wc}$
(^{B}As-∗-Br)	0.1060	–0.0010	–0.0555	0.0555	181.0	–0.196	198.2	10.0	SS/Cov-w
7-8a$^{+}_{s\text{-}ns:TS}$ (^{A}Sb--∗--H: C_1)	0.0706	–0.0007	–0.0287	0.0287	181.5	1.935	176.1	20.9	SS/Cov-w
(^{B}Sb-∗-H)	0.0812	–0.0034	–0.0355	0.0357	185.4	1.154	170.3	39.9	SS/Cov-w
7-8b$^{+}_{s\text{-}ns:TS}$ (^{A}Sb--∗--F: C_3)	0.0507	0.0203	–0.0062	0.0212	106.9	0.724	98.4	7.6	*r*-CS/*t*-HB$_{wc}$
(^{B}Sb-∗-F)	0.0904	0.0514	–0.0193	0.0549	110.6	0.334	108.6	4.7	*r*-CS/*t*-HB$_{wc}$
7-8c$^{+}_{s\text{-}ns:TS}$ (^{A}Sb--∗--Cl: C_3)	0.0492	0.0091	–0.0124	0.0154	143.7	0.553	139.6	39.5	*r*-CS/*t*-HB$_{wc}$
(^{B}Sb-∗-Cl)	0.0828	0.0163	–0.0298	0.0339	151.4	0.202	117.8	28.1	*r*-CS/*t*-HB$_{wc}$

[a] See Table 7-1 in the text for BSS-B. [b] Data are given at the BCPs. [c] The u and v are the position numbers of C or C bonding to H. [d] $c\nabla^2\rho_b(\boldsymbol{r}_c) = H_b(\boldsymbol{r}_c) - V_b(\boldsymbol{r}_c)/2$, where $c = \hbar^2/8m$. [e] $R = (x^2 + y^2)^{1/2}$, where $(x, y) = (H_b(\boldsymbol{r}_c) - V_b(\boldsymbol{r}_c)/2, H_b(\boldsymbol{r}_c))$. [f] $\theta = 90º - \tan^{-1}(y/x)$. [g] $C_{ij} = \partial^2 E/\partial f_i \partial f_j$, where i and j refer to internal coordinates, and f_i and f_j corresponding to i and j, respectively, are the external force components acting on the system. [h] $\theta_p = 90º - \tan^{-1}(dy/dx)$. [i] $\kappa_p = |d^2y/dx^2|/[1 + (dy/dx)^2]^{3/2}$. [j] Data from $w = \pm0.05$, ±0.025, and 0.0 were employed for the calculating θ_p and κ_p, because a poor correlation is obtained for the data from $w = \pm0.1$, ±0.05, and 0.0. [k] Data from $w = –0.075$, $–0.05$, $–0.025$, 0.0, and 0.025 were employed for the calculating θ_p and κ_p because the BCPs were not detected for $w = 0.05$ and 0.1. [l] Data from $w = \pm0.05$, ±0.025, and 0.0 were employed for the calculating θ_p and κ_p because the BCPs were not detected for $w = 0.1$. [m] Data from $w = –0.1$, $–0.075$, $–0.05$, $–0.025$, and 0.0 were employed for the calculating θ_p and κ_p because the BCPs were not detected for $w = 0.025$.

(Table 7-A6 continued)

Species (^{u}A-∗-^{v}B^c: symm)	$\rho_b(\boldsymbol{r}_c)$ (ea_o^{-3})	$c\nabla^2\rho_b(\boldsymbol{r}_c)^d$ (au)	$H_b(\boldsymbol{r}_c)$ (au)	R^e (au)	θ^f (º)	$C_{it}{}^g$ (Å mdyn^{-1})	$\theta_p{}^h$ (º)	$\kappa_p{}^i$ (au^{-1})	Predicted nature
X-∗-C and H-∗-H interactions									
7-7a$^+_{tp:TS}$ (^{3}H-∗-^{8}H: C_3)	0.0118	0.0041	0.0000	0.0041	89.3	9.563	131.2	127.5	*p*-CS/*t*-HB$_{nc}$
7-1b$^+_{s\text{-}ns:TS}$ (F-∗-^{3}C: C_3)	0.0506	0.0328	–0.0008	0.0328	91.4	0.537	130.0	25.2	*r*-CS/*t*-HB$_{wc}$
7-2b$^+_{s\text{-}ns:TS}$ (F-∗-^{3}C: C_3)^k	0.0332	0.0234	0.0041	0.0238	80.1	0.914	106.6	34.4	*p*-CS/*t*-HB$_{nc}$
7-3a$^+_{s\text{-}ns:TS}$ (^{2}H-∗-^{7}H: C_3)	0.0072	0.0033	0.0012	0.0035	69.6	25.983	96.9	307.5	*p*-CS/*t*-HB$_{nc}$
7-3b$^+_{s\text{-}ns:TS}$ (^{2}H-∗-^{7}H: C_3)	0.0085	0.0039	0.0011	0.0040	73.6	13.537	107.8	370.2	*p*-CS/*t*-HB$_{nc}$
7-4a$^+_{s\text{-}ns:TS}$ (^{2}H-∗-^{7}H: C_3)	0.0079	0.0034	0.0011	0.0036	72.8	20.372	103.0	416.0	*p*-CS/*t*-HB$_{nc}$
7-5b$^+_{s\text{-}ns:TS}$ (^{3}H-∗-^{8}H: C_3)	0.0056	0.0025	0.0010	0.0027	68.3	16.014	87.0	455.7	*p*-CS/vdW
7-6a$^+_{s\text{-}ns:TS}$ (^{3}H-∗-^{8}H: C_1)	0.0094	0.0035	0.0005	0.0035	81.8	14.451	122.5	299.1	*p*-CS/*t*-HB$_{nc}$
7-6b$^+_{s\text{-}ns:TS}$ (^{3}H-∗-^{8}H: C_3)	0.0098	0.0037	0.0005	0.0037	82.2	11.828	132.8	237.0	*p*-CS/*t*-HB$_{nc}$
7-6c$^+_{s\text{-}ns:TS}$ (Cl-∗-^{3}C: C_1)	0.0264	0.0137	0.0014	0.0138	84.1	1.167	114.7	1.5	*p*-CS/*t*-HB$_{nc}$
7-6d$^+_{s\text{-}ns:TS}$ (Br-∗-^{3}C: C_1)^l	0.0289	0.0137	0.0006	0.0137	87.5	1.139	119.7	44.1	*p*-CS/*t*-HB$_{nc}$
7-7b$^+_{s\text{-}ns:TS}$ (F-∗-^{3}C: C_1)^l	0.0164	0.0110	0.0036	0.0115	71.9	1.898	74.7	42.7	*p*-CS/vdW
(^{3}H-∗-^{8}H)	0.0112	0.0041	0.0003	0.0041	85.2	10.014	125.4	167.3	*p*-CS/*t*-HB$_{nc}$
7-7c$^+_{s\text{-}ns:TS}$ (Cl-∗-^{3}C: C_1)^l	0.0240	0.0128	0.0019	0.0130	81.6	1.403	108.5	42.8	*p*-CS/*t*-HB$_{nc}$
7-7d$^+_{s\text{-}ns:TS}$ (Br-∗-^{3}C: C_1)	0.0267	0.0130	0.0011	0.0130	85.1	1.487	112.2	49.6	*p*-CS/*t*-HB$_{nc}$
7-8a$^+_{s\text{-}ns:TS}$ (^{3}H-∗-^{8}H: C_1)	0.0132	0.0047	0.0000	0.0047	89.6	7.525	130.1	98.6	*p*-CS/*t*-HB$_{nc}$
7-8b$^+_{s\text{-}ns:TS}$ (F-∗-^{3}C: C_3)	0.0149	0.0098	0.0033	0.0103	71.1	2.184	72.2	25.3	*p*-CS/vdW
(F-∗-^{4}C)^m	0.0151	0.0099	0.0033	0.0105	71.7	2.17	72.1	67.2	*p*-CS/vdW
(^{3}H-∗-^{8}H)	0.0107	0.0041	0.0005	0.0041	83.3	10.544	122.8	201.0	*p*-CS/*t*-HB$_{nc}$
7-8c$^+_{s\text{-}ns:TS}$ (Cl-∗-^{3}C: C_3)	0.0208	0.0114	0.0023	0.0116	78.6	2.358	101.5	69.1	*p*-CS/*t*-HB$_{nc}$

[a] See Table 7-1 in the text for BSS-B. [b] Data are given at the BCPs. [c] The *u* and *v* are the position numbers of C or C bonding to H. [d] $c\nabla^2\rho_b(\boldsymbol{r}_c) = H_b(\boldsymbol{r}_c) - V_b(\boldsymbol{r}_c)/2$, where $c = \hbar^2/8m$. [e] $R = (x^2 + y^2)^{1/2}$, where $(x, y) = (H_b(\boldsymbol{r}_c) - V_b(\boldsymbol{r}_c)/2, H_b(\boldsymbol{r}_c))$. [f] $\theta = 90^o - \tan^{-1}(y/x)$. [g] $C_{ij} = \partial^2 E/\partial f_i \partial f_j$, where *i* and *j* refer to internal coordinates, and f_i and f_j corresponding to *i* and *j*, respectively, are the external force components acting on the system. [h] $\theta_p = 90^o - \tan^{-1}(dy/dx)$. [i] $\kappa_p = |d^2y/dx^2|/[1 + (dy/dx)^2]^{3/2}$. [j] Data from $w = \pm0.05$, ±0.025, and 0.0 were employed for the calculating θ_p and κ_p, because a poor correlation is obtained for the data from $w = \pm0.1$, ±0.05, and 0.0. [k] Data from $w = -0.075$, -0.05, -0.025, 0.0, and 0.025 were employed for the calculating θ_p and κ_p because the BCPs were not detected for $w = 0.05$ and 0.1. [l] Data from $w = \pm0.05$, ±0.025, and 0.0 were employed for the calculating θ_p and κ_p because the BCPs were not detected for $w = 0.1$. [m] Data from $w = -0.1$, -0.075, -0.05, -0.025, and 0.0 were employed for the calculating θ_p and κ_p because the BCPs were not detected for $w = 0.025$.

Table 7-A7. Atomic charges (*Qn*) on ^{A}Pn, ^{B}Pn, and/or X for **7-1**–**7-8** and **7-1a**$^{+}$–**7-8c**$^{+}$ of **7-*mx*$^{+}_{sym}$** and/or **7-*mx*$^{+}_{nsym}$**, calculated by NBO analysis under the M06-2X/BSS-B//MP2/BSS-B conditions.[a]

Species (^{A}Pn (^{B}Pn), X)	*Qn*(^{A}Pn) (*e*)	*Qn*(X) (*e*)	*Qn*(^{B}Pn) (*e*)	*Qn*(T)[b] (*e*)
7-1 (N, null)	–0.62		–0.62	–1.23
7-2 (P, null)	0.78		0.78	1.55
7-3 (As, null)	0.85		0.85	1.71
7-4 (Sb, null)	1.14		1.14	2.29
7-5 (N, null)	–0.62		–0.62	–1.25
7-6 (P, null)	0.78		0.82	1.60
7-7 (As, null)	0.85		0.85	1.71
7-8 (Sb, null)	1.12		1.12	2.24
7-1a$^{+}_{nsym}$ (N, H)	–0.67	0.59	–0.67	–0.75
7-1b$^{+}_{sym}$ (N, F)	–0.23	–0.34	–0.23	–0.80
7-1b$^{+}_{nsym}$ (N, F)	–0.52	–0.27	0.05	–0.74
7-1c$^{+}_{sym}$ (N, Cl)	–0.54	0.32	–0.54	–0.75
7-2a$^{+}_{sym}$ (P, H)	0.90	–0.09	0.90	1.71
7-2a$^{+}_{nsym}$ (P, H)	0.84	–0.03	1.23	2.04
7-2b$^{+}_{sym}$ (P, F)	1.27	–0.69	1.27	1.86
7-2b$^{+}_{nsym}$ (P, F)	0.85	–0.63	1.83	2.05
7-3a$^{+}_{sym}$ (As, H)	0.95	–0.12	0.95	1.78
7-3a$^{+}_{nsym}$ (As, H)	0.92	–0.08	1.24	2.08
7-3b$^{+}_{sym}$ (As, F)	1.32	–0.70	1.32	1.94
7-3b$^{+}_{nsym}$ (As, F)	0.94	–0.67	1.80	2.07
7-4a$^{+}_{sym}$ (Sb, H)	1.29	–0.26	1.29	2.32
7-4a$^{+}_{nsym}$ (Sb, H)	1.23	–0.23	1.55	2.55
7-4b$^{+}_{sym}$ (Sb, F)	1.75	–0.79	1.75	2.71
7-5a$^{+}_{nsym}$ (N, H)	–0.66	0.55	–0.66	–0.78
7-5b$^{+}_{sym}$ (N, F)	–0.24	–0.38	–0.24	–0.86
7-5b$^{+}_{nsym}$ (N, F)	–0.58	–0.25	0.07	–0.77
7-5c$^{+}_{sym}$ (N, Cl)	–0.50	0.25	–0.50	–0.76
7-5d$^{+}_{sym}$ (N, Br)	–0.57	0.45	–0.57	–0.70
7-5e$^{+}_{sym}$ (N, I)	–0.65	0.71	–0.65	–0.60
7-6a$^{+}_{sym}$ (P, H)	0.98	–0.09	0.98	1.86
7-6a$^{+}_{nsym}$ (P, H)	0.81	0.13	1.22	2.16
7-6b$^{+}_{sym}$ (P, F)	1.31	–0.69	1.31	1.93
7-6b$^{+}_{nsym}$ (P, F)	0.82	–0.59	2.01	2.24
7-6c$^{+}_{sym}$ (P, Cl)	1.02	–0.31	1.02	1.72
7-6c$^{+}_{nsym}$ (P, Cl)	0.81	–0.17	1.43	2.06
7-6d$^{+}_{sym}$ (P, Br)	0.90	–0.10	0.90	1.71
7-6d$^{+}_{nsym}$ (P, Br)	0.79	–0.02	1.22	1.99
7-6e$^{+}_{sym}$ (P-*-I)	0.76	0.21	0.76	1.72
7-7a$^{+}_{nsym}$ (As, H)	0.90	0.04	1.34	2.28
7-7b$^{+}_{sym}$ (As, F)	1.36	–0.70	1.36	2.02
7-7b$^{+}_{nsym}$ (As, F)	0.92	–0.63	2.06	2.34
7-7c$^{+}_{sym}$ (As, Cl)	1.05	–0.35	1.06	1.76
7-7c$^{+}_{nsym}$ (As, Cl)	0.89	–0.26	1.46	2.08
7-7c$^{+}_{sym}$ (As, Br)	0.94	–0.15	0.94	1.74
7-7c$^{+}_{nsym}$ (As, Br)	0.87	–0.11	1.18	1.94
7-8a$^{+}_{sym}$ (Sb, H)	1.30	–0.29	1.30	2.31
7-8a$^{+}_{nsym}$ (Sb, H)	1.19	–0.19	1.84	2.83
7-8b$^{+}_{sym}$ (Sb, F)	1.74	–0.78	1.74	2.71
7-8b$^{+}_{nsym}$ (Sb, F)	1.23	–0.72	2.39	2.90
7-8c$^{+}_{sym}$ (Sb, Cl)	1.41	–0.47	1.41	2.36
7-8c$^{+}_{nsym}$ (Sb, Cl)	1.18	–0.42	1.84	2.61

[a] See Table 7-1 in the text for BSS-B. [b] *Qn*(T) = *Qn*(^{A}Pn) + *Qn*(X) + *Qn*(^{B}Pn).

Order of $H_b(\boldsymbol{r}_c)$ for ^{A}Pn--*--X, $^{A/B}$Pn-*-X, and ^{B}Pn-*-X (X = F, Cl, Br, and I):

^{B}N-*-F (**7-1b**$^{+}_{nsym}$: $H_b(\boldsymbol{r}_c)$/au = –0.332) > ^{B}N-*-H (**7-1a**$^{+}_{nsym}$: $H_b(\boldsymbol{r}_c)$ = –0.296) > ^{B}N-*-F (**7-5b**$^{+}_{nsym}$: $H_b(\boldsymbol{r}_c)$ = –0.283) > ^{B}N-*-H (**7-5a**$^{+}_{nsym}$: $H_b(\boldsymbol{r}_c)$ = –0.252) > ^{B}P-*-H (**7-2a**$^{+}_{nsym}$: $H_b(\boldsymbol{r}_c)$ = –0.221) > ^{B}P-*-H (**7-6a**$^{+}_{nsym}$: $H_b(\boldsymbol{r}_c)$ = –0.204) > ^{A}N--*--H (**7-1a**$^{+}_{nsym}$: $H_b(\boldsymbol{r}_c)$ = –0.181) > ^{B}P-*-Cl (**7-6c**$^{+}_{nsym}$: $H_b(\boldsymbol{r}_c)$ = –0.166) > ^{B}P-*-Br (**7-6d**$^{+}_{nsym}$: $H_b(\boldsymbol{r}_c)$ = –0.159) > ^{B}As-*-H (**7-3a**$^{+}_{nsym}$: $H_b(\boldsymbol{r}_c)$ = –0.146) > ^{B}As-*-H (**7-7a**$^{+}_{nsym}$: $H_b(\boldsymbol{r}_c)$ = –0.134) > ^{B}P-*-F (**7-2b**$^{+}_{nsym}$: $H_b(\boldsymbol{r}_c)$ = –0.134) > ^{A}N--*--H (**7-5a**$^{+}_{nsym}$: $H_b(\boldsymbol{r}_c)$ = –0.129) > ^{B}P-*-F (**7-6b**$^{+}_{nsym}$: $H_b(\boldsymbol{r}_c)$ = –0.125) > ^{B}As-*-F (**7-3b**$^{+}_{nsym}$: $H_b(\boldsymbol{r}_c)$ = –0.120) > $^{A/B}$N-*-Cl (**7-1c**$^{+}_{sym}$: $H_b(\boldsymbol{r}_c)$ = –0.115) > ^{B}As-*-F (**7-7b**$^{+}_{nsym}$: $H_b(\boldsymbol{r}_c)$ = –0.109) > $^{A/B}$N-*-Cl (**7-5c**$^{+}_{sym}$: $H_b(\boldsymbol{r}_c)$ = –0.104) > ^{B}As-*-Cl (**7-7c**$^{+}_{nsym}$: $H_b(\boldsymbol{r}_c)$ = –0.097) > $^{A/B}$N-*-Br (**7-5d**$^{+}_{sym}$: $H_b(\boldsymbol{r}_c)$ = –0.096) > ^{B}As-*-Br (**7-7d**$^{+}_{nsym}$: $H_b(\boldsymbol{r}_c)$ = –0.076) > ^{B}Sb-*-H (**7-8a**$^{+}_{nsym}$: $H_b(\boldsymbol{r}_c)$ = –0.075) > ^{B}Sb-*-H (**7-4a**$^{+}_{nsym}$: $H_b(\boldsymbol{r}_c)$ = –0.074) > $^{A/B}$P-*-H (**7-6a**$^{+}_{sym}$: $H_b(\boldsymbol{r}_c)$ = –0.074) > $^{A/B}$N-*-I (**7-5e**$^{+}_{sym}$: $H_b(\boldsymbol{r}_c)$ = –0.073) > $^{A/B}$P-*-H (**7-2a**$^{+}_{sym}$: $H_b(\boldsymbol{r}_c)$ = –0.071) > $^{A/B}$P-*-F (**7-2b**$^{+}_{sym}$: $H_b(\boldsymbol{r}_c)$ = –0.065) > $^{A/B}$N-*-F (**7-1b**$^{+}_{sym}$: $H_b(\boldsymbol{r}_c)$ = –0.059) > $^{A/B}$P-*-Cl (**7-6c**$^{+}_{sym}$: $H_b(\boldsymbol{r}_c)$ = –0.049) = ^{B}Sb-*-Cl (**7-8c**$^{+}_{nsym}$: $H_b(\boldsymbol{r}_c)$ = -0.049_{8}) > $^{A/B}$As-*-H (**7-3a**$^{+}_{sym}$: $H_b(\boldsymbol{r}_c)$ = -0.048_{7}) > ^{B}Sb-*-F (**7-8b**$^{+}_{nsym}$: $H_b(\boldsymbol{r}_c)$ = –0.047) > $^{A/B}$P-*-Br (**7-6d**$^{+}_{sym}$: $H_b(\boldsymbol{r}_c)$ = –0.045) > $^{A/B}$P-*-I (**7-6e**$^{+}_{sym}$: $H_b(\boldsymbol{r}_c)$ = –0.040) > $^{A/B}$P-*-F (**7-6b**$^{+}_{sym}$: $H_b(\boldsymbol{r}_c)$ = –0.035) > $^{A/B}$As-*-F (**7-3b**$^{+}_{sym}$: $H_b(\boldsymbol{r}_c)$ = –0.032) > $^{A/B}$Sb-*-H (**7-4a**$^{+}_{sym}$: $H_b(\boldsymbol{r}_c)$ = –0.031) > $^{A/B}$As-*-Cl (**7-7c**$^{+}_{sym}$: $H_b(\boldsymbol{r}_c)$ = –0.030) > $^{A/B}$As-*-Br (**7-7d**$^{+}_{sym}$: $H_b(\boldsymbol{r}_c)$ = –0.0300) > $^{A/B}$Sb-*-H (**7-8a**$^{+}_{sym}$: $H_b(\boldsymbol{r}_c)$ = –0.027) > $^{A/B}$N-*-F (**7-5b**$^{+}_{sym}$: $H_b(\boldsymbol{r}_c)$ = –0.026) > $^{A/B}$As-*-F (**7-7b**$^{+}_{sym}$: $H_b(\boldsymbol{r}_c)$ = –0.019) > $^{A/B}$Sb-*-Cl (**7-8c**$^{+}_{sym}$: $H_b(\boldsymbol{r}_c)$ = –0.018) > ^{A}N--*--F (**7-1b**$^{+}_{nsym}$: $H_b(\boldsymbol{r}_c)$ = –0.016) > $^{A/B}$Sb-*-F (**7-4b**$^{+}_{sym}$: $H_b(\boldsymbol{r}_c)$ = –0.011) > ^{A}P--*--Br (**7-6d**$^{+}_{nsym}$: $H_b(\boldsymbol{r}_c)$ = -0.010_{9}) > ^{A}P--*--H (**7-2a**$^{+}_{nsym}$: $H_b(\boldsymbol{r}_c)$ = -0.010_{8}) > ^{A}As--*--H (**7-3a**$^{+}_{nsym}$: $H_b(\boldsymbol{r}_c)$ = -0.010_{1}) > ^{A}As--*--Br (**7-7d**$^{+}_{nsym}$: $H_b(\boldsymbol{r}_c)$ = -0.009_{8}) > ^{A}Sb--*--H (**7-4a**$^{+}_{nsym}$: $H_b(\boldsymbol{r}_c)$ = -0.009_{7}) > ^{A}P--*--Cl (**7-6c**$^{+}_{nsym}$: $H_b(\boldsymbol{r}_c)$ = -0.007_{4}) > $^{A/B}$Sb-*-F (**7-8b**$^{+}_{sym}$: $H_b(\boldsymbol{r}_c)$ = -0.007_{2}) > ^{A}As--*--Cl (**7-7c**$^{+}_{nsym}$: $H_b(\boldsymbol{r}_c)$ = –0.006) > ^{A}Sb--*--Cl (**7-8c**$^{+}_{nsym}$: $H_b(\boldsymbol{r}_c)$ = –0.005) > ^{A}P--*--F (**7-2b**$^{+}_{nsym}$: $H_b(\boldsymbol{r}_c)$ = -0.003_{9}) > ^{A}As--*--F (**7-3b**$^{+}_{nsym}$: $H_b(\boldsymbol{r}_c)$ = -0.003_{6}) > ^{A}Sb--*--H (**7-8a**$^{+}_{nsym}$: $H_b(\boldsymbol{r}_c)$ = -0.001_{9}) > ^{A}N--*--F (**7-5b**$^{+}_{nsym}$: $H_b(\boldsymbol{r}_c)$ = -0.001_{5}) > ^{A}As--*--H (**7-7a**$^{+}_{nsym}$: $H_b(\boldsymbol{r}_c)$ = -0.001_{4}) > ^{A}P--*--H (**7-6a**$^{+}_{nsym}$: $H_b(\boldsymbol{r}_c)$ = -0.000_{3}) > ^{A}Sb--*--F (**7-8b**$^{+}_{nsym}$: $H_b(\boldsymbol{r}_c)$ = 0.001) > ^{A}As--*--F (**7-7b**$^{+}_{nsym}$: $H_b(\boldsymbol{r}_c)$ = 0.002_{0}) > ^{A}P--*--F (**7-6b**$^{+}_{nsym}$: $H_b(\boldsymbol{r}_c)$ = 0.002_{3}) (7-A1)

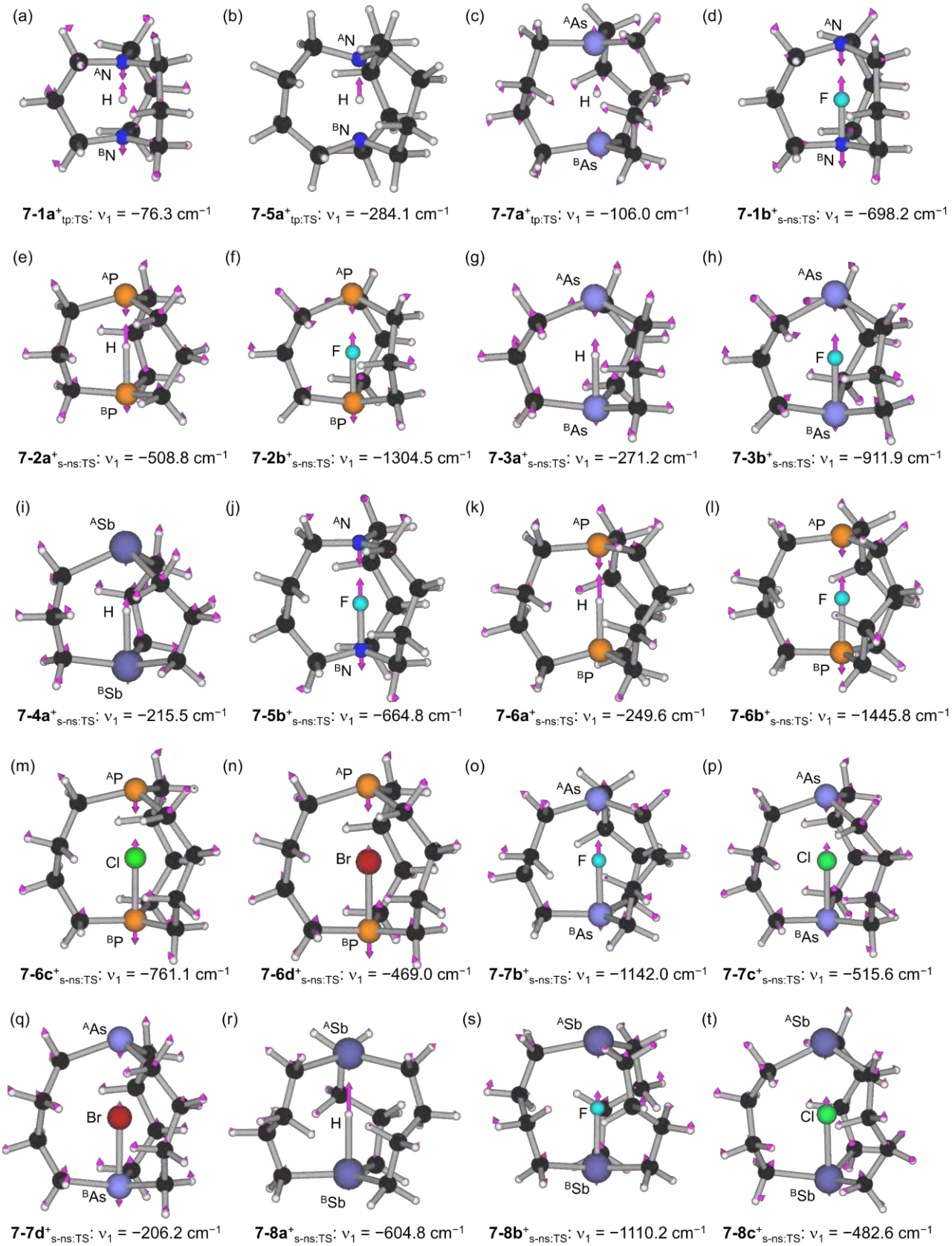

Figure 7-A1. The internal vibration motions corresponding to imaginary frequency for the transition structures of **7-1a**$^+$, **7-5a**$^+$, and **7-7a**$^+$ for **7-*mx***$^+_{\text{tp:TS}}$ and **7-1b**$^+$–**7-8c**$^+$ for **7-*mx***$^+_{\text{s-ns:TS}}$ ((a)–(t), respectively), together with the ν_1, calculated with MP2/BSS-B. Carbon, hydrogen, nitrogen, phosphorus, arsenic, antimony, fluorine, chlorine, and bromine atoms are shown in black, grey, blue, orange, light purple, purple, light green, green, and dark red, respectively.

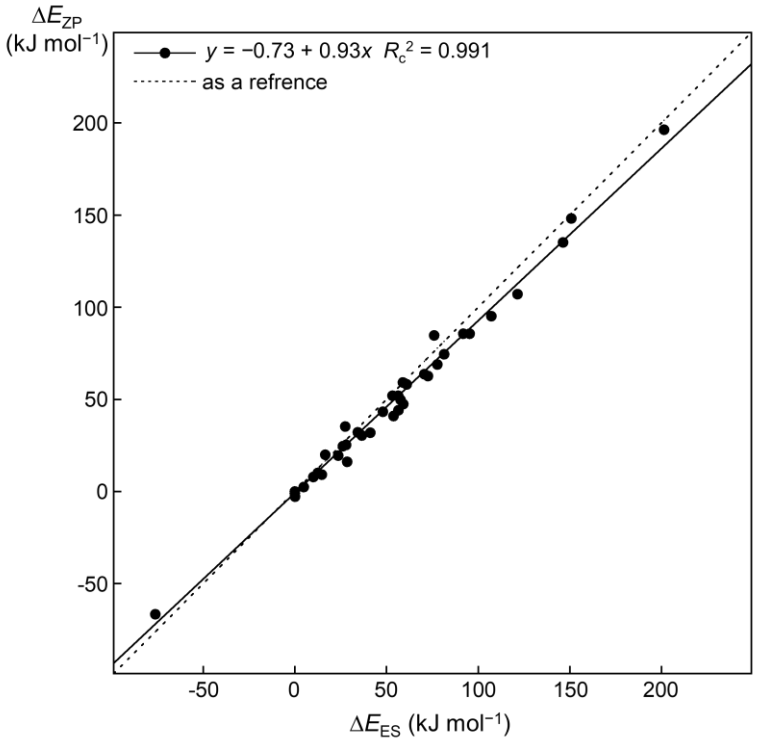

Figure 7-A2. Plot of ΔE_{ZP} versus ΔE_{ES} for **7-1a**$^{+}$–**7-8c**$^{+}$, calculated with MP2/BSS-B.

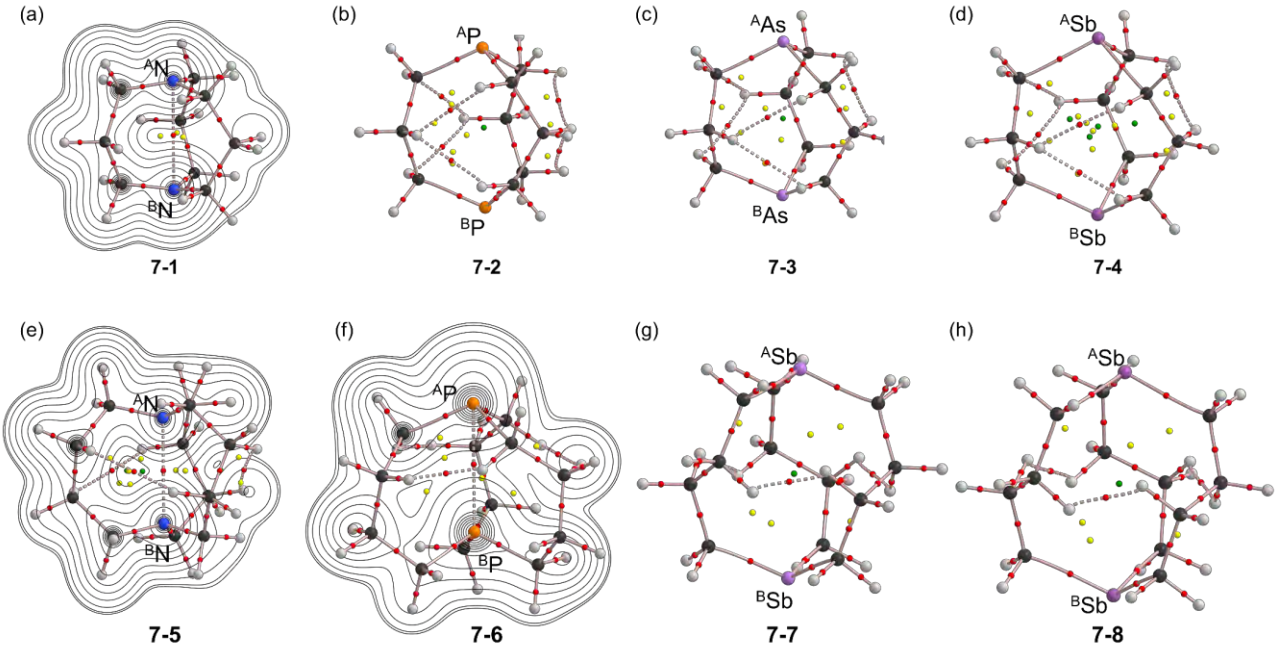

Figure 7-A3. Molecular graphs with contour plots for **7-1** (a), **7-5** (e), and **7-6** (f), and without contour plots for **7-2**–**7-4** ((b–d), respectively), **7-7** (g), and **7-8** (h), evaluated with MP2/BSS-B. BCPs are denoted by red dots, RCPs (ring critical points) by yellow dots, CCPs (cage critical points) by green dots, and BPs by pink lines. Carbon, hydrogen, nitrogen, phosphorus, arsenic, and antimony atoms are shown in black, grey, blue, orange, light purple, and purple, respectively. Contour plots are drawn on the planes containing at least ^{A}Pn and ^{B}Pn atoms.

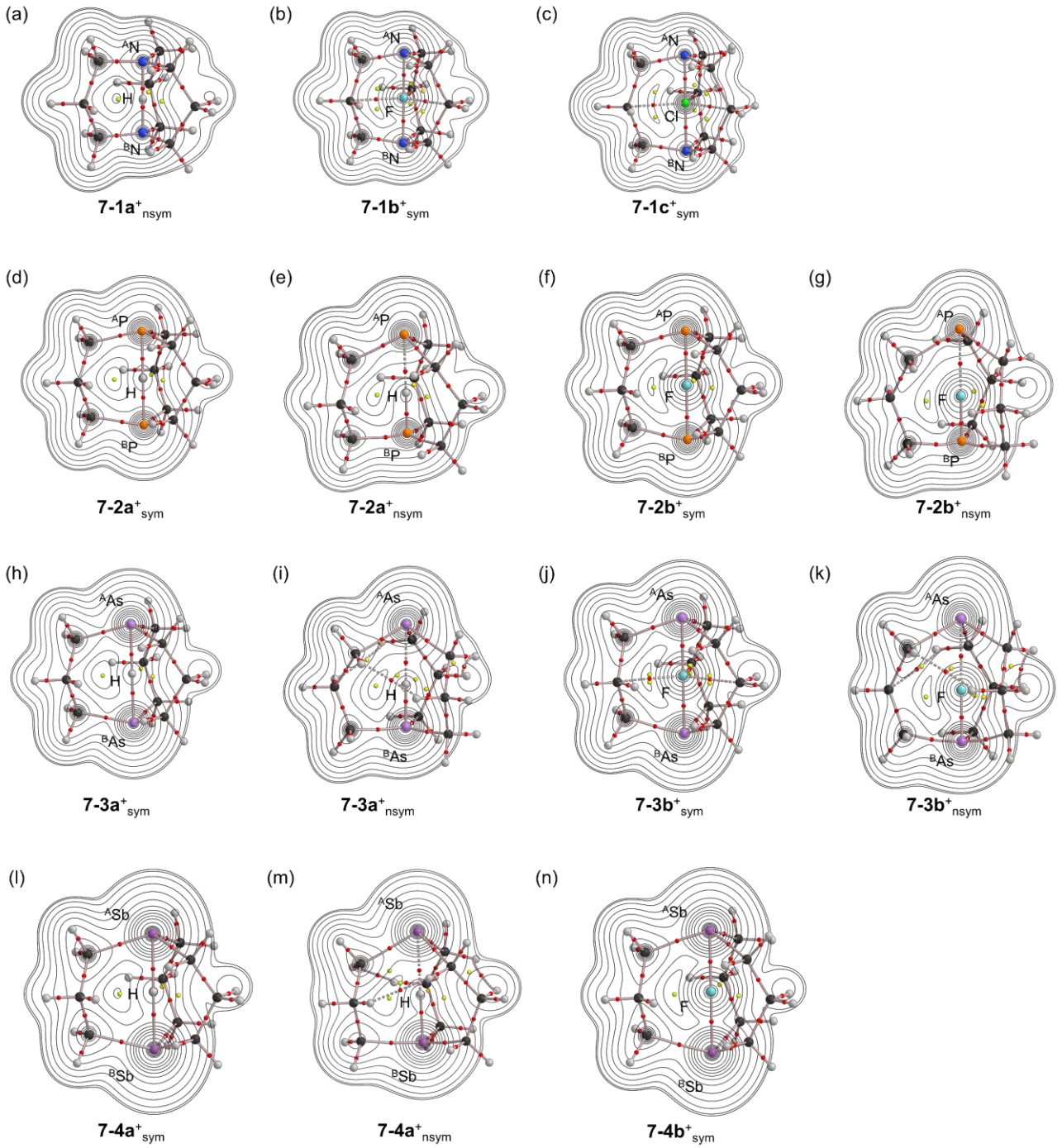

Figure 7-A4. Molecular graphs with contour plots for **7-1a**$^{+}_{nsym}$ (a), **7-1b**$^{+}_{sym}$ (b), **7-1c**$^{+}_{sym}$ (c), **7-2a**$^{+}_{sym}$ (d), **7-2a**$^{+}_{nsym}$ (e), **7-2b**$^{+}_{sym}$ (f), **7-2b**$^{+}_{nsym}$ (g), **7-3a**$^{+}_{sym}$ (h), **7-3a**$^{+}_{nsym}$ (i), **7-3b**$^{+}_{sym}$ (j), **7-3b**$^{+}_{nsym}$ (k), **7-4a**$^{+}_{sym}$ (l), **7-4a**$^{+}_{nsym}$ (m), and **7-4b**$^{+}_{sym}$ (n), evaluated with MP2/BSS-B. BCPs are denoted by red dots, RCPs (ring critical points) by yellow dots, CCPs (cage critical points) by green dots, and BPs by pink lines. Carbon, hydrogen, nitrogen, phosphorus, arsenic, antimony, fluorine, chlorine, bromine, and iodine atoms are shown in black, grey, blue, orange, light purple, purple, light green, green, dark red, and dark purple, respectively. Contour plots are drawn on the planes containing at least ^{A}Pn, ^{B}Pn, and X atoms.

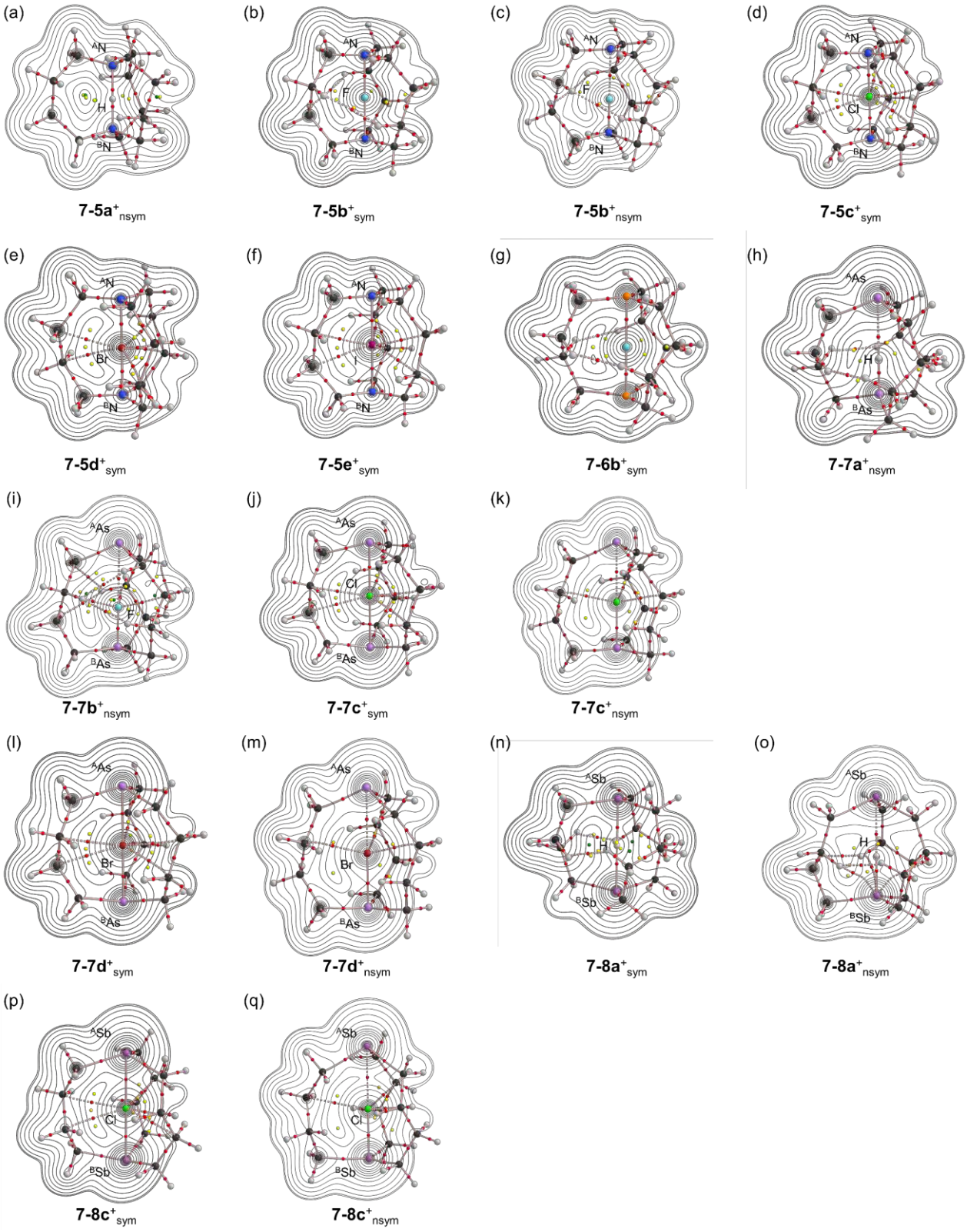

Figure 7-A5. Molecular graphs with contour plots for **7-5a**$^{+}_{nsym}$ (a), **7-5b**$^{+}_{sym}$ (b), **7-5b**$^{+}_{nsym}$ (c), **7-5c**$^{+}_{sym}$ (d), **7-5d**$^{+}_{sym}$ (e), **7-5e**$^{+}_{sym}$ (f), **7-6b**$^{+}_{sym}$ (g), **7-7a**$^{+}_{nsym}$ (h), **7-7b**$^{+}_{nsym}$ (i), **7-7c**$^{+}_{sym}$ (j), **7-7c**$^{+}_{nsym}$ (k), **7-7d**$^{+}_{sym}$ (l), **7-7d**$^{+}_{nsym}$ (m), **7-8a**$^{+}_{sym}$ (n), **7-8a**$^{+}_{nsym}$ (o), **7-8c**$^{+}_{sym}$ (p), and **7-8c**$^{+}_{nsym}$ (q), evaluated with MP2/BSS-B. BCPs are denoted by red dots, RCPs (ring critical points) by yellow dots, CCPs (cage critical points) by green dots, and BPs by pink lines. Carbon, hydrogen, nitrogen, phosphorus, arsenic, antimony, fluorine, chlorine, bromine, and iodine atoms are shown in black, grey, blue, orange, light purple, purple, light green, green, dark red, and dark purple, respectively. Contour plots are drawn on the planes containing at least ^{A}Pn, ^{B}Pn, and X atoms.

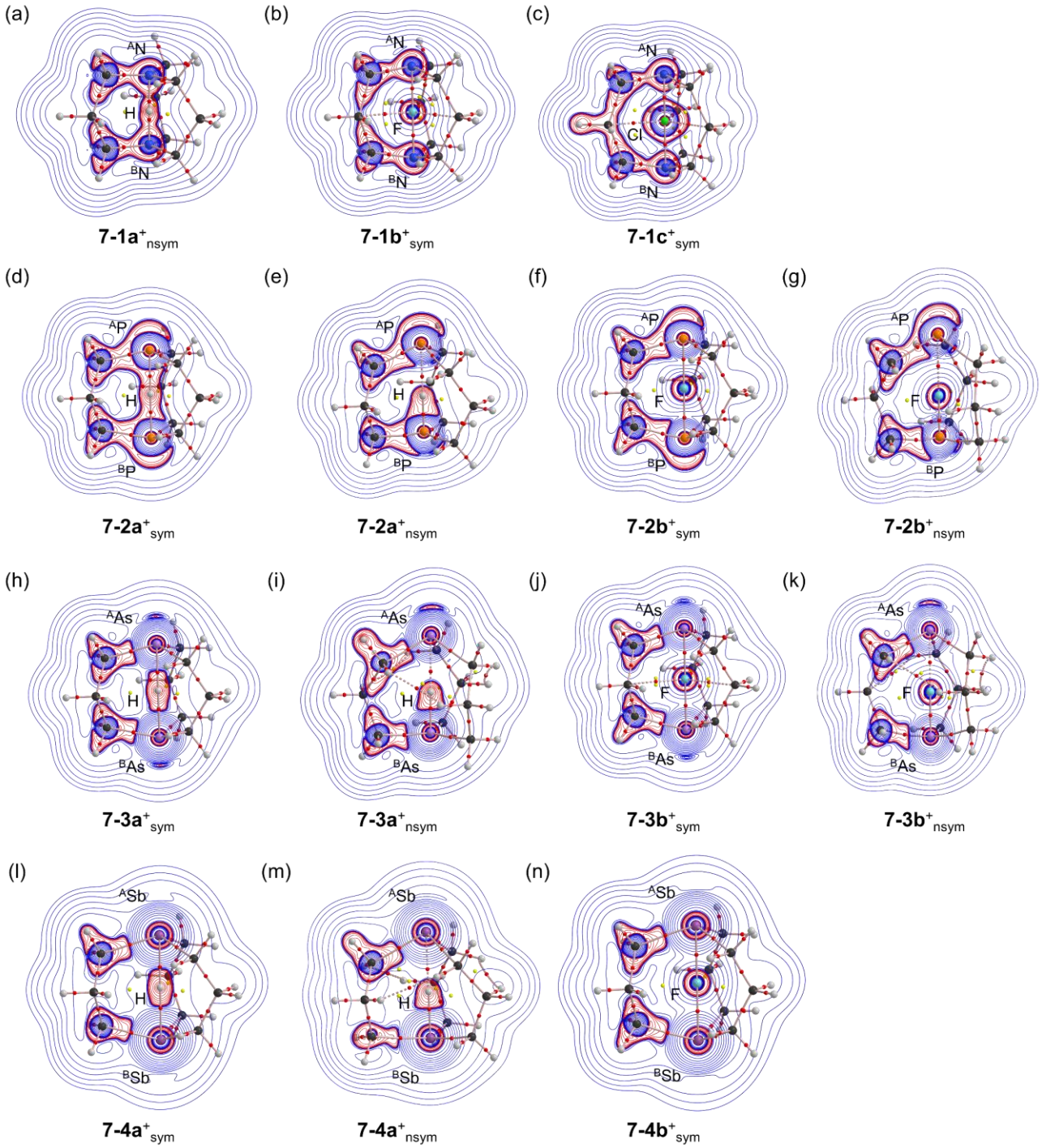

Figure 7-A6. Negative Laplacian maps of **7-1a**$^{+}_{nsym}$ (a), **7-1b**$^{+}_{sym}$ (b), **7-1c**$^{+}_{sym}$ (c), **7-2a**$^{+}_{sym}$ (d), **7-2a**$^{+}_{nsym}$ (e), **7-2b**$^{+}_{sym}$ (f), **7-2b**$^{+}_{nsym}$ (g), **7-3a**$^{+}_{sym}$ (h), **7-3a**$^{+}_{nsym}$ (i), **7-3b**$^{+}_{sym}$ (j), **7-3b**$^{+}_{nsym}$ (k), **7-4a**$^{+}_{sym}$ (l), **7-4a**$^{+}_{nsym}$ (m), and **7-4b**$^{+}_{sym}$ (n), evaluated with MP2/BSS-B. BCPs are denoted by red dots, RCPs (ring critical points) by yellow dots, CCPs (cage critical points) by green dots, and BPs by pink lines. Carbon, hydrogen, nitrogen, phosphorus, arsenic, antimony, fluorine, chlorine, bromine, and iodine atoms are shown in black, grey, blue, orange, light purple, purple, light green, green, dark red, and dark purple, respectively. Contour plots are drawn on the planes containing at least ^{A}Pn, ^{B}Pn, and X atoms. The red and blue lines correspond to the negative and positive areas of $\nabla^2\rho(\boldsymbol{r})$, respectively.

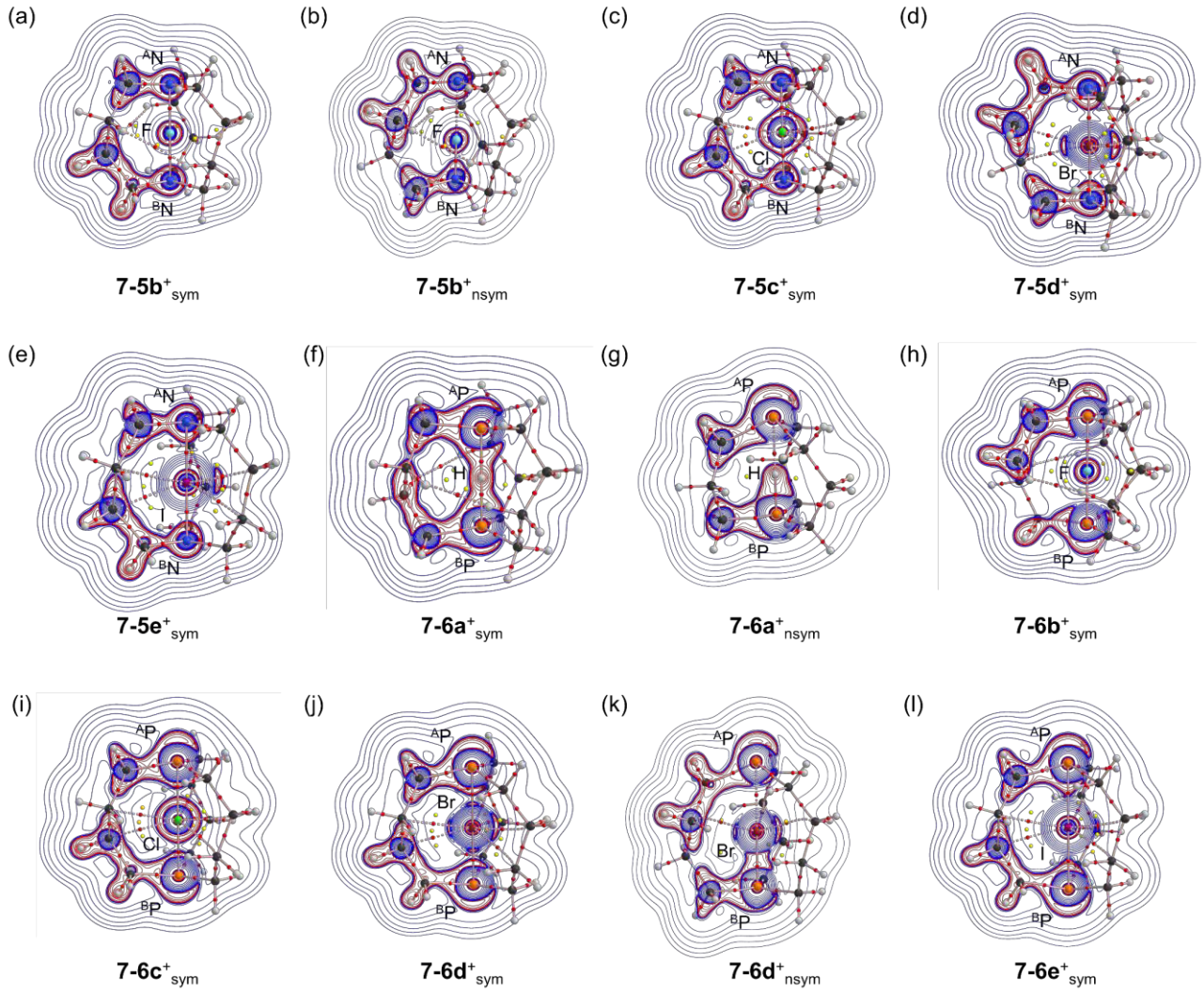

Figure 7-A7. Negative Laplacian maps of **7-5b**$^{+}_{sym}$ (a), **7-5b**$^{+}_{nsym}$ (b), **7-5c**$^{+}_{sym}$ (c), **7-5d**$^{+}_{sym}$ (d), **7-5e**$^{+}_{sym}$ (e), **7-6a**$^{+}_{sym}$ (f), **7-6a**$^{+}_{nsym}$ (g), **7-6b**$^{+}_{sym}$ (h), **7-6c**$^{+}_{sym}$ (i), **7-6d**$^{+}_{sym}$ (j), **7-6d**$^{+}_{nsym}$ (k), **7-6e**$^{+}_{sym}$ (l), **7-7a**$^{+}_{nsym}$ (m), **7-7b**$^{+}_{sym}$ (n), **7-7b**$^{+}_{nsym}$ (o), **7-7c**$^{+}_{sym}$ (p), **7-7c**$^{+}_{nsym}$ (q), **7-7d**$^{+}_{sym}$ (r), **7-7d**$^{+}_{nsym}$ (s), **7-8a**$^{+}_{sym}$ (t), **7-8b**$^{+}_{sym}$ (u), **7-8b**$^{+}_{nsym}$ (v), **7-8c**$^{+}_{sym}$ (w), and **7-8c**$^{+}_{nsym}$ (x), evaluated with MP2/BSS-B. BCPs are denoted by red dots, RCPs (ring critical points) by yellow dots, CCPs (cage critical points) by green dots, and BPs by pink lines. Carbon, hydrogen, nitrogen, phosphorus, arsenic, antimony, fluorine, chlorine, bromine, and iodine atoms are shown in black, grey, blue, orange, light purple, purple, light green, green, dark red, and dark purple, respectively. Contour plots are drawn on the planes containing at least ^{A}Pn, ^{B}Pn, and X atoms. The red and blue lines correspond to the negative and positive areas of $\nabla^2\rho(\boldsymbol{r})$, respectively.

(Figure 7-A7 continued.)

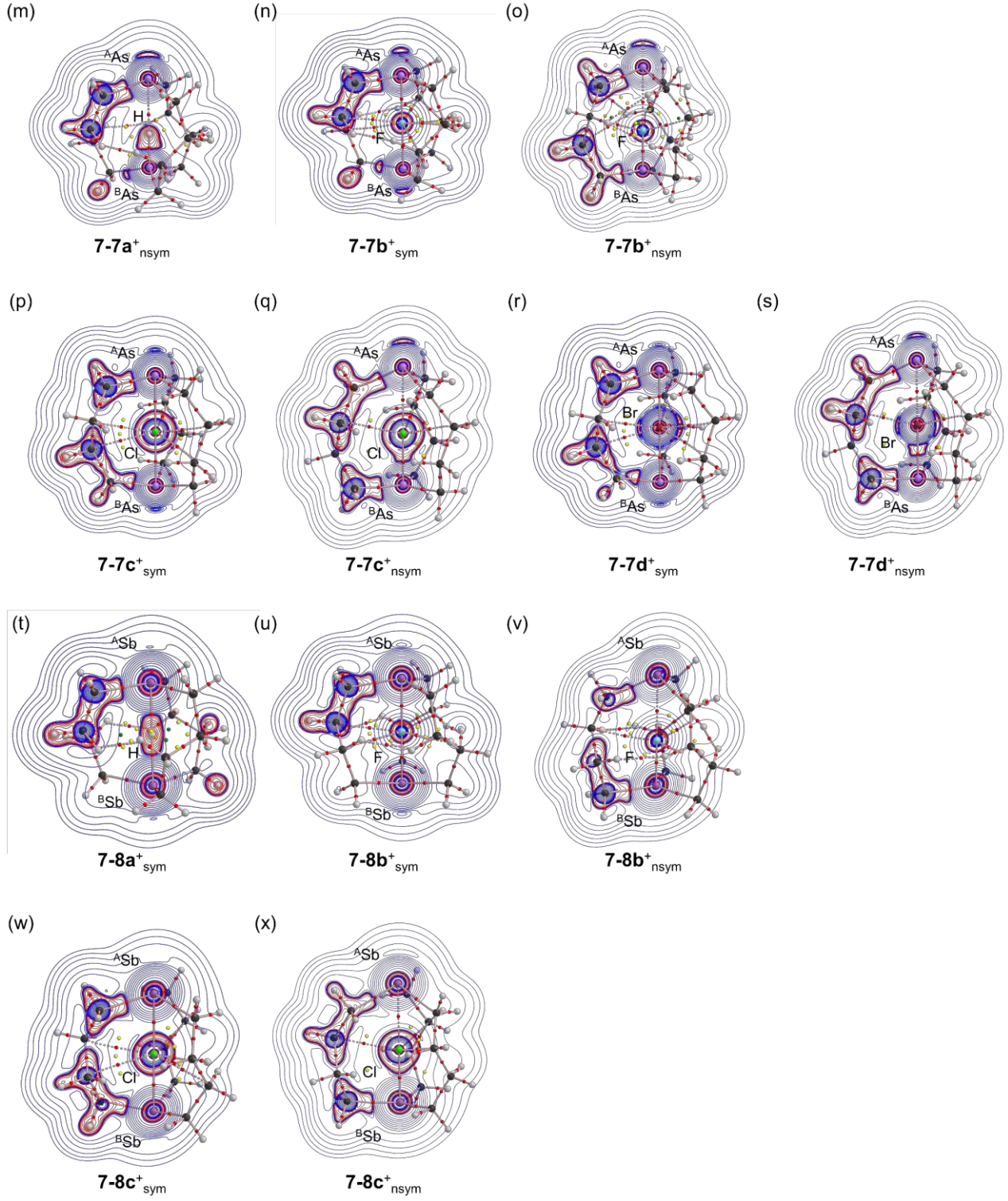

Figure 7-A7. Negative Laplacian maps of **7-5b**$^{+}_{sym}$ (a), **7-5b**$^{+}_{nsym}$ (b), **7-5c**$^{+}_{sym}$ (c), **7-5d**$^{+}_{sym}$ (d), **7-5e**$^{+}_{sym}$ (e), **7-6a**$^{+}_{sym}$ (f), **7-6a**$^{+}_{nsym}$ (g), **7-6b**$^{+}_{sym}$ (h), **7-6c**$^{+}_{sym}$ (i), **7-6d**$^{+}_{sym}$ (j), **7-6d**$^{+}_{nsym}$ (k), **7-6e**$^{+}_{sym}$ (l), **7-7a**$^{+}_{nsym}$ (m), **7-7b**$^{+}_{sym}$ (n), **7-7b**$^{+}_{nsym}$ (o), **7-7c**$^{+}_{sym}$ (p), **7-7c**$^{+}_{nsym}$ (q), **7-7d**$^{+}_{sym}$ (r), **7-7d**$^{+}_{nsym}$ (s), **7-8a**$^{+}_{sym}$ (t), **7-8b**$^{+}_{sym}$ (u), **7-8b**$^{+}_{nsym}$ (v), **7-8c**$^{+}_{sym}$ (w), and **7-8c**$^{+}_{nsym}$ (x), evaluated with MP2/BSS-B. BCPs are denoted by red dots, RCPs (ring critical points) by yellow dots, CCPs (cage critical points) by green dots, and BPs by pink lines. Carbon, hydrogen, nitrogen, phosphorus, arsenic, antimony, fluorine, chlorine, bromine, and iodine atoms are shown in black, grey, blue, orange, light purple, purple, light green, green, dark red, and dark purple, respectively. Contour plots are drawn on the planes containing at least ^{A}Pn, ^{B}Pn, and X atoms. The red and blue lines correspond to the negative and positive areas of $\nabla^2\rho(\boldsymbol{r})$, respectively.

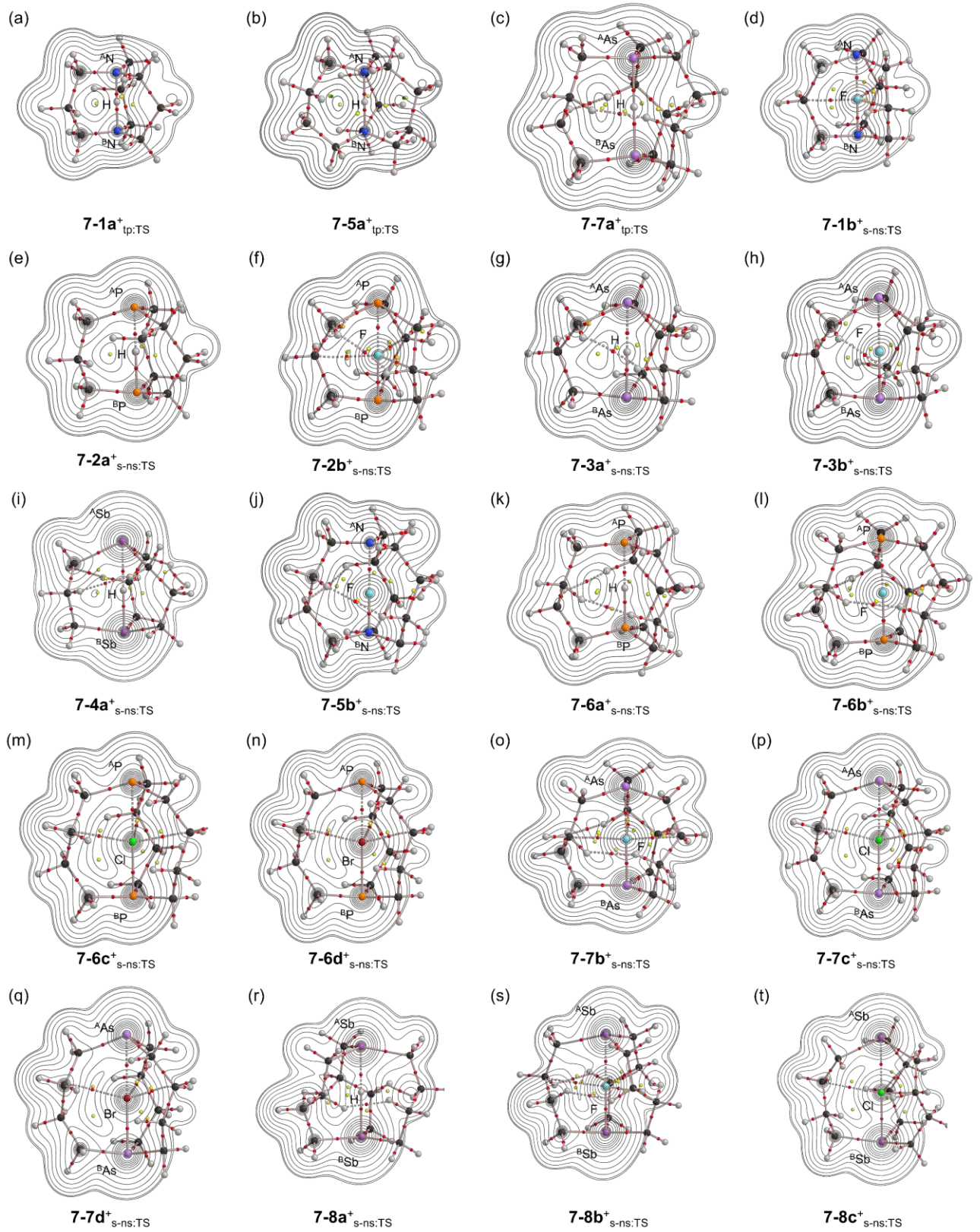

Figure 7-A8. Molecular graphs with contour plots for **7-1a**$^+$, **7-5a**$^+$, and **7-7a**$^+$ for **7-*mx***$^+_{\text{tp:TS}}$ and **7-1b**$^+$–**7-8c**$^+$ for **7-*mx***$^+_{\text{s-ns:TS}}$ ((a)–(t), respectively), evaluated with MP2/BSS-B. BCPs are denoted by red dots, RCPs (ring critical points) by yellow dots, CCPs (cage critical points) by green dots, and BPs by pink lines. Carbon, hydrogen, nitrogen, phosphorus, arsenic, antimony, fluorine, chlorine, bromine, and iodine atoms are shown in black, grey, blue, orange, light purple, purple, light green, green, dark red, and dark purple, respectively. Contour plots are drawn on the planes containing at least $^{\text{A}}$Pn, $^{\text{B}}$Pn, and X atoms.

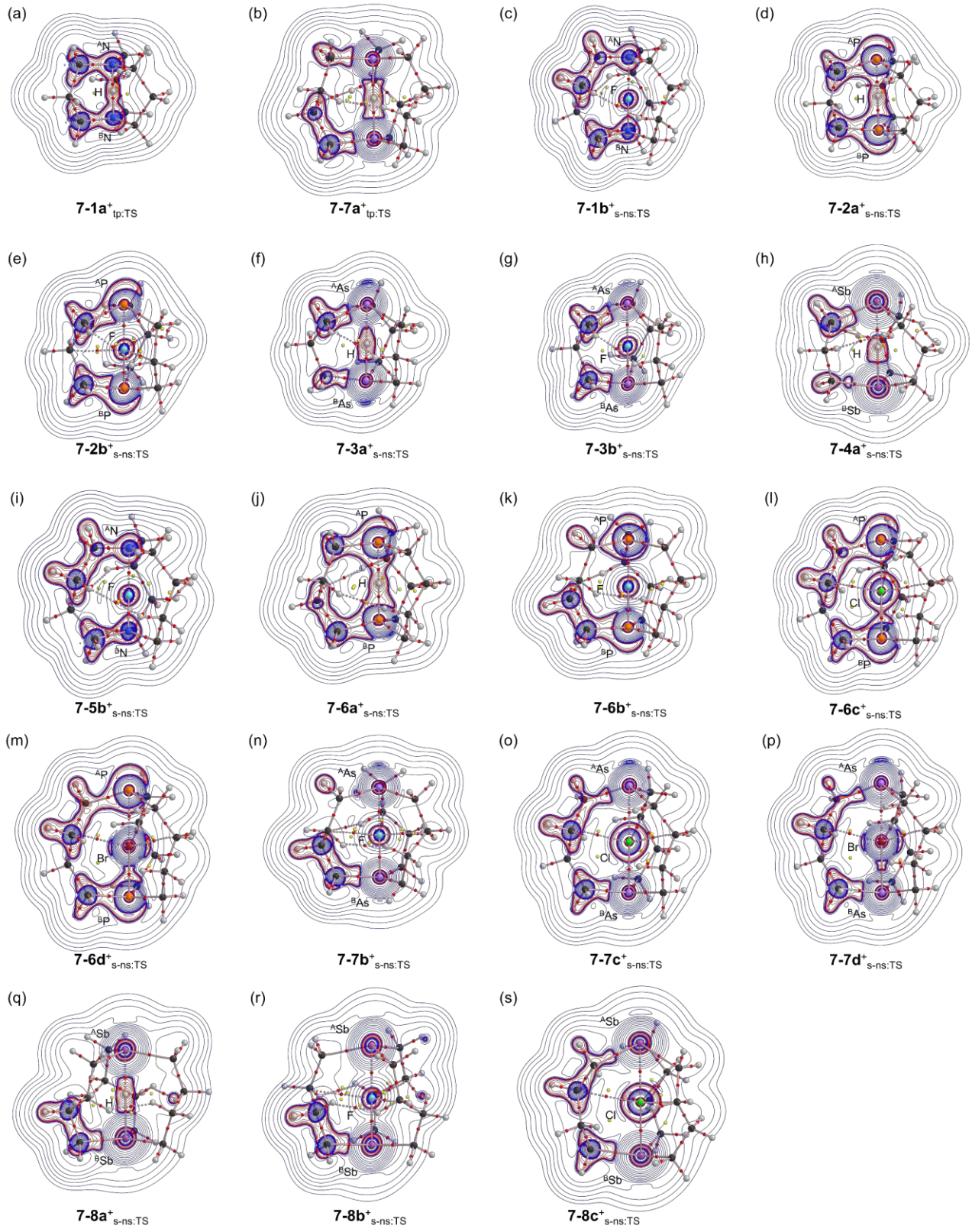

Figure 7-A9. Negative Laplacian maps of **7-1a**$^+$ and **7-7a**$^+$ for **7-*mx***$^+_{tp:TS}$ and **7-1b**$^+$–**7-8c**$^+$ for **7-*mx***$^+_{s\text{-}ns:TS}$ ((a)–(s), respectively), evaluated with MP2/BSS-B. BCPs are denoted by red dots, RCPs (ring critical points) by yellow dots, CCPs (cage critical points) by green dots, and BPs by pink lines. Carbon, hydrogen, nitrogen, phosphorus, arsenic, antimony, fluorine, chlorine, bromine, and iodine atoms are shown in black, grey, blue, orange, light purple, purple, light green, green, dark red, and dark purple, respectively. Contour plots are drawn on the planes containing at least ^{A}Pn, ^{B}Pn, and X atoms. The red and blue lines correspond to the negative and positive areas of $\nabla^2\rho(\boldsymbol{r})$, respectively.

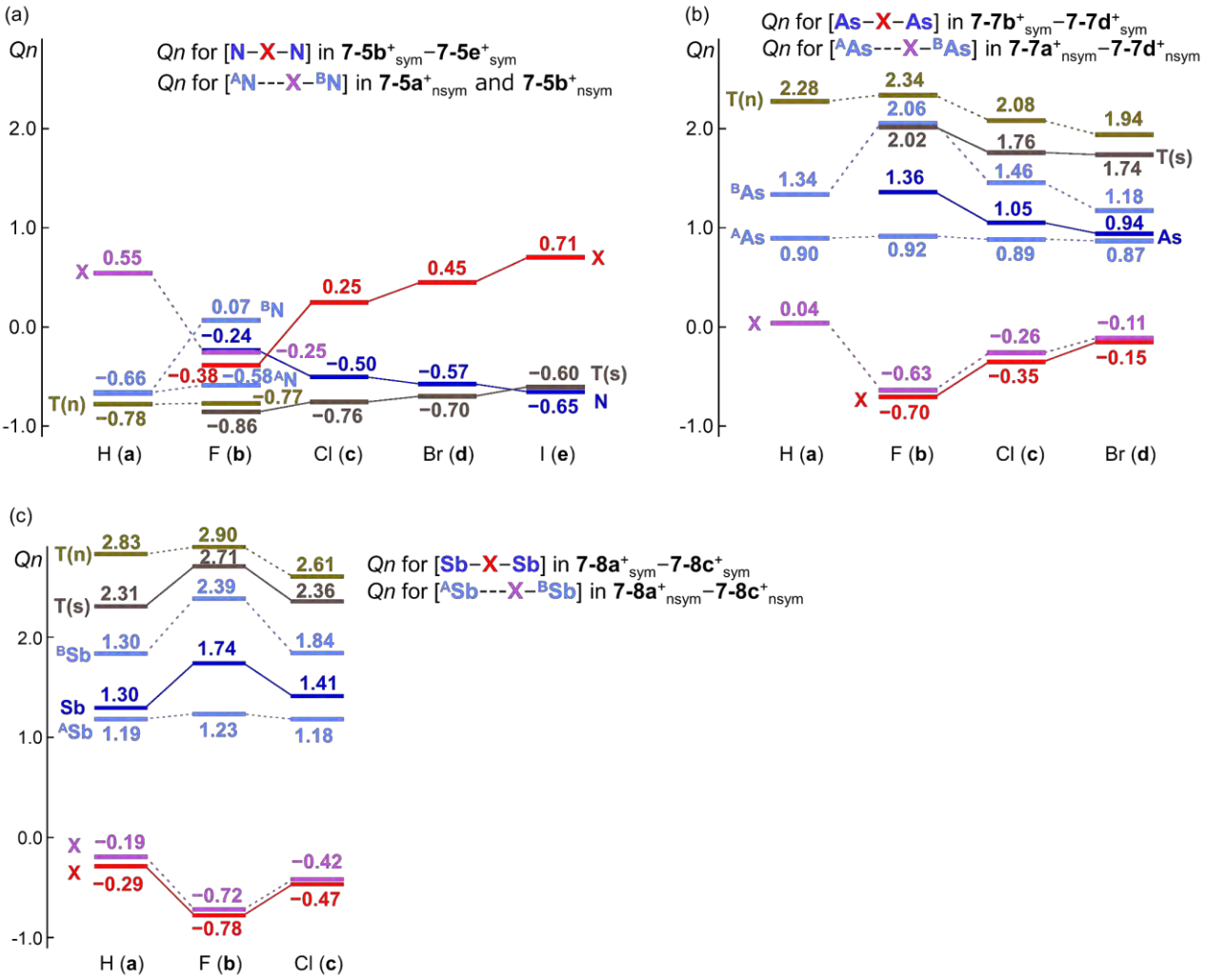

Figure 7-A10. Plots of *Qn* (^{A}Pn), *Qn* (X), *Qn* (^{B}Pn), and *Qn* (T) versus X for **7-5a**$^{+}$–**7-5e**$^{+}$ (a), **7-7a**$^{+}$–**7-7d**$^{+}$ (b), and **7-8a**$^{+}$–**7-8c**$^{+}$ (c), where the values of *Qn* were calculated by NBO analysis under M06-2X/BSS-B//MP2/BSS-B conditions. The *Qn* for T(s) and T(n) are sum of *Qn* (^{A}Pn), *Qn* (X), and *Qn* (^{B}Pn) for **7-*mx***$^{+}_{sym}$ and **7-*mx***$^{+}_{nsym}$, respectively.

References and Notes

1. G. Montà-González, F. Sancenón, R. Martínez-Máñez, V. Martí-Centelles, *Chem. Rev.* **2022**, *122*, 13636–13708.
2. X. Yang, Z. Ullah, J. F. Stoddart, C. T. Yavuz, *Chem. Rev.* **2023**, *123*, 4602–4634.
3. R. W. Alder, *Tetrahedron* **1990**, *46*, 683–713.
4. J. G. Verkade, *Coord. Chem. Rev.* **1994**, *137*, 233–295.
5. R. W. Alder, D. Read, *Coord. Chem. Rev.* **1998**, *176*, 113–133.
6. J. L. Vennerstrom, *J. Med. Chem.* **1989**, *32*, 64–67.
7. R. Gleiter, K. Hövermann, J. Ritter, B. Nuber, *Angew. Chem. Int. Ed.* **1995**, *34*, 789–791.
8. J. Kobayashi, K. Goto, T. Kawashima, M. W. Schmidt, S. Nagase, *J. Am. Chem. Soc.* **2002**, *124*, 3703–3712.
9. S. Nakafuji, J. Kobayashi, T. Kawashima, M. W. Schmidt, *Inorg. Chem.* **2005**, *44*, 6500–6502.
10. J. Kobayashi, K. Goto, T. Kawashima, M. W. Schmidt, S. Nagase, *Chem. A Eur. J.* **2006**, *12*, 3811–3820.
11. J. Kobayashi, T. Kawashima, *C. R. Chim.* **2010**, *13*, 1249–1259.
12. J. Tang, J. Dopke, J. G. Verkade, *J. Am. Chem. Soc.* **1993**, *115*, 5015–5020.
13. P. B. Kisanga, J. G. Verkade, R. Schwesinger, *J. Org. Chem.* **2000**, *65*, 5431–5432.
14. J. G. Verkade, *New Aspects in Phosphorus Chemistry II* (Ed.: JP, Majoral), Springer, Berlin, Heidelberg, **2003**, pp. 1–44.
15. M.-Y. Xu, W.-T. Jiang, Y. Li, Q.-H. Xu, Q.-L. Zhou, S. Yang, B. Xiao, *J. Am. Chem. Soc.* **2019**, *141*, 7582–7588.
16. D. Tanaka, A. Konishi, M. Yasuda, *Chem. Asian. J.* **2021**, *16*, 3118–3123.
17. M.-Y. Xu, B. Xiao, *Chem. Comm.* **2021**, *57*, 11764–11775.
18. J. K. Puri, R. Singh, V. K. Chahal, *Chem. Soc. Rev.* **2011**, *40*, 1791–1840.
19. S. N. Adamovich, *Appl. Organomet. Chem.* **2019**, *33*, e4940.
20. V. V. Istratov, V. A. Vasnev, G. D. Markova, *Molecules* **2021**, *26*, 1893.
21. S. N. Adamovich, I. A. Ushakov, E. N. Oborina, S. V. Lukyanova, V. Y. Komarov, *Int. J. Mol. Sci.* **2023**, *24*, 9965.
22. R. W. Alder, R. B. Sessions, J. M. Mellor, M. F. Rawlins, *J. Chem. Soc., Chem. Commun.* **1977**, 747–748.
23. R. W. Alder, R. B. Sessions, *J. Am. Chem. Soc.* **1979**, *101*, 3651–3652.
24. R. W. Alder, D. D. Ellis, R. Gleiter, C. J. Harris, H. Lange, A. G. Orpen, D. Read, P. N. Taylor, *J. Chem. Soc., Perkin trans. 1* **1998**, 1657–1668.
25. R. W. Alder, C. P. Butts, A. G. Orpen, D. Read, *J. Chem. Soc. Perkin Trans. 2* **2001**, 288–295.
26. R. W. Alder, A. Casson, R. B. Sessions, *J. Am. Chem. Soc.* **1979**, *101*, 3652–3653.
27. R. W. Alder, R. J. Arrowsmith, A. Casson, R. B. Sessions, E. Heilbronner, B. Kovac, H. Huber, M. Taagepera, *J. Am. Chem. Soc.* **1981**, *103*, 6137–6142.
28. R. W. Alder, R. E. Moss, R. B. Sessions, *J. Chem. Soc. Chem. Commun.* **1983**, 997–998.
29. R. W. Alder, A. G. Orpen, R. B. Sessions, *J. Chem. Soc. Chem. Commun.* **1983**, 999–1000.

30. R. W. Alder, R. E. Moss, R. B. Sessions, *J. Chem. Soc. Chem. Commun.* **1983**, 1000–1002.
31. S. A. Harry, S. Vemulapalli, T. Dudding, T. Lectka, *J. Org. Chem.* **2022**, *87*, 8413–8419.
32. Y. Wang, Z.-X. Yu, *J. Org. Chem.* **2020**, *85*, 397–402.
33. Cage compounds with compressed CX-π interactions, called "iron maiden," were also studied.[62,63]
34. A. Karim, M. Reitti, A.-C. C. Carlsson, J. Gräfenstein, M. Erdélyi, *Chem. Sci.* **2014**, *5*, 3226–3233.
35. M. Bedin, A. Karim, M. Reitti, A.-C. C. Carlsson, F. Topić, M. Cetina, F. Pan, V. Havel, F. Al-Ameri, V. Sindelar, K. Rissanen, J. Gräfenstein, M. Erdélyi, *Chem. Sci.* **2015**, *6*, 3746–3756.
36. S. Lindblad, K. Mehmeti, A. X. Veiga, B. Nekoueishahraki, J. Gräfenstein, M. Erdélyi, *J. Am. Chem. Soc.* **2018**, *140*, 13503–13513.
37. L. Turunen, M. Erdélyi, *Chem. Soc. Rev.* **2020**, *49*, 2688–2700.
38. A. C. Reiersølmoen, S. Battaglia, S. Øien-Ødegaard, A. K. Gupta, A. Fiksdahl, R. Lindh, M. Erdélyi, *Chem. Sci.* **2020**, *11*, 7979–7990.
39. W. Nakanishi, S. Hayashi, K. Narahara, *J. Phys. Chem. A* **2009**, *113*, 10050–10057.
40. W. Nakanishi, S. Hayashi, *Curr. Org. Chem.* **2010**, *14*, 181–197.
41. W. Nakanishi, S. Hayashi, *J. Phys. Chem. A* **2010**, *114*, 7423–7430.
42. W. Nakanishi, S. Hayashi, K. Matsuiwa, M. Kitamoto, *Bull. Chem. Soc. Jpn.* **2012**, *85*, 1293–1305.
43. R. F. W. Bader, *Atoms in Molecules. A Quantum Theory*; Oxford University Press, Oxford, UK, **1990**.
44. C. F. Matta, R. J. Boyd, *An Introduction to the Quantum Theory of Atoms in Molecules* in *The Quantum Theory of Atoms in Molecules: From Solid State to DNA and Drug Design* (Eds.: C. F. Matta, R. J. Boyd), WILEY-VCH: Weinheim, Germany, **2007**, Ch. 1.
45. W. Nakanishi, S. Hayashi, *Int. J. Quantum Chem.* **2018**, *118*, e25590.
46. *Gaussian 09, Revision D.01 and E. 01*, M. J. Frisch, G. W. Trucks, H. B. Schlegel, G. E. Scuseria, M. A. Robb, J. R. Cheeseman, G. Scalmani, V. Barone, B. Mennucci, G. A. Petersson, H. Nakatsuji, M. Caricato, X. Li, H. P. Hratchian, A. F. Izmaylov, J. Bloino, G. Zheng, J. L. Sonnenberg, M. Hada, M. Ehara, K. Toyota, R. Fukuda, J. Hasegawa, M. Ishida, T. Nakajima, Y. Honda, O. Kitao, H. Nakai, T. Vreven, J. A. Montgomery, Jr., J. E. Peralta, F. Ogliaro, M. Bearpark, J. J. Heyd, E. Brothers, K. N. Kudin, V. N. Staroverov, R. Kobayashi, J. Normand, K. Raghavachari, A. Rendell, J. C. Burant, S. S. Iyengar, J. Tomasi, M. Cossi, N. Rega, J. M. Millam, M. Klene, J. E. Knox, J. B. Cross, V. Bakken, C. Adamo, J. Jaramillo, R. Gomperts, R. E. Stratmann, O. Yazyev, A. J. Austin, R. Cammi, C. Pomelli, J. W. Ochterski, R. L. Martin, K. Morokuma, V. G. Zakrzewski, G. A. Voth, P. Salvador, J. J. Dannenberg, S. Dapprich, A. D. Daniels, Ö. Farkas, J. B. Foresman, J. V. Ortiz, J. Cioslowski, D. J. Fox, Gaussian, Inc., Wallingford CT, **2009**.
47. T. Noro, M. Sekiya, T. Koga, *Theor. Chem. Acc.* **2012**, *131*, 1–8.
48. C. Møller, M. S. Plesset, *Phys. Rev.* **1934**, *46*, 618–622.

49. K. Brandhorst, J. Grunenberg, *Chem. Soc. Rev.* **2008**, *37*, 1558–1567.
50. K. Brandhorst, J. Grunenberg, *J. Chem. Phys.* **2010**, *132*, 184101.
51. E. D. Glendening, C. R. Landis, F. Weinhold, *J. Comput. Chem.* **2013**, *34*, 1429–1437.
52. F. Biegler-König, *J. Comput. Chem.* **2000**, *21*, 1040–1048.
53. T. A. Keith, AIMAll (Version 17.11.14), TK Gristmill Software, Overland Park, KS, USA, **2017**, http://www.aim.tkgristmill.com.
54. R. W. Alder, S. P. East, *Chem. Rev.* **1996**, *96*, 2097–2112.
55. The postulated symmetry was often broken during the optimizations, but not significantly altered.
56. P. Pyykkö, M. Atsumi, *Chem. A Eur. J.* **2009**, *15*, 186–197.
57. A. Bondi, *J. Phys. Chem.* **1964**, *68*, 441–451.
58. M. Mantina, A. C. Chamberlin, R. Valero, C. J. Cramer, D. G. Truhlar, *J. Phys. Chem. A* **2009**, *113*, 5806–5812.
59. W. Nakanishi, S. Hayashi, R. Imanaka, T. Nishide, E. Tanaka, H. Matsuoka, *Int. J. Mol. Sci.* **2023**, *24*, 2798.
60. D. B. DuPré, *J. Phys. Chem. A* **2003**, *107*, 10142–10148.
61. D. Cremer, E. Kraka, *Croat. Chem. Acta, CCA* **1984**, *57*, 1259–1281.
62. R. A. Pascal, *Eur. J. Org. Chem.* **2004**, 3763–3771.
63. M. Jabłoński, *J. Comput. Chem.* **2022**, *43*, 1206–1220.

Chapter 8

Intrinsic Dynamic and Static Nature of π···π Interactions in Fused Benzene-Type Helicenes and Dimers, Elucidated with QTAIM Dual Functional Analysis

Abstract

The intrinsic dynamic and static nature of the π···π interactions between the phenyl groups in proximity of **8-*n*** (*n* = 3–12 in [*n*]helicenes) are elucidated with the quantum theory of atoms-in-molecules dual functional analysis (QTAIM-DFA). The C···C interactions corresponding to π···π interactions are detected, together with H···H and C···H in **8-3**–**8-12**. The interactions of **8-3**–**8-12** are all predicted to have a *p*-CS/vdW nature (vdW nature of the pure closed-shell interaction), except for ^{2}C···^{7}C in bay area of **8-10**, which has a *p*-CS/*t*-HB$_{nc}$ nature (typical-HBs with no covalency). The natures of the interactions are similarly elucidated between the components of [*n*]helicene dimers **8-*n*:*n*** (*n* = 6, 7, 8, and 10) with QTAIM-DFA, which have a *p*-CS/vdW nature. The characteristic electronic structures of helicenes are clarified through the natures predicted with QTAIM-DFA. Some bond paths (BPs) in helicenes appeared or disappeared, depending on the calculation methods. The static nature of C···C in cape area is very similar to that of C···C in bay area in **8-9**–**8-12**, whereas the dynamic nature of C···C in cape area appears to be very different from that of C···C in bay area. The results will be a guide to design the helicene-containing materials of high functionality.

Introduction

Helicenes, which are ortho-fused polycyclic aromatic or heteroaromatic compounds with all rings angularly arranged to form helically shaped molecules, are of current and continuing interest. Helicenes are chiral; as a result, they are expected to have specific functionalities. Recently, helicenes have been widely applied in various fields,[1–5] such as organic semiconductors,[6–10] asymmetric catalysis,[11–16] and molecular recognition,[17–22] due to their diverse functionalities in materials. Many studies have also been reported on self-assembly phenomena at metal surfaces,[23–26] caused by interactions with the π-orbitals of helicenes. The π-orbitals will cause intramolecular π···π interactions between adjacent aromatic rings of helicenes, which play an important role in effective interactions. It is crucial to clarify the nature of π···π interactions for future high-functioning material developments based on helicenes. The discussion in this work will be limited to π···π interactions between the aromatic rings, the nature of which needs to be clarified, since helicenes of the fused benzene type were chosen as the target.

The noncovalent distances between the aromatic planes in close proximity to the helicenes were determined as the total effect of the attractive and repulsive forces between the atoms on the planes. The restoring forces from the deviated planarity in the helicenes should be a main factor for the

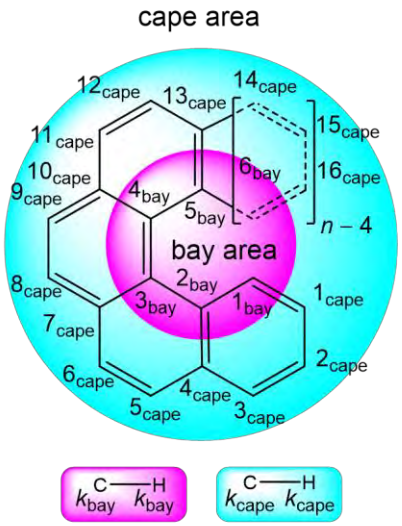

n:	1	2	3	4	5	6
8-*n*:	**8-1**	**8-2**	**8-3**	**8-4**	**8-5**	**8-6**
n:	7	8	9	10	11	12
8-*n*:	**8-7**	**8-8**	**8-9**	**8-10**	**8-11**	**8-12**

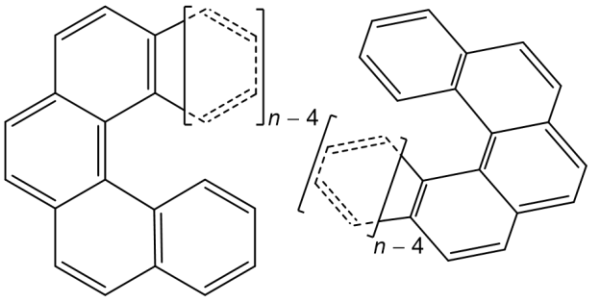

n:*n*:	6:6	7:7	8:8	10:10
8-*n*:*n*:	**8-6:6**	**8-7:7**	**8-8:8**	**8-10:10**

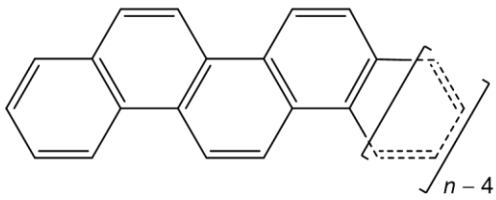

n:	1	2	3	4	5	6
8-*n*$_p$:	**8-1$_p$**	**8-2$_p$**	**8-3$_p$**	**8-4$_p$**	**8-5$_p$**	**8-6$_p$**
n:	7	8	9	10	11	12
8-*n*$_p$:	**8-7$_p$**	**8-8$_p$**	**8-9$_p$**	**8-10$_p$**	**8-11$_p$**	**8-12$_p$**

Chart 8-1. Helicenes, **8-1**–**8-12**, dimers, **8-6**:**6**–**8-8**:**8** and **8-10**:**10**, and [*n*]phenacenes, **8-1$_p$**–**8-12$_p$**. The bay and cape areas in **8-1**–**8-12** are illustrated. The number of C is shown, where the number of H is the same for C–H. Benzene, naphthalene, and phenanthrene are defined corresponding to *n* = 1, 2, and 3, respectively.

attractive and repulsive forces due to π-orbital overlapping in the helicenes. The noncovalent distances between the planes in close proximity to the helicenes are defined as the balanced distances of the two factors. The noncovalent intramolecular distances between atoms in close proximity to the helicenes must be (much) shorter than the noncovalent intermolecular distances between the unrestricted nonhelical aromatic species. The shorter distances in helicenes result from the π···π interactions between the planes in close proximity in space, which operate under very severe conditions. Clarifying the nature of the π···π interactions in helicenes under such severe conditions will enable to understand the factors that control the structures and the nature of the interactions. The results will also provide a starting point for understanding the nature of π···π interactions and will hint at designs for materials with high functionality based on the interactions.

The author has been particularly interested in the π···π interactions that operate under severe conditions, as these should be the factors that control the fine details of the structures. Interactions are also expected to result in materials with high functionalities. The nature of π···π interactions under such severe conditions was investigated in a series of fused benzene-type helicenes **8-1**–**8-12** and concave-type dimers **8-6**:**6**–**8-8**:**8** and **8-10**:**10**, where **8-1**–**8-3** are analyzed as helicenes in this work, although they are usually not. Chart 8-1 shows the structures of helicenes **8-1**–**8-12**, dimers **8-6**:**6**–**8-8**:**8**, **8-10**:**10**, and [*n*]phenacenes **8-1$_p$**–**8-12$_p$**, where **8-1$_p$**–**8-12$_p$** are the comparative compounds and **p** stands for phenacenes. The bay and cape areas used in this work are also illustrated. The nature of the benzene π···π interactions in cyclophanes has been reported, previously.[27] The π···π interactions in the helicenes must correspond to the extended π···π interactions of the species.

The dynamic and static nature of π···π interactions in the helicenes and those dimers were analyzed with QTAIM dual functional analysis (QTAIM-DFA),[28–31] by employing perturbed structures generated with CIV.[32] The QTAIM-DFA with CIV would be suitable method to analyze the π···π interactions, which are more complex as larger helicenes.

The QTAIM-DFA is explained in Chapter 2, together with the basic concept of the QTAIM approach.[33,34]

Herein, the author presents the results of the investigations into the natures of the π···π interactions in **8-1**–**8-12**, **8-6**:**6**–**8-8**:**8**, and **8-10**:**10**. The structural features and the energy profile are also discussed to provide a solid basis for the discussion.

Methodological Details in Calculations

Calculations were performed with the Gaussian 09 program package.[35] The 6-311+G(3d,p) basis set was used for the calculations at the DFT level of M06-2X [36] (M06-2X/6-311+G(3d,p)). The optimized structures were confirmed by frequency analysis. The results of the frequency analysis were used to calculate the coordinates derived from compliance force constants (C_{ii}) for internal vibrations.[37–39] Calculations were also performed with M06-2X/6-311+G(2d,p) and LC-ωPBE[40]/6-311+G(2d,p) to examine the basis set and level dependence, containing the optimized π···π distances, on the results. The results with M06-2X/6-311+G(3d,p) are discussed, while the results with M06-2X/6-311+G(2d,p) and LC-ωPBE/6-311+G(2d,p) are also discussed if necessary. The author should be careful with the basis set and level dependence on the QTAIM-DFA parameters, which has been examined carefully.[41] Similar methodology was also employed for the theoretical studies of the π-stacking.[42,43]

QTAIM functions were calculated using the same basis set system and the level as in the optimizations, unless otherwise noted, and were analyzed with the AIM2000[44] and AIMAll[45] programs. In QTAIM-DFA, $H_b(\boldsymbol{r}_c)$ are plotted versus $H_b(\boldsymbol{r}_c) - V_b(\boldsymbol{r}_c)/2$ for the five data points of w = 0, ±0.025, and ±0.05 (see Chapter 2).

Results and Discussion

Structural Features of 8-1–8-12 and Their Energy Profile

The structures of **8-1**–**8-12** were optimized with M06-2X/6-311+G(3d,p), M06-2X/6-311+G(2d,p), and LC-ωPBE/6-311+G(2d,p), retaining C_2 symmetry. The selected noncovalent X···Y distances (X, Y = C, H) in the optimized structures with M06-2X/6-311+G(3d,p), M06-2X/6-311+G(2d,p), and LC-ωPBE/6-311+G(2d,p) are shown in Table 8-A1 of the Appendix, along with the observed values.[46–53]

How can the behavior of the energies of the helicenes be explained? The energies of the helicenes were compared with the energies of [*n*]phenacene, a nonhelical species, evaluated with M06-2X/6-311+G(3d,p). The energy profiles will be discussed based on the energy differences, ΔE(**8-*n***) = E(**8-*n***) − E(**8-(*n* – 1)**) for helicenes (**8-1**–**8-12**) and ΔE(**8-*n*$_p$**) = E(**8-*n*$_p$**) − E(**8-(*n*$_p$ – 1)**) for [*n*]phenacenes (**8-1$_p$**–**8-12$_p$**). The ΔE(**8-*n***) values correspond to the energy differences in the formation of **8-*n*** from **8-(*n* – 1)**, and the ΔE(**8-*n*$_p$**) values similarly correspond to **8-*n*$_p$** from (**8-(*n*$_p$** − 1)). The E(**8-*n***), E(**8-*n*$_p$**), ΔE(**8-*n***), and ΔE(**8-*n*$_p$**) values were calculated on the energy surface, which are described by E_{ES}(**8-*n***), E_{ES}(**8-*n*$_p$**), ΔE_{ES}(**8-*n***), and ΔE_{ES}(**8-*n*$_p$**), respectively. The E_{ES} corrected with zero-point energies were also calculated, which are described by E_{ZP}(**8-*n***), E_{ZP}(**8-*n*$_p$**), ΔE_{ZP}(**8-*n***), and ΔE_{ZP}(**8-*n*$_p$**). The values calculated with M06-2X/6-311+G(3d,p) are collected in Table 8-A2 of the Appendix. The plot of ΔE_{ZP}(**8-*n***) versus ΔE_{ES}(**8-*n***) revealed an excellent correlation (y = 1.0042x + 0.6859; R_c^2 = 0.980, see Figure 8-A1 of the Appendix). As a result, ΔE_{ES}(**8-*n***) can be used to analyze the energy terms.

Figure 8-1 shows the plots of ΔE_{ES}(**8-*n***) and ΔE_{ES}(**8-*n*$_p$**) versus n. Both the ΔE_{ES}(**8-*n***) and ΔE_{ES}(**8-*n*$_p$**) values (ΔE_{ES}(**8-*n***; **8-*n*$_p$**)) decrease when n increases from 2 to 3. The extension of the π system appears to contribute more to the formation of phenanthrene from naphthalene than the repulsive noncovalent H···H interaction. The ΔE_{ES}(**8-3**; **8-3$_p$**) values are less than the ΔE_{ES}(**8-2**; **8-2$_p$**) values; however, the ΔE_{ES}(**8-*n***; **8-*n*$_p$**) values increase from **8-3**; **8-3$_p$** to **8-4**; **8-4$_p$**. In the case of ΔE_{ES}(**8-*n*$_p$**), the ΔE_{ES}(**8-4$_p$**) value is somewhat larger than ΔE_{ES}(**8-3$_p$**) but slightly smaller than ΔE_{ES}(**8-2$_p$**). The ΔE_{ES}(**8-*n*$_p$**) value decreases again slightly from **8-4$_p$** to **8-5$_p$**. Then, the values are nearly constant for $n_p \geq 5_p$. The results show that the repulsive energy from the noncovalent H···H interaction does not appear to be as severe as the stabilization factor from the extended π systems in **8-1$_p$**–**8-12$_p$**. Namely, the **8-*n*$_p$** system stabilizes almost constantly as the size of the species increase, especially for $n_p \geq 5_p$, although a change in ΔE_{ES}(**8-*n*$_p$**) is detected for $2_p \leq n_p < 5_p$.

The data points for ΔE_{ES}(**8-*n***) appear to be greater than those for ΔE_{ES}(**8-*n*$_p$**) when $n \geq 4$. The observations must be due to the severe steric repulsion in ΔE_{ES}(**8-*n***) ($n \geq 4$), where the plot for ΔE_{ES}(**8-*n*$_p$**) corresponds to that without such severe steric repulsion. The ΔE_{ES}(**8-4**) value is much larger than those of ΔE_{ES}(**8-2**) and ΔE_{ES}(**8-3**). The results can be explained by considering the much larger

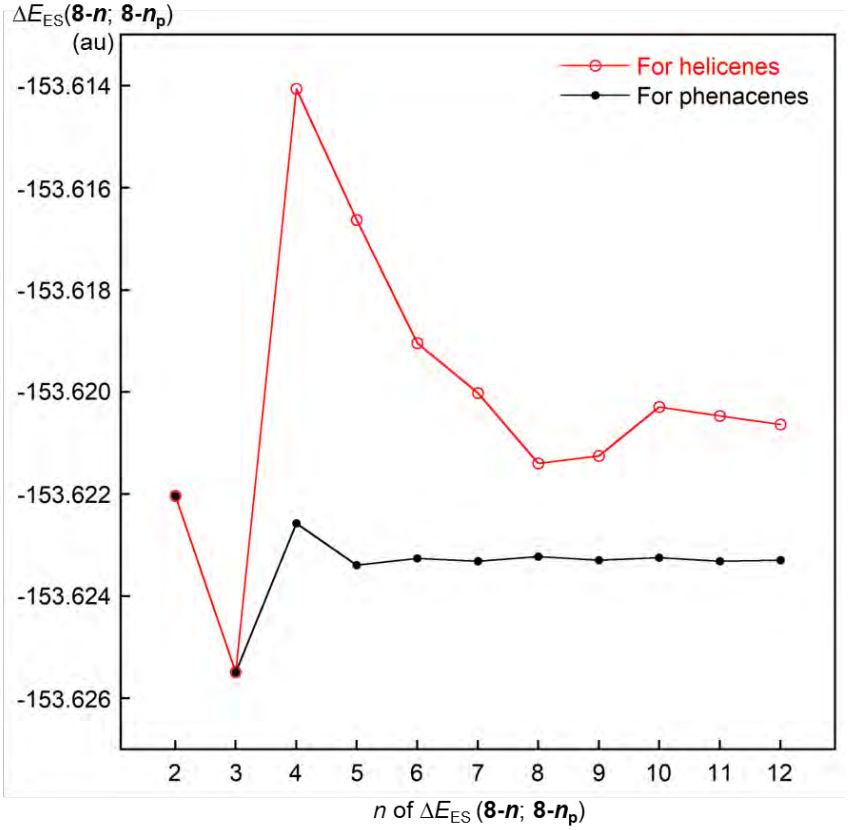

Figure 8-1. Plots of ΔE_{ES}(**8-*n***) and ΔE_{ES}(**8-*n*$_p$**) versus *n*, evaluated with M06-2X/6-311+G(3d,p), where ΔE_{ES}(**8-*n***) = E_{ES}(**8-*n***) − E_{ES}(**8-(*n* – 1)**) and ΔE_{ES}(**8-*n*$_p$**) = E_{ES}(**8-*n*$_p$**) – E_{ES}(**8-(*n*$_p$ – 1)**).

contribution from the repulsive noncovalent H···H interaction in **8-4** than in **8-3**. This consideration is supported by the optimized structure of **8-4**, drawn in Figure 8-3, as the molecular graph type. The ΔE_{ES}(**8-*n***) values decrease in the following order: ΔE_{ES}(**8-4**) > ΔE_{ES}(**8-5**) > ΔE_{ES}(**8-6**) > ΔE_{ES}(**8-7**) > ΔE_{ES}(**8-8**). The contribution of steric repulsion to ΔE_{ES}(**8-*n***) due to noncovalent interactions is expected to increase as *n* increases in this process. However, the observed results are the opposite of what was expected. Therefore, the observed trend should be attributed to the increased energy-lowering effect by the extended π systems in **8-4**–**8-8** relative to the repulsive interactions.

The ΔE_{ES}(**8-*n***) value becomes somewhat larger again from *n* = 8 to 9 and 9 to 10, and then decreases again from 10 to 11 and 11 to 12. The subtle conditions in the steric repulsion contribute to the complex behavior of ΔE_{ES}(**8-*n***) (8 ≤ *n* ≤ 12). The behavior of ΔE_{ES}(**8-2**)–ΔE_{ES}(**8-12**) shown in Figure 8-1 should be affected both by the repulsive factor of the noncovalent H-∗-H, C-∗-H, and C-∗-C interactions and by the energy-lowering factor of the extended π system. The ΔE_{ES}(**8-4**) value is the largest among ΔE_{ES}(**8-2**)–ΔE_{ES}(**8-12**). The results are of great interest since the repulsive noncovalent H···H interaction in **8-4** from **8-3** appears to be very large among **8-2**–**8-12** when evaluated by ΔE_{ES}(**8-*n***). The trend in ΔE_{ES}(**8-*n***) seems to be in good agreement with those reported by Rulíšek et al. calculated with PBE-D/TZVP//PBE-D/6-31G(d), except for ΔE_{ES}(**8-8**) and ΔE_{ES}(**8-9**).[54]

It is also instructive to analyze the aromaticities of acenes, phenacenes, and helicenes after investigating the energy profiles. The aromaticities were analyzed by the HOMA (harmonic oscillator model of aromaticity) method.[55] The HOMA values are collected in Table 8-A3 of the Appendix. The HOMA values of the acenes and phenacenes are plotted versus those of the helicenes, which are shown in Figure 8-2. The plot of the data for phenacenes versus those for helicenes gave a very good correlation ($y = 0.964x + 0.042$; $R_c^2 = 0.981$), whereas the correlations of the plots for acenes versus helicenes were very poor ($y = -0.685x + 0.995$; $R_c^2 = 0.492$ if calculated under the closed-shell singlet conditions and $y = -0.399x + 0.880$; $R_c^2 = 0.317$ under the open-shell singlet conditions). The very good correlation of the former demonstrates that the aromaticities of the helicenes appear to be very similar to those of the phenacenes, irrespective of the very severe steric deformations in the structures of helicenes. However, the very poor correlations with the negative correlation constants show that the aromaticities of the helicenes are very different from those of acenes.

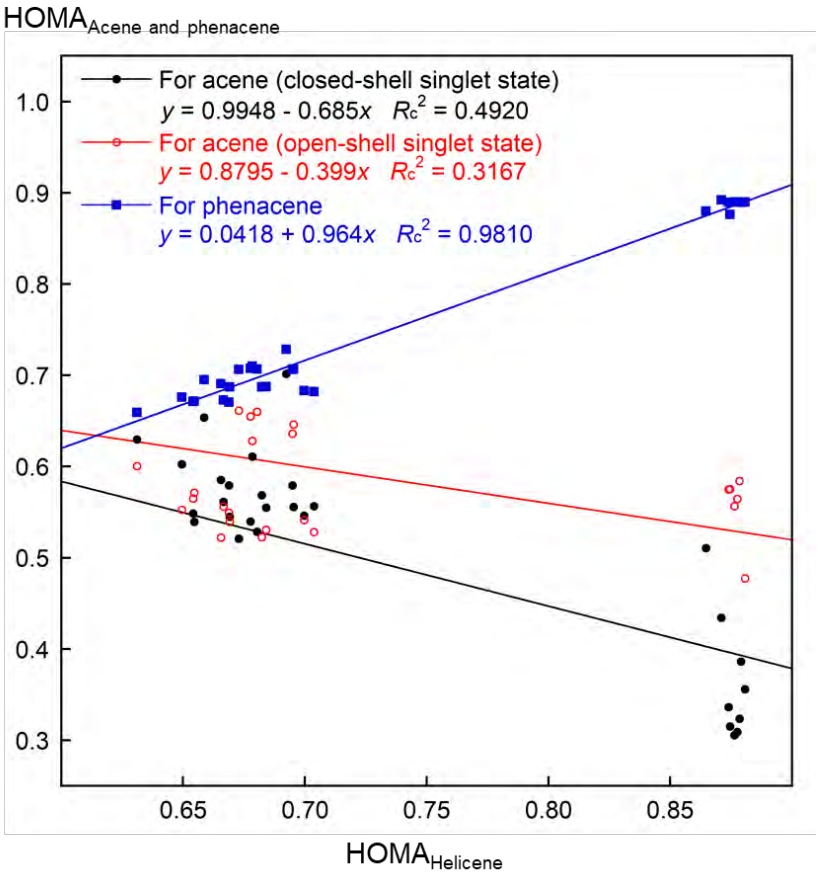

Figure 8-2. Plots of HOMA indices for [*n*]acenes (*n* = 4−12) at closed-shell singlet state, [*n*]acenes (*n* = 7−12) at open-shell singlet state and [*n*]phenacenes (*n* = 4−12) versus those for [*n*]helicenes (*n* = 4−12), calculated with MP2/6-311+G(3d,p).

Survey of X-∗-Y (X, Y = C and H) in 8-3–8-12 with the Molecular Graphs

Figure 8-3 shows the molecular graphs for by **8-3**–**8-12**. Many BPs with BCPs are detected in the π···π interactions between the phenyl rings in close proximity to the helicenes.

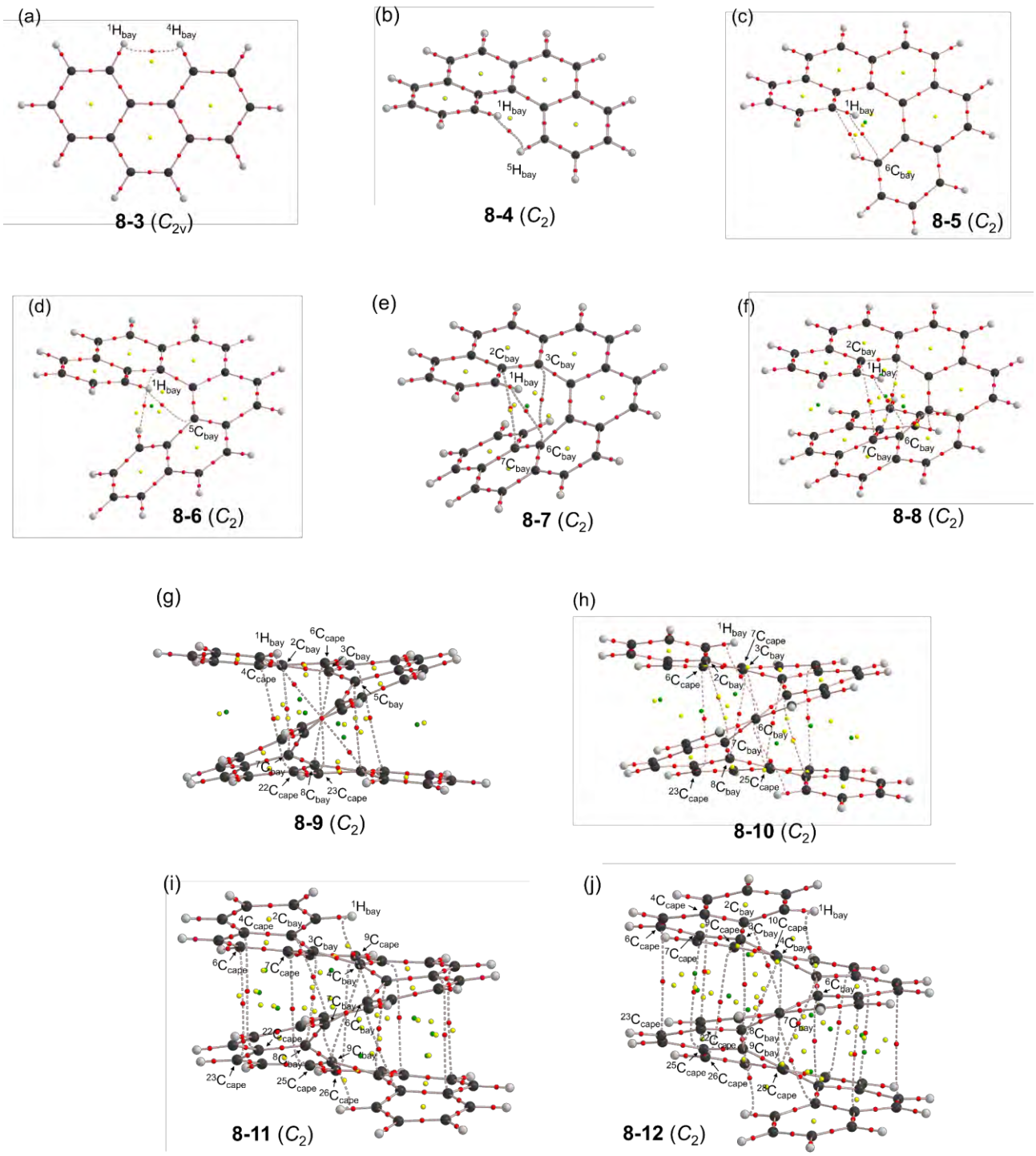

Figure 8-3. Molecular graphs for **8-3**–**8-12** ((a)–(j), respectively), calculated with M06-2X/6-311+G(3d,p), where BPs with BCPs corresponding to intramolecular noncovalent interactions are detected. The BCPs are denoted by red dots, RCPs (ring critical points) by yellow dots, CCPs (cage critical points) by green dots, and BPs by pink lines. The carbon atoms are in black and, the hydrogen atoms are in grey.

The BPs corresponding to X-*-Y (X and Y = C and H) appear almost straight, as shown in Figure 8-3, although some appear somewhat bent. To examine the linearity of the BPs further, the lengths of the BPs (r_{BP}) were calculated for all X-*-Y of **8-3**–**8-12**, along with the corresponding straight-line distances (R_{SL}). The values are collected in Table 8-A4 of the Appendix, along with the differences between them ($\Delta r_{BP} = r_{BP} - R_{SL}$). The averaged values of Δr_{BP} were 0.2040, 0.4006, 0.0588, and 0.1451 Å for H_{bay}-*-H_{bay}, C_{bay}-*-H_{bay}, C_{bay}-*-C_{bay}, and C_{cape}-*-C_{cape}, respectively. As a result, Δr_{BP} for H_{bay}-*-H_{bay} and C_{bay}-*-H_{bay} were larger than 0.20 Å, while those for C_{bay}-*-C_{bay} and C_{cape}-*-C_{cape} were less than 0.15 Å. Therefore, the BPs corresponding to C_{bay}-*-C_{bay} and C_{cape}-*-C_{cape} can be roughly approximated as straight lines since the Δr_{BP} values are less than 0.20 Å (see also Figure 8-A2 of the Appendix).

The QTAIM functions were calculated at BCPs on X-*-Y of **8-3**–**8-12** with M06-2X/6-311+G(3d,p). Table 8-1 collects the $\rho_b(\boldsymbol{r}_c)$, $H_b(\boldsymbol{r}_c) - V_b(\boldsymbol{r}_c)/2$, and $H_b(\boldsymbol{r}_c)$ values for one of the X-*-Y if it is doubly degenerated due to the C_2 symmetry of the optimized structures. Figure 8-4 shows the plots of $H_b(\boldsymbol{r}_c)$ versus $H_b(\boldsymbol{r}_c) - V_b(\boldsymbol{r}_c)/2$ for each X-*-Y, exemplified by **8-3**–**8-6**, **8-8**, **8-10**, and **8-12**, where H-*-H was detected in **8-3** and **8-4**, and C-*-H and C-*-C were detected in **8-8**, **8-10**, and **8-12**. (See Figure 8-A3 of the Appendix for **8-7**, **8-9**, and **8-11**.)

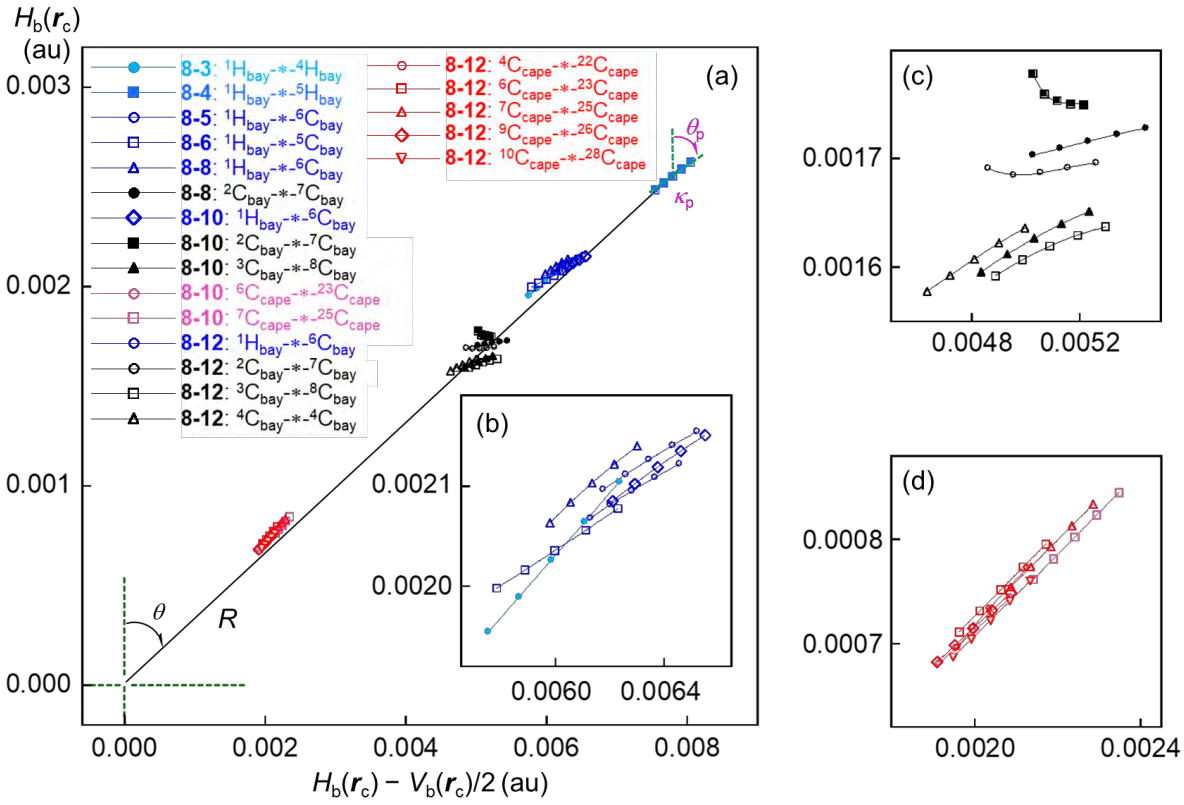

Figure 8-4. Plots of $H_b(\boldsymbol{r}_c)$ versus $H_b(\boldsymbol{r}_c) - V_b(\boldsymbol{r}_c)/2$ for H-*-H, C-*-H, and C-*-C, exemplified by those in **8-3**–**8-6**, **8-8**, **8-10**, and **8-12** (a). Whole picture (b). Magnified picture of the C-*-H area (c). Magnified picture of the C-*-C bay area (d). Magnified picture of the C-*-C cape area. The definitions of (R, θ) and (θ_p, κ_p) are illustrated, exemplified by H-*-H in **8-4**.

Table 8-1 also collects the QTAIM-DFA parameters of (R, θ) and (θ_p, κ_p) for each X-∗-Y of **8-3**–**8-12**, along with the C_{ii} values. The QTAIM functions and QTAIM-DFA parameters calculated with M06-2X/6-311+G(2d,p) and LC-ωPBE/6-311+G(2d,p) are collected in Tables 8-A5 and A6 of the Appendix, respectively.

Nature of Each X-∗-Y in 8-3–8-12

The C atoms in helicenes **8-3**–**8-12** were subdivided into C_{bay} and C_{cape} based on the positions of the atoms in the species, as were the H atoms into H_{bay} and H_{cape}. The bay and cape areas (positions) in the species are illustrated in Chart 8-1. While both the C_{bay} and C_{cape} atoms of **8-3**–**8-12** participate in the interactions as BPs, only H_{bay} atoms participate as BPs. The θ and θ_p values for H-∗-H, C-∗-H, and C-∗-C of **8-3**–**8-12**, collected in Table 8-1, are all less than 90º, except for θ_p of $^2C_{bay}$-∗-$^7C_{bay}$ in **8-10**, where (θ, θ_p) = (70.5º, 94.2º). The $^2C_{bay}$-∗-$^7C_{bay}$ interaction in **8-10** is denoted by **8-10** ($^2C_{bay}$-∗-$^7C_{bay}$) (see also Table 8-1). Therefore, the H-∗-H, C-∗-H, and C-∗-C interactions of **8-3**–**8-12** are all classified as *p*-CS interactions and characterized to have a vdW nature, which is denoted by *p*-CS/vdW, except for **8-10** ($^2C_{bay}$-∗-$^7C_{bay}$), which is predicted to have a *p*-CS/*t*-HB_{nc} nature.

Next, the interactions were individually examined. The (θ, θ_p) values are (71.3º, 72.8º) and (71.8º, 74.5º) for **8-3** ($^1H_{bay}$-∗-$^4H_{bay}$) and **8-4** ($^1H_{bay}$-∗-$^5H_{bay}$), respectively. The θ values for **8-3** ($^1H_{bay}$-∗-$^4H_{bay}$) and **8-4** ($^1H_{bay}$-∗-$^5H_{bay}$) are larger than those of A-∗-HF (A = He, Ne, and Ar: (θ, θ_p) = (59.9–70.9º, 64.0–88.0º)), whereas the θ_p values are larger than those of A-∗-HF (A = He and Ar). The interaction in **8-4** is estimated to be slightly stronger than that in **8-3**, although the real image of **8-3** ($^1H_{bay}$-∗-$^4H_{bay}$) has been much debated.[56–58] The detection of BPs with BCPs for **8-3** ($^1H_{bay}$-∗-$^4H_{bay}$) would not show enough strength for the interaction. It could be the mathematical results of the treatment. Nevertheless, **8-3** ($^1H_{bay}$-∗-$^4H_{bay}$) and **8-4** ($^1H_{bay}$-∗-$^5H_{bay}$) are discussed as very weak interactions in this work because the (θ, θ_p) values are larger than those of A-∗-HF (A = He, Ne, and Ar). Double H_{bay}-∗-C_{bay} interactions are detected for each of **8-5**–**8-12**, with (θ, θ_p) values of (70.7–71.6º, 76.7–80.8º). The (θ, θ_p) values are very close to those of A-∗-HF (A = He, Ne, and Ar). The BP (H_{bay}-∗-C_{bay}) in **8-6** and **8-9** connect the H_{bay} and C_{bay} atoms. However, they are not located at the nearest positions, as shown in Table 8-1 and Figure 8-3. Therefore, the BP (H_{bay}-∗-C_{bay}) in **8-6** and **8-9** should be analyzed carefully.

Table 8-1. QTAIM functions and QTAIM-DFA parameters evaluated for the fused benzene-type helicenes of monomers (**8-3**–**8-12**), employing the perturbed structures generated with CIV.[a–c]

Species (X-*-Y)	$\rho_b(\boldsymbol{r}_c)$ (ea_o^{-3})	$c\nabla^2\rho_b(\boldsymbol{r}_c)$[d] (au)	$H_b(\boldsymbol{r}_c)$ (au)	R[e] (au)	θ[f] (°)	C_{il}[g] (Å mdyn^{-1})	θ_p[h] (°)	κ_p[i] (au^{-1})	Predicted Nature
8-3 ($^1H_{bay}$-*-$^4H_{bay}$)	0.0130	0.0060	0.0020	0.0063	71.3	3.29	72.8	12.4	*p*-CS/vdW
8-4 ($^1H_{bay}$-*-$^5H_{bay}$)	0.0165	0.0078	0.0026	0.0082	71.8	6.67	74.5	11.4	*p*-CS/vdW
8-5 ($^1H_{bay}$-*-$^6C_{bay}$)	0.0131	0.0063	0.0021	0.0066	71.6	6.12	80.8	136	*p*-CS/vdW
8-6 ($^1H_{bay}$-*-$^5C_{bay}$)	0.0131	0.0060	0.0020	0.0063	71.3	3.82	79.9	31.8	*p*-CS/vdW
8-7 ($^1H_{bay}$-*-$^6C_{bay}$)	0.0135	0.0063	0.0021	0.0067	71.5	5.47	77.9	188	*p*-CS/vdW
8-7 ($^2C_{bay}$-*-$^7C_{bay}$)	0.0114	0.0051	0.0017	0.0054	71.9	3.33	80.6	128	*p*-CS/vdW
8-8 ($^1H_{bay}$-*-$^6C_{bay}$)	0.0130	0.0061	0.0021	0.0065	71.1	5.51	76.7	189	*p*-CS/vdW
8-8 ($^2C_{bay}$-*-$^7C_{bay}$)	0.0117	0.0052	0.0017	0.0055	71.8	2.01	86.4	28.5	*p*-CS/vdW
8-9 ($^1H_{bay}$-*-$^5C_{bay}$)	0.0134	0.0062	0.0022	0.0066	70.7	3.40	79.5	627	*p*-CS/vdW
8-9 ($^2C_{bay}$-*-$^7C_{bay}$)	0.0113	0.0050	0.0016	0.0053	72.1	1.83	81.6	119	*p*-CS/vdW
8-9 ($^3C_{bay}$-*-$^8C_{bay}$)	0.0122	0.0053	0.0016	0.0056	72.9	1.87	85.0	196	*p*-CS/vdW
8-9 ($^4C_{cape}$-*-$^{22}C_{cape}$)[j]	0.0055	0.0020	0.0007	0.0022	70.7	5.25	66.9	135	*p*-CS/vdW
8-9 ($^6C_{cape}$-*-$^{23}C_{cape}$)	0.0061	0.0021	0.0007	0.0022	70.4	8.51	69.4	37.7	*p*-CS/vdW
8-10 ($^1H_{bay}$-*-$^6C_{bay}$)	0.0137	0.0064	0.0021	0.0067	71.6	5.74	79.2	123	*p*-CS/vdW
8-10 ($^2C_{bay}$-*-$^7C_{bay}$)[k]	0.0113	0.0050	0.0018	0.0053	70.5	1.86	94.2	2890	*p*-CS/*t*-HB$_{nc}$
8-10 ($^3C_{bay}$-*-$^8C_{bay}$)	0.0114	0.0050	0.0016	0.0053	72.1	1.78	82.0	182	*p*-CS/vdW
8-10 ($^6C_{cape}$-*-$^{23}C_{cape}$)	0.0059	0.0020	0.0007	0.0021	70.4	9.02	69.7	7.0	*p*-CS/vdW
8-10 ($^7C_{cape}$-*-$^{25}C_{cape}$)	0.0061	0.0022	0.0008	0.0024	70.3	3.42	68.0	10.3	*p*-CS/vdW
8-11 ($^1H_{bay}$-*-$^6C_{bay}$)	0.0136	0.0063	0.0021	0.0067	71.6	5.41	79.8	113	*p*-CS/vdW
8-11 ($^2C_{bay}$-*-$^7C_{bay}$)	0.0116	0.0051	0.0017	0.0054	71.5	1.84	87.1	142	*p*-CS/vdW
8-11 ($^3C_{bay}$-*-$^8C_{bay}$)	0.0115	0.0050	0.0016	0.0053	72.0	1.91	82.6	166	*p*-CS/vdW
8-11 ($^4C_{bay}$-*-$^9C_{bay}$)	0.0111	0.0049	0.0016	0.0052	71.7	1.69	79.5	155	*p*-CS/vdW
8-11 ($^4C_{cape}$-*-$^{22}C_{cape}$)	0.0053	0.0019	0.0007	0.0020	70.1	6.81	68.3	13.5	*p*-CS/vdW
8-11 ($^6C_{cape}$-*-$^{23}C_{cape}$)	0.0059	0.0020	0.0007	0.0021	70.2	10.21	69.7	7.5	*p*-CS/vdW
8-11 ($^7C_{cape}$-*-$^{25}C_{cape}$)	0.0059	0.0022	0.0008	0.0023	70.2	3.58	67.8	7.2	*p*-CS/vdW
8-11 ($^9C_{cape}$-*-$^{26}C_{cape}$)	0.0062	0.0021	0.0007	0.0022	70.4	5.80	69.5	64.7	*p*-CS/vdW
8-12 ($^1H_{bay}$-*-$^6C_{bay}$)	0.0136	0.0063	0.0021	0.0067	71.5	4.84	80.5	103	*p*-CS/vdW
8-12 ($^2C_{bay}$-*-$^7C_{bay}$)	0.0115	0.0051	0.0017	0.0053	71.5	1.77	87.8	349	*p*-CS/vdW
8-12 ($^3C_{bay}$-*-$^8C_{bay}$)	0.0117	0.0051	0.0016	0.0053	72.3	1.74	83.6	241	*p*-CS/vdW
8-12 ($^4C_{bay}$-*-$^9C_{bay}$)	0.0110	0.0048	0.0016	0.0051	71.5	1.72	80.7	87.8	*p*-CS/vdW
8-12 ($^4C_{cape}$-*-$^{22}C_{cape}$)	0.0055	0.0020	0.0007	0.0022	70.2	4.80	66.3	697	*p*-CS/vdW
8-12 ($^6C_{cape}$-*-$^{23}C_{cape}$)	0.0060	0.0021	0.0008	0.0022	70.0	6.78	68.0	8.6	*p*-CS/vdW
8-12 ($^7C_{cape}$-*-$^{25}C_{cape}$)	0.0059	0.0022	0.0008	0.0023	70.0	3.41	68.2	3.3	*p*-CS/vdW
8-12 ($^9C_{cape}$-*-$^{26}C_{cape}$)	0.0059	0.0020	0.0007	0.0021	70.3	6.95	69.4	24.7	*p*-CS/vdW
8-12 ($^{10}C_{cape}$-*-$^{28}C_{cape}$)	0.0056	0.0020	0.0007	0.0022	70.5	4.09	68.6	65.4	*p*-CS/vdW

[a] Calculated with M06-2X/6-311+G(3d,p). [b] Data are given at the BCPs. [c] All interactions are predicted to have the *p*-CS/vdW nature, except for **8-10** ($^2C_{bay}$-*-$^7C_{bay}$), which has the *p*-CS/*t*-HB$_{nc}$ nature. [d] $c\nabla^2\rho_b(\boldsymbol{r}_c) = H_b(\boldsymbol{r}_c) - V_b(\boldsymbol{r}_c)/2$, where $c = \hbar^2/8m$. [e] $R = (x^2 + y^2)^{1/2}$, where $(x, y) = (H_b(\boldsymbol{r}_c) - V_b(\boldsymbol{r}_c)/2, H_b(\boldsymbol{r}_c))$. [f] $\theta = 90° - \tan^{-1}(y/x)$. [g] $C_{ij} = \partial^2 E/\partial f_i \partial f_j$, where i and j refer to internal coordinates, and the external force components acting on the system f_i and f_j correspond to i and j, respectively. [h] $\theta_p = 90° - \tan^{-1}(dy/dx)$. [i] $\kappa_p = |d^2y/dx^2|/[1 + (dy/dx)^2]^{3/2}$. [j] Data from $w = \pm0.0125$, ±0.025, and 0 were used for the plot since BCPs were not detected at $w = 0.05$. [k] Data from $w = -0.05$, -0.0375, -0.025, -0.0125, and 0 were used for the plot since BCPs were not detected when $w > 0$.

One, one, four, four, seven, and eight different types of C-∗-C interactions are detected for **8-7**–**8-12**, respectively. The (θ, θ_p) values for C-∗-C in **8-7**–**8-12** are (70.0–72.9º, 66.3–94.2º). It appears better to separately examine the values for two groups of C_{bay}-∗-C_{bay} and C_{cape}-∗-C_{cape}. While the (θ, θ_p) values of C_{bay}-∗-C_{bay} in **8-7**–**8-12** are (71.5–72.9º, 79.5–87.8º), the values are (70.0–70.7º, 66.3–69.7º) for C_{cape}-∗-C_{cape}. The θ values for C_{cape}-∗-C_{cape} are slightly smaller than those of C_{bay}-∗-C_{bay} (by 0.5–2.2º), but the θ_p values for C_{cape}-∗-C_{cape} are much smaller than those of C_{bay}-∗-C_{bay} (by 13.2–24.5º). In this case, $\theta_p < \theta$ for C_{cape}-∗-C_{cape}, whereas $\theta_p > \theta$ for C_{bay}-∗-C_{bay}. Interactions with $\theta_p > \theta$ are usually observed, but interactions with $\theta_p < \theta$ are rare.

Interactions with $\theta > \theta_p$ occur under some specific conditions. To examine the behavior of θ and θ_p in **8-7**–**8-12**, the $\Delta\theta_p$ (= $\theta_p - \theta$) values are plotted versus θ_p for C-∗-C, H-∗-H, and C-∗-H in **8-3**–**8-12**. Figure 8-5 shows this plot. The plot showed a very good correlation for all data ($y = 0.918x - 64.88$: $R_c^2 = 0.995$). (A substantial correlation was not found in the plot of $\Delta\theta_p$ versus θ_p due to the very small range of θ (= 70–72.9º).) The two areas for C-∗-C interactions with $\Delta\theta_p > 0$ and $\Delta\theta_p < 0$ are clearly illustrated by the green dotted lines in Figure 8-5. The $\Delta\theta_p$ values for the interactions are positive if the θ_p values are larger than 70.7º, whereas $\Delta\theta_p < 0$ if $\theta_p < 70.7$º. Figure 8-5 clearly shows that C_{bay}-∗-C_{bay} and C_{cape}-∗-C_{cape} in **8-9**–**8-12** belong to the areas where $\Delta\theta_p > 0$ and $\Delta\theta_p < 0$, respectively.

It seems difficult to clearly explain the results shown in Figure 8-5; however, the explanation is as follows: The static nature of the interactions described by θ should be a measure of the strength of

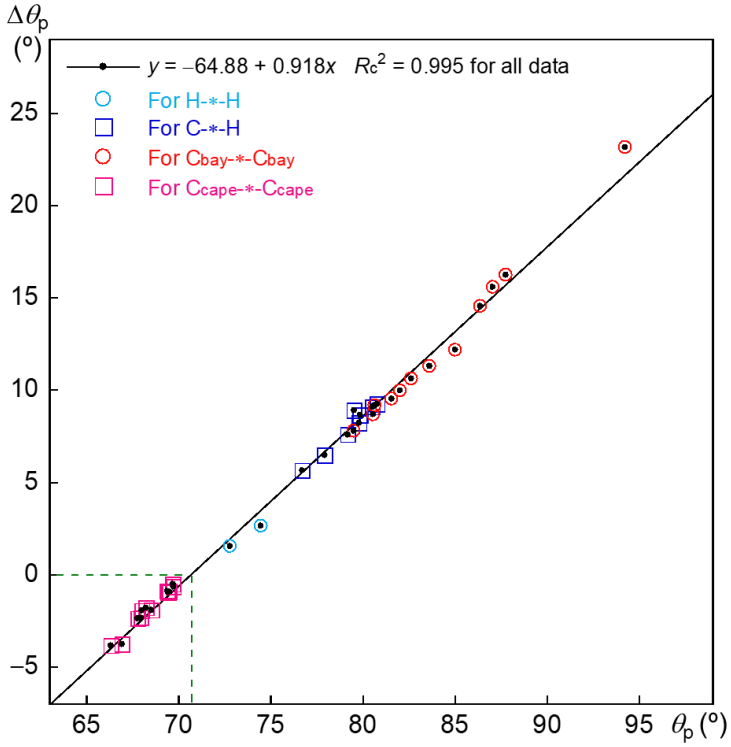

Figure 8-5. Plot of $\Delta\theta_p$ versus θ_p for H-∗-H, C-∗-H, and C-∗-C in **8-3**–**8-12**, evaluated with M06-2X/6-311+G(3d,p), where $\Delta\theta_p = (\theta_p - \theta)$.

the interactions. If so, the steric compression on C_{cape}-∗-C_{cape} in **8-9**–**8-12** appears to be similar to that on C_{bay}-∗-C_{bay} in fully optimized structures. Namely, the C_{cape}-∗-C_{cape} and C_{bay}-∗-C_{bay} interactions in the fully optimized structures of **8-9**–**8-12** would be affected similarly to steric compression, according to the θ values. On the other hand, the dynamic nature of the interactions is defined by θ_p based on the behavior of the interactions in the perturbed structures. The C_{bay}-∗-C_{bay} interactions in the perturbed structures will be affected by steric compression, similar to the usual cases of interactions, whereas the C_{cape}-∗-C_{cape} interactions will be inversely affected compared with the usual cases when measured by the θ_p values at the BCPs of the interactions.

Nature of Each X-∗-Y in 8-6:6 and 8-7:7

What is the behavior of the interactions when the helicenes form concave-type dimers? The behavior was elucidated, exemplified by **8-6**:**6** (C_i) and **8-7**:**7** (C_i) with M06-2X/6-311+G(3d,p). Figure 8-6 shows molecular graphs of **8-6**:**6** and **8-7**:**7**. Five and four independent BPs with BCPs were detected in **8-6**:**6** and **8-7**:**7**, respectively, between the components of H-∗-H and C-∗-H, as well as two independent BPs with BCPs for the intramolecular C-∗-H interactions in each component of **8-6**:**6** and **8-7**:**7**. The behavior of the interactions was also investigated for **8-7**:**7** (C_i), **8-8**:**8** (C_i), and/or **8-10**:**10** (C_i) with M06-2X/6-311+G(2d,p) and LC-ωPBE/6-311+G(2d,p). The results are collected in Tables 8-A7 and A8 of the Appendix. The QTAIM functions were similarly calculated for the intermolecular interactions at the BCPs on the BPs of **8-6**:**6** and **8-7**:**7** with M06-2X/6-311+G(3d,p).

Table 8-2 collects the $\rho_b(\boldsymbol{r}_c)$, $H_b(\boldsymbol{r}_c) - V_b(\boldsymbol{r}_c)/2$, and $H_b(\boldsymbol{r}_c)$ values for one of the doubly degenerate interactions due to the C_i symmetry of the optimized structures. Figure 8-7 shows the plots of $H_b(\boldsymbol{r}_c)$ versus $H_b(\boldsymbol{r}_c) - V_b(\boldsymbol{r}_c)/2$ for each interaction between the components at **8-6**:**6** and **8-7**:**7**. (The plots

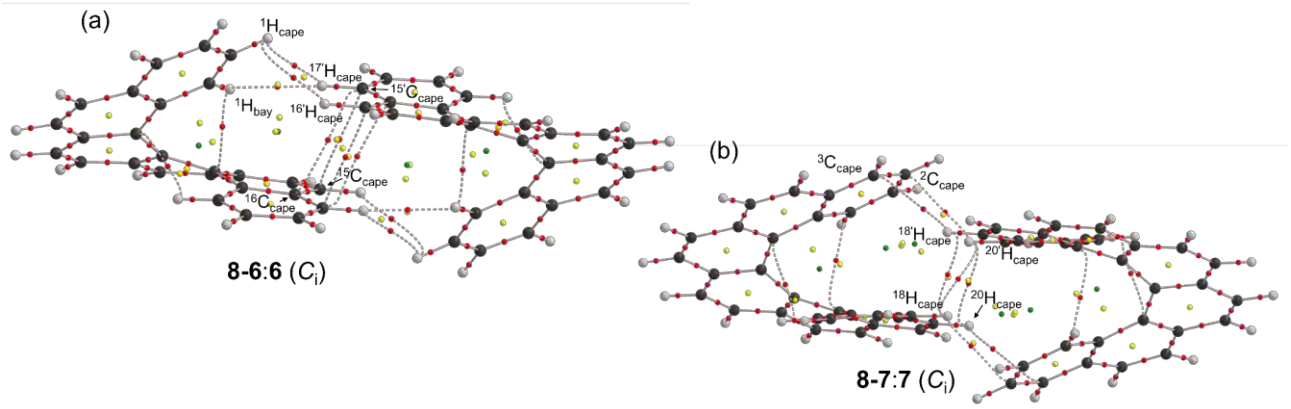

Figure 8-6. Molecular graphs for helicene dimers, **8-6**:**6** (a) and **8-7**:**7** (b), calculated with M06-2X/6-311+G(3d,p), where BPs with BCPs corresponding to intra- and intermolecular noncovalent interactions are detected. The BCPs are denoted by red dots, RCPs (ring critical points) by yellow dots, CCPs (cage critical points) by green dots, and BPs by pink lines. The carbon atoms are in black, and the hydrogen atoms are in grey.

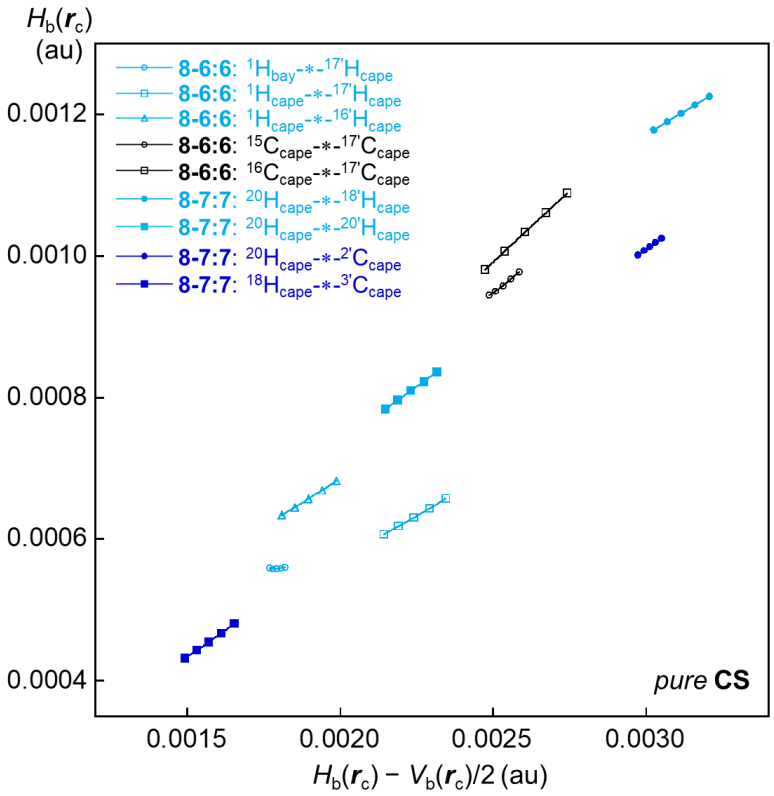

Figure 8-7. Plots of $H_b(\boldsymbol{r}_c)$ versus $H_b(\boldsymbol{r}_c) - V_b(\boldsymbol{r}_c)/2$ for H-∗-H, C-∗-H, and C-∗-C at **8-6**:**6** (C_i) and **8-7**:**7** (C_i), calculated with M06-2X/6-311+G(3d,p).

for **8-8**:**8** and **8-10**:**10** are shown in Figure 8-A5 of the Appendix, and the data are collected in Table 8-A8 of the Appendix.)

The plots were analyzed similarly to the case of **8-3**–**8-12**. Table 8-2 also collects the QTAIM-DFA parameters of (R, θ) and (θ_p, κ_p) for the intermolecular interactions in question at **8-6**:**6** and **8-7**:**7**, together with the C_{ii} values. The (θ, θ_p) values for the three H-∗-H and two C-∗-C intermolecular independent interactions of **8-6**:**6** are (70.9–74.3º, 74.9–88.1º) and (68.3–69.2º, 68.0–70.8º), respectively. The (θ, θ_p) values for the couple of H-∗-H and two C-∗-H intermolecular independent interactions at **8-7**:**7** are (68.9–70.0º, 72.7–75.5º) and (71.4–73.8º, 73.2–73.3º), respectively. The θ and θ_p values for the intermolecular H-∗-H, C-∗-H, and C-∗-C interactions at **8-6**:**6** and **8-7**:**7** are all less than 90º; therefore, the interactions are all predicted to have a *p*-CS/vdW nature. The interactions appear to be very weak, based on the (θ, θ_p) values. However, (θ, θ_p) = (72.6º, 88.1º) for **8-6**:**6** ($^{1}H_{bay}$-∗-$^{17'}H_{cape}$), of which nature seems close to *p*-CS/*t*-HB_{nc}.

In the case of intramolecular interactions, $^{1}H_{bay}$-∗-$^{5}C_{bay}$ and $^{3}C_{bay}$-∗-$^{7}H_{bay}$ were detected at **8-6**:**6**. The former was also observed in **8-6**, whereas the latter was newly detected in **8-6**:**6**. The new appearance of **8-6** ($^{3}C_{bay}$-∗-$^{7}H_{bay}$) may be due to a structural change at **8-6**:**6** relative to **8-6**. Similarly, $^{1}H_{bay}$-∗-$^{6}C_{bay}$ and $^{3}C_{bay}$-∗-$^{8}H_{bay}$ were detected at **8-7**:**7**. The former was observed in **8-7**, while

Table 8-2. QTAIM functions and QTAIM-DFA parameters evaluated for the fused benzene-type helicenes of concave-type dimers (**8-6**:**6** and **8-7**:**7**), employing the perturbed structures generated with CIV.[a–c]

Species X-∗-Y	$\rho_b(\boldsymbol{r}_c)$ (ea_o^{-3})	$c\nabla^2\rho_b(\boldsymbol{r}_c)$ (au)	$H_b(\boldsymbol{r}_c)$ (au)	R (au)	θ (º)	C_{ii} (Å mdyn^{-1})	θ_p (º)	κ_p (au^{-1})	Predicted Nature
8-6:**6**									
$^{1}H_{bay}$-∗-$^{17'}H_{cape}$[d]	0.0045	0.0018	0.0006	0.0019	72.6	25.02	88.1	5163	*p*-CS/vdW
$^{1}H_{cape}$-∗-$^{17'}H_{cape}$	0.0061	0.0022	0.0006	0.0023	74.3	35.63	76.2	184.2	*p*-CS/vdW
$^{1}H_{cape}$-∗-$^{16'}H_{cape}$	0.0051	0.0019	0.0007	0.0020	70.9	42.01	74.9	69.9	*p*-CS/vdW
$^{15}C_{cape}$-∗-$^{17'}C_{cape}$[e]	0.0065	0.0025	0.0009	0.0027	69.2	12.64	70.8	1066	*p*-CS/vdW
$^{16}C_{cape}$-∗-$^{17'}C_{cape}$	0.0066	0.0026	0.0010	0.0028	68.3	8.63	68.0	53.5	*p*-CS/vdW
$^{1}H_{bay}$-∗-$^{5}C_{bay}$	0.0128	0.0057	0.0019	0.0060	71.9	3.817	78.3	32.3	*p*-CS/vdW
$^{3}C_{bay}$-∗-$^{7}H_{bay}$	0.0134	0.0061	0.0020	0.0064	71.7	3.414	79.3	29.5	*p*-CS/vdW
8-7:**7**									
$^{20}H_{cape}$-∗-$^{18'}H_{cape}$	0.0073	0.0031	0.0012	0.0033	68.9	14.61	75.5	24.6	*p*-CS/vdW
$^{20}H_{cape}$-∗-$^{20'}H_{cape}$	0.0054	0.0022	0.0008	0.0024	70.0	27.90	72.7	36.5	*p*-CS/vdW
$^{20}H_{cape}$-∗-$^{2'}C_{cape}$	0.0079	0.0030	0.0010	0.0032	71.4	10.01	73.3	125.7	*p*-CS/vdW
$^{18}H_{cape}$-∗-$^{3'}C_{cape}$	0.0050	0.0016	0.0005	0.0016	73.8	17.36	73.2	181.8	*p*-CS/vdW
$^{1}H_{bay}$-∗-$^{6}C_{bay}$	0.0132	0.0062	0.0021	0.0065	70.8	5.557	80.0	93.5	*p*-CS/vdW
$^{3}C_{bay}$-∗-$^{8}H_{bay}$	0.0138	0.0065	0.0021	0.0068	71.9	5.024	78.8	154.1	*p*-CS/vdW

[a] Calculated with M06-2X/6-311+G(3d,p). [b] Data are given at the BCPs. [c] See footnotes of Table 8-1 for the QTAIM-DFA parameters and C_{ii}. [d] Data from $w = -0.0375$, -0.025, -0.0125, 0, and 0.0125 were used for the plot, since BCPs for **8-6**:**6** ($^{1}H_{bay}$-∗-$^{17'}H_{cape}$) were not detected when $w > 0.0125$. [e] Data from $w = -0.05$, -0.0375, -0.025, -0.0125, and 0 were used for the plot, since BCPs for **8-6**:**6** ($^{15}C_{cape}$-∗-$^{17'}C_{cape}$) were not detected when $w > 0$.

$^{3}C_{bay}$-∗-$^{8}H_{bay}$ in **8-7**:**7** appeared in place of $^{2}C_{bay}$-∗-$^{7}C_{bay}$ in **8-7**. The change in the optimized structures between **8-7** and **8-7**:**7** would again be responsible for the results. However, clarifying the reason for the appearance/disappearance of BPs is very complex and difficult in helicenes, and it is beyond the scope of this work.

Highly theoretical treatment must be necessary to clarify the reason for the appearance and disappearance of BPs/BCPs. Pendás and coworkers discussed BPs as privileged exchange channels, using the interacting quantum atom (IQA) framework.[59] They have investigated how BPs between an atom A and atoms B in its environment appear to be determined by competition among the A–B exchange correlation energies that always contribute to stabilize the A–B interactions. And they have predicted that a BP is found between two atoms by examining a number of archetypal simple systems: (1) there is no other competing atom in its vicinity, so there must be a direct exchange route between them or (2) its $\mathbf{V}_{xc}$ term is the largest among several possibilities, where $\mathbf{V}_{xc}$ stands for a quantum-mechanical correction coming from the exchange correlation second-order density.[59] It has also indicated that interaction energies between both atoms cannot be universally used to predict the existence of a BP between them.[60] Moreover, they are not correlated to distances or to the density values at BCPs. On the contrary, the exchange contribution is shown to be an appropriate descriptor.[60]

Similarly, theoretical treatments are applied to various interactions, employing QTAIM-defined an atomic interaction line (AIL: Presence or absence), IQA-defined interaction energy and its components, NCI (non-covalent interactions)-defined isosurfaces, and deformation density.[61] The reason for the appearance and disappearance of BPs/BCPs in the helicenes would be rationalized by applying above theory.

The (θ, θ_p) values for the intramolecular interactions at **8-6**:**6** and **8-7**:**7** are (70.8–71.9º, 78.3–80.0º). As a result, the interactions are all predicted to have a *p*-CS/vdW nature. The predicted natures of the interactions in **8-6**:**6** and **8-7**:**7** appear to be similar to those in **8-6** and **8-7**, perhaps due to the very weak nature of both dimers and monomers.

Basis Set and Level Dependence of the Predicted Natures

The basis set and level dependence of the predicted natures was investigated, exemplified by **8-7** and **8-7**:**7**, to attempt to determine the reason why the optimized structures can easily change. Table 8-3 shows the QTAIM-DFA parameters of (R, θ) and (θ_p, κ_p) and the C_{ii} values, calculated with M06-2X/6-311+G(3d,p), M06-2X/6-311+G(2d,p), and LC-ωPBE/6-311+G(2d,p). Table 8-3 includes the distances in question as well as some internal vibration(s) ν_n corresponding to the interactions in question, which are closely related to (θ_p, κ_p). Figure 8-8 shows the motions of the internal vibrations for ν_1 of **8-7** and **8-7**:**7** calculated with M06-2X/6-311+G(3d,p), M06-2X/6-311+G(2d,p), and LC-ωPBE/6-311+G(3d,p).

The calculated $r(^1H_{bay}\cdots{}^6C_{bay})$ and $r(^2C_{bay}\cdots{}^7C_{bay})$ distances were 2.590 Å and 2.975 Å, respectively, for **8-7**, when calculated with M06-2X/6-311+(3d,p), while the values were 2.590 Å and 3.003 Å, respectively, when calculated with M06-2X/6-311+(2d,p). The differences are less than 0.001 Å for $r(^1H_{bay}\cdots{}^6C_{bay})$ and 0.028 Å for $r(^2C_{bay}\cdots{}^7C_{bay})$. The results show that the structure of **8-7** optimized with M06-2X/6-311+(2d,p) appears to be nearly identical to that optimized with M06-2X/6-311+(3d,p). On the other hand, the $r(^1H_{bay}\cdots{}^6C_{bay})$ and $r(^2C_{bay}\cdots{}^7C_{bay})$ of **8-7** were 2.561 Å and 3.227 Å, respectively, if calculated with LC-ωPBE/6-311+(2d,p). The difference was −0.029 Å for the former but 0.224 Å for the latter relative to the corresponding values calculated with M06-2X/6-311+(2d,p). The structure of **8-7** optimized with LC-ωPBE/6-311+(2d,p) appears to be (very) different from that optimized with M06-2X/6-311+(2d,p), especially around $r(^2C_{bay}\cdots{}^7C_{bay})$. In the case of $^1H_{bay}\cdots{}^5C_{bay}$, the distance was optimized to be 2.468 Å with LC-ωPBE/6-311+(2d,p), which is shorter than the $r(^1H_{bay}\cdots{}^6C_{bay})$ distance optimized with M06-2X/6-311+(2d,p) (2.590 Å) by 0.122 Å. BPs (with BCPs) were detected for $^1H_{bay}$-*-$^6C_{bay}$ and $^2C_{bay}$-*-$^7C_{bay}$ in **8-7** if calculated with M06-2X/6-311+(3d,p) and M06-2X/6-311+(2d,p), while a BP was detected for $^1H_{bay}$-*-$^5C_{bay}$ if calculated with LC-ωPBE/6-311+(2d,p). The $^2C_{bay}$-*-$^7C_{bay}$ and $^1H_{bay}$-*-$^5C_{bay}$ distances in **8-7**, optimized with LC-ωPBE/6-311+(2d,p), were (much) longer and shorter than those optimized with M06-2X/6-311+(2d,p), respectively.

The differences in the optimized distances appear to be the main factor for the appearance/disappearance of the BPs, although predicting the appearance/disappearance of the BPs is very difficult and complex. Despite such different results, the motion of ν_1 appears to be very similar when calculated at both the M06-2X and LC-ωPBE levels, indicating that ν_1 is a good measure for imaging the dynamic nature of the π···π interactions in **8-7** among the internal vibrations. Small differences in the dynamic nature of the interactions predicted at both the M06-2X and LC-ωPBE levels result from the (very) similar motion of ν_1. The magnitudes of the displacements in the cape area seem (much) larger than those in the bay area in ν_1. This will be instructive if the relationship is clarified for that between the magnitudes of the displacements and the $\Delta\theta_p$ values. This issue will be investigated in a future work. The very low energy of ν_1 in **8-7** suggests the basis set and level dependence can easily change the optimized structure.

Table 8-3. QTAIM functions and QTAIM-DFA parameters evaluated for the fused benzene-type helicene (**8-7**) and the concave-type dimer (**8-7**:**7**), employing the perturbed structures generated with CIV, together with the X-∗-Y distances and the corresponding internal vibrations, with the frequencies closely related to the interactions in question.[a,b]

Species X-∗-Y	r(X···Y) (Å)	R (au)	θ (º)	C_{ii} (Å mdyn^{-1})	θ_p (º)	κ_p (au^{-1})	Predicted Nature
8-7 (M06-2X/6-311+G(3d,p): ν_1 = 43.4 cm^{-1})							
$^{1}H_{bay}$-∗-$^{6}C_{bay}$	2.5902	0.0067	71.5	5.47	77.9	187.5	*p*-CS/vdW
$^{2}C_{bay}$-∗-$^{7}C_{bay}$	2.9751	0.0054	71.9	3.33	80.6	128.2	*p*-CS/vdW
8-7 (M06-2X/6-311+G(2d,p): ν_1 = 46.6 cm^{-1})							
$^{1}H_{bay}$-∗-$^{6}C_{bay}$	2.5896	0.0067	70.4	5.49	81.6	39.9	*p*-CS/vdW
$^{2}C_{bay}$-∗-$^{7}C_{bay}$	3.0025	0.0054	69.9	3.06	78.7	120.2	*p*-CS/vdW
8-7 (LC-ωPBE/6-311+G(2d,p): ν_1 = 40.1 cm^{-1})[c,d]							
$^{1}H_{bay}$-∗-$^{5}C_{bay}$	2.4681	0.0066	70.5	3.72	82.2	46.4	*p*-CS/vdW
8-7:**7** (M06-2X/6-311+G(3d,p): ν_1 = 14.0 cm^{-1}; ν_4 = 24.2 cm^{-1}; ν_5 = 29.3 cm^{-1}; ν_{11} = 81.2 cm^{-1})							
$^{20}H_{cape}$-∗-$^{18'}H_{cape}$	2.5423	0.0033	68.9	14.61	75.5	24.6	*p*-CS/vdW
$^{20}H_{cape}$-∗-$^{20'}H_{cape}$	2.7155	0.0024	70.0	27.90	72.7	36.5	*p*-CS/vdW
$^{20}H_{cape}$-∗-$^{2'}C_{cape}$	2.6769	0.0032	71.4	10.01	73.3	125.7	*p*-CS/vdW
$^{18}H_{cape}$-∗-$^{3'}C_{cape}$	2.9640	0.0016	73.8	17.36	73.2	181.8	*p*-CS/vdW
8-7:**7** (M06-2X/6-311+G(2d,p): ν_1 = 13.0 cm^{-1}; ν_4 = 22.1 cm^{-1}; ν_5 = 27.3 cm^{-1}; ν_{11} = 78.6 cm^{-1})							
$^{20}H_{cape}$-∗-$^{18'}H_{cape}$	2.5643	0.0032	67.9	16.63	75.2	60.1	*p*-CS/vdW
$^{20}H_{cape}$-∗-$^{20'}H_{cape}$	2.7287	0.0024	68.6	29.20	71.9	42.2	*p*-CS/vdW
$^{20}H_{cape}$-∗-$^{2'}C_{cape}$	2.6881	0.0031	70.2	11.44	69.4	12.4	*p*-CS/vdW
$^{18}H_{cape}$-∗-$^{3'}C_{cape}$	2.9857	0.0016	73.0	31.43	73.2	181.9	*p*-CS/vdW
8-7:**7** (LC-ωPBE/6-311+G(2d,p): ν_1 = 2.1 cm^{-1}; ν_5 = 15.8 cm^{-1}; ν_6 = 28.8 cm^{-1}; ν_8 = 48.2 cm^{-1})[e,f]							
$^{20}C_{cape}$-∗-$^{18'}H_{cape}$	3.2357	0.0015	63.8	65.63	67.4	40.4	*p*-CS/vdW
$^{20}H_{cape}$-∗-$^{20'}H_{cape}$	3.0148	0.0014	63.6	96.42	66.9	90.7	*p*-CS/vdW
$^{20}H_{cape}$-∗-$^{2'}C_{cape}$	3.0656	0.0014	67.2	52.66	70.0	10.9	*p*-CS/vdW
$^{18}H_{cape}$-∗-$^{3'}C_{cape}$	3.6594	0.0005	62.9	73.99	73.9	394.0	*p*-CS/vdW

[a] See footnotes of Table 8-1 for the QTAIM-DFA parameters and C_{ii}. [b] The motions of the internal vibrations for ν_1 are shown in Figure 8-8. [c] BPs and BCPs were not detected for $^{1}H_{bay}$-∗-$^{6}C_{bay}$ and $^{2}C_{bay}$-∗-$^{7}C_{bay}$. [d] r($^{1}H_{bay}$-∗-$^{6}C_{bay}$) = 2.5609 Å and r($^{2}C_{bay}$-∗-$^{7}C_{bay}$) = 3.2265 Å. [e] BPs and BCPs were not detected for $^{20}H_{cape}$-∗-$^{18'}H_{cape}$. [f] r($^{20}H_{cape}$-∗-$^{18'}H_{cape}$) = 2.9473 Å.

In the case of **8-7**:**7**, the $r(^{20}H_{cape}\cdots{}^{18'}H_{cape})$, $r(^{20}H_{cape}\cdots{}^{20'}H_{bay})$, $r(^{20}H_{cape}\cdots{}^{2'}C_{cape})$, and $r(^{8}H_{cape}\cdots{}^{3'}C_{cape})$ distances were 2.543 Å, 2.716 Å, 2.677 Å, and 2.964 Å, respectively, when calculated with M06-2X/6-311+(3d,p), while the values were 2.564 Å, 2.729 Å, 2.688 Å, and 2.986 Å, respectively, when calculated with M06-2X/6-311+(2d,p). The differences are 0.011–0.022 Å, which are less than approximately 0.02 Å. The results show that the optimized structures of **8-7**:**7** are very similar with both M06-2X/6-311+(3d,p) and M06-2X/6-311+(2d,p). On the other hand, the distances are optimized to be 2.947 Å, 3.015 Å, 3.066 Å, and 3.659 Å with LC-ωPBE/6-311+(2d,p). The differences with the corresponding values of M06-2X/6-311+(2d,p) are 0.286–0.674 Å. Namely, the structure of **8-7**:**7** optimized with LC-ωPBE/6-311+(2d,p) appears to be very different from that optimized with M06-2X/6-311+(2d,p), similar to the case of **8-7**.

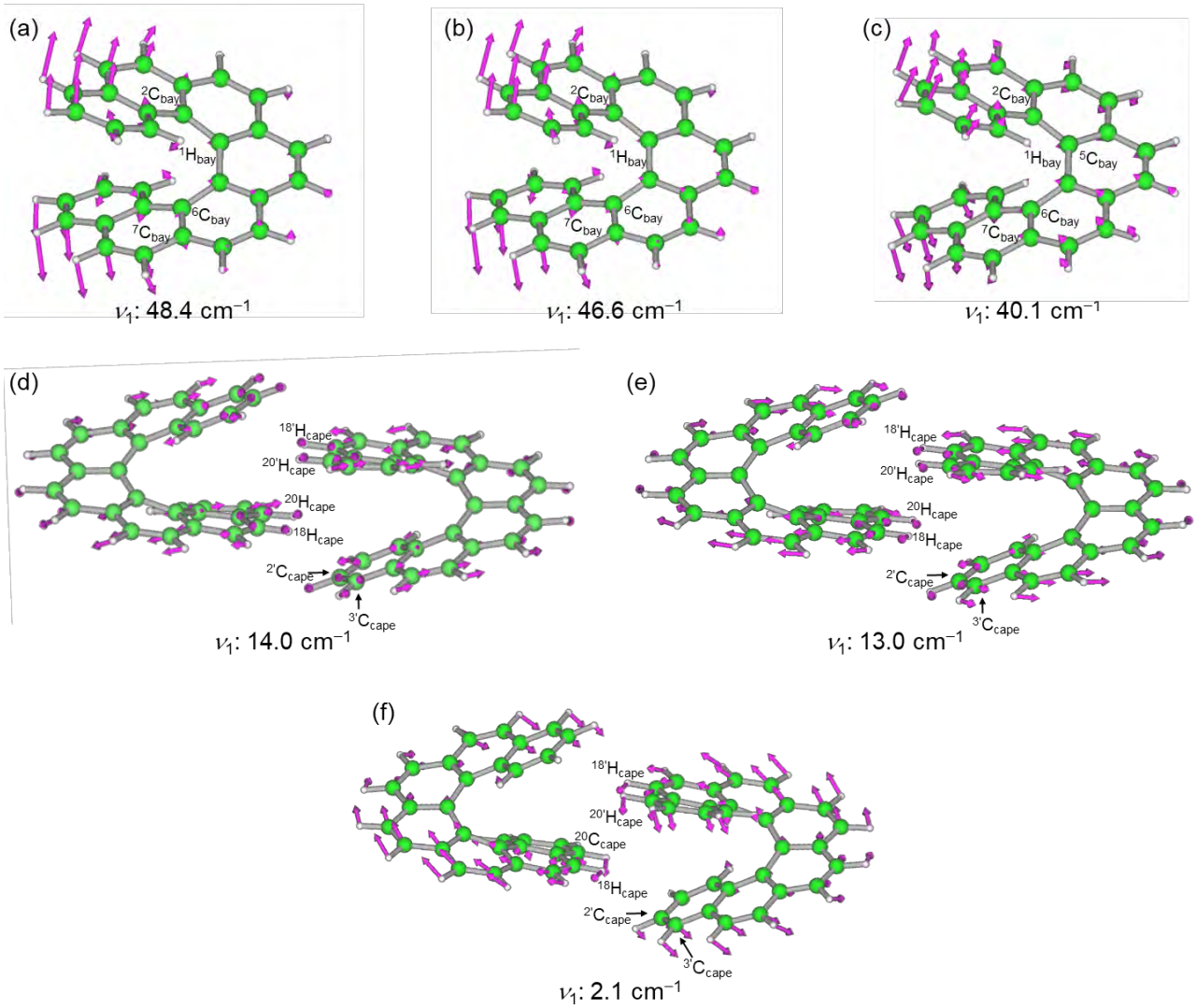

Figure 8-8. The internal vibrational motions of ν_1 for **8-7** (C_2) and **8-7**:**7** (C_i). For **8-7** (C_2) calculated with M06-2X/6-311+G(3d,p) (a), for **8-7** (C_2) calculated with M06-2X/6-311+G(2d,p) (b), for **8-7** (C_2) calculated with LC-ωPBE/6-311+G(2d,p) (c), for **8-7**:**7** (C_i) calculated with M06-2X/6-311+G(3d,p) (d), for **8-7**:**7** (C_i) calculated with M06-2X/6-311+G(2d,p) (e), for **8-7**:**7** (C_i) calculated with LC-ωPBE/6-311+G(2d,p) (f).

The $^{20}C_{cape}$-*-$^{18'}H_{cape}$ distance was optimized to be 3.236 Å, which is longer than $r(^{20}H_{cape}\cdots{}^{18'}H_{cape})$ (2.947 Å) by 0.288 Å with LC-ωPBE/6-311+(2d,p). However, a BP was detected for $^{20}C_{cape}$-*-$^{18'}H_{cape}$ but not for $^{20}H_{cape}$-*-$^{18'}H_{cape}$. The difference in the atomic size between C and H, such as the van der Waals radii, may be responsible for the predicted results, in this case. The $^{20}C_{cape}$-*-$^{18'}H_{cape}$, $^{20}H_{cape}$-*-$^{20'}H_{bay}$, $^{20}H_{cape}$-*-$^{2'}C_{cape}$, and $^{8}H_{cape}$-*-$^{3'}C_{cape}$ distances at **7**:**7**, optimized with LC-ωPBE/6-311+(2d,p), were much longer than the corresponding distances, optimized with M06-2X/6-311+(2d,p). BPs were detected for $^{20}H_{cape}$-*-$^{18'}H_{cape}$, $^{20}H_{cape}$-*-$^{20'}H_{bay}$, $^{20}H_{cape}$-*-$^{2'}C_{cape}$, and $^{18}H_{cape}$-*-$^{3'}C_{cape}$ when calculated with M06-2X/6-311+(2d,p), while they were detected for $^{20}C_{cape}$-*-$^{18'}H_{cape}$, $^{20}H_{cape}$-*-$^{20'}H_{bay}$, $^{20}H_{cape}$-*-$^{2'}C_{cape}$, and $^{8}H_{cape}$-*-$^{3'}C_{cape}$ when calculated with LC-ωPBE/6-311+(2d,p). The differences in the optimized distances appear to be the main factor for the appearance/disappearance of the BPs, similar to the case of **8**-**7**.

Table 8-3 contains the ν_1 values for **8**-**7** and **8**-**7**:**7**, calculated with M06-2X/6-311+(3d,p), M06-2X/6-311+(2d,p), and LC-ωPBE/6-311+(2d,p). Table 8-3 also contains some vibrations closely related to the interactions in question (corresponding to the perturbed structures) at **8**-**7**:**7**, where most candidates were found to be less than ν_n of ν_{20}. The ν_1 values for **8**-**7** were 48.4 cm^{-1}, 46.6 cm^{-1}, and 40.2 cm^{-1} when calculated with the three methods, respectively. The ν_1 motion of **8**-**7** appears to be very similar when calculated with the three methods. For **8**-**7**:**7**, the frequencies of ν_1 calculated with M06-2X/6-311+G(3d,p) and M06-2X/6-311+G(2d,p) were 14.0 cm^{-1} and 13.1 cm^{-1}, respectively, while the value calculated with LC-ωPBE was 2.1 cm^{-1}. Very large differences are predicted for ν_1 at **8**-**7**:**7** when calculated with M06-2X and LC-ωPBE. The ν_1 value with the motion should correspond to the strength of the interactions in the direction of the perturbed structures.

The (θ, θ_p) values of **8**-**7**:**7** are (67.9–73.0º, 69.4−75.2º) and (62.9−67.2º, 67.4−73.9º) with M06-2X/6-311+(2d,p) and LC-ωPBE/6-311+(2d,p), respectively. The differences seem large relative to the case of **8**-**7**, with (θ, θ_p) values of (70.4º, 81.6º) and (70.5º, 82.2º) when calculated with M06-2X/6-311+(2d,p) and LC-ωPBE/6-311+(2d,p), respectively, although **8**-**7** ($^{1}H_{bay}$-*-$^{6}C_{bay}$) was detected with M06-2X/6-311+(2d,p) and **8**-**7** ($^{1}H_{bay}$-*-$^{5}C_{bay}$) was detected with LC-ωPBE/6-311+(2d,p). The (optimized) structures of **8**-**7**:**7** would be affected more easily by surroundings containing the calculation methods than the case of **8**-**7**. The basis set and level dependence of the interactions in **8**-**7** and **8**-**7**:**7** can help to better understand the interactions in helicenes.

The unit of C_{ii} (Å $mdyn^{-1}$) is the inverse of that of the force constant, which corresponds to the frequency. Therefore, the strengths of the interactions should be roughly inversely proportional to the C_{ii} values. As shown in Table 8-3, the C_{ii} values for the π···π interactions of **8**-**7** are 3.1–5.5 Å $mdyn^{-1}$ for H_{bay}-*-C_{bay} and C_{bay}-*-C_{bay} with the three methods. The values for the π···π interactions of **8**-**7**:**7** are 10.0–27.9, 11.4–31.4, and 52.7–96.4 Å $mdyn^{-1}$ for H_{cape}-*-H_{cape} and H_{cape}-*-C_{cape} when calculated with M06-2X/6-311+(3d,p), M06-2X/6-311+(2d,p), and LC-ωPBE/6-311+(2d,p), respectively. This consideration explains the above results.

Summary

It is challenging to clarify the natures of π···π interactions in helicenes since the interactions are factors that control the fine details of structures and are expected to give rise to specific functionalities for the species. The repulsive interactions between the benzene rings in helicenes must be very strong; therefore, the π···π interactions would be considered strong. The π···π interactions in the helicenes are described by the H-∗-H, C-∗-H, and C-∗-C forms with BPs and BCPs. The π···π interactions in helicenes **8-1**–**8-12**, as well as in dimers **8-6**:**6** and **8-7**:**7,** were analyzed with QTAIM-DFA after clarifying the structural features and the energy profile.

The interactions were analyzed by dividing the C atoms of **8-3**–**8-12** into C_{bay} and C_{cape} and the H atoms into H_{bay} and H_{cape}. While both C_{bay} and C_{cape} atoms of **8-3**–**8-12** take part in the interactions, only H_{bay} atoms participate as BPs. The θ and θ_p values for H-∗-H, C-∗-H, and C-∗-C of **8-3**–**8-12** are all less than 90º, except for **8-10** ($^2C_{bay}$-∗-$^7C_{bay}$), where (θ, θ_p) = (70.5º, 94.2º). Therefore, the H-∗-H, C-∗-H, and C-∗-C interactions of **8-3**–**8-12** are all predicted to have a *p*-CS/vdW nature, except for **8-10** ($^2C_{bay}$-∗-$^7C_{bay}$), which is predicted to have a *p*-CS/*t*-HB_{nc} nature. While the (θ, θ_p) values of C_{bay}-∗-C_{bay} in **8-7**–**8-12** are (71.5–72.9º, 79.5–87.8º), the values are (70.0–70.7º, 66.3–69.7º) for C_{cape}-∗-C_{cape}. The θ values for C_{cape}-∗-C_{cape} are slightly smaller than those of C_{bay}-∗-C_{bay} (by 0.5–2.2º), but the θ_p values for C_{cape}-∗-C_{cape} are much smaller than those of C_{bay}-∗-C_{bay} (by 13.2–24.5º). In this case, $\theta < \theta_p$ for C_{bay}-∗-C_{bay}, whereas $\theta > \theta_p$ for C_{cape}-∗-C_{cape}. Interactions with $\theta < \theta_p$ are usually observed, whereas interactions with $\theta > \theta_p$ are rare.

The H-∗-H, C-∗-H, and C-∗-C interactions of dimers **8-6**:**6** and **8-7**:**7** were similarly analyzed. The interactions were predicted to have a *p*-CS/vdW nature, although **8-6**:**6** ($^1H_{bay}$-∗-$^{17'}H_{cape}$) has a nature close to *p*-CS/*t*-HB_{nc}, since (θ, θ_p) = (72.6º, 88.1º). The interactions at **8-3**–**8-12** and **8-6**:**6** and **8-7**:**7** were predicted to be much weaker than expected. The very low energy of v_1 of **8-7**:**7** supports the very weak nature predicted for interactions and the easy dependence of the levels on the nature of the interactions. The strength of the interactions can also be estimated by the C_{ii}^{-1} values. Detecting the interactions and predicting the nature of helicenes will provide a solid basis for investigating and applying the interactions in helicenes.

Appendix

Table 8-A1. The observed and calculated C···C length (r_{obsd} and r_{calcd}, respectively), which are located in the bay area for **8-3**–**8-5** and the bay and cape area between adjacent aromatic rings for **8-6**–**8-12**, together with the differences, Δr_{calcd} (= $r_{calcd:XY} - r_{obsd:XY}$) in each C···C for **8-3**–**8-12**, elucidated with various methods.

Compds	r_{obsd}/Å [a]	r_{calcd}/Å [b]	Δr_{calcd}/Å [c]	r_{calcd}/Å [b]	Δr_{calcd}/Å [c]	r_{calcd}/Å [b]	Δr_{calcd}/Å [c]
C···C		M06-2X/6-311+G(3d,p)		M06-2X/6-311+G(2d,p)		LC-ωPBE/6-311+G(2d,p)	
8-3							
$^{1}C_{bay}\cdots{}^{4}C_{bay}$	2.9574	2.9860	0.0286	2.9842	0.0268	2.9763	0.0189
8-4							
$^{1}C_{bay}\cdots{}^{5}C_{bay}$	3.0387	3.0252	–0.0134	3.0237	–0.0149	3.0175	–0.0212
8-5							
$^{1}C_{bay}\cdots{}^{6}C_{bay}$	2.9216	2.9191	–0.0025	2.9212	–0.0004	2.9189	–0.0027
$^{1}C_{cape}\cdots{}^{16}C_{cape}$	4.5765	4.5735	–0.0030	4.5823	0.0058	4.5798	0.0034
8-6							
$^{1}C_{bay}\cdots{}^{7}C_{bay}$	3.2496	3.0813	–0.1683	3.0862	–0.1634	3.1262	–0.1234
$^{1}C_{cape}\cdots{}^{19}C_{cape}$	4.6285	4.1555	–0.4729	4.1751	–0.4534	4.3244	–0.3041
8-7							
$^{1}C_{bay}\cdots{}^{7}C_{bay}$	3.1120	3.1234	0.0114	3.1276	0.0155	3.2265	0.1145
$^{1}C_{cape}\cdots{}^{19}C_{cape}$	3.8256	3.7521	–0.0736	3.7682	–0.0574	4.0750	0.2493
$^{2}C_{cape}\cdots{}^{20}C_{cape}$	4.4119	4.2392	–0.1727	4.2704	–0.1415	4.7973	0.3854
8-8							
$^{1}C_{bay}\cdots{}^{7}C_{bay}$	*d*	3.1381		3.1402		3.1914	
$^{2}C_{bay}\cdots{}^{8}C_{bay}$	*d*	3.2329		3.2363		3.3357	
$^{1}C_{cape}\cdots{}^{19}C_{cape}$	*d*	3.6197		3.6271		3.8147	
$^{2}C_{cape}\cdots{}^{20}C_{cape}$	*d*	3.9039		3.9183		4.2797	
$^{3}C_{cape}\cdots{}^{21}C_{cape}$	*d*	3.8336		3.8495		4.2516	
$^{4}C_{cape}\cdots{}^{22}C_{cape}$	*d*	3.5915		3.6019		3.8866	
8-9							
$^{1}C_{bay}\cdots{}^{7}C_{bay}$	3.1722	3.1704	–0.0018	3.1721	–0.0001	3.2160	0.0438
$^{2}C_{bay}\cdots{}^{8}C_{bay}$	3.2816	3.2510	–0.0306	3.2546	–0.0270	3.3437	0.0620
$^{1}C_{cape}\cdots{}^{19}C_{cape}$	3.7598	3.6490	–0.1109	3.6551	–0.1047	3.8212	0.0614
$^{2}C_{cape}\cdots{}^{20}C_{cape}$	4.1287	3.8984	–0.2303	3.9105	–0.2182	4.2264	0.0977
$^{3}C_{cape}\cdots{}^{21}C_{cape}$	3.9874	3.7392	–0.2482	3.7529	–0.2345	4.0909	0.1034
$^{4}C_{cape}\cdots{}^{22}C_{cape}$	3.6385	3.4874	–0.1511	3.4973	–0.1413	3.7322	0.0937
$^{5}C_{cape}\cdots{}^{23}C_{cape}$	3.7783	3.5574	–0.2209	3.5739	–0.2044	3.9030	0.1247
8-10							
$^{1}C_{bay}\cdots{}^{7}C_{bay}$	3.1762	3.1650	–0.0112	3.1682	–0.0080	3.2230	0.0468
$^{2}C_{bay}\cdots{}^{8}C_{bay}$	3.3432	3.2954	–0.0478	3.2995	–0.0436	3.3860	0.0428
$^{3}C_{bay}\cdots{}^{9}C_{bay}$	3.3756	3.2894	–0.0862	3.2929	–0.0827	3.3659	–0.0097
$^{1}C_{cape}\cdots{}^{19}C_{cape}$	3.6952	3.6328	–0.0624	3.6407	–0.0545	3.8208	0.1256
$^{2}C_{cape}\cdots{}^{20}C_{cape}$	4.0115	3.9069	–0.1046	3.9210	–0.0905	4.2513	0.2398
$^{3}C_{cape}\cdots{}^{21}C_{cape}$	3.9003	3.7707	–0.1295	3.7857	–0.1146	4.1196	0.2193
$^{4}C_{cape}\cdots{}^{22}C_{cape}$	3.6520	3.5250	–0.1269	3.5349	–0.1170	3.7505	0.0985
$^{5}C_{cape}\cdots{}^{23}C_{cape}$	3.8432	3.5855	–0.2578	3.5985	–0.2447	3.8632	0.0200
$^{6}C_{cape}\cdots{}^{24}C_{cape}$	3.8282	3.5254	–0.3028	3.5362	–0.2919	3.7621	–0.0660
$^{7}C_{cape}\cdots{}^{25}C_{cape}$	3.6419	3.4321	–0.2098	3.4387	–0.2032	3.5921	–0.0498

[a] Observed values for C···C length. [b] Calculated values for C···C length. [c] $\Delta r_{calcd} = r_{obsd} - r_{calcd}$. [d] No X-ray crystal structure. [e] The mean absolute error, defined by $[1/n\sum_i^n |r_{obsd} - r_{calcd}|]$.

(Table 8-A1 continued.)

Compds C···C	r_{obsd}/Å [a]	r_{calcd}/Å [b] M06-2X/6-311+G(3d,p)	Δr_{calcd}/Å [c]	r_{calcd}/Å [b] M06-2X/6-311+G(2d,p)	Δr_{calcd}/Å [c]	r_{calcd}/Å [b] LC-ωPBE/6-311+G(2d,p)	Δr_{calcd}/Å [c]
8-11							
$^{1}C_{bay}\cdots{}^{7}C_{bay}$	3.0854	3.1484	0.0629	3.1517	0.0663	3.2017	0.1162
$^{2}C_{bay}\cdots{}^{8}C_{bay}$	3.3389	3.2965	–0.0424	3.3015	–0.0374	3.3913	0.0525
$^{3}C_{bay}\cdots{}^{9}C_{bay}$	3.4422	3.3277	–0.1144	3.3312	–0.1109	3.4041	–0.0380
$^{1}C_{cape}\cdots{}^{19}C_{cape}$	3.5310	3.6144	0.0834	3.6229	0.0919	3.7677	0.2367
$^{2}C_{cape}\cdots{}^{20}C_{cape}$	3.9002	3.8963	–0.0039	3.9109	0.0107	4.1924	0.2921
$^{3}C_{cape}\cdots{}^{21}C_{cape}$	3.8595	3.7663	–0.0932	3.7828	–0.0767	4.0909	0.2315
$^{4}C_{cape}\cdots{}^{22}C_{cape}$	3.6578	3.5279	–0.1300	3.5395	–0.1183	3.7550	0.0972
$^{5}C_{cape}\cdots{}^{23}C_{cape}$	3.9128	3.6038	–0.3089	3.6194	–0.2934	3.8931	–0.0197
$^{6}C_{cape}\cdots{}^{24}C_{cape}$	3.9267	3.5461	–0.3806	3.5580	–0.3686	3.7954	–0.1312
$^{7}C_{cape}\cdots{}^{25}C_{cape}$	3.7478	3.4523	–0.2955	3.4583	–0.2895	3.6140	–0.1339
$^{8}C_{cape}\cdots{}^{26}C_{cape}$	3.9754	3.5190	–0.4564	3.5258	–0.4496	3.7333	–0.2420
8-12							
$^{1}C_{bay}\cdots{}^{7}C_{bay}$	*d*	3.1408		3.1436		3.2004	
$^{2}C_{bay}\cdots{}^{8}C_{bay}$	*d*	3.2687		3.2722		3.3704	
$^{3}C_{bay}\cdots{}^{9}C_{bay}$	*d*	3.3218		3.3256		3.4091	
$^{4}C_{bay}\cdots{}^{10}C_{bay}$	*d*	3.3609		3.3646		3.4395	
$^{1}C_{cape}\cdots{}^{19}C_{cape}$	*d*	3.6102		3.6173		3.7649	
$^{2}C_{cape}\cdots{}^{20}C_{cape}$	*d*	3.8752		3.8865		4.1672	
$^{3}C_{cape}\cdots{}^{21}C_{cape}$	*d*	3.7273		3.7383		4.0410	
$^{4}C_{cape}\cdots{}^{22}C_{cape}$	*d*	3.4895		3.4967		3.7129	
$^{5}C_{cape}\cdots{}^{23}C_{cape}$	*d*	3.5687		3.5783		3.8538	
$^{6}C_{cape}\cdots{}^{24}C_{cape}$	*d*	3.5248		3.5337		3.7794	
$^{7}C_{cape}\cdots{}^{25}C_{cape}$	*d*	3.4478		3.4539		3.6199	
$^{8}C_{cape}\cdots{}^{26}C_{cape}$	*d*	3.5330		3.5414		3.7592	
$^{9}C_{cape}\cdots{}^{27}C_{cape}$	*d*	3.5397		3.5481		3.7592	
$^{10}C_{cape}\cdots{}^{28}C_{cape}$	*d*	3.4744		3.4806		3.6294	
r_{MAE}/Å [e]			0.1419		0.1344		0.1167

[a] Observed values for C···C length. [b] Calculated values for C···C length. [c] $\Delta r_{calcd} = r_{obsd} - r_{calcd}$. [d] No X-ray crystal structure. [e] The mean absolute error, defined by $[1/n\sum_i^n |r_{obsd} - r_{calcd}|]$.

Table 8-A2. The total energy E_{ES} and zero-point energy E_{ZP} values for **8-*n*** and **8-n_p**, where n = 1 to 12, along with the ΔE_{ES} and ΔE_{ZP}(**8-*n***; **8-n_p**) values, evaluated with M06-2X/6-311+G(3d,p).

[*n*]	E_{ES}(**8-*n***)[a] (au)	E_{ZP}(**8-*n***)[b] (au)	E_{ES}(**8-n_p**)[c] (au)	E_{ZP}(**8-n_p**)[d] (au)
1	–232.204406	–232.103648	–232.204406	–232.103648
2	–385.826436	–385.678728	–385.826436	–385.678728
3	–539.451928	–539.257087	–539.451928	–539.257087
4	–693.065985	–692.823727	–693.074499	–692.832694
5	–846.682614	–846.393864	–846.697891	–846.409144
6	–1000.301653	–999.966434	–1000.321148	–999.985238
7	–1153.921671	–1153.538937	–1153.944463	–1153.561852
8	–1307.543065	–1307.113731	–1307.567690	–1307.137460
9	–1461.164313	–1460.688171	–1461.190980	–1460.714495
10	–1614.784600	–1614.261465	–1614.814222	–1614.290352
11	–1768.405064	–1767.835590	–1768.437538	–1767.867216
12	–1922.025696	–1921.408804	–1922.060826	–1921.443585

[a] ΔE_{ES} (**8-*n***) = E_{ES} (**8-*n***) – E_{ES} (**8-(*n* – 1)**). [b] ΔE_{ZP} (**8-*n***) = E_{ZP} (**8-*n***) – E_{ZP} (**8-(*n* – 1)**). [c] ΔE_{ES} (**8-n_p**) = E_{ES} (**8-n_p**) – E_{ES} (**8-(n_p – 1)**). [d] ΔE_{ZP} (**8-n_p**) = E_{ZP} (**8-n_p**) – E_{ZP} (**8-(n_p – 1)**).

(Table 8-A2 continued.)

[*n*]	ΔE_{ES}(**8-*n***)[a] (au)	ΔE_{ZP}(**8-*n***)[b] (au)	ΔE_{ES}(**8-n_p**)[c] (au)	ΔE_{ZP}(**8-n_p**)[d] (au)
1				
2	–153.622030	–153.575080	–153.622030	–153.575080
3	–153.625492	–153.578359	–153.625492	–153.578359
4	–153.614057	–153.566640	–153.622571	–153.575607
5	–153.616629	–153.570137	–153.623392	–153.576450
6	–153.619039	–153.572570	–153.623257	–153.576094
7	–153.620018	–153.572503	–153.623315	–153.576614
8	–153.621394	–153.574794	–153.623227	–153.575608
9	–153.621248	–153.574440	–153.623290	–153.577035
10	–153.620287	–153.573294	–153.623242	–153.575857
11	–153.620464	–153.574125	–153.623316	–153.576864
12	–153.620632	–153.573214	–153.623288	–153.576369

[a] ΔE_{ES} (**8-*n***) = E_{ES} (**8-*n***) – E_{ES} (**8-(*n* – 1)**). [b] ΔE_{ZP} (**8-*n***) = E_{ZP} (**8-*n***) – E_{ZP} (**8-(*n* – 1)**). [c] ΔE_{ES} (**8-n_p**) = E_{ES} (**8-n_p**) – E_{ES} (**8-(n_p – 1)**). [d] ΔE_{ZP} (**8-n_p**) = E_{ZP} (**8-n_p**) – E_{ZP} (**8-(n_p – 1)**).

Table 8-A3. The HOMA indices for [*n*]acenes, [*n*]phenacenes, and [*n*]helicenes, evaluated with M06-2X/6-311+G(3d,p).[a,b]

[*n*]	Ring[c]	Acene[d]	Acene[e]	Phenacene	Helicene
1	A	0.9989			
2	A	0.8150			
3	A	0.6325		0.9072	
3	B	0.8178		0.3181	
4	A	0.5106		0.8801	0.8646
4	B	0.7263		0.6393	0.5836
5	A	0.4342		0.8923	0.8709
5	B	0.6408		0.5742	0.5402
5	C	0.7019		0.7284	0.6924
6	A	0.3862		0.8898	0.8789
6	B	0.5787		0.5910	0.5566
6	C	0.6535		0.6954	0.6587
7	A	0.3557	0.4776	0.8900	0.8807
7	B	0.5360	0.6395	0.5861	0.5807
7	C	0.6111	0.6284	0.7099	0.6784
7	D	0.6296	0.6003	0.6594	0.6311
8	A	0.3362	0.5751	0.8897	0.8740
8	B	0.5073	0.7165	0.5881	0.5872
8	C	0.5791	0.6362	0.7066	0.6948
8	D	0.6024	0.5528	0.6760	0.6495
9	A	0.3236	0.5843	0.8898	0.8783
9	B	0.4881	0.7305	0.5869	0.5664
9	C	0.5560	0.6461	0.7070	0.6953
9	D	0.5793	0.5493	0.6707	0.6689
9	E	0.5853	0.5223	0.6909	0.6655
10	A	0.3151	0.5754	0.8764	0.8745
10	B	0.4750	0.7295	0.5875	0.5944
10	C	0.5398	0.6548	0.7076	0.6777
10	D	0.5615	0.5562	0.6730	0.6666
10	E	0.5686	0.5224	0.6874	0.6824
11	A	0.3094	0.5644	0.8898	0.8775
11	B	0.4663	0.7239	0.5870	0.5635
11	C	0.5287	0.6599	0.7068	0.6804
11	D	0.5487	0.5648	0.6714	0.6541
11	E	0.5551	0.5305	0.6879	0.6842
11	F	0.5565	0.5282	0.6819	0.7037
12	A	0.3055	0.5567	0.8898	0.8763
12	B	0.4603	0.7186	0.5872	0.5638
12	C	0.5210	0.6613	0.7066	0.6729
12	D	0.5394	0.5713	0.6718	0.6546
12	E	0.5449	0.5396	0.6872	0.6691
12	F	0.5460	0.5414	0.6834	0.6997

[a] The HOMA index is defined by $[1 - \alpha/m\sum_i^n (R_{opt} - R_i)^2]$, where m, α, R_{opt}, and R_i are the number of bonds considered, empirical constant for CC bonds α = 257.7, 1.388 Å for CC bonds, and running bond length, respectively. [b] The one of HOMA indices collected, due to the D_{2h}, C_{2v} or C_{2h}, C_2 symmetry for acene, phenacene, and helicene, respectively. [c] Defined alphabetically, starting with the terminal ring. [d] At the closed-shell singlet state. [e] At the open-shell singlet state.

Table 8-A4. The observed and calculated X-∗-Y lengths ($R_{obsd:XY}$ and $R_{calcd:XY}$, respectively; X, Y = C and H) and the length of the bond paths ($r_{BP:XY}$) and the corresponding straight-line distances ($R_{SL:XY}$), together with the differences, $\Delta R_{calcd:XY}$ (= $R_{calcd:XY} - R_{obsd:XY}$) in each X-∗-Y for **8-3**–**8-12**, **8-6**:**6** and **8-7**:**7**, evaluated with M06-2X/6-311+G(3d,p), where $R_{SL:XY} = R_{calcd:XY}$, together with **8-8**:**8** and **8-10**:**10**, calculated with M06-2X/6-311+G(2d,p).

Compds X-∗-Y	$R_{calcd:XY}$ (= $R_{SL:XY}$ [a]) (Å)	$R_{obsd:XY}$ [b] (Å)	$\Delta R_{calcd:XY}$ [c] (Å)	$r_{BP:XY}$ [d] (Å)	$\Delta r_{BP:XY}$ [e] (Å)
8-3					
$^{1}H_{bay}$-∗-$^{4}H_{bay}$	2.0020	(2.0349)	(–0.0329)	2.1901	0.1882
8-4					
$^{1}H_{bay}$-∗-$^{5}H_{bay}$	1.9931	(1.8963)	(0.0969)	2.2127	0.2196
8-5					
$^{1}H_{bay}$-∗-$^{6}H_{bay}$	2.5512	(2.8170)	(–0.2658)	2.8426	0.2914
8-6					
$^{1}H_{bay}$-∗-$^{5}C_{bay}$	2.4796	(2.5059)	(–0.0263)	2.7315	0.2519
8-7					
$^{1}H_{bay}$-∗-$^{6}C_{bay}$	2.5902	(2.5356)	(0.0547)	2.9988	0.4086
$^{2}C_{bay}$-∗-$^{7}C_{bay}$	2.9751	3.0374	–0.0623	3.0126	0.0374
8-8					
$^{1}H_{bay}$-∗-$^{6}C_{bay}$	2.5193	*f*		3.0250	0.5057
$^{2}C_{bay}$-∗-$^{7}C_{bay}$	2.9947	*f*		3.0239	0.0292
8-9					
$^{1}H_{bay}$-∗-$^{5}C_{bay}$	2.4930	(2.4976)	(–0.0046)	3.2466	0.7535
$^{2}C_{bay}$-∗-$^{7}C_{bay}$	2.9977	3.0504	–0.0527	3.0258	0.0281
$^{3}C_{bay}$-∗-$^{8}C_{bay}$	2.9422	2.9820	–0.0398	2.9642	0.0220
$^{4}C_{cape}$-∗-$^{22}C_{cape}$	3.4874	3.6385	–0.1511	3.5596	0.0723
$^{6}C_{cape}$-∗-$^{23}C_{cape}$	3.4400	3.6886	–0.2487	3.5176	0.0776
8-10					
$^{1}H_{bay}$-∗-$^{6}C_{bay}$	2.5813	(2.5782)	(0.0031)	2.9305	0.3493
$^{2}C_{bay}$-∗-$^{7}C_{bay}$	3.0042	3.0427	–0.0385	3.1844	0.1802
$^{3}C_{bay}$-∗-$^{8}C_{bay}$	2.9889	3.0443	–0.0553	3.0272	0.0383
$^{6}C_{cape}$-∗-$^{23}C_{cape}$	3.4723	3.6982	–0.2260	3.6152	0.1430
$^{7}C_{cape}$-∗-$^{25}C_{cape}$	3.4321	3.6419	–0.2098	3.5442	0.1121
8-11					
$^{1}H_{bay}$-∗-$^{6}C_{bay}$	2.5795	(2.5038)	(0.0758)	2.9102	0.3306
$^{2}C_{bay}$-∗-$^{7}C_{bay}$	2.9877	3.0425	–0.0548	3.0686	0.0809
$^{3}C_{bay}$-∗-$^{8}C_{bay}$	2.9888	3.1037	–0.1149	3.0296	0.0408
$^{4}C_{bay}$-∗-$^{9}C_{bay}$	3.0149	3.1655	–0.1506	3.0712	0.0563
$^{4}C_{cape}$-∗-$^{22}C_{cape}$	3.5279	3.6578	–0.1300	3.8606	0.3328
$^{6}C_{cape}$-∗-$^{23}C_{cape}$	3.4710	3.9133	–0.4423	3.6022	0.1312
$^{7}C_{cape}$-∗-$^{25}C_{cape}$	3.4523	3.7059	–0.2536	3.6740	0.2217
$^{9}C_{cape}$-∗-$^{26}C_{cape}$	3.4429	4.0056	–0.5627	3.5337	0.0908
8-12					
$^{1}H_{bay}$-∗-$^{6}C_{bay}$	2.5753	*f*		2.8893	0.3140
$^{2}C_{bay}$-∗-$^{7}C_{bay}$	2.9947	*f*		3.0789	0.0842
$^{3}C_{bay}$-∗-$^{8}C_{bay}$	2.9736	*f*		3.0015	0.0279
$^{4}C_{bay}$-∗-$^{9}C_{bay}$	3.0269	*f*		3.1074	0.0805
$^{4}C_{cape}$-∗-$^{22}C_{cape}$	3.4895	*f*		3.6126	0.1232
$^{6}C_{cape}$-∗-$^{23}C_{cape}$	3.4535	*f*		3.5720	0.1185
$^{7}C_{cape}$-∗-$^{25}C_{cape}$	3.4478	*f*		3.6954	0.2476
$^{9}C_{cape}$-∗-$^{26}C_{cape}$	3.4756	*f*		3.5788	0.1032
$^{10}C_{cape}$-∗-$^{28}C_{cape}$	3.4744	*f*		3.5873	0.1129

[a] Straight-line distances. [b] Average values were calculated, since all X-ray crystal structures for **8-3**–**8-7**, **8-9**–**8-11** are C_1 symmetry. [c] $\Delta R_{calcd:XY} = R_{calcd:XY} - R_{obsd:XY}$. [d] The length of bond paths. [e] $\Delta r_{BP} = r_{BP} - R_{SL}$. [f] No X-ray crystal structure.

(Table 8-A4 continued.)

Compd X-∗-Y	$R_{calcd:XY}$ (= $R_{SL:XY}$ [a]) (Å)	$R_{obsd:XY}$ [b] (Å)	$\Delta R_{calcd:XY}$ [c] (Å)	$r_{BP:XY}$ [d] (Å)	$\Delta r_{BP:XY}$ [e] (Å)
8-6:**6**					
$^{1}H_{bay}$-∗-$^{17'}H_{cape}$	2.4840			2.7464	0.2624
$^{1}H_{cape}$-∗-$^{16'}H_{cape}$	2.5169			2.7517	0.2347
$^{1}H_{cape}$-∗-$^{17'}H_{cape}$	2.3329			2.4122	0.0793
$^{15}C_{cape}$-∗-$^{17'}C_{cape}$	3.3236			3.3712	0.0476
$^{16}C_{cape}$-∗-$^{17'}C_{cape}$	3.3531			3.4838	0.1307
8-7:**7**					
$^{20}H_{bay}$-∗-$^{18'}H_{cape}$	2.5423			2.9823	0.4400
$^{20}H_{cape}$-∗-$^{20'}H_{cape}$	2.7155			3.1351	0.4196
$^{18}H_{cape}$-∗-$^{3'}C_{cape}$	2.6769			2.7251	0.2726
$^{20}C_{cape}$-∗-$^{2'}C_{cape}$	2.9640			3.2255	0.2615
8-8:**8**					
$^{21}H_{cape}$-∗-$^{21'}H_{cape}$	2.3000			2.5725	0.2726
$^{3}C_{cape}$-∗-$^{23'}H_{cape}$	2.8407			3.0958	0.2550
$^{5}C_{cape}$-∗-$^{21'}H_{cape}$	2.7037			3.0824	0.3787
$^{21}C_{cape}$-∗-$^{23'}H_{cape}$	3.1228			3.4954	0.3726
8-10:**10**					
$^{21}H_{cape}$-∗-$^{21'}H_{cape}$	2.2151			2.3799	0.1648
$^{3}C_{cape}$-∗-$^{23'}H_{cape}$	2.9636			3.2375	0.2739
$^{5}C_{cape}$-∗-$^{21'}H_{cape}$	2.6685			3.0243	0.3558
$^{21}C_{cape}$-∗-$^{23'}H_{cape}$	3.0891			3.1308	0.0417

[a] Straight-line distances. [b] Average values were calculated, since all X-ray crystal structures for **8-3**–**8-7**, **8-9**–**8-11** are C_1 symmetry. [c] $\Delta R_{calcd:XY} = R_{calcd:XY} - R_{obsd:XY}$. [d] The length of bond path. [e] $\Delta r_{BP} = r_{BP} - R_{SL}$. [f] No X-ray crystal data.

Table 8-A5. QTAIM functions and QTAIM-DFA parameters for the fused-benzene type helicenes of monomers (**8-3**–**8-12** (C_2)), together with the nature of each noncovalent interaction, elucidated with M06-2X/6-311+G(2d,p).[a]

Compds (X-∗-Y)	$\rho_b(\boldsymbol{r}_c)$ (au)	$c\nabla^2\rho_b(\boldsymbol{r}_c)$[b] (au)	$H_b(\boldsymbol{r}_c)$ (au)	$k_b(\boldsymbol{r}_c)$[c]	R[d] (au)	θ[e] (°)	C_{ii}[f] (unit[i])	θ_p[g] (°)	κ_p[h] (au^{-1})	Predicted Nature
8-3 ($^1H_{bay}$-∗-$^4H_{bay}$)	0.0129	0.0060	0.0022	–0.780	0.0064	70.2	3.25	73.8	15.4	*p*-CS/vdW
8-4 ($^1H_{bay}$-∗-$^5H_{bay}$)	0.0164	0.0078	0.0026	–0.796	0.0082	71.3	6.66	75.1	13.7	*p*-CS/vdW
8-5 ($^1H_{bay}$-∗-$^6C_{bay}$)	0.0129	0.0063	0.0022	–0.781	0.0066	70.2	9.88	81.3	15.3	*p*-CS/vdW
8-6 ($^1H_{bay}$-∗-$^5C_{bay}$)	0.0130	0.0060	0.0021	–0.786	0.0063	70.6	3.83	64.6	91.9	*p*-CS/vdW
8-7 ($^1H_{bay}$-∗-$^6C_{bay}$)	0.0134	0.0063	0.0022	–0.784	0.0067	70.4	5.49	81.6	39.9	*p*-CS/vdW
8-7 ($^2C_{bay}$-∗-$^7C_{bay}$)	0.0111	0.0051	0.0019	–0.777	0.0054	69.9	3.06	78.7	120.2	*p*-CS/vdW
8-8 ($^1H_{bay}$-∗-$^6C_{bay}$)	0.0130	0.0061	0.0022	–0.780	0.0065	70.2	5.77	80.2	35.2	*p*-CS/vdW
8-8 ($^2C_{bay}$-∗-$^7C_{bay}$)	0.0116	0.0052	0.0019	–0.777	0.0056	70.0	2.09	82.9	12.2	*p*-CS/vdW
8-9 ($^1H_{bay}$-∗-$^5C_{bay}$)	0.0133	0.0062	0.0022	–0.784	0.0066	70.4	3.43	81.3	91.4	*p*-CS/vdW
8-9 ($^2C_{bay}$-∗-$^7C_{bay}$)	0.0111	0.0050	0.0018	–0.777	0.0054	69.9	1.90	79.8	12.8	*p*-CS/vdW
8-9 ($^3C_{bay}$-∗-$^8C_{bay}$)	0.0120	0.0054	0.0019	–0.788	0.0057	70.7	2.09	82.9	165.1	*p*-CS/vdW
8-9 ($^4C_{cape}$-∗-$^{22}C_{cape}$)	0.0054	0.0020	0.0008	–0.761	0.0021	68.9	6.17	65.8	152.5	*p*-CS/vdW
8-9 ($^6C_{cape}$-∗-$^{23}C_{cape}$)	0.0059	0.0020	0.0007	–0.778	0.0021	70.0	11.60	68.6	5.9	*p*-CS/vdW
8-10 ^{1}(H_{bay}-∗-$^6C_{bay}$)	0.0136	0.0063	0.0022	–0.788	0.0067	70.7	5.94	82.0	50.1	*p*-CS/vdW
8-10 ($^3C_{bay}$-∗-$^8C_{bay}$)	0.0112	0.0050	0.0018	–0.776	0.0054	69.9	1.85	79.8	157.8	*p*-CS/vdW
8-10 ($^4C_{cape}$-∗-$^{22}C_{cape}$)[j]	0.0051	0.0018	0.0007	–0.763	0.0020	69.0	7.55	65.2	505.4	*p*-CS/vdW
8-10 ($^6C_{cape}$-∗-$^{23}C_{cape}$)	0.0059	0.0020	0.0007	–0.780	0.0021	70.2	9.85	68.2	22.2	*p*-CS/vdW
8-10 ($^7C_{cape}$-∗-$^{25}C_{cape}$)	0.0059	0.0022	0.0008	–0.757	0.0023	68.7	3.93	66.3	15.2	*p*-CS/vdW
8-11 ($^1H_{bay}$-∗-$^6C_{bay}$)	0.0135	0.0063	0.0022	–0.788	0.0067	70.7	5.50	81.8	48.2	*p*-CS/vdW
8-11 ($^2C_{bay}$-∗-$^7C_{bay}$)[k]	0.0114	0.0051	0.0019	–0.772	0.0054	69.7	1.89	84.5	682.9	*p*-CS/vdW
8-11 ($^3C_{bay}$-∗-$^8C_{bay}$)	0.0113	0.0050	0.0018	–0.775	0.0054	69.8	1.97	80.2	148.8	*p*-CS/vdW
8-11 ($^4C_{bay}$-∗-$^9C_{bay}$)	0.0109	0.0049	0.0018	–0.772	0.0053	69.6	1.72	77.4	137.1	*p*-CS/vdW
8-11 ($^4C_{cape}$-∗-$^{22}C_{cape}$)	0.0051	0.0018	0.0007	–0.759	0.0020	68.8	7.67	66.6	18.8	*p*-CS/vdW
8-11 ($^6C_{cape}$-∗-$^{23}C_{cape}$)	0.0058	0.0019	0.0007	–0.778	0.0021	70.0	11.51	68.1	14.3	*p*-CS/vdW
8-11 ($^7C_{cape}$-∗-$^{25}C_{cape}$)	0.0058	0.0021	0.0008	–0.759	0.0023	68.7	3.91	66.1	5.2	*p*-CS/vdW
8-11 ($^9C_{cape}$-∗-$^{26}C_{cape}$)	0.0062	0.0021	0.0008	–0.778	0.0022	70.0	6.14	68.6	42.0	*p*-CS/vdW
8-12 ($^1H_{bay}$-∗-$^6C_{bay}$)	0.0136	0.0063	0.0022	–0.787	0.0067	70.6	4.89	81.4	63.6	*p*-CS/vdW
8-12 ($^2C_{bay}$-∗-$^7C_{bay}$)[l]	0.0113	0.0050	0.0019	–0.770	0.0054	69.5	1.79	84.6	587.9	*p*-CS/vdW
8-12 ($^3C_{bay}$-∗-$^8C_{bay}$)	0.0115	0.0051	0.0018	–0.780	0.0054	70.2	1.75	80.8	193.2	*p*-CS/vdW
8-12 ($^4C_{bay}$-∗-$^9C_{bay}$)[m]	0.0108	0.0048	0.0018	–0.767	0.0052	69.3	1.73	78.2	86.8	*p*-CS/vdW
8-12 ($^4C_{cape}$-∗-$^{22}C_{cape}$)	0.0054	0.0020	0.0008	–0.755	0.0021	68.5	5.05	65.5	62.0	*p*-CS/vdW
8-12 ($^6C_{cape}$-∗-$^{23}C_{cape}$)	0.0060	0.0020	0.0008	–0.774	0.0022	69.7	7.11	68.0	33.1	*p*-CS/vdW
8-12 ($^7C_{cape}$-∗-$^{25}C_{cape}$)	0.0058	0.0021	0.0008	–0.756	0.0023	68.6	3.61	66.0	9.3	*p*-CS/vdW
8-12 ($^9C_{cape}$-∗-$^{26}C_{cape}$)	0.0059	0.0020	0.0007	–0.779	0.0021	70.1	7.28	68.6	16.2	*p*-CS/vdW
8-12 ($^{10}C_{cape}$-∗-$^{28}C_{cape}$)	0.0054	0.0020	0.0008	–0.758	0.0021	68.7	4.40	66.3	24.7	*p*-CS/vdW

[a] Data are given at BCPs. [b] $c\nabla^2\rho_b(\boldsymbol{r}_c) = H_b(\boldsymbol{r}_c) - V_b(\boldsymbol{r}_c)/2$, where $c = \hbar^2/8m$. [c] $k_b(\boldsymbol{r}_c) = V_b(\boldsymbol{r}_c)/G_b(\boldsymbol{r}_c)$. [d] $R = (x + y)^{1/2}$, where $(x, y = H_b(\boldsymbol{r}_c) - V_b(\boldsymbol{r}_c)/2, H_b(\boldsymbol{r}_c))$. [e] $\theta = 90° - \tan^{-1}(y/x)$. [f] Compliance force constants. [g] $\theta_p = 90° - \tan^{-1}(dy/dx)$. [h] $\kappa_p = |d^2y/dx^2|/[1 + (dy/dx)^2]^{3/2}$. [i] Å $mdyn^{-1}$. [j] Data from $w = –0.05$, $–0.0375$, $–0.025$, $–0.0125$, and 0, were employed for the evaluation of dynamic nature, since BCP for $^4C_{cape}$-∗-$^{22}C_{cape}$ in the case of $w > 0$ were not detected. [k] Data from $w = 0$, ±0.0125, and ±0.025 were employed for the evaluation of dynamic nature, since BCP for $^2C_{bay}$-∗-$^7C_{bay}$ in the case of $w > 0.05$ were not detected. [l] Data from $w = –0.0375$, $–0.025$, $–0.0125$, 0, 0.0125 were employed for the evaluation of dynamic nature, since BCP for $^2C_{bay}$-∗-$^7C_{bay}$ in the case of $w > 0.025$ were not detected. [m] Data from $w = –0.0375$, $–0.025$, $–0.0125$, 0, and 0.0125 were employed for the evaluation of dynamic nature, since BCP for $^4C_{bay}$-∗-$^9C_{bay}$ in the case of $w > 0.025$ were not detected.

Table 8-A6. QTAIM functions and QTAIM-DFA parameters for the fused benzene-type helicenes of monomers (**8-3**–**8-12** (C_2)), along with the nature of each noncovalent interaction, elucidated with LC-ωPBE/6-311+G(2d,p).[a]

Compds (X-*-Y)	$\rho_b(\boldsymbol{r}_c)$ (au)	$c\nabla^2\rho_b(\boldsymbol{r}_c)^b$ (au)	$H_b(\boldsymbol{r}_c)$ (au)	$k_b(\boldsymbol{r}_c)^c$	R^d (au)	θ^e (º)	$C_{ii}{}^f$ (unit[i])	$\theta_p{}^g$ (º)	$\kappa_p{}^h$ (au^{-1})	Predicted Nature
8-3 ($^1H_{bay}$-*-$^4H_{bay}$)	0.0132	0.0062	0.0023	–0.776	0.0066	69.9	3.47	76.0	9.4	*p*-CS/vdW
8-4 ($^1H_{bay}$-*-$^5H_{bay}$)	0.0169	0.0079	0.0026	–0.800	0.0083	71.6	6.72	77.9	22.8	*p*-CS/vdW
8-5 ($^1H_{bay}$-*-$^6C_{bay}$)	0.0130	0.0062	0.0022	–0.778	0.0066	70.0	6.71	83.7	55.5	*p*-CS/vdW
8-6 ($^1H_{bay}$-*-$^5C_{bay}$)	0.0134	0.0060	0.0020	–0.793	0.0063	71.1	3.86	81.6	46.3	*p*-CS/vdW
8-7 ($^1H_{bay}$-*-$^5C_{bay}$)	0.0139	0.0062	0.0022	–0.789	0.0066	70.8	3.70	82.2	45.7	*p*-CS/vdW
8-8 ($^1H_{bay}$-*-$^5C_{bay}$)[j]	0.0135	0.0061	0.0021	–0.786	0.0064	70.6	3.77	96.0	12303.9	*p*-CS/*t*-HB_{nc}
8-9 ($^1H_{bay}$-*-$^5C_{bay}$)	0.0141	0.0062	0.0021	–0.797	0.0066	71.4	3.47	83.2	42.9	*p*-CS/vdW
8-9 ($^3C_{bay}$-*-$^8C_{bay}$)	0.0106	0.0046	0.0018	–0.758	0.0050	68.7	2.49	81.2	176.1	*p*-CS/vdW
8-9 ($^6C_{cape}$-*-$^{23}C_{cape}$)	0.0033	0.0011	0.0005	–0.741	0.0012	67.7	12.43	68.2	22.8	*p*-CS/vdW
8-10 ($^1H_{bay}$-*-$^6C_{bay}$)	0.0143	0.0064	0.0022	–0.796	0.0067	71.3	5.74	82.8	191.9	*p*-CS/vdW
8-10 ($^3C_{bay}$-*-$^8C_{bay}$)	0.0101	0.0044	0.0018	–0.750	0.0048	68.2	2.67	78.3	323.9	*p*-CS/vdW
8-10 ($^6C_{cape}$-*-$^{23}C_{cape}$)	0.0037	0.0013	0.0005	–0.746	0.0014	67.9	13.90	68.7	404.7	*p*-CS/vdW
8-11 ($^1H_{bay}$-*-$^6C_{bay}$)	0.0141	0.0063	0.0021	–0.795	0.0067	71.2	5.63	83.6	171.4	*p*-CS/vdW
8-11 ($^3C_{bay}$-*-$^8C_{bay}$)	0.0099	0.0044	0.0018	–0.747	0.0047	68.0	2.70	78.4	174.0	*p*-CS/vdW
8-11 ($^4C_{bay}$-*-$^9C_{bay}$)	0.0097	0.0043	0.0018	–0.745	0.0047	67.9	2.76	77.3	163.4	*p*-CS/vdW
8-11 ($^6C_{cape}$-*-$^{24}C_{cape}$)[k]	0.0036	0.0013	0.0005	–0.743	0.0014	67.7	13.86	70.0	2078.2	*p*-CS/vdW
8-11 ($^9C_{cape}$-*-$^{26}C_{cape}$)	0.0040	0.0014	0.0006	–0.745	0.0015	67.9	14.90	68.2	10.0	*p*-CS/vdW
8-12 ($^1H_{bay}$-*-$^6C_{bay}$)	0.0143	0.0064	0.0022	–0.796	0.0067	71.3	5.68	81.9	180.6	*p*-CS/vdW
8-12 ($^3C_{bay}$-*-$^8C_{bay}$)	0.0102	0.0045	0.0018	–0.753	0.0048	68.4	2.64	80.2	178.3	*p*-CS/vdW
8-12 ($^6C_{cape}$-*-$^{23}C_{cape}$)	0.0038	0.0013	0.0006	–0.739	0.0014	67.5	13.59	67.6	150.4	*p*-CS/vdW
8-12 ($^9C_{cape}$-*-$^{26}C_{cape}$)	0.0039	0.0013	0.0005	–0.743	0.0014	67.8	14.52	68.3	11.7	*p*-CS/vdW

[a] Data are given at BCPs. [b] $c\nabla^2\rho_b(\boldsymbol{r}_c) = H_b(\boldsymbol{r}_c) - V_b(\boldsymbol{r}_c)/2$, where $c = \hbar^2/8m$. [c] $k_b(\boldsymbol{r}_c) = V_b(\boldsymbol{r}_c)/G_b(\boldsymbol{r}_c)$. [d] $R = (x + y)^{1/2}$, where $(x, y = H_b(\boldsymbol{r}_c) - V_b(\boldsymbol{r}_c)/2, H_b(\boldsymbol{r}_c))$. [e] $\theta = 90^o - \tan^{-1}(y/x)$. [f] Compliance force constants. [g] $\theta_p = 90^o - \tan^{-1}(dy/dx)$. [h] $\kappa_p = |d^2y/dx^2|/[1 + (dy/dx)^2]^{3/2}$. [i] Å $mdyn^{-1}$. [j] No intrinsic dynamic behavior for $^1H_{bay}$-*-$^5C_{bay}$ was observed, since BCPs were detected between $^1H_{bay}$ and $^6C_{bay}$ in the case of $0.0 < w$, while if $w \leq 0.0$, BCP were detected between $^1H_{bay}$ and $^5C_{bay}$. [k] Data from $w = –0.05$, –0.0375, –0.025, –0.0125, and 0 were employed for the evaluation of dynamic nature, since BCPs for $^6C_{cape}$-*-$^{24}C_{cape}$ in the case of $w > 0$ were not detected.

Table 8-A7. The E_{ES} (au), ΔE_{ES} (kJ mol^{-1}), and ΔE_{ZP} (kJ mol^{-1}) values for **8-6**:**6**–**8-8**:**8** and **8-10**:**10**, evaluated with various methods.[a]

Compds (symm)	$E_{ES:dim}$[b] (au)	$E_{ES:mono}$[c] (au)	ΔE_{ES}[d] (kJ mol^{-1})
M06-2X/6-311+G(3d,p)			
8-6:**6** (C_i)	–2000.613340	–1000.301869	–25.2
8-7:**7** (C_i)	–2307.855458	–1153.921673	–31.8
M06-2X/6-311+G(2d,p)			
8-7:**7** (C_i)	–2307.865224	–1153.926727	–30.9
8-8:**8** (C_i)	–2615.109370	–1307.548324	–33.4
8-10:**10** (C_i)	–3229.593523	–1614.790462	–33.1
LC-ωPBE/6-311+G(2d,p)			
8-7:**7** (C_i)	–2306.940209	–1153.468598	–7.9

[a] Ultrafine integration grid (corresponding to Int=ultrafine keyword) was employed for the calculations, since very low imaginary frequencies were predicted for frequency analysis under default condition (finegrid) of the Gaussian 09 program. [b] For concave-type dimers. [c] For monomers. [d] $\Delta E_{ES} = E_{ES:dim} - 2E_{ES:mono}$.

Table 8-A8. QTAIM functions and QTAIM-DFA parameters for the concave-type dimer of helicenes (**8-8**:**8**–**8-10**:**10** (C_i)), together with the nature of each noncovalent interaction, elucidated with M06-2X/6-311+G(2d,p).[a]

Compds X-∗-Y	$\rho_b(\boldsymbol{r}_c)$ (au)	$c\nabla^2\rho_b(\boldsymbol{r}_c)$[b] (au)	$H_b(\boldsymbol{r}_c)$ (au)	$k_b(\boldsymbol{r}_c)$[c]	R[d] (au)	θ[e] (º)	C_{ii}[f] (unit[i])	θ_p[g] (º)	κ_p[h] (au^{-1})	Predicted Nature
8-8:**8** (C_i)										
$^{21}H_{cape}$-∗-$^{21'}H_{cape}$	0.0103	0.0045	0.0016	–0.776	0.0048	69.9	9.12	75.0	44.8	*p*-CS/vdW
$^{3}C_{cape}$ -∗-$^{23'}H_{cape}$	0.0063	0.0024	0.0009	–0.773	0.0026	69.7	14.48	70.6	14.2	*p*-CS/vdW
$^{5}C_{cape}$ -∗-$^{21'}H_{cape}$	0.0077	0.0032	0.0011	–0.782	0.0034	70.3	8.83	70.6	16.2	*p*-CS/vdW
$^{21}C_{cape}$ -∗-$^{23'}H_{cape}$	0.0045	0.0015	0.0005	–0.803	0.0016	71.8	24.95	73.2	197.1	*p*-CS/vdW
8-10:**10** (C_i)										
$^{21}H_{cape}$-∗-$^{21'}H_{cape}$	0.0104	0.0043	0.0015	–0.792	0.0046	71.0	7.85	72.5	39.1	*p*-CS/vdW
$^{3}C_{cape}$ -∗-$^{23'}H_{cape}$	0.0052	0.0020	0.0008	–0.762	0.0021	69.0	24.13	71.5	26.9	*p*-CS/vdW
$^{5}C_{cape}$ -∗-$^{21'}H_{cape}$	0.0083	0.0035	0.0013	–0.779	0.0037	70.1	7.62	70.3	2.6	*p*-CS/vdW
$^{21}C_{cape}$ -∗-$^{23'}H_{cape}$	0.0045	0.0016	0.0006	–0.791	0.0017	70.9	28.07	76.2	502.6	*p*-CS/vdW

[a] Data are given at BCPs. [b] $c\nabla^2\rho_b(\boldsymbol{r}_c) = H_b(\boldsymbol{r}_c) - V_b(\boldsymbol{r}_c)/2$, where $c = \hbar^2/8m$. [c] $k_b(\boldsymbol{r}_c) = V_b(\boldsymbol{r}_c)/G_b(\boldsymbol{r}_c)$. [d] $R = (x + y)^{1/2}$, where $(x, y = H_b(\boldsymbol{r}_c) - V_b(\boldsymbol{r}_c)/2, H_b(\boldsymbol{r}_c))$. [e] $\theta = 90^o - \tan^{-1}(y/x)$. [f] Compliance force constants. [g] $\theta_p = 90^o - \tan^{-1}(dy/dx)$. [h] $\kappa_p = |d^2y/dx^2|/[1 + (dy/dx)^2]^{3/2}$. [i] Å mdyn^{-1}.

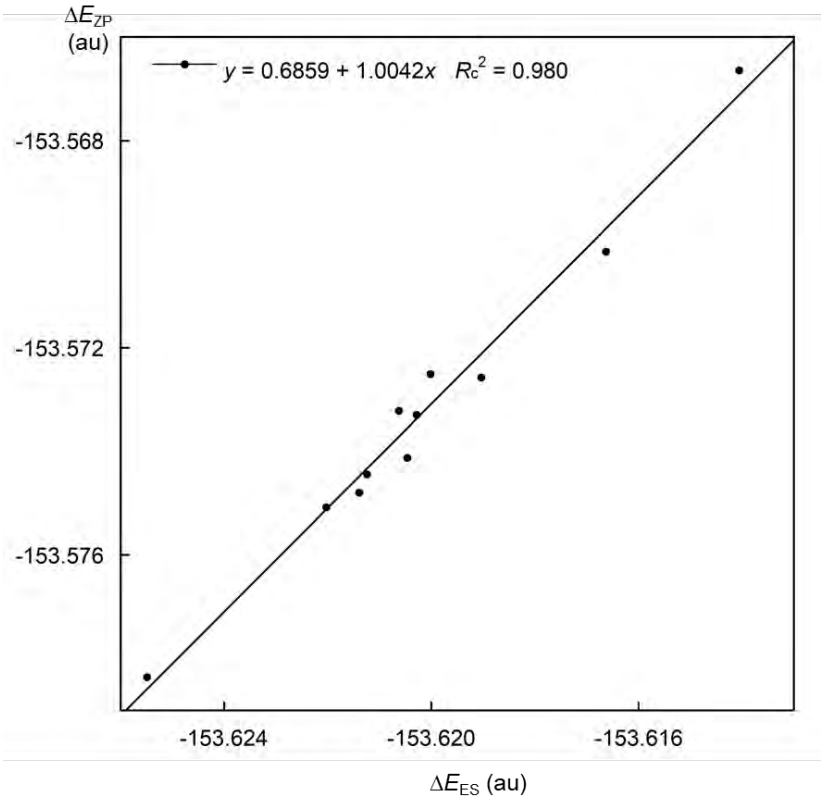

Figure 8-A1. Plots of ΔE_{ZP}(**8-*n***) versus ΔE_{ES}(**8-*n***), calculated with M06-2X/6-311+G(3d,p), where ΔE_{ES}(**8-*n***) (= E_{ES}(**8-*n***) – E_{ES}(**8-(*n* – 1)**)) and ΔE_{ZP}(**8-*n***) (= E_{ZP}(**8-*n***) – E_{ZP}(**8-(*n* – 1)**)).

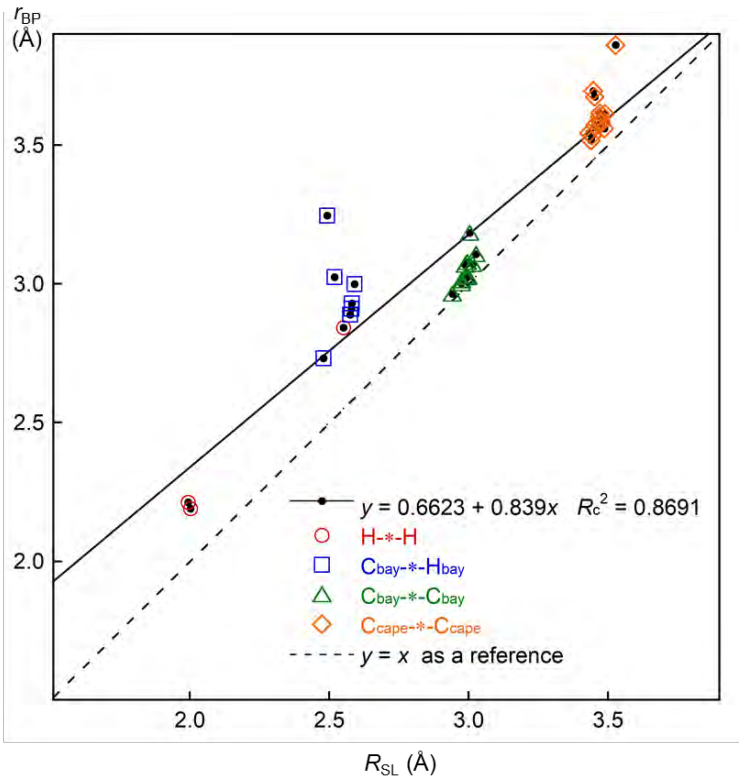

Figure 8-A2. Plots of r_{BP} versus R_{SL} for H_{bay}-*-H_{bay}, C_{bay}-*-H_{bay}, C_{bay}-*-C_{bay}, and C_{cape}-*-C_{cape} in **8-3**–**8-12**, calculated with M06-2X/6-311+G(3d,p).

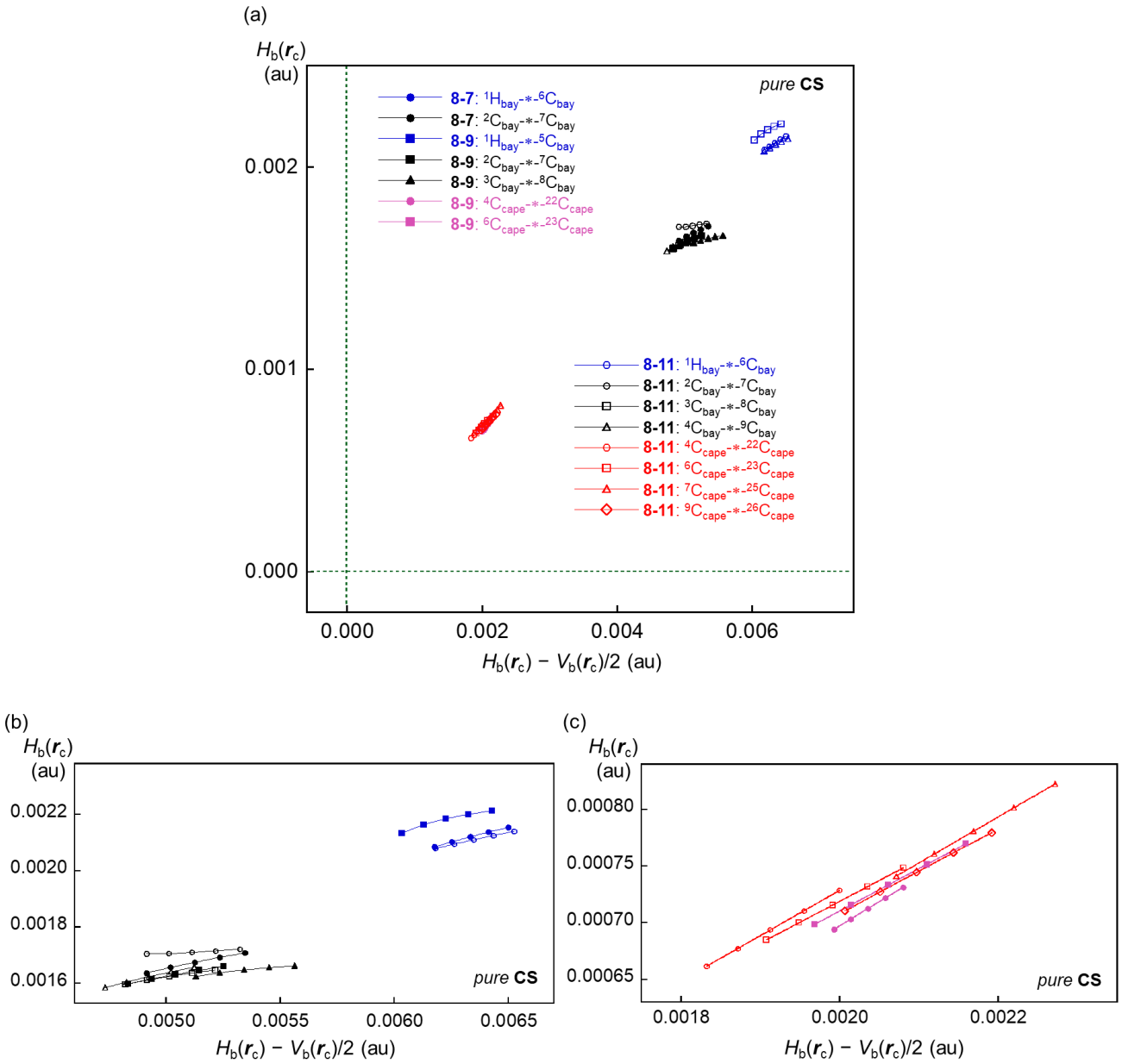

Figure 8-A3. Plots of $H_b(\boldsymbol{r}_c)$ versus $H_b(\boldsymbol{r}_c) - V_b(\boldsymbol{r}_c)/2$ for H-*-H, C-*-H, and C-*-C for **8-7**, **8-9**, and **8-11**. Whole picture (a), magnified picture for C-*-H and C-*-C in the bay area (b), magnified picture for C-*-C in the cape area (c).

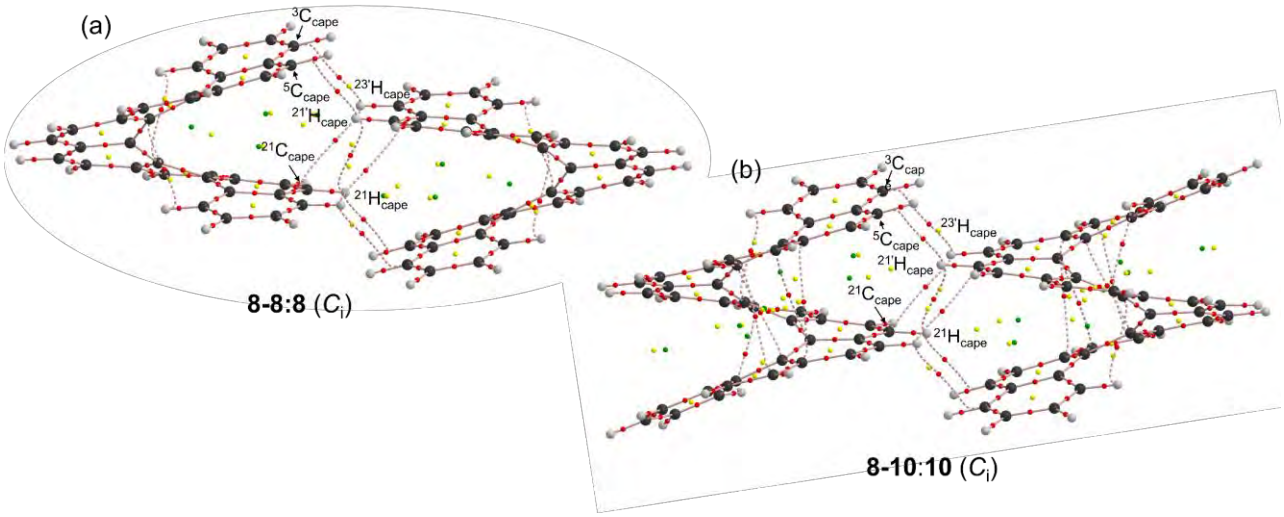

Figure 8-A4. Molecular graphs for **8-8**:**8** (C_i) and **8-10**:**10** (C_i) calculated with M06-2X/6-311+G(2d,p) (shown by (a) and (b), respectively, in the figure), where BPs with BCPs corresponding to intramolecular non-covalent interactions are detected. The BCPs are denoted by red dots, RCPs (ring critical points) by yellow dots, CCPs (cage critical points) by green dots and BPs by pink lines. The carbon atoms are in black with hydrogen atoms in grey.

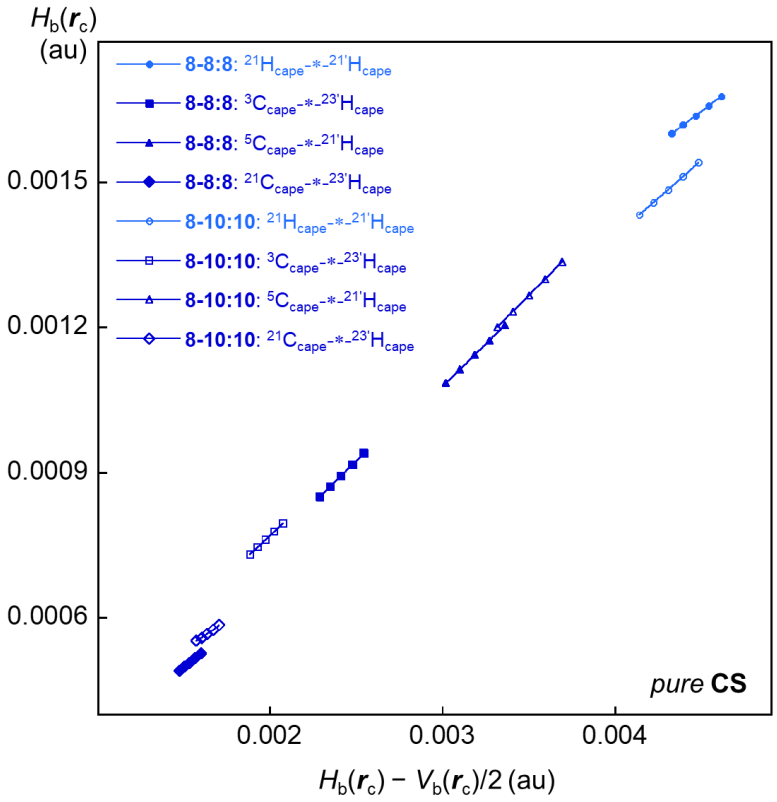

Figure 8-A5. Plots of $H_b(\boldsymbol{r}_c)$ versus $H_b(\boldsymbol{r}_c) - V_b(\boldsymbol{r}_c)/2$ for H-*-H, C-*-H, and C-*-C for **8-8**:**8** and **8-10**:**10**.

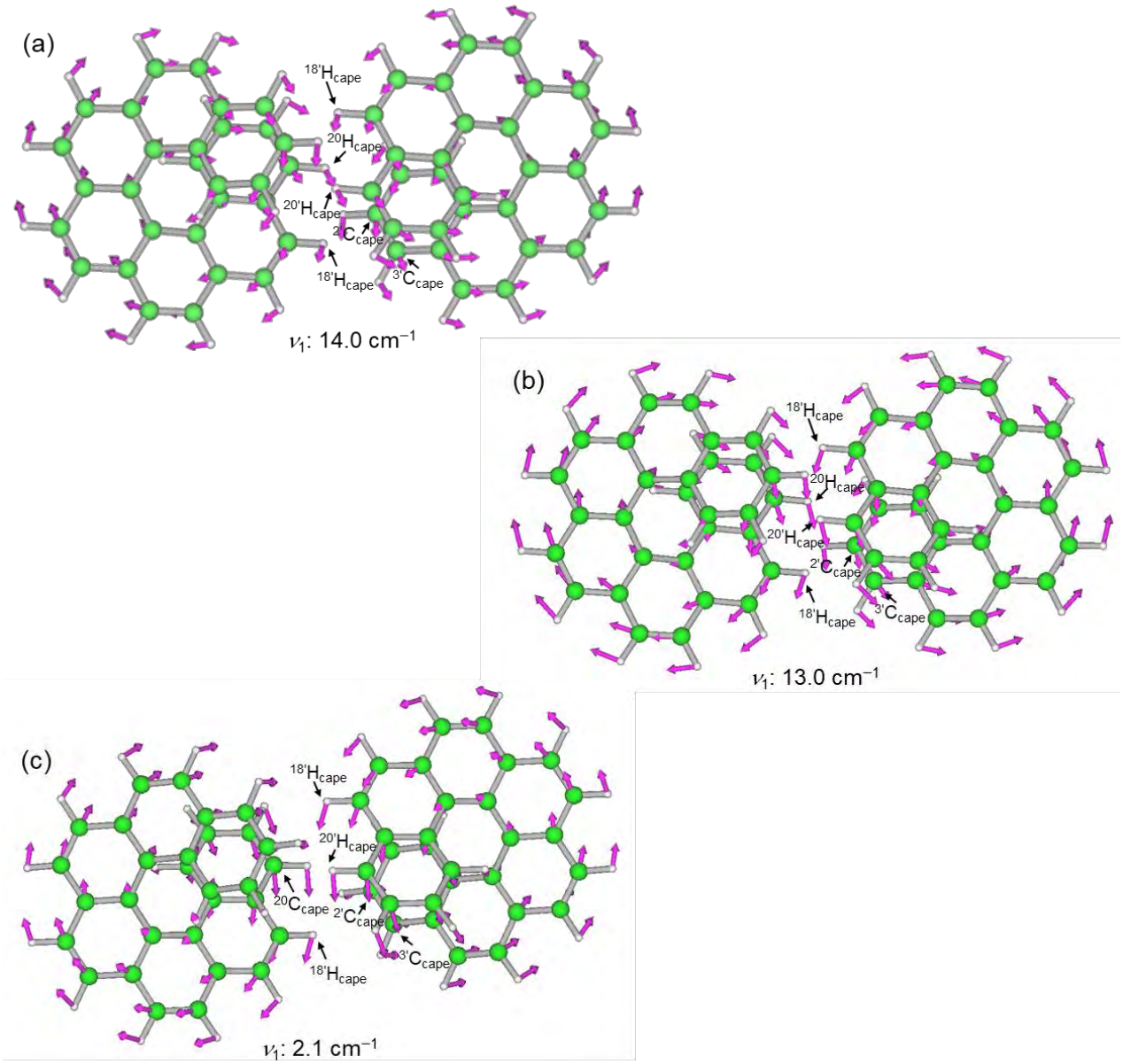

Figure 8-A6. The internal vibration motions of ν_n for **8-7**:**7** (C_i) from the top view. ν_1 for **8-7**:**7** (C_i) calculated with M06-2X/6-311+G(3d,p) (a), ν_1 for **8-7**:**7** (C_i) calculated with M06-2X/6-311+G(2d,p) (b), ν_1 for **8-7**:**7** (C_i) calculated with LC-ωPBE/6-311+G(2d,p) (c).

References and Notes

1. Y. Shen, C.-F. Chen, *Chem. Rev.* **2012**, *112*, 1463–1535.
2. C.-F. Chen, Y. Shen, *Helicene Chemistry: From Synthesis to Applications*, Springer, Berlin, Germany, **2017**.
3. K. Dhbaibi, L. Favereau, J. Crassous, *Chem. Rev.* **2019**, *119*, 8846–8953.
4. F. Tani, M. Narita, T. Murafuji, *ChemPlusChem* **2020**, *85*, 2093–2104.
5. M. Jakubec, J. Storch, *J. Org. Chem.* **2020**, *85*, 13415–13428.
6. M. Ren, J. Wang, X. Xie, J. Zhang, P. Wang, *ACS Energy Lett.* **2019**, *4*, 2683–2688.
7. N. Xu, Y. Li, D. Ricciarelli, J. Wang, E. Mosconi, Y. Yuan, F. De Angelis, S. M. Zakeeruddin, M. Grätzel, P. Wang, *iScience* **2019**, *15*, 234–242.
8. J. Wang, H. Shi, N. Xu, J. Zhang, Y. Yuan, M. Lei, L. Wang, P. Wang, *Adv. Funct. Mater.* **2020**, *30*, 2002114.
9. Y. Wei, A. Zheng, X. Xie, J. Zhang, L. He, P. Wang, *ACS Mater. Lett.* **2021**, *3*, 947–955.
10. J. Wang, Y. Wang, X. Xie, Y. Ren, B. Zhang, L. He, J. Zhang, L.-D. Wang, P. Wang, *ACS Energy Lett.* **2021**, *6*, 1764–1772.
11. T. Tsujihara, N. Inada-Nozaki, T. Takehara, D.-Y. Zhou, T. Suzuki, T. Kawano, *Eur. J. Org. Chem.* **2016**, 4948–4952.
12. K. Yamamoto, T. Shimizu, K. Igawa, K. Tomooka, G. Hirai, H. Suemune, K. Usui, *Sci. Rep.* **2016**, *6*, 36211.
13. C. S. Demmer, A. Voituriez, A. Marinetti, *C. R. Chim.* **2017**, *20*, 860–879.
14. S. Cauteruccio, E. Licandro, M. Panigati, G. D'Alfonso, S. Maiorana, *Coord. Chem. Rev.* **2019**, *386*, 119–137.
15. T. Beránek, J. Žádný, T. Strašák, J. Karban, I. Císařová, J. Sýkora, J. Storch, *ACS Omega* **2020**, *5*, 882–892.
16. C. Medena, C. Aubert, E. Derat, L. Fensterbank, G. Gontard, O. Khaled, C. Ollivier, N. Vanthuyne, M. Petit, M. Barbazanges, *ChemCatChem* **2021**, *13*, 4543–4548.
17. O. Kel, A. Fürstenberg, N. Mehanna, C. Nicolas, B. Laleu, M. Hammarson, B. Albinsson, J. Lacour, E. Vauthey, *Chem. Eur. J.* **2013**, *19*, 7173–7180.
18. K. Kawara, G. Tsuji, Y. Taniguchi, S. Sasaki, *Chem. Eur. J.* **2017**, *23*, 1763–1769.
19. Y. Kalachyova, O. Guselnikova, R. Elashnikov, I. Panov, J. Žádný, V. Církva, J. Storch, J. Sykora, K. Zaruba, V ík, O. Lyutakov, *ACS Appl. Mater. Interfaces* **2019**, *11*, 1555–1562.
20. T. R. Schulte, J. J. Holstein, G. H. Clever, *Angew. Chem.* **2019**, *131*, 5618–5622.
21. A. Petdum, N. Faichu, J. Sirirak, P. Khammultri, V. Promarak, W. Panchan, T. Sooksimuang, A. Charoenpanich, N. Wanichacheva, *J. Photochem. Photobiol. A* **2020**, *394*, 112473.
22. X.-H. Gu, Y. Lei, S. Wang, F. Cao, Q. Zhang, S. Chen, K.-P. Wang, Z.-Q. Hu, *Spectrochim. Acta A Mol. Biomol. Spectrosc.* **2020**, *229*, 118003.
23. J. Li, K. Martin, N. Avarvari, C. Wäckerlin, K.-H. Ernst, *Chem. Commun.* **2018**, *54*, 7948–7951.
24. A. Shiotari, K. Tanaka, T. Nakae, S. Mori, T. Okujima, H. Uno, H. Sakaguchi, Y. Sugimoto, *J. Phys. Chem. C* **2018**, *122*, 4997–5003.
25. H. Zhang, H. Liu, C. Shen, F. Gan, X. Su, H. Qiu, B. Yang, P. Yu, *Int. J. Mol. Sci.* **2019**, *20*, 2018.

26. B. Irziqat, J. Berger, J. I. Mendieta-Moreno, M. S. Sundar, A. V. Bedekar, K. Ernst, *ChemPhysChem* **2021**, *22*, 293–297.
27. K. Matsuiwa, S. Hayashi, W. Nakanishi, *ChemistrySelect* **2017**, *2*, 1774–1782. See also refs 62 and 63.
28. W. Nakanishi, S. Hayashi, K. Narahara, *J. Phys. Chem. A* **2008**, *112*, 13593–13599.
29. W. Nakanishi, S. Hayashi, K. Narahara, *J. Phys. Chem. A* **2009**, *113*, 10050–10057.
30. W. Nakanishi, S. Hayashi, *Curr. Org. Chem.* **2010**, *14*, 181–197.
31. W. Nakanishi, S. Hayashi, K. Matsuiwa, M. Kitamoto, *Bull. Chem. Soc. Jpn.* **2012**, *85*, 1293–1305.
32. W. Nakanishi, S. Hayashi, *Int. J. Quantum Chem.* **2018**, *118*, e25590.
33. R. F. W. Bader, *Atoms in Molecules. A Quantum Theory*; Oxford University Press, Oxford, UK, **1990**.
34. C. F. Matta, R. J. Boyd, *An Introduction to the Quantum Theory of Atoms in Molecules* in *The Quantum Theory of Atoms in Molecules: From Solid State to DNA and Drug Design* (Eds.: C. F. Matta, R. J. Boyd), WILEY-VCH: Weinheim, Germany, **2007**, Ch. 1.
35. *Gaussian 09, Revision D.01*, M. J. Frisch, G. W. Trucks, H. B. Schlegel, G. E. Scuseria, M. A. Robb, J. R. Cheeseman, G. Scalmani, V. Barone, B. Mennucci, G. A. Petersson, H. Nakatsuji, M. Caricato, X. Li, H. P. Hratchian, A. F. Izmaylov, J. Bloino, G. Zheng, J. L. Sonnenberg, M. Hada, M. Ehara, K. Toyota, R. Fukuda, J. Hasegawa, M. Ishida, T. Nakajima, Y. Honda, O. Kitao, H. Nakai, T. Vreven, J. A. Montgomery, Jr., J. E. Peralta, F. Ogliaro, M. Bearpark, J. J. Heyd, E. Brothers, K. N. Kudin, V. N. Staroverov, R. Kobayashi, J. Normand, K. Raghavachari, A. Rendell, J. C. Burant, S. S. Iyengar, J. Tomasi, M. Cossi, N. Rega, J. M. Millam, M. Klene, J. E. Knox, J. B. Cross, V. Bakken, C. Adamo, J. Jaramillo, R. Gomperts, R. E. Stratmann, O. Yazyev, A. J. Austin, R. Cammi, C. Pomelli, J. W. Ochterski, R. L. Martin, K. Morokuma, V. G. Zakrzewski, G. A. Voth, P. Salvador, J. J. Dannenberg, S. Dapprich, A. D. Daniels, Ö. Farkas, J. B. Foresman, J. V. Ortiz, J. Cioslowski, D. J. Fox, Gaussian, Inc., Wallingford CT, **2009**.
36. Y. Zhao, D. G. Truhlar, *Theor. Chem. Acc.* **2008**, *120*, 215–241.
37. The C_{ij} values and the coordinates corresponding to C_{ii} were calculated by using the Compliance 3.0.2 program released by J. Grunenberg and K. Brandhorst.
38. K. Brandhorst, J. Grunenberg, *J. Chem. Phys.* **2010**, *132*, 184101.
39. K. Brandhorst, J. Grunenberg, *Chem. Soc. Rev.* **2008**, *37*, 1558–1567.
40. O. A. Vydrov, G. E. Scuseria, *J. Chem. Phys.* **2006**, *125*, 234109.
41. S. Hayashi, T. Nishide, K. Ueda, K. Hayama, W. Nakanishi, *ChemistrySelect* **2019**, *4*, 6198–6208.
42. D. M. Ivanov, Y. V. Kirina, A. S. Novikov, G. L. Starova, V. Yu. Kukushkin, *J. Mol. Struct.* **2016**, *1104*, 19–23.
43. A. A. Mukhacheva, V. Yu. Komarov, V. V. Kokovkin, A. S. Novikov, P. A. Abramov, M. N. Sokolov, *CrystEngComm* **2021**, *23*, 4125–4135.
44. F. Biegler–König, *J. Comput. Chem.* **2000**, *21*, 1040–1048.

45. T. A. Keith, AIMAll (Version 17.11.14), TK Gristmill Software, Overland Park, KS, USA, **2017**, http://www.aim.tkgristmill.com.
46. M. I. Kay, Y. Okaya, D. E. Cox, *Acta Crystallogr. Sect. B Struct. Crystallogr. Cryst. Chem.* **1971**, *27*, 26–33.
47. M. K. Lakshman, P. L. Kole, S. Chaturvedi, J. H. Saugier, H. J. C. Yeh, J. P. Glusker, H. L. Carrell, A. K. Katz, C. E. Afshar, W.-M. Dashwood, G. Kenniston, W. M. Baird, *J. Am. Chem. Soc.* **2000**, *122*, 12629–12636.
48. A.-C. Bédard, A. Vlassova, A. C. Hernandez-Perez, A. Bessette, G. S. Hanan, M. A. Heuft, S. K. Collins, *Chem. Eur. J.* **2013**, *19*, 16295–16302.
49. Y. Yoshida, Y. Nakamura, H. Kishida, H. Hayama, Y. Nakano, H. Yamochi, G. Saito, *CrystEngComm* **2017**, *19*, 3626–3632.
50. S. Fujino, M. Yamaji, H. Okamoto, T. Mutai, I. Yoshikawa, H. Houjou, F. Tani, *Photochem. Photobiol. Sci.* **2017**, *16*, 925–934.
51. K. Mori, T. Murase, M. Fujita, *Angew. Chem.* **2015**, *127*, 6951–6955.
52. G. L. Bas, A. Navaza, Y. Mauguen, C. D. Rango, *Cryst. Struct. Commun.* **1976**, *5*, 357–361.
53. G. L. Bas, A. Navaza, M. Knossow, C. D. Rango, *Cryst. Struct. Commun.* **1976**, *5*, 713–718.
54. L. Rulíšek, O. Exner, L. Cwiklik, P. Jungwirth, I. Starý, L. Pospíšil, Z. Havlas, *J. Phys. Chem. C* **2007**, *111*, 14948–14955.
55. T. M. Krygowski, *J. Chem. Inf. Comput. Sci.* **1993**, *33*, 70–78.
56. R. F. W. Bader, *J. Phys. Chem. A* **2009**, *113*, 10391–10396.
57. S. Grimme, C. Mück-Lichtenfeld, G. Erker, G. Kehr, H. Wang, H. Beckers, H. Willner, *Angew. Chem. Int.* **2009**, *48*, 2592–2595.
58. I. Cukrowski, *Wiley Interdiscip. Rev. Comput. Mol. Sci.* **2021**, e1579.
59. A. M. Pendás, E. Francisco, M. A. Blanco, C. Gatti, *Chem. Eur. J.* **2007**, *13*, 9362–9371.
60. V. Tognetti, L. Joubert, *J. Chem. Phys.* **2013**, *138*, 024102.
61. I. Cukrowski, J. H. de Lange, A. S. Adeyinka, P. Mangondo, *Comput. Theor. Chem.* **2015**, *1053*, 60–76.
62. K. Matsuiwa, S. Hayashi, W. Nakanishi, *ChemistrySelect* **2016**, *1*, 2344–2353.
63. K. Matsuiwa, Y. Sugibayashi, Y. Tsubomoto, S. Hayashi, W. Nakanishi, *ChemistrySelect* **2017**, *2*, 90–100.

Chapter 9

Conclusions

Inter- and intramolecular interactions are vital in materials science because their nature must be closely related to structural properties and stability. For further development of materials science, it is inevitable to gain a comprehensive understanding of the interactions in question. Therefore, the author aimed to establish and apply the QTAIM-DFA with CIV to various inter- and intramolecular interactions to elucidate the "intrinsic dynamic behavior" of the interactions involved.

As a first step, the high applicability of the QTAIM-DFA with CIV is demonstrated by employing a variety of neutral intermolecular HBs, which have a wide range of interactions. Some characteristics of HBs, well-characterized based on their intrinsic dynamic and static behaviors, are shown as follows: *p*-CS/vdW for H_2Se-∗-HSeH and H_3N-∗-HNH_2; *p*-CS/*t*-HB_{nc} for H_2S-∗-HSH, H_2O-∗-HOH, and HX-∗-HX (X = Cl, Br, and I); *r*-CS/*t*-HB_{wc} for HF-∗-HF, H_2S-∗-HX (X = Cl and Br), and H_2O-∗-HX (X = Cl and Br); *r*-CS/CT-MC for H_2C=O-∗-HX (X = F, Cl, and Br); and *r*-CS/CT-TBP for H_3N-∗-HX (F, CI, Br, and I).

The dynamic behavior of CIV demonstrates an excellent correlation with that of POM in terms of error calculation. Therefore, the CIV substantially generates the same perturbed structures. The high applicability of the QTAIM-DFA with CIV to various neutral intermolecular HBs is demonstrated along with typical interactions.

Furthermore, the QTAIM-DFA with CIV is also applied to the intramolecular OH···π interactions in π systems for ethynyl, vinyl, and phenyl groups. Seventy-two conformers are obtained by changing all torsion angles for each species. Stability in terms of the energy of conformers for each species is not solely explained by the steric hindrance. Consequently, the intramolecular interactions are expected to contribute to stabilization. Notably, OH-∗-C(π), O-∗-C(π), and O-∗-H(π) interactions are detected for some species, in which C(π) and H(π) show a C atom with π-orbital and H joined directly to C(π). The OH-∗-C(π) interactions appear in the six-membered ring, whereas O-∗-C(π) or O-∗-H(π) appear in the five-, six-, or seven-membered rings. The nature of OH-∗-C(π) is predicted to be *p*-CS/*t*-HB_{nc}, except for one *p*-CS/vdW nature. However, two *p*-CS/vdW and *p*-CS/*t*-HB_{nc} natures are obtained for O-∗-C(π). For O-∗-H(π), the *p*-CS/vdW nature is predicted. The OH-∗-C(π) interactions are somewhat stronger than the intermolecular interactions because of the steric compression between the H and C(π) atoms.

The high applicability of the QTAIM-DFA with CIV can also be demonstrated by employing the intramolecular OH···π interactions in various π systems.

The methodology elucidating the dynamic and static behavior of multi-HBs formed in close proximity is established by employing an acetic acid dimer and related species. The dynamic and

static behavior of OH-∗-O in acetic acid dimer and NH-∗-O in acetamide dimer are close to those of OH-∗-O and NH-∗-O in acetic acid-acetamide complex, respectively. Therefore, the QTAIM-DFA with CIV would elucidate the dynamic behavior of each HB in multi-HB systems. The *r*-CS/CT-MC nature is predicted for each HB in multi-HBs of acetic acid dimer and the related species. Consequently, the HBs in multi-HB systems seem stronger than single HBs. The isomers of acetic acid dimer and related species, mainly stabilized by single HBs, are also examined. Each HB in the multi-HB system is confirmed to be stronger than single HBs in the isomers because of the enhancement by the formation of multi-HBs in close proximity. Notably, the QTAIM-DFA with CIV is highly applicable to each HB in the multi-HB system and single HBs.

Subsequently, the QTAIM-DFA with CIV is applied to the nucleobase pairs to elucidate the nature of each HB in multi HBs, which will be more complex than the case of acetic acid dimers and related species. The nature of each HB in multi HBs is characterized based on its intrinsic dynamic and static behavior. For instance, the natures of N-∗-HN, NH-∗-O, and CH-∗-O in A-T are predicted to be *r*-CS/CT-TBP, *r*-CS/*t*-HB_{wc}, and *p*-CS/vdW, respectively. In contrast, the *r*-CS/CT-MC nature is predicted for NH-∗-O and N-∗-HN in C-G, together with *r*-CS/*t*-HB_{wc} for O-∗-HN. In addition, the ΔE values are proportional to the sum of the $1/C_{ii}$ values of each HB in plural HBs of nucleobase pairs. Hence, the ΔE values are closely related to the C_{ii} values, indicating that the ΔE values can be fractionalized to each HB in the multi-HB system by employing the ratio of each $1/C_{ii}$ value. These results demonstrate that the QTAIM-DFA with CIV and C_{ii} will be a valuable tool for elucidating the intrinsic dynamic and static nature of intermolecular interactions.

Furthermore, the QTAIM-DFA with CIV is applied to 3c–4e interactions in bicyclo[3.3.3] and [4.4.4] systems, in which the two bridgehead atoms are replaced by pnictogen ($^{A}Pn = {}^{B}Pn$ = N, P, As, and Sb). The possibility of large X^+ (X = H, F, Cl, Br, and I) atoms inside the cage is revealed, as well as the structural features. The optimized structures are obtained as follows: (Pn, X) = (N, H–Cl) and (P–Sb, H and F) for bicyclo[3.3.3] system and (Pn, X) = (N and P, H–I), (As, H–Br), and (Sb, H–Cl) for bicyclo[4.4.4] system. The stability between the symmetric and nonsymmetric shapes is also clarified, along with their transition states. Their stabilization would be attributed to the interactions between Pn and X. The different natures of $^{A}Pn\cdot\cdot X\cdot\cdot {}^{B}Pn/{}^{A}Pn\cdots X{-}{}^{B}Pn$ interactions are predicted from *p*-CS/*t*-HB_{nc} to SS/Cov-s, along with the secondary interactions for H-∗-H and X-∗-C, of which natures are *p*-CS/vdW, *p*-CS/*t*-HB_{nc}, *r*-CS/*t*-HB_{wc}, and *r*-CS/CT-MC. Therefore, the QTAIM-DFA with CIV can be applied to the 3c–4e interactions to reveal the factor to stabilize the structures, such as bicyclo[3.3.3] and [4.4.4] systems.

Finally, the nature of π···π interactions in [*n*]helicenes (*n* = 1–12) and intermolecular interactions in [*n*]helicene dimers (*n* = 6–8 and 10) is elucidated by applying the QTAIM-DFA with CIV. The π···π interactions in [*n*]helicenes are detected for $n \geq 7$ as expected, although H-∗-H and H-∗-C

interactions are obtained for $n \geq 3$. These interactions would contribute to stabilizing the structures and determining the fine structures of helicenes. The π···π interactions are analyzed by dividing the C atoms into C_{bay} and C_{cape}, corresponding to the C atoms in the bay and cape areas, respectively. The H atoms are denoted by H_{bay} and H_{cape}, as well as the C atoms. Moreover, the π···π interactions for C_{cape}-*-C_{cape} are detected for $n \geq 9$, in addition to C_{bay}-*-C_{bay}. The natures of H-*-H, H-*-C, and C-*-C interactions are predicted to be *p*-CS/vdW ($\theta_p < 90^o$), except for one C_{bay}-*-C_{bay} in [10]helicene, of which the nature is *p*-CS/*t*-HB_{nc} ($\theta_p = 94.2^o$). The different trends of the π···π interactions between C_{bay}-*-C_{bay} and C_{cape}-*-C_{cape} are observed by comparing the dynamic and static behaviors (θ_p and θ, respectively). The θ_p values are larger than the θ values for C_{bay}-*-C_{bay} and smaller than the θ values for C_{cape}-*-C_{cape}. Interactions with $\theta_p > \theta$ are usually observed, whereas interactions with $\theta_p < \theta$ are rare. This result would be related to the steric compression under the different conditions between C_{bay}-*-C_{bay} and C_{cape}-*-C_{cape}. The dynamic behavior of C_{bay}-*-C_{bay} would be affected by the steric compression similar to the usual cases of interactions. However, those of C_{cape}-*-C_{cape} would be inversely affected relative to the usual cases.

Conversely, the intermolecular interactions in [*n*]helicene dimers (n = 6–8 and 10) are detected for H_{cape}-*-H_{cape}, H_{cape}-*-C_{cape}, and C_{cape}-*-C_{cape}, together with two H_{bay}-*-C_{cape} in [6]helicene dimers. Therefore, the stabilization of helicene dimers would be mainly contributed by atoms in the cape area. The nature of the intermolecular interactions is predicted to be *p*-CS/vdW. However, the ΔE values of [*n*]helicene dimers for n = 6, 7, 8, and 10 are −25.2, −31.8, −33.4, and −33.1 kJ mol^{-1}, respectively. These results indicate that the ΔE values are contributed by numerous intermolecular interactions with vdW nature.

The complex π···π interactions in helicenes and the intermolecular interactions in helicene dimers demonstrate the excellent applicability of the QTAIM-DFA with CIV.

This thesis demonstrated that the QTAIM-DFA with CIV possesses remarkable applicability in elucidating the intrinsic dynamic and static behaviors of various inter- and intramolecular interactions, which are neutral HBs, intramolecular OH-*-π interactions, multi-HBs, sterically compressed 3c–4e interactions, and π···π interactions in characteristic systems. The QTAIM-DFA with CIV can also elucidate the nature of σ(3c–4e) in benzene and naphthalene systems, extended-hypervalent bonds such as I_4 σ(4c–6e) in tellurolane system and Se_2Br_5 σ(7c–10e) in selenanthrene system, and Br···Br interactions in Br_2 clusters, along with the interactions previously mentioned. The results will be valuable for revealing the nature of similar inter- and intramolecular interactions. Therefore, the QTAIM-DFA with CIV, in addition to POM and NIV, will provide a comprehensive understanding of the nature of the interactions in question for the development of materials science, including various fields, such as molecular design with functionality and elucidation of biological phenomena.

List of Research Achievements

List of Publications

1. S. Hayashi, T. Nishide, H. Matsuoka, R, Imanaka, W. Nakanishi, Proposal of Pseudo-Intrinsic Dynamic Nature of Interactions: Simple Methods to Generate the Perturbed Structures and to Analyze for the Prediction of the Nature of High Reliability, with the Applications, *Arkivoc* **2022**, *part v*, 93–116 (Chapter 2).

2. T. Nishide, S. Hayashi, W. Nakanishi, Intrinsic Dynamic Nature of Neutral Hydrogen Bonds Elucidated with QTAIM Dual Functional Analysis: Role of the Compliance Force Constants and QTAIM-DFA Parameters in Stability, *ChemistryOpen* **2018**, *7*, 565–575 (Chapter 3).

3. S. Hayashi, T. Nishide, W. Nakanishi, Nature of Intramolecular O–H···π Interactions as Elucidated by QTAIM Dual Functional Analysis with QC Calculations, *RSC Adv.* **2019**, *9*, 15521–15530 (Chapter 4).

4. S. Hayashi, T. Nishide, W. Nakanishi, Behavior of Multi-HBs in Acetic Acid Dimer and Related Species: QTAIM Dual Functional Analysis Employing Perturbed Structures Generated Using Coordinates from Compliance Force Constants, *Bull. Chem. Soc. Jpn*. **2019**, *92*, 87–96 (Chapter 5).

5. W. Nakanishi, S. Hayashi, T. Nishide, Intrinsic Dynamic and Static Nature of Each HB in the Multi-HBs between Nucleobase Pairs and its Behavior, Elucidated with QTAIM Dual Functional Analysis and QC Calculations, *RSC Adv.* **2020**, *10*, 24730–24742 (Chapter 6).

6. T. Nishide, W. Nakanishi, S. Hayashi, Intrinsic Dynamic and Static Natures of $^{A}Pn\cdot\cdot X^{+}\cdot\cdot{}^{B}Pn$ σ(3c–4e) Type Interactions (^{A}Pn = ^{B}Pn = N, P, As, and Sb; X = H, F, Cl, Br, and I) in Bicyclo[3.3.3] and Bicyclo[4.4.4] Systems and the Behaviour, Elucidated with QTAIM Dual Functional Analysis, *RSC Adv.* **2024**, *14*, 5675–5689. (Chapter 7).

7. T. Nishide, S. Hayashi, Intrinsic Dynamic and Static Nature of π···π Interactions in Fused Benzene-Type Helicenes and Dimers, Elucidated with QTAIM Dual Functional Analysis, *Nanomaterials* **2022**, *12*, 321-1–19 (Chapter 8).

List of Other Publications

1. S. Hayashi, T. Nishide, W. Nakanishi, M. Saito, Relativistic Effect on ^{1}J(M, C) in Me_4M, Me_3M^-, Ph_4M, and Ph_3M^- (M = Pb, Sn, Ge, Si, and/or C): Role of s-type Lone Pair Orbitals in the Distinct Effect for the Anionic Species, *ChemPhysChem* **2017**, *18*, 2466–2474.

2. S. Hayashi, T. Nishide, W. Nakanishi, Behavior of I_4 σ(4c–6e) in Tellurolane System and Related Species, Elucidated by QTAIM Dual Functional Analysis with QC Calculations, *Heteroat. Chem.* **2018**, *29*, e21462-1–12.

3. S. Hayashi, T. Nishide, K. Ueda, K. Hayama, W. Nakanishi, Effects from Basis Sets and Levels of Calculations on the Nature of Interactions Predicted by QTAIM Dual Functional Analysis with QTAIM Functions, *ChemistrySelect* **2019**, *4*, 6198–6208.

4. S. Hayashi, M. Uegaito, T. Nishide, E. Tanaka, W. Nakanishi, T. Sasamori, N. Tokitoh, M. Minoura, Nature of the E···E′ Interactions (E, E′ = O, S, Se, and Te) at Naphthalene 1,8-Positions with Fine Details of the Structures: Experimental and Theoretical Investigations, *New J. Chem.* **2019**, *43*, 14224–14237.

5. W. Nakanishi, S. Hayashi, T. Nishide, S. Otsuki, Dynamic and Static Nature of Activated Interactions in Transition States as Elucidated by Quantum Theory of Atoms-in-Molecules Dual Functional Analysis: A Case of Ligand Exchange at the N of Sulfonylimino-λ^3-Bromanes, *Int. J. Quantum Chem.* **2019**, *120*, e26073-1–14.

6. S. Hayashi, T. Nishide, W. Nakanishi, L. Sancineto, C. Santi, The Nature of G···E–Y σ(3c–4e) in *o*-$Me_nGCH_2C_6H_4EY$ (Me_nG = Me_2N and MeE; E = O, S, Se, and Te; Y = F, Cl, Br, EMe, and Me) with Contributions from CT and Compliance Constants in Noncovalent G···E Interactions, *RSC Adv.* **2019**, *9*, 39435–39446.

7. S. Hayashi, T. Nishide, W. Nakanishi, Dynamic and Static Nature of Br_4 σ(4c–6e) and Se_2Br_5 σ(7c–10e) in the Selenanthrene System and Related Species Elucidated by QTAIM Dual Functional Analysis with QC Calculations, *Bioinorg. Chem. Appl.* **2020**, 2901439-1–14.

8. S. Hayashi, T. Nishide, K. Nagata, W. Nakanishi, Linear Multiselenium Interactions in Dicationic Oligomers of 1,5-(diselena)canes: Behavior of Se_{mc} $\sigma(m_c c–n_e e)$ ($6 \leq m_c \leq 16$) Elucidated with QTAIM Dual Functional Analysis, *ChemistryOpen* **2021**, *10*, 1–10.

9. S. Hayashi, T. Nishide, E. Tanaka, W. Nakanishi, Intrinsic Dynamic and Static Nature of Halogen Bonding in Neutral Polybromine Clusters, with the Structural Feature Elucidated by QTAIM Dual-functional Analysis and MO Calculations, *Molecules* **2021**, *26*, 2936-1–18.

10. W. Nakanishi, S. Hayashi, R. Imanaka, T. Nishide, E. Tanaka, H. Matsuoka, Inverse Versus Normal Behavior of Interactions, Elucidated Based on the Dynamic Nature with QTAIM Dual-functional Analysis, *Int. J. Mol. Sci.* **2023**, *24*, 2798-1–27.

List of International Conferences

1. T. Nishide, K. Matsuiwa, N. Nishizawa, S. Hayashi, W. Nakanishi, Nature of the $^{A}E\cdots{}^{B}E$ Interactions in Neutral and Charged Forms of $^{A}E(CH_2CH_2CH_2)_2\ E^{B}$ (^{A}E, ^{B}E = S, Se, Te, and O), Elucidated by Improved QTAIM-DFA, *The 12th International Conference on Heteroatom Chemistry* (ICHAC-12), June 11th–16th, **2017**, the University of British Columbia in Vancouver (Vancouver, Canada), P-20.

2. A. Okumura, T. Nishide, S. Hayashi, W. Nakanishi, Nature of E–E in Neutral and Charged Forms of Cyclo-1,2-EE$(CH_2)_3$ (E = S, Se, Te, and O), Elucidated by Improved Method of QTAIM Approach, *The 12th International Conference on Heteroatom Chemistry* (ICHAC-12), June 11th–16th, **2017**, the University of British Columbia in Vancouver (Vancouver, Canada), P-22.

3. S. Hayashi, M. Uegaito, T. Nishide, E, Tanaka, W. Nakanishi, T. Sasamori, N. Tokitoh, M. Minoura, Nature of E···E' (E, E' = O, S, Se, and Te) at Naphthalene 1,8-Positions: Theoretical and Experimental Investigations, *14th International Conference on the Chemistry of Selenium and Tellurium* (ICCST-14), June 3rd–7th, **2019**, Hotel Resort Flamingo (Sardinia, Italy), PP47.

4. M. Minoura, S. Kobayashi, T. Nishide, S. Hayashi, W. Nakanishi, Synthesis and Structure of Tetraaryltellurium(IV), *14th International Conference on the Chemistry of Selenium and Tellurium* (ICCST-14), June 3rd–7th, **2019**, Hotel Resort Flamingo (Sardinia, Italy), OC28.

5. S. Hayashi, T. Nishide, W. Nakanishi, L. Sancineto, C. Santi, The Nature of G···E–Y σ(3c–4e) in *o*-$Me_nGCH_2C_6H_4EY$ (Me_nG = Me_2N and MeE; E = O, S, Se, and Te) with Contributions from CT and Compliance Constants in Noncovalent G···E Interactions, *The 9th International Meeting on Halogen Chemistry* (Halchem-IX), September 23rd–26th, **2019**, University of PERUGIA (Italy), PP20.

Acknowledgements

The author would like to express the deepest appreciation to Professor Satoko Hayashi and Professor Emeritus Waro Nakanishi at Wakayama University for their valuable and helpful suggestions, discussion, and encouragement during this work.

He greatly appreciates the financial support received through TOBE MAKI Scholarship Foundation for financial support.

Acknowledgements are also extended to the members of Structural Organic Chemistry Laboratory at Wakayama University.

Furthermore, many appreciations are dedicated to his friends and former colleagues, especially, Mr. Ken Hamada and Mr. Ippei Shimozaki in SUMCO corporation.

Finally, the author would like to thank his parents, Reiko Nishide and Yoshihide Nishide, uncle, Tetsuya Yoshinaga, and grandmother, Choko Yoshinaga, for their warm encouragement.

March 2024

Taro Nishide

Graduate School of Systems Engineering
Wakayama University